

SUBAQUEOUS VOLCANISM, FROM ANCIENT SUCCESSIONS TO MODERN VOLCANOES AND MODELLING

EDITED BY: Carles Soriano, Nancy Riggs and Guido Giordano
PUBLISHED IN: Frontiers in Earth Science



frontiers

Frontiers eBook Copyright Statement

The copyright in the text of individual articles in this eBook is the property of their respective authors or their respective institutions or funders. The copyright in graphics and images within each article may be subject to copyright of other parties. In both cases this is subject to a license granted to Frontiers.

The compilation of articles constituting this eBook is the property of Frontiers.

Each article within this eBook, and the eBook itself, are published under the most recent version of the Creative Commons CC-BY licence.

The version current at the date of publication of this eBook is CC-BY 4.0. If the CC-BY licence is updated, the licence granted by Frontiers is automatically updated to the new version.

When exercising any right under the CC-BY licence, Frontiers must be attributed as the original publisher of the article or eBook, as applicable.

Authors have the responsibility of ensuring that any graphics or other materials which are the property of others may be included in the CC-BY licence, but this should be checked before relying on the CC-BY licence to reproduce those materials. Any copyright notices relating to those materials must be complied with.

Copyright and source acknowledgement notices may not be removed and must be displayed in any copy, derivative work or partial copy which includes the elements in question.

All copyright, and all rights therein, are protected by national and international copyright laws. The above represents a summary only. For further information please read Frontiers' Conditions for Website Use and Copyright Statement, and the applicable CC-BY licence.

ISSN 1664-8714

ISBN 978-2-88963-699-0

DOI 10.3389/978-2-88963-699-0

About Frontiers

Frontiers is more than just an open-access publisher of scholarly articles: it is a pioneering approach to the world of academia, radically improving the way scholarly research is managed. The grand vision of Frontiers is a world where all people have an equal opportunity to seek, share and generate knowledge. Frontiers provides immediate and permanent online open access to all its publications, but this alone is not enough to realize our grand goals.

Frontiers Journal Series

The Frontiers Journal Series is a multi-tier and interdisciplinary set of open-access, online journals, promising a paradigm shift from the current review, selection and dissemination processes in academic publishing. All Frontiers journals are driven by researchers for researchers; therefore, they constitute a service to the scholarly community. At the same time, the Frontiers Journal Series operates on a revolutionary invention, the tiered publishing system, initially addressing specific communities of scholars, and gradually climbing up to broader public understanding, thus serving the interests of the lay society, too.

Dedication to Quality

Each Frontiers article is a landmark of the highest quality, thanks to genuinely collaborative interactions between authors and review editors, who include some of the world's best academicians. Research must be certified by peers before entering a stream of knowledge that may eventually reach the public - and shape society; therefore, Frontiers only applies the most rigorous and unbiased reviews.

Frontiers revolutionizes research publishing by freely delivering the most outstanding research, evaluated with no bias from both the academic and social point of view. By applying the most advanced information technologies, Frontiers is catapulting scholarly publishing into a new generation.

What are Frontiers Research Topics?

Frontiers Research Topics are very popular trademarks of the Frontiers Journals Series: they are collections of at least ten articles, all centered on a particular subject. With their unique mix of varied contributions from Original Research to Review Articles, Frontiers Research Topics unify the most influential researchers, the latest key findings and historical advances in a hot research area! Find out more on how to host your own Frontiers Research Topic or contribute to one as an author by contacting the Frontiers Editorial Office: researchtopics@frontiersin.org

SUBAQUEOUS VOLCANISM, FROM ANCIENT SUCCESSIONS TO MODERN VOLCANOES AND MODELLING

Topic Editors:

Carles Soriano, Instituto de Ciencias de la Tierra Jaume Almera (ICTJA), Spain

Nancy Riggs, Northern Arizona University, United States

Guido Giordano, Roma Tre University, Italy

Citation: Soriano, C., Riggs, N., Giordano, G., eds. (2020). Subaqueous Volcanism, From Ancient Successions to Modern Volcanoes and Modelling.

Lausanne: Frontiers Media SA. doi: 10.3389/978-2-88963-699-0

Table of Contents

- 04 Editorial: Subaqueous Volcanism, From Ancient Successions to Modern Volcanoes and Modelling**
Carles Soriano, Nancy Riggs and Guido Giordano
- 06 The Eruption of Submarine Rhyolite Lavas and Domes in the Deep Ocean – Havre 2012, Kermadec Arc**
Fumihiko Ikegami, Jocelyn McPhie, Rebecca Carey, Rhiannan Mundana, Adam Soule and Martin Jutzeler
- 26 A Recent Volcanic Eruption Discovered on the Central Mariana Back-Arc Spreading Center**
William W. Chadwick Jr., Susan G. Merle, Edward T. Baker, Sharon L. Walker, Joseph A. Resing, David A. Butterfield, Melissa O. Anderson, Tamara Baumberger and Andra M. Bobbitt
- 42 Why Deep-Water Eruptions are so Different From Subaerial Eruptions**
Raymond A. F. Cas and Jack M. Simmons
- 63 Characteristics and Deposit Stratigraphy of Submarine-Erupted Silicic Ash, Havre Volcano, Kermadec Arc, New Zealand**
Arran P. Murch, James D. L. White and Rebecca J. Carey
- 84 Structure of Lō'ihi Seamount, Hawai'i and Lava Flow Morphology From High-Resolution Mapping**
David A. Clague, Jennifer B. Paduan, David W. Caress, Craig L. Moyer, Brian T. Glazer and Dana R. Yoerger
- 101 Internal Structures and Growth Style of a Quaternary Subaerial Rhyodacite Cryptodome at Ogariyama, Usu Volcano, Hokkaido, Japan**
Yoshihiko Goto and Akihiko Tomiya
- 115 Geochemistry of CO₂-Rich Gases Venting From Submarine Volcanism: The Case of Kolumbo (Hellenic Volcanic Arc, Greece)**
Andrea Luca Rizzo, Antonio Caracausi, Valérie Chavagnac, Paraskevi Nomikou, Paraskevi N. Polymenakou, Manolis Mandalakis, Georgios Kotoulas, Antonios Magoulas, Alain Castillo, Danai Lampridou, Nicolas Maruszczak and Jeroen E. Sonke
- 135 The Graham Volcanic Field Offshore Southwestern Sicily (Italy) Revealed by High-Resolution Seafloor Mapping and ROV Images**
Danilo Cavallaro and Mauro Coltelli



Editorial: Subaqueous Volcanism, From Ancient Successions to Modern Volcanoes and Modelling

Carles Soriano^{1*}, Nancy Riggs^{2*} and Guido Giordano^{3*}

¹ Instituto de Ciencias de la Tierra Jaume Almera, CSIC, Barcelona, Spain, ² Merriam-Powell Center for Environmental Research, Northern Arizona University, Flagstaff, AZ, United States, ³ Department of Science, Roma Tre University, Rome, Italy

Keywords: processes, products, underwater eruptions, underwater vehicles, bathymetry

Editorial on the Research Topic

Subaqueous Volcanism, From Ancient Successions to Modern Volcanoes and Modelling

Understanding the processes and products of subaqueous volcanism has been traditionally based on the study of ancient successions and deposits; only a few studies are based on deposits from recent subaqueous eruptions and fewer yet on the direct observation of underwater eruptions. This situation has rapidly changed during last decades of the twentieth century and first decades of the twenty-first century, during which scientific and technological development has allowed an increasing exploration of the sea floor. Understanding of subaqueous volcanism has benefited from such exploration and from an increasing number of studies on modern volcanoes under the sea. As a result, the processes and products of subaqueous eruptions are now much better understood than ever before. Nevertheless, the study of ancient volcanic successions around the world still is a major source of models for subaqueous eruptions and, together with experimental and numerical modeling, is a major contribution to our understanding.

The present Research Topic showcases current trends in research on subaqueous volcanism, with a dominance of oceanographic surveys aimed toward the study of modern volcanoes and their deposits by using a number of techniques such as different types of underwater vehicles (AUVs, ROVs) and of high-resolution sonar bathymetries.

Cas and Simmons is a review with a summary of the physical properties of water and on how these may affect magma properties and eruptive processes like magma decompression, volatile exsolution and, ultimately, volcanic explosiveness. This contribution discusses a major issue in subaqueous volcanism that has driven a long-standing controversy: the hydrostatic pressure exerted by water column and its capability to inhibit explosive eruptions. It also addresses a process that has been increasingly investigated in both subaerial and subaqueous volcanic studies, as is the non-explosive production of ash by pumice-to-pumice abrasion.

The Havre volcano in the Kermadec arc erupted in 2012 and is likely one of the best-documented recent deep-water eruptions on Earth. Two contributions in the Research Topic are devoted to the study of this eruption of silicic magma. Ikegami et al. focuses on the chronostratigraphic relations of lavas and domes to reconstruct the chronologic history of the Havre eruption based on vent distribution and on lava and dome stratigraphy. They also provide a critical comparison of the Havre lavas and domes with subaerial counterparts, finding close similarities between them.

Murch et al. analyzed the Ash with Lapilli unit from Havre volcano by means of ROV sampling and detailed imagery. They use their results to highlight the important role that small-volume ash beds play in understanding subaqueous volcanic activity as a whole.

OPEN ACCESS

Edited and reviewed by:

Valerio Acocella,
Roma Tre University, Italy

*Correspondence:

Carles Soriano
csoriano@ictja.csic.es
Nancy Riggs
nancy.riggs@nau.edu
Guido Giordano
guido.giordano@uniroma3.it

Specialty section:

This article was submitted to
Volcanology,
a section of the journal
Frontiers in Earth Science

Received: 15 January 2020

Accepted: 04 February 2020

Published: 21 February 2020

Citation:

Soriano C, Riggs N and Giordano G
(2020) Editorial: Subaqueous
Volcanism, From Ancient Successions
to Modern Volcanoes and Modelling.
Front. Earth Sci. 8:42.
doi: 10.3389/feart.2020.00042

Clague et al. report on the construction and destruction processes in a volcanic seamount to the southeast of Hawaii Island. Construction events were followed by vertical collapses due to lateral migration of basaltic magma to feed flank rift eruptions, yielding morphology of nested calderas, pit craters, and resurgent caldera blocks. Down-talus emplacement of basaltic pillows during eruption and syn-eruptive landslides on volcano flanks modified volcanic edifices.

Chadwick et al. present documentation of the first known historical eruption in the Mariana spreading center in December 2015, with a depth of >4,000 m below sea level. Multiple surveys, both from ships and using submersible ROVs, let the authors pinpoint the timing of eruption within a 3-year period. Although the Mariana system has a slow spreading rate, the study concludes that an active magmatic system is clearly present.

Cavallaro and Coltelli investigates the morphology of the Graham Volcanic Field (Sicily Channel, Italy) based on High-Resolution Seafloor Mapping and ROV Images. Their results show the tectonic control on the N-S and NW-SE alignment of monogenetic cones, which include the remnant of the 1,831 submarine-to-emergent eruption that formed the now totally dismantled Ferdinandea Island.

Rizzo et al. analyzed the geochemistry of CO₂-rich gases associated with the Kolumbo submarine volcano, which lies next to Santorini (Hellenic Volcanic Arc, Greece). Their results show that magmatic gases equilibrate within the Kolumbo hydrothermal system at about 270°C and at a depth of ~1 km b.s.l.

Goto and Tomiya's contribution discusses a Quaternary subaerial cryptodome, highlighting commonalities and differences with respect to domes that grow in underwater settings.

These contributions have improved our empirical and theoretical understanding of the processes and products of subaqueous volcanism. As scientific and technological development proceeds, more studies of modern sea-floor volcanoes will provide empirical data on which refinement of theoretical models will be based. This assures that our understanding of subaqueous volcanism will continue to improve.

AUTHOR CONTRIBUTIONS

All authors listed have made a substantial, direct and intellectual contribution to the work, and approved it for publication.

Conflict of Interest: The authors declare that the research was conducted in the absence of any commercial or financial relationships that could be construed as a potential conflict of interest.

Copyright © 2020 Soriano, Riggs and Giordano. This is an open-access article distributed under the terms of the Creative Commons Attribution License (CC BY). The use, distribution or reproduction in other forums is permitted, provided the original author(s) and the copyright owner(s) are credited and that the original publication in this journal is cited, in accordance with accepted academic practice. No use, distribution or reproduction is permitted which does not comply with these terms.



The Eruption of Submarine Rhyolite Lavas and Domes in the Deep Ocean – Havre 2012, Kermadec Arc

Fumihiko Ikegami¹, Jocelyn McPhie^{1*}, Rebecca Carey¹, Rhiannan Mundana¹, Adam Soule² and Martin Jutzeler¹

¹ School of Natural Sciences, University of Tasmania, Hobart, TAS, Australia, ² Woods Hole Oceanographic Institution, Woods Hole, MA, United States

OPEN ACCESS

Edited by:

Carles Soriano,
Instituto de Ciencias de la Tierra
Jaume Almera (ICTJA), Spain

Reviewed by:

Jonathan Fink,
Portland State University,
United States
Ilya Bindeman,
University of Oregon, United States

*Correspondence:

Jocelyn McPhie
j.mcphie@utas.edu.au

Specialty section:

This article was submitted to
Volcanology,
a section of the journal
Frontiers in Earth Science

Received: 29 June 2018

Accepted: 14 September 2018

Published: 17 October 2018

Citation:

Ikegami F, McPhie J, Carey R,
Mundana R, Soule A and Jutzeler M
(2018) The Eruption of Submarine
Rhyolite Lavas and Domes
in the Deep Ocean – Havre 2012,
Kermadec Arc.
Front. Earth Sci. 6:147.
doi: 10.3389/feart.2018.00147

Silicic effusive eruptions in deep submarine environments have not yet been directly observed and very few modern submarine silicic lavas and domes have been described. The eruption of Havre caldera volcano in the Kermadec arc in 2012 provided an outstanding database for research on deep submarine silicic effusive eruptions because it produced 15 rhyolite (70–72 wt.% SiO₂) lavas and domes with a total volume of ~0.21 km³ from 14 separate seafloor vents. Moreover, in 2015, the seafloor products were observed, mapped and sampled in exceptional detail (1-m resolution) using AUV *Sentry* and ROV *Jason2* deployed from R/V Roger Revelle. Vent positions are strongly aligned, defining NW-SE and E-W trends along the southwestern and southern Havre caldera margin, respectively. The alignment of the vents suggests magma ascent along dykes which probably occupy faults related to the caldera margin. Four vents part way up the steeply sloping southwestern caldera wall at 1,200–1,300 m below sea level (bsl) and one on the caldera rim (1,060 m bsl) produced elongate lavas. On the steep caldera wall, the lavas consist of narrow tongues that have triangular cross-section shapes. Two of the narrow-tongue segments are connected to wide lobes on the flat caldera floor at ~1,500 m bsl. The lavas are characterized by arcuate surface ridges oriented perpendicular to the propagation direction. Eight domes were erupted onto relatively flat sea floor from vents at ~1,000 m bsl along the southern and southwestern caldera rim. They are characterized by steep margins and gently convex-up upper surfaces. With one exception, the domes have narrow spines and deep clefts above the inferred vent positions. One dome has a relatively smooth upper surface. The lavas and domes all consist of combinations of coherent rhyolite and monomictic rhyolite breccia. Despite eruption from deep-water vents (most >900 m bsl), the Havre 2012 rhyolite lavas and domes are very similar to subaerial rhyolite lavas and domes in terms of dimensions, volumes, aspect ratio, textures and morphology. They show that lava morphology was strongly controlled by the pre-existing seafloor topography: domes and wide lobes formed where the rhyolite was emplaced onto flat sea floor, whereas narrow tongues formed where the rhyolite was emplaced on the steep slopes of the caldera wall.

Keywords: lava, dome, submarine effusive eruption, rhyolite, Havre

INTRODUCTION

Silicic effusive eruptions in deep submarine environments have not yet been directly observed, partly because the deep sea floor is a difficult environment to explore and partly because such eruptions are apparently rare. The majority of our knowledge comes from the study of silicic lavas and domes in ancient submarine successions now exposed on land (e.g., Cas, 1978; Yamagishi and Dimroth, 1985; Kano et al., 1991). However, such studies have yielded only limited information on the lava morphology and dimensions; also, the duration of lava emplacement, the details of the original setting and the water depth at the vent are typically poorly constrained.

Recently, autonomous underwater vehicles (AUVs) and remotely operated vehicles (ROVs) have allowed high-resolution observation and strategic sampling of silicic lavas on the modern sea floor, adding significantly to data on their characteristics. For example, Allen et al. (2010) utilized ROV to document the morphological and textural differences among rhyolite lava domes at Sumisu-I knoll, Izu-Bonin arc. At Myojin-knoll caldera, 70 km farther north, Honsho et al. (2016) produced a high-resolution AUV map of an intracaldera rhyolite dome. A series of studies in the Manus Basin, Papua New Guinea, including high-resolution bathymetry, seafloor observation, and sampling by underwater vehicles as well as drilling (Ocean Drilling Program Leg 193), provided a detailed description of a deep submarine dacite dome and lava complex on the modern sea floor (Bartetzko et al., 2003; Paulick et al., 2004; Binns et al., 2007; Thal et al., 2014). Embley and Rubin (2018) described dacitic lavas and domes in the northeastern Lau Basin that had been explored using multibeam sonar, camera tow and dredging.

This paper extends our understanding of deep submarine silicic lavas by adding examples produced during the 2012 eruption at Havre caldera, the first of such eruptions to be witnessed (Carey et al., 2018). The eruption produced 15 separate rhyolite lavas and domes from 14 vents between ~880 m and 1,280 m bsl. In some cases, rhyolite was erupted onto flat sea floor and in others, it traversed steep slopes. The lavas and domes have been mapped using exceptionally high-resolution bathymetry, observed by video and still photography, and sampled. We present detailed information on dimensions, volumes, aspect ratios, textures, surface features, and morphology, and explore the influence of vent depth and substrate slope on lava morphology. We also compare these submarine rhyolite lavas and domes with subaerial counterparts, and demonstrate that despite eruption in more than 900 m of seawater, the Havre rhyolite lavas and domes are very similar to subaerial rhyolite lavas and domes.

HAVRE 2012 ERUPTION AND MESH CRUISE IN 2015

The eruption of Havre caldera volcano (31°6.5' S, 179°2.45' W) in the Kermadec arc in 2012 (**Figure 1A**) was first detected by the appearance of extensive floating pumice rafts on 18th July, 2012 (Global Volcanism Program, 2012; Carey et al., 2014; Jutzeler et al., 2014; Carey et al., 2018). Carey et al. (2018) estimated the

bulk volume of pumice in the rafts to be ~1.2 km³. On the 15th October, 90 days after the production of the pumice rafts, R/V Tangaroa of NIWA (National Institute of Water and Atmospheric Research) visited the area and acquired bathymetry at Havre. In 2015, the MESH (Mapping, Exploration, & Sampling at Havre) voyage was conducted in order to perform more detailed investigation of the 2012 eruption products on the sea floor. As well as rhyolite lavas and domes, the 2012 eruption generated a layer of giant pumice (GP) clasts (GP deposit; ~0.1 km³ bulk) and small-volume pyroclastic deposits (ash-lapilli-block deposit and ash-lapilli deposit; <0.07 km³ bulk) on the sea floor (Carey et al., 2018). Data were collected using two unmanned vehicles, *Jason2* ROV and *Sentry* AUV from the US National Deep Submersible Facility. The AUV *Sentry* created a high-resolution bathymetry map covering the Havre caldera and adjacent areas. The ROV *Jason2* operated in tandem, traversing the sea floor and sampling.

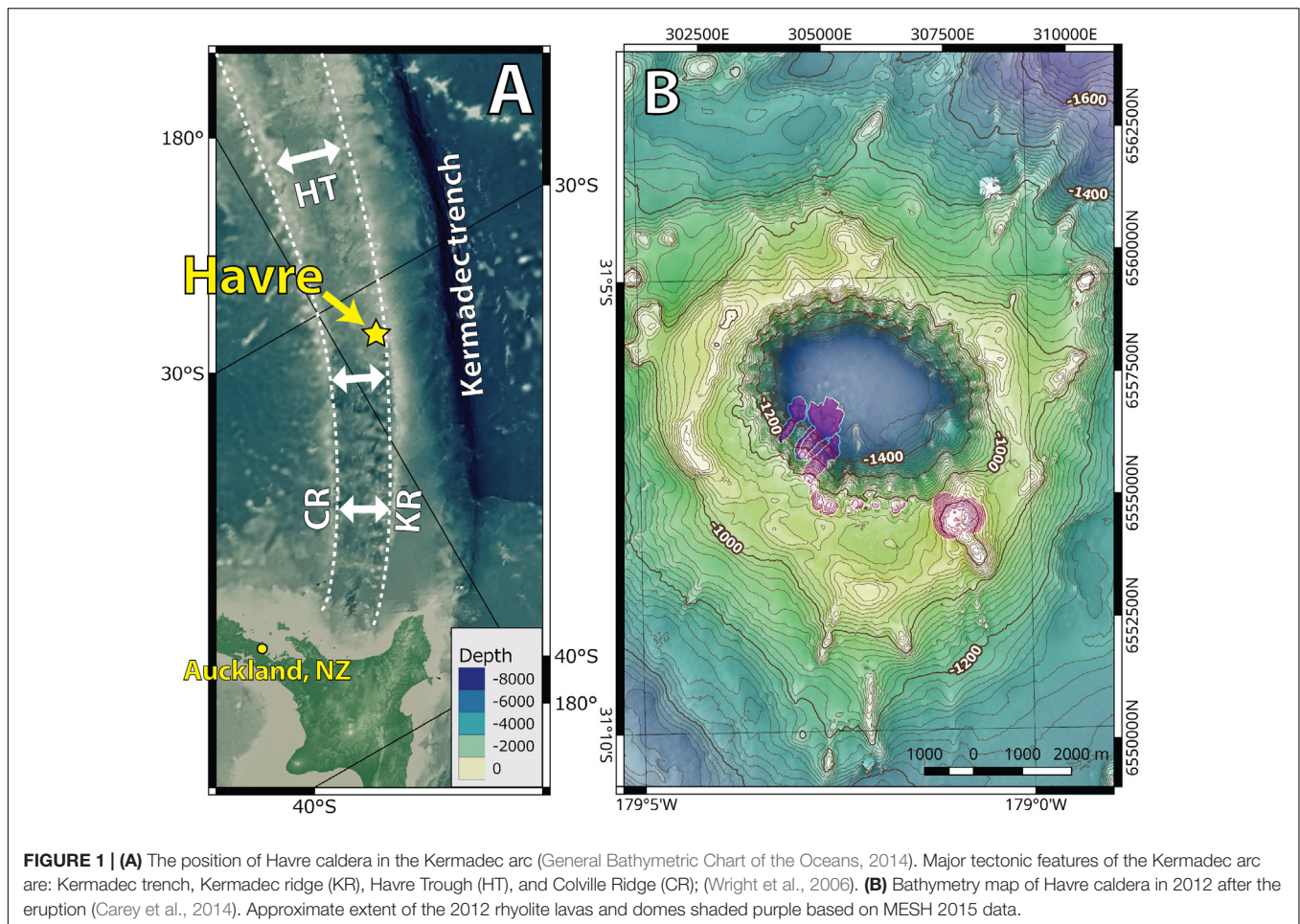
Bathymetry Acquisition and Comparisons

The MESH cruise acquired two bathymetry datasets with different platforms. The EM122 multi-beam echo sounder (12 kHz) on R/V Roger Revelle provided data resolution to create a 25-m gridded Digital Elevation Model (DEM) of the Havre caldera and surrounding areas. High-resolution bathymetry data (1-m gridded DEM) were collected with a Reson SeaBat 7125 multi-beam echo sounder (400 kHz) on the AUV *Sentry*. The *Sentry* bathymetry data cover 56.5 km² (total 465 km track; **Supplementary Figure S1**).

Two other bathymetric DEMs acquired in the past are also used for comparison. The earlier data were acquired in 2002 (Wright et al., 2006) by the R/V Tangaroa which was equipped with a Simrad EM300 multi-beam echo sounder (30 kHz). The later data were acquired by the same R/V Tangaroa in 2012, 90 days after the pumice rafts appeared in the satellite imagery (Carey et al., 2014), using a Kongsberg EM302 multi-beam echo sounder (30 kHz) which allows the creation of an approximately 24-m gridded DEM. The topographic differences between the DEMs were calculated by Raster Calculator of QGIS 2.14 after datum and projection of the grids were adjusted to Zone 1S of Universal Transverse Mercator projection. The DEMs are referenced to best fit the AUV bathymetry data.

Visual Observations and Sampling by ROV

The ROV *Jason2* conducted 12 dives (J2-802–J2-813) and traversed 50 km of sea floor over 238.5 h. The traverses were recorded by three video cameras and two still cameras. The dives covered the floor, walls, and rims of the Havre caldera (**Supplementary Figure S2**). Dives 802–808, 811, and 813 were dedicated to the investigation of the 2012 rhyolite lavas and domes, whereas the other dives observed the eastern, northern, and western part of the caldera. Eighty-nine lava and dome samples were collected during the ROV *Jason2* traverses (**Supplementary Figures S3–S5**). A subset of 41 lava and dome samples was examined by both an optical



microscope and scanning electron microscope (SEM). Whole-rock X-ray Fluorescence analyses of samples from each of the lavas and domes have been published in Carey et al. (2018).

SETTING OF HAVRE 2012 LAVAS AND DOMES IN HAVRE CALDERA

Havre is a 5-km-wide caldera (Wright et al., 2006); the caldera rim is situated at ~1,000 m bsl and the floor is at ~1,500 m bsl (Figure 1B). Very little is known about the formation of Havre caldera. Wright et al. (2006) recovered samples of basalt, andesite, and dacite lavas and intrusions thought to form the pre-caldera sequence.

Comparison of the 2002 and 2012/2015 bathymetry shows that the 2012 eruption changed the southern and southwestern caldera margin dramatically, with the appearance of 15 new lavas and domes (Figure 2 and Supplementary Figure S6). Syn-eruptive mass-wasting events also modified the western and southwestern caldera margin and the caldera floor. No significant changes have been recognized elsewhere on the edifice. The lavas and domes have been labeled A to P from west to east. Note that J is also a silicic dome but it was already present in 2002. The

2012 lavas and domes are rhyolitic, ranging between 70.7 and 72.5 wt.% SiO₂ (Carey et al., 2018). Vents for the lavas and domes are located around the southwestern and southern margin of the caldera (Figure 2). The vents extend along 4.2 km of the caldera perimeter, the total length of which is 15 km. Five of the vents (A to E) are part way up the steep southwestern caldera wall and the rest (F to I, K to P) are on the southwestern and southern rim of the caldera.

PETROGRAPHY OF THE 2012 RHYOLITE LAVAS AND DOMES

The typical texture is porphyritic (<5 modal% phenocrysts, 100–500 μm) (Figure 3) and microlite-rich (>60 modal%) in glassy groundmass (Figure 4). The phenocryst population comprises plagioclase, pyroxene, and Fe-Ti oxides, and a minor amount of quartz and apatite. The microlites are mainly plagioclase (>70 modal%); pyroxene (~20 modal%) and Fe-Ti oxides (~10 modal%) make up the rest. The vesicularity varies from <5 modal% to >50 modal%. The most vesicular samples (>50 modal%; e.g., L and the carapace of G) have a pumiceous texture and are exceptionally poor (<5 modal%) in microlites although their phenocryst populations are the same as in other samples

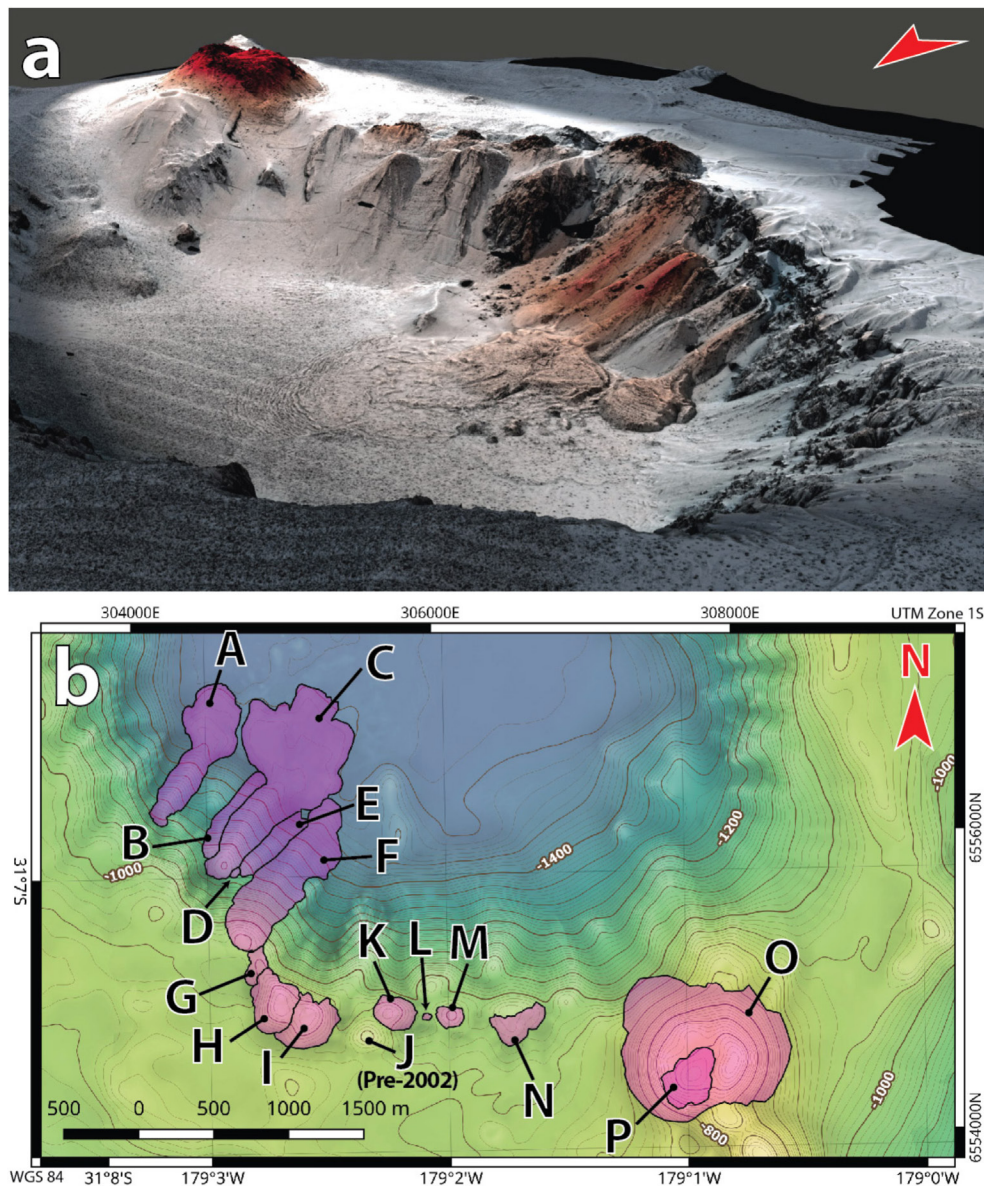


FIGURE 2 | (a) 3D-rendered high-resolution AUV bathymetry map (2015) showing the southern margin of Havre caldera, viewed from the northwest. The red shade indicates areas where there is a positive topographic change between 2002 and 2015. (b) Contour map showing the southern caldera margin and the extent of 2012 lavas and domes determined by morphological and visual observations. Note that J is a pre-2002 dome which was already present in 2002 bathymetry.

collected. Extremely elongate vesicles and bands characterized by different microlite contents are common in the carapace of G (Figures 3c, 4d); L samples are microvesicular.

Cristobalite is common in the microlite-rich samples. Cristobalite is a high-temperature devitrification or vapor-phase crystallization product (Baxter et al., 1999; Horwell et al., 2013). The size (typically $\sim 50 \mu\text{m}$) and amount of cristobalite are highly variable in the Havre rhyolite samples although the abundance is commonly higher in microlite-rich samples. Cristobalite occurs in vesicles or groundmass (Figure 4b), and in extreme cases, cristobalite has completely replaced the groundmass (Figure 4c). The Havre cristobalite is identical to cristobalite found in

subaerial silicic lava domes (e.g., Horwell et al., 2013; Schipper et al., 2015).

MORPHOLOGY AND DIMENSIONS OF THE HAVRE 2012 RHYOLITE LAVAS AND DOMES

The Havre 2012 rhyolites are divided into lavas (A, B, C, E, F) and domes (D, G to I, K to P) (Figure 5) based on overall morphology. All the lavas and domes consist of combinations of coherent rhyolite and monomictic rhyolite breccia. Monomictic

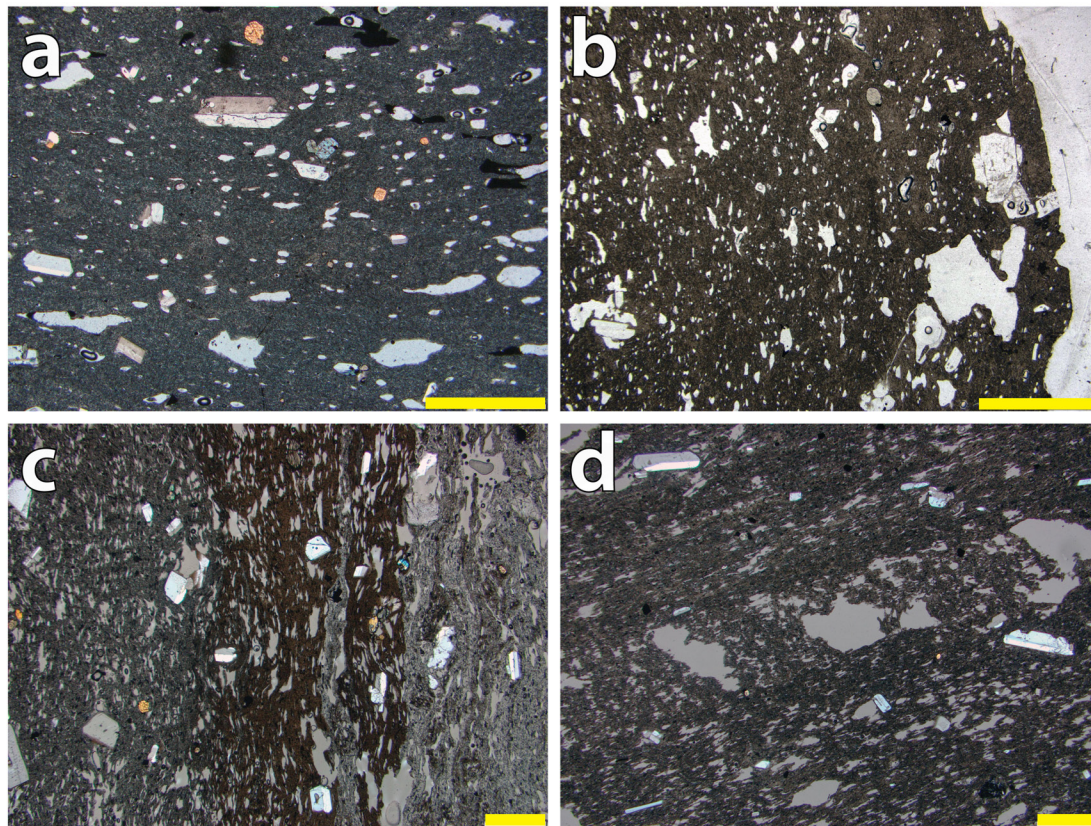


FIGURE 3 | Photomicrographs of Havre 2012 rhyolite lava and dome samples. The yellow bars are 1 mm long. **(a)** XPL image of HVR141 from C, representing typical low-vesicularity texture (<15 modal% vesicles) and glassy groundmass. Plagioclase and pyroxene phenocrysts are <1 mm and sparse (<10 modal%). **(b)** PPL image of HVR144 from C, showing abundant small vesicles. The groundmass contains abundant microlites. **(c)** XPL image of HVR099 from L, showing dark gray, black, and pale gray groundmass bands defined mainly by differences in microlite abundance. **(d)** XPL image of HVR090 from I, showing heterogeneous vesicularity and irregular-shaped vesicles forming a band.

rhyolite breccia comprises coarse, angular fragments of dense to pumiceous, massive or flow-banded rhyolite; the fragments are prismatic or polyhedral and bounded by curvilinear surfaces.

The lavas are narrow, elongate tongues of rhyolite that were erupted from the vents on the southwestern caldera wall and rim, and descended 300–600 m to the caldera floor (**Figure 5a**). Lavas A and C extended farther across the caldera floor (A, ~450 m; C, ~650 m) and also spread laterally. The lavas have relatively high aspect ratios (lateral extent:thickness; Walker, 1973; 5.5–47.7; **Supplementary Table S1**). The domes on the other hand were erupted from vents on the southwestern and southern caldera rim (**Figures 5b,c**), except for D which is on the southwestern caldera wall. The domes are round or oval in plan view although G, H, and I have been truncated along their northeastern edges by a mass-wasting scarp. The domes have relatively low aspect ratios (lateral extent:thickness; 2.0–3.8; **Supplementary Table S1**).

The combination of bathymetric differences (2002 versus 2015; **Supplementary Figure S7**) as well as the precisely mapped extents of the Havre 2012 lavas and domes, have been used to calculate their median thicknesses and volumes (**Supplementary Table S1**). Near-vent thicknesses of the lavas (A, B, C, E, F) range from 50 to 100 m, and they maintain near-uniform thickness with

distance from the source down the steep caldera wall (**Figure 6a** and **Supplementary Figure S8**). Most of the domes (G–I, K–N) have maximum thicknesses between 50 and 110 m (**Figure 6b**). The exception is the largest dome pair, OP, which has a maximum thickness of 210 m. The total volume of all lavas and domes is 0.21 km³. The largest component (>50%; 0.11 km³) of this volume is contained by the dome pair, OP, on the southern caldera margin (**Figure 2**). The aggregate volume erupted from vents on the southwestern caldera wall (A–F) is also significant (0.08 km³). In comparison, the domes on the southwestern and southern caldera rim (G–I, K–N) are very small (aggregate volume 0.02 km³). The smallest “dome” is L which comprises the top of a rhyolite body still largely contained in its vent and too small to measure.

Lavas

All the lavas traversed the ~40° slope of the caldera wall (**Figure 7a**). On this steep slope, the lavas are narrow tongues, more-or-less triangular in cross-section (~200 m across and ~50 m high; **Figure 7b**). The surfaces of the narrow tongues are almost entirely monomictic rhyolite breccia; sparse exposures of coherent rhyolite occur exclusively at the top of the narrow

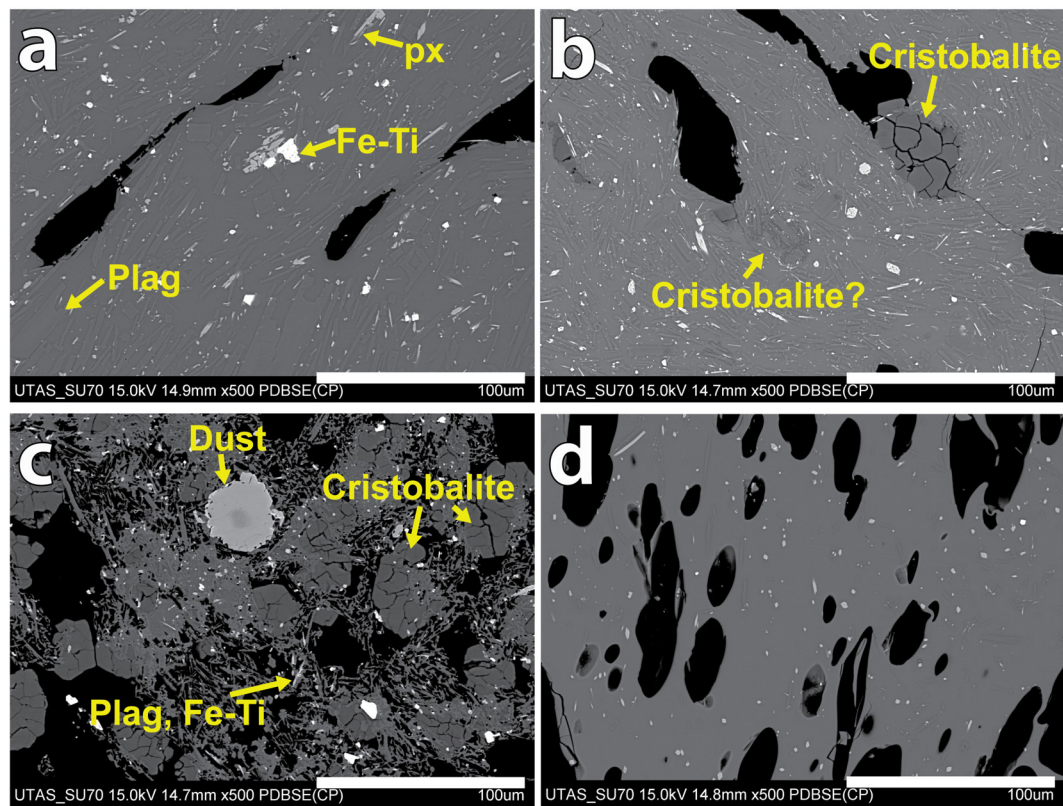


FIGURE 4 | Backscatter Scanning Electron Microscope images of Havre 2012 rhyolite lava and dome samples. **(a)** Microlite-rich (~70 modal% microlites) groundmass of HVR147 from C which is typical of Havre 2012 lavas. The microlites consist of plagioclase (gray, almost indistinguishable from the glass), pyroxene (pale gray), and Fe-Ti oxides (white) which are ubiquitous in all Havre 2012 lavas. **(b)** Microlite-rich groundmass of HVR088 from H. Cristobalite is present in the both groundmass and within vesicles. A patch of cristobalite is also present in the groundmass. **(c)** Glass-free groundmass texture of HVR010 from O. Cristobalite is abundant; plagioclase and Fe-Ti oxide microlites are also present. Note that the large pale gray feature is aluminum foil dust attached during drying of the section. **(d)** Microlite-poor (<5 modal% microlites) groundmass of HVR085 from the vesicular carapace of G.

tongues. Along much of the narrow-tongue segment of A, there is a shallow depression (~15 m across and <10 m deep; **Figure 7b**). Lavas A and C also have wide-lobe segments emplaced on the flat caldera floor (**Figures 2, 7a,c**). The wide-lobe segments have similar rough surfaces to the narrow-tongue segments, composed of monomictic rhyolite breccia; coarsely vesicular coherent rhyolite is locally exposed beneath the breccia.

Arcuate surface ridges are present on the wide-lobe segments of A and C, and on parts of the narrow-tongue segments of A, B, C, and F (**Supplementary Figure S9**), though the best example of this feature is on A (**Figure 8**). The ridges are oriented perpendicular to the long axes of the lavas and curve away from the leading edge of the lavas. On A, the ridges are sub-parallel and have wavelengths of 10–30 m and amplitudes of 1–2 m (**Figures 8d,e**). There is one small domain in which the pattern of ridges is slightly offset (**Figure 8b**). The pattern of ridges on the wide-lobe segment of C is complex and includes several domains where the ridges have different orientations (**Figure 2a** and **Supplementary Figure S9**). Also, the distal margin of C is indistinct where it meets variably deformed caldera-floor sediment. The emplacement of the wide-lobe segment of C and its

impact on the caldera-floor sediment are the subject of a separate study.

Breakout lobes are present on the wide-lobe segment of A (“x” on **Figures 5a, 9a,b**) and the narrow-tongue segment of E (“y” on **Figures 5a, 9c,d**). On the western margin of A close to the start of the wide-lobe segment, there is a stack of three breakout lobes. The largest is at the base and is 150 m long and ~15 m high; two smaller breakout lobes occur immediately above. The largest breakout lobe appears to connect directly with the narrow-tongue segment of A on the steep caldera wall. The breakout lobe on E is 50 m long, 60 m across, and 15 m high. It emerges from the crest of the narrow tongue about two-thirds of the way down the caldera wall.

Domes

All the domes have very rough surfaces composed of jagged and spiny coherent rhyolite (**Figures 10a,b**), surrounded by aprons of coarse breccia. The spines rise almost vertically and have widths of a few m and heights up to 20 m; their surfaces are smooth and planar or gently curved (**Figure 10c**), or very rough and irregular. In some cases, spines form a ridge 10–100 m across and ~40 m high at the center of the dome (**Figures 10a,b**). The ridges are

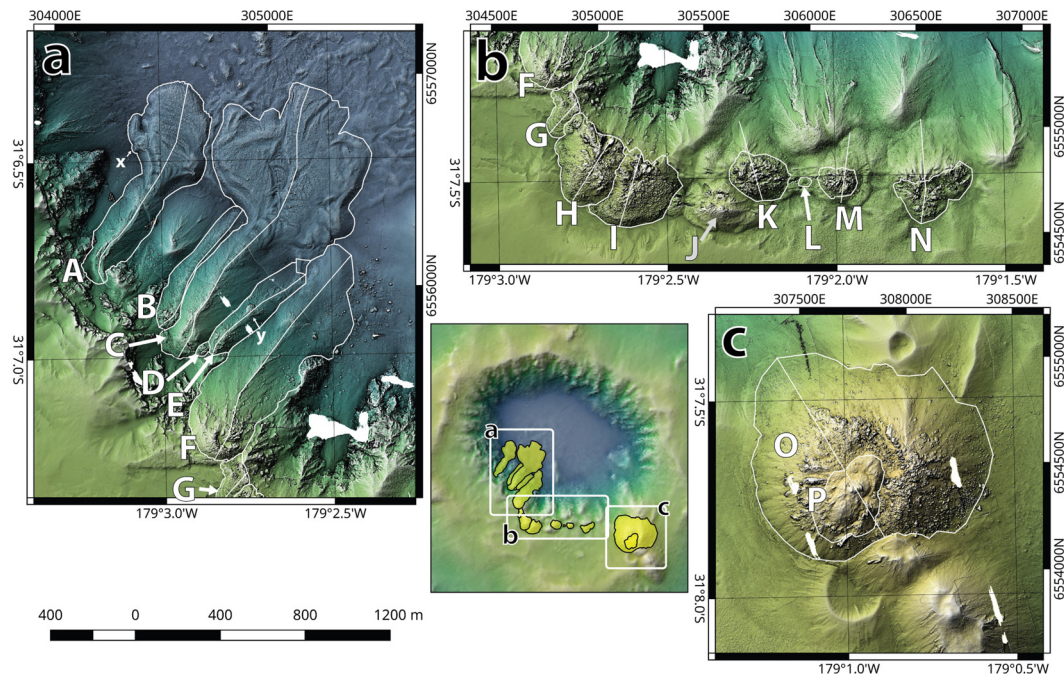


FIGURE 5 | Enlarged relief maps (a–c) based on AUV bathymetry map (2015) of the Havre 2012 lavas and domes. The extent of each map is shown in the small inset map. The capital letters identify the lavas and domes following **Figure 2b**. The bright lines are the profiles given in **Figure 6**. Lower case letters “x” and “y” indicate the areas shown in detail in **Figure 9**.

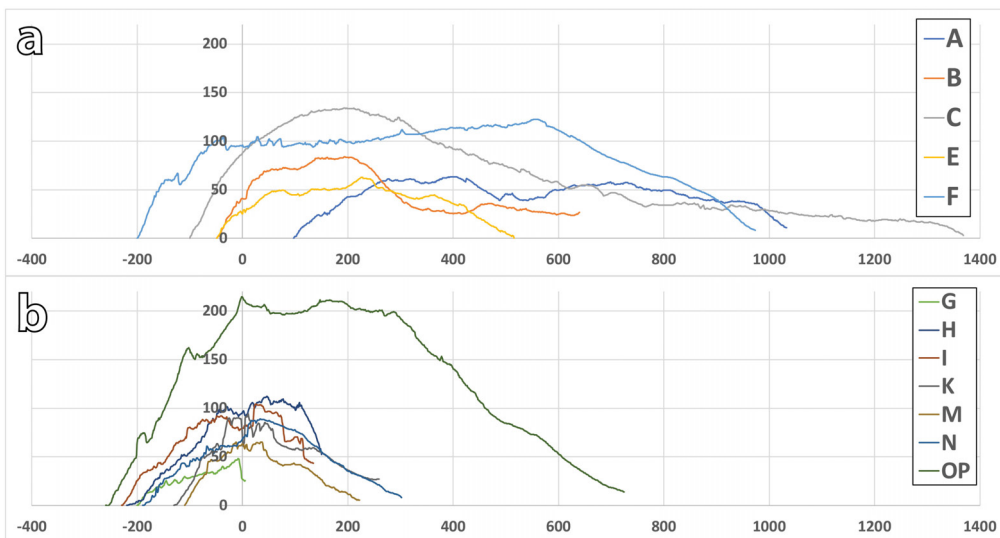


FIGURE 6 | Comparison of cross-sections through Havre 2012 lavas and domes. The sections are oriented parallel to the longest dimension of each unit. The profile locations are shown on **Figure 5**. The caldera rim is at the left and the caldera wall and floor are at the right. The horizontal and vertical scales are in metres. The vertical axis is exaggerated 200% and adjusted to the surrounding topography. The cross-sections are aligned so all the vents are at zero. **(a)** The lavas that descended the caldera wall (A, B, C, E, F). **(b)** The domes on the caldera rim (G–I, K–OP). D and L are excluded from the comparison as they are too small. Domes O and P are shown together as the basal topography of dome P is not known.

aligned either parallel to the caldera rim (K and N) or radially (H, I, and M). On K, the central ridge is cut by a narrow, deep (~30 m) cleft (**Figure 10b**) parallel to fissures that extend between K and M (**Figure 10a**).

The large dome pair OP has a more complicated morphology due to the two extrusions apparently sharing one vent. Dome O is slightly elongate in a NE–SW direction (**Figure 5b**). The top surface slopes gently westward and consists of numerous spines

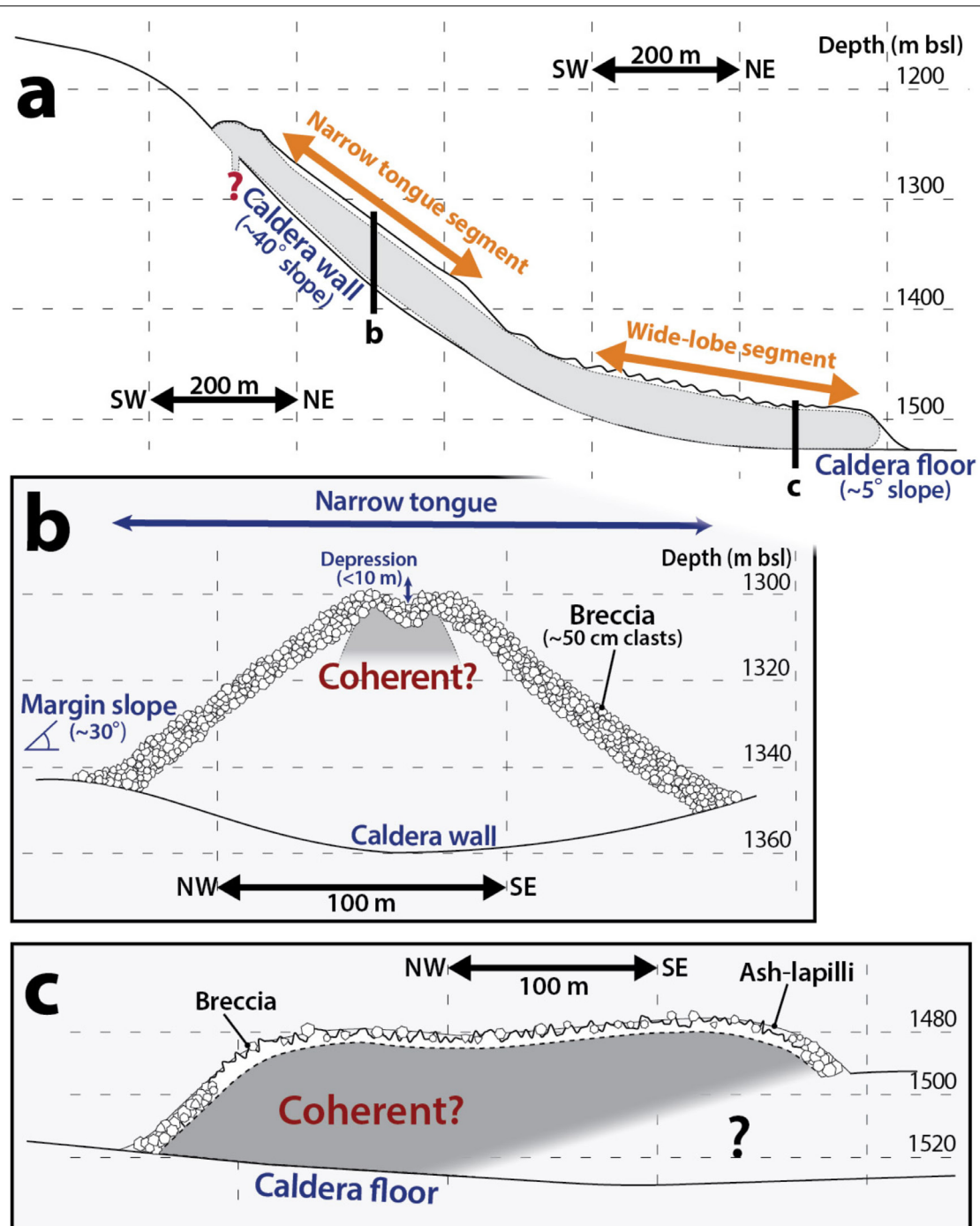


FIGURE 7 | (a) Cross-section of lava A parallel to its length, showing the steep slope of the caldera wall and gentle slope of the caldera floor. (b) Transverse cross-section of the narrow-tongue segment of A [position shown on (a)]. (c) Transverse cross-section of the wide-lobe segment of A [position shown on (a)]. The brecciated surface of the lava is covered by thin pyroclastic deposits (ash-lapilli deposit; <20 cm). Note that each of the figures has a different scale and 150% vertical exaggeration.

and ridges. The ridges define weak horseshoe-shaped alignments opening to the west and the highest point of the dome (635 m bsl) is located on its eastern margin. The top is surrounded by steep aprons of breccia (~40° for 200 m of height). Dome P sits on the top of O and its highest point is 50 m higher than the

top of O. P is elongate, being slightly longer in the northeasterly direction (~450 m) than the northwesterly direction (~300 m). The southwestern margin of P overlaps that of O, making their boundaries hard to distinguish. The surface of P slopes gently and is composed of decimeter-sized rhyolite fragments which

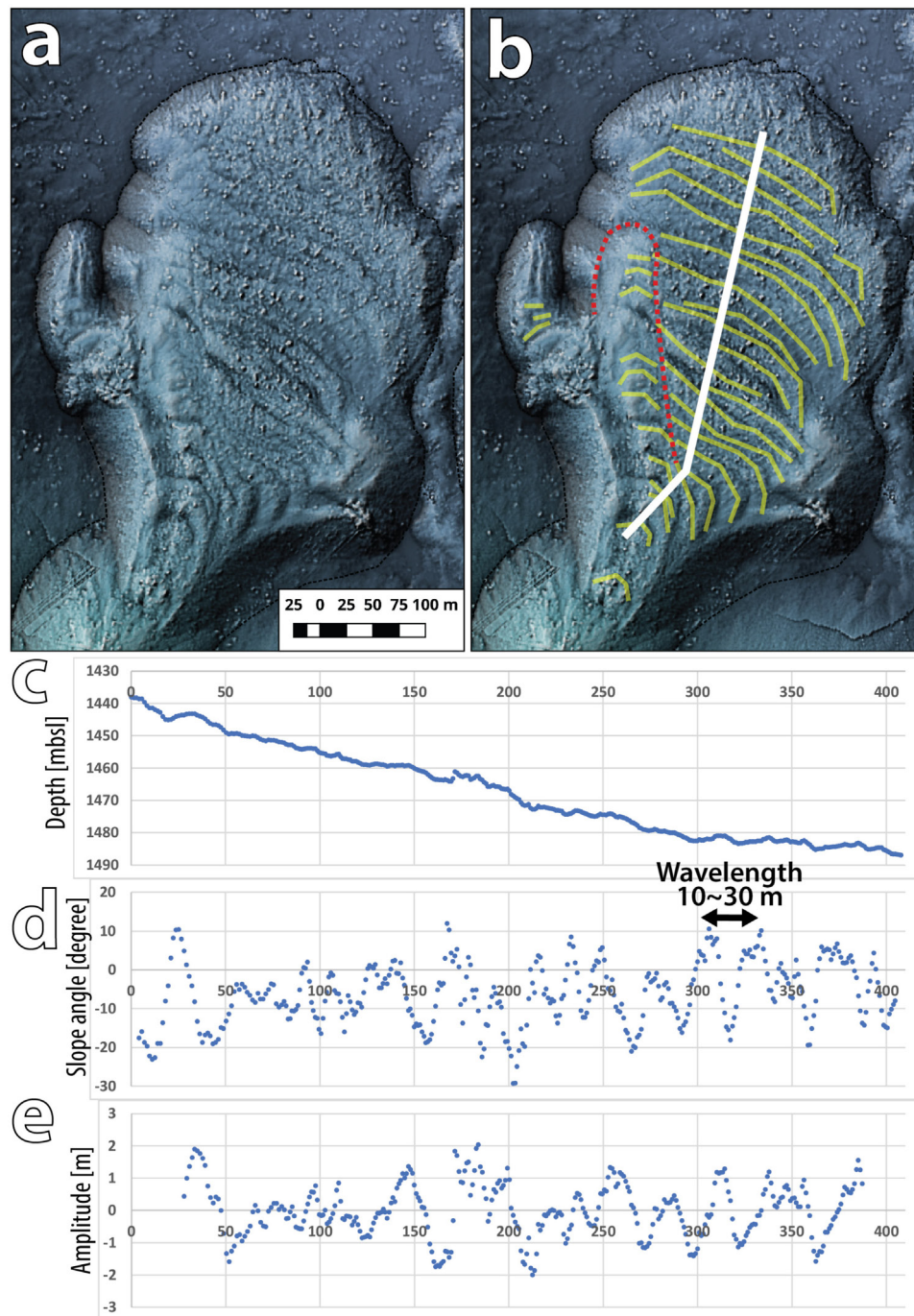


FIGURE 8 | High-resolution AUV bathymetry maps and topographic profiles showing arcuate surface ridges on lava A. **(a)** Plain relief map showing the morphology. **(b)** Traces of arcuate surface ridges (yellow) on A. The red dotted outline traces the boundary of a domain in which the pattern of surface ridges has been slightly offset from the main pattern. The white stroke indicates the position of the data shown in **(c–e)**. **(c)** Depth of the surface of A along the longitudinal profile [white stroke on **(b)**]. **(d)** Slope angle profile with an averaging of approximately 6 m. The cyclic variations suggest the presence of surface ridges separated by 10–30 m intervals. **(e)** Amplitude profile with an averaging of approximately 41 m. The data indicate amplitudes of 1–2 m for the surface ridges.

produce a smooth morphology on the AUV bathymetric map (**Figure 5b**). A half-dome shaped spine (3 m across, 5–10 m high) which is the highest point on P (650 m bsl) sits at the center.

Dome G is the only dome with arcuate surface ridges, similar to the arcuate surface ridges on lava A in terms of wavelength (10–20 m) and amplitude (~2 m). The carapace of G was sampled at the top of a mass-wasting scarp that faces the caldera, and

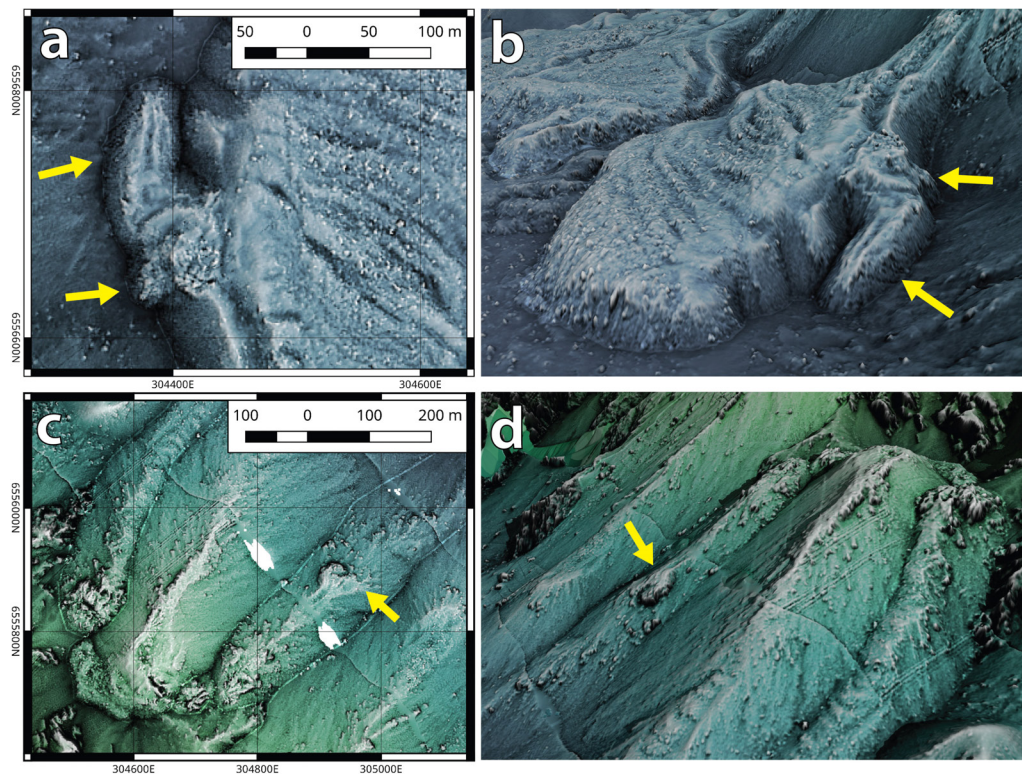


FIGURE 9 | (a) Enlarged relief map and **(b)** 3D rendered image of the breakout lobes on A (indicated by yellow arrows). The area is marked as “x” on **Figure 5a**. The largest breakout lobe is 150 m long and ~15 m thick, and has a depression < 2 m deep on the top. Multiple smaller lobes < 10 m thick are also present beside and above the large breakout lobe. **(c)** Enlarged relief map and **(d)** 3D rendered image of the breakout lobe on the narrow-tongue segment of E (indicated by yellow arrows). The area is marked as “y” in **Figure 5a**. The breakout lobe is 60 m across, 50 m long and surrounded by a cliff ~15 m high. White patches are places where bathymetric data capture was incomplete. All maps and images based on AUV bathymetry data collected in 2015.

about 120 m Southwest of the scarp (**Figure 11**). The carapace is vesicular and glassy (**Figure 4d**). The interior of G was observed and sampled on the mass-wasting scarp. The vesicular coherent rhyolite extends ~2 m into the interior. Dome F also has a vesicular carapace. The inner part of G consists of massive coherent rhyolite that grades deeper down into jointed coherent rhyolite.

Most of the surface of N is rough and jagged, similar to the other domes, but part of its northern edge is smoother and shows subtle tonal differences (**Figure 12**). This northern area was uplifted ~100 m between 2002 and 2012, and both morphologically and visually, the surface resembles the surface of the nearby caldera rim, rather than the rough rhyolite. One explanation is that N is partially intrusive, a portion of the northern side of the dome having stalled and intruded instead of emerging at the sea-floor. Intrusion resulted in subtle local uplift of the caldera rim that can be detected in the detailed bathymetry.

STRATIGRAPHIC RELATIONSHIPS OF HAVRE 2012 LAVAS AND DOMES

The order of emplacement of the 15 rhyolite lavas and domes has been deciphered using a combination of stratigraphic

relationships with other 2012 seafloor products and contact relationships between adjacent lavas or domes. Among the 2012 seafloor products, the deposit of GP clasts is most useful because it was formed by settling from suspension of temporarily buoyant pumice clasts (Carey et al., 2018) and serves as a stratigraphic marker. This deposit is distinguishable in the high-resolution bathymetry map and was sampled in many places. One limitation of using the GP deposit as a marker is that its dispersal area is strongly elongate in a northwesterly direction (Carey et al., 2018) and some domes (G, H, I) on the caldera rim are outside the dispersal area. A second limitation is that the GP clasts can be found only on flat sea floor so relationships could not be identified for B, D, and E, all of which are limited to the steep caldera wall. For F, the top is on the caldera rim but outside the GP dispersal area, and the rest of F is on the steep caldera wall. Nevertheless, among the 15 lavas and domes, only A and C are overlain by numerous clasts of GP whereas K, L, M, N, and OP (all within the dispersal area and on flat sea floor) are not. Considering A in more detail, a small breakout lobe on its northwestern margin is not covered by GP clasts (**Figures 9a,b** and **Supplementary Figure S10**), implying that the breakout occurred after the GP deposit. Therefore, most of A and all of C pre-date the GP deposit whereas the breakout lobe on A, and K, L, M, N, and OP

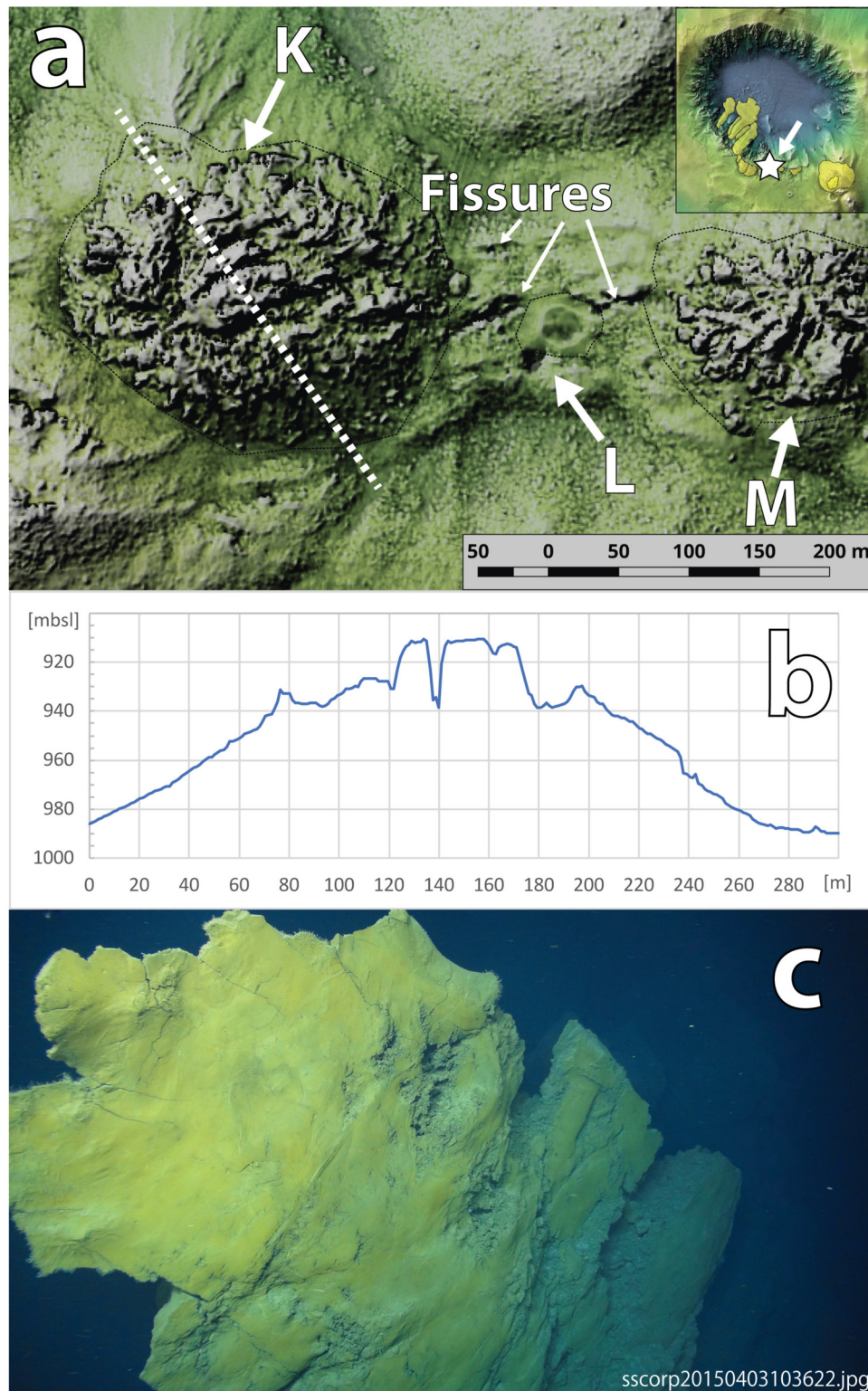


FIGURE 10 | (a) Map of domes K, L and M, and connecting fissures, based on AUV bathymetric map of the area. The white dashed line across K shows the position of the topographic profile given in **(b)** and the small inset map shows the location of these domes on the caldera rim. The fissures extend east-west across the gap between K and M, to the north of L. They are a few m across and 150–180 m long. The fissures lie within a bench that extends from K to M and has been uplifted by ~10 m. **(b)** Northwest (LHS)-southeast (RHS) topographic profile of K, showing the central ridge > 30 m tall and 50 m across with a steep axial cleft more than 20 m deep. **(c)** Full view of a spine on H. The spine is ~5 m across.

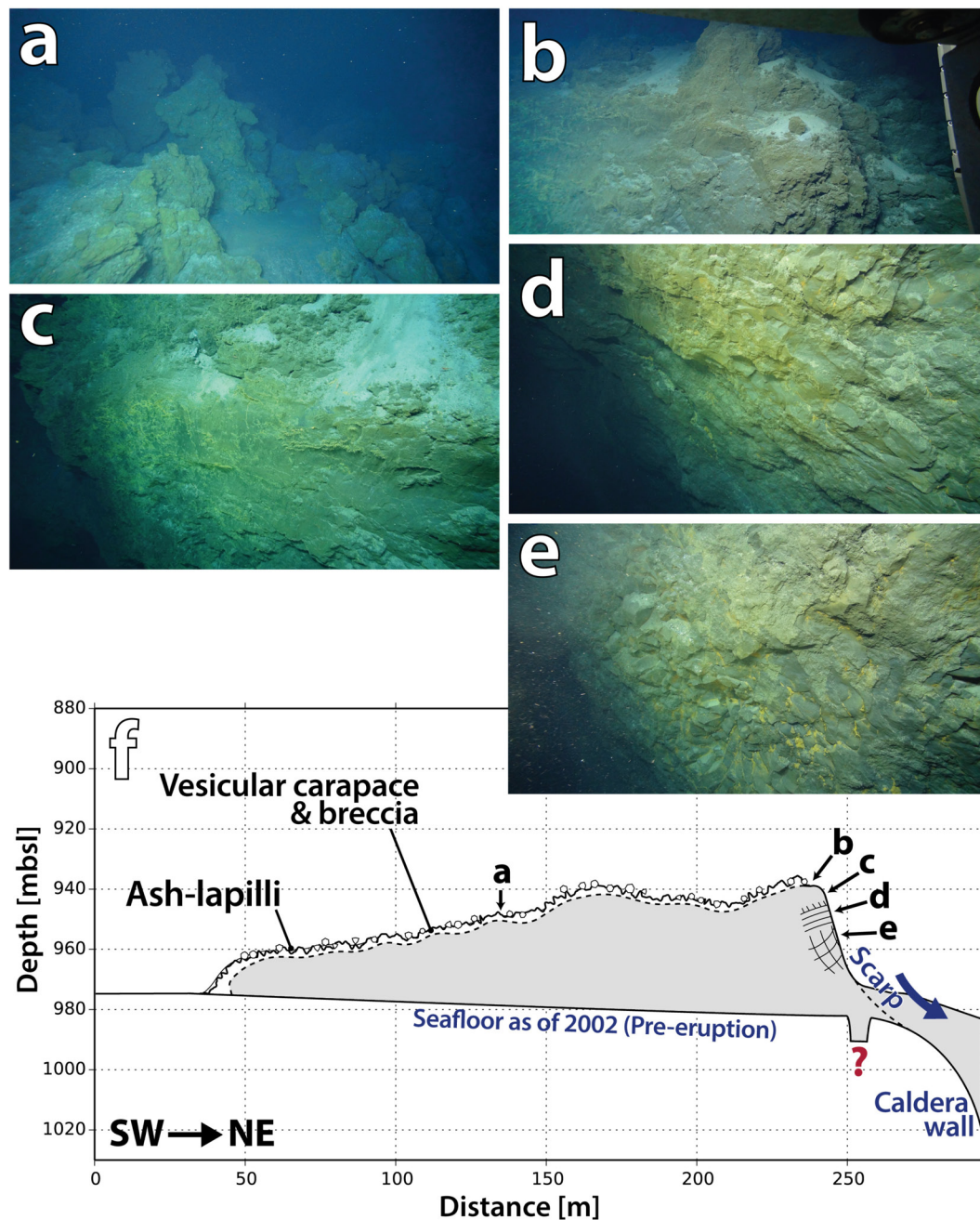


FIGURE 11 | Dome G morphology and facies exposed in a scarp facing the caldera wall. **(a)** Vesicular carapace. The rough surface is created by ~1-m-high spines and breccia, both of which are covered by the thin ash-lapilli deposit. **(b)** At the edge of the scarp, the vesicular carapace is less than a few meters thick. **(c)** Massive coherent core at the top of the scarp. **(d)** Laterally jointed coherent rhyolite in the middle of the scarp. **(e)** Complex radial joints in coherent rhyolite at the base of the scarp. **(f)** Schematic cross-section of G based on the pre- and post-eruption bathymetry in 2002 and 2015, and the facies exposed in the scarp.

post-date the GP deposit (Figure 13). The relationship between the GP deposit and each of B, D, E, F, G, H, and I is not known.

Some contact relationships between adjacent lavas or domes imply their order of emplacement. On the steep southwestern caldera wall, well-sorted decimeter-sized talus breccia of C overlies less-sorted coarser breccia of B to the northwest and E

to the southeast (Figures 14a–c). Although these observations imply only the final relationship when the lavas stopped moving, the simplest interpretation is that B, E, and probably D (a small dome between C and E) either preceded or are contemporaneous with C. This finding therefore suggests that all of the units erupted from vents on the southwestern caldera wall (A–E) except the small breakout on A were emplaced before the GP deposit.

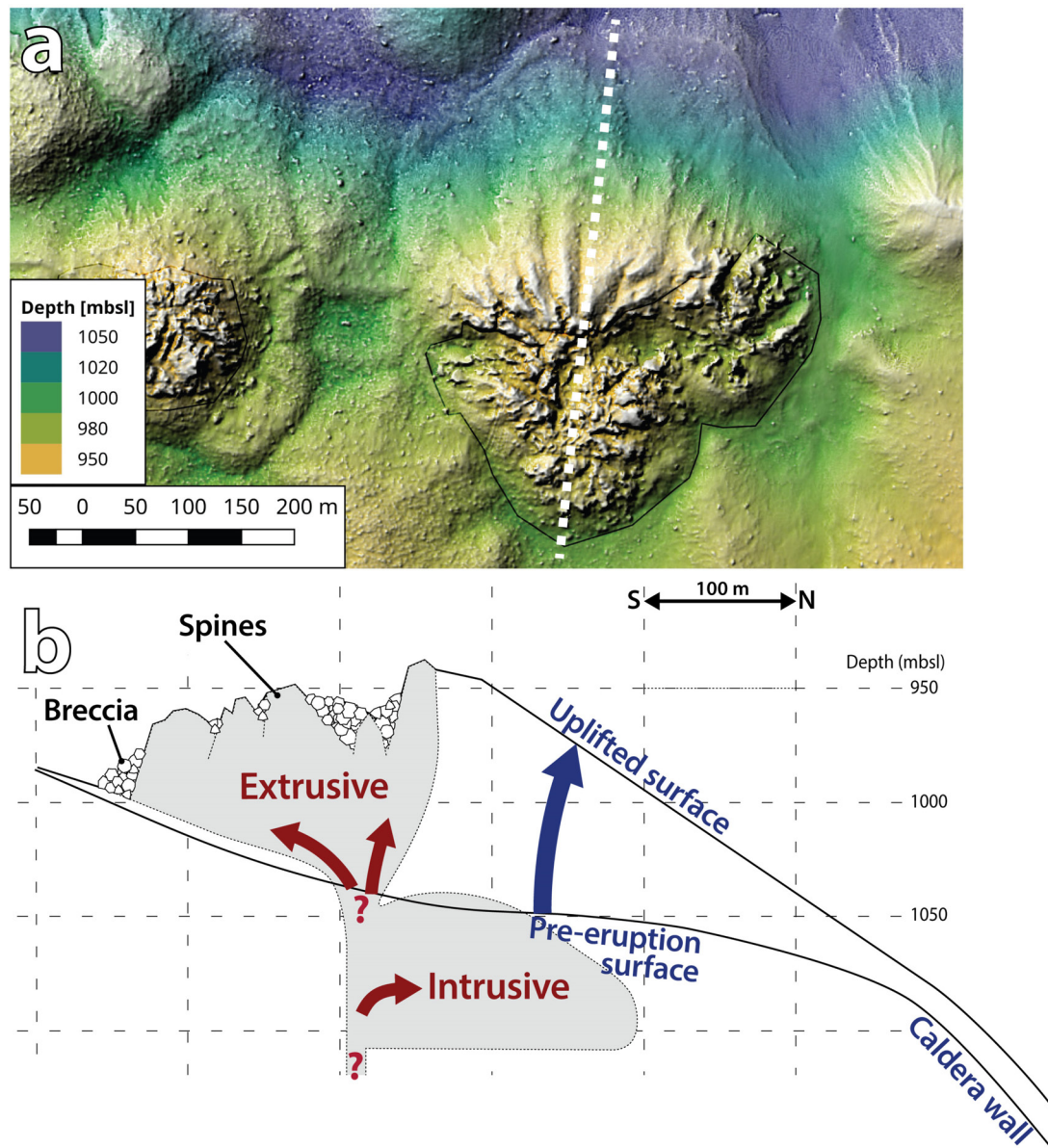


FIGURE 12 | Partially intrusive dome N. **(a)** Relief map of N showing the subtle contrast in surface texture between the northern and southern parts. The white dashed line shows the position of the cross-section in **(b)**. **(b)** Cross-section of N, showing the interpreted subsurface intrusion responsible for the uplift on the northern side of the extrusive part.

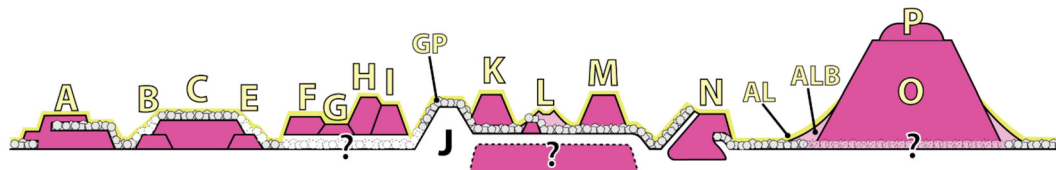


FIGURE 13 | Stratigraphic relationships among the Havre 2012 lavas and domes, the giant pumice deposit (GP), ash-lapilli deposit (AL), and ash-lapilli-block deposit (ALB), along the southwestern and southern caldera margin. Note that J is a pre-2002 feature. The pink shape below K, L, and M represents a possible shallow intrusion responsible for the uplifted bench that connects K, L, and M. The small cone beside L post-dates the GP deposit but was not systematically examined. Part of N was extrusive; this part is not covered by the GP deposit; the GP deposit covers the surface above the intrusive part of N.

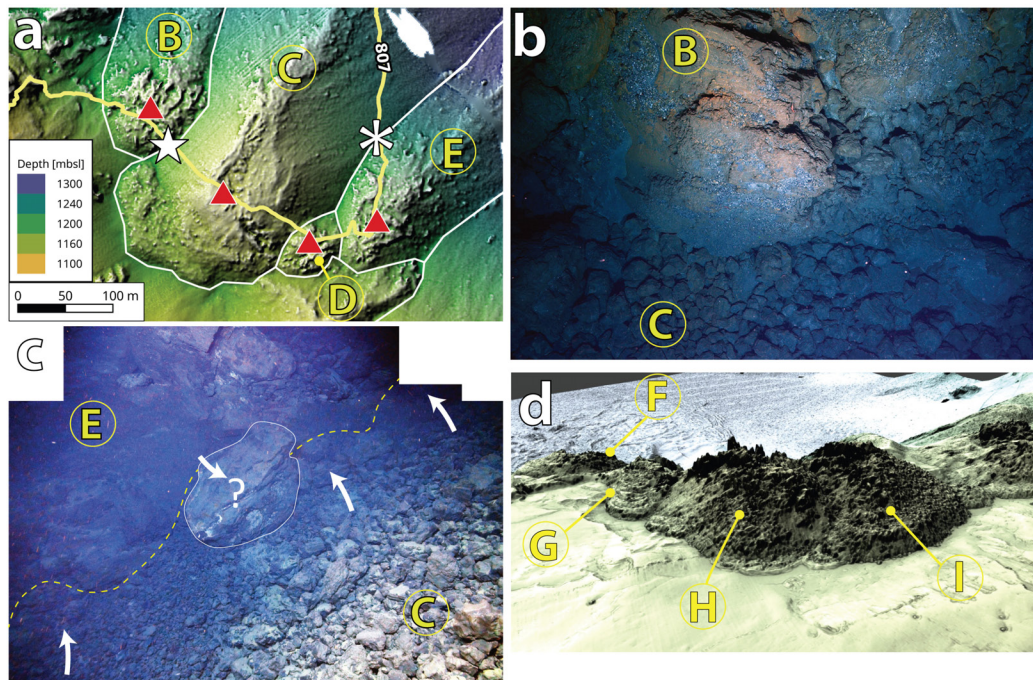


FIGURE 14 | Observations used to determine relative ages of the lavas and domes. **(a)** AUV bathymetry map of the southwestern caldera wall. The extents and inferred vents of B, C, and E are highlighted by solid borders and red triangles, respectively. The yellow line is the ROV dive traverse J2-807. The white star and asterisk show the positions of the outcrops in **(b,c)**, respectively. White patch lacks bathymetric data. **(b)** Talus of C overlies the carapace of B. Image from down-looking still camera on ROV Jason. Field of view is ~4 m across. **(c)** Talus of C overlies the carapace of E. Composite image from front-looking still camera on ROV Jason. The rock outlined in the center is ~1 m across. **(d)** 3D AUV bathymetry map of the southern caldera rim showing that the edges of H overlap I and G. The 2D map in **Figure 5** gives an orthographic view of the area.

Overlapping relationships also exist among G, H and I on the southwestern caldera rim. Their morphologies suggest that H overlaps G and I (**Figure 14d**) and is therefore younger than both. However, the relationship between these domes and the GP deposit remains unknown as they are outside of the GP dispersal area.

DISCUSSION

The Chronology of the Havre 2012 Eruption

Using the GP deposit as a marker on the sea floor and the recorded formation of the pumice raft at the sea surface, three main stages can be defined for the Havre 2012 eruption. This approach requires assuming that the GP deposit on the sea floor is the counterpart of the pumice raft recorded in satellite imagery on July 18, 2012, and is valid only if this correlation is correct.

The first stage involved the effusion of A, B, C, D, and E from vents at 1,200 to 1,300 m bsl on the southwestern caldera wall (**Figures 15a,b**). A small dome formed at D while lavas with greater volumes descended the steep caldera wall to the caldera floor at 1,500 m bsl. A and C advanced hundreds of meters farther across the flat surface of the caldera floor. At least 0.05 km³ of rhyolite was erupted at this stage, including C (0.034 km³) which is the longest (1.35 km) among the Havre 2012

lavas. The beginning and duration of the first stage are unknown. However, a rhyolitic lava as long as C may have taken months to be fully emplaced. For comparison, the obsidian lava from the 2011 eruption of Cordón-Caulle in Chile took ~3 months to reach ~3 km from the source (Tuffen et al., 2013), and was active for another 18 months (Farquharson et al., 2015).

The second stage is defined by the widespread deposition of GP on the sea floor (**Figure 15c**) and is based on the observation that most of A, and all of C are overlain by the GP deposit. The breakout lobe on A formed after deposition of the GP deposit, implying that the initial lava- and dome-producing stage immediately preceded the second stage (rather than being a long time earlier). Assuming the GP deposit correlates with the pumice raft, the second stage began on 18 July, 2012, and lasted less than 24 h (Jutzeler et al., 2014). The dispersal trajectory of the GP deposit and lateral grain size variations within it (Carey et al., 2018) strongly suggest that the source was the same vent that subsequently produced the large dome pair OP on the southern caldera rim. The significant seismicity associated with this stage (Global Volcanism Program, 2012), the short duration, and the large combined volume of the GP deposit and the pumice raft (~1.3 km³ bulk; 0.3 km³ DRE; Jutzeler et al., 2014; Carey et al., 2018) indicate that this stage involved rapid ascent of newly supplied magma.

The third stage is characterized by the eruption of lava domes K, L, M, N, and OP along the southwestern and southern rim of

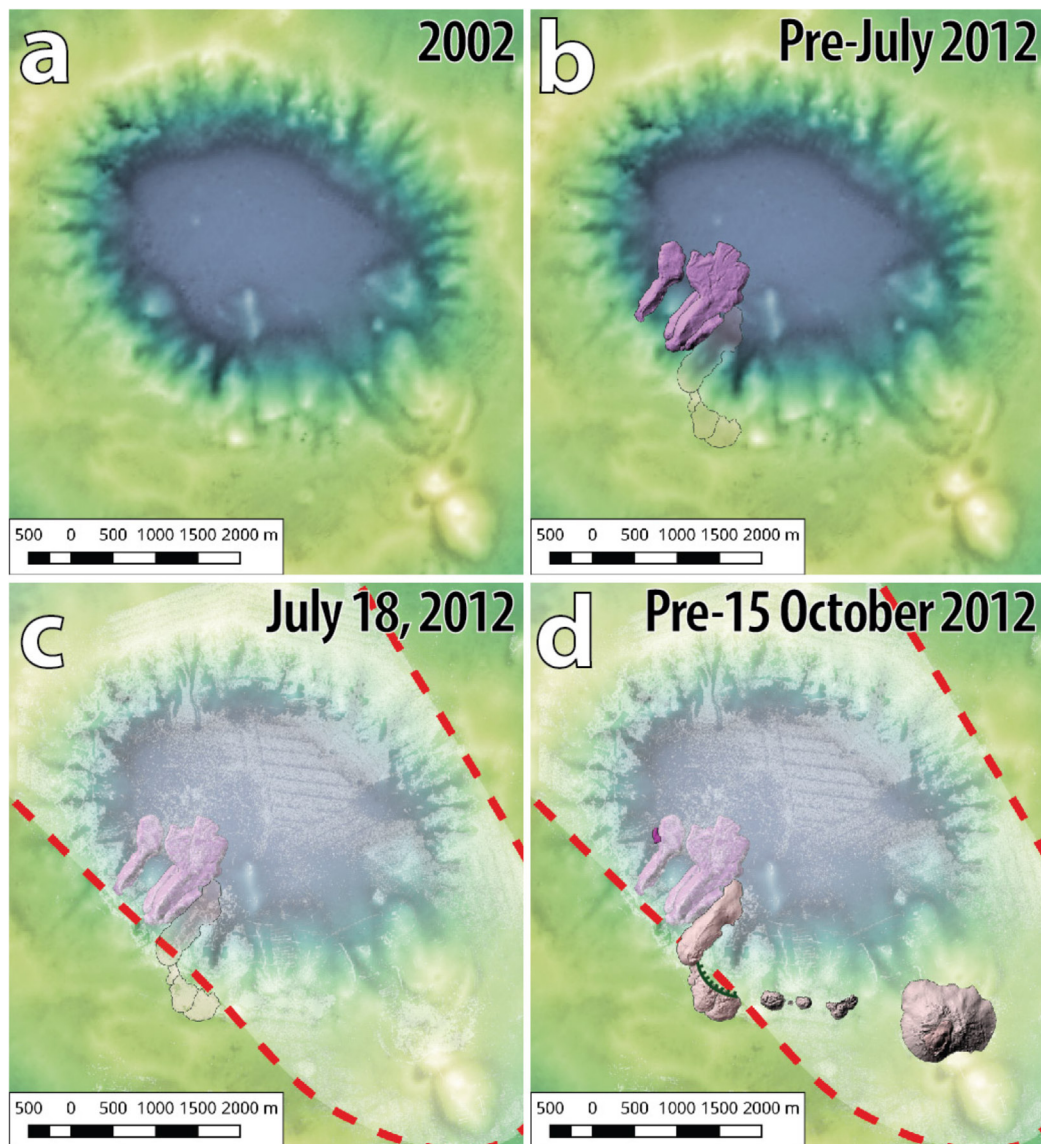


FIGURE 15 | Chronology of the Havre 2012 lava and dome eruptions. **(a)** Havre caldera in 2002 (based on Wright et al., 2006). **(b)** Effusive eruption of A, B, C, D, and E from vents at 1,200 to 1,300 m bsl on the southwestern caldera wall. A small dome formed at D; lavas A, B, C, E descended the steep caldera wall. F, G, H, and I may have also been erupted during this stage, or else after the GP deposit. **(c)** Eruption of the GP; providing the correlation of the GP deposit and the pumice raft is correct, then the GP-forming event began on July 18th, 2012. The GP deposit has a northwesterly dispersal area that covers all the caldera floor but only parts of the caldera rim. **(d)** Effusive eruption of domes K, L, M, N, O, and P and breakout of a small lobe on intracaldera lava A, before October 2012 when Havre was surveyed by R/V Tangaroa. F, G, H, and I may have also been erupted during this stage, or else before the GP deposit. After or during emplacement, part of G, H, and I collapsed, forming a scarp along their northern margins.

the caldera (Figure 15d). The breakout lobe on A (Figures 9a,b and Supplementary Figure S10) was also extruded during this stage, and requires that the earlier part of A (pre-GP) was still sufficiently mobile to undergo farther advance. The vent on the southern caldera margin inferred to have been the source of the GP deposit (Carey et al., 2018) in the second stage now became the vent for dome pair OP which is exceptionally large among the Havre 2012 rhyolite units ($\sim 0.11 \text{ km}^3$). The ash-lapilli-block deposit is found only around OP and probably underlies, and therefore predates them (Carey et al., 2018). After the majority of

dome O was built, a small-volume effusion created P, displacing O sideways so that O now forms an annulus around P. The domes K–N emerged from vents on benches along the caldera rim. Although the aggregate erupted volume of K–N is small ($\sim 0.0063 \text{ km}^3$), the 1.4-km-long alignment of these domes, and fissures connecting them (Figure 10), suggest that an additional volume of rhyolite was intruded as a dyke at the same time.

The timing of the emplacement of F, G, H, and I is not clear because they are beyond the dispersal area of the GP deposit. They could have been emplaced about the same time as A–E,

before the GP (**Figure 15b**), or about the same time as K to OP, after the GP (**Figure 15d**). The northern parts of G, H, and I are truncated by an arcuate scarp (**Figure 5c** and **Supplementary Figure S11**), indicating that they underwent partial collapse after emplacement. The collapse event occurred after the emplacement of the GP deposit because GP clasts on the caldera floor are partly buried by mass-wasting deposits.

The widespread ash-lapilli deposit is found on the GP deposit and on all the lavas and domes except P. However, its stratigraphic and temporal relationships are complex (Murch et al., unpublished). Internal subdivisions appear to record deposition that began following the eruption of the GP deposit, and persisted at least until the emplacement of P. It is inferred to have been produced by explosive and effusive events, as well as intracaldera mass-wasting events, none of which was large enough to have an expression above the sea surface.

The major part of the Havre 2012 eruption is considered to have ended by October 15, 2012, because there was no significant change in the bathymetry data between October 15, 2012 when R/V Tangaroa completed mapping the area and 2015 (MESH voyage). This chronology suggests that the Havre 2012 eruption began and ended with relatively slow lava effusion from multiple vents, which was interrupted by a brief period of higher discharge rate on July 18, 2012 when the pumice raft and GP deposit were erupted.

Structurally Controlled Vents

The Havre 2012 lavas and domes were erupted from vents distributed along ~one third (4.2 km) of the 15-km-long perimeter of the caldera. In detail, the 4.2 km of vents is made up of shorter linear segments (**Supplementary Figure S6**): BCDE, 0.3 km long, trend 120°; FGHI, 0.7 km long, trend 145°; KLMN, 1.1 km long, trend 090°. The vent of A is located on the northwestern extension of the BCDE vent alignment, but there is a 250 m gap between A and B. The BCDE and FGHI vent alignments have similar trends but are offset and separated by a 400-m-wide gap and an elevation difference of 200 m. The large dome pair OP does not fall on any of the other 2012 vent alignments but it lies at the northwestern end of a line of older vents with a trend of 150° (**Supplementary Figure S6**).

The linear arrangement of the 2012 vents, proximity of adjacent vents and the uniform composition of the rhyolite erupted (Carey et al., 2018) suggest that the 2012 lavas and domes were fed by three structurally controlled dykes (e.g., Fink and Pollard, 1983; Mastin and Pollard, 1988), corresponding to the three distinct vent alignments. The three segments evident from the vents at the surface could be connected at depth, as has been demonstrated in studies of dyke-fed subaerial rhyolite eruptions (e.g., Reches and Fink, 1988). At least for the KLMN vent alignment, there are additional surface features consistent with this interpretation. In particular, domes K and M on the KLMN vent alignment have large spines and clefts parallel to the vent alignment (**Figure 10a**). A bench ~10 m high and ~150 m wide extends between K and M (**Figure 10a**); the bench is cut by fissures to the north of L; the bench and the fissures are both parallel to the KLMN vent alignment. The uplift and extension associated with the bench and fissures could result from

a shallow syn-eruptive intrusion (pink shape beneath K, L, and M, **Figure 13**). Uplift inferred to be related to a shallow syn-eruptive intrusion has been identified at Cordón-Caulle (Castro et al., 2016) and at Medicine Lake Volcano (Fink and Anderson, 2017). Given the location of the vent alignments along the caldera perimeter, we conclude that the prime structural control on the 2012 rhyolite feeder dyke(s) was a new or pre-existing caldera-margin fault or fault set.

It is also possible to infer that shallow-level dyke emplacement proceeded from the west to south around the perimeter of the caldera during the course of the whole eruption. The basis for this interpretation is the fact that the lavas (A, B, C, E) and dome (D) at the western end predate the domes on the southwestern and southern caldera rim. Furthermore, available compositional data suggest the 2012 Havre rhyolites become progressively more silicic from the west to the south though the overall change is very small (<2 wt.% SiO₂; Carey et al., 2018). The western dyke may have tapped slightly deeper (less evolved) and the southern dyke slightly shallower (more evolved) levels of a weakly vertically zoned magma source.

Comparison of the Havre 2012 Lavas and Domes With Subaerial Rhyolite Lavas and Domes

Here, we consider whether the Havre 2012 lavas and domes, erupted in ~900 to 1,300 m of water, differ significantly from subaerial counterparts in terms of dimensions, volumes, aspect ratios, surface features, textures, eruption rates, and structural controls on vents.

The range in diameter (tens of meters to 720 m), maximum thickness (~20 to 270 m) and volume (0.0003 to 0.11 km³) of the ten Havre 2012 domes is comparable to that of subaerial dacitic and rhyolitic domes (e.g., Walker, 1973; Calder et al., 2015). The surface features of the submarine Havre domes are also similar to those of small subaerial domes, particularly those named spiny or Pelean domes, characterized by tall vertical spines (e.g., Fink and Griffiths, 1998; Fink and Anderson, 2000). The overall organization of a coherent (though jagged and spiny) core surrounded by talus is shared by both subaerial domes (e.g., Swanson et al., 1987; Calder et al., 2015) and the Havre submarine domes, and in both settings, the outer part of the core is vesicular (**Figures 11a,b**). Texturally, the Havre domes match the “obsidian dome” category of Calder et al. (2015), given the low abundance of phenocrysts, but the proportion of genuine obsidian (dense glass) within them is unknown.

Being covered almost entirely by breccia, the Havre 2012 lavas resemble subaerial, intermediate to silicic, blocky lavas (Kilburn, 2000; Harris and Rowland, 2015). In both settings, the breccia is autoclastic; in the Havre case, both quench fragmentation and dynamic stressing probably operated. Among the best subaerial examples of silicic, blocky lavas are the Roche Rosse rhyolite lava (Italy; ~2 km long, 0.03 km³; Bullock et al., 2018), the Cordón-Caulle obsidian lava (Chile; ~3.6 km long, 0.8 km³; Tuffen et al., 2013) and rhyolite lavas of Newberry volcano (e.g., Big Obsidian Flow, 1.8 km long, ~0.13 km³; Interlake Obsidian

Flow, 1.8 km long, 0.025 km^3 ; MacLeod et al., 1995), all of which have dimensions comparable to the Havre 2012 lavas. The arcuate surface ridges on the Havre lavas, especially those on A (**Figure 8**), appear to be identical to similar ridges on subaerial silicic lavas (commonly referred to as surface folds, compressional ridges or ogives). In subaerial settings, surface ridges form where the crust buckles in response to compression behind a stalled lava-flow front (Fink, 1980). The same explanation appears valid in the case of the arcuate surface ridges on the Havre submarine lavas. Although not common or not widely recognized, subaerial rhyolite lavas may include small breakout lobes emplaced after the main lava advance ceased (e.g., breakouts associated with the 2011–2012 Cordón-Caulle obsidian lava, Tuffen et al., 2013). Among the lavas produced during the Havre 2012 eruption, both A and E include small breakout lobes.

The aspect ratios of the Havre 2012 lavas (**Supplementary Table S1**) fall in the range considered typical of subaerial high-viscosity lavas by Walker (1973; <50 and commonly <8). Lava C has an aspect ratio of 47.7, near the high end of the range whereas the other lavas (A, B, E, F) have much lower aspect ratios (5.5–16; **Supplementary Table S1**).

The narrow-tongue segments of the Havre 2012 lavas on the steep caldera wall superficially resemble channelized lavas (e.g., Harris and Rowland, 2015). However, the strongly triangular cross-section shape and very shallow depth of the central depression (**Figures 7a,b**) are important differences, especially with regard to the identification of levees which are an integral part of channelized lavas. Although there are very few exposures of coherent rhyolite on the narrow-tongue segments, it is reasonable to infer that the interior of the ridges comprised molten rhyolite while the lavas were active, because (1) in the cases of A and C, the narrow-tongue segments fed the wide-lobe segments on the caldera floor, and (2) there is a breakout lobe on the narrow-tongue segment of E (**Figures 9c,d**). In this respect, the narrow-tongue segments appear to have delivered molten rhyolite to the flow front beneath an insulating cover of breccia. This mechanism of propagation strongly resembles that of subaerial a'a and blocky lavas (Kilburn, 1993; Harris and Rowland, 2015).

By assuming that the GP deposit and the observed pumice raft were contemporaneous, and noting that there was no significant topographical change between the bathymetry mapped on October 15, 2012 and March 2015, Carey et al. (2018) concluded that domes K to P were likely erupted within (or less than) 90 days. The minimum mean discharge rate of dome OP (0.11 km^3) was $14.4 \text{ m}^3/\text{s}$ whereas the rates for each of K, M, and N were between 0.14 and $0.37 \text{ m}^3/\text{s}$.

Recent subaerial eruptions of Chaiten in 2008 and Puyehue Cordón-Caulle in 2011 demonstrated that rhyolitic effusive eruptions can have maximum discharge rates as high as $70 \text{ m}^3/\text{s}$ (Pallister et al., 2013; Bertin et al., 2015) which surpasses the rate for typical subaerial dacitic dome eruptions such as Mt. St. Helens ($\sim 0.59 \text{ m}^3/\text{s}$; Fink et al., 1990), Unzen ($\sim 3.5 \text{ m}^3/\text{s}$; Nakada and Fujii, 1993) or Santiaguito ($\sim 1.4 \text{ m}^3/\text{s}$; Harris et al., 2003) by more than an order of magnitude. However, the mean discharge rates of Chaiten ($\sim 16 \text{ m}^3/\text{s}$) and Puyehue Cordón-Caulle ($16.7 \text{ m}^3/\text{s}$)

were much lower than the maxima, and comparable to the minimum mean discharge rate of Havre dome OP. The rates for other small Havre 2012 domes K, M and N are comparable to those of small subaerial silicic domes.

We have interpreted the linear alignment of the vents for the Havre 2012 lavas and domes to result from structural control, most likely a fault or fault set. Alignment of multiple vents along faults is commonly shown by subaerial rhyolite lava and dome fields. Well-studied examples include Cordón-Caulle (Lara et al., 2004), the Inyo volcanic chain (Sampson, 1987; Miller, 1985), Newberry volcano (MacLeod et al., 1995), South Sister volcano (Scott, 1987) and Kaharoa domes (Leonard et al., 2002) (**Supplementary Figure S12**).

Controls on Morphology

Comparison of rhyolitic lavas and domes in subaerial and deep submarine (Havre 2012 rhyolitic lavas and domes) settings has shown the two are closely similar. Deep water above vents might be expected to influence morphology, because elevated confining pressure favors retention of volatiles that lowers the magma viscosity (Murase and McBirney, 1973). On the other hand, enhanced cooling, due to the greater heat capacity of water versus air, might be expected to raise the viscosity (Murase and McBirney, 1973). It could be that in the case of Havre 2012, the two influences were balanced or that neither was significant. The latter option appears most plausible: the Havre melts were probably relatively low in dissolved water, given the anhydrous phenocryst assemblage of the lavas and domes, so elevated confining pressure did little to modify the viscosity of the melt. Enhanced cooling probably influenced only the rate of crust development, and once formed, the crust very effectively insulated the interior from any further cooling by seawater.

Because some Havre 2012 lavas and domes were erupted on a steep slope and others onto flat sea floor, we can assess the influence of substrate slope on morphology. Clearly, the influence was profound – narrow tongues formed in all cases where the rhyolite propagated across the steep caldera wall, and either wide lobes or domes formed where the rhyolite propagated across flat sea floor, both within the caldera or on the caldera rim. On the flat sea floor, the contrast between wide lobes and domes was probably primarily controlled by the available magma volume, small volumes producing domes and larger volumes producing wide lobes.

Observations of active subaerial domes and analog experiments of dome growth have shown that the ratio of discharge rate to cooling rate has a strong influence on dome morphology (e.g., Fink and Griffiths, 1998). In this approach, dome morphology can be used to infer discharge rate. The Havre 2012 domes except G are spiny or Pelean domes; this dome morphology is associated with the lowest discharge and highest cooling rates. The discharge rates for domes K, M, and N (between 0.4 and $1.2 \text{ m}^3/\text{s}$; Carey et al., 2018) are at the low end of the known range, consistent with the prediction based on morphology alone. However, the effusion rate of the dome pair OP was substantially higher ($14.4 \text{ m}^3/\text{s}$; Carey et al., 2018). This much higher effusion rate relates mainly to the effusion of O because P is a lot smaller than O. The morphological

interpretation of O is complicated because it was modified when P was emplaced, but it best fits the spiny category of Fink and Griffiths (1998), despite the much higher effusion rate. It could be that application of this morphological approach to the Havre domes requires that the original scaling and dimensional analysis be revisited for the different ambient conditions in the submarine environment.

Among the domes, G is distinctive in being much lower in relief than the other domes and having well-developed arcuate surface ridges rather than spines typical of the other domes (Figures 6c, 14d). This morphology matches the axisymmetric dome category of Fink and Griffiths (1998), associated with relatively high discharge and low cooling rates. This difference in effusion style was presumably viscosity-controlled, the viscosity of the magma that produced G being lower than that of the other domes. Lower viscosity favors higher discharge rate which in turn influences crust development and outflow distance (e.g., Walker, 1973; Fink and Griffiths, 1990). The cause of G rhyolite having a lower viscosity than the rhyolite that formed the other domes has not been identified.

CONCLUSION

The Havre 2012 eruption produced 15 submarine rhyolite lavas and domes with a collective volume of 0.21 km^3 from 14 separate vents. Five vents (A–E) are aligned along the steep caldera wall between 1,200 and 1,300 m bsl. Four of the five vents produced lavas that flowed to the base of caldera wall, two of which (A, C) extended 450–650 m farther across the flat caldera floor. On the caldera rim (960–1,060 m bsl), eight vents produced domes (G–I, K–P) and one vent produced a lava (F) that flowed 1,070 m down the caldera wall. One caldera-rim vent built two domes (OP), the collective volume of which ($\sim 0.11 \text{ km}^3$) is the largest of all the Havre 2012 lavas and domes.

On the steep caldera wall, the lavas consist of narrow tongues. The narrow-tongue segments of lavas A and C are connected to wide lobes on the caldera floor. Although covered by breccia, the narrow tongues probably fed molten rhyolite to the lava flow fronts and also to small breakout lobes. Well-developed arcuate surface ridges on the lavas are the crests of folds developed in response to compression during flowage. With the exception of G, the surfaces of the domes consist of jagged, spiny coherent rhyolite surrounded by aprons of talus and have morphologies typical of low discharge rates. The low profile of G and its lobate morphology imply higher discharge rates which in turn probably reflect lower magma viscosity. The presence of narrow-tongue morphology on the steeply sloping caldera wall versus domes and wide lobes on flat sea floor demonstrates that substrate slope was a major control on morphology. Additional analysis of the Havre lava and dome morphologies could yield information on discharge rates for the lavas erupted from the caldera-wall vents and the domes that lie outside the dispersal of the GP deposit.

The dome and lavas erupted from vents on the caldera wall are older than the GP deposit but probably only slightly older because a breakout lobe from one of them (A) is younger than the GP deposit. Domes K, L, M, N, and OP on the caldera rim are

younger than the GP deposit. For these domes, minimum mean eruption rates from 0.14 to $14.4 \text{ m}^3/\text{s}$ can be estimated providing correlation of the GP deposit with the pumice raft witnessed on July 18, 2012, is correct. The ages of lava F and domes G, H, and I relative to the GP deposit could not be established because they are located outside the dispersal area of the GP deposit.

The Havre 2012 vents define three alignments close to the caldera margin. The similar magma composition, strong alignment of vents, small separation between adjacent vents and local presence of ground fissures suggest the vents were fed by fault-controlled dykes.

The Havre 2012 lavas and domes are very similar to subaerial rhyolite lavas and domes in terms of dimensions, volumes, aspect ratios, textures, morphology, discharge rate, and structural controls on vent positions.

AUTHOR CONTRIBUTIONS

FI, JM, RC, AS, and MJ were on the 2015 MESH voyage. FI, JM, and RC led the writing and revision of the article and created the figures. RM conducted a scientific study on one component of this study which has been used in this manuscript. AS contributed to expertise on bathymetry and vehicle data. AS and MJ contributed to discussions, and revision of text and figures.

FUNDING

This research was funded by an Australian Research Council Postdoctoral fellowship to RJC (DP110102196 and DE150101190), and National Science Foundation grants OCE1357443 and OCE1357216. FI was supported by a Tasmanian Government Postgraduate Award.

ACKNOWLEDGMENTS

This science would not be possible without the captain, operations teams, marine technicians and crew of the RV Roger Revelle, who we thank for their expert help at sea. We thank the Operations team of the ROV *Jason* and the AUV *Sentry*. We particularly thank Dana Yoerger from WHOI for the significant level of assistance on the ship preparing AUV surveys and data processing during and after the MESH voyage. We also thank Sandrin Feig, Karsten Goemann and staff of the Central Science Laboratory at the University of Tasmania. Comments from reviewers Jon Fink and Ilya Bindeman are gratefully acknowledged.

SUPPLEMENTARY MATERIAL

The Supplementary Material for this article can be found online at: <https://www.frontiersin.org/articles/10.3389/feart.2018.00147/full#supplementary-material>

REFERENCES

- Allen, S. R., Fiske, R. S., and Tamura, Y. (2010). Effects of water depth on pumice formation in submarine domes at Sumisu, Izu-Bonin arc, western Pacific. *Geology* 38, 391–394. doi: 10.1130/G30500.1
- Bartetzko, A., Paulick, H., Iturrino, G., and Arnold, J. (2003). Facies reconstruction of a hydrothermally altered dacite extrusive sequence: evidence from geophysical downhole logging data (ODP Leg 193). *Geochem. Geophys. Geosyst.* 4:1087. doi: 10.1029/2003GC000575
- Baxter, P. J., Bonadonna, C., Dupree, R., Hards, V. L., Kohn, S. C., Murphy, M. D., et al. (1999). Cristobalite in volcanic ash of the Soufriere Hills Volcano, Montserrat, British West Indies. *Science* 283, 1142–1145. doi: 10.1126/science.283.5405.1142
- Bertin, D., Lara, L. E., Basualto, D., Amigo, Á., Cardona, C., Franco, L., et al. (2015). High effusion rates of the Cordon Caulle 2011–2012 eruption (Southern Andes) and their relation with the quasi-harmonic tremor: effusion rates and quasi-harmonic tremor. *Geophys. Res. Lett.* 42, 7054–7063. doi: 10.1002/2015GL064624
- Binns, R. A., Barriga, F. J. A. S., and Miller, D. J. (2007). “Leg 193 synthesis: anatomy of an active felsic-hosted hydrothermal system, eastern Manus basin, Papua New Guinea,” in *Proceedings of the Ocean Drilling Program, 194 Scientific Results Proceedings of the Ocean Drilling Program*, eds F. J. A. S. Barriga, R. A. Binns, D. J. Miller, and P. M. Herzig (College Station, TX: Joint Oceanographic Institutions). doi: 10.2973/odp.proc.sr.193.201.2007
- Bullock, L. A., Gertisser, R., and O’Driscoll, B. (2018). Emplacement of the Rocche Rosse rhyolite lava flow (Lipari, Aeolian Islands). *Bull. Volcanol.* 80:48. doi: 10.1007/s00445-018-1222-4
- Calder, E. S., Lavallée, Y., Kendrick, J. E., and Bernstein, M. (2015). “Chapter 18 - Lava Dome Eruptions,” in *The Encyclopedia of Volcanoes*, 2nd Edn, ed. H. Sigurdsson (Amsterdam: Academic Press), 343–362. doi: 10.1016/B978-0-12-385938-9.00018-3
- Carey, R., Soule, A. S., Manga, M., White, J., McPhie, J., Wysoczanski, R., et al. (2018). The largest deep-ocean silicic volcanic eruption of the past century. *Sci. Adv.* 4:e1701121. doi: 10.1126/sciadv.1701121
- Carey, R. J., Wysoczanski, R., Wunderman, R., and Jutzeler, M. (2014). Discovery of the largest historic silicic submarine eruption. *EOS Trans. AGU* 95, 157–159. doi: 10.1002/2014EO190001
- Cas, R. (1978). Silicic lavas in Paleozoic flyschlike deposits in New South Wales, Australia: behavior of deep subaqueous silicic flows. *Geol. Soc. Am. Bull.* 89, 1708–1714. doi: 10.1130/0016-7606(1978)89<1708:SLIPFD>2.0.CO;2
- Castro, J. M., Cordonnier, B., Schipper, I. C., Tuffen, H., Baumann, T. S., and Feisel, Y. (2016). Rapid laccolith intrusion driven by explosive volcanic eruption. *Nat. Commun.* 7:13585. doi: 10.1038/ncomms13585
- Embley, R. W., and Rubin, K. H. (2018). Extensive young silicic volcanism produces large deep submarine lava flows in the NE Lau Basin. *Bull. Volcanol.* 80:36. doi: 10.1007/s00445-018-1211-7
- Farquharson, J. I., James, M. R., and Tuffen, H. (2015). Examining rhyolite lava flow dynamics through photo-based 3D reconstructions of the 2011–2012 lava flow field at Cordón-Caulle, Chile. *J. Volcanol. Geotherm. Res.* 304, 336–348. doi: 10.1016/j.jvolgeores.2015.09.004
- Fink, J. A., and Anderson, S. W. (2017). *Emplacement of Holocene Silicic lava flows and Domes at Newberry, South Sister, and Medicine Lake volcanoes, California and Oregon*. Reston: US Geological Survey.
- Fink, J. H. (1980). Surface folding and viscosity of rhyolite flows. *Geology* 8, 250–254. doi: 10.1130/0091-7613(1980)8<250:SFAVOR>2.0.CO;2
- Fink, J. H., and Griffiths, R. W. (1990). Radial spreading of viscous gravity currents with solidifying crust. *J. Fluid Mech.* 221, 485–509. doi: 10.1017/S0022112090003640
- Fink, J. H., and Griffiths, R. W. (1998). Morphology, eruption rates, and rheology of lava domes: insights from laboratory models. *J. Geophys. Res.* 103, 527–545. doi: 10.1029/97JB02838
- Fink, J. H., Malin, M. C., and Anderson, S. W. (1990). Intrusive and extrusive growth of the Mount St Helens lava dome. *Nature* 348, 435–437. doi: 10.1038/348435a0
- Fink, J. H., and Pollard, D. D. (1983). Structural evidence for dikes beneath silicic domes, Medicine Lake Highland Volcano, California. *Geology* 11, 458–461. doi: 10.1130/0091-7613(1983)11<458:SEFDBS>2.0.CO;2
- Fink, J. H., and Anderson, S. W. (2000). “Lava domes and coulees,” in *The Encyclopedia of Volcanoes*, 1st Edn, ed. H. Sigurdsson (Amsterdam: Academic Press), 307–319.
- General Bathymetric Chart of the Oceans (2014). *GEBCO 2014 Grid*. Available at: <https://www.gebco.net/> [accessed July 28, 2015].
- Global Volcanism Program (2012). Report on Havre Seamount (New Zealand), in *Bulletin of the Global Volcanism Network*, Vol. 37, ed. R. Wunderman (Washington, D.C.: Smithsonian Institution)
- Harris, A. J., Rose, W. I., and Flynn, L. P. (2003). Temporal trends in lava dome extrusion at Santiaguito 1922–2000. *Bull. Volcanol.* 65, 77–89. doi: 10.1007/s00445-002-0243-0
- Harris, A. J. L., and Rowland, S. K. (2015). “Lava flows and rheology,” in *The Encyclopedia of Volcanoes*, 2nd Edn, ed. H. Sigurdsson (Amsterdam: Academic Press), 321–362. doi: 10.1016/B978-0-12-385938-9.00018-3
- Honsho, C., Ura, T., Kim, K., and Asada, A. (2016). Post-caldera volcanism and hydrothermal activity revealed by autonomous underwater vehicle surveys in Myojin Knoll caldera, Izu-Ogasawara arc. *J. Geophys. Res.* 121, 4085–4102. doi: 10.1002/2016JB012971
- Horwell, C. J., Williamson, B. J., Llewellyn, E. W., Damby, D. E., and Le Blond, J. S. (2013). The nature and formation of cristobalite at the Soufrière Hills volcano, Montserrat: implications for the petrology and stability of silicic lava domes. *Bull. Volcanol.* 75, 1–19. doi: 10.1007/s00445-013-0696-3
- Jutzeler, M., Marsh, R., Carey, R. J., White, J. D. L., Talling, P. J., and Karlstrom, L. (2014). On the fate of pumice rafts formed during the 2012 Havre submarine eruption. *Nat. Commun.* 5:3660. doi: 10.1038/ncomms4660
- Kano, K., Takeuchi, K., Yamamoto, T., and Hoshizumi, H. (1991). Subaqueous rhyolite block lavas in the Miocene Ushikiri Formation, Shimane Peninsula, SW Japan. *J. Volcanol. Geotherm. Res.* 46, 241–253. doi: 10.1016/0377-0273(91)90086-F
- Kilburn, C. (1993). “Lava crusts, aa flow lengthening and the pahoehoe-aa transition,” in *Active Lavas: Monitoring And Modelling*, eds C. R. Kilburn and G. Luongo (London: UCL Press), 263–280.
- Kilburn, C. (2000). “Lava flows and flow fields,” in *The Encyclopedia of Volcanoes*, 1st Edn, ed. H. Sigurdsson (Amsterdam: Academic Press), 291–305.
- Lara, L. E., Naranjo, J. A., and Moreno, H. (2004). Rhyodacitic fissure eruption in Southern Andes (Cordon Caulle; 40.5°S) after the 1960 (Mw:9.5) Chilean earthquake: a structural interpretation. *J. Volcanol. Geotherm. Res.* 138, 127–138. doi: 10.1016/j.jvolgeores.2004.06.009
- Leonard, G. S., Cole, J. W., Nairn, I. A., and Self, S. (2002). Basalt triggering of the c. AD 1305 Kaharoa rhyolite eruption, Tarawera Volcanic Complex, New Zealand. *J. Volcanol. Geotherm. Res.* 115, 461–486. doi: 10.1016/S0377-0273(01)00326-2
- MacLeod, N. S., Sherrod, D. R., Chitwood, L. A., and Jensen, R. A. (1995). *Geologic map of Newberry Volcano, Deschutes, Klamath, and Lake Counties, Oregon*. Available at: <https://pubs.usgs.gov/imap/2455/> [accessed June 1, 2017].
- Mastin, L. G., and Pollard, D. D. (1988). Surface deformation and shallow dike intrusion processes at Inyo Craters, Long Valley, California. *J. Geophys. Res.* 93, 13221–13235. doi: 10.1029/JB093iB11p13221
- Miller, C. D. (1985). Holocene eruptions at the Inyo volcanic chain, California: implications for possible eruptions in Long Valley caldera. *Geology* 13, 14–17. doi: 10.1130/0091-7613(1985)13<14:HEATIV>2.0.CO;2
- Murase, T., and McBirney, A. R. (1973). Properties of some common igneous rocks and their melts at high temperatures. *Geol. Soc. Am. Bull.* 84, 3563–3592. doi: 10.1130/0016-7606(1973)84<3563:POSCIR>2.0.CO;2
- Nakada, S., and Fujii, T. (1993). Preliminary report on the activity at Unzen Volcano (Japan), November 1990–November 1991: dacite lava domes and pyroclastic flows. *J. Volcanol. Geotherm. Res.* 54, 319–333. doi: 10.1016/0377-0273(93)90070-8
- Pallister, J. S., Diefenbach, A. K., Burton, W. C., Muñoz, J., Griswold, J. P., Lara, L. E., et al. (2013). The Chaitén rhyolite lava dome: eruption sequence, lava dome volumes, rapid effusion rates and source of the rhyolite magma. *Andean Geol.* 40, 277–294. doi: 10.5027/andgeoV40n2-a06
- Paulick, H., Vanko, D. A., and Yeats, C. J. (2004). Drill core-based facies reconstruction of a deep-marine felsic volcano hosting an active hydrothermal system (Pual Ridge, Papua New Guinea, ODP Leg 193). *J. Volcanol. Geotherm. Res.* 130, 31–50. doi: 10.1016/S0377-0273(03)00275-0
- Reches, Z., and Fink, J. (1988). The mechanism of intrusion of the Inyo Dike, Long Valley Caldera, California. *J. Geophys. Res.* 93, 4321–4334. doi: 10.1029/JB093iB05p04321

- Sampson, D. E. (1987). Textural heterogeneities and vent area structures in the 600-year-old lavas of the Inyo volcanic chain, eastern California. *Geol. Soc. Am. Special Paper* 212, 89–102. doi: 10.1130/SPE212-p89
- Schipper, C. I., Castro, J. M., Tuffen, H., Wadsworth, F. B., Chappell, D., Pantoja, A. E., et al. (2015). Cristobalite in the 2011–2012 Cordón Caulle eruption (Chile). *Bull. Volcanol.* 77:193. doi: 10.1007/s00445-015-0925-z
- Scott, W. E. (1987). Holocene rhyodacite eruptions on the flanks of South Sister volcano, Oregon. *Geol. Soc. Am. Special Paper* 212, 35–54. doi: 10.1130/SPE212-p35
- Swanson, D. A., Dzurisin, D., Holcomb, R. T., Iwatsubo, E. Y., Chadwick, W., Casadevall, T. J., et al. (1987). Growth of the lava dome at Mount St. Helens, Washington, (USA), 1981–1983. *Geol. Soc. Am. Special Paper* 212, 1–16. doi: 10.1130/SPE212-p1
- Thal, J., Tivey, M., Yoerger, D., Jöns, N., and Bach, W. (2014). Geologic setting of PACManus hydrothermal area — High resolution mapping and in situ observations. *Mar. Geol.* 355, 98–114. doi: 10.1016/j.margeo.2014.05.011
- Tuffen, H., James, M. R., Castro, J. M., and Schipper, I. C. (2013). Exceptional mobility of an advancing rhyolitic obsidian flow at Cordón Caulle volcano in Chile. *Nat. Commun.* 4:2709. doi: 10.1038/ncomms3709
- Walker, G. P. L. (1973). Lengths of Lava Flows [and Discussion]. *Philos. Trans. R. Soc. Lond. A* 274, 107–118. doi: 10.1098/rsta.1973.0030
- Wright, I. C., Worthington, T. J., and Gamble, J. A. (2006). New multibeam mapping and geochemistry of the 30°–35° S sector, and overview, of southern Kermadec arc volcanism. *J. Volcanol. Geotherm. Res.* 149, 263–296. doi: 10.1016/j.jvolgeores.2005.03.021
- Yamagishi, H., and Dimroth, E. (1985). A comparison of Miocene and Archean rhyolite hyaloclastites: evidence for a hot and fluid rhyolite lava. *J. Volcanol. Geotherm. Res.* 23, 337–355. doi: 10.1016/0377-0273(85)90040-X

Conflict of Interest Statement: The authors declare that the research was conducted in the absence of any commercial or financial relationships that could be construed as a potential conflict of interest.

Copyright © 2018 Ikegami, McPhie, Carey, Mundana, Soule and Jutzeler. This is an open-access article distributed under the terms of the Creative Commons Attribution License (CC BY). The use, distribution or reproduction in other forums is permitted, provided the original author(s) and the copyright owner(s) are credited and that the original publication in this journal is cited, in accordance with accepted academic practice. No use, distribution or reproduction is permitted which does not comply with these terms.



A Recent Volcanic Eruption Discovered on the Central Mariana Back-Arc Spreading Center

William W. Chadwick Jr.^{1*}, Susan G. Merle², Edward T. Baker³, Sharon L. Walker⁴, Joseph A. Resing³, David A. Butterfield³, Melissa O. Anderson^{5,6†}, Tamara Baumberger² and Andra M. Bobbitt²

¹ NOAA Pacific Marine Environmental Laboratory, Newport, OR, United States, ² CIMRS, Oregon State University, Newport, OR, United States, ³ JISAO, University of Washington, Seattle, WA, United States, ⁴ NOAA Pacific Marine Environmental Laboratory, Seattle, WA, United States, ⁵ Department of Earth Sciences, University of Ottawa, Ottawa, ON, Canada, ⁶ GEOMAR, Helmholtz Centre for Ocean Research, Kiel, Germany

OPEN ACCESS

Edited by:

Nancy Riggs,
Northern Arizona University,
United States

Reviewed by:

James D. L. White,
University of Otago, New Zealand
Jan Marie Lindsay,
University of Auckland, New Zealand

*Correspondence:

William W. Chadwick Jr.
william.w.chadwick@noaa.gov

†Present address:

Melissa O. Anderson,
Department of Earth Sciences,
University of Toronto, Toronto, ON,
Canada

Specialty section:

This article was submitted to
Volcanology,
a section of the journal
Frontiers in Earth Science

Received: 29 June 2018

Accepted: 02 October 2018

Published: 23 October 2018

Citation:

Chadwick WW Jr, Merle SG,
Baker ET, Walker SL, Resing JA,
Butterfield DA, Anderson MO,
Baumberger T and Bobbitt AM (2018)
A Recent Volcanic Eruption
Discovered on the Central Mariana
Back-Arc Spreading Center.
Front. Earth Sci. 6:172.
doi: 10.3389/feart.2018.00172

Submarine volcanic eruptions are difficult to detect because they are hidden from view at the bottom of the ocean and far from land-based sensors. However, most of Earth's volcanic activity is in the oceans along tectonic plate boundaries, and modern tools of oceanography now allow us to find and study recent eruptions in the deep sea. The first known historical eruption on the Mariana back-arc spreading center was discovered in December 2015 during exploration of the southern back-arc for new hydrothermal vent sites. A water-column survey along the axis of the back-arc showed hydrothermal plumes over the site characterized by low particle concentrations and relatively high reduced chemical anomalies. A dive with the autonomous underwater vehicle *Sentry* collected high-resolution (1 m) multibeam sonar bathymetry over the site, followed by a near-bottom photographic survey of a smaller area. The photo survey revealed the presence of a pristine, dark, glassy lava flow on the seafloor with no sediment cover. Venting of milky hydrothermal fluid indicated that the lava flow was still warm and therefore very young. A comparison of multibeam sonar bathymetry collected by *R/V Falkor* in December 2015, to the most recent previous survey of the area by *R/V Melville* in February 2013, revealed large depth changes in the same area, effectively bracketing the timing of the eruption within a window of less than 3 years. The bathymetric comparison shows the eruption produced a string of lava flows with maximum thicknesses of 40–138 m along a distance of 7.3 km (from latitude 15°22.3' to 15°26.3'N) between depths of 4050–4450 m bsl (meters below sea level), making this the deepest known historical submarine volcanic eruption on Earth. The cross-axis width of the lava flows is 200–800 m. The *Sentry* bathymetry shows that the new lava flows are constructed of steep-sided hummocky pillow mounds and are surrounded by older flows with similar morphology. In April and December 2016, two dives were made on the new lava flows by remotely operated vehicles *Deep Discoverer* and *SuBastian*. The pillow lavas have many small glassy buds on the steep flanks of the mounds, locally thick accumulations of hydrothermal sediment near the tops of mounds, and small cones of radiating pillows at their summits. The 2015–2016 observations show a rapidly declining hydrothermal system on the lava flows, suggesting that the eruption had occurred only

months before its discovery in December 2015. The morphology of the pillow lavas is similar to other historical eruption sites, so the greater depth and ambient pressure of this site had no apparent effect on the processes of lava extrusion and emplacement. This study reveals that some segments of the Mariana back-arc have active magmatic systems despite the relatively low spreading rate, and that other eruptions are possible in the near future.

Keywords: submarine eruption, mariana back-arc spreading center, mariana trough, high-resolution mapping, submarine lava flow morphology

INTRODUCTION

Documented historical volcanic eruptions in the deep-sea are relatively rare, because they usually have no expression at the ocean surface and only produce small earthquakes which are difficult to detect in the ocean basins. For example, Rubin et al. (2012) highlighted the fact that only 17 deep [>500 m bsl (meters below sea level)] submarine eruptions were known to have occurred in the last 500 years, compared to 497 known eruptions on land. Historical deep-sea eruptions have been found in a variety of ways, including by distinctive hydrothermal plumes detected during water-column surveys, repeated bathymetric mapping showing depth changes, time-series visual observations by camera or submersible, radiometric dating of young lava flows, remote detection of seismic swarms by hydrophone or seismometers, and rarely by pumice rafts appearing on the ocean surface (Cowen et al., 2004; Dziak et al., 2011; Baker et al., 2012; Rubin et al., 2012; Carey et al., 2018). Only two seamounts have been directly observed erupting, NW Rota-1 in the Mariana arc and West Mata in the NE Lau Basin (probably both long-lived eruptions) (Chadwick et al., 2008; Resing et al., 2011; Embley et al., 2014; Schnur et al., 2017). More recently, a cabled observatory established at Axial Seamount captured an eruption in 2015 (Kelley et al., 2014; Chadwick et al., 2016; Nooner and Chadwick, 2016; Wilcock et al., 2016). Most of these known eruptions have been found on mid-ocean ridges or in submarine volcanic arcs. We know even less about the character and frequency of deep-sea eruptions in back-arc settings.

Recent systematic exploration of the southern Mariana back-arc between 13 and 18.5°N during research cruises on *R/V Falkor* in 2015 and 2016 (FK151121 and FK161129) led to the discovery of new hydrothermal vent sites along the back-arc spreading axis (Baker et al., 2017; Butterfield et al., 2018). That work included the collection of new EM302 multibeam sonar bathymetry along the back-arc that permitted a refined mapping of the axis of spreading, and allowed geologic interpretation of the back-arc spreading segments and their tectonic and magmatic character (Anderson et al., 2017). The *R/V Falkor* cruises also included high-resolution bathymetric mapping of selected sites with the autonomous underwater vehicle (AUV) *Sentry* in 2015, followed by dives with the remotely operated vehicles (ROV) *SuBastian* in 2016. In between those, the NOAA Ship *Okeanos Explorer* made three exploratory dives with the ROV *Deep Discoverer* (D2).

During the exploration for new vent sites we discovered evidence of a very recent eruption on the axis of the

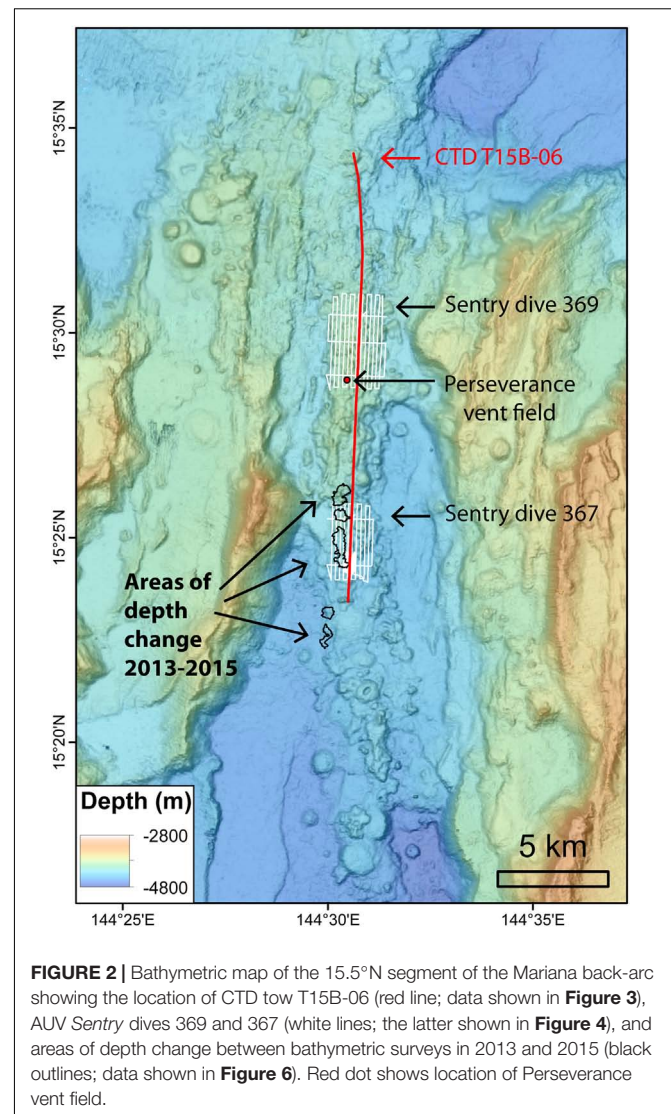
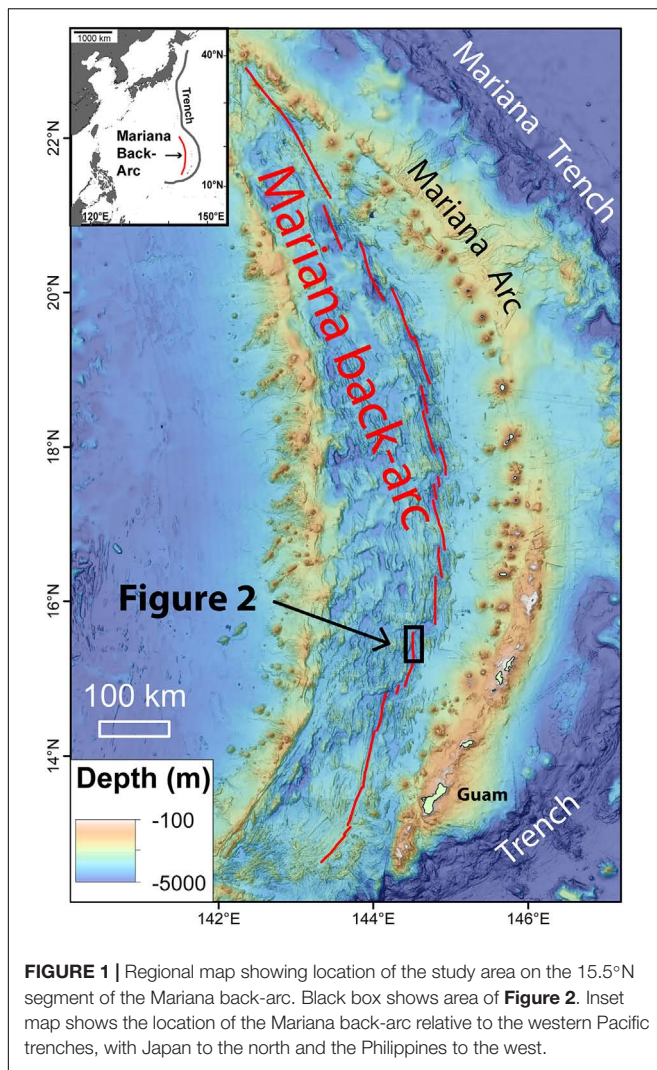
central Mariana back-arc. The only other known historical submarine eruptions on back-arc spreading centers are on the NE Lau Spreading Center (NELSC), including one discovered in November 2008 when hydrothermal event plumes were encountered by chance in the overlying water column during a regional survey (Baker et al., 2011; Rubin et al., 2012), and eruptions near Tatu cone on the NELSC that were recently discovered by before-and-after bathymetric surveys and confirmed by ROV dives (Rubin et al., 2018a,b).

Here, we describe the physical setting of the recent eruption site, constrain the timing of the eruption to within a 3-year period based on before-and-after surveys, show high-resolution bathymetry and ROV visual observations of the young lava flows that provide information about their emplacement, and present observations and sensor data that show a rapidly diminishing hydrothermal system associated with the new lava flows. These results confirm the value of collecting repeated ship-based bathymetry in potentially active submarine volcanic settings for detecting eruptions, illustrate how AUV-based high-resolution bathymetry helps interpret submarine lava flow morphology and emplacement, and reveal that some segments of the Mariana back-arc have active magmatic systems, despite the relatively low spreading rate.

Geologic Setting

The Mariana back-arc spreading center is an example of upper plate spreading in an oceanic subduction setting (Fryer, 1995; Stern et al., 2003). Here the Pacific plate subducts beneath the Philippine Sea plate forming the Mariana trench and the active volcanic arc, which is made up of nine islands and over 60 seamounts, a third of which are hydrothermally active (Embley et al., 2007; Baker et al., 2008; Resing et al., 2009). The Mariana back-arc spreading center is located to the west of the volcanic arc and transitions from a relatively shallow ridge in the south (~ 3000 m bsl) to a series of deep basins (up to 5000 m bsl) north of 13°N that are segmented and arranged in an en-echelon pattern (Figure 1).

In this paper, we focus on the Mariana back-arc segment centered at 15.5°N [following the naming scheme of Anderson et al. (2017)], which has a spreading rate of ~ 25 –40 mm/yr (Kato et al., 2003). This segment is ~ 34 km long, with an axial valley that is ~ 22 –25 km wide, with a maximum depth that ranges from 4650 m bsl in the south to 4350 m bsl in the north (Figure 2). The neovolcanic zone is dominated by hummocky volcanic morphology with little or no faulting and has an axial



volcanic ridge that rises up to ~ 1050 m above the surrounding seafloor with a shallowest depth of 3820 m bsl near 15.5°N (Anderson et al., 2017). Anderson et al. (2017) classified this segment as a tectonic segment currently undergoing magmatic extension, where extension is accommodated by the intrusion of dikes, and the morphology is characterized by an axial valley with moderate-to-high relief at the segment center (600–1300 m), a prominent hummocky axial volcanic ridge (800–1050 m) without a central graben, and limited faulting within the axial valley. Anderson et al. (2017) also calculated the volume of neovolcanic material on this segment as a first-order estimate of eruption rates and magma supply, in comparison to the other segments in the Mariana back-arc. Interestingly, the 15.5°N segment had the second-lowest calculated eruption rate per kilometer ($3912 \text{ m}^3/\text{yr}/\text{km}$) of all the segments in their study area (from 12.7°N to 18.3°N). So, in some ways, this segment was the least likely to have hosted a recent eruption. However, the calculated long-term eruption rate is based on its morphology produced by activity over perhaps the last 100,000 years. In contrast, the recent eruption is a manifestation of the present-day (or very

recent) magma supply. Therefore, the recent eruption on this segment is consistent with the characterization that the segment is undergoing recent magmatic rejuvenation, as is the discovery of high-temperature black-smoker vents at the Perseverance vent field located on the along-axis high just 5 km north of the eruption site (**Figure 2**; Baker et al., 2017; Butterfield et al., 2018; Chadwick et al., 2018).

Discovery of the Recent Eruption Site at 15.4°N in December 2015

The search for new hydrothermal vent sites along the southern Mariana back-arc during the FK151121 expedition included first using a towed Conductivity, Temperature, Depth (CTD) instrument package. The CTD was raised and lowered from 10 s to several hundred meters above the seafloor as the ship slowly drove forward, resulting in the CTD producing a saw-tooth path in a vertical 2D profile above the seafloor along the tow track (Baker et al., 2017). Where hydrothermal plumes were

discovered with the CTD, we deployed the *Sentry* to collect high-resolution bathymetry in those areas, which was used later when ROV dives were made to localize the source of the plume on the seafloor. Hydrothermal plumes can be detected by CTD sensors that measure temperature, light scattering [turbidity (ΔNTU , Nephelometric Turbidity Units) from hydrothermal particles], and oxidation reduction potential [or ORP (ΔE), for detecting reduced chemicals such as Fe_2+ , HS^- , H_2]. On the *Sentry* mapping dives these same sensors were housed in a self-contained instrument called a Miniature Autonomous Plume Recorder, or MAPR (Walker et al., 2007). The MAPR data from the *Sentry* dives were complementary to the CTD data (Walker et al., 2016a; Baker et al., 2017).

CTD tow T15B-06 was conducted along the axis of the back-arc segment centered at $15.5^\circ N$ (Figure 2), and revealed two plumes with distinctly different character (Figure 3). To the south of the highest part of the segment, between $15^\circ 23.4'$ to $15^\circ 27.6' N$ a plume was detected with relatively low ΔNTU values but high ΔE values. Further north, between $15^\circ 27.6'$ to $15^\circ 33.0' N$, the opposite was found in a plume that had relatively high ΔNTU values and lower ΔE values (Figure 3). This was interpreted as evidence for low-temperature diffuse venting in the south and high-temperature focused venting in the north (Baker et al., 2017).

To investigate further, we deployed *Sentry* for dive 367, which collected multibeam sonar and plume data in a 2×3.5 -km area at an altitude of 70 m above the bottom, and then conducted a photo survey at a lower altitude of 5 m over a smaller area ($500 \text{ m} \times 1000 \text{ m}$) centered on the highest ΔE anomaly from the CTD tow (Figure 4). We had anticipated that we might photograph some vent animals at a diffuse venting site, but unexpectedly

the *Sentry* photo survey revealed pristine young pillow lavas covering some of the area (Figures 5a,b). The young lava flow was dark, glassy, and completely lacking in any sessile animals or even pelagic sediment. A very light dusting of hydrothermal sediment could be seen in a few areas at the tops of pillow mounds (Figure 5c), and within one of those areas a cloud of milky hydrothermal fluid was photographed coming out of the flow (Figure 5d). The surrounding lava flows are clearly much older with a few cm of sediment completely mantling the lava lobes (Figure 5e). On the eastern edge of the photo survey, in low-lying areas below 4300 m bsl that are noticeably more faulted, the older seafloor is locally completely buried by sediment (Figure 5f).

The MAPR data collected by *Sentry* during dive 367 (Walker et al., 2016b) showed multiple ΔE anomalies indicative of hydrothermal venting in the western half of the survey area during the mapping at 70 m above bottom (Figure 4A). During the photo survey at 5 m altitude, a large ΔE anomaly was recorded at the same time and location that the milky vent fluid was photographed (Figure 4B). The photograph of active venting and the number of anomalies detected by the MAPR on *Sentry* suggest that the lava flows were young enough to be still warm and actively cooling (implying the lavas were only months to years old). On the other hand, chemical analysis of water samples from the CTD tow over the young lava flows showed low levels of hydrogen, indicating that the eruption had ended at least days to weeks beforehand. Active submarine eruptions produce high levels of hydrogen from magma-water interaction, which has a short residence time in the water column (McLaughlin-West et al., 1999; Lilley et al., 2003; Baker et al., 2011; Resing et al., 2011; Baumberger et al., 2014). The 1-m resolution bathymetry collected by *Sentry* during dive 367 shows

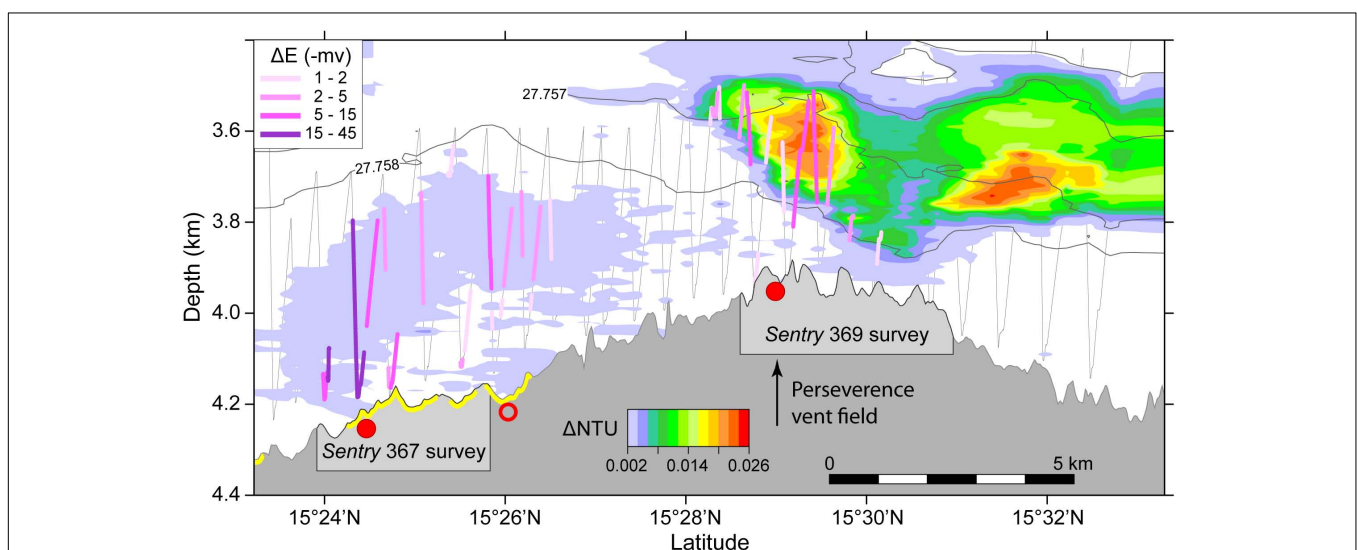


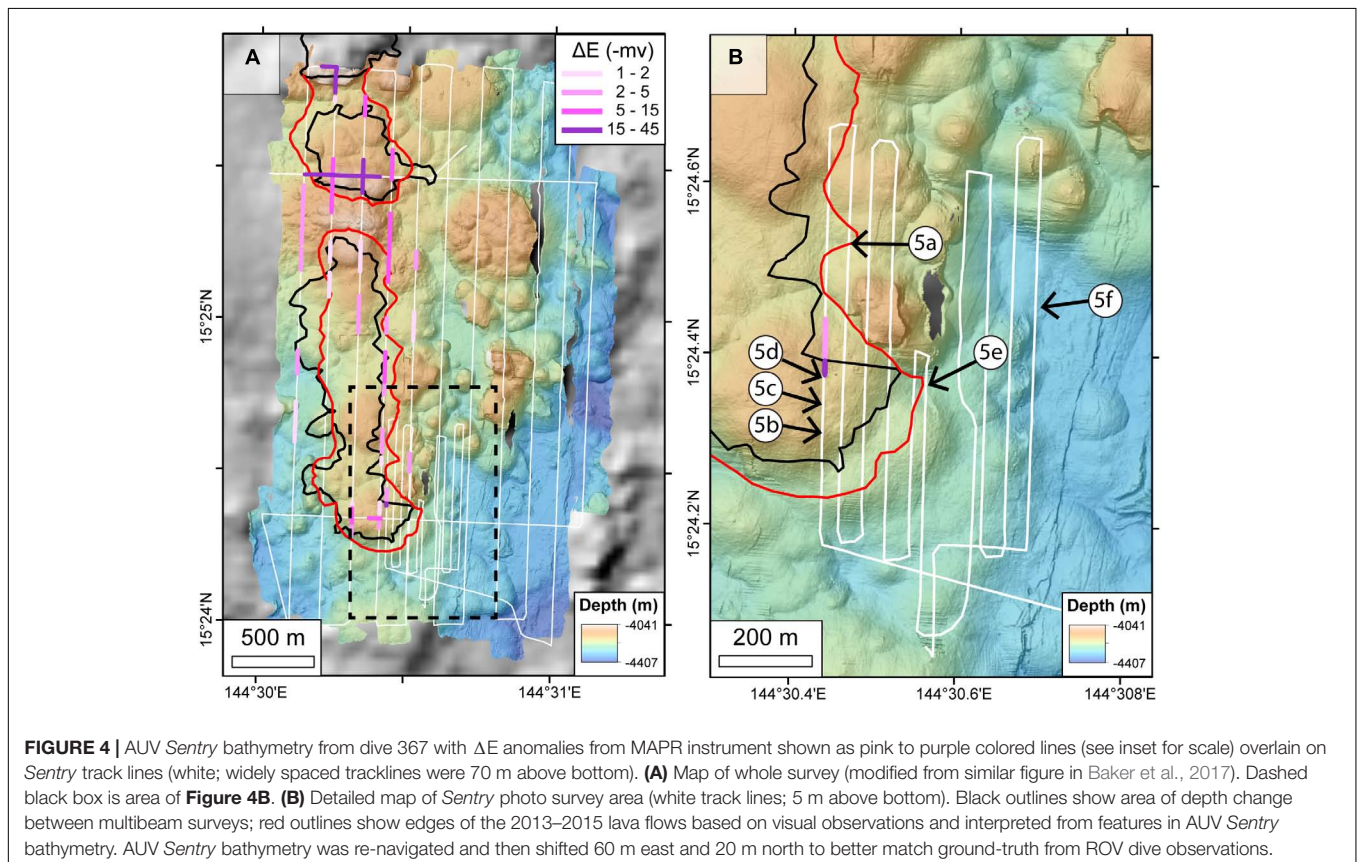
FIGURE 3 | Depth cross-section along the axis of the $15.5^\circ N$ segment of the Mariana back-arc showing data from CTD tow T15B-06 (from Baker et al., 2017). Gray is seafloor profile. Colors above seafloor show turbid particle plumes as ΔNTU anomalies. Colored lines along CTD tow path (gray zigzag lines) show ΔE anomalies in millivolts from ORP sensor (see inset for scale). Red dots are confirmed (solid) or inferred (open) hydrothermal sites from Baker et al. (2017). Yellow highlight on the bathymetry profile indicates extent of new lava flows. Note relatively high ΔE but low ΔNTU anomalies over new lava flows, and high ΔNTU and lower ΔE anomalies over northern-most hydrothermal site, at the Perseverance vent field with black-smoker chimneys.

that the areas within the young lava flow photographed by *Sentry* have smooth (unfaulted) hummocky morphology, typical of pillow lava mounds (**Figure 4B**).

To constrain the age of the young lava flow eruption, we compared (post-eruption) ship-based multibeam bathymetry collected by *R/V Falkor* with its EM302 sonar system on 01 December 2015 [expedition FK151121 (Resing, 2016b)], with the last survey of the area collected by *R/V Melville* with its EM122 sonar on 14 February 2013 (expedition MV1302a). Comparing the two surveys revealed a string of five areas with maximum depth change from 40 m up to 138 m (**Table 1**), extending over a distance of 7.3 km along the back-arc spreading axis from latitude 15°22.3' to 15°26.3'N (**Figure 6**). The cross-axis width of these depth changes was 200–800 m. For convenience, we number the areas of depth change 1 to 5, from north to south (**Table 1**). The third area of depth change includes the area photographed and mapped by *Sentry* (**Figures 4, 6**). The timing of the eruption can be bracketed within the 2.8-year period between the two bathymetric surveys. However, the fact that the young flows were still emitting hydrothermal fluids when first photographed suggests that the eruption was probably late within that time period (Baker et al., 2018). A search for anomalous seismicity in the area that might have narrowed the eruption time window further did not uncover any unusual activity¹, so the eruption was not detected remotely.

¹ Matt Haney, USGS, personal communication, 2015.

The 2013–2015 eruption is the deepest known historical submarine volcanic eruption, and extends over a depth range of 4050 to 4450 m bsl. The post-eruption bathymetry, the photo survey, and the relatively large magnitude of the depth changes between the surveys indicates that the eruption produced a chain of hummocky pillow lava mounds, which commonly accumulate to thicknesses of tens to over 100 m in divergent plate boundary settings (Caress et al., 2012; Yeo et al., 2012; Chadwick et al., 2013; Yeo et al., 2013; Chadwick et al., 2016; Clague et al., 2017). The outlines of the depth changes (and young lava flows) shown in **Figure 6** are minimum areas, since the detection threshold used was a depth difference of 5 m, and therefore any areas where the flow thickness is less than that (including flow margins) are not resolved. For example, observations from later ROV dives show that some of the separate areas of depth change are actually connected by young lavas (described below). Nevertheless, the before-and-after bathymetry can be used to constrain the thickness and area of the lava flows and the volume of lava erupted (**Table 1**). Our analysis shows that the total area of the young flows is $1.81 \times 10^6 \text{ m}^2$ and the total eruptive volume was $66.3 \times 10^6 \text{ m}^3$. For comparison, this volume is larger than all the previously documented historical eruptions on the Juan de Fuca and Gorda spreading ridges in the NE Pacific, except for the 2011 and 2015 eruptions at Axial Seamount, which is a hot spot volcano superposed on the Juan de Fuca spreading ridge (Chadwick et al., 1998; Rubin et al., 2012; Yeo et al., 2013; Clague et al., 2017).



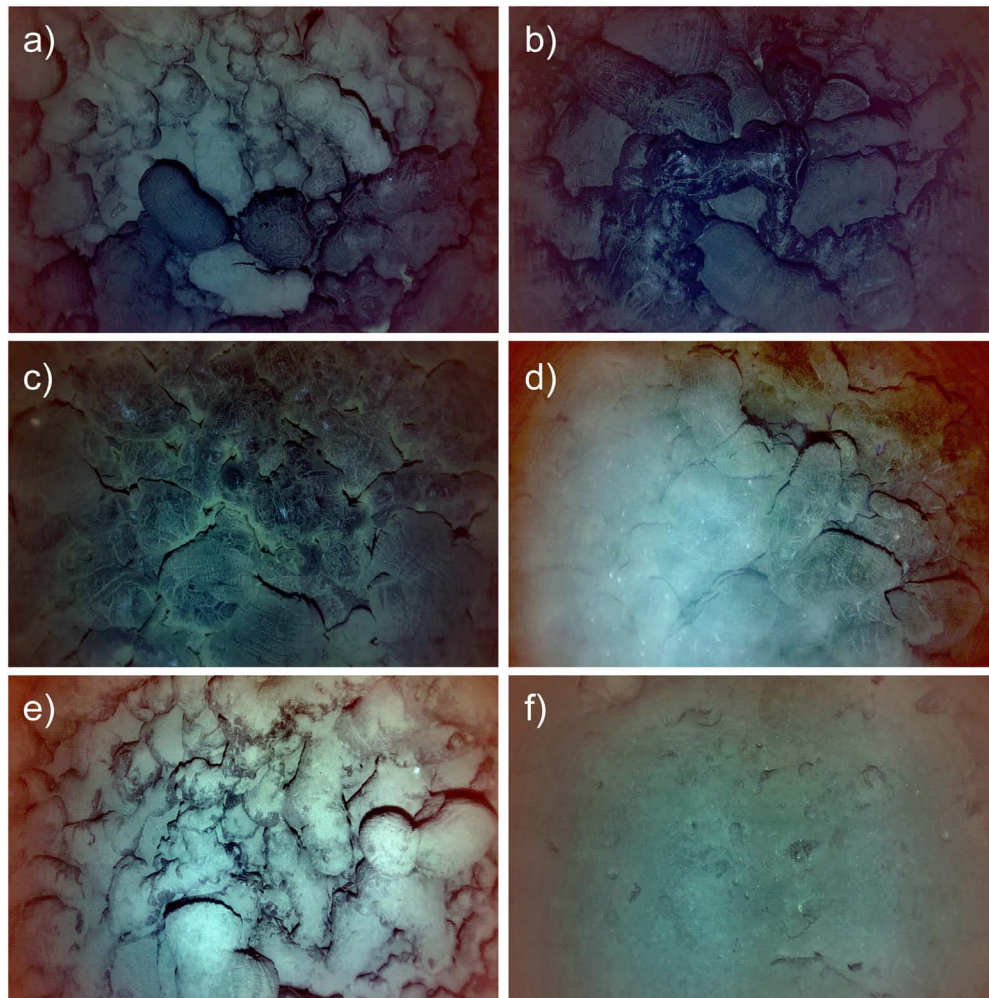


FIGURE 5 | Images from AUV *Sentry* dive 367 photo survey on 03 December 2015 showing young lava flow, evidence of hydrothermal venting, and surrounding older seafloor. Horizontal dimension of photos is ~5 m. See **Figure 4B** for photo locations. Numbers in parentheses are time of photo in GMT. **(a)** Contact between young and old lava (07:33:20), **(b)** glassy young pillow lava (07:03:43), **(c)** hydrothermal sediment on young flow (07:04:43), **(d)** milky hydrothermal venting from young flow (07:05:53), **(e)** surrounding older lava (09:42:10), **(f)** older seafloor at east edge of survey with almost complete sediment cover (12:05:26).

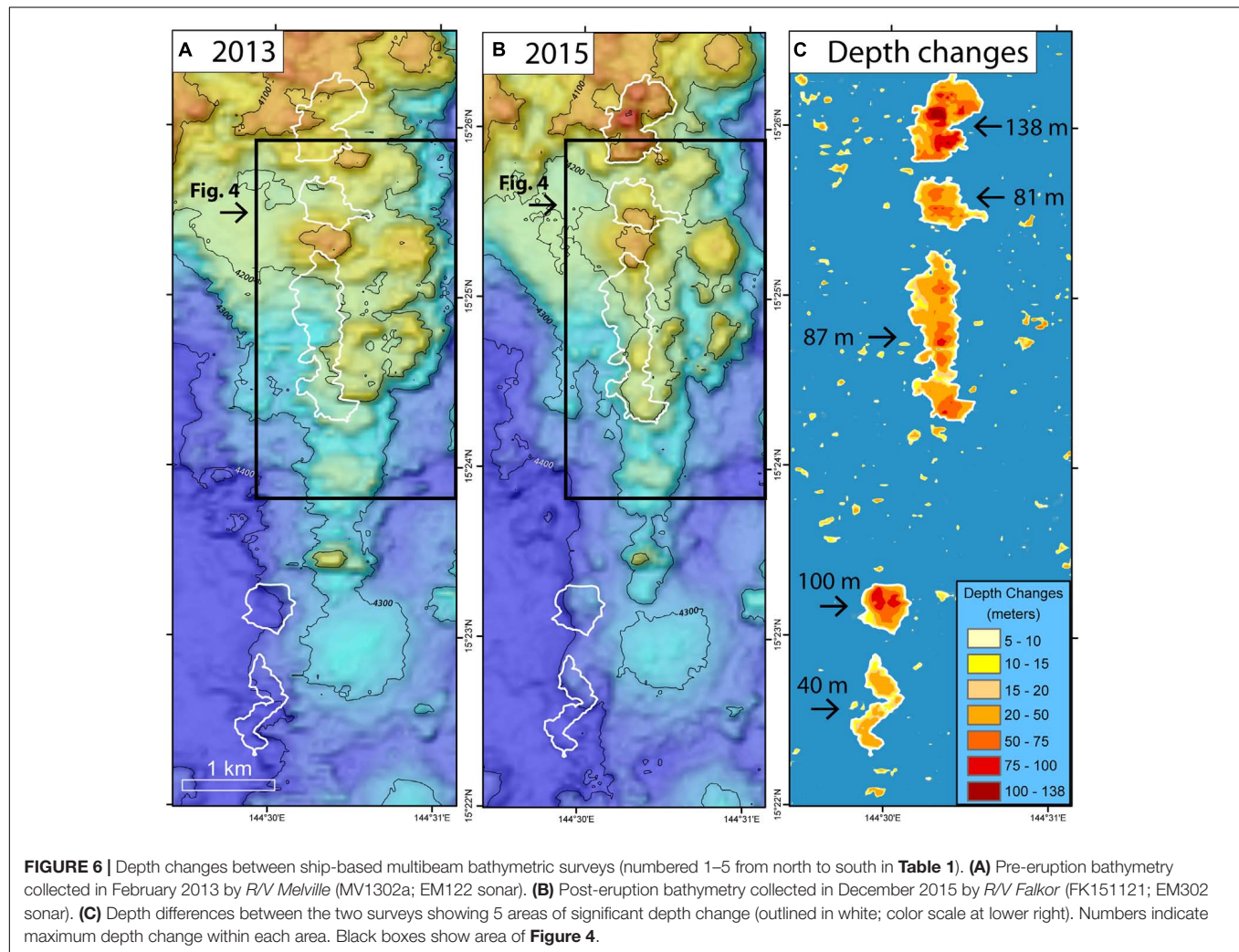
The area surveyed during AUV *Sentry* dive 367 (Resing, 2016a) covered part of the northern half of the chain of lava flows along the back-arc spreading axis (covering the second and third areas of depth change), but did not extend all the way to the northern end where the thickest of the flows was located (**Figures 4, 6**). Superposing the outlines of the areas of depth change determined by the ship-based bathymetric comparison on the high-resolution *Sentry* bathymetry shows that all the ΔE anomalies recorded by the MAPR on *Sentry* were located over relatively thick accumulations of lava (**Figures 4, 6**). The *Sentry* bathymetry also shows that the hummocky flows produced by this most recent eruption (on the west side of the *Sentry* survey area) are very similar in morphology to previous eruptions along this segment of the back-arc (on the east side of **Figure 4A**). In fact, it would be impossible to map the boundaries of 2013–2015 lava flows on the AUV bathymetry without the additional information from multibeam depth changes and the visual

observations. In general, the young lava flows have a smooth but hummocky morphology in the AUV bathymetry, which shows that they were emplaced from multiple local eruption centers along a N-S fissure system. The *Sentry* photo survey was fortuitously located spanning the southeastern edge of the third area of depth change (**Figure 4B**). The navigation of AUV *Sentry* dive 367 bathymetry was reprocessed using mbsystem navadjust software (Caress and Chayes, 2016) based on matching features in overlapping swaths, and then was shifted 60 m east and 20 m north to best match the ship-based EM302 bathymetry. The location of the edge of the young lavas mapped by the *Sentry* data and the ROV dives (described below) compared to the areas of depth change between bathymetric surveys gives an idea of the uncertainty in the ship-based multibeam comparison method. The lava flow boundary mapped by visual ground truth (red lines in **Figure 4**) is generally within 50–100 m of the depth change boundary (black outlines in **Figure 4**).

TABLE 1 | Estimates of the thicknesses, areas, and volumes of new lava flows, based on depth changes between 2013 and 2015 bathymetric surveys.

Area name	Mean depth change (lava thickness) in meters	Maximum depth change (lava thickness) in meters	Area of depth change ($\times 10^6 \text{ m}^2$)*	Volume of depth change ($\times 10^6 \text{ m}^3$)*
Area 1	48	138	0.468	22.488
Area 2	32	81	0.246	7.989
Area 3	32	87	0.681	21.854
Area 4	47	100	0.207	9.726
Area 5	20	40	0.213	4.198
Totals			1.815	66.255

* The areas and volumes of depth change are minimum estimates of the areas and volumes of the new lava flows, since they do not include the thin margins of the flows.



Visual Characterization of the 2013–2015 Lava Flows and Changes Over Time

After the discovery of the recent eruption site in December 2015, two later expeditions with ROVs visited the site in 2016: NOAA ship *Okeanos Explorer* cruise EX1605L1 with ROV *Deep Discoverer* (D2) in April 2016, and *R/V Falkor* cruise FK161129 with ROV *SuBastian* in December 2016. Each expedition made one ROV dive on the new lava flows, which allowed for visual

observations over different parts of the eruption site, sampling of the lava flows, and a search for evidence of any on-going hydrothermal activity.

ROV *Deep Discoverer* (D2) made dive EX1605L1-09 on 29–30 April 2016 on the northern-most and thickest of the 2013–2015 lava flows (**Figure 7**), for which we only have ship-based bathymetry (~40 m resolution), because it is north of the *Sentry* survey. The ROV dive made a north-to-south zig-zag traverse

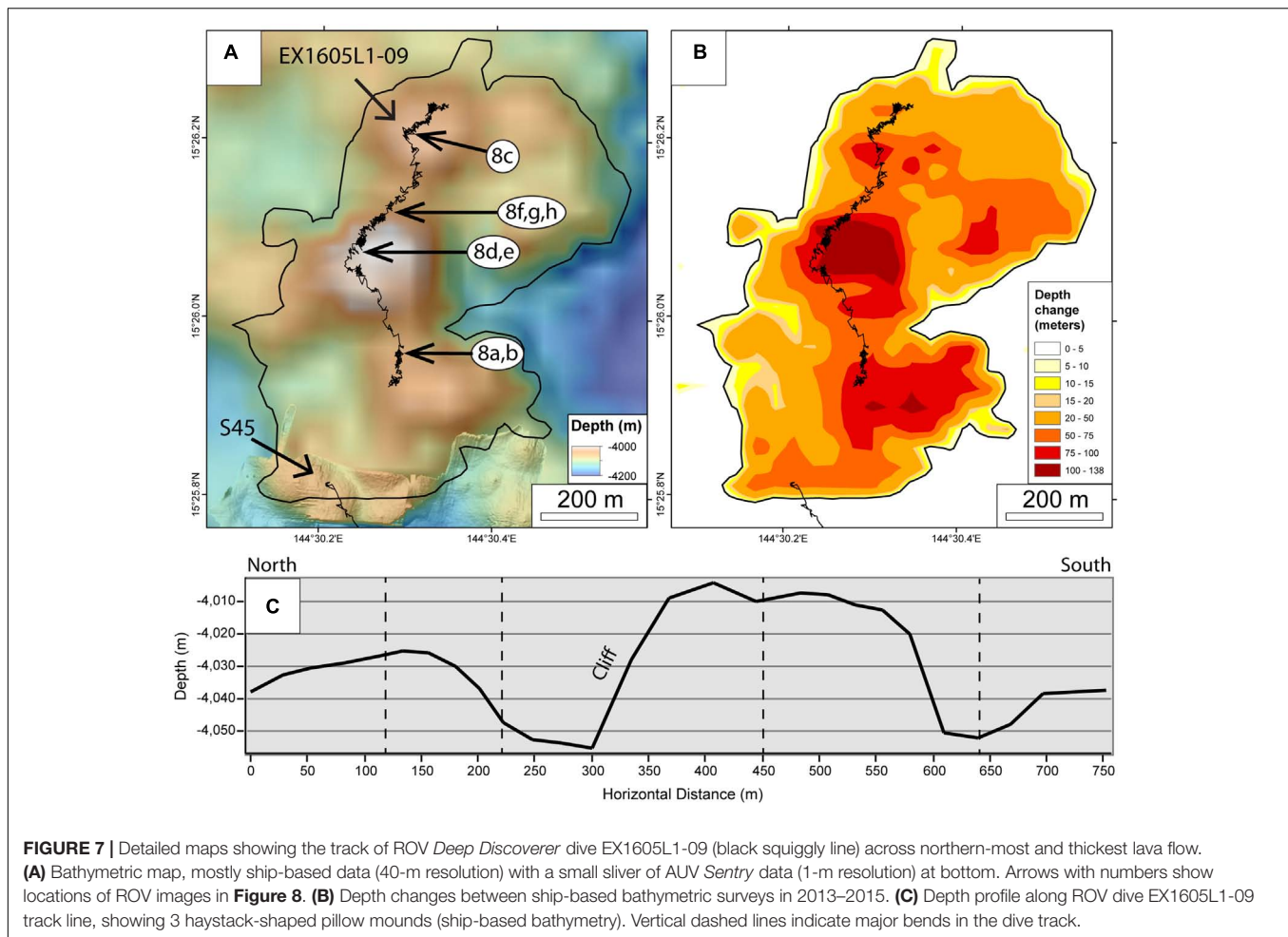


FIGURE 7 | Detailed maps showing the track of ROV *Deep Discoverer* dive EX1605L1-09 (black squiggly line) across northern-most and thickest lava flow. **(A)** Bathymetric map, mostly ship-based data (40-m resolution) with a small sliver of AUV *Sentry* data (1-m resolution) at bottom. Arrows with numbers show locations of ROV images in **Figure 8**. **(B)** Depth changes between ship-based bathymetric surveys in 2013–2015. **(C)** Depth profile along ROV dive EX1605L1-09 track line, showing 3 haystack-shaped pillow mounds (ship-based bathymetry). Vertical dashed lines indicate major bends in the dive track.

over three haystack-shaped mounds of young pillow lavas, each 50–100 m high and 200–400 m wide, along a horizontal traverse of ~750 m, during ~5.5 h of time on the bottom. The second of the three mounds has the thickest accumulation of pillow lavas, with a maximum depth difference of 138 m, although the ROV track skirted the very thickest part (**Figure 7**). The pillow lavas on the relatively steep sides of the mounds frequently were decorated with an extraordinary number of extremely glassy “buds” or “fingers” of lava (5–10 cm in diameter) extending outward for a few 10s of cm from the main pillow tubes (0.5–1.0 m in diameter) (**Figures 8a,b**). These are similar to the “knobby pillows” described by Ballard and Moore (1977) on the mid-Atlantic ridge, interpreted to be indicative of faster flow rates on the steeper flanks of pillow constructs. The flanks of the mounds had little or no hydrothermal sediment on the lava. In contrast, the tops of the pillow mounds had much broader and flatter pillows and were commonly dusted with low-temperature hydrothermal sediment composed mainly of iron oxy-hydroxide, which locally accumulated into thicker deposits between the lobes (**Figures 8c,d**). The pillow mounds were topped with small conical constructs that were ~10 m high and ~5 m in diameter and formed of radiating pillow tubes (**Figures 8d,e**), apparently representing late-stage eruption centers. These are

similar to the “pillowed cones” described in Ballard and Moore (1977).

The north slope of the second, thickest mound was nearly vertical and consisted of a mix of intact and truncated pillows (**Figures 7, 8f**), with an apron of talus at the bottom consisting of pillow fragments (**Figure 8g**). The talus was likely primary and formed by auto-brecciation during lava flow emplacement and mound construction, rather than due to later tectonism. Beyond the apron of talus, smaller angular glassy fragments were deposited on top of pillow lavas and extended outward for 50–75 m from the base of the cliff (**Figure 8h**), a more distal component of auto-brecciation, also formed by pillow fragments tumbling down the cliff. The dive started and ended within the new lavas and no contacts with older lavas were seen.

During the dive we saw one area of noticeable diffuse hydrothermal venting where we measured a temperature of 7.0°C with the ROV’s temperature probe, well above the ambient temperature of 1.65°C (**Figure 9a**). Vent endemic species were commonly sighted throughout the dive, including polychaetes (**Figure 9b**), shrimp (**Figure 9c**), and squat lobsters (**Figure 9d**). This is additional evidence that the lava flows were still actively cooling in April 2016, and had hosted diffuse hydrothermal venting long enough to be colonized by mobile vent animals,

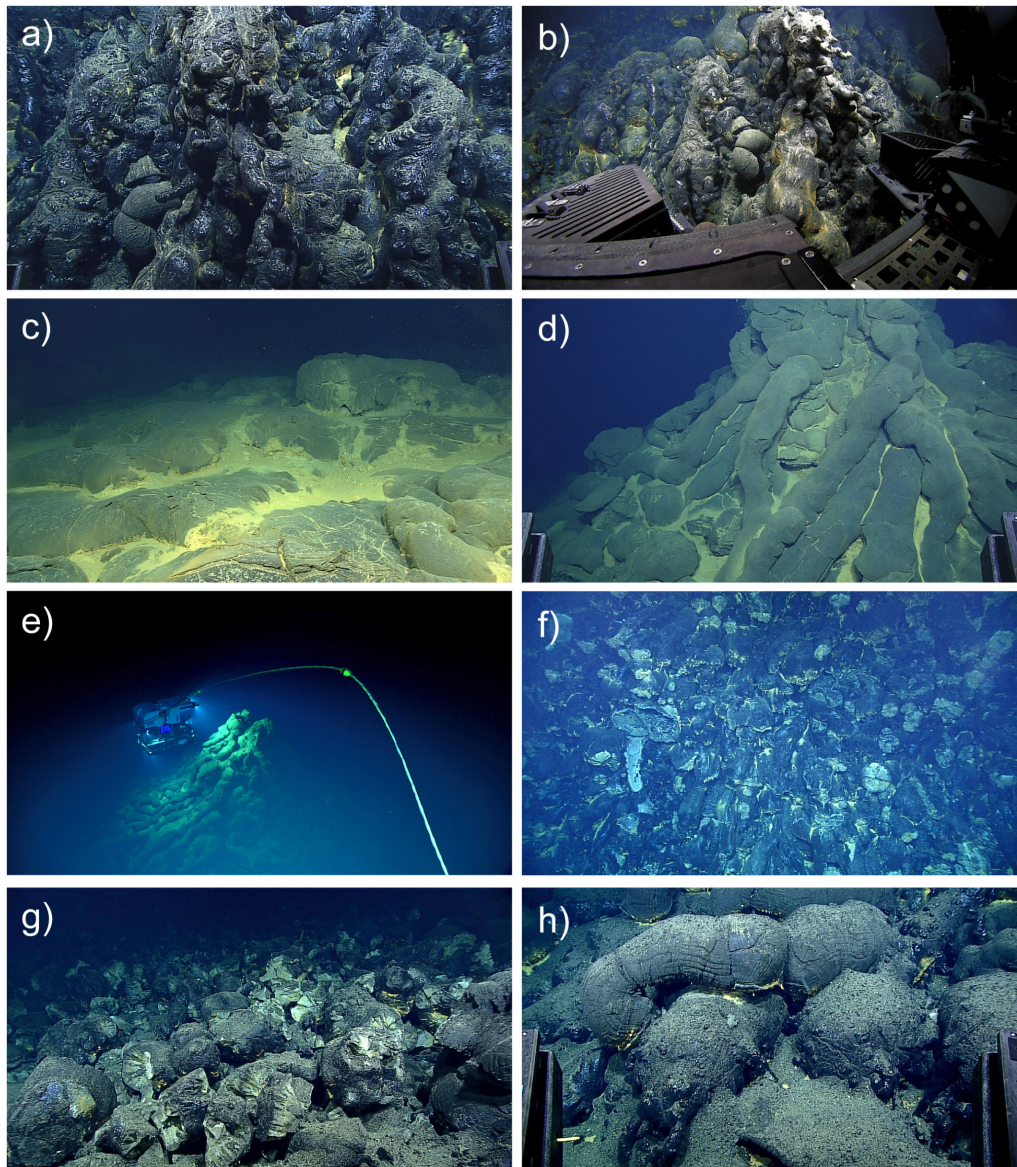


FIGURE 8 | Images from ROV *Deep Discoverer* dive EX1605L1-09 on 29–30 April 2016, which crossed the northern-most and thickest of the 2013–2015 lava flows. See **Figure 7** for photo locations. Numbers in parentheses are time of photo in GMT and horizontal scale. **(a)** Pillow lavas with extremely glassy finger-like buds (03:41:31, 2 m). **(b)** ROV set up to sample a glassy pillow bud (03:49:32, 4 m). **(c)** Broader lobes on top of one of the pillow mounds with hydrothermal sediment (00:03:48, 5 m). **(d)** Conical eruptive center at the top of a mound with radiating pillow tubes and hydrothermal sediment (02:43:00, 6 m). **(e)** View of ROV illuminating a conical eruptive center (02:40:20, 20 m). **(f)** Nearly vertical cliff with intact and truncated pillows (01:12:11, 10 m). **(g)** Primary pillow talus at base of cliff (01:06:06, 3 m). **(h)** Fragmental deposit on top of pillows beyond the talus apron (01:03:14, 2 m).

but not by sessile species that take longer to colonize. This is consistent with the lava flows only being months to years old when first discovered. The nearest known hydrothermal site is the Perseverance vent field located ~ 5 km to the north on the segment high (**Figures 3, 4**).

Seven months later on 12 December 2016, a second ROV dive was made during expedition FK161129 from *R/V Falkor* with ROV *SuBastian*. Dive S45 started 240 m SSE of the end of the previous ROV dive and explored areas further south where high resolution bathymetry had been collected by AUV *Sentry* a

year earlier (**Figure 10**) and where the MAPR on *Sentry* detected ΔE anomalies, indicating hydrothermal activity (**Figure 4A**). The dive started at a depth of 4045 m bsl in young lava with a light dusting of yellow hydrothermal sediment (**Figure 11a**) at the top of a pillow mound at the SW end of the northern-most area of depth change (**Figure 10**). The south side of that pillow mound was a nearly vertical cliff, over 110 m high, that was mantled by almost completely intact young pillow lavas (**Figure 11b**). The pillows on the cliff face were narrow glassy elongated tubes appearing like elephant trunks or the drips of wax

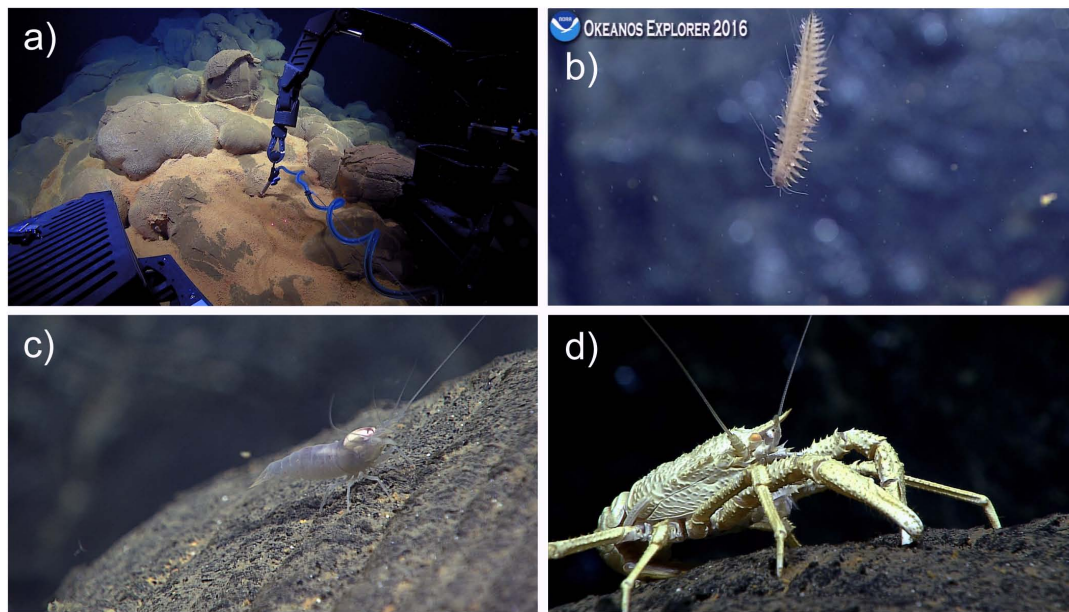


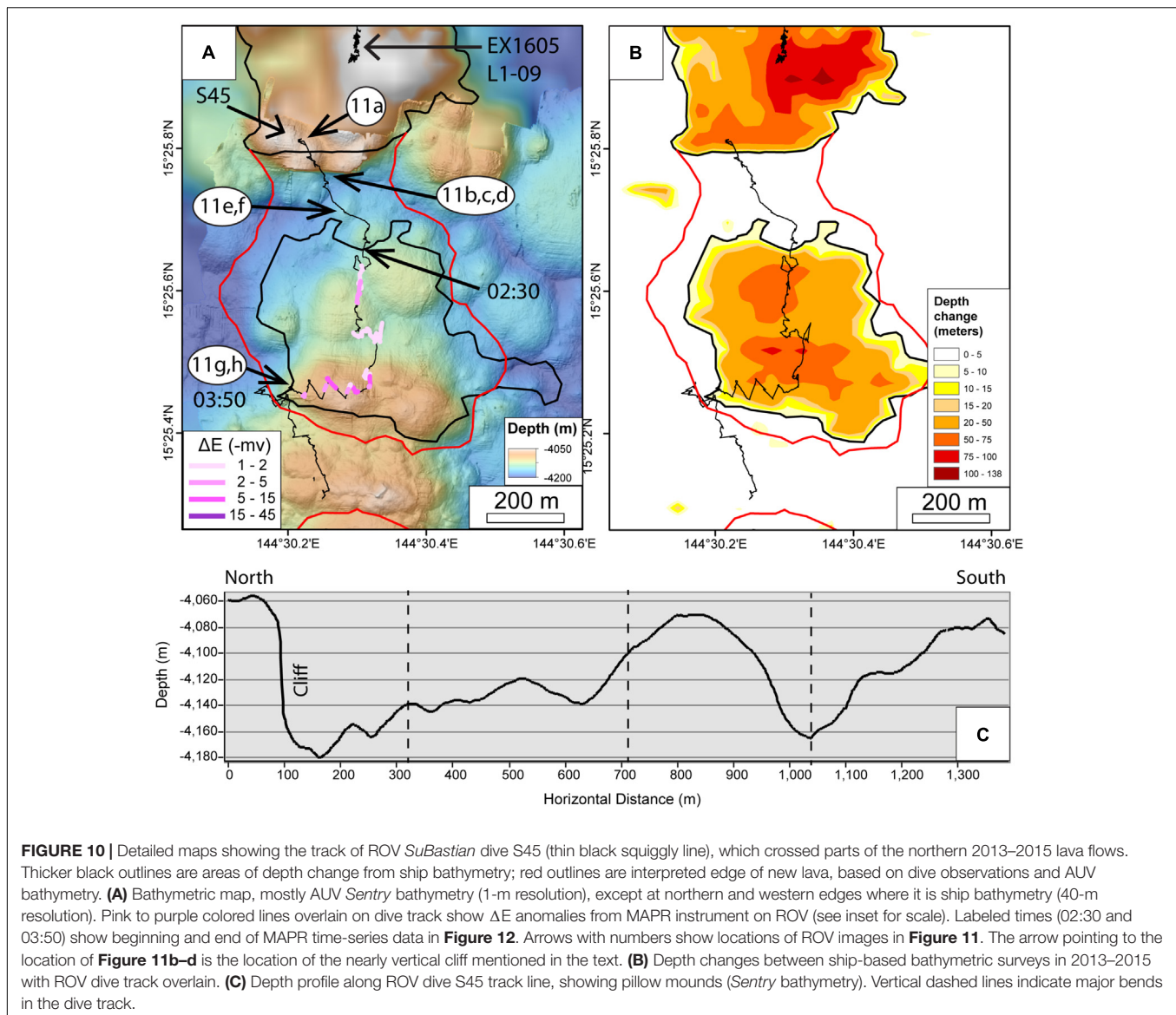
FIGURE 9 | Images of hydrothermal vent animals observed on the new lavas during ROV Deep Discoverer dive EX1605L1-09 on 29–30 April 2016. Numbers in parentheses are time of photo in GMT and horizontal scale. **(A)** ROV manipulator arm measuring temperature of 7.0°C (ambient = 1.65°C) in an area of very diffuse venting (02:17:21, ~5 m). **(B)** One of many polychaetes seen swimming above the bottom (23:03:48, ~6 cm). **(C)** Shrimp (00:11:20, ~3 cm). **(D)** Squat lobster (00:24:51, ~5 cm).

on the outside of a candle (**Figures 11c,d**). It was remarkable how little talus was at the base of the cliff, in strong contrast to the cliff encountered on the previous dive (**Figures 8f–h**), apparently because these lavas were emplaced at a higher extrusion rate so the pillows remained intact even though the lava was flowing down such a steep slope. Extrusion rate would affect the thickness of lava crusts during pillow emplacement, with more rapidly emplaced pillows more likely to have a thinner plastic crust before solidification, rather than a thicker brittle crust that is more likely to result in auto-brecciation. The location of this cliff on the *Sentry* bathymetry coincides with a navigation artifact, so on the map it appears even more steep than it actually is (**Figure 10**). The cliff on the map is between the northern-most two areas of multibeam depth change, but this ROV dive showed that young lavas are continuous and actually connect the two areas (but the lava must be relatively thin there). On **Figures 4, 10**, the red outlines show our interpreted mapping of the extent of the young lava flows, based on ROV observations and the *Sentry* high-resolution bathymetry.

South of the cliff, the ROV track crossed over several low pillow mounds, each 20–25 m high and 70–100 m wide. At the top of the first one, we found another steep-sided pillow cone representing a local eruptive center, covered with a fine dusting of hydrothermal sediment (**Figure 11e**). The high-resolution bathymetry shows that many of the pillow mounds in this area (both young and old) have these pillow cones at the shallowest points (they appear as small dimples on the map). The dive proceeded southward to the top of the highest of the pillow mounds within the second area of multibeam depth change, which is located near the southern edge of the area of depth

change, and is topped by a ridge with an E-W orientation (**Figure 10**). Here the ROV turned and headed west, zigzagging along the crest of the E-W pillow ridge and followed it down to the western contact between young and old lavas (**Figures 11g,h**). There, the young lavas were again characterized by larger pillows with many glassy pillow buds. The remainder of the dive continued south onto an older pillow ridge that separates the second and third areas of depth change (**Figure 10**). The older lavas had moderate sediment accumulation and were colonized by sessile animals such as sponges, anemones, and crinoids (**Figures 11g,h**). The dive covered 1.6 km on the bottom in 3.75 h (twice as far as the ROV D2 dive in less time), but the dive had to be terminated early due to deteriorating weather.

While traversing over the younger lavas during ROV *SuBastian* dive S45, we saw several areas with thick accumulations of yellow hydrothermal sediment (**Figure 11f**), but no visible fluid flow (shimmering water). However, we had a MAPR instrument on the ROV and the data show minor temperature and ΔE anomalies in the areas with thick hydrothermal sediment (**Figure 12**) especially on the E-W pillow ridge near the end of the dive, indicating that hydrothermal fluids must still have been seeping out, but so diffusely that they were not visible. Although the two ROV dives were in different (but adjacent) areas, the observations are consistent with a rapidly waning hydrothermal system as the lava flows were cooling in the aftermath of the eruption. *Sentry* saw robust ΔE anomalies 70 m above the lava flows in December 2015, then ROV D2 found only one area of visible venting and elevated temperature on the flows in April 2016, and finally ROV *SuBastian* did not encounter any visible diffuse flow,



but still detected barely measurable instrumental anomalies near the seafloor. Likewise, CTD tow T15B-06 and vertical cast V15B-06 in 2015 showed the rise height of ΔE anomalies was > 400 m above bottom (**Figure 3**), whereas CTD cast V16A-03 in 2016 near the same location had only a weak ΔE anomaly at less than 100 m above bottom. In terms of biological colonization, on ROV *SuBastian* dive S45 we saw some of the same vent-endemic animals as on the previous ROV D2 dive (polychaetes, shrimp, and squat lobsters), but in much fewer numbers, also consistent with a rapidly waning hydrothermal system. All these observations suggest that the eruption occurred relatively late in the 2013–2015 time window constrained by the multibeam sonar surveys. They also imply that the hydrothermal activity from the lava flows was likely temporary and short-lived, consistent with observations of the hydrothermal response after multiple eruptions at Axial Seamount (Chadwick et al., 2013; Baker et al., 2018).

DISCUSSION

This study was a fortuitous outgrowth of a large-scale exploration of the spreading axis of the southern Mariana back-arc for new hydrothermal vent sites between 13 and 18.2°N, an area that had not been systematically surveyed previously. The discovery of the new vent sites (Baker et al., 2017) and characterization of their chemistry and biological communities (Tunnicliffe et al., 2017; Butterfield et al., 2018) will fill a knowledge gap to help interpret the biogeography of the region and the connections between geology, chemistry, and chemosynthetic ecosystems (Chadwick et al., 2018). Understanding such links will have important implications for management plans of the Mariana Trench Marine National Monument.

Judging from the relatively low spreading rate of the central Mariana back-arc segments [~ 25 – 40 mm/yr (Kato et al., 2003)], individual eruptions would be expected to be relatively rare

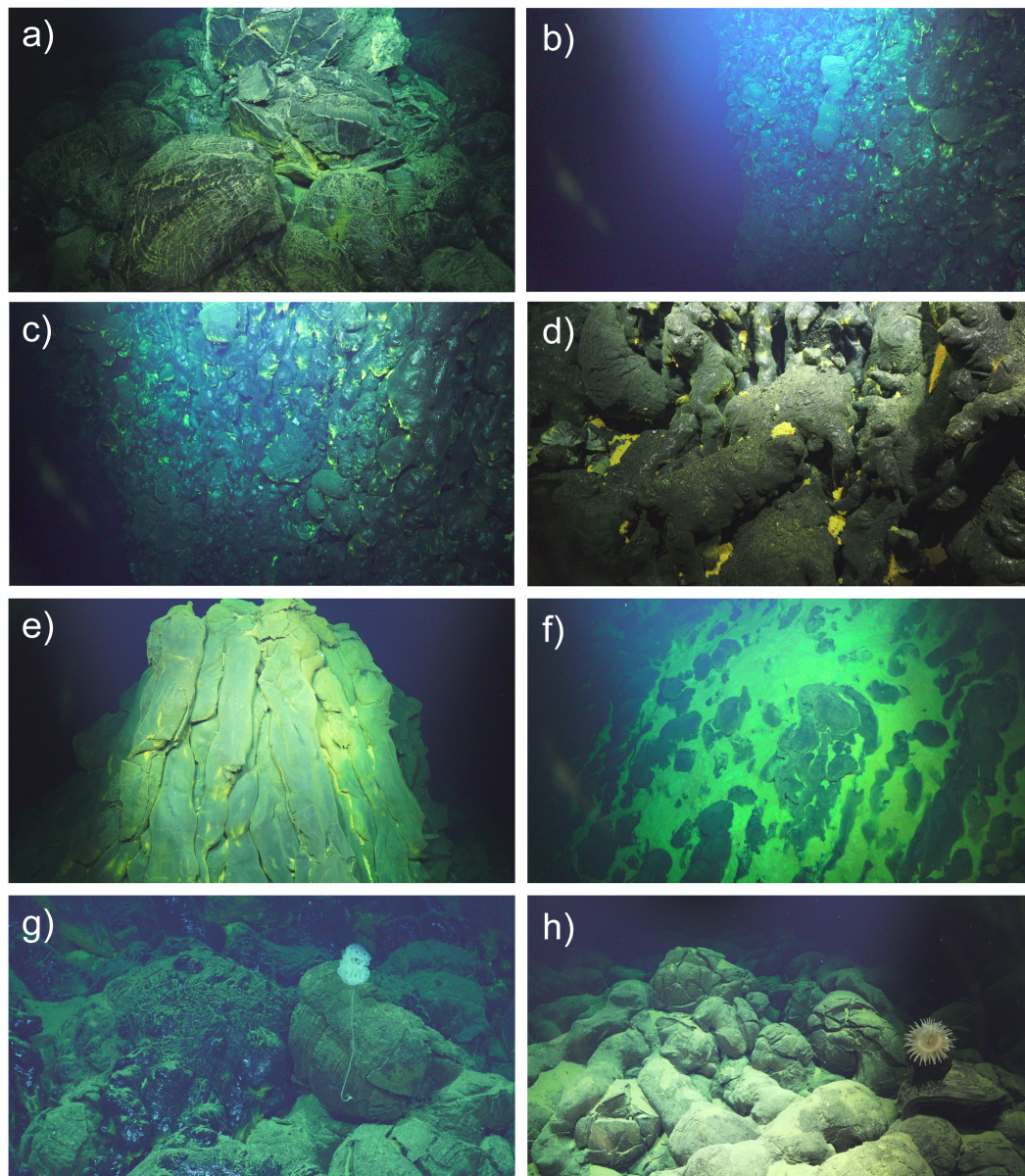


FIGURE 11 | Images from ROV *SuBastian* dive S45 on 12 December 2016. See **Figure 10** for photo locations. Numbers in parentheses are time of photo in GMT and horizontal scale. **(a)** Young pillow lava at the top of a mound at the beginning of the dive (01:31:24, 4 m). **(b)** Nearly vertical cliff mantled by intact young pillow lavas (01:47:42, 15 m). **(c)** Glassy narrow pillow tubes on the cliff face (01:48:26, 12 m). **(d)** Close up of glassy pillow buds about mid-way down the cliff face (01:57:36, 2 m). **(e)** Pillow cone atop a low pillow mound dusted with yellow hydrothermal sediment (02:14:58, 8 m). **(f)** Locally thick accumulation of hydrothermal sediment on a young pillow mound (02:21:05, 10 m). **(g)** Western contact of the young lavas (glassy in upper left) with surrounding older lavas (with sponge attached at lower right) (04:19:45, 5 m). **(h)** Surrounding older lavas with anemone attached (04:22:14, 5 m).

(perhaps only every 100 years or more). On the other hand, Baker et al. (2017) point out that back-arc basins can have both enhanced incidence of hydrothermal venting and an enhanced magma supply where they are close to adjacent magmatic arcs, although this back-arc segment is not particularly close to the Mariana arc. In any case, it was surprising to discover fresh new lava flows on the 15.5°N segment of the Mariana back-arc. There have been relatively few deep-sea (>500 m depth) eruptions documented worldwide (<40), due to the difficulty in detecting

them far away from land-based sensor networks (Dziak et al., 2012; Rubin et al., 2012), despite the fact that ~75% of Earth's volcanic output is in the oceans (Crisp, 1984). That makes finding and characterizing recent deep-sea eruptions rare, valuable, and informative. The investigation of these historical eruption sites provides information on the frequency of eruptions, their volumes, and their chemical and biological impacts in the deep-sea. They also give us a glimpse of the fundamental process of seafloor spreading and ocean crust formation.

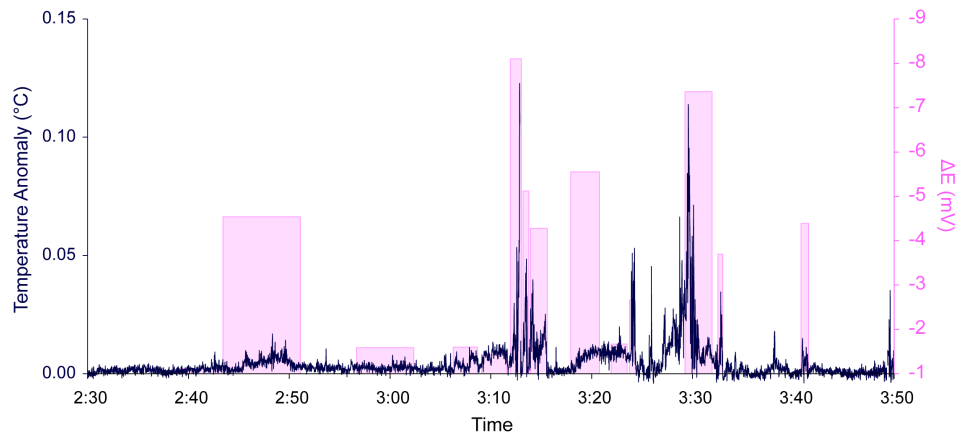


FIGURE 12 | Time-series data from MAPR instrument on ROV *SuBastian* dive S45 showing that temperature and ΔE anomalies (black line and pink bars, respectively) are well-correlated, providing evidence of weak hydrothermal activity associated with the new lava flow. The largest anomalies are where the ROV crossed over the thickest parts of the pillow mound within the second area of depth change (see **Figure 10**). This was the same time interval when thick accumulations of hydrothermal sediments were observed (**Figure 11f**) along with occasional sightings of vent fauna.

It is known from laboratory analog experiments that pillow lavas form at relatively low extrusion rates whereas sheet flows form at higher extrusion rates (Griffiths and Fink, 1992; Gregg and Fink, 1995). More recent studies have interpreted larger constructional volcanic features in terms of extrusion rate. For example, studies at the hotspot-influenced Axial Seamount on the Juan de Fuca ridge in the NE Pacific have used 1-m resolution AUV bathymetry and ROV observations to document a range of morphologies on lava flows erupted in 1998, 2011, and 2015 (Caress et al., 2012; Chadwick et al., 2013, 2016; Clague et al., 2017). Chadwick et al. (2013) introduced the concept of map-scale lava flow morphology to describe features that are on the scale of hundreds of meters, which are discernable in high-resolution AUV bathymetry. They proposed three types: inflated lobate flows, inflated pillow flows, and pillow mounds, mainly distinguished by the extent of a molten lava core within the interior of each flow type during emplacement. “Pillow mounds” were interpreted to be map-scale constructions without a significant molten core. Clague et al. (2017) modified this terminology and used the terms “channelized flows” and “hummocky flows” instead. The “channelized flows” of Clague et al. (2017) include the “inflated lobate flows” and “inflated pillow flows” of Chadwick et al. (2013), and are interpreted as near-vent and distal facies, respectively, of the same flow type. The “hummocky flows” of Clague et al. (2017) are pillow lavas that form mounds, coalesced mounds, or ridges. The main difference to the “pillow mounds” of Chadwick et al. (2013) is that “hummocky flows” also have small to voluminous molten cores, evident from summit collapses, levee-bounded lava ponds, surface tumuli, and off-fissure hummocky flows fed through tubes.

In this paper, we have used the terms “pillow mounds” and “hummocky flows” interchangeably, and we agree with Clague et al. (2017)’s interpretation that these flow types are commonly emplaced with molten cores in their interiors.

However, although the “hummocky flows” erupted at Axial Seamount often show more obvious morphologic evidence of a molten interior, the 2013–2015 flows on the Mariana back-arc do not. While there were clearly multiple eruption centers distributed along their lengths and widths, based on the multiple pillow-cones encountered during the ROV dives and that are evident in the *Sentry* bathymetry, there are no areas of lava drain-out and collapse or the other features described above. This, and the prevalence of locally steep constructional pillow-lava slopes in some places suggest that the Mariana back-arc hummocky flows were emplaced relatively rapidly, perhaps within a time window of only a few days. This interpretation is based on the observation that the thickest hummocky flows emplaced during the 2015 eruption at Axial Seamount, which had levee-bounded lava ponds at their summits as mapped by Clague et al. (2017), were emplaced over a time period of nearly a month, based on the duration of summit deflation (Nooner and Chadwick, 2016) and the explosion-like sounds recorded by a local network of seismometers and hydrophones (Wilcock et al., 2016; Caplan-Auerbach et al., 2017). The Mariana back-arc flows are more consistent with the observations of “lava domes” or pillow mounds on the axis of the southern East Pacific Rise by White et al. (2000) who interpreted that they formed directly over eruptive fissures over time periods of days. The discontinuous distribution of the hummocky flows along-axis on the Mariana back-arc may be evidence of pre-eruption focusing of magma within a mildly overpressurized feeder dike as it rose to the surface, similar to the discontinuous pillow mounds documented by Yeo et al. (2013) on the Juan de Fuca and Gorda ridges.

This eruption in the central Mariana back-arc produced a series of hummocky pillow lava mounds along the spreading axis that were comparable in size and morphology to other recent eruption sites at back-arc and mid-ocean ridge spreading

centers, as well as the older lavas at this site. In fact, despite being the deepest historical eruption documented thus far on Earth (>4000 m bsl), the morphology of the pillow lavas is otherwise indistinguishable from other historical eruption sites, so the greater depth and ambient pressure had no apparent effect on the processes of extrusion, flow, volcanic construction, and solidification. However, it was unusual in that it was one of the first discovered in an active back-arc setting. It was also one of the largest historical seafloor eruptions in terms of volume, $66.3 \times 10^6 \text{ m}^3$ based on before-and-after bathymetric surveys, but that may also reflect the small number of documented submarine eruptions to date. Smaller eruptions are probably more frequent, and if so larger less frequent events will only become apparent over time (Perfit and Chadwick, 1998). Perhaps most significantly, this eruption, and the discovery of the Perseverance high-temperature vent field 5 km to the north, indicate that there is probably magma currently stored under the axial high of this segment of the Mariana back-arc, and that other eruptions on this segment may be possible in the not-too-distant future.

CONCLUSIONS

- (1) A very recent volcanic eruption was discovered on the central Mariana back-arc spreading center between latitude $15^\circ 22.3'$ to $15^\circ 26.3' \text{N}$, and between depths of 4050–4450 m bsl. This is the first known historical eruption on the Mariana back-arc, and the deepest one documented anywhere on Earth.
- (2) The date of the eruption is constrained between February 2013 and December 2015 by before-and-after bathymetric surveys, and the rapid decline in hydrothermal venting observed in 2015–2016 suggests it occurred only months before its discovery.
- (3) The eruption produced a discontinuous chain of hummocky pillow lava mounds along a distance of 7.3 km that are 200–800 m wide and up to 40–138 m thick. The lack of collapse features or evidence of lava drain-out suggests they were emplaced relatively rapidly, perhaps in less than a week.
- (4) The volume of lava erupted was at least $66.3 \times 10^6 \text{ m}^3$, making this one of the largest historical submarine eruptions documented so far.
- (5) The high ambient pressure at >4000 m bsl had no apparent effect on the eruptive processes that controlled the morphology of the lava flows, since they appear similar to those at other shallower eruption sites.
- (6) This eruption shows there is magma currently stored beneath the 15.5°N segment of the Mariana back-arc spreading center that is likely providing heat to the newly discovered Perseverance vent field (5 km to the north), and could be mobilized to feed additional eruptions.

DATA AVAILABILITY STATEMENT

The data presented in this study are available at the NOAA Centers for Environmental Information (ship bathymetry), the Rolling Deck to Repository (CTD data), the IEDA Marine Geoscience Data System (*Sentry* AUV and *SuBastian* ROV data), and ROV video is available on the Schmidt Ocean Institute YouTube channel.

AUTHOR CONTRIBUTIONS

WC wrote the manuscript and made most of the figures, was co-Chief scientist on the FK151121 and FK161129 expeditions, and directed the ROV dives described here. SM processed and analyzed ship-based and AUV-based multibeam sonar bathymetric data. EB and SW collected and processed the CTD and MAPR data. JR and DB were Chief Scientists on the FK151121 and FK161129 expeditions respectively. MA mapped the young lava flow contact from the *Sentry* photo survey. TB analyzed CTD water samples for methane and hydrogen on FK151121. AB assisted with GIS data management, volume calculations, and figure preparation.

FUNDING

We gratefully acknowledge the funding of the NOAA Ocean Exploration and Research (OER) Program and NOAA's Pacific Marine Environmental Laboratory (PMEL) for support of the science at sea and on shore. This research was supported by the PMEL Earth-Ocean Interactions Program, the Cooperative Institute for Marine Resources Studies (CIMRS), and the Joint Institute for the Study of the Atmosphere and Ocean (JISAO) under NOAA Cooperative Agreements NA11OAR4320091 and NA15OAR4320063. JISAO contribution number 2018-0157 and PMEL contribution number 4806.

ACKNOWLEDGEMENTS

We thank Patrick Shore and Doug A. Wiens of Washington University in St. Louis for collecting the 2013 multibeam sonar bathymetry during *R/V Melville* expedition MV1302a. We also thank the Schmidt Ocean Institute for supporting expeditions FK151121 and FK161129 on *R/V Falkor*, as well as the ship's crews and the teams that operated AUV *Sentry* and ROV *SuBastian*, especially expedition leaders Karl Kaiser (*Sentry*) and Jason Williams (*SuBastian*). In addition, we also thank NOAA OER for supporting the *Okeanos Explorer* operations in the Mariana region in 2016, including the ship's crew, science leads at sea, Deborah Glickson and Diva Amon, and the ROV *Deep Discoverer* team. The manuscript was improved by the helpful comments from reviewers JL and JW.

REFERENCES

- Anderson, M. O., Chadwick, W. W. Jr., Hannington, M. D., Merle, S. G., and Resing, J. A. (2017). Geological interpretation of volcanism and segmentation of the Mariana back-arc spreading center between 12.7°N and 18.3°N. *Geochem. Geophys. Geosyst.* 18, 2240–2274. doi: 10.1002/2017GC006813
- Baker, E. T., Chadwick, W. W. Jr., Cowen, J. P., Dziak, R. P., and Rubin, K. H. (2012). Hydrothermal discharge during submarine eruptions: the importance of detection, response, and new technology. *Oceanography* 25, 128–141. doi: 10.5670/oceanog.2012.11
- Baker, E. T., Embley, R. W., Walker, S. L., Resing, J. A., Lupton, J. E., Nakamura, K., et al. (2008). Hydrothermal activity and volcano distributions along the Mariana Arc. *J. Geophys. Res.* 113:B08S09. doi: 10.1029/2007JB005423
- Baker, E. T., Lupton, J. E., Resing, J. A., Baumberger, T., Lilley, M., Walker, S. L., et al. (2011). Unique event plumes from a 2008 eruption on the Northeast Lau spreading center. *Geochem. Geophys. Geosyst.* 12:Q0AF02. doi: 10.1029/2011GC003725
- Baker, E. T., Walker, S. L., Chadwick, W. W. Jr., Butterfield, D. A., Buck, N. J., et al. (2018). Post-eruption enhancement of hydrothermal activity: a 33-year, multi-eruption time-series at Axial Seamount (Juan de Fuca Ridge). *Geochem. Geophys. Geosyst.* 19. doi: 10.1002/2018GC007802
- Baker, E. T., Walker, S. L., Resing, J. A., Chadwick, W. W. Jr., and Merle, S. G. (2017). The effect of arc proximity on hydrothermal activity along spreading centers: new evidence from the Mariana back-arc (12.7°–18.3°N). *Geochem. Geophys. Geosyst.* 18, 4211–4228. doi: 10.1002/2017GC007234
- Ballard, R. D., and Moore, J. G. (1977). *Photographic Atlas of the Mid-Atlantic Ridge Rift Valley*. New York, NY: Springer-Verlag. doi: 10.1007/978-1-4612-9920-2
- Baumberger, T., Lilley, M. D., Resing, J. A., Lupton, J. E., Baker, E. T., Butterfield, D. A., et al. (2014). Understanding a submarine eruption through time series hydrothermal plume sampling of dissolved and particulate constituents: West Mata, 2008–2012. *Geochem. Geophys. Geosyst.* 15, 4631–4650. doi: 10.1002/2014GC005460
- Butterfield, D. A., Chadwick, W. W. Jr., Larson, B., Tunncliffe, V., Bates, A. E., et al. (2018). 2016 exploration shows contrasting fluid chemistry and hydrothermal vent communities between the Mariana arc and back-Arc. *Paper Presented at 2018 Ocean Sciences Meeting*, Portland, OR.
- Caplan-Auerbach, J., Dziak, R. P., Haxel, J., Bohnenstiehl, D. R., and Garcia, C. (2017). Explosive processes during the 2015 eruption of Axial Seamount, as recorded by seafloor hydrophones. *Geochem. Geophys. Geosyst.* 18, 1761–1774. doi: 10.1002/2016GC006734
- Caress, D. W., and Chayes, D. N. (2016). *MB-System: Mapping the Seafloor. Open Source Software Distributed From the MBARI and L-DEO Web Sites*. Available at: <http://www.mbari.org/data/mbsystem/>
- Caress, D. W., Clague, D. A., Paduan, J. B., Martin, J., Dreyer, B., Chadwick, W. W., et al. (2012). Repeat bathymetric surveys at 1-metre resolution of lava flows erupted at Axial Seamount in April 2011. *Nat. Geosci.* 5, 483–488. doi: 10.1038/NGEO1496
- Carey, R., Soule, S. A., Manga, M., White, J., McPhie, J., Wysockanski, R., et al. (2018). The largest deep-ocean silicic volcanic eruption of the past century. *Sci. Adv.* 4:e1701121. doi: 10.1126/sciadv.1701121
- Chadwick, W. W. Jr., Cashman, K. V., Embley, R. W., Matsumoto, H., and Dziak, R. P. (2008). Direct video and hydrophone observations of submarine explosive eruptions at NW Rota-1 Volcano, Mariana Arc. *J. Geophys. Res.* 113:B08S10. doi: 10.1029/2007JB005215
- Chadwick, W. W. Jr., Clague, D. A., Embley, R. W., Perfit, M. R., and Butterfield, D. A. (2013). The 1998 eruption of Axial Seamount: new insights on submarine lava flow emplacement from high-resolution mapping. *Geochem. Geophys. Geosyst.* 14, 3939–3968. doi: 10.1002/ggge20202
- Chadwick, W. W. Jr., Embley, R. W., and Shank, T. M. (1998). The 1996 Gorda Ridge eruption: geologic mapping, sidescan sonar, and SeaBeam comparison results. *Deep Sea Res. II* 45, 2547–2570. doi: 10.1016/S0967-0645(98)00083-6
- Chadwick, W. W. Jr., Paduan, B. P., Clague, D. A., Dreyer, B. M., and Merle, S. G. (2016). Voluminous eruption from a zoned magma body after an increase in supply rate at Axial Seamount. *Geophys. Res. Lett.* 43, 12063–12070. doi: 10.1002/2016GL071327
- Chadwick, W. W. Jr., Tunncliffe, V., Butterfield, D. A., Bates, A. E., Huber, J., Trembath-Reichert, E., et al. (2018). Newly discovered hydrothermal vent sites along the Mariana back-arc spreading center support hypothesis of geological and chemical control on chemosynthetic ecosystems. *Paper Presented at 2018 Ocean Sciences Meeting*, Portland, OR.
- Clague, D. A., Paduan, J. B., Caress, D. W., Chadwick, W. W. Jr., and Saout, M. L. (2017). High-resolution AUV mapping and targeted ROV observations of three historical lava flows at Axial Seamount. *Oceanography* 30, 82–99. doi: 10.5670/oceanog.2017.426
- Cowen, J. P., Baker, E. T., and Embley, R. W. (2004). “Detection of and response to mid-ocean ridge magmatic events: implications for the subsurface biosphere,” in *The Seafloor Biosphere at Mid-Ocean Ridges*, eds W. S. D. Wilcock, E. F. Delong, D. S. Kelley, J. A. Baross, and S. C. Cary (Washington, DC: American Geophysical Union), 227–243. doi: 10.1029/144GM15
- Crisp, J. A. (1984). Rates of magma emplacement and volcanic output. *J. Volcanol. Geotherm. Res.* 20, 177–211. doi: 10.1016/0377-0273(84)90039-8
- Dziak, R. P., Bohnenstiehl, D. R., and Smith, D. K. (2012). Hydroacoustic monitoring of oceanic spreading centers: past, present, and future. *Oceanography* 25, 116–127. doi: 10.5670/oceanog.2012.10
- Dziak, R. P., Hammond, S. R., and Fox, C. G. (2011). A 20-year hydroacoustic time series of seismic and volcanic events in the Northeast Pacific Ocean. *Oceanography* 24, 280–293. doi: 10.5670/oceanog.2011.79
- Embley, R. W., Baker, E. T., Butterfield, D. A., Chadwick, W. W. Jr., and Lupton, J. E. (2007). Exploring the submarine ring of fire: Mariana Arc - Western Pacific. *Oceanography* 20, 69–80. doi: 10.5670/oceanog.2007.07
- Embley, R. W., Merle, S. G., Baker, E. T., Rubin, K. H., Lupton, J. E., Resing, J. A., et al. (2014). Eruptive modes and hiatus of volcanism at West Mata seamount, NE Lau Basin: 1996–2012. *Geochem. Geophys. Geosyst.* 15, 4093–4115. doi: 10.1002/2014GC005387
- Fryer, P. (1995). “Geology of the Mariana trough,” in *Backarc Basins: Tectonics and Magmatism*, ed. B. Taylor (New York, NY: Plenum), 237–279.
- Gregg, T. K. P., and Fink, J. H. (1995). Quantification of submarine lava-flow morphology through analog experiments. *Geology* 23, 73–76. doi: 10.1130/0091-7613(1995)023<0073:QOSLFM>2.3.CO;2
- Griffiths, R. W., and Fink, J. H. (1992). Solidification and morphology of submarine lavas: a dependence on extrusion rate. *J. Geophys. Res.* 97, 19729–19737. doi: 10.1029/92JB01594
- Kato, T., Beavan, J., Matsushima, T., Kotake, Y., Camacho, J. T., and Nakao, S. (2003). Geodetic evidence of back-arc spreading in the Mariana trough. *Geophys. Res. Lett.* 30:1625. doi: 10.1029/2002GL016757
- Kelley, D. S., Delaney, J. R., and Juniper, S. K. (2014). Establishing a new era of submarine volcanic observatories: cabling Axial seamount and the endeavour segment of the Juan de Fuca Ridge. *Mar. Geol.* 352, 426–450. doi: 10.1016/j.margeo.2014.03.010
- Lilley, M. D., Butterfield, D. A., Lupton, J. E., and Olson, E. J. (2003). Magmatic events can produce rapid changes in hydrothermal vent chemistry. *Nature* 422, 878–881. doi: 10.1038/nature01569
- McLaughlin-West, E. A., Olsen, E. J., Lilley, M. D., Resing, J. A., Lupton, J. E., Baker, E. T., et al. (1999). Variations in hydrothermal methane and hydrogen following the 1998 eruption at Axial Volcano. *Geophys. Res. Lett.* 26, 3453–3456. doi: 10.1029/1999GL002336
- Nooner, S. L., and Chadwick, W. W. Jr. (2016). Inflation-predictable behavior and co-eruption deformation at Axial Seamount. *Science* 354, 1399–1403. doi: 10.1126/science.aah4666
- Perfit, M. R., and Chadwick, W. W. Jr. (1998). “Magmatism at mid-ocean ridges: constraints from volcanological and geochemical investigations,” in *Faulting and Magmatism at Mid-Ocean Ridges*, eds W. R. Buck, P. T. Delaney, J. A. Karson, and Y. Lagabriele (Washington, DC: American Geophysical Union), 59–116.
- Resing, J. A. (2016a). *Processed Gridded Near-Bottom AUV Sentry Bathymetric Sonar Data from the Izu-Bonin-Mariana Volcanic Arc Acquired During the Falkor Expedition FK151121 (2015)*. Palisades, NY: Integrated Earth Data Applications (IEDA).
- Resing, J. A. (2016b). *Processed Ship-Based Swath Bathymetry and Acoustic Backscatter Sonar Data (EM302) from the Izu-Bonin-Mariana Volcanic Arc Acquired During the Falkor Expedition FK151121 (2015)*. Palisades, NY: Integrated Earth Data Applications (IEDA).

- Resing, J. A., Baker, E. T., Lupton, J. E., Walker, S. L., Butterfield, D. A., Massoth, G. J., et al. (2009). Chemistry of hydrothermal plumes above submarine volcanoes of the Mariana Arc. *Geochem. Geophys. Geosyst.* 10:Q02009. doi: 10.101029/02008GC002141
- Resing, J. A., Rubin, K. H., Embley, R. W., Lupton, J. E., Baker, E. T., Dziak, R. P., et al. (2011). Active submarine eruption of boninite in the northeast Lau Basin. *Nat. Geosci.* 4, 799–806. doi: 10.1038/NGEO1275
- Rubin, K. H., Embley, R. W., Chadwick, W. W. Jr., Resing, J. A., Butterfield, D. A., Shank, T. M., et al. (2018a). Submarine volcanoes, ecosystems and landscape evolution in the NE Lau Basin. *Paper Presented at 2018 Ocean Sciences Meeting*, Portland, OR.
- Rubin, K. H., Embley, R. W., Hellebrand, E., and Chadwick, W. W. Jr. (2018b). Weird magmas all over the place: young boninite-dacite-basalt occurrences in the NE Lau Basin. *Paper Presented at 2018 Goldschmidt Conference*, Boston, MA.
- Rubin, K. H., Soule, S. A., Chadwick, W. W. Jr., Fornari, D. J., and Clague, D. A. (2012). Volcanic eruptions in the deep sea. *Oceanography* 25, 142–157. doi: 10.5670/oceanog.2012.12
- Schnur, S. R., Chadwick, W. W. Jr., Embley, R. W., Ferrini, V. L., and De Ronde, C. E. J. (2017). A decade of volcanic construction and destruction at the summit of NW Rota-1 seamount: 2004–2014. *J. Geophys. Res.* 122, 1558–1584. doi: 10.1002/2016JB013742
- Stern, R. J., Fouch, M. J., and Klemperer, S. L. (2003). “An overview of the Izu-Bonin-Mariana subduction factory,” in *Inside the Subduction Factory*, ed. J. Eiler (Washington, DC: American Geophysical Union), 175–222.
- Tunnicliffe, V., Bates, A. E., Butterfield, D. A., and Larson, B. I. (2017). Diversity of the Mariana beogeographic region with a closer look at *Alviniconcha hessleri*, the original “hairy snail. *Paper Presented at the 6th International Symposium on Chemosynthesis-Based Ecosystems (CBE6)*, Woods Hole, MA.
- Walker, S. L., Baker, E. T., Resing, J. A., Chadwick, W. W. Jr., Merle, S. G., et al. (2016a). High resolution mapping of hydrothermal plumes in the Mariana back-arc relate seafloor sources to above-bottom plumes. *Paper Presented at 2016 Fall Meeting, AGU*, San Francisco, CA.
- Walker, S. L., Baker, E. T., Resing, J. A., Chadwick, W. W. Jr., Merle, S. G., et al. (2016b). *Raw Near-Bottom MAPR Data from the Izu-Bonin-Mariana Volcanic Arc Acquired by AUV Sentry During the Falkor Expedition FK151121* (2015). Palisades, NY: Integrated Earth Data Applications (IEDA).
- Walker, S. L., Baker, E. T., Resing, J. A., Nakamura, K., and McLain, P. D. (2007). “A new tool for detecting hydrothermal plumes: an ORP sensor for the PMEL MAPR,” in *Proceedings of the American Geophysical Union, Fall Meeting 2007*, San Francisco, CA.
- White, S. M., Macdonald, K. C., and Haymon, R. M. (2000). Basaltic lava domes, lava lakes, and volcanic segmentation on the southern East Pacific Rise. *J. Geophys. Res.* 103B, 25519–25536. doi: 10.1029/2000JB900248
- Wilcock, W. S. D., Tolstoy, M., Waldhauser, F., Garcia, C., Tan, Y. J., Bohnenstiehl, D. R., et al. (2016). Seismic constraints on caldera dynamics from the 2015 Axial Seamount eruption. *Science* 354, 1395–1399. doi: 10.1126/science.aah5563
- Yeo, I., Searle, R. C., Achenbach, K. L., Le Bas, T. P., and Murton, B. J. (2012). Eruptive hummocks: building blocks of the upper ocean crust. *Geology* 40, 91–94. doi: 10.1130/G31892.1
- Yeo, I. A., Clague, D. A., Martin, J. F., Paduan, J. B., and Caress, D. W. (2013). Preeruptive flow focussing in dikes feeding historical pillow ridges on the Juan de Fuca and Gorda Ridges. *Geochem. Geophys. Geosyst.* 14, 3586–3599. doi: 10.1002/ggge.20210

Conflict of Interest Statement: The authors declare that the research was conducted in the absence of any commercial or financial relationships that could be construed as a potential conflict of interest.

Copyright © 2018 Chadwick, Merle, Baker, Walker, Resing, Butterfield, Anderson, Baumberger and Bobbitt. This is an open-access article distributed under the terms of the Creative Commons Attribution License (CC BY). The use, distribution or reproduction in other forums is permitted, provided the original author(s) and the copyright owner(s) are credited and that the original publication in this journal is cited, in accordance with accepted academic practice. No use, distribution or reproduction is permitted which does not comply with these terms.



Why Deep-Water Eruptions Are So Different From Subaerial Eruptions

Raymond A. F. Cas^{1,2*} and Jack M. Simmons¹

¹ School of Earth, Atmosphere and Environment (EAE), Monash University, Clayton, VIC, Australia, ² Centre for Ore Deposit and Earth Sciences (CODES), School of Physical Sciences, University of Tasmania, Hobart, TAS, Australia

OPEN ACCESS

Edited by:

Carles Soriano,
Instituto de Ciencias de la Tierra
Jaume Almera (ICTJA), Spain

Reviewed by:

Rodney Allen,
Volcanic Resources AB, Sweden
Margherita Polacci,
The University of Manchester,
United Kingdom

*Correspondence:

Raymond A. F. Cas
ray.cas@monash.edu

Specialty section:

This article was submitted to
Volcanology,
a section of the journal
Frontiers in Earth Science

Received: 29 June 2018

Accepted: 22 October 2018

Published: 20 November 2018

Citation:

Cas RAF and Simmons JM (2018)
Why Deep-Water Eruptions Are So
Different From Subaerial Eruptions.
Front. Earth Sci. 6:198.
doi: 10.3389/feart.2018.00198

Magmas erupted in deep-water environments (>500 m) are subject to physical constraints very different to those for subaerial eruptions, including hydrostatic pressure, bulk modulus, thermal conductivity, heat capacity and the density of water mass, which are generally orders of magnitude greater than for air. Generally, the exsolved volatile content of the erupting magma will be lower because magmas decompress to hydrostatic pressures orders of magnitude greater than atmospheric pressure. At water depths and pressures greater than those equivalent to the critical points of H₂O and CO₂, exsolved volatiles are supercritical fluids, not gas, and so have limited ability to expand, let alone explosively. Gas overpressures are lower in deep submarine magmas relative to subaerial counterparts, limiting explosive expansion of gas bubbles to shallower waters. Explosive intensity is further minimized by the higher bulk modulus of water, relative to air. Higher retention of volatiles makes subaqueously erupted magmas less viscous, and more prone to fire fountaining eruption style compared with compositionally equivalent subaerial counterparts. The high heat capacity and thermal conductivity of (ambient) water makes effusively (and/or explosively) erupted magmas more prone to rapid cooling and quench fragmentation, producing non-explosive hyaloclastite breccia. Gaseous subaqueous eruption columns and hot water plumes form above both explosive and non-explosive eruptions, and these can entrain pyroclasts and pumice autoclats upward. The height of such plumes is limited by the water depth and will show different buoyancy, dynamics, and height and dispersal capacity compared with subaerial eruption columns. Water ingress and condensation erosion of gas bubbles will be major factors in controlling column dynamics. Autoclats and pyroclasts with an initial bulk density less than water can rise buoyantly, irrespective of plume buoyancy, which they cannot do in the atmosphere. Dispersal and sedimentation of clasts in water is affected by the rate at which buoyant clasts become water-logged and sink, and by wind, waves, and oceanic currents, which can produce very circuitous dispersal patterns in floating pumice rafts. Floating pumice can abrade by frictional interaction with neighbors in a floating raft, and generate in transit, post-eruptive ash fallout unrelated to explosive activity or quench fragmentation.

Keywords: submarine eruptions, hydrostatic pressure, bulk modulus, limited volatile exsolution, supercritical fluid, magma properties, pumice raft dispersal

INTRODUCTION

Understanding the physical processes controlling the dynamics, style and intensity of volcanic eruptions has historically relied upon observations of recent subaerial eruptions (e.g., 1980 Mt St Helens, Lipman and Mullineaux, 1981; 1991 Mt Pinatubo, Newhall and Punongbayan, 1996; 1982 – present Hawai'i, Poland et al., 2014; Soufriere Hills, Montserrat, 1995–2012, Druitt and Kokelaar, 2002) and well-preserved subaerial eruption deposits (e.g., Askja, Carey et al., 2010; Colli Albano, Giordano et al., 2010; Vesuvius, Shea et al., 2011; Santorini, Druitt et al., 1999; Simmons et al., 2016; Tenerife, Marti and Geyer 2009, Edgar et al., 2017). However, volcanism on Earth principally occurs in the submarine realm (at mid-ocean ridge systems, intraplate hotspots/seamounts, oceanic plateaus, oceanic volcanic arcs), under eruptive conditions distinct from atmospheric or subaerial vent settings (McBirney, 1963; Cas, 1992; Head and Wilson, 2003; White et al., 2003, 2015a,b; Wohletz et al., 2013; Cas and Giordano, 2014; Carey et al., 2018; Manga et al., 2018). The heat capacity, thermal conductivity, density, viscosity, pressure gradient and bulk modulus of (sea)water, in particular, are each generally orders of magnitude larger than the properties of the atmosphere at subaerial vents (**Table 1**), which will greatly affect eruption processes. Studies of uplifted subaqueous volcanic deposits preserved in the geological rock record (e.g., Cas, 1978, 1992; Dimroth et al., 1978; de Rosen-Spence et al., 1980; Furnes et al., 1980; Busby-Spera, 1984, 1986; Cas and Wright, 1987; Allen, 1992; Mueller and White, 1992; McPhie et al., 1993; Kano et al., 1996; Scutler et al., 1998; Hunns and McPhie, 1999; Gifkins et al., 2002; Cas et al., 2003; Fujibayashi and Sakai, 2003; Goto and Tsuchiya, 2004; Cas and Giordano, 2014; Soriano et al., 2016; and many others) and relatively recent observations of modern sea floor volcanism and deposits (e.g., Moore, 1975; Batiza et al., 1984; Fornari, 1986; Cashman and Fiske, 1991; Fiske et al., 1995, 1998; Batiza and White, 2000; Wright et al., 2006; Deardorff et al., 2011; Resing et al., 2011; Clague et al., 2013; Embley et al., 2014; Chadwick et al., 2016; Carey et al., 2018; Embley and Rubin, 2018; Manga et al., 2018; and many others) have provided important insights into

the processes governing submarine volcanism and the deposit characteristics.

Although study of both modern and ancient submarine volcanic settings and successions have benefits, they also have limitations as to how much information can be accessed, documented and interpreted (**Table 1**). In ancient deep-water volcanic successions, the major limitation is the lack of understanding of the actual water depth at the time and place of eruption and deposition. As we will see, water depth determines the ambient hydrostatic pressure, and as a result magma properties, eruption style and the deposit characteristics. In modern submarine settings, even if the water depth and hydrostatic pressure are known, unless the physics of the processes at those water depths are carefully evaluated and understood, mistakes in interpreting the eruption processes and origins of deposits are commonly made, including erroneous assignment of some subaerial eruption styles to deep water settings.

In this review, we will outline the physical properties and effects of an ambient water mass on magma properties and eruption dynamics in deep-water environments (>500 m), discuss the deposits or products of subaqueous eruptions from observations in modern and ancient deep-water seafloor settings, and highlight the differences between subaqueous and subaerial eruptions. There are few papers which have attempted this to date (e.g., McBirney, 1963; Cas and Wright, 1987; Head and Wilson, 2003; White et al., 2003; Cas and Giordano, 2014). This current paper represents a significant and comprehensive update.

EFFECTS OF HYDROSTATIC PRESSURE ON SUBMARINE ERUPTIONS AND MAGMA PROPERTIES

Magma erupting from vents in subaerial settings decompress to atmospheric pressures of approximately 0.1 MPa (1 bar, at sea level). This contrasts to magma erupting on the sea floor, which decompress to the hydrostatic pressure corresponding to the

TABLE 1 | Advantages and limitations of studies of ancient submarine successions and modern seafloor settings.

	Ancient submarine successions	Modern seafloor settings
ADVANTAGES	<ul style="list-style-type: none"> • May preserve stratigraphy (including contact relationships) that provides a 4-D perspective on the evolution of a volcanic center. • Depositional textures may be well preserved. • Deposits are usually accessible. • Fieldwork is relatively inexpensive. • Requires minimal equipment. • Sampling of volcanic material is easy. 	<ul style="list-style-type: none"> • Preserve modern submarine edifices. • Preserve deposits without significant reworking or erosion. • Physical setting well constrained (e.g., water depth, topography, tectonic setting).
LIMITATIONS	<ul style="list-style-type: none"> • Outcrop is often discontinuous. • Field work can be time consuming if significant mapping is required. • The possible effects of uplift, deformation, hydrothermal alteration, and erosion need to be considered. • Physical setting is NOT well constrained (e.g., water depth, topography etc.). • Regional context may not be well understood. 	<ul style="list-style-type: none"> • Limited access to the deep-sea and volcanic stratigraphy. • Very time consuming. • Research is very expensive. • Requires technology to visualize volcanic forms and sample volcanic material.

water depth of the seafloor at the location of the vent. Hydrostatic pressure, P_{HYD} , is calculated as follows:

$$P_{HYD} = g\rho d \quad (1)$$

where g is gravitational acceleration (9.8 m s^{-2}), ρ is the density of water (1000 kg m^{-3} for fresh water and $1020\text{--}1030 \text{ kg m}^{-3}$ for sea water), and d is the depth or thickness of the overlying water column (in meters; **Figure 1** and **Table 2**). Hydrostatic pressure thus increases at a rate of $\sim 9.8 \text{ MPa km}^{-1}$ of water depth, which is $\sim 10,000\times$ greater than the atmospheric pressure gradient of about $-0.009 \text{ MPa km}^{-1}$ with altitude (**Table 2**). At a water depth of 100 m, the hydrostatic pressure is 1 MPa ($10\times$ atmospheric pressure, AP), at 500 m, 5 MPa ($50\times$ AP), at 1000 m, 10 MPa ($100\times$ AP), at 1500 m, 15 MPa ($150\times$ AP), at 2000 m, 20 MPa ($200\times$ AP; **Figure 1**), and so on. The increasing pressure with increasing water depth has the effect of modifying the physical properties of the erupting magmas, particularly the timing of volatile saturation and exsolution, the state of exsolved volatiles, and magma viscosity (McBirney, 1963; Wallace and Anderson, 2000; Wallace et al., 2015).

Effects of Hydrostatic Pressure on Volatile Saturation and Exsolution in Magmas

The saturation pressure of volatile species in magmas, particularly H_2O and CO_2 , is strongly dependent on the initial volatile content, magma composition and properties, and the confining

pressure (**Figure 2**; Wallace et al., 2015). If the volatile content is sufficiently high, volatiles can exsolve from a melt at any pressure/depth in the crust (**Figure 2**; Wallace et al., 2015). When the confining pressure, whether it be hydrostatic, magmatic or lithostatic, or a combination of these, exceeds the volatile saturation pressure, which is volatile content dependent, volatile exsolution is prevented. For example, a rhyolitic magma containing 4 wt. % H_2O and a basaltic magma containing 3 wt. % H_2O rising through continental crust in subaerial settings are saturated at confining pressures of $\sim 100 \text{ MPa}$. Assuming a typical continental lithostatic pressure gradient of $24.5\text{--}25 \text{ MPa km}^{-1}$ (**Figure 2**, Wallace et al., 2015), this is equivalent to 4 km depth in continental crust (**Figures 1, 2**). In submerged crust, the confining pressures will be the sum of lithostatic pressure and the hydrostatic pressure of the water column at the eruption water depth (add $\sim 9.8 \text{ MPa}$ per kilometer of water depth), and the depth in the crust below the seafloor at which volatile exsolution occurs will be:

$$D_{CR} = (P_{sat} - P_{HYD})/L_{gr} \quad (2)$$

where D_{CR} is the depth in the crust at which exsolution occurs in meters, P_{sat} is the volatile saturation pressure (MPa), P_{HYD} (MPa) is the hydrostatic pressure at the depth of the vent in the water body, and L_{gr} is the lithostatic pressure gradient (MPa km^{-1}) for submerged continental, arc, or oceanic crust. For example, at a water depth of 1 km, rhyolite magma with 4 wt. % dissolved H_2O , or a basalt magma with 3 wt. % dissolved H_2O , becomes water saturated at crustal pressures of 90.2 MPa ($=100 \text{ MPa} - 9.8 \text{ MPa}$), equivalent to a submarine crustal depth of $\sim 3.6 \text{ km}$. At 2 km water depth, with a hydrostatic pressure of 19.6 MPa, the lithostatic pressure component is 80.4 MPa, equivalent to a volatile saturation depth in the crust of $\sim 3.2 \text{ km}$, and at 3 km water depth the volatile saturation pressure equivalent depth in the crust is $\sim 2.8 \text{ km}$.

Equally importantly, the exsolution of volatiles will cease earlier in submarine settings compared to their subaerial counterpart because the erupting magma decompresses to higher ambient eruption pressures with increasing vent water depths. Consequently, less of the dissolved volatile component will exsolve, meaning a smaller fraction of volatiles is potentially available to drive explosive eruptions in submarine settings. This principle also applies to sub-glacial settings and other planetary bodies with dense atmospheres. For example, on Venus, the atmospheric pressure is 9.2 MPa (Taylor, 2010; Airey et al., 2015), which is equivalent to a depth of $\sim 1 \text{ km}$ in the Earth's oceans.

Geochemical compositional data and pre-eruptive volatile content can be used to determine degrees of exsolution and residual H_2O volatile content in magmas rising and decompressing in a conduit at various pressures, using the modeling software CONFORT 15 (Campagnola et al., 2016; **Figure 3**). Using data from Carey et al. (2018) and Manga et al. (2018) for rhyolite samples erupted at water depths of 900 m at the wholly submarine Havre volcano in the Kermadec arc, Southwest Pacific in 2012 (9 MPa confining hydrostatic pressure; pre-eruptive water content of 5.8 wt%; eruption temperature of $\sim 850^\circ\text{C}$), we calculate that the residual water content after

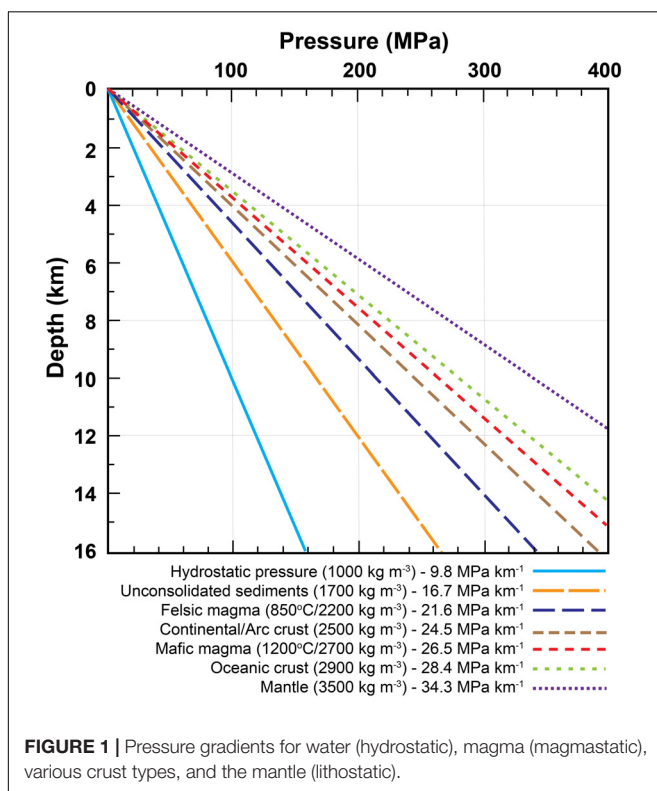
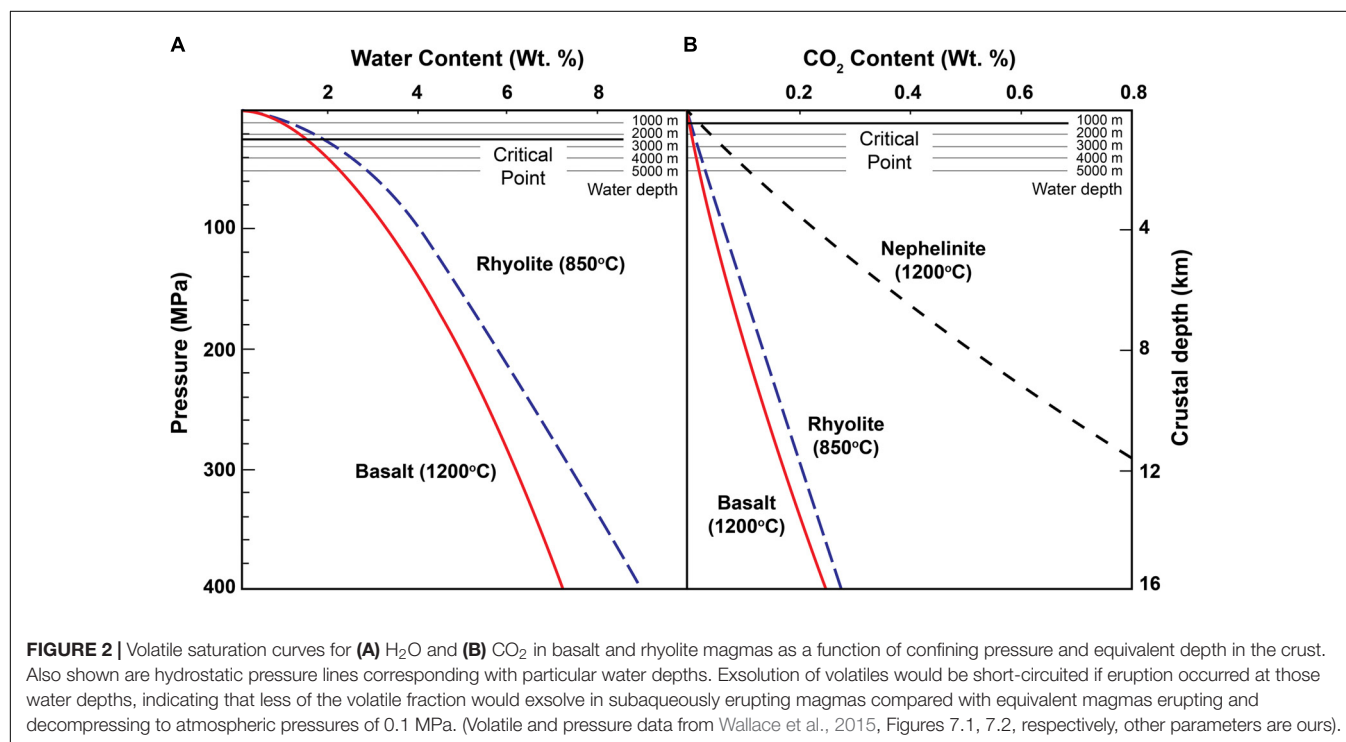


TABLE 2 | Physical properties of water and air (from Cas et al., in press).

Physical property	Seawater	Air/atmosphere	Difference factor (Sw/A)
Pressure gradient	$\sim 9.8 \text{ MPa km}^{-1}$	$\sim 0.0009 \text{ MPa km}^{-1}$	10,000×
Viscosity	$\sim 0.001 \text{ Pa s}$	0.000018 Pa s	1,000×
Bulk modulus	2,340 MPa	0.142 MPa	16,500×
Heat capacity	$\sim 4.0 \text{ kJ kg}^{-1} \text{ K}^{-1}$	$1.005 \text{ kJ kg}^{-1} \text{ K}^{-1}$	4×
Thermal conductivity	$0.61 \text{ W m}^{-1} \text{ K}^{-1}$ at 25°C	$0.025 \text{ W m}^{-1} \text{ K}^{-1}$ for air at 15°C	25×
Density	$1020\text{--}1030 \text{ kg m}^{-3}$	1 kg m^{-3}	1,000×



exsolution at 900 m water depth, and assuming ascent through a 20 m diameter cylindrical conduit, is about one quarter the original magmatic water content (**Figure 3B**).

Confining (Hydrostatic) Pressure and the Physical State and Specific Volume of Exsolved Magmatic Volatiles, and Effects on Eruption Styles

Even high levels of vesiculation in erupting subaqueous magmas do not ensure an explosive eruption because the physical state (vapor/gas versus supercritical fluid versus liquid) and the specific volume of exsolved volatiles in magma in conduits or lavas, and of volatile bubbles released into water masses is directly related to the confining pressure (McBirney, 1963; Wallace and Anderson, 2000; Cas and Giordano, 2014; Wallace et al., 2015). The transition between liquid and vapor states occurs at the critical point pressure and temperature of a particular volatile species. At and above the critical point, the fluid is supercritical, which is almost incompressible, and the liquid and vapor states are indistinguishable. The critical point pressure and

temperature for fresh H₂O (magmatic volatiles) are $\sim 22 \text{ MPa}$ and 374°C , respectively, and for CO₂ they are $\sim 7.8 \text{ MPa}$ and 31°C , respectively.

For magma in a closed conduit in continental or arc crust under lithostatic pressure, exsolved magmatic H₂O bubbles are supercritical at depths $>900 \text{ m}$ (i.e., the lithostatic pressure is 22 MPa at $\sim 900 \text{ m}$ in the crust). In oceanic crust, the equivalent supercritical pressure depth is $\sim 750 \text{ m}$, due to the higher lithostatic pressure. In comparison, the supercritical depth of exsolved magmatic H₂O in an open column of silicic and basaltic magma in continental crust is $\sim 980 \text{ m}$ and in oceanic crust, $\sim 830 \text{ m}$. In an open body of water, the water depth that coincides with the supercritical pressure for exsolving magmatic H₂O (fresh) is 2200 m, meaning that H₂O exsolving in an erupting magma, or released from a vent as fluid bubbles at those depths, is a supercritical fluid. The equivalent critical pressure depth for CO₂ is $\sim 800 \text{ m}$.

Supercritical fluids are dense ($\sim 322 \text{ kg m}^{-3}$; Pioro and Mokry, 2011), almost incompressible, and volumetrically limited compared with their gaseous form, and therefore cannot expand explosively (**Figure 4**; McBirney, 1963). If magma

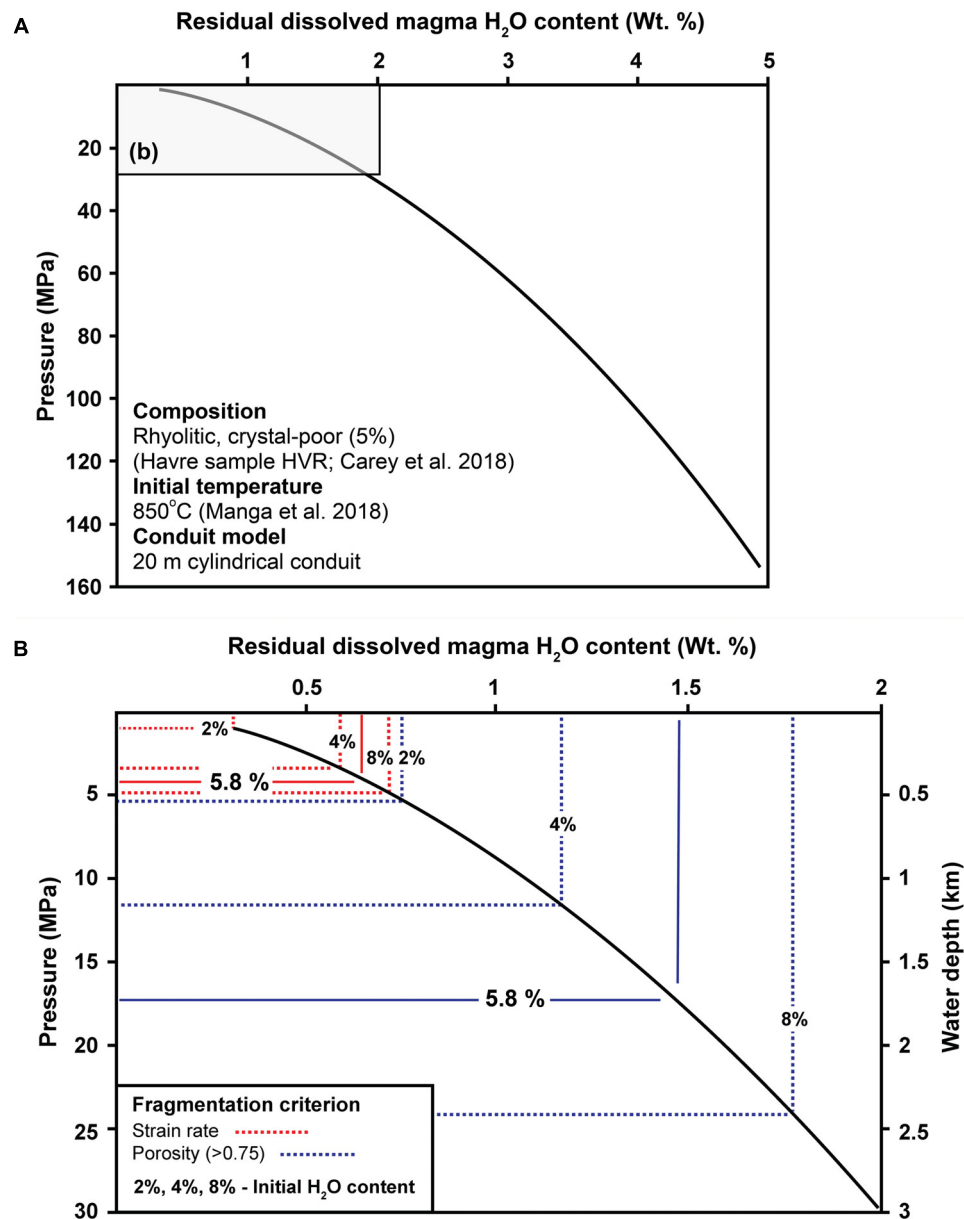
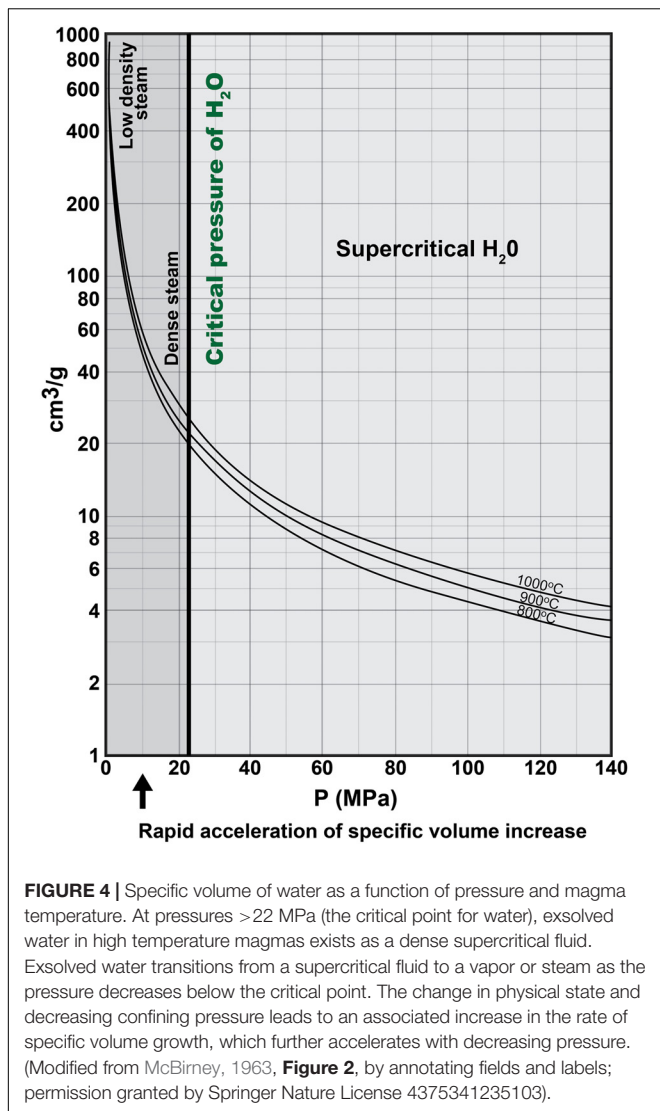


FIGURE 3 | (A) Modeled variation in residual dissolved magma H₂O content in a crystal-poor, rhyolitic magma during magma decompression and ascent in a 20 m diameter cylindrical conduit, based on compositional data from Carey et al. (2018) and Manga et al. (2018) for samples from the 2012 submarine eruption of Havre volcano, Kermadec arc, southwest Pacific, using CONFORT 15 modeling program of Campagnola et al. (2016). **(B)** Enlargement of the field shown in the box in **(A)**. The solid and dotted blue lines show the residual magmatic water content left after the magma had vesiculated to ~75 vol% for varying volatile contents. The solid blue line represents the initial 2012 Havre magma H₂O content of 5.8 wt% (Manga et al., 2018). Red lines show the calculated depths and residual water contents coinciding with the conditions for the strain rate criterion that would cause explosive fragmentation. In each modeled simulation, a fraction of the available initial volatile content remains dissolved in the magma (top axis) at the point of fragmentation and the depth of fragmentation increases as a function of increasing initial volatile content. Note, strain rate driven fragmentation only occurs at depths of <500 m, even if the initial magmatic water content was 8 wt. %.

risers to confining pressures less than the critical pressure, the supercritical fluid transforms through boiling to dense steam ($\sim 10 \text{ kg m}^{-3}$), leading to a slight increase in specific volume, which then increases exponentially at lower pressures as dense steam transforms into low density steam or gas ($\sim 1 \text{ kg m}^{-3}$; **Figure 4**). At $P < 10 \text{ MPa}$ (equivalent to 1 km water depth), the rate of change in specific volume and abundance of exsolved

water bubbles in magma increases dramatically, which reduces the bulk density, but dramatically increases the bulk vesiculated volume, buoyancy and ascent rates of the magma in the crust. The vesiculated magma then has the potential to fragment explosively (**Figure 4**; McBirney, 1963).

Volatile bubbles grow in magma if the exsolved gas bubble (over)pressure, ΔP , exceeds the sum of the yield strength of



the magma, γ_s (which for most magmas is several pascals to kilopascals), and the ambient pressure, P (atmospheric, hydrostatic, glaciostatic, lithostatic):

$$\Delta P > \gamma_s + \text{ambient } P \quad (3)$$

Where the yield strength is given by:

$$\gamma_s = \sigma - \eta \gamma^n \quad (4)$$

where σ is the total shear stress applied, η is the viscosity, γ is the strain rate, and n is a constant that is <1 for pseudo-plastic behavior and = 1 for Bingham behavior.

However, vesiculation alone does not ensure that explosive fragmentation, involving brittle bubble wall rupturing, will occur. This can only occur if the gas overpressure, ΔP , exceeds the tensile strength, τ , of the magma (<5–6 MPa) and the ambient pressure:

$$\Delta P > \tau + \text{ambient } P \quad (5)$$

Papale (1999) recognized that magmas can also fragment during explosive eruptions if the buoyancy driven strain rate that a vesiculating magma is subject to in the conduit exceeds a critical level whereby brittle failure occurs. This criterion for fragmentation in terms of strain rate, γ , and viscosity, η , is based on Maxwell's Law, as follows (Papale, 1999):

$$\gamma > kG\eta^{-1} \quad (6)$$

where k is a constant, G is the magma elastic or shear modulus, and η is the viscosity.

This process requires very rapid growth rates of steam-filled bubbles and high magma decompression rates (Cashman et al., 2000; Spieler et al., 2004; Cashman and Scheu, 2015; Gonnermann, 2015), which readily occurs in subaerial settings, even if the volatile content is only moderately high (Shea et al., 2011; Simmons et al., 2017a,b).

In subaqueous settings, as water depth and hydrostatic pressure increase, it becomes increasingly difficult for the gas over-pressure (= gas bubble pressure – ambient pressure) to exceed the tensile strength of magma (Eq. 5), which is ~5–6 MPa. At water depths of 500 m the ambient pressure is 5 MPa, so the gas pressure in vesicles in an erupting magma would have to be >10 MPa, unless gas bubble content released into the water column above the vent is high enough (~50–100%, depending on the magma volatile content and vesicle gas pressure) to significantly lower the density and ambient pressure of the water column, so reducing the minimum gas over-pressure required to initiate an explosive eruption (cf. Mitchell et al., 2018). At 1 and 2 km water depth, the hydrostatic pressures are ~10 and 20 MPa, and the gas pressure in bubbles would have to be >15 MPa and >25 MPa, respectively, in order to initiate an explosive eruption. However, 25 MPa is well above the critical pressure of water, and consequently the exsolved magmatic water in the magma would be supercritical, or pseudo-critical fluid with an extremely low expansivity factor ($\ll 0.1$; Piro and Mokry, 2011).

To put this into context, Thomas et al. (1994) calculated that the gas pressures during the highly explosive, subaerial, caldera-forming 3.6 ka Minoan eruption on Santorini was 18 MPa, during the 232 AD Taupo eruption (New Zealand) it was 20 MPa, and during the 780 ka Bishop Tuff eruption from Long Valley caldera, California, it was 27 MPa. If these eruptions were to occur in submarine environments, they would be ineffectual at water depths of 1300, 1500, and 2200 m water depths, respectively, but probably at even shallower water depths, given the effects of hydrostatic pressures on the specific volumes and expansion rates in gas bubbles.

Manga et al. (2018) determined that the strain rate in vesiculated rhyolite magma rising in the conduit toward a vent at water depth of 900 m during the 2012 submarine Havre volcano eruption was orders of magnitude below the strain rate threshold criterion for explosive fragmentation of magma determined by Papale (1999). Our calculations using CONFORT 15 (Campagnola et al., 2016), using whole-rock compositions and pre-eruption melt inclusion data for erupted 2012 Havre pumice from Carey et al. (2018) and Manga et al. (2018), demonstrate that explosive strain driven fragmentation would only be possible

at water depths <500 m (**Figure 3B**). Even if the Havre magma had 8 wt% H₂O, it would not erupt explosively at depths >500 m using the strain-rate driven fragmentation criterion (**Figure 3B**).

In some cases, weak explosive eruptions may occur at water depths from 1500 to 500 m, while more intense explosive eruptions can occur at depths <500 m (Cas, 1992; Fiske et al., 1998; White et al., 2015b), but only if the volatile content, strain rate affecting magma in the conduit and gas over-pressures are high enough. Otherwise, coherent lavas, including highly vesicular pumice lavas, can form, as occurred during the 2012 submarine Havre eruption (Carey et al., 2018; Ikegami et al., 2018; Manga et al., 2018). Our calculations for deep-water pumiceous submarine rhyolite from Sumisu volcano, Izu-Bonin arc (Allen et al., 2010), are very similar. In both the Havre and Sumisu eruptions (as well as other cases), abundant pumice was produced, but NOT by explosive mechanisms.

Non-explosive Growth of Vesicles Producing Coherent Subaqueous Pumice Lavas

In subaerial, low atmospheric pressure settings, there are many lavas that are erupted with highly pumiceous, coherent or autobrecciated carapaces (**Figure 5a**; 50–80% vesicles; e.g., Fink and Manley, 1987; Fink et al., 1992). This indicates that volatile content and gas over-pressure were greater than the yield strength

of the magma so allowing bubble growth under low strain conditions, but less than the tensile strength of the magma in the bubble walls (i.e., $\gamma_s < \Delta P < \tau$), so preventing brittle explosive fragmentation.

Since subaqueously erupting magmas decompress to much higher ambient pressures, particularly in deep water, compared with subaerial eruptions, this will significantly lower volatile exsolution and vesicle growth rates (**Figure 2**), and the level of gas over-pressure with increasing water depths. In magmas erupted at water depths (or under thick ice) and pressures where the rate of decompression, and the level of gas over-pressure are too low to drive explosive fragmentation, highly vesicular lavas, even with rhyolite compositions (**Figures 5b–d**; de Rosen-Spence et al., 1980; Furnes et al., 1980; Cas and Wright, 1987; Cas, 1992; McPhie et al., 1993; Scutcher et al., 1998; Binns, 2003; Kano, 2003; Allen et al., 2010; Rotella et al., 2015; Carey et al., 2018; Ikegami et al., 2018; Manga et al., 2018), can form because gas bubbles will grow more slowly than under atmospheric conditions. The pre-historic rhyolite lava dome-forming eruption of Sumisu volcano at water depths from 430 to 1210 m (Allen et al., 2010), in which the magmatic H₂O content was ~5.5 wt%, produced highly vesicular, coherent pumice lava dome carapaces (**Figures 5b–d**). Similarly, the 2012 submarine Havre volcano eruption, at a water depth of ~900 m, involving rhyolite magma with pre-eruption magmatic H₂O content of 5.8 wt% was effusive,

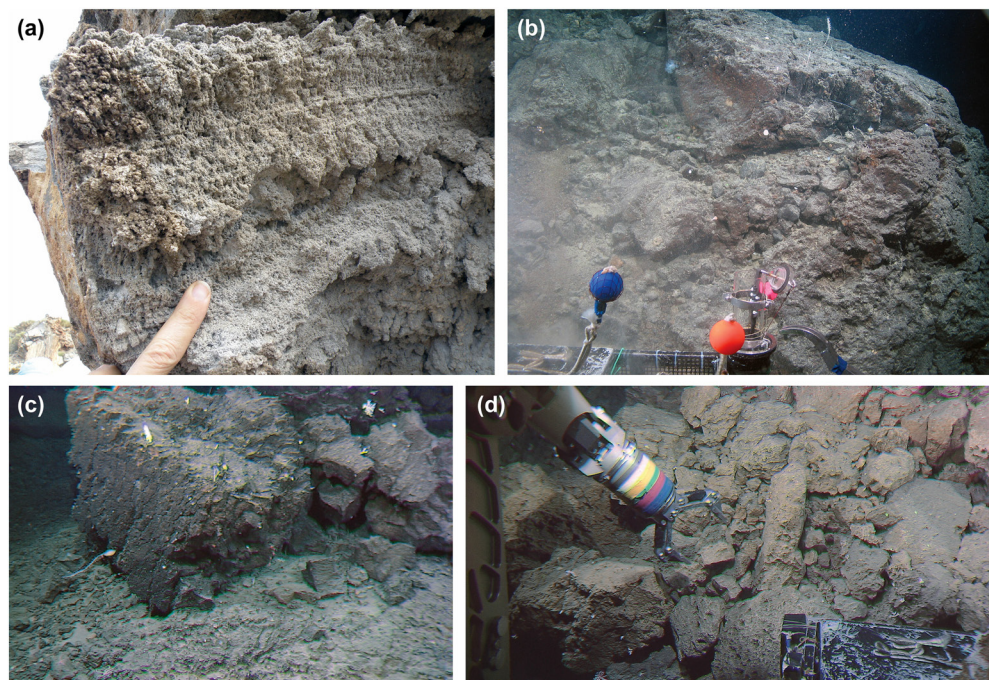


FIGURE 5 | Coherent and autoclastic pumice carapaces on felsic lavas. **(a)** Subaerial rhyolitic Rocche Rosse lava, Lipari Island, Italy, showing an *in situ*, flow-banded, highly vesicular, coherent pumice domain. **(b)** Highly vesicular, coherent rhyolitic pumice surface of submarine lava dome at water depth of 1210 m, from Sumisu submarine volcano, Izu-Bonin arc, Japan, showing a rough columnar jointing on curvi-planar surface on right side. Field of view: 5 m wide. **(c)** polygonal giant pumice blocks, Sumisu volcano, 960 m water depth. The large block is 3 m in diameter and the left hand planar surface shows small scale polygonal, cooling jointing. **(d)** 5–30 cm diameter pumice blocks, some with planar surfaces and polygonal form, Sumisu volcano, water depth of 430 m. [(b–d) are from Allen et al. (2010), parts a, c, e, of **Figure 2**, reproduced with permission of the senior author S. Allen, and under “fair use” provisions of the Geological Society of America: <https://www.geosociety.org/GSA/Publications/InfoServices/Copyright/GSA/Pubs/guide/copyright.aspx>].

and produced lava domes with highly vesicular pumice carapaces (70% vesicles; Carey et al., 2018; Ikegami et al., 2018; Manga et al., 2018). Subaerially, such lavas would almost certainly have erupted explosively because gas over-pressures would have been much higher. The presence of highly vesicular deep-water basalt lava (56% vesicles; Dixon et al., 1997; 44% vesicles; Fujibayashi and Sakai, 2003) indicates that the same constraints affect lower viscosity magmas as well. Empirical observations that there is a decrease in pyroclastic deposits with increasing ocean depths (e.g., Gregg and Fink, 1995; Grosfils et al., 2000; Wright et al., 2006) also provide support for this theory.

IMPLOSIONS: INCREASINGLY LIKELY IN DEEP-WATER

So far, this review has focused on scenarios involving gas over-pressures relative to hydrostatic pressures in subaqueous settings. However, at increasing water depths and hydrostatic pressure there is an increasing probability that significant under-pressures can occur in some cavities in erupted volcanic deposits and even in erupting gas bubbles released into the water column as they cool and condense. At high enough under-pressures, catastrophic cavitation or implosions will occur. In implosions, debris is concentrated by collapse rather than being energetically dispersed far from source, as occurs during explosions. As subaqueous lavas cool, gas in cavities may escape, cool and condense, creating a low-pressure cavity, or lava may drain from an internal lava tube creating a cavity that is under-pressured. If the hydrostatic pressure exceeds the pressure in the cavity and the strength of the chilled glassy surface lava crust (~ 7 MPa, but less if that crust has micro-fracture flaws, which is likely during chilling and contraction of glass), the cavity will collapse or cavitate energetically and implausively. Moore (1975) documented this during an eruption of Kilauea volcano, Hawai'i, when lava entered the sea and formed pillow lava tubes off-shore. As lava drained from some pillow tubes, gasses cooled leading to implosive cavitation of evacuated pillow tubes. The glassy lava crust of subaqueous lavas will be weakened by *in situ*, contractional cooling cracks at all scales. Visible and cryptic networks of cracks result in loss of tensile strength, which facilitates cavitation collapse of the crusts of drained lava tubes and pillows subject to high hydrostatic pressure. If water permeates into the cavities before cavitation occurs, the hydrostatic pressure in the cavity will balance that outside, and no collapse will occur.

Gas bubbles in a liquid can also cavitate implausively (Rayleigh, 1917; Fujikawa and Akamatsu, 1980; Brennen, 1995). This also requires an under-pressure differential between the gas bubbles and the external fluid. Spherical bubbles are the most difficult to cavitate because of the effects of surface tension forces (Brennen, 1995). If gas filled bubbles are compressed, this normally leads to significant pressure and temperature increase (Brennen, 1995). However, cooling and condensation can reduce both (Fujikawa and Akamatsu, 1980), and if bubbles are deformed by asymmetric pressure gradients or by stretching, they are more prone to collapse (Brennen, 1995).

Gas bubbles in vesiculating magmas erupting on the seafloor, and superheated bubbles of gas or ambient water being released from deep subaqueous vents into the overlying water mass, will be subject to rapid cooling, leading to condensation of gas in the bubbles, rapid decrease in internal bubble pressure, facilitating collapse or implosions. Some acoustic pulses detected during modern submarine eruptions and described as explosions, could in fact be largely implosions (e.g., some gas release events from the 2009 West Mata submarine eruption, Lau Basin at 1200 m water depth; Resing et al., 2011; lava tube collapse during the 2015 eruption at Axial Seamount volcano, East Pacific Rise at water depths >1500 m; Chadwick et al., 2016).

Although implosions trigger an immediate shock or pressure wave and acoustic signals, and the implosion motion is inwards, there can then be a rebound against solid surfaces leading to limited ejection of solids and disintegrating bubbles away from the implosion source, mimicking explosions.

EFFECTS OF (HYDROSTATIC) PRESSURE ON MAGMA VISCOSITY

The viscosity of a magma is a function of pressure, temperature and composition, including dissolved magmatic water content and crystallinity (Scarfe et al., 1987; Spera, 2000; Giordano et al., 2008; Wohletz et al., 2013; Leshner and Spera, 2015; Persikov et al., 2017). Increasing water depths and corresponding increases in confining (hydrostatic) pressures, in particular, reduce magma viscosity by reducing polymerization (Scarfe et al., 1987) and suppressing volatile exsolution, ensuring a larger fraction of the volatile budget remains dissolved in the melt (Figure 2; Leshner and Spera, 2015). Magmas erupting on the seafloor at high hydrostatic pressure are therefore likely to be initially less viscous and more fluidal than their subaerial counterparts. This has several important consequences:

- First, magmas will be prone to erupt through fire fountaining on the sea-floor if magma ascent rates are high. Exsolved volatiles at high hydrostatic pressures, whether they are supercritical fluids (density $\sim 322 \text{ kg m}^{-3}$; Pioro and Mokry, 2011) or dense steam (density $\sim 10 \text{ kg m}^{-3}$), will lower bulk magma density, and enhance buoyancy and rise rate. Even silicic magmas may erupt through submarine fire fountaining if the magma viscosity is low and discharge rate is high (e.g., Mueller and White, 1992).
- Secondly, if magma viscosity is lower, even silicic magmas can produce unusually far flowing submarine lavas in deep water (e.g., Early Devonian Merriam dacitic lavas, >60 km flow distance; Cas, 1978; Lau Basin dacitic lavas, >10 km flow distance at 2500 m water depth; Embley and Rubin, 2018).
- Third, because viscosity is inversely proportional to strain rate (Eq. 6), vesicles in magma erupting on the deep-sea floor will grow more easily than subaerial counterparts because magma viscosity is lower. However,

lower viscosities require higher strain rates (Eq. 6) to meet the strain rate induced brittle explosive fragmentation criterion of Papale (1999), Campagnola et al. (2016), and because gas bubble overpressures are lower than in subaerial counterparts, they are less likely to disrupt explosively, again reinforcing the likelihood of finding more coherent, highly vesicular lavas on the deep-sea floor than in subaerial settings.

However, counteracting the effects of pressure in lowering magma viscosity in deep-water are the effects of increased cooling rates of the surfaces of submarine lavas that cause rapid formation of a solid strong crust (Griffiths and Fink, 1992; Gregg and Fink, 1995). Strong, thick crusts may confine the liquid magma, enhance lava flow inflation and limit flow mobility. This effect is likely to be more significant at low effusion rates than at high effusion rates because a larger proportion of the lava can solidify quickly (Griffiths and Fink, 1992; Gregg and Fink, 1995). In addition, quench crystallization of microlites as a result of rapid cooling of flow margins could enhance bulk viscosity of some erupted lavas and affect their flow behavior (e.g., Saar et al., 2001). Unfortunately, the effects of a cooling confining crust, pressure and crystal content cannot be modeled in an integrated way at present using viscosity modeling packages such as those of Giordano et al. (2008), which is based on chemical composition, temperature, volatile content at atmospheric pressure and a crystal free basis.

In addition, slope upon which lavas are erupted and flow can significantly affect the flow behavior and morphology of lavas (Ikegami et al., 2018).

BULK MODULUS OF WATER: AN OVERLOOKED CONSTRAINT ON EXPLOSIVITY AND ERUPTION INTENSITY

The intensity of an explosive eruption, or the extent to which it affects its surroundings, can be measured by the bulk modulus of the surrounding material (i.e., its resistance to compressibility, or the rate of change of volume decreases as pressure is changed).

The Bulk Modulus can be calculated as

$$K = -dP/(dV/V_0) \\ = -(P_1 - P_0)/((V_1 - V_0)/V_0) \quad (7)$$

where K = Bulk Modulus of Elasticity (Pa, N/m²), dP = differential change in pressure on the object (Pa, N/m²), dV = differential change in volume of the object (m³), V_0 = initial volume of the object (m³), P_0 = initial pressure (Pa, N/m²), P_1 = final pressure (Pa, N/m²), and V_1 = final volume (m³)¹.

Alternatively, Bulk Modulus can be expressed as:

$$K = d\rho/(d\rho/\rho_0) \\ = (\rho_1 - \rho_0)/((\rho_1 - \rho_0)/\rho_0) \quad (8)$$

where $d\rho$ = differential change in density of the object (kg m⁻³), ρ_0 = initial density of the object (kg m⁻³), and ρ_1 = final density of the object (kg m⁻³).

The adiabatic bulk modulus of air/atmosphere is 0.142 MPa, meaning it is extremely deformable or compressible (Table 2). Explosive eruptions in subaerial environments are therefore often intense and far-reaching. In contrast, the bulk modulus of water is 2340 MPa, four orders of magnitude less compressible or deformable than air (Table 2; but >10× times smaller than the Young's modulus of rock, 20000–70000 MPa; Karagianni et al., 2010). The intensity of explosive eruptions will therefore be greatly suppressed in submarine settings relative to their subaerial counterparts, and explosive shock waves produced during the eruption will be greatly attenuated close to source (Resnyansky and Delaney, 2006). Likewise, the attenuation effects of solid rock during subterranean explosions will result in only a very limited cone of deformation. The relationships summarized indicate that with increasing pressure, the Bulk Modulus rises and a material becomes less compressible. So, with increasing water depth, water becomes less compressible, less deformable, and will suppress explosive pressure or intensity more than at shallow water depths.

HEAT CAPACITY AND THERMAL CONDUCTIVITY OF WATER: QUENCH FRAGMENTATION AND BRECCIA FORMATION, THERMO-HYDRAULIC EXPLOSIONS, AND SUBAQUEOUS ERUPTION COLUMN DYNAMICS

Film Boiling and Its Role in Subaqueous Quench Fragmentation, Coherent Lava Formation and Thermo-Hydraulic (Phreatomagmatic, Phreatic) Explosions

Water at the interface between erupting magma and an ambient body of water can be superheated, in a process called film boiling, as a result of the extreme temperature difference between hot magma (800–1200°C) and cold water (<20°C; Figure 6a; Mills, 1984). High temperature contrasts and low ambient or hydrostatic pressures favor stable film boiling at the magma-water interface (Zimanowski and Büttner, 2003; Wohletz et al., 2013; Zimanowski et al., 2015). Diffusion of heat across the vapor film, which may be only mm to cm thick, is slow, so insulating the erupted magma and allowing viscous elastic crusts and coherent lavas to develop and propagate (Leidenfrost phenomenon). If the vapor film collapses, due to fluid instabilities related to decreasing magma temperatures, increasing confining pressures and shear between lavas and the water mass (Wohletz, 1986), direct magma-water interaction

¹ www.EngineeringToolbox.com

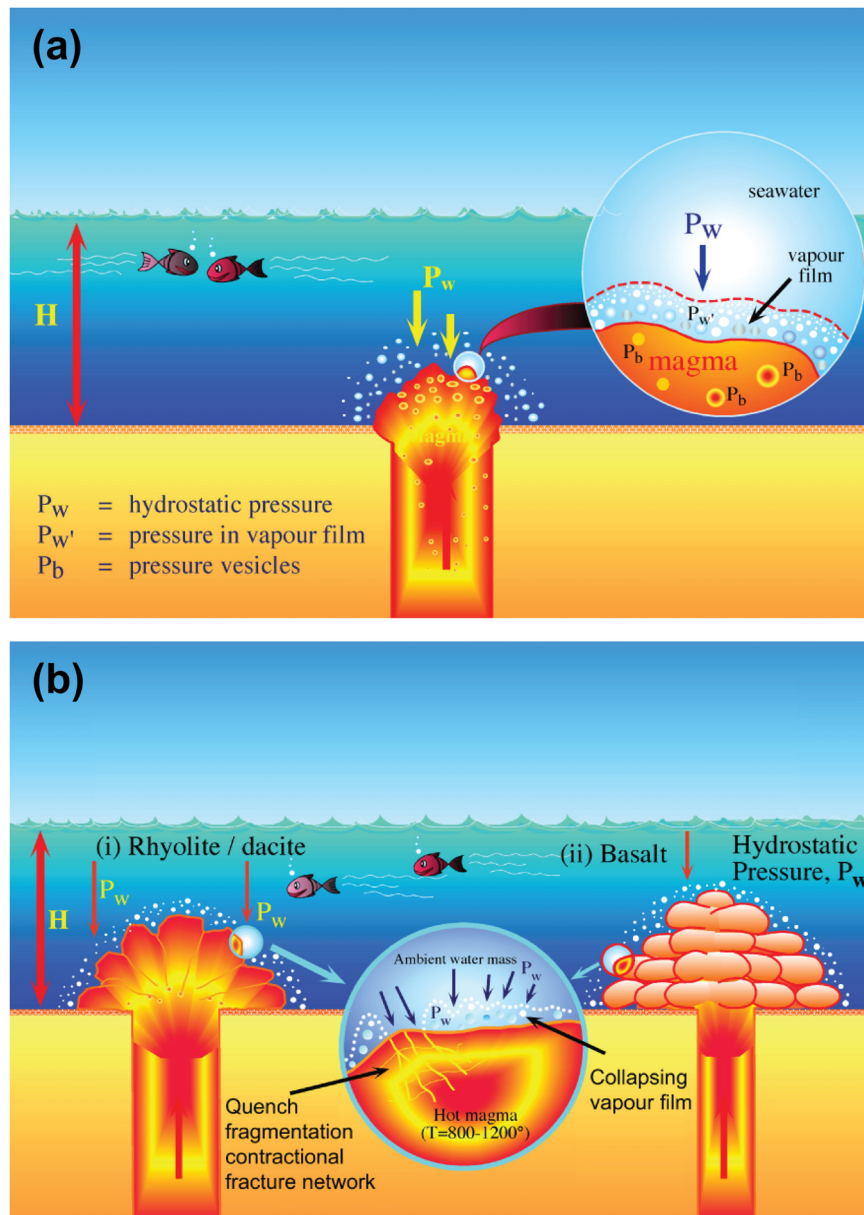


FIGURE 6 | Film boiling at the interface between hot magma and a body of water. **(a)** Stable film boiling at the interface, leading to controlled heat lost across the vapor film and formation of a visco-elastic and progressively a coherent crust to the lava flow. **(b)** Vapor film collapse, leading to *in situ* rapid cooling of the magma at the interface through the glass transition, and rapid cooling contraction fracturing of the glass into an *in situ*, jigsaw-fit breccia.

will occur leading to chilling of the magma to glass. Cooling contraction fractures will propagate instantaneously, and quench fragmentation and breccias will result (Figure 6b; van Otterloo et al., 2015). Film boiling can even occur at pressures and depths greater than the critical point of water (<22 MPa for fresh water and <30 MPa for sea water – 3 km deep at $\sim 407^\circ\text{C}$ with 3.2 wt. % NaCl; Bischoff and Rosenbauer, 1988; Wohletz, 2003; Wohletz et al., 2013; Zimanowski et al., 2015).

At low confining pressures and water depths (<10 MPa, 1000 m, and generally much less), the sudden collapse of the

vapor film can lead to thermal detonation of liquid water as it hits the magma surface, resulting from instantaneous superheating and explosive boiling of the liquid water at the interface, leading to phreatomagmatic and/or explosive activity. Although phreatomagmatic activity could occur in water depths up to 1000 m, it generally only occurs in water depths up to a few hundred meters, because it requires a low density and pressure vapor film to be able to collapse instantaneously (Zimanowski and Büttner, 2003; Wohletz et al., 2013). Alternatively, vapor film collapse could lead to quench fragmentation.

Quench Fragmentation and Hyaloclastite Breccia Formation

The heat capacity of water is $4\times$ greater than air, and its thermal conductivity $25\times$ higher (Table 2). Magmas erupting in deep-sea settings or lavas flowing into the sea, lakes or rivers are therefore prone to extremely high rates of cooling relative to subaerially erupted magmas or lavas because water acts as a heat sink. When in direct contact with cold liquid water, magmas or lavas instantaneously chill through the glass transition, causing thermal tensile stress, contraction and cracking of the glass, in a process called quench fragmentation or thermal granulation (Figure 6b; Kokelaar, 1986; Wohletz, 1986; Cas and Wright, 1987; Cas, 1992; van Otterloo et al., 2015; Cas et al., in press). Quench fragmentation is also a brittle fracturing process and should emit strong acoustic signals under water. Some acoustic signals associated with modern deep-water eruptions and interpreted as due to explosions (e.g., 2015 Axial Seamount lava forming eruption, Chadwick et al., 2016) could in fact result from tensile brittle fracturing of the glassy crusts of lavas during quench fragmentation.

Quench fragmentation produces *in situ* breccias, commonly with angular blocks to ash size fragments of glassy debris called hyaloclastite (Pichler, 2011; de Rosen-Spence et al., 1980; Furnes et al., 1980; Cas and Wright, 1987; Cas, 1992; Cas and Giordano, 2014; van Otterloo et al., 2015; Figure 7). Hyaloclastite deposits preserve gradations from coherent lava in the core to *in situ* jigsaw-fit breccias to clast-rotated aggregates at the margins of a subaqueous lava (Figures 7a–d; Furnes et al., 1980; Cas and Wright, 1987; Cas, 1992; Batiza and White, 2000; White et al., 2000; Goto and Tsuchiya, 2004; Maeno and Taniguchi, 2006; Cas and Giordano, 2014; van Otterloo et al., 2015; White et al., 2015a; Soriano et al., 2016). When lavas or syn-depositional intrusions are in contact with water-saturated, unconsolidated sediments, they can also be quench fragmented, and the heated pore water in the sediments can convect vigorously and boil, leading to dynamic mixing of hyaloclasts and sediment, producing a chaotic volcanic clast-sediment breccia deposit called peperite (Figure 7e), which also grades back into jigsaw-fit breccia and coherent lava or intrusive rock in the core (Busby-Spera and White, 1987; Cas and Wright, 1987; Cas, 1992; Hunns and McPhie, 1999; Batiza and White, 2000; White et al., 2000; Gifkins et al., 2002; Skilling et al., 2002; Goto and Tsuchiya, 2004; Maeno and Taniguchi, 2006; Cas and Giordano, 2014; van Otterloo et al., 2015; White et al., 2015a; Soriano et al., 2016).

Quench fragmentation is an *in situ* fragmentation process that can produce very large volumes of hyaloclastite breccia (Figures 7a–e), which is not explosive in origin and does not occur subaerially, unless lava flows into water (e.g., in Hawai'i) or erupts sub-glacially (e.g., Iceland). It has been underestimated as the origin for volcanic breccias in subaqueous settings, which are often described as explosive or pyroclastic in origin, when in fact they are much more likely to be autoclastic. When volcanic breccias and even ash-size deposits are found in subaqueous settings, the first and most likely

hypothesis to test is: are these hyaloclastite, and if not, what is the evidence based on textural characteristics, context, analysis or physical processes, rather than assuming that they are pyroclastic? The high heat capacity, thermal conductivity, and hydrostatic pressure constraints of water indicate that explosive origins become less likely with increasing water depths.

For lavas that have vesiculated to high degrees, but have not been fragmented explosively, the pumice carapaces can also be quench fragmented, producing pumice hyaloclastite (Figures 5c,d, 7c; de Rosen-Spence et al., 1980; Furnes et al., 1980; Cas and Wright, 1987; Kurokawa, 1991; Cas, 1992; McPhie et al., 1993; Scutter et al., 1998; Scutter, 1999; Binns, 2003; Carey et al., 2018; Manga et al., 2018).

In addition, spatter ejected from submarine fire fountains will be subject to quench fragmentation in the water column and plume above the vent (Figure 8A), producing blocky, ash size glassy fragments and fractured spatter fragments (Figure 7f), that then become entrained and dispersed in thermal plumes of seawater above the fountain (Cas et al., 2003), again producing non-explosive, hyaloclastic ash-size fallout deposits.

Another effect of the high heat capacity and thermal conductivity of water is that water directly above a vent and above propagating seafloor lava flows is quickly heated, decreasing its density by 10% relative to cold seawater ($\sim 900 \text{ kg m}^{-3}$ vs. $1,027 \text{ kg m}^{-3}$; Safarov et al., 2009; Sharqawy et al., 2010), so producing buoyant plumes of hot seawater. In deep water, as lavas propagate and form a chilled glassy crust, the thermal stresses associated with cooling cause ash size glass particles to exfoliate ("popping") from the surfaces of lavas (White et al., 2015a). Hot thermal plumes of water that rise above the vent and above propagating seafloor lavas (cf. Barreyre et al., 2011) can entrain such ash size glassy fragments and disperse them, forming ash fallout deposits of hyaloclastite debris. Deep-sea "ash" deposits associated with young seafloor lavas (e.g., ash found after the 2015 seafloor lava-forming eruption from Axial Seamount on the East Pacific Rise), are often interpreted as pyroclastic in origin (e.g., Chadwick et al., 2016), which is unlikely given the water depth of $>1500 \text{ m}$, as discussed above. They are more likely to be hyaloclastic fallout deposits dispersed by thermal seawater plumes rising above the newly erupting lavas.

Cooling of Subaqueous Eruption Columns

The heat capacity and thermal conductivity of water also plays a critical role in determining the dynamics of subaqueous eruption columns, through heat exchange between the eruption column and the ambient water body (e.g., physical ingress and mixing of cold water along the margins of eruption columns into the core, the cooling and condensation of gas bubbles by the water mass). The change in plume dynamics results from a change in the physical state of the plume, particularly temperature, density, and the proportions of water and gas. These factors each influence the

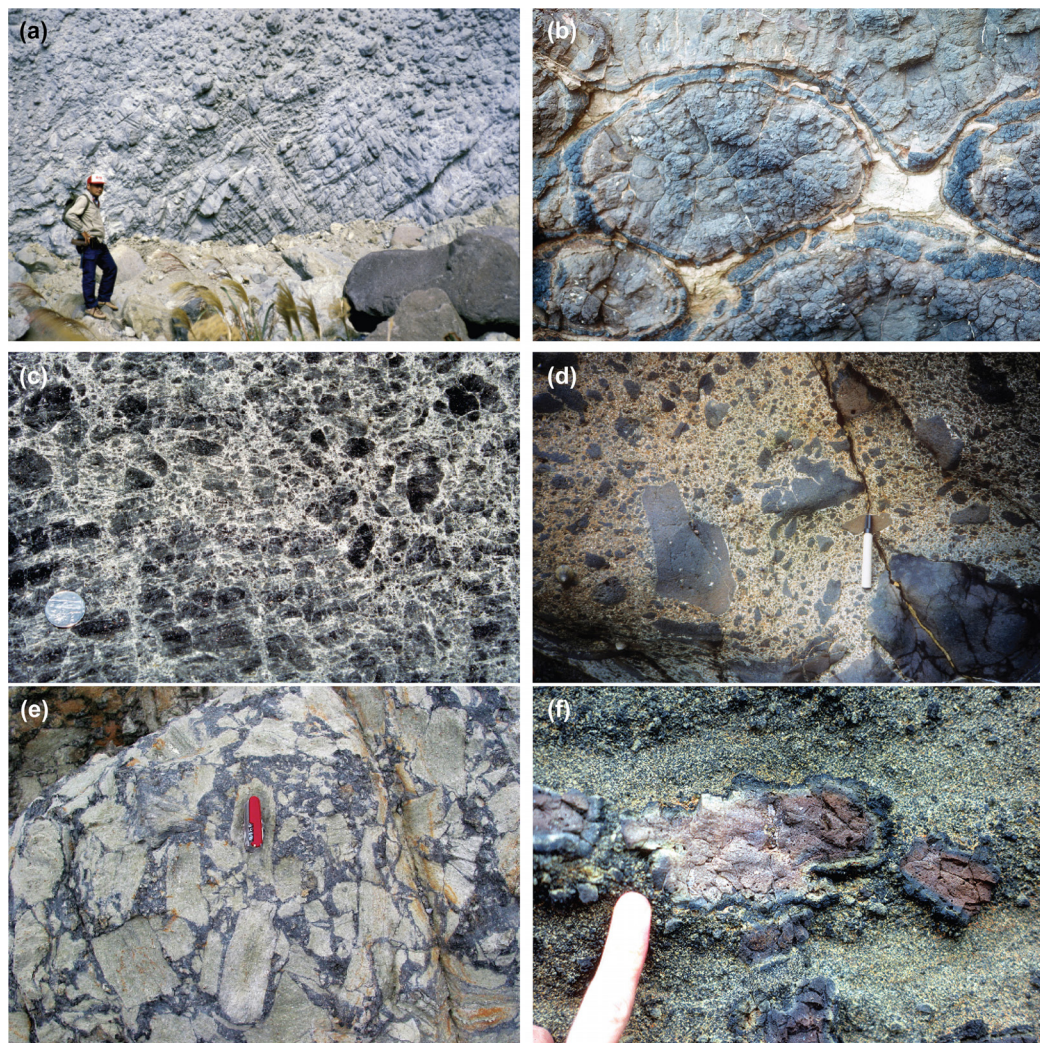


FIGURE 7 | Prehistoric subaqueous lavas and hyaloclastite. **(a)** Quench fragmented submarine Miocene dacite lava dome with *in situ* hyaloclastite breccia, Kariba, Hokkaido, Japan. Note the transition from the coherent to *in situ*, jigsaw-fit brecciated, flow-banded core, to progressively more intensively fragmented, finer breccia outwards. **(b)** Coherent to *in situ* fractured, Eocene-Oligocene, basaltic pillow lava with black, chilled, polygonally quench fractured glassy margins, and an internal fracture network, separated by bioclastic limestone (pale color), Boatmans Harbour, Oamaru, New Zealand. **(c)** *In situ* to clast-rotated pumice hyaloclastite breccia, Cala di Feola, Ponza, Italy. **(d)** Clast-rotated, probably resedimented, basaltic hyaloclastite breccia resulting from pervasive quench fragmentation of fluidal Eocene-Oligocene pillow lavas, Oamaru, New Zealand. **(e)** Rhyolite clast (pale) peperite breccia with black mudstone matrix, Late Devonian Boyd Volcanic Complex, Mimosa Rocks National Park, New South Wales, Australia. **(f)** Fractured and broken, poorly vesicular, submarine fire fountain spatter clast, in a matrix of blocky, coarse ash size, glassy fragments, fragmented by quench fragmentation in the submarine fire fountain, Miocene, Ryugasaki, Oshoro Peninsula, Hokkaido, Japan. (From Cas et al., 2003, **Figure 8**, reproduced under rights granted to authors by American Geophysical Union <https://publications.agu.org/author-resource-center/usage-permissions/>).

dispersal capacity of submarine plumes, which will be discussed below.

Cooling of Pumice Clasts and Vesicle Gases and Effects on Eruption Column Behavior and Dispersal Properties

Whitham and Sparks (1986) first demonstrated that if hot pumice with gas filled vesicles comes in contact with cold water, a large proportion of them quickly become water-logged, denser and sink. This process can affect both pyroclastic and autoclastic

(hyaloclastite) pumice. It is due to the cooling and condensation of hot gasses in vesicles, resulting in a pressure gradient from high in the host, dense water mass to low in vesicles in pumice clasts, which forces external water into the vesicles if permeability pathways exist. This then increases the bulk density of the pumices, in some cases to higher values than water, which causes them to sink (cf. **Figure 5d**). Water-logging and densification of pumice by this process can occur syn-eruptively in subaqueous eruption columns (Whitham and Sparks, 1986; Allen et al., 2008; Carey et al., 2018; Manga et al., 2018), whereas pumices with low permeability will retain a density lower than water, will be

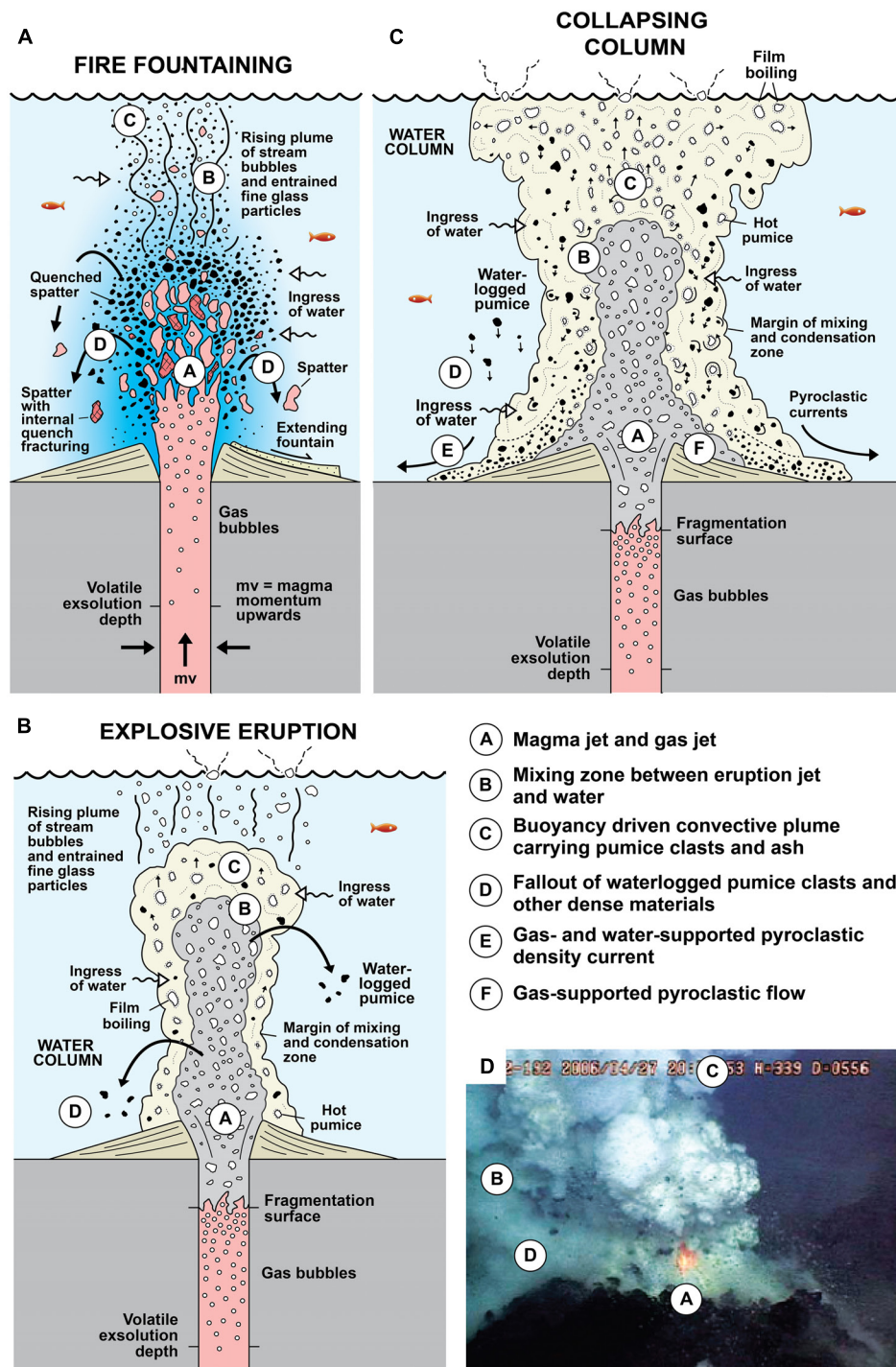


FIGURE 8 | Subaqueous eruption column characteristics. **(A)** Deep-water fire fountain column, showing quench fragmentation of spatter clasts in the column and the water mass above the vent. (After Cas et al., 2003, Figure 14A, under rights granted to authors by American Geophysical Union <https://publications.agu.org/author-resource-center/usage-permissions/>). **(B)** Complex processes contributing to the dynamics of a relatively deep-water, subaqueous explosive eruption column as a result of initial bubble decompression and expansion, then cooling, condensation and water ingress into a subaqueous eruption column upward. **(C)** Schematic diagram of a relatively shallow water (tens to hundreds of meters) explosive eruption column collapsing around the vent. The rising buoyant column is subject to condensation of gasses and mixing in of ambient water. Large pumice clasts become water-logged, contributing to collapse of the column, forming a hot mass-flow of pyroclastic debris, steam and water on the seafloor. (After Kano et al., 1996, Figure 12; Permission from Elsevier). **(D)** Small, suppressed explosion of small ejecta, with a core of incandescent lava or fire fountain, in 2006, Brimbank Crater, NW Rota 1 volcano, Marianas arc, water depth ~550 m. (From Chadwick et al., 2008, **Figure 9E**, under usage permissions for academic works policy of the American Geophysical Union <https://publications.agu.org/author-resource-center/usage-permissions/>).

buoyant and will float for a long time (Fauria et al., 2017). Some may, however, eventually become water-logged through slow infiltration of water, even when cold after drifting around for weeks to years on the sea surface (Fauria et al., 2017).

WATER DENSITY: BUOYANCY OF SUBAQUEOUS AUTOCLASTIC AND PYROCLASTIC ERUPTION COLUMNS AND WATER PLUMES, AND DISPERSAL OF PUMICE

Factors Affecting the Buoyancy of Subaqueous Autoclastic and Pyroclastic Eruption Columns

Subaerial eruption columns and plumes result from the buoyant rise or uplift of a mixture of mostly hot gas, with dispersed water droplets, and solids, driven initially by explosive gas thrust, and the low density and buoyancy of hot gas relative to the density of the atmosphere. In subaerial settings, in addition to hot volcanic gas from the vent, the heating of cold air entrained from the atmosphere through turbulent mixing into the eruption column at its margins helps to maintain a low bulk density and contributes to turbulent plume rise. The decreasing density of the atmosphere with increasing altitude, from $\sim 1.225 \text{ kg m}^{-3}$ at sea level to 0.004 kg m^{-3} at 40 km altitude (United States Standard Atmosphere Air Properties), results in a decrease in relative plume buoyancy and rise rates with increasing height in the atmosphere, becoming neutrally buoyant at a height governed by plume density relative to the surrounding atmosphere; they can rise to 50 km above the vent.

In subaqueous settings, plumes of (super-)heated water, supercritical fluid and gas (\pm solids) form above submarine vents and advancing lava flows away from the vent. Theoretically, the plumes can rise through the entirety of the water column and breach the sea surface if their upward momentum is high, after which they behave more or less like subaerial eruption columns. However, this is more likely from shallow water vents where the eruption column is gas-charged, or seawater has been explosively superheated (e.g., 1952–1953 Myojinsho shallow submarine eruption, Japan; Fiske et al., 1998). From deep-water vents, eruption columns can be significantly modified above the vent by cooling, condensation of gasses and mixing in of cold, dense ambient water, so that their heights are often limited to the depth of the ocean/water body at the location of the eruption. Considering all submarine eruptions occur at water depths of $< 5000 \text{ m}$, submarine eruption columns are generally limited in height to a few kilometers to hundreds of meters, which constrains how column behavior controls pyroclast dispersal, compared with usually higher subaerial eruption columns.

Heated seawater at several hundred $^{\circ}\text{C}$ can be 10% less dense ($\sim 900 \text{ kg m}^{-3}$; Safarov et al., 2009; Sharqawy et al., 2010) than the density of cold sea water (1020 kg m^{-3} at sea level to 1030 kg m^{-3} at depths $> 1000 \text{ m}$; Garrison, 2012; Gladkikh and Tenzer, 2012), and therefore is buoyant. However, cold seawater can be mixed into the margins of the column, particularly if there is a significant

density difference between the column and the ambient water, creating a pressure difference between the two, which will drive cold seawater laterally into the column. As a result, a hot plume of seawater above a vent will cool, become denser and lose buoyancy upward (Whitham and Sparks, 1986; Allen et al., 2008). If volatile bubbles are released from a subaqueous vent, they will further reduce the density of the water column or eruption plume rising above the vent. Bubbles will be densest at the vent because the hydrostatic pressure is greatest at the seafloor. As bubbles rise buoyantly in the eruption column to shallower water depths and lower hydrostatic pressures, they decompress and theoretically should expand and cause the eruption column to become less dense and become more buoyant upward.

However, subaqueous eruption columns with a significant gas bubble fraction are also affected by cooling and condensation erosion of gas bubbles, due to the high heat capacity and thermal conductivity of the water column (Kano et al., 1996; Allen et al., 2008; Cas and Giordano, 2014), and by water ingress driven by a density and pressure gradient from the dense ambient water mass into the gaseous eruption column (Figures 8B,C). Gas bubbles under high ambient pressure can also collapse or implode as they cool and adjust to ambient pressure. For example, the only imaged subaqueous explosive events (NW Rota, Marianas arc, Chadwick et al., 2008; Deardorff et al., 2011; West Mata eruption, Lau Basin, Resing et al., 2011; Embley et al., 2014) formed very small, eruption columns only meters high. The gas-rich column from the 2006 submarine eruption of NW Rota (Marianas arc) at a depth of $\sim 550 \text{ m}$ and temperature of 700°C dissipated within 2 m of leaving vent (e.g., Figure 8D; Chadwick et al., 2008; Deardorff et al., 2011). This could be due to cooling condensation effects and implosions of under-pressured volatile bubbles in magma or in the subaqueous eruption column.

Mitchell et al. (2018) integrated some of these concepts into a model for the eruption column resulting from the wholly submarine eruption of Havre volcano, Kermadec arc, north of New Zealand in 2012 (Carey et al., 2018; Manga et al., 2018). Mitchell et al. (2018) proposed that the release of gasses at the vent affected the eruption column by making it less dense and highly buoyant, although cooling upward made it denser. They also suggest that such reductions in density and therefore hydraulic pressure in the eruption column at the depth of the vent have the capacity to change eruption styles (e.g., triggering explosive activity where otherwise non-explosive activity would be expected because of normal hydrostatic pressure constraints). However, their argument is based on speculative gas bubble abundances in the eruption column, not based on quantitative modeling of likely gas release rates from the erupting vesiculating lava domes. In particular, one of the free gas bubble abundances proposed, 75 vol% in the water column, is highly unlikely at depths of 900 m. This assumed bubble abundance may be based on the fact that the vesicularity of the Havre pumice is very high ($\sim 70 \text{ vol. \%}$) suggesting that this volume of free gas bubbles is released into the water mass at the same time as the pumice is being released. This could only happen if all bubble walls in the erupting pumiceous magma were bursting at the time of the eruption or in the column, which should then produce more ash glass shards than pumice clasts, for which there is little

evidence. The concept could perhaps work where vents lie at shallow water depths of a few hundred meters or less, at much lower hydrostatic pressure, and higher gas overpressure, almost simulating subaerial conditions with high gas overpressures.

In addition, syn-eruptive cooling and water logging of pumice clasts in rising subaqueous eruption columns will cause the columns to cool and become denser and may even lead to gravitational collapses of parts of eruption columns, producing subaqueous volcanoclastic density currents and deposits around the vent, which are water-supported mass flows of volcanic debris (Figure 8C; Kano et al., 1996; Allen et al., 2008). This is analogous to subaerial pyroclastic density currents, which are gas supported. If eruption mass flux is high enough, column collapse-generated subaqueous mass flows that are briefly gas-supported could travel limited distances from vent, producing limited true subaqueous pyroclastic density current deposits (e.g., Busby-Spera, 1984, 1986; Cas and Wright, 1987, 1991), before water mixes into such flows and condensation of gas occurs, transforming them into water-supported mass-flows (Cas and Wright, 1987, 1991).

In summary, subaqueous eruption columns and plumes are therefore likely to have very different buoyancy properties, experience greater ephemeral changes to buoyancy properties, and therefore different dynamics, compared with subaerial eruptions columns. In particular, every subaqueous eruption, including both effusive and explosive eruptions, will produce a subaqueous eruption column or hot water plume. Subaqueous eruption columns resulting from effusive eruptions can disperse non-explosively generated autoclastic pumice and ash size hyaloclasts to produce autoclast fallout deposits. This is very different from subaerial effusive eruptions, which can generate gas plumes capable of carrying very fine glassy ash popped off the surfaces of cooling lavas, but not coarse pumice clasts. Furthermore, deep-water subaqueous eruption columns are much more height limited than subaerial counterparts, which has implications for dispersal of pyroclasts, compared with subaerial eruption columns.

Buoyancy of Pyroclasts Due to the Density of Subaqueous Environments

During subaerial explosive eruptions, no clasts are spontaneously buoyant if ejected into the still atmosphere, because $\rho_{\text{allclasts}} > \rho_{\text{atmosphere}}$. However, buoyant eruption columns can entrain pyroclasts if the gas turbulence velocity and column up-rise velocity exceeds the terminal fall velocity of the pyroclasts. In seawater, however, all vesiculated pyroclasts or autoclasts with $\rho < 1020 \text{ kg m}^{-3}$ are spontaneously buoyant, irrespective of the dynamics of the associated subaqueous plume, and can rise to the surface of the water column if they do not become water-logged in transit. Even clasts with $\rho > 1020 \text{ kg m}^{-3}$ have a reduced effective weight in water relative to air and can be more easily entrained and transported in subaqueous plumes compared with subaerial plumes. Conversely, the rise (and settling) velocities of clasts in the water column are reduced relative to pyroclasts erupted at subaerial vents, because of the high density, relative viscosity and the viscous drag effects of water compared with air (Figure 9; Cashman and Fiske, 1991; Fiske et al., 1998).

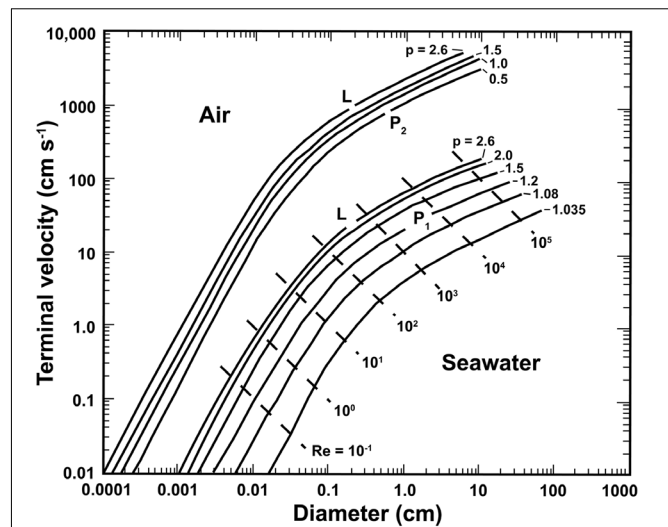


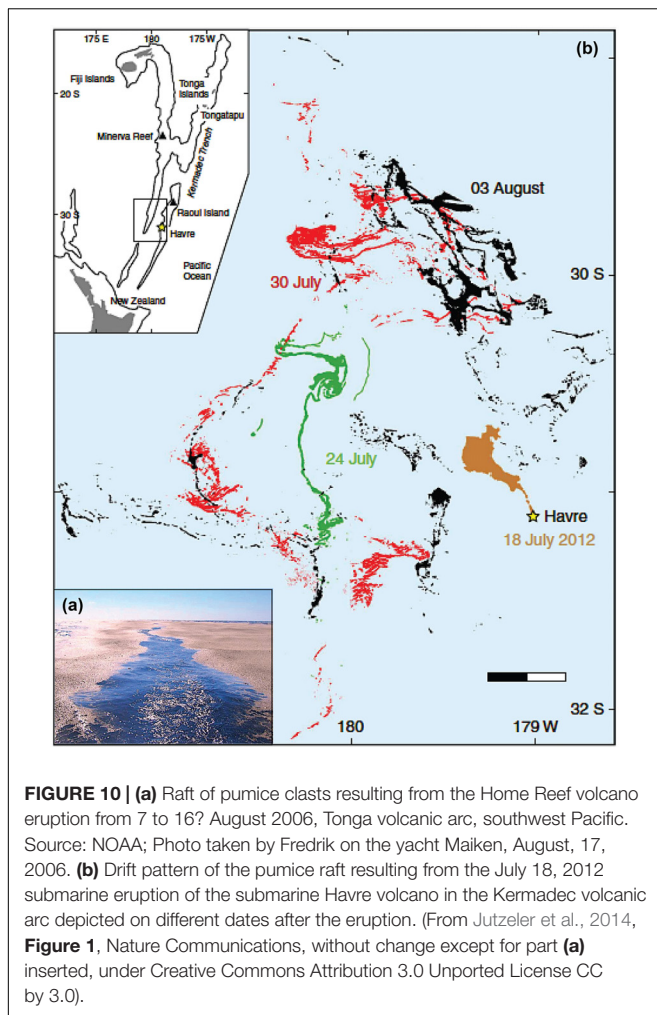
FIGURE 9 | Terminal settling velocities of pyroclasts of different grain sizes and densities in air and in water according to the Stokes' Settling Law, showing orders of magnitude slower velocities in water than in air. (After Cashman and Fiske, 1991, Figure 2; permission American Association for Advancement of Science).

Dispersal of Pumice From Subaqueous Eruption Columns

The dispersal and sedimentation behavior of pumice clasts by subaqueous eruption columns through the water column and from floating masses of pumice (called “pumice rafts”) that form at the sea surface reflects the grain size, vesicularity characteristics (e.g., vesicle size and distribution pattern, permeability), the rate at which clasts become infiltrated by water, the resultant density of clasts, and the prevailing currents and wave patterns (Whitham and Sparks, 1986; Kato, 1987; Manville et al., 1998; Allen and McPhie, 2000; Bryan et al., 2004, 2012; Allen et al., 2008; Fauria et al., 2017; Manga et al., 2018).

Water-logged pumice clasts whose bulk density exceeds that of water can sink and be deposited around the eruption vent, although Cashman and Fiske (1991) noted that the settling velocity of pumice clasts is markedly slower in water than in air (Figure 9). However, pumice clasts that do not have a permeable network of vesicles can retain their low bulk density and float (Fauria et al., 2017), often forming extensive “rafts” of pumice debris that float away from the vent area, pushed thousands of kilometers by marine currents, waves and wind to foreign shores (Bryan et al., 2004, 2012; Jutzeler et al., 2014). For example, pumice from the submarine eruptions along the Tonga arc in 2001 (Bryan et al., 2004), 2006 (Home Reef volcano eruption; Figure 10a; Bryan et al., 2012), and the 2012 Havre volcano eruption in the Kermadec arc (Figure 10b; Jutzeler et al., 2014), was deposited along Australia's eastern seaboard for years after those eruptions, transported thousands of kilometers by flotation by currents and waves.

Surface currents and waves can produce very irregular, changing and circuitous dispersal patterns, reflected by changing pumice raft shapes and drift directions (Figure 10b;



Bryan et al., 2004; Carey et al., 2014; Jutzeler et al., 2014). Different current directions at different depths in the ocean may also affect the distribution and dispersal of clasts. Water settled seafloor deposits of rafted pumice pyroclasts and autoclasts also often coarsen or show no systematic down current variations in grain size (Jutzeler et al., 2014; cf. subaerial fallout deposits). In addition, ash sized particles within deep-sea tephra layers could in fact be generated by abrasion between pumice clasts during transit in pumice rafts (Jutzeler et al., 2014), or through quench spalling from the surfaces of hot lava flows. Such fine “ash” deposits are not syn-eruptive pyroclastic fallout and do not reflect eruption intensity. This contrasts with true subaerial pyroclastic pumice fall deposits, which are dispersed radially around the vent on a windless day, or asymmetrically by strong atmospheric winds following relatively linear paths away from the vent. The deposit grain size decreases downwind with increasing distance from the vent, and exhibits distribution patterns that reflect plume height, and prevailing wind direction and strength (Carey and Sparks, 1986; Bonadonna and Costa, 2013). Few of these controls apply to submarine pumice-forming eruptions and their columns.

DIVERSE POSSIBLE ORIGINS OF PUMICE AND ASH DEPOSITS IN THE OCEANS

Although it is tempting to assign the origin of pumice deposits in submarine settings to a nearby submarine or subaerial explosive eruption, pumice and ash deposits in marine settings can in fact originate from a range of possible processes, many of which are very different from those in subaerial settings. Possible origins (Cas and Giordano, 2014), include:

- (1) Pyroclastic fallout from subaerial vents and fallout through the water column.
- (2) Near-vent fallout from subaqueous vents.
- (3) *In situ* autoclastic pumice (mostly quench fragmentation of erupting submarine vesicular magma = *in situ* pumice hyaloclastite).
- (4) Buoyant detachment of block (incl. house size) to lapilli size pumice from autoclastically fragmenting erupting vesicular magma and dispersal by flotation.
- (5) Post-eruptive sedimentation from far traveling pumice rafts originating from subaqueous vents from either explosive or effusive eruptions.
- (6) Syn- and post-eruptive mass flow resedimentation from shallow water into deep-water.

TERMINOLOGY FOR SUBAQUEOUS ERUPTION STYLES AND DEPOSITS

Cas and Giordano (2014) have briefly considered this topic and advise against using terms ascribed to subaerial explosive eruption styles and deposits for subaqueous eruptions and deposits. Subaerial explosive eruption styles and deposits are defined on measurable quantitative parameters, such as eruption column height, dispersal patterns and distances of the deposits, grain size and sorting characteristics relative to dispersal patterns and areas, etc. (Walker, 1973; Cas and Wright, 1987; Cas et al., in press). These parameters cannot be easily applied to subaqueously erupted deposits because the dispersal processes of vesiculated clasts are influenced by very different processes and conditions in marine environments, and data on dispersal and grain size characteristics are very rarely available or collectable. We first need to decide on what descriptive and measurable parameters are most useful and what the significance of those parameters is before we can begin to develop a terminological approach.

DIRECTIONS FOR FUTURE RESEARCH

The data base on both modern and ancient deep-water submarine volcanic successions is much less than for subaerial volcanic successions, which is reflected in the much more limited understanding of the properties of magmas erupting in deep-water, the physics of eruption processes and submarine eruption plumes, pyroclast dispersal processes and behavior

of both autoclaves and pyroclasts during transport/dispersal and sedimentation. In most cases we don't actually know the location of the source vents, so we can't relate deposit characteristics to distance from vent. As a result, to further advance understanding of submarine volcanic processes we need continuing documentation of both modern and ancient volcanic settings through detailed mapping, logging of sections and sample collection. In ancient settings, this will involve traditional mapping methods as well as application of remote sensing methods and data sets such as LiDAR, radiometrics, magnetics, drone based imagery, aerial image interpretation, and in some cases diamond drilling. In modern settings, high resolution seafloor bathymetric surveying using submersibles including "manned" submersibles, remotely operated submersible vehicles (ROV's) and autonomous underwater vehicles (AUVs), imagery and sampling using submersible vessels are essential, together with coring.

In addition, further modeling of the physics of deep-water eruptions, eruption columns, magma properties, volatile properties, fragmentation processes (including autoclastic and pyroclastic) and dispersal processes based on factual data is required to help better understand them and to bring understanding to the same level as for subaerial eruption processes.

CONCLUSIONS

- Vesiculation can occur at any depth in the crust and at any water depth if the magmatic volatile content is sufficiently high, but the state of the exsolved fluids (supercritical fluid, gas) depends on the water depth and confining pressure.
- The growth rates of exsolved volatiles (bubbles) at pressures approaching 22 MPa (the critical point of water; ~2200 m water depth) are insufficient to drive explosive fragmentation. Explosive eruptions at water depths <1000 m are more likely.
- Slow, non-explosive vesiculation of magma at high pressures can produce highly vesicular lavas and even coherent pumice, which if quench fragmented produces pumice hyaloclastite breccia. High levels of vesicularity are not an indicator of explosivity.
- Magmas erupting in deep-sea settings are initially less viscous than subaerial counterparts, and more prone to erupt effusively or as fountains because of suppressed volatile exsolution. Deep-water fountains are jets of fluid magma, but not explosive.
- Magmas erupting into water are prone to high rates of cooling because of the high heat capacity and thermal

conductivity of water, commonly leading to quench fragmentation and formation of hyaloclastite breccia, which is rare subaerially.

- Submarine eruption columns and particulate hot water plumes can be generated by both explosive and effusive eruptions. Submarine eruption columns behave differently to subaerial columns, and can be dissipated by cooling condensation effects, implosions of gas bubbles, and ingress of cold ambient water.
- Subaqueous effusive eruptions can produce subaqueous fallout deposits of ash size autoclastic vitric material and even fallout deposits of autoclastic pumice.
- The height of submarine eruption columns is limited to the water depth at the vent (<5 km high), except in shallow water, which affects dispersal processes, whereas subaerial explosive eruption columns are not comparably height limited, being potentially an order of magnitude higher (<50 km high).
- Dispersal of pumice (autoclastic or pyroclastic) from submarine eruption columns is much more circuitous than for subaerial columns, is a function of changing wind, wave and current directions, and can take months to years.
- Pumice deposits in the oceans are not necessarily pyroclastic, and can be autoclastic or resedimented in origin.
- Terminology developed for subaerial explosive eruption styles and deposits is unsuitable for subaqueous eruption processes, styles and deposits, and is often incorrect. A new approach to classifying submarine eruption styles and deposits is required, based on careful assessment of deposit characteristics.

AUTHOR CONTRIBUTIONS

RC and JS worked jointly on the text and the preparation of figures.

ACKNOWLEDGMENTS

This review has resulted from decades of interest and research on submarine volcanic processes by the senior author and numerous insightful discussions with volcanological colleagues at Monash University, the University of Tasmania, and the international volcanological community at scientific meetings. We thank RA, MP, guest editor CS and journal editor Valerio Acocella for helpful comments and suggestions that improved the manuscript.

REFERENCES

- Airey, M. W., Mather, T. A., Pyle, D. M., Glaze, L. S., Ghail, R. C., and Wilson, C. F. (2015). Explosive volcanic activity on Venus: the roles of volatile contribution, degassing, and external environment. *Planet. Space Sci.* 113, 33–48. doi: 10.1016/j.pss.2015.01.009
- Allen, R. L. (1992). Reconstruction of the tectonic, volcanic, and sedimentary setting of strongly deformed Zn-Cu massive sulfide deposits at Benambra, Victoria. *Econ. Geol.* 87, 825–854. doi: 10.2113/gsecongeo.87.3.825
- Allen, S. R., Fiske, R. S., and Cashman, K. V. (2008). Quenching of steam-charged pumice: implications for submarine pyroclastic volcanism. *Earth Planet. Sci. Letts.* 274, 40–49. doi: 10.1016/j.epsl.2008.06.050

- Allen, S. R., Fiske, R. S., and Tamura, Y. (2010). Effects of water depth on pumice formation in submarine domes at Sumisu, Izu-Bonin arc, western Pacific. *Geology* 38, 391–394. doi: 10.1130/G30500.1
- Allen, S. R., and McPhie, J. (2000). Water-settling and resedimentation of submarine rhyolitic pumice at Yali, eastern Aegean, Greece. *J. Volcanol. Geotherm. Res.* 95, 285–307. doi: 10.1016/S0377-0273(99)00127-4
- Barreyre, T., Soule, S. A., and Sohn, R. A. (2011). Dispersal of volcaniclasts during deep-sea eruptions: settling velocities and entrainment in buoyant seawater plumes. *J. Volcanol. Geotherm. Res.* 205, 84–93. doi: 10.1016/j.jvolgeores.2011.05.006
- Batiza, R., Fornari, D. J., Vanko, D. A., and Lonsdale, P. (1984). Craters, calderas, and hyaloclastites on young Pacific seamounts. *J. Geophys. Res. Solid Earth* 8371–8390. doi: 10.1029/JB089iB10p08371
- Batiza, R., and White, J. D. L. (2000). “Submarine lavas and hyaloclastite,” in *Encyclopedia of Volcanoes*, eds H. Sigurdsson, J. Stix, B. F. Houghton, S. R. McNutt, and H. Rymer (San Diego, CA: Academic Press), 361–382.
- Binns, R. A., (2003). “Deep marine pumice from the Woodlark and Manus Basins, Papua New Guinea,” in *Explosive Subaqueous Volcanism*, eds J. D. L. White, J. L. Smellie, and D. A. Clague (Washington, DC: American Geophysical Union), 329–343.
- Bischoff, J. L., and Rosenbauer, R. J. (1988). Liquid-vapor relations in the critical region of the system NaCl-H₂O from 380 to 415°C: a refined determination of the critical point and two-phase boundary of seawater. *Geochim. Cosmochim. Acta* 52, 2121–2126. doi: 10.1016/0016-7037(88)90192-5
- Bonadonna, C., and Costa, A. (2013). Plume height, volume, and classification of explosive volcanic eruptions based on the Weibull function. *Bull. Volcanol.* 75, 1–19. doi: 10.1007/s00445-013-0742-1
- Brennen, C. E. (1995). *Cavitation and Bubble Dynamics*. Oxford: Oxford University Press.
- Bryan, S. E., Cook, A., Evans, J. P., Colls, P. W., Wells, M. G., Lawrence, M. G., et al. (2004). Pumice rafting and faunal dispersion during 2001–2002 in the Southwest Pacific: record of a dacitic submarine explosive eruption from Tonga. *Earth Planet. Sci. Letts.* 227, 135–154. doi: 10.1016/j.epsl.2004.08.009
- Bryan, S. E., Cook, A. G., Evans, J. P., Hebden, K., Hurrey, L., Colls, P., et al. (2012). Rapid, long-distance dispersal by pumice rafting. *PLoS One* 7:e40583. doi: 10.1371/journal.pone.0040583
- Busby-Spera, C. J. (1986). Depositional features of rhyolitic and andesitic volcaniclastic rocks of the Mineral King submarine caldera complex, Sierra Nevada, California. *J. Volcanol. Geotherm. Res.* 27, 43–76. doi: 10.1016/0377-0273(86)90080-6
- Busby-Spera, C. J., and White, J. D. (1987). Variation in peperite textures associated with differing host-sediment properties. *Bull. Volcanol.* 49, 765–776. doi: 10.1007/BF01079827
- Busby-Spera, C. J. (1984). Large-rhyolite ash flow eruptions and submarine caldera collapse in the Lower Mesozoic Sierra Nevada, California. *J. Geophys. Res. Solid Earth* 89, 8417–8427. doi: 10.1029/JB089iB10p08417
- Campagnola, S., Romano, C., Mastin, L. G., and Vona, A. (2016). Confort 15 model of conduit dynamics: applications to Pantelleria Green Tuff and Etna 122 BC eruptions. *Contribs. Mineral. Petrol.* 171:60. doi: 10.1007/s00410-016-1265-5
- Carey, R., Soule, S. A., Manga, M., White, J. D., McPhie, J., Wysoczanski, R., et al. (2018). The largest deep-ocean silicic volcanic eruption of the past century. *Sci. Adv.* 4:e1701121. doi: 10.1126/sciadv.1701121
- Carey, R. J., Houghton, B. F., and Thordarson, T. (2010). Tephra dispersal and eruption dynamics of wet and dry phases of the 1875 eruption of Askja Volcano, Iceland. *Bull. Volcanol.* 72, 259–278. doi: 10.1007/s00445-009-0317-3
- Carey, R. J., Wysoczanski, R., Wunderman, R., and Jutzeler, M. (2014). Discovery of the largest historic silicic submarine eruption, Eos. *Trans. Amer. Geophys. Union* 95, 157–159. doi: 10.1002/2014EO190001
- Carey, S., and Sparks, R. S. J. (1986). Quantitative models of the fallout and dispersal of tephra from volcanic eruption columns. *Bull. Volcanol.* 48, 109–125. doi: 10.1007/BF01046546
- Cas, R. A. F. (1978). Silicic lavas in Paleozoic flyschlike deposits in New South Wales, Australia: behavior of deep subaqueous silicic flows. *Geol. Soc. Amer. Bull.* 89, 1708–1714. doi: 10.1130/0016-7606197889<1708:SLIPFD>2.0.CO;2
- Cas, R. A. F. (1992). Submarine volcanism; eruption styles, products, and relevance to understanding the host-rock successions to volcanic-hosted massive sulfide deposits. *Econ. Geol.* 87, 511–541. doi: 10.2113/gsecongeo.87.3.511
- Cas, R. A. F., and Giordano, G. (2014). Submarine volcanism: a review of the constraints, processes and products, and relevance to the Cabo de Gata volcanic succession. *Ital. J. Geosci.* 133, 362–377. doi: 10.3301/IJG.2014.46
- Cas, R. A. F., Giordano, G., and Wright, J. V. (in press). *Volcanology – Processes, Deposits, Geology and Resources*. Berlin: Springer.
- Cas, R. A. F., and Wright, J. V. (1987). *Volcanic Successions: Modern and Ancient*. London: Allen & Unwin, 528. doi: 10.1007/978-94-009-3167-1
- Cas, R. A. F., and Wright, J. V. (1991). Subaqueous pyroclastic flows and ignimbrites: an assessment. *Bull. Volcanol.* 53, 357–380.
- Cas, R. A. F., Yamagishi, H., Moore, L., and Scutter, C. R. (2003). “Miocene submarine fire fountain deposits, Ryugasaki Headland, Oshoro Peninsula, Hokkaido, Japan: implications for submarine fountain dynamics and fragmentation processes,” in *Explosive Subaqueous Volcanism*, Vol. 140, eds J. D. L. White, J. L. Smellie, and D. A. Clague (Washington, DC: American Geophysical Union), 299–316.
- Cashman, K. V., and Fiske, R. S. (1991). Fallout of pyroclastic debris from submarine volcanic eruptions. *Science* 253, 275–280. doi: 10.1126/science.253.5017.275
- Cashman, K. V., and Scheu, B. (2015). “Magmatic fragmentation,” in *The Encyclopedia of Volcanoes*, eds H. Sigurdsson, B. Houghton, S. R. McNutt, H. Rymer, and J. Stix (Cambridge: Academic Press), 459–471. doi: 10.1016/B978-0-12-385938-9.00025-0
- Cashman, K. V., Sturevant, B., Papale, P., and Navon, O. (2000). “Magmatic fragmentation,” in *Encyclopedia of Volcanoes*, eds H. Sigurdsson, J. Stix, B. F. Houghton, S. R. McNutt, and H. Rymer (San Diego, CA: Academic Press), 421–430.
- Chadwick, W. W., Paduan, J. B., Clague, D. A., Dreyer, B. M., Merle, S. G., Bobbitt, A. M., et al. (2016). Voluminous eruption from a zoned magma body after an increase in supply rate at Axial Seamount. *Geophys. Res. Letts.* 43, 12063–12070. doi: 10.1002/2016GL071327
- Chadwick, W. W., Cashman, K. V., Embley, R. W., Matsumoto, H., Dziak, R. P., De Ronde, C. E. J., et al. (2008). Direct video and hydrophone observations of submarine explosive eruptions at NW Rota-1 volcano, Mariana arc. *J. Geophys. Res. Solid Earth* 113. doi: 10.1029/2007JB005215
- Clague, D. A., Dreyer, B. M., Paduan, J. B., Martin, J. F., Chadwick, W. W., Caress, D. W., et al. (2013). Geologic history of the summit of Axial Seamount, Juan de Fuca Ridge. *Geochem. Geophys. Geosyst.* 14, 4403–4404. doi: 10.1002/ggge.20240
- de Rosen-Spence, A. F., Provost, G., Dimroth, E., Gochner, K., and Owen, V. (1980). Archean subaqueous felsic flows, Rouyn-Noranda, Quebec, Canada, and their Quaternary equivalents. *Precamb. Res.* 12, 43–77. doi: 10.1016/0301-9268(80)90023-6
- Deardorff, N. D., Cashman, K. V., and Chadwick, W. W. Jr. (2011). Observations of eruptive plume dynamics and pyroclastic deposits from submarine explosive eruptions at NW Rota-1, Mariana arc. *J. Volcanol. Geotherm. Res.* 202, 47–59. doi: 10.1016/j.jvolgeores.2011.01.003
- Dimroth, E., Cousineau, P., Leduc, M., and Sanschagrin, Y. (1978). Structure and organization of Archean subaqueous basalt flows, Rouyn-Noranda area, Quebec, Canada. *Can. J. Earth Sci.* 15, 902–918. doi: 10.1139/e78-101
- Dixon, J. E., Clague, D. A., Wallace, P., and Poreda, R. (1997). Volatiles in alkalic basalts form the North Arch Volcanic Field, Hawaii: extensive degassing of deep submarine-erupted alkalic series lavas. *J. Petrol.* 38, 911–939. doi: 10.1093/ptro/38.7.911
- Druitt, T. H., Edwards, L., Mellors, R. M., Pyle, D. M., Sparks, R. S., Lanphere, M., et al. (1999). Santorini volcano. *Geol. Soc. Lond. Mem.* 19:165.
- Druitt, T. H., and Kokelaar, B. P. (eds.) (2002). The eruption of Soufrière Hills volcano, Montserrat, from 1995 to 1999. *Geol. Soc. Lond. Mem.* 21:645.
- Edgar, C. J., Cas, R. A. F., Olin, P., Wolff, J. A., Marti, J., and Simmons, J. M. (2017). Causes of complexity in one of the largest known Plinian fallout eruption sequences: the 312 ka Fasnía Member of the Diego Hernandez Formation, Tenerife, Spain. *J. Volcanol. Geotherm. Res.* 345, 21–45. doi: 10.1016/j.jvolgeores.2017.07.008
- Embley, R. W., Merle, S. G., Baker, E. T., Rubin, K. H., Lupton, J. E., Resing, J. A., et al. (2014). Eruptive modes and hiatus of volcanism at West Mata seamount,

- NE Lau basin: 1996–2012. *Geochem. Geophys. Geosyst.* 15, 4093–4115. doi: 10.1002/2014GC005387
- Embley, R. W., and Rubin, K. H. (2018). Extensive young silicic volcanism produces large deep submarine lava flows in the NE Lau Basin. *Bull. Volcanol.* 80:36. doi: 10.1007/s00445-018-1211-7
- Fauria, K. E., Manga, M., and Wei, Z. (2017). Trapped bubbles keep pumice afloat and gas diffusion makes pumice sink. *Earth Planet. Sci. Lett.* 460, 50–59. doi: 10.1016/j.epsl.2016.11.055
- Fink, J. H., and Manley, C. R. (1987). Origin of pumiceous and glassy textures in rhyolite flows and domes. *Geol. Soc. Am. Spec. Pap.* 212, 77–88. doi: 10.1130/SPE212-p77
- Fink, J. H., Anderson, S. W., Manley, C. R. (1992). Textural constraints on effusive silicic volcanism: beyond the permeable foam model. *J. Geophys. Res. Solid Earth* 97, 9073–9083. doi: 10.1029/92JB00416
- Fiske, R. S., Cashman, K. V., Shibata, A., and Watanabe, K. (1998). Tephra dispersal from Myojinsho, Japan, during its shallow submarine eruption of 1952–1953. *Bull. Volcanol.* 59, 262–275. doi: 10.1007/s004450050190
- Fiske, R. S., Naka, J., Iizasa, K., and Yuasa, M. (1995). Caldera-forming submarine pyroclastic eruption at Myojin Knoll, Izu-Bonin arc. *JAMSTEC J. Deep Sea Res.* 11, 315–322.
- Fornari, D. J. (1986). Submarine lava tubes and channels. *Bull. Volcanol.* 48, 291–298. doi: 10.1007/BF01081757
- Fujibayashi, N., and Sakai, U. (2003). “Vesiculation and eruption processes of submarine effusive and explosive rocks from the middle miocene ogi basalt, Sado Island, Japan,” in *Explosive Subaqueous Volcanism*, eds J. D. L. White, J. L. Smellie, and D. A. Clague (Washington, DC: American Geophysical Union), 259–272.
- Fujikawa, S., and Akamatsu, T. (1980). Effects of the non-equilibrium condensation of vapour on the pressure wave produced by the collapse of a bubble in a liquid. *J. Fluid Mech.* 97, 481–512. doi: 10.1017/S0022112080002662
- Furnes, H., Fridleifsson, I. B., and Atkins, F. B. (1980). Subglacial volcanics — On the formation of acid hyaloclastites. *J. Volcanol. Geother. Res.* 8, 95–110. doi: 10.1016/0377-0273(80)90009-8
- Garrison, T. S. (2012). *Essentials of Oceanography*. Belmont, CA: Brooks/Cole Cengage Learning.
- Giffkins, C. C., McPhie, J., and Allen, R. L. (2002). Pumiceous rhyolitic peperite in ancient submarine volcanic successions. *J. Volcanol. Geother. Res.* 114, 181–203. doi: 10.1016/S0377-0273(01)00284-0
- Giordano, D., Russell, J. K., and Dingwell, D. B. (2008). Viscosity of magmatic liquids: a model. *Earth Planet. Sci. Lett.* 271, 123–134. doi: 10.1016/j.epsl.2008.03.038
- Giordano, G., de Benedetti, A. A., Diana, A., Diano, G., Esposito, A., Fabbri, M., et al. (2010). Stratigraphy, volcano tectonics and evolution of the Colli Albani volcanic field. *Geol. Soc. Lon. Spec. Publ.* 3, 43–98.
- Gladkikh, V., and Tenzer, R. (2012). A mathematical model of the global ocean saltwater density distribution. *Pure Appl. Geophys.* 169, 249–257. doi: 10.1007/s00024-011-0275-5
- Gonnermann, H. M. (2015). Magma fragmentation. *Annu. Rev. Earth Planet. Sci.* 43, 431–458. doi: 10.1146/annurev-earth-060614-105206
- Goto, Y., and Tsuchiya, N. (2004). Morphology and growth style of a Miocene submarine dacite lava dome at Atsumi, northeast Japan. *J. Volcanol. Geother. Res.* 134, 255–275. doi: 10.1016/j.jvolgeores.2004.03.015
- Gregg, T. K. P., and Fink, J. H. (1995). Quantification of submarine lava-flow morphology through analog experiments. *Geology* 23, 73–76. doi: 10.1130/0091-7613(1995)023<0073:QOSLFM>2.3.CO;2
- Griffiths, R. W., and Fink, J. H. (1992). Solidification and morphology of submarine lavas: a dependence on extrusion rate. *J. Geophys. Res. Solid Earth* 97, 19729–19737. doi: 10.1029/92JB01594
- Grosfils, E. B., Aubele, J., Crumpler, L., Gregg, T. K. P., and Sakimoto, S. (2000). “Volcanism on earth’s seafloor and Venus,” in *Environmental Effects on Volcanic Eruptions*, eds J. R. Zimbelman and K. P. Gregg (Berlin: Springer), 113–142. doi: 10.1007/978-1-4615-4151-6_5
- Head, J. W. III, and Wilson, L. (2003). Deep submarine pyroclastic eruptions: theory and predicted landforms and deposits. *J. Volcanol. Geother. Res.* 121, 155–193. doi: 10.1016/S0377-0273(02)00425-0
- Hunns, S. R., and McPhie, J. (1999). Pumiceous peperite in a submarine volcanic succession at Mount Chalmers, Queensland, Australia. *J. Volcanol. Geother. Res.* 88, 239–254. doi: 10.1016/S0377-0273(99)00015-3
- Ikegami, F., McPhie, J., Carey, R., Mundana, R., Soule, S. A., and Jutzeler, M. (2018). The eruption of submarine rhyolite lavas and domes in the deep ocean—Havre 2012, Kermadec Arc. *Front. Earth Sci.* 6:147. doi: 10.3389/feart.2018.00147
- Jutzeler, M., Marsh, R., Carey, R. J., White, J. D. L., Talling, P. J., and Karlstrom, L. (2014). On the fate of pumice rafts formed during the 2012 Havre submarine eruption. *Nat. Commun.* 5:3660. doi: 10.1038/ncomms4660
- Kano, K. (2003). “Subaqueous pumice eruptions and their products: a review,” in *Explosive Subaqueous Volcanism*, eds J. D. L. White, J. L. Smellie, and D. A. Clague (Washington, DC: American Geophysical Union), 213–229. doi: 10.1029/140GM14
- Kano, K., Yamamoto, T., and Ono, K. (1996). Subaqueous eruption and emplacement of the Shinjima Pumice, Shinjima (Moeshima) Island, Kagoshima Bay, SW Japan. *J. Volcanol. Geother. Res.* 71, 187–206. doi: 10.1016/0377-0273(95)00077-1
- Karagianni, A., Karoutzos, G., Ktena, S., Vagenas, N., Vlachopoulos, I., Sabatakakis, N., et al. (2010). Elastic properties of rocks. *Bull. Geol. Soc. Greece* 43, 1165–1168. doi: 10.12681/bgsg.11291
- Kato, Y. (1987). Woody pumice generated with submarine eruption. *J. Geol. Soc. Jpn.* 77, 193–206. doi: 10.5575/geosoc.77.193
- Kokelaar, B. P. (1986). Magma-water interactions in subaqueous and emergent basaltic volcanism. *Bull. Volcanol.* 48, 275–289. doi: 10.1007/BF01081756
- Kurokawa, A. (1991). Formation of fesc pumiceous hyaloclastites a case study from Tadami district, Fukushima Prefecture, Japan. *J. Mineral. Petrol. Econ. Geol.* 86, 439–458. doi: 10.2465/ganko.86.439
- Leshner, C., and Spera, F. J. (2015). “Thermodynamic and transport properties of silicate melts and magma,” in *The Encyclopedia of Volcanoes*, eds H. Sigurdsson, B. Houghton, S. R. McNutt, H. Rymer, and J. Stix (San Diego, CA: Academic Press), 113–141.
- Lipman, P. W., and Mullineaux, D. R. (1981). *The 1980 Eruptions of Mount St. Helens, Washington*, Washington, DC: US Geological Survey, 844. doi: 10.3133/pp1250
- Maeno, F., and Taniguchi, H. (2006). Silicic lava dome growth in the 1934–1935 Showa Iwo-jima eruption, Kikai caldera, south of Kyushu, Japan. *Bull. Volcanol.* 68, 673–688. doi: 10.1007/s00445-005-0042-5
- Manga, M., Fauria, K. E., Lin, C., Mitchell, S. J., Jones, M., Conway, C. E., et al. (2018). The pumice raft-forming 2012 Havre submarine eruption was effusive. *Earth Planet. Sci. Lett.* 489, 49–58. doi: 10.1016/j.epsl.2018.02.025
- Manville, V., White, J. D. L., Houghton, B. F., and Wilson, C. J. N. (1998). The saturation behaviour of pumice and some sedimentological implications. *Sedimen. Geol.* 119, 5–16. doi: 10.1016/S0037-0738(98)00057-8
- McBirney, A. R. (1963). Factors governing the nature of submarine volcanism. *Bull. Volcanol.* 26, 455–469. doi: 10.1007/BF02597304
- McPhie, J., Doyle, M., and Allen, R. (1993). *Volcanic Textures: A Guide to the Interpretation of Textures in Volcanic Rocks*. Hobart TAS: CODES Key Centre, University of Tasmania, 196.
- Mills, A. A. (1984). Pillow lavas and the Leidenfrost effect. *J. Geol. Soc.* 141, 183–186. doi: 10.1144/gsjgs.141.1.0183
- Mitchell, S. J., McIntosh, I. M., Houghton, B. F., Carey, R. J., and Shea, T. (2018). Dynamics of a powerful deep submarine eruption recorded in H₂O contents and speciation in rhyolitic glass: the 2012 Havre eruption. *Earth Planet. Sci. Lett.* 494, 135–147. doi: 10.1016/j.epsl.2018.04.053
- Moore, J. G. (1975). Mechanism of formation of pillow lava: pillow lava, produced as fluid lava cools underwater, is the most abundant volcanic rock on earth, but only recently have divers observed it forming. *Am. Sci.* 63, 269–277.
- Mueller, W., and White, J. D. (1992). Felsic fire-fountaining beneath Archean seas: pyroclastic deposits of the 2730 Ma Hunter Mine Group, Quebec, Canada. *J. Volcanol. Geother. Res.* 54, 117–134. doi: 10.1016/0377-0273(92)90118-W

- Newhall, C. G., and Punongbayan, R. (eds). (1996). *Fire and Mud: Eruptions and Lahars of Mount Pinatubo*, Philippines: Philippine Institute, 1126.
- Papale, P. (1999). Strain-induced magma fragmentation in explosive eruptions. *Nature* 397, 425–428. doi: 10.1038/17109
- Persikov, E. S., Bukhtiyarov, P. G., and Sokol, A. G. (2017). Viscosity of hydrous kimberlite and basaltic melts at high pressures. *Russ. Geol. Geophys.* 58, 1093–1100. doi: 10.1016/j.rgg.2017.08.005
- Pichler, H. (1965). Acid hyaloclastites. *Bull. Volcanol.* 28, 293–310. doi: 10.1186/s40517-015-0031-7
- Pioro, I., and Mokry, S. (2011). “Thermophysical properties at critical and supercritical pressures,” in *Heat Transfer-Theoretical Analysis, Experimental Investigations and Industrial Systems*. ed. A. Belmiloudi (Rijeka: InTech published), 573–592.
- Poland, M. P., Takahashi, T. J., and Landowski, C. M. (eds). (2014). *Characteristics of Hawaiian Volcanoes: U.S. Geological Survey Professional*. Heidelberg: Springer.
- Rayleigh, L. (1917). On the pressure developed in a liquid during the collapse of a spherical cavity. *Philos. Mag.* 34, 94–98. doi: 10.1080/14786440808635681
- Resing, J. A., Rubin, K. H., Embley, R. W., Lupton, J. E., Baker, E. T., Dziak, R. P., et al. (2011). Active submarine eruption of boninite in the northeastern Lau Basin. *Nat. Geosci.* 4, 799–806. doi: 10.1038/ngeo1275
- Resnyansky, A. D., and Delaney, T. G. (2006). *Experimental Study of Blast Mitigation in a Water Mist Weapons Systems Division*. Edinburgh, SA: Defence Science and Technology Organisation.
- Rotella, M. D., Wilson, C. J. N., Barker, S. J., Schipper, I. C., Wright, I. C., and Wysoczanski, R. J. (2015). Dynamics of deep submarine silicic explosive eruptions in the Kermadec arc, as reflected in pumice vesicularity textures. *J. Volcanol. Geother. Res.* 301, 314–332. doi: 10.1016/j.jvolgeores.2015.05.021
- Saar, M. O., Manga, M., Cashman, K. V., and Fremouw, S. (2001). Numerical models of the onset of yield strength in crystal-melt suspensions. *Earth Planet. Sci. Lett.* 187, 367–379. doi: 10.1016/S0012-821X(01)00289-8
- Safarov, J., Millero, F., Feistel, R., Heintz, A., and Hassel, E. (2009). Thermodynamic properties of standard seawater: extensions to high temperatures and pressures. *Ocean Sci.* 5, 235–246. doi: 10.5194/os-5-235-2009
- Scarfe, C. M., Mysen, B. O., and Virgo, D. (1987). Pressure dependence of the viscosity of silicate melts. *Magmat. Process. Physicochem. Princip.* 1, 59–67.
- Scutcher, C. R., Cas, R. A. F., Moore, C. L., Rita, and Dd. (1998). Facies architecture and origin of a submarine rhyolitic lava flow-dome complex, Ponza, Italy. *J. Geophys. Res. Solid Earth* 103, 27551–27566. doi: 10.1029/98JB01121
- Scutcher, C. R. (1999). *Characteristics and Origins of Subaqueous Silicic Hyaloclastites, Ponza, Italy and Southwestern Hokkaido, Japan*. Ph.D. thesis, Monash University, Melbourne, VIC, 550.
- Sharqawy, M. H., Lienhard, J. H., and Zubair, S. M. (2010). Thermophysical properties of seawater: a review of existing correlations and data. *Desalinat. Water Treat.* 16, 354–380. doi: 10.5004/dwt.2010.1079
- Shea, T., Gurioli, L., Houghton, B. F., Cioni, R., and Cashman, K. V. (2011). Column collapse and generation of pyroclastic density currents during the AD 79 eruption of Vesuvius: the role of pyroclast density. *Geology* 39, 695–698. doi: 10.1130/G32092.1
- Simmons, J. M., Carey, R. J., Cas, R. A. F., and Druitt, T. H. (2017a). High magma decompression rates at the peak of a violent caldera-forming eruption (Lower Pumice 1 eruption, Santorini, Greece). *Bull. Volcanol.* 79:42. doi: 10.1007/s00445-017-1120-1
- Simmons, J. M., Cas, R. A. F., Druitt, T. H., and Carey, R. J. (2017b). The initiation and development of a caldera-forming Plinian eruption (172ka Lower Pumice 2 eruption, Santorini, Greece). *J. Volcanol. Geother. Res.* 341, 332–350. doi: 10.1016/j.jvolgeores.2017.05.034
- Simmons, J. M., Cas, R. A. F., Druitt, T. H., and Folkes, C. B. (2016). Complex variations during a caldera-forming Plinian eruption, including precursor deposits, thick pumice fallout, co-ignimbrite breccias and climactic lag breccias: the 184ka Lower Pumice 1 eruption sequence, Santorini, Greece. *J. Volcanol. Geother. Res.* 324, 200–219. doi: 10.1016/j.jvolgeores.2016.05.013
- Skilling, I. P., White, J. D. L., and McPhie, J. (2002). Peperite: a review of magma-sediment mingling. *J. Volcanol. Geother. Res.* 114, 1–17. doi: 10.1016/S0377-0273(01)00278-5
- Soriano, C., Cas, R. A. F., Riggs, N. R., and Giordano, G. (2016). “Submarine volcanism of the cabo de gata magmatic arc in the betic-rif orogen, se spain: processes and products,” in *Updates in Volcanology – From Volcano Modelling to Volcano Geology*, Chap. 12, ed. K. Nemeth (Rijeka: InTech).
- Spera, F. J. (2000). “Physical properties of magma,” in *Encyclopedia of Volcanoes*, eds H. Sigurdsson, J. Stix, B. F. Houghton, S. R. McNutt, and H. Rymer (San Diego, CA: Academic Press), 171–190.
- Spieler, O., Kennedy, B., Kueppers, U., Dingwell, D. B., Scheu, B., and Taddeucci, J. (2004). The fragmentation threshold of pyroclastic rocks. *Earth Planet. Sci. Lett.* 226, 139–148. doi: 10.1016/j.epsl.2004.07.016
- Taylor, F. W. (2010). Planetary atmospheres. *Meteorol. Appl.* 17, 393–403. doi: 10.1002/met.212
- Thomas, N., Jaupart, C., and Vergnolle, S. (1994). On the vesicularity of pumice. *J. Geophys. Res.* 99, 633–615. doi: 10.1029/94JB00650
- van Otterloo, J., Cas, R. A. F., and Scutcher, C. R. (2015). The fracture behaviour of volcanic glass and relevance to quench fragmentation during formation of hyaloclastite and phreatomagmatism. *Earth-Sci. Rev.* 151, 79–116. doi: 10.1016/j.earscirev.2015.10.003
- Walker, G. P. L. (1973). Explosive volcanic eruptions—a new classification scheme. *Geol. Rundschau* 62, 431–446. doi: 10.1007/BF01840108
- Wallace, P. J., and Anderson, A. T. (2000). “Volatiles in magmas,” in *Encyclopedia of Volcanoes*, eds H. Sigurdsson, J. Stix, B. F. Houghton, S. R. McNutt, and H. Rymer (San Diego, CA: Academic Press), 149–170.
- Wallace, P. J., Plank, T., Edmonds, M., and Hauri, E. H. (2015). “Volatiles in magmas,” in *The Encyclopedia of Volcanoes*, eds H. Sigurdsson, B. Houghton, S. R. McNutt, H. Rymer, and J. Stix (San Diego, CA: Academic Press), 163–184. doi: 10.1016/B978-0-12-385938-9.00007-9
- White, J. D. L., McPhie, J., and Skilling, I. (2000). Peperite: a useful genetic term. *Bull. Volcanol.* 62, 65–66. doi: 10.1007/s004450050293
- White, J. D. L., McPhie, J., and Soule, S. A. (2015a). “Submarine lavas and hyaloclastite,” in *Encyclopedia of Volcanoes*, eds H. Sigurdsson, J. Stix, B. F. Houghton, S. R. McNutt, and H. Rymer (San Diego, CA: Academic Press), 363–376. doi: 10.1016/B978-0-12-385938-9.00019-5
- White, J. D. L., Schipper, C. A., and Kano, K. (2015b). “Submarine explosive eruptions,” in *Encyclopedia of Volcanoes*, eds H. Sigurdsson, B. Houghton, S. R. McNutt, H. Rymer, and J. Stix (San Diego, CA: Academic Press), 553–569. doi: 10.1016/B978-0-12-385938-9.00031-6
- White, J. D. L., Smellie, J. L., and Clague, D. A. (2003). “Introduction: a deductive outline and topical overview of subaqueous explosive volcanism,” in *Explosive subaqueous Volcanism. Geophysical Monograph*, eds J. D. L. White, J. L. Smellie, and D. A. Clague (Washington, DC: American Geophysical Union), 1–23.
- Whitham, A. G., and Sparks, R. S. J. (1986). Pumice. *Bull. Volcanol.* 48, 209–223. doi: 10.1007/BF01087675
- Wohletz, K., Zimanowski, B., and Büttner, R. (2013). “Magma-water interactions,” in *Modeling Volcanic Processes: The Physics and Mathematics of Volcanism*, eds S. A. Fagents, T. K. P. Gregg, and R. M. C. Lopes (New York, NY: Cambridge University Press), 230–257. doi: 10.1017/CBO9781139021562.011
- Wohletz, K. H. (1986). Explosive magma-water interactions: thermodynamics, explosion mechanisms, and field studies. *Bull. Volcanol.* 48, 245–264. doi: 10.1007/BF01081754
- Wohletz, K. H. (2003). “Water/Magma interaction: physical considerations for the deep submarine environment,” in *Explosive Subaqueous Volcanism*, eds J. D. L. White, J. L. Smellie, and D. A. Clague (Washington, DC: American Geophysical Union), 25–49. doi: 10.1029/140GM02

- Wright, I. C., Worthington, T. J., and Gamble, J. A. (2006). New multibeam mapping and geochemistry of the 30o–35o S sector, and overview, of southern Kermadec arc volcanism. *J. Volcanol. Geother. Res.* 149, 263–296. doi: 10.1016/j.jvolgeores.2005.03.021
- Zimanowski, B., and Büttner, R. (2003). “Phreatomagmatic explosions in subaqueous volcanism,” in *Explosive Subaqueous Volcanism*, eds J. D. L. White, J. L. Smellie, and D. A. Clague (Washington, DC: American Geophysical Union), 51–60. doi: 10.1029/140GM03
- Zimanowski, B., Büttner, R., Dellino, P., White, D. L., and Wohletz, K. H. (2015). “Magma-water interaction and phreatomagmatic fragmentation,” in *The Encyclopedia of Volcanoes*, eds H. Sigurdsson, B. Houghton, S. R. McNutt, H. Rymer, and J. Stix (Amsterdam: Elsevier), 473–484.

Conflict of Interest Statement: The authors declare that the research was conducted in the absence of any commercial or financial relationships that could be construed as a potential conflict of interest.

The handling Editor declared a past co-authorship with the author RC.

Copyright © 2018 Cas and Simmons. This is an open-access article distributed under the terms of the Creative Commons Attribution License (CC BY). The use, distribution or reproduction in other forums is permitted, provided the original author(s) and the copyright owner(s) are credited and that the original publication in this journal is cited, in accordance with accepted academic practice. No use, distribution or reproduction is permitted which does not comply with these terms.



Characteristics and Deposit Stratigraphy of Submarine-Erupted Silicic Ash, Havre Volcano, Kermadec Arc, New Zealand

Arran P. Murch¹, James D. L. White^{1*} and Rebecca J. Carey²

¹ Department of Geology, University of Otago, Dunedin, New Zealand, ² School of Physical Sciences, University of Tasmania, Hobart, TAS, Australia

OPEN ACCESS

Edited by:

Nancy Riggs,
Northern Arizona University,
United States

Reviewed by:

Laura Pioli,
Università degli Studi di Cagliari, Italy
Katharine F. Bull,
Geological Survey of New South
Wales (GSNSW), Australia

*Correspondence:

James D. L. White
james.white@otago.ac.nz

Specialty section:

This article was submitted to
Volcanology,
a section of the journal
Frontiers in Earth Science

Received: 16 June 2018

Accepted: 04 January 2019

Published: 23 January 2019

Citation:

Murch AP, White JDL and
Carey RJ (2019) Characteristics
and Deposit Stratigraphy
of Submarine-Erupted Silicic Ash,
Havre Volcano, Kermadec Arc,
New Zealand. *Front. Earth Sci.* 7:1.
doi: 10.3389/feart.2019.00001

Submarine eruptions dominate volcanism on Earth, but few are observed or even identified. Knowledge of how they operate is largely based on inference from ancient deposits, lagging by a decade or more our understanding of subaerial eruptions. In 2012, the largest wholly deep-subaqueous silicic eruption with any observational record occurred 700–1220 m below sea level at Havre volcano, Kermadec Arc, New Zealand. Pre- and post-eruption shipboard bathymetry surveys, acquisition by autonomous underwater vehicle of meter-scale-resolution bathymetry, and sampling by remote-operated vehicle revealed 14 seafloor lavas and three major seafloor clastic deposits. Here we analyze one of these clastic deposits, an Ash with Lapilli (AL) unit, which drapes the Havre caldera, and interpret the fragmentation and dispersal processes that produced it. Seafloor images of the unit reveal multiple subunits, all ash-dominated. Sampling destroyed layering in all but two samples, but by combining seafloor imagery with granulometry and componentry, we were able to determine the subunits' stratigraphy and spatial extents throughout the study area. Five subunits are distinguished; from the base these are Subunit 1, Subunit 2a, Subunit 3, Subunit 4 (comprising the coeval Subunit 4 west and Subunit 4 east), and Subunit 2b. The stratigraphic relationships of the four AL unit subunits to other seafloor products of the 2012 Havre eruption, coupled with the wealth of remote-operated vehicle observations and detailed AUV bathymetry, allow us to infer the overall order of events through the eruption. Ash formed by explosive fragmentation of a glassy vesicular magma and was dispersed by a buoyant thermal plume and dilute density currents from which Subunits 1 and 2 were deposited. Following a time break (days/weeks?), effusion of lava along the southern caldera rim led to additional ash generation; first by syn-extrusive ash venting, quenching, brecciation, and comminution (S3 and S4e) and then by gravitational collapse of a dome (S4w). Slow deposition of extremely fine ash sustained S2 deposition across the times of S3 and S4 emplacement, so that S2 ash was the last deposited. These thin ash deposits hold information critical for interpretation of the overall eruption, even though they are small in volume and bathymetrically unimpressive. Ash deposits formed during other submarine eruptions are similarly likely to offer new perspectives on associated lavas and coarse pumice beds, both modern and ancient, and on the

eruptions that formed them. Submarine ash is widely dispersed prior to deposition, and tuff is likely to be the first product of eruption identified in reconnaissance exploration; it is the start of the trail to vent hydrothermal systems and associated mineralized deposits of submarine volcanoes, as well as a sensitive indicator of submarine eruptive processes.

Keywords: submarine, Havre volcano, seafloor ash, fragmentation, stratigraphy, pyroclastic eruption

INTRODUCTION

Eruption into a deep subaqueous environment is complex. In addition to influences of magma composition and rheology (Walker and Croasdale, 1971; Dingwell and Webb, 1990), volatile content of the magma, and magma flux (Gonnermann and Manga, 2003; Namiki and Manga, 2008), submarine eruptions are significantly modulated by the physical properties of water, both indirectly (hydrostatic pressure, increased viscosity of water relative to air) and directly (rapid heat transfer, rapid volume expansion of vaporized seawater) (Head and Wilson, 2003; White et al., 2003, 2015; Cas and Giordano, 2014). Hydrostatic pressure will suppress the magnitude of volatile exsolution and expansion, and is presumed to limit explosive expansion and related fragmentation (Fisher, 1984; Staudigel and Schmincke, 1984). Rapid heat transfer on direct contact between magma and water, however, can induce both explosive (Zimanowski et al., 1997; Austin-Erickson et al., 2008) and passive fragmentation (Carlisle, 1963; Kokelaar, 1986; Schmid et al., 2010; van Otterloo et al., 2015).

The cost and difficulty of collecting seafloor samples that can be linked directly to subaqueous eruptive dynamics, and the complexity of modeling these processes (both physically and computationally), has led to diverse interpretations of eruptive processes in the subaqueous environment (Head and Wilson, 2003; Allen and McPhie, 2009; Schipper et al., 2010; Rotella et al., 2013; White and Valentine, 2016). Much of our understanding comes from studies of uplifted subaqueous volcanic successions (e.g., Cas, 1978; Dimroth and Demarcke, 1978; Staudigel and Schmincke, 1984; Busby-Spera, 1986; Dimroth and Yamagishi, 1987; Kano et al., 1996; Allen and McPhie, 2000; Simpson and McPhie, 2001; Allen and Stewart, 2003; Cas et al., 2003; Stewart and McPhie, 2004; Allen and McPhie, 2009; Jutzeler et al., 2015).

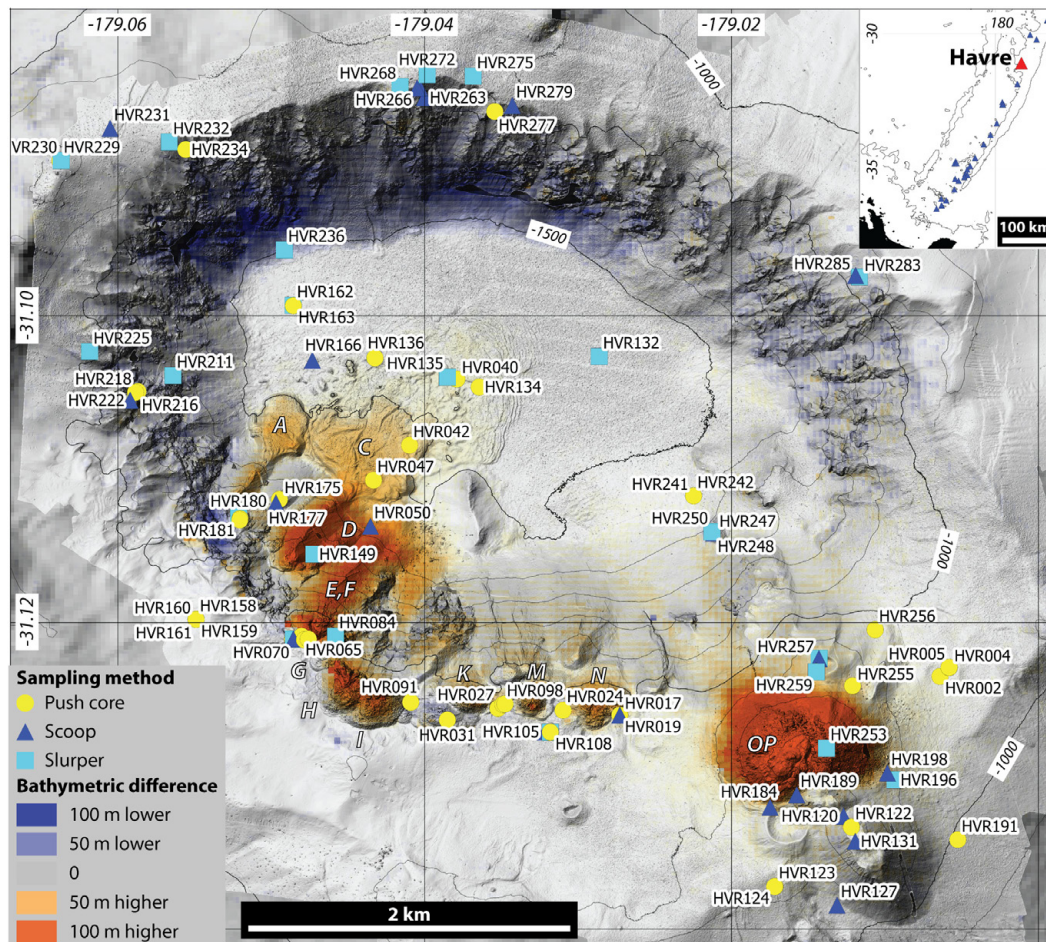
In this paper, we present observations and data on a proximal seafloor ash deposit called the Ash with Lapilli unit (AL unit), sampled 3 years after the deep submarine eruption of Havre volcano (Carey et al., 2014, 2018; Manga et al., 2018; Mitchell et al., 2018). Sampling and observations by remote-operated vehicle (ROV) Jason, guided by high-resolution bathymetry from the autonomous underwater vehicle (AUV) Sentry (Carey et al., 2018), show that the AL unit contains different layers of ash formed during the eruption. The differing distributions of the AL unit ash layers, together with textural differences among deposits and their ash particles, allow us to interpret their origins during the eruption sequence. The study of the AL deposit provides a vital stratigraphic framework for the eruption allowing us to interpret the temporal evolution in processes of the largest known historic wholly deep-subaqueous (>0.5 km; well below wave base) silicic eruption.

GEOLOGICAL SETTING

Havre is a seamount volcano first described by Wright et al. (2006), located at 31° 05'S 179° 5'W (−31.10, −179.03) along the Kermadec arc (**Figure 1a**). The edifice rises from 1500–2000 m below sea level (mbsl) to a peak along the caldera wall at 600 mbsl. The caldera is 4 km long and 3 km wide, elongate northwest–southeast, and has an average caldera-rim depth of 900 m. The caldera floor is at 1500 mbsl (**Figure 1b**).

Havre volcano erupted most recently in 2012 (Carey et al., 2014, 2018; Jutzeler et al., 2014). Satellite images acquired at 1050 18 July 2012 UTC (universal coordinated time; all subsequent times in UTC) show an eruption plume and hot spot emanating from a point source above Havre (**Figure 1a**). An image taken 11 h later at 2151 shows a 400 km² pumice raft. Satellite imagery indicates that eruptive activity affecting the sea-surface, including origination of the atmospheric plume, pumice raft, and of a plume of discolored, ash-stained, water, extended over 21.5 h. An image taken at 0209 20 July 2012 shows the pumice raft detached from its source and no atmospheric plume, indicating the eruption was no longer powerful enough to produce effects at the sea surface. From 17 to 21 July frequent earthquakes of magnitude 3–5 were also recorded from Havre. After 21 July 2012, there is no record in satellite imagery or recorded seismicity of further activity at Havre.

Comparison of shipboard bathymetry surveys conducted in 2002 (Wright et al., 2006) and after the eruption, on 26 October 2012, revealed substantial topographic changes on the volcano (Carey et al., 2014, 2018). Several dome/cone shaped features had been produced on the southern caldera rim along with a large “bulge” on the southwest caldera wall. The seafloor products of the Havre eruption were subsequently mapped at high resolution, imaged, and sampled in a 2015 cruise using AUV Sentry and ROV Jason (**Figure 1b**). Fifteen domes and lavas were erupted (A–P) along the southern and southwestern caldera rim (**Figure 1b**; Carey et al., 2018). Three clastic units were mapped on the seafloor. The lowest observed stratigraphic unit is a widespread deposit composed of giant pumice clasts >1 m in diameter [Giant Pumice unit (GP unit)] extending and coarsening to the NW and inferred to predate Dome OP in the southwest. No clear exposures were found of the contact between GP unit and the pre-2012 substrate, but observations on caldera walls and rims indicate that no other deposits of significant thickness there underlie the GP unit. Surrounding Dome OP is a local unit with lobate distribution, the Ash, Lapilli, and Block unit (ALB unit). The ALB unit overlies, and near the dome buries, the GP unit, with several lobes extending from Dome OP onto the caldera rim and into the caldera. The AL unit, which over most of its extent consists almost entirely of ash, is the most widespread unit, found



data to the fraction of the sieved sample below the chosen point [i.e., if 20% of the sieved sample was less than 1 ϕ (the chosen merge point) then the Mastersizer® data were rescaled to reflect its wt% in the whole sample]. The chosen point produced the lowest difference from 100 wt% when adding the sieving and Mastersizer® data.

Componentry was conducted at whole ϕ steps on material from -2 to 2 ϕ (4 mm to 125 μm). For larger particles, -2 ϕ to 0 ϕ (4–1 mm), categorization and identification were done with the naked eye and for 1 ϕ and 2 ϕ (500–250 μm) fractions, by binocular microscope. For each size fraction, at least 300 grains were analyzed as sample splits or entire samples. Three first-order juvenile component groups were identified based on grain color and morphology. These first-order groups were then subdivided into several second-order subgroups defined on surface morphology and texture. Grain counts of SEM-SE-imaged populations (see below) were also made for particle size fractions 3 ϕ (125 μm), 4 ϕ (63 μm), and smaller than 4 ϕ .

Grain morphology and microtextures were investigated using secondary electron (SE) and back-scattered electron (BSE) methods on a Zeiss Sigma VP® Field-Emission-Gun scanning electron microscope (SEM) at the University of Otago. For SE (morphological) imaging, grains were mounted on an SEM stub using carbon tape and then carbon coated. BSE imaging was undertaken on sectioned grains mounted in a carbon-coated polished briquette. In both cases, imaging was undertaken using a 15-keV accelerating voltage and a working distance of between 7.1 and 9.5 mm.

RESULTS

Identification of Strata Within the AL Unit

Seafloor observations did not reveal natural vertical exposures through the AL unit, but layering was observed in incisions (**Figures 2a–d**) produced by sampling at several sites (HVR042, HVR132, HVR163, HVR196, HVR229, HVR232, and HVR272). In addition, two push cores (HVR159 and HVR134) preserved distinct layers. By combining observations of the seafloor (e.g., 2e–k) and preserved samples, four distinct layers are identified in the AL unit.

Four layers were observed at sites HVR132 and HVR163 (**Figures 2a,b**) and had similar characteristics and thicknesses at each. Two layers were observed at site HVR196 (**Figure 2c**), and a single layer at sites HVR229, HVR232, and HVR272. In each case, the observed layers displayed similar characteristics and thicknesses to one of the layers observed at HVR132 and HVR163 (**Figure 2d**). Detailed observation descriptions of each site are presented in **Supplement 1.2**.

Pushcore HVR159 is the most important single AL sample. It is from the southwest caldera rim and was taken through a thick deposit of the AL unit, beyond the boundary of the GP unit and away from any significant slopes. Here the push core sampled and preserved at least four layers, the upper three of which were visible (**Supplementary Figure 2**). The basal part of the sample, which mostly collapsed when removed from the push core, was a light-colored layer between 4 and 5 cm thick composed of fine to

coarse ash. Stratigraphically overlying this layer was a 1 cm-thick layer rich in elongate coarse ash grains. Next, above a sharp basal contact, was a 2.5 cm-thick dark-colored, medium-to-coarse-ash layer. The uppermost layer was cohesive and 2 cm thick.

Pushcore HVR134 was taken on the caldera floor, northeast of Lava C through a thick deposit of the AL unit near the base of a slight slope, in an area with hummocky topography (**Figure 1b**). The push core shows only two layers: a basal gray cohesive fine-grained layer ~ 20 cm thick, overlain by a dark gray layer 8 cm thick.

Remote-operated vehicle images of the AL unit overlying 2012 Havre lavas show reduced deposit coverage and thickness compared with AL deposits on older lavas of similar morphology. Atop pre-2012 lavas on the southern caldera rim the AL unit is consistently thick (**Figures 2g,h**). In contrast, the AL unit overlying Lavas H, I, K, M, and OP (**Figures 2i–k**) comprises thin patchy deposits. Across Lava N a sharp divide in deposit coverage is observed. Most of Lava G has GP clasts on it and a thick, consistent mantling AL deposit, but the central part of Lava G shows only a thin, patchy AL deposit.

Granulometry and Componentry of HVR134 and HVR159

A critically useful feature of the two samples that did preserve layering (HVR134 and HVR159) is that particles making up the layers have distinctive characteristics. Both HVR134 and HVR159 pushcores were subsampled on the ship from their basal and top layers. The material that remained after removal of the subsamples formed a mixed sample containing material from both subsampled layers and the remainder of the sample. In HVR159, two additional layers are visible in the middle of the sample which were not separately subsampled. Granulometry and componentry were conducted on both the mixed samples and the basal- and top-layer subsamples of HVR134 and HVR159 and reveal common layer-particle characteristics.

Granulometry of mixed samples from HVR134 and HVR159 shows two main grain size peaks, determined using GRADISTATv8 (Blott and Pye, 2001). A 6–5 ϕ (16–32 μm) fraction dominates HVR134, and one of 2–1 ϕ (250–500 μm) is dominant in HVR159, with a minor peak between 0 and -1.5 ϕ (1–2.8 mm) (**Figure 3**). In both samples, the basal layer subsample displays a bimodal grain size distribution with modes at 2–1 ϕ and 0 to -1.5 ϕ (**Figure 3**). The top layer subsample of both HVR134 and HVR159 displays a unimodal distribution with a mode of extremely fine ash (White and Houghton, 2006) at 6–5 ϕ . We used the granulometry modes in mixed samples taken from around the caldera to map the distribution of specific layers.

Componentry was conducted in 1 ϕ steps from -2 to 2 ϕ (4 mm to 250 μm) for 27 samples. Grains were counted into three first-order groups: glassy vesicular, microcrystalline, and elongate tube-vesicle particles (**Figure 3c**). These first-order groups are subdivided into secondary classes based on particle vesicularity and morphology (**Figure 3c**). No lithic component was recognized in any sample examined.



FIGURE 2 | Seafloor images of AL unit layering exposed during sampling from atop GPs at locations HVR132 **(a)**, HVR163 **(b)**, HVR196 **(c)**, and HVR272 **(d)**. At both HVR132 **(a)** and HVR163 **(b)** a similar stratigraphy can be observed showing four layers with comparable layer thicknesses, apparent grainsize, and color. At HVR196 **(c)** only two layers can be seen. At HVR272 **(d)** only a single layer can be seen **(e and f)** show a clastic deposit consisting of lapilli and ash with dominantly elongate tube morphologies at HVR070 **(e)** and overlying the carapace of Lava G **(f)**. In **(g–k)**, the variation in the AL unit coverage overlying lavas around the caldera is shown. Thick deposits of the AL unit can be seen overlying an apparently older part of Lava N **(g)** and also overlying a lava produced prior to the 2012 Havre eruption **(h)**. Over the more-recent part of Dome N **(i)**, and on Domes M **(j)**, and I **(k)**, the AL unit is thinner and patchier. Domes with similar shapes were chosen to provide a consistent context for observed variations in the AL unit.

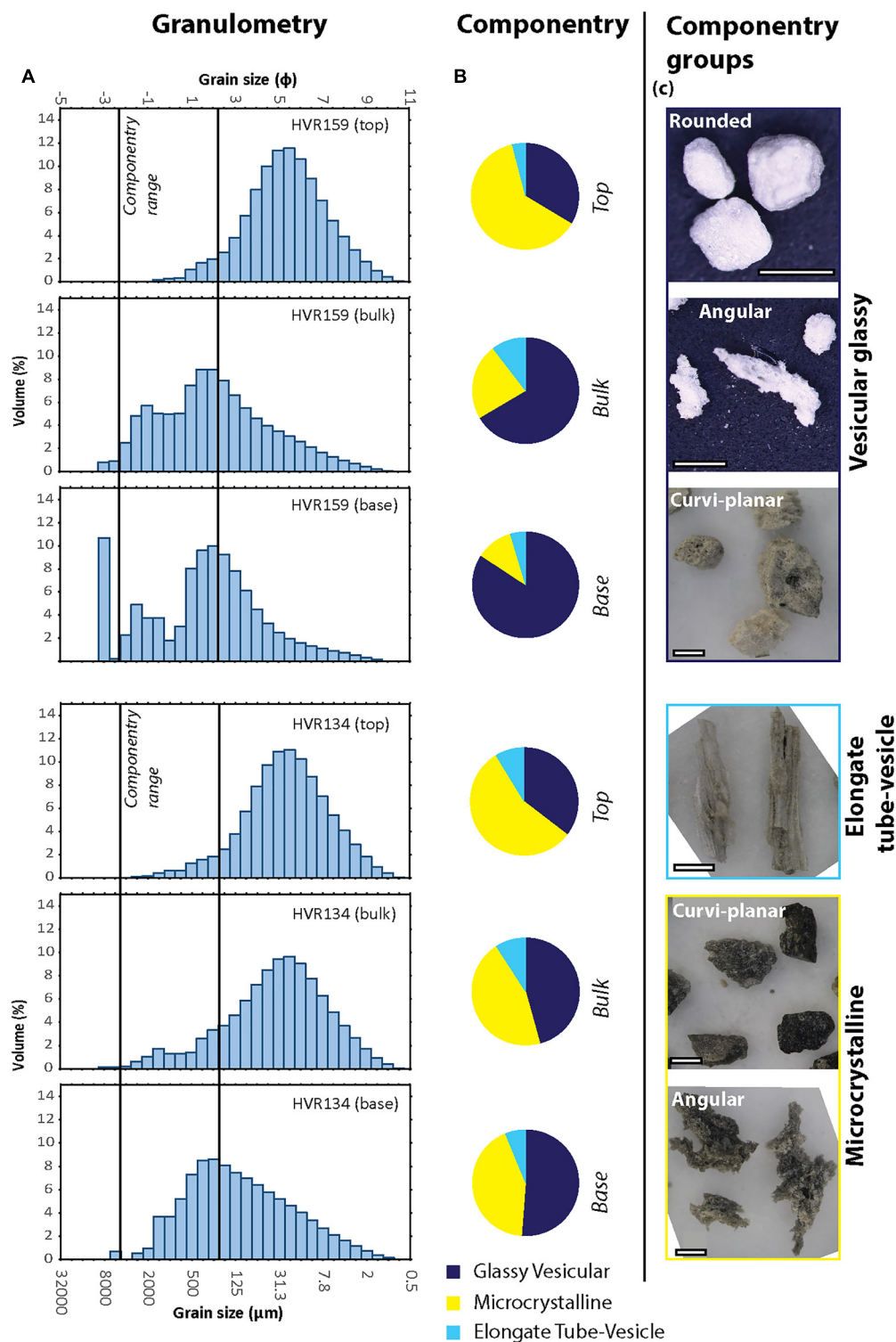


FIGURE 3 | Grainsize distribution **(a)** and componentry **(b)** for samples HVR159 mixed, HVR134 mixed, and their basal and upper layer subsamples. The upper sub-sample is finer grained, shows a decrease in glassy vesicular particles, and a concurrent increase in microcrystalline particles from its bottom to top. In the mixed sample, there is a concentration of elongate tube-vesicle particles. Componentry range indicated for both samples. Small subsamples removed from mixed samples (<5% mixed-sample mass) slightly reduce measured proportions of subsampled ash in mixed samples. **(c)** Optical images that show the componentry classes and their morphological subclasses. Color differences in particles are due to groundmass microcrystallinity, where microcrystalline particles show a higher crystallinity than glassy vesicular, and elongate tube-vesicle particles.

Glassy vesicular grains are white to creamy gray glass of moderate to high vesicularity (**Figure 3c**). Microcrystalline grains are black to dark gray, microcrystalline, and weakly to non-vesicular (**Figure 3c**). Elongate tube-vesicle clasts are white to cream-colored glass with elongate shapes defined by tube vesicles; they have a woody/fibrous appearance (**Figure 3c**).

Componentry of individual layers preserved in the HVR159 and HVR134 was used in parallel with granulometry (**Figure 3**) to determine layer distributions. In HVR159, there is an increase in the proportion of microcrystalline clasts from 11% in the basal layer subsample, to 23% in the mixed sample and 62% in the top layer subsample. Glassy vesicular clasts decrease from 83% in the basal layer to 66% in the mixed sample, to 25% in the top layer. The broad trend of increasing microcrystalline clasts and decreasing glassy vesicular clasts from the base to the top of the AL unit is repeated in sample HVR134, with microcrystalline clasts comprising 42%, 45%, and 54% of the basal layer, mixed sample, and top layer, respectively. The mixed sample of HVR159 also shows the highest percentage of elongate tube-vesicle clasts, 10% compared to 5% and 4% in the basal layer and top layer, respectively (**Figure 3**).

Nomenclature and Stratigraphy of Layers Within the AL Unit

Seafloor observations, plus granulometry and componentry from preserved stratigraphy in push cores, indicate that there are four subunits within the AL unit.

Subunit 1 (S1) – The basal layer in seafloor images of the AL unit and in sample HVR159 is a >6-cm-thick, light-cream-colored deposit of coarse ash (**Figures 2a–c, 3**). We identify grainsize modes at 2–1 ϕ and 0 to –1.5 ϕ (the large mode is subdued) (**Figure 3**). Overall S1 is dominated by glassy vesicular clasts. Subunit 1 is also shown in seafloor images at HVR132 and HVR163 to directly overlie the GP unit.

Subunit 2 (S2) – Subunit 2 was observed on the seafloor as a cohesive extremely fine ash and has a measured modal grainsize of 6–5 ϕ . It overlies S1 across a gradational contact (**Figures 2a–c** and **Supplementary Figure 1**). The fine modal grainsize of particles in S2 precluded standard componentry, but they were examined by SEM (see below). Observations from HVR132 and HVR163 show that Subunit 2 is locally divided into lower (a) and upper (b) where separated by subunits 3 and 4 (**Figure 6**). Elsewhere S2 is a single layer without any visible internal contact(s). Subunit 2a was observed at sites HVR132 and HVR163 (**Figures 2e,f**) where it is approximately 2 cm thick (**Figures 2e,f, 6**). Subunit 2b is 4–10 cm thick on the caldera floor and 2–3 cm thick on the southern, eastern, and western caldera rims. Subunit 2 particles are characterized by their consistent 6–5 ϕ modal grainsize.

Subunit 3 (S3) – Push core HVR159 has in its midsection an approximately 3 cm thick layer rich in elongate clasts. Subunit 3 is dominated by elongate tube-vesicle clasts. It overlies Subunit layer 2a.

Subunit 4 (S4) – This subunit is 2 cm thick and composed of medium/coarse dark colored ash at seafloor locations HVR132 and HVR163 (**Figures 2a,b**), and in push core HVR159. Subunit

4 directly overlies S3 across a sharp boundary. The granulometry of S4 is uncertain because it was not directly sampled, but comparison of the characteristics observed in push core HVR159 with identified components indicates that Subunit 4 is dominated by microcrystalline particles.

Mapping Subunits Using “Mixed” Samples

Observed seafloor stratigraphy at HVR132, HVR163, and granulometry and componentry characteristics of subunits from push core HVR159 allow us to establish the presence or absence of subunits in the other, mixed, samples where no layering was preserved. For example, the presence of the 6–5 ϕ grain size mode indicates the presence of Subunit 2. By establishing the presence of subunits in mixed samples, we can map the distribution of the subunits across the study area. For our sampling locations, the proportional depth of sampling within the overall deposit is unknown, so deeper layers may not have been sampled or have been under-sampled. This limitation would most strongly affect the mapped distribution of S1 (the basal layer). Subunit 1 was, however, identified in all samples, apart from a few taken on steep slopes and on lavas on the southern caldera rim, indicating that samples acquired contain the full sequence.

Granulometry of 81 mixed samples of the AL unit shows that they are composed of >90% ash with complex multimodal grainsize distributions. The grainsize distributions are unimodal and bimodal, with common modes identified at 6–5 ϕ (16–32 μm) associated with Subunit 2, and between 3.5 and 0.25 ϕ (88–840 μm) associated with Subunit 1 (**Figure 4**). Seven ash-dominated samples also show grainsize modes in the 0 to –2 ϕ (1–4 mm) range. The presence of subunits inferred from granulometry was confirmed by componentry showing the presence of particle types also characteristic of the subunits (see the section “Nomenclature and Stratigraphy of Layers Within the AL Unit,” **Figure 5**). Subunit characteristics are summarized in **Table 1**.

Subunit 1

Seafloor images show S1 thicknesses of 2–6 cm (**Figures 2a–c, 6**). Common seafloor ripples and strong seafloor currents encountered during ROV *Jason* dives suggest deposit reworking, so observed layers may not preserve their original thicknesses. The glassy vesicular clasts that characterize S1 have been identified in all clastic samples, indicating that S1 extends across all the study area and beyond it (**Figure 5**). The grainsize mode of S1 in pushcore HVR159 is 2–1 ϕ (0.25–0.5 mm). The mixed samples show a regular fining of the coarser grain size mode from 0 ϕ (1000 μm) near dome OP, toward 3.5 ϕ (88 μm) to the WNW on the far caldera rim (**Figure 4**).

Subunit 2

Subunit 2 is locally divided into lower (a) and upper (b) where separated by Subunits 3 and/or 4 (**Figure 6**). Elsewhere Subunit 2 is a single layer without any visible internal contact(s). Subunit 2a was observed at sites HVR132 and HVR163 (**Figures 2e,f**) where it is approximately 2 cm thick (**Figures 2e,f, 6**). Subunit 2b is 4–10 cm thick on the caldera floor and 2–3 cm thick

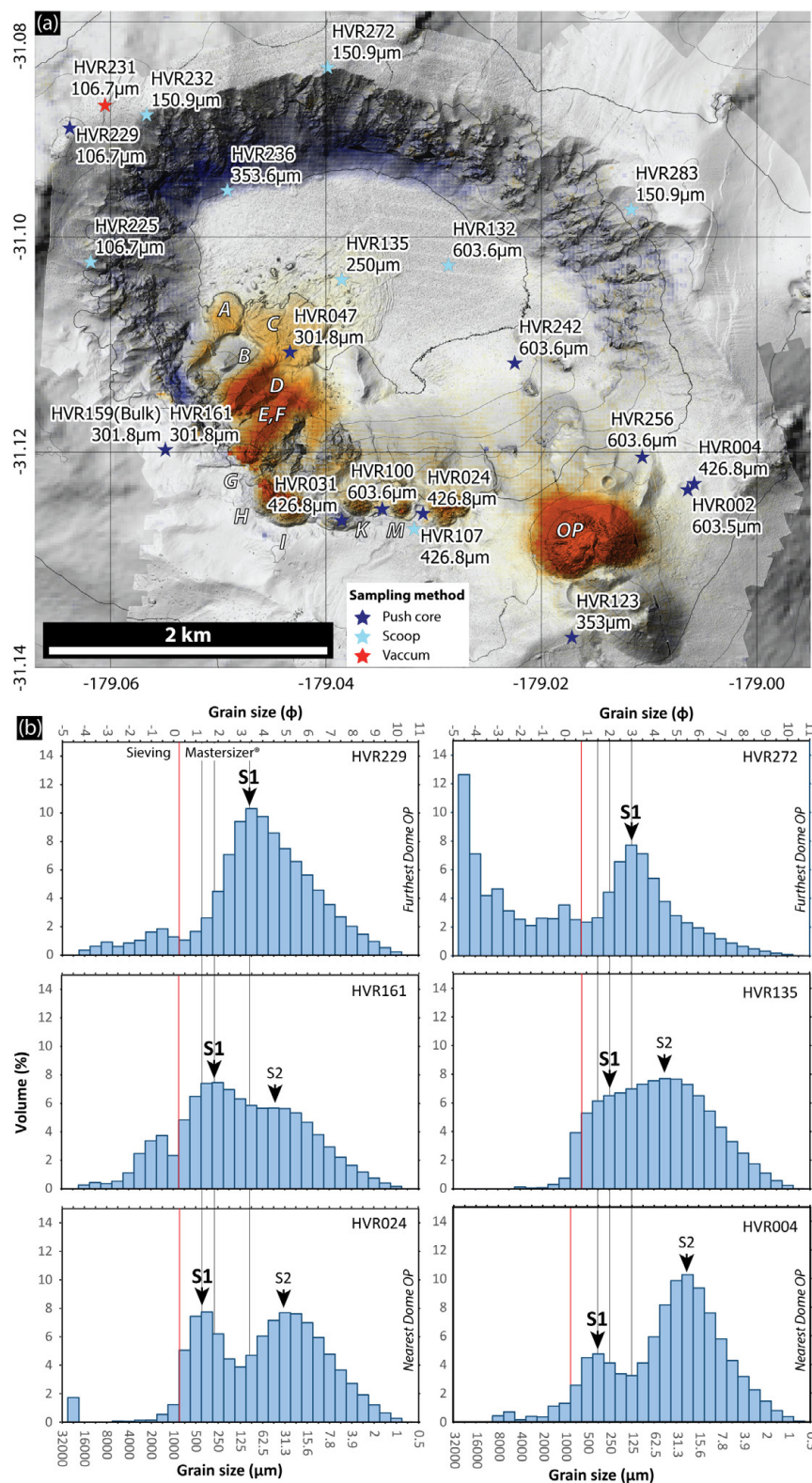


FIGURE 4 | (a) Sample numbers and grainsize peaks for samples of the AL unit from 0.25ϕ ($\sim 240 \mu\text{m}$) and 3.5ϕ ($\sim 88 \mu\text{m}$), inferred to represent S1, across the Havre caldera. **(b)** Representative grain size distributions for samples of the AL unit, with samples closest to Dome OP at the bottom and samples farthest away at the top. The dark lines show the location of the inferred S1 peak in each sample for comparison across the caldera. Note the lack of the 5–6 ϕ mode on the northern caldera rim in samples HVR229 and HVR272.

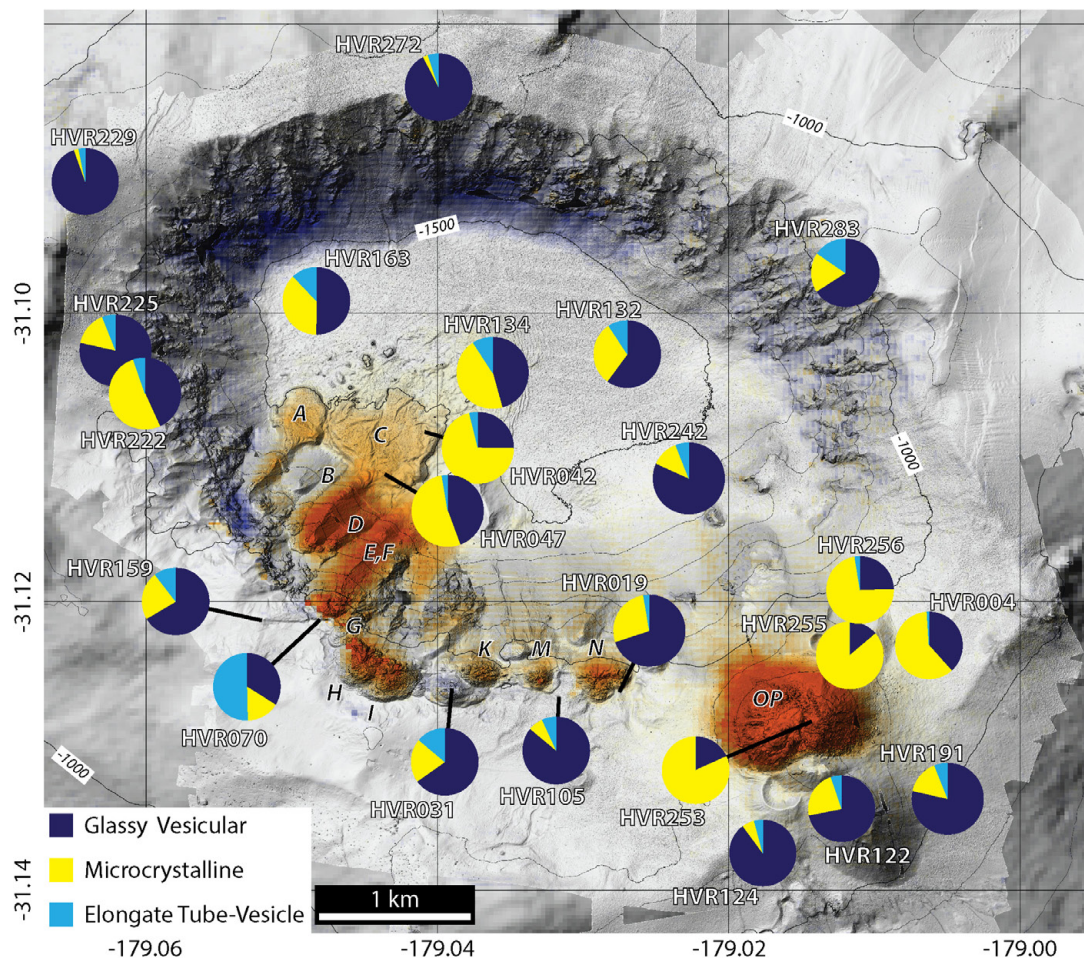


FIGURE 5 | Spatial distribution of componentry data plotted by sample location. Note concentrations in elongate tube-vesicle particles (light blue) around Lava G. Microcrystalline particles (yellow) concentrations are present around Dome OP and the lava flows A–E on the southwest caldera wall, and caldera floor. Glassy vesicular particles (dark blue) are found in every sample and are the dominant component of the overall deposit. Several samples are offset from their sampling location, denoted with a black-tie line.

on the southern, eastern, and western caldera rims. Subunit 2 particles are characterized by their consistent 6–5 ϕ modal grainsize. Subunit 2 can be identified in all clastic samples south of a boundary that roughly follows the east–west trend of the northern caldera wall (Figure 4). To the south, east, and west, Subunit 2 is present to the edge of the investigated area with no notable change in thickness or grainsize. It is inferred to extend well beyond the area, as does Subunit 1.

Subunit 3

Subunit 3 was observed *in situ* in the HVR159 push core where it had a thickness of ~ 3 cm (Figure 6). In mixed samples, componentry shows that elongate tube-vesicle particles are a minor fraction (6–15%) of samples taken from the southwest caldera rim, caldera floor, and a single sample taken on the northeast caldera rim (Figure 5). The highest concentration of elongate tube-vesicle clasts occurs at HVR070 (50%) where the deposit is approximately 0.5 m thick and comprises ash to coarse lapilli (Figures 2e, 5). A similar-looking but unsampled deposit

overlies Lava G (Figure 2f). Three samples taken south of Dome OP contain 4–6% of these clasts (Figure 5). The granulometry and componentry of mixed samples indicate fining of elongate tube-vesicle clasts away from Lava G. This can be seen as a decrease in modal elongate tube-vesicle clasts from larger than -2ϕ (4 mm) in HVR070 (nearest sample to Lava G) to smaller than 2ϕ (0.25 mm) in HVR283 (4 km from Lava G). A general fining trend in elongate tube-vesicle clasts away from Lava G is also observed through samples HVR031, HVR159, HVR163, and HVR132.

Subunit 4

Subunit 4 is a ~ 2 cm thick layer (Figure 6) observed on the seafloor at locations HVR132, and HVR163, and in push core HVR159. Microcrystalline grains characterize Subunit 4, and these are found in samples from two separate areas (Figure 5). A western area trends northeast across the caldera floor from the southwest caldera rim and is denoted S4w (Figure 5). An eastern area, S4e, with microcrystalline particles is around Dome

TABLE 1 | Summary table of subunit dispersal, stratigraphic, and depositional characteristics.

Subunit	Dispersal	Stratigraphic relations	Depositional characteristics	Grainsize/componentry characteristics
S1	<ul style="list-style-type: none"> Entire study area. 	<ul style="list-style-type: none"> Basal contact not seen. Overlies the GP unit. Relation to the ALB unit unknown. 	<ul style="list-style-type: none"> At least 5 cm thick at all sites observed. Drapes topography with no thinning or thickening. No internal sedimentary features observed. 	<ul style="list-style-type: none"> Grain size of 0.5–3.5 ϕ. Composed of glassy vesicular ash. No lithic clasts.
S2	<ul style="list-style-type: none"> Sharp boundary at the northern caldera wall. South of the boundary deposit extends to the edges of the study area. 	<ul style="list-style-type: none"> S2 is split in to lower (S2a) and upper (S2b) sections. Forms current seafloor. Overlies S1 and ALB unit. S2a has diffusive contact with S1. S2b overlies domes. 	<ul style="list-style-type: none"> S2a thickness of ~2 cm on caldera floor. Thickness poorly resolved on rim. S2b on caldera floor 3–14 cm thick vs. ~2 cm on rim. Thickest on Lava C (10–14 cm). Ripples occasionally observed on upper surface (seafloor). Appears to drape GP clasts to some degree. No internal sedimentary features observed. 	<ul style="list-style-type: none"> Characteristic grain size of 6 ϕ. Composed of glassy vesicular ash. No lithic clasts.
S3	<ul style="list-style-type: none"> Deposit extends NE–SW across the caldera with boundaries approximately at either caldera wall. 	<ul style="list-style-type: none"> In proximal locations overlies S2a. Distally a diffusive layer at the top of S2a. 	<ul style="list-style-type: none"> Thickens toward the area of Lava G. >0.5 m thick at HVR070. Diffusive layer of unknown thickness at HVR283 (most distal). S3 deposited on topography ~50 m higher than Lava G. Topography has little influence on grain size or thickness. S3 drapes topography. No internal sedimentary features observed. 	<ul style="list-style-type: none"> Maximum grain size drops from >70 mm on Lava G to <250 μm at HVR283 (most distal). Characterized by elongate tube-vesicle particles. No lithic clasts.
S4a	<ul style="list-style-type: none"> Deposit extends NE–SW across the caldera. Thins toward the NE. 	<ul style="list-style-type: none"> Overlies S3. Overlain by S2b. Sharp boundary with S3 and S2b. 	<ul style="list-style-type: none"> Subunit ~2 cm thick on the caldera floor (HVR132 and 163) and on the SW rim (HVR159). Topography does not appear to affect thickness. S4 drapes topography. 	<ul style="list-style-type: none"> Characterized by microcrystalline ash. No lithic clasts.
S4b	<ul style="list-style-type: none"> Surrounds Dome OP and extends toward the north down slope. 	<ul style="list-style-type: none"> Overlies the ALB unit. 	<ul style="list-style-type: none"> Visually the deposit appears to thin away from Dome OP. Deposit elongated downslope to the north. Deposit poorly observed. 	<ul style="list-style-type: none"> Meter scale blocks proximal to Dome OP. Maximum grainsize reduces away from Dome OP. Characterized by microcrystalline ash. No lithic clasts.

OP (Figure 5). All seafloor observations of Subunit 4 were made in the western S4w area (Figure 5). There are no apparent differences between clasts of S4w and S4e (Figure 5).

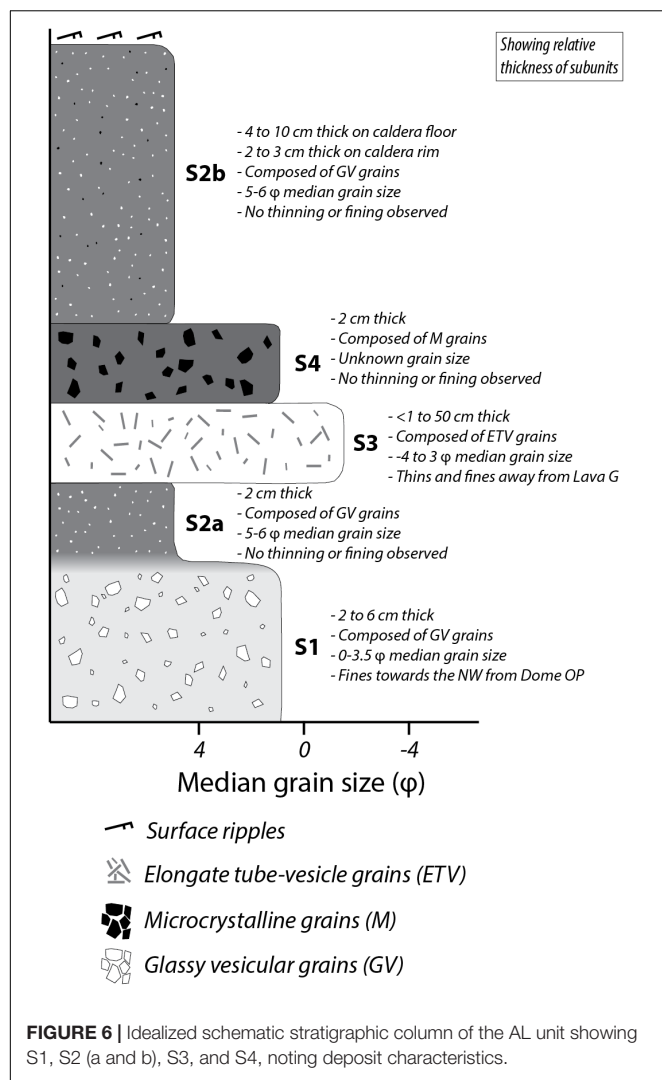
Limitations

The stratigraphic framework presented above (Figure 6) represents a best estimate from the available data, but we recognize significant potential sources of error. Our ROV sampling techniques did not generally preserve layering, and did not always produce a surface that would allow visual observations of layering. Sampling of the AL unit was also restricted to the proximal depositional areas studied. Despite these limitations, the combination of ROV observations, key samples with preserved layering, and distinctive particle populations give

us confidence that the proposed subunits and their mapped distributions adequately represent the seafloor deposits.

Grain Morphology

Glassy vesicular, elongate tube-vesicle, and microcrystalline particles are split into subclasses based on morphology or vesicle form. Glassy vesicular grains show three subclasses; curvi-planar, angular, and fluidal particles (Figures 3c, 7). Curvi-planar clasts are defined by planar and curvi-planar surfaces that intersect to form sharp edges (Figures 3c, 7a–c) and include both platy and sub-equant blocky clasts. Vesicles in curvi-planar clasts are cross-cut by fracture surfaces, which show no deformation around the bubble (Figure 7a). Angular clasts have prominent concavities



defined by brittle-fractured vesicle walls (**Figures 3e, 7d-f**). Fluidal clasts have exterior features indicating surface-tension or fluid-dynamic reshaping of the grains while molten. Fluidal clasts include both those with a wholly fluidal form, and those that preserve a single fluidal surface (**Figures 3c, 7g,h**). Fluidal particles are often cross cut by undeformed curvi-planar fracture surfaces (**Figures 7g,h**).

Microcrystalline particles, by contrast, show only two subclasses; curvi-planar and angular grains (**Figure 3c**). Curvi-planar clasts are typically weakly- to non-vesicular, defined by planar and curvi-planar surfaces that intersect to form sharp edges and include both platy and sub-equant blocky clasts (**Figure 3c**). Angular clasts generally show moderate-vesicularity, with vesicle walls producing complex particle shapes (**Figure 3c**).

Elongate-tube particles are categorized into three different subclasses; elongate tube-angular, elongate tube-ribbed, and elongate tube-fluidal (**Figures 7j-l**). Elongate-tube angular particles are elongate with concave surfaces defined by brittle-fractured bubble walls (**Figure 7j**). Elongate-tube ribbed grains show surface ribs that run parallel to the vesicle and clast

elongation direction (inferred to be outer tube-vesicle walls) (**Figure 7k**). The surface ribs have smoothly undulating surfaces and are typically unmarked by vesicles. Elongate tube-fluidal particles have flowing, molten, surfaces on which peaks or droplet-like features are present; they show evidence of ductile necking (**Figure 7l**).

SEM SE images were montaged and used to count particles of different shapes for 3 φ (125 μm), 4 φ (63 μm), and smaller than 4 φ (63 μm) fractions in samples containing few or no microcrystalline clasts. Subunits 1 and 2 are composed dominantly of curvi-planar particles smaller than 3 φ (**Figure 8**). These curvi-planar particles make up between 50 and 86% of the total sample, with a relatively consistent abundance in each grainsize fraction (**Figure 8**). Over the same grainsize range, there are between 2 and 45% angular clasts in S1 and S2, showing an increase in abundance with decreasing grainsize; 12% at 3 φ, to 22% for smaller than 4 φ (**Figure 8**). Fluidal clasts make up 3–35% of clasts in S1 and S2, decreasing with particle size from an average of 19% at 3 φ to 7% for smaller than 4 φ (**Figure 8**).

Microtextural Descriptions

Microtextures of AL unit ash from -1 φ (2 mm) particles to those smaller than 4 φ (63 μm) are characterized by distinctive vesicle and microlite textures. In all clast types phenocrysts compose <5% by solid area, generally in 70–300 μm clusters of euhedral plagioclase and pyroxene.

The groundmass of glassy vesicular clasts is >95% glass, with a microlite population of acicular plagioclase and pyroxene (**Figures 9a,b**). Glassy vesicular clasts are typically moderately to highly vesicular and show a wide range of vesicle size populations, textures, and degrees of vesicle deformation. Vesicles are typically sub-round to round in 2D and range in cross-sectional diameter from <6 up to ~500 μm. Vesicles smaller than 20 μm are typically isolated, while larger vesicles display more-complex shapes resulting from coalescence and bubble interaction. Vesicles in fluidal glassy vesicular clasts exhibit a range of features indicating ductile behavior of the melt during and after fragmentation, such as inflated bubble walls which protrude from outer clast surfaces, and dense rims unbroken by vesicles enclosing highly vesicular clast cores (**Figures 9g-h**). Some fluidal grains also display several domains in single clasts defined by vesicular cores surrounded by a convex dense fluidal rim (**Figure 9h**).

The groundmass of microcrystalline grains contains 8–35% acicular plagioclase, pyroxene, and Fe-Ti oxide microlites, calculated using ImageJ (**Figures 9c,d**). Plagioclase microlites display swallowtail and hopper forms (**Figures 9c,d**). The characteristics and textures of microcrystalline particles differ between grains (**Figures 9c,d**). One grain also shows apparent mingling of two melts of differing microlite populations (**Figure 9d**). There is cristobalite, both vesicle-hosted and groundmass-replacing, in ~20% of observed microcrystalline clasts. Vesicles in microcrystalline clasts are generally isolated from one another and have ragged forms that result from the interaction of bubble walls with the microlite population (**Figure 9d**).

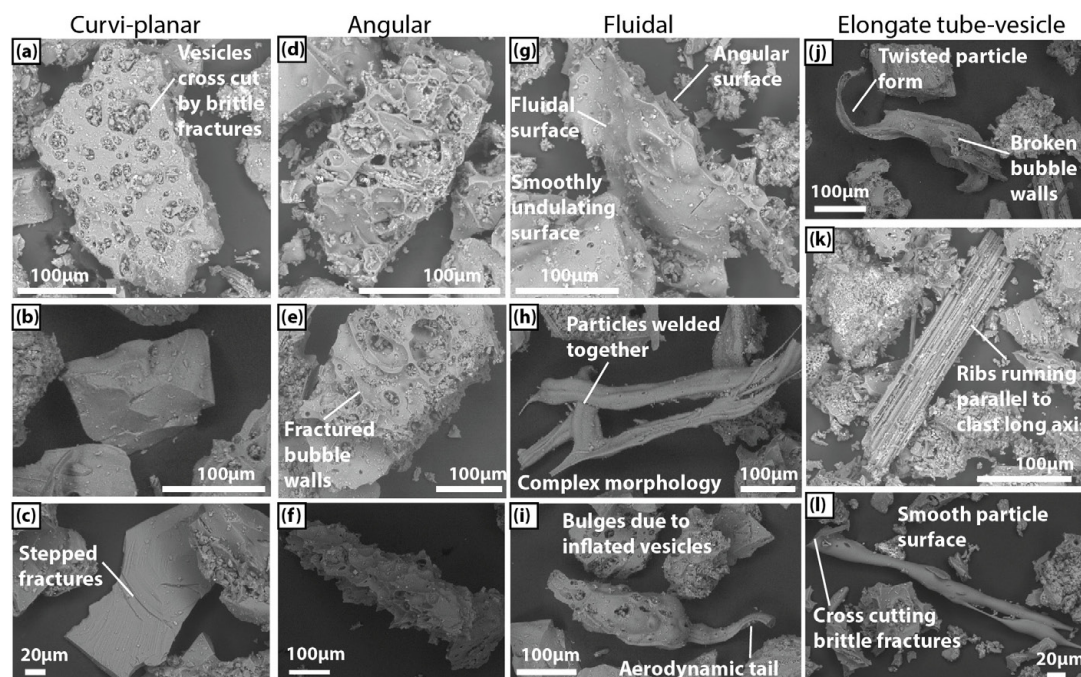


FIGURE 7 | SEM images of representative particles from the different componentry classes; curvi-planar (a–c), angular (d–f), fluidal (g–i), and elongate tube (j–l). In curvi-planar clasts, fracture surfaces cross cut vesicles. Angular particles are bound by fractured vesicle walls with grain morphology dominantly controlled by vesicle texture (d–f). Fluidal particles are defined based on features that are indicative of molten behavior syn/post-fragmentation. This includes ductile reshaping (g), particle welding (h), and post-fragmentation vesicle inflation (i). (j–l) Clast-surface textures of elongate tube particles. Note the different scales across images.

Elongate tube-vesicle clasts have >95% groundmass glass with dominantly acicular pyroxene microlites and minor plagioclase (Figures 9e,f). Elongate tube-vesicle clasts show generally weak to moderate vesicularity. Vesicles are generally highly elongate, with tube to pipe-like morphologies in 3D and lengths from ~10 µm to those that traverse the whole length of clasts. The microlites in elongate tube-vesicle clasts are aligned parallel with the vesicle- and clast-elongation direction (Figures 9e,f). The smallest vesicles in some particles (<20%) (<10 µm) have circular cross-sectional forms and appear undeformed. Asymmetrical strain shadows can be observed around phenocrysts with vesicles and microlites wrapping around in distinctly flow-like patterns. In the strain shadows vesicles display rounded to sub-rounded forms.

INTERPRETATIONS

Timing, Eruption, and Pyroclast Transport Processes

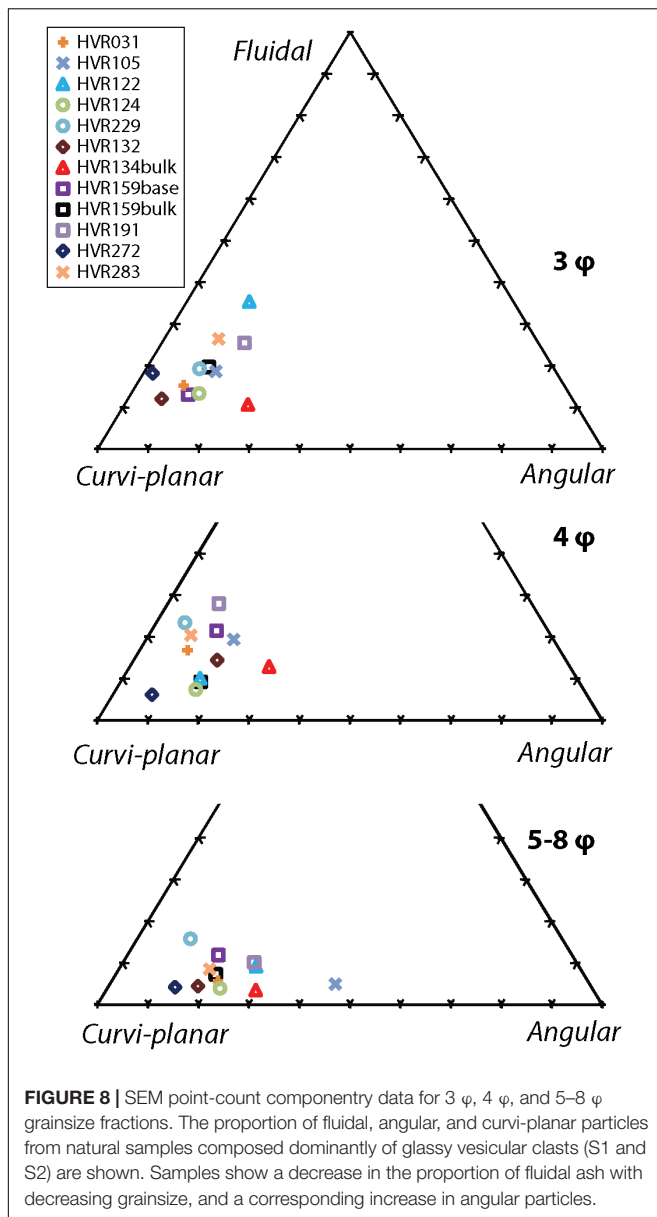
Subunit 1

Subunit 1 drapes topography, which suggests deposition from suspension in the water column. The wide distribution of this subunit (Figure 10a) requires that the height from which the bulk of the grains settled must have been shallower than 700 mbsl, the highest point on the caldera rim. No thinning of Subunit 1 is apparent, but it does fine with distance from Dome OP; we infer that this indicates eruption from a source vent now covered by Dome OP (Figure 4). The lack of any apparent internal

stratification indicates that the deposition of S1 was broadly continuous (Figures 2a–d).

The dominance of glassy vesicular ash in S1 indicates fragmentation of a relatively homogeneous magma (Figures 3, 5). The extremely low microlite content (Figures 9a,b,g,h) indicates a high degree of magma undercooling. The modal grain size of S1, 0.5–3.5 φ (Figures 4, 6) suggests reasonably energetic fragmentation of the magma (Büttner et al., 2002; Zimanowski et al., 2003; Dürig et al., 2012a), while predominant curvi-planar ash morphologies indicate brittle fragmentation (Heiken, 1972; Dürig et al., 2012b; Gonnermann, 2015; Liu et al., 2015; Figure 8). Although direct fingerprinting of hydromagmatic fragmentation is difficult (White and Valentine, 2016), the combination of fine particles <0.5 mm across the dispersal area and even proximal to the vent, and the dominance of curvi-planar particles with stepped fractures, points toward magma water interaction-driven fragmentation (e.g., Wohletz, 1983; Büttner et al., 1999, 2002; Austin-Erickson et al., 2008). Fluidal rhyolitic ash grains in S1 (Figure 7) indicate that viscous fragmentation mechanisms were also important (Walker and Croasdale, 1971; Porritt et al., 2012). Fluidal ash grains also suggest unusual magma rheology during fragmentation in the Havre eruption. Wholly fluidal clasts cannot have been produced by abrasion from larger particles and must have been produced by a primary volcanic fragmentation mechanism.

Clasts in Subunit 1, the raft pumice, the GP unit, and the ALB unit are all composed of dominantly glassy material with variable vesicle populations and textures (Rotella et al., 2015;



Carey et al., 2018; **Figures 9a,b,g,h**), and are distinct from clasts of S3 and S4. Stratigraphically, S1 directly overlies the GP unit, and almost all our seafloor observations of S1 were made from deposits lying on GP clasts. It is not known whether any S1-equivalent ash underlies the GP unit, and the relationship of S1 to the ALB unit is also unknown. The AL unit is much thinner and patchier where it overlies the caldera rim lava domes (**Figures 2g–k**), and there is little or no S1 signature in sample HVR255 (**Figure 5**) from on top of Dome O. These relationships suggest that deposition of S1 began prior to effusion of the caldera rim domes F–O. Given its groundmass microtextural similarities to pumice in the GP unit and raft pumice (Rotella et al., 2015; **Figure 9**), its position immediately overlying GP (**Figure 10b**), and observational evidence that it possibly predates domes F–P (**Figures 2g–k**), we infer that Subunit 1 is associated with the

eruption phase that produced the raft pumice, synchronous with or subsequent to deposition of the GP unit (Manga et al., 2018; Mitchell et al., 2018). The presence of a discolored water plume associated with the Havre pumice raft in MODIS images (Carey et al., 2014, 2018; Jutzeler et al., 2014) indicates significant quantities of ash in the water column during emplacement of the pumice raft (**Figure 1**).

The S1 deposit is inferred to have formed through settling of ash dispersed over a wide area by a buoyant plume (**Figure 11a**). The eruption that generated the plume is inferred to have occurred from the same vent that produced the pumice raft and the GP unit now below Dome OP. Modal S1 grains, 500–125 μm , would have settled through 700–1500 m of seawater over 3–52 h if released from the top of the water column (Ferguson and Church, 2004). This settling rate could have been significantly increased through the formation of vertical density currents (e.g., Manville and Wilson, 2004), or somewhat reduced by hindered-settling effects (Druitt, 1995). To produce the observed stratigraphic relationship of S1 overlying GP clasts, we suggest that S1 and the GP deposits were generated during distinct events, with intervening time sufficient that settling produced the GP deposit before deposition of S1 began (**Figure 11a**). Particle morphology of S1 ash grains is inconsistent with an origin by abrasion of raft pumice, and the presence of fluidal ash in S1 further suggests that part of the magma was fragmented without direct water contact. Fragmentation to produce S1 ash is thus inferred to have been driven by a range of processes, some “dry,” but overall mostly driven by direct magma–water interaction, and most probably at the same time as the pumice raft was formed.

Subunit 2 (a and b)

Subunit 2 has a well-defined depositional limit along the northern caldera wall and is thicker on the caldera floor than on the caldera rim (**Figure 10**), indicating a strong topographic control on its deposition. Subunit 2 shows no internal stratification or grading, indicating continuous deposition (**Figures 2a–c**). The lack of S2 deposits on the northern caldera rim suggests that S2 ash was erupted from a vent on the southern caldera rim. The extremely fine modal grainsize of S2 would result in particle settling times of ~ 1 –3 months in still water (Ferguson and Church, 2004) from a height of 500 m above the depositional surface (the height of the caldera walls), though the formation of vertical density currents (e.g., Fiske et al., 1998; Manville and Wilson, 2004) or particle aggregation (Wiesner et al., 1995) could have increased the rate of deposition. The presence of S3 and S4 as discrete layers within S2 is consistent with an inference of prolonged S2 deposition (**Figure 10b**).

Subunit 2 is composed of glassy vesicular ash, indicating fragmentation of a highly undercooled broadly homogeneous magma. The modal grainsize of 6–5 ϕ indicates highly energetic fragmentation (Büttner et al., 2002; Zimanowski et al., 2003; Dürig et al., 2012a).

Like those of S1, S2 ash grains are broadly similar in groundmass microtexture to the raft pumice (Rotella et al., 2015), the GP unit blocks, and particles of the ALB unit. All comprise dominantly glassy material with varied vesicle populations and

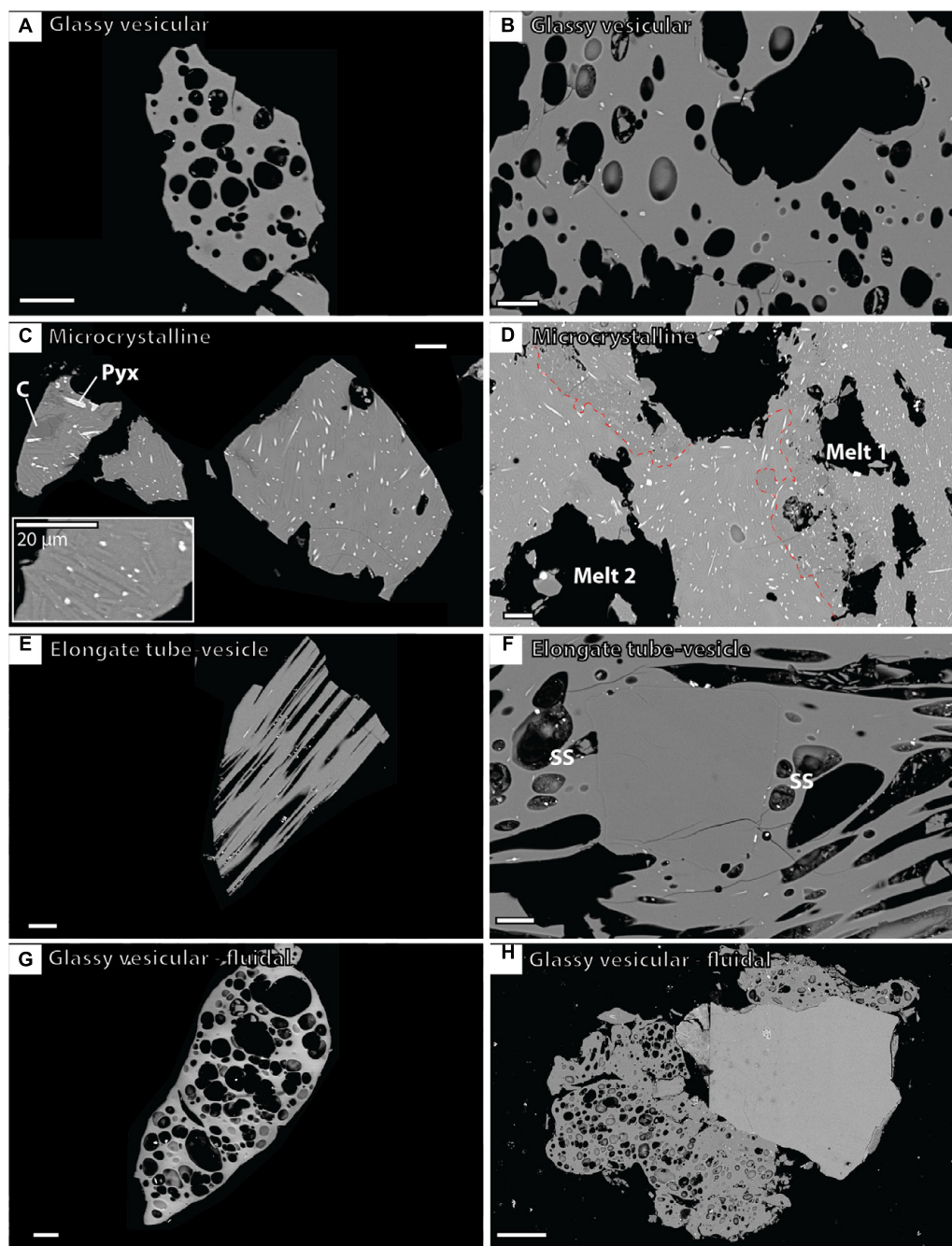


FIGURE 9 | SEM images illustrating representative microtextures of glassy vesicular (a,b), microcrystalline (c,d), elongate tube-vesicle (e,f), and glassy vesicular fluidal (g,h) components (scale bars are 100 μm unless otherwise noted). Glassy vesicular particles show rounded vesicles and dominantly glassy groundmasses. Microcrystalline particles show a range of both groundmass crystallinity and vesicle textures (c,d), in (c) three microcrystalline grains can be observed each showing differing crystallinities show plagioclase (Plg) and pyroxene (Pyx) microlites. Groundmass-hosted cristobalite (C) is common (c), textures of mingling between melt of different crystallinities are rarely observed (d). Elongate tube-vesicle grains are generally glassy with aligned sheared vesicles and microlites (e,f). Around phenocrysts strain shadows (SS) can occasionally be observed (f). The fluidal particles show a Pele's Tear-like structure with a highly vesicular core and a dense glassy rim (g,h). In the case of (h) the Pele's Tear structure appears domainal with several separate vesicular cores and dense rims.

textures. Subunit 2 overlies S1 across a gradational contact (Figures 2a–c), suggesting continuous deposition; we infer that S1 and S2 are probably both deposits from the same eruptive event.

Subunit 2 is inferred to have been emplaced from an extremely dilute suspension flow, shed from the same eruption column from which S1 was dispersed (Figure 11a). The flow spread radially from an eruption column fed by the vent

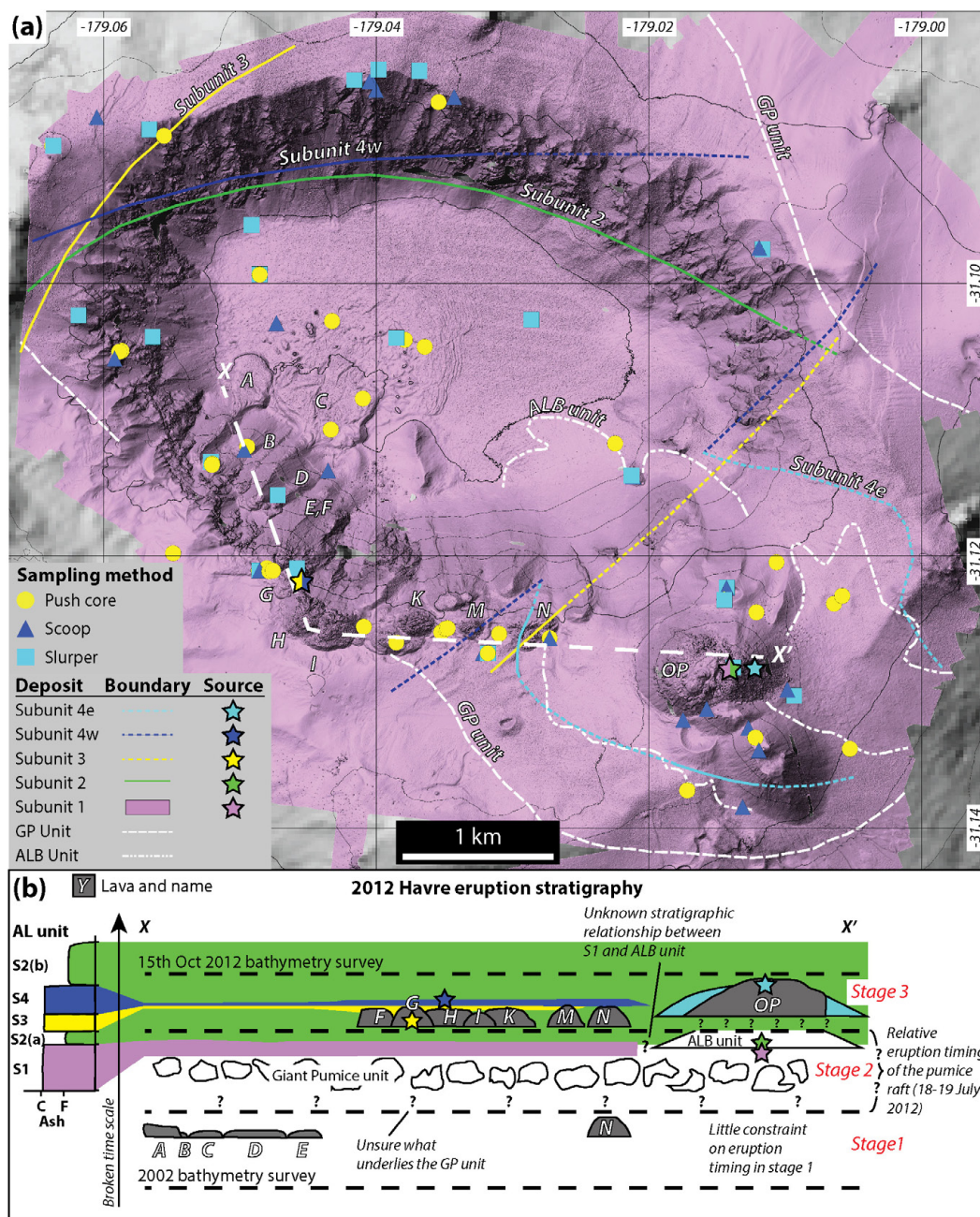


FIGURE 10 | (a) Bathymetric map showing Havre caldera along with the distributions/outlines of the clastic deposits produced during the 2012 Havre eruption where: GP unit – white dashed, ALB unit – white dash and dots, S2 – green, S3 – yellow, S4w – dark blue, and S4e – light blue. Solid line indicates a deposit boundary constrained by sample characteristics, while the dashed boundary are constrained by bathymetry, seafloor texture, etc. Subunit 1 (purple) is present at all sample sites with no change in thickness or grainsize, and is interpreted to extend well beyond AUV-mapped area. The inferred locations of the sources for each subunit are denoted by stars. **(b)** An idealized stratigraphic cross section through the Havre eruption deposits [generalized location shown on (a)] showing temporal and spatial relations of deposits from various vents. Three stages have been identified for the Havre eruption reflecting changes in style and location, from dispersed effusive to fragmental eruption focused on a single vent, then to dispersed effusive with weakly pyroclastic behavior.

now filled with Dome OP. On entering the caldera the flow is inferred to have acted in a similar manner to a density current entering a restricted basin (e.g., Pickering et al., 1992; Edwards et al., 1994; Mulder et al., 2009; Pickering and Hiscott, 2009; Talling et al., 2012). Reflection between steep caldera walls

caused the flow to pond, resulting in a thickened deposit of S2 compared with outside the caldera. We infer that S2 comprises more-distal and dilute deposits of density currents that also emplaced the ALB unit (Figure 10). Rapid slowing of the flow by condensation of any volatile component and

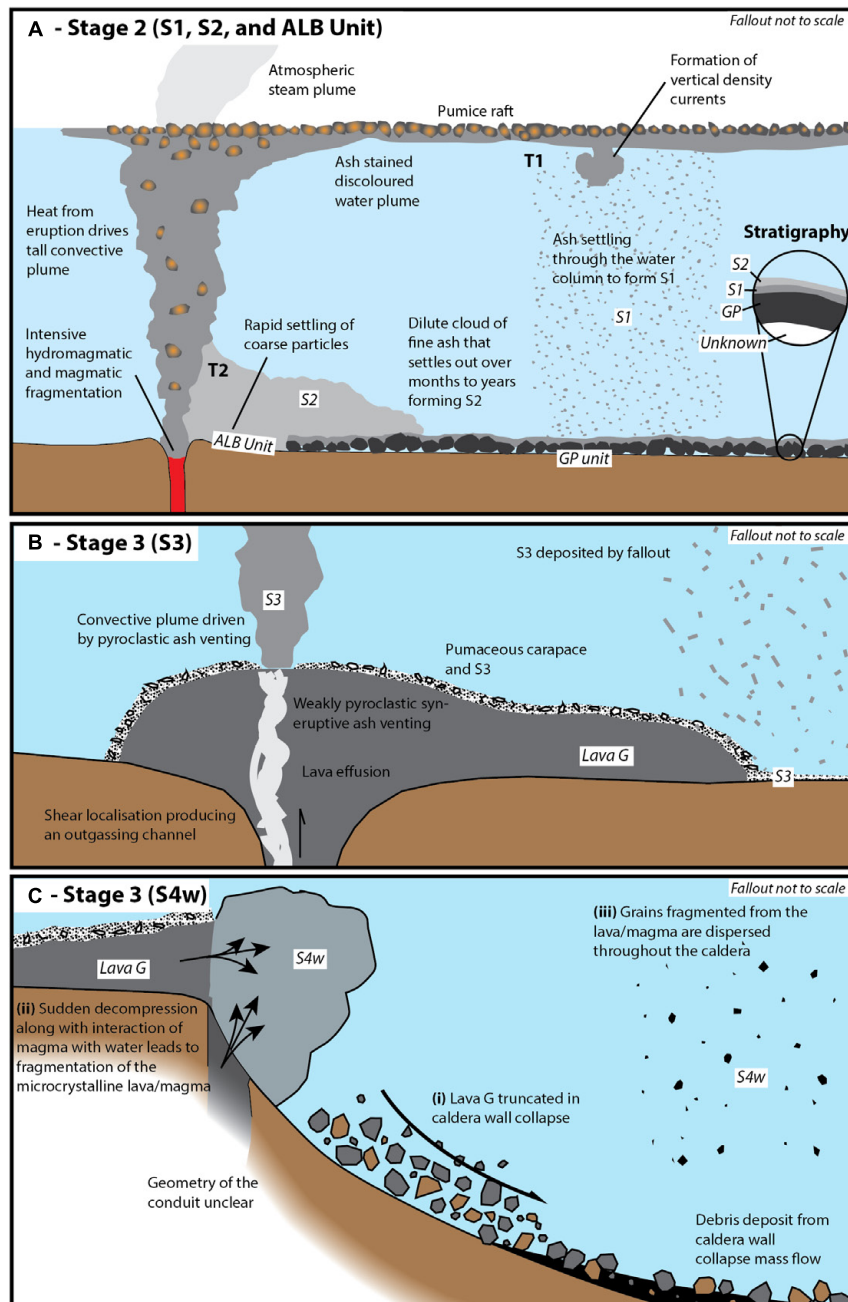


FIGURE 11 | Conceptual model for generation of the various subunits of the seafloor AL unit at Havre. **(a)** Subunits 1 and 2 are inferred to have been formed from the same eruption [at time 1 (T1) and time 2 (T2), respectively], along with the ALB unit and pumice raft. Energetic wet and dry fragmentation of a highly undercooled, ascending, vesiculating magma generated abundant fine particles that were dispersed in an overlying convective column, fallout from which formed S1. Partial or whole-scale collapse of the column, possibility due to vent widening, lead to the formation of density currents. Rapid deposition of the coarse fraction produced the ALB unit surrounding the vent. The remaining dilute flow was then dispersed widely, and from it S2 was deposited. **(b)** Subunit 3 formed during weakly pyroclastic ash venting during the eruption of Lava G. Far-reaching dispersal of the ash occurred in a weak convective column overlying the source of the pyroclastic activity. **(c)** Subunit 4w is inferred to have been formed following caldera wall collapse. Exposure of the hot microcrystalline core of Lava G (+H and I?) to the ambient water resulted in fine-scale fragmentation and dispersal.

friction of the water would result in rapid deposition of coarse suspended material to produce the ALB unit. The deposition of S2 is inferred to have been slow, but the initial generation and injection into the water column of particles was rapid. Over the

time during which S2 was being deposited, eruptive activity at the caldera-rim domes and syn-eruptive mass-wasting activity rapidly emplaced S3 and S4, with deposition of S2 continuing afterward (Figure 10b).

Subunit 3

Subunit 3 drapes topography, indicating deposition by settling from the water column, and fines and thins away from Lava G (**Figure 10a**). No vent structure is apparent at or near Lava G and we cannot confidently infer a precise source location. The morphological similarity between elongate tube-vesicle clasts that compose S3 and the carapace of Lava G, in addition to S3's thinning and fining trends, suggests that Lava G was the source of S3. Stratigraphically S3 overlies S2a above a gradational contact. Our interpretation is that the deposition of S3 closely followed the eruptive phase that produced the GP deposit, the raft pumice, the ALB, S1, and S2a deposits. Rapid thinning of S3 from ~0.5 m thick at 150 m distance (HVR070) to 2 cm thick at 900 m distance (HVR159) along with fining away from Lava G suggest a low-intensity eruptive mechanism.

Subunit 3 is composed of elongate tube-vesicle clasts characterized by tube/pipe vesicles (**Figures 7j–l, 9e,f**). Elongate tube-vesicle clast morphology in S3 indicates both brittle and viscous deformation, before or during fragmentation (**Figures 7j–l**; Heiken, 1972).

The generation of an ash deposit by fallout from a lava flow implies an additional process(es) that drove extensive fragmentation and vertical transport of particles. Viscous fragmentation, as suggested by particle morphology in S3, indicates that fragmentation cannot have been driven by quenching alone, since water contact would rapidly cool the magma preventing viscous deformation. Subunit 3 is therefore inferred to be a fallout deposit produced by weak pyroclastic activity during explosive–effusive effusion of Lava G (**Figure 11b**).

The inference that S3 was generated by explosive–effusive activity implies that Lava G was being actively extruded at the time of S3 deposition (Schipper et al., 2013; Cole et al., 2014; Black et al., 2016). The apparently sharp upper contact of S3 with S4w indicates termination of S3 ash venting prior to onset of S4w deposition.

Transitional explosive–effusive ash venting in subaerial eruptions of silicic magma appears relatively common (e.g., Kennedy and Russell, 2012; Schipper et al., 2013; Cole et al., 2014; Black et al., 2016). The generation of S3 in the deep subaqueous environment would result in modified explosive–effusive behavior, with decreased volatile exsolution due to increased hydrostatic pressure. This would result in a proportional decrease in the depth at which shear induced permeability begins, and a decrease in explosivity. In addition, a reduced magma viscosity, due to decreased exsolution, would result in a greater influence of ductile deformation on permeability development as opposed to brittle fracturing.

Subunit 4w

Subunit 4w occurs both on the caldera rim and caldera floor with microcrystalline clasts apparently concentrated around Lava C on the caldera floor (**Figure 5**). Stratigraphically S4w directly overlies S3 across a sharp boundary (pushcore HVR159; **Figure 3**), and at other sites where S3 is not present overlies 2 cm of S2a (HVR132 and HVR163; **Figures 2a,b**). The sharp basal contact of S4w suggests a rapid onset to deposition at around the same time as

production of S3 ceased. Slow inferred accumulation of S2 and its consistent 2 cm thickness below S4w suggest that deposition of S4w began a significant time (weeks?) after the termination of the S2 – forming phase of the Havre eruption.

The microcrystalline clasts that characterize both S4w and S4e were derived from a relatively dense crystalline sources (**Figures 9c,d**). We infer from this that dome-forming lavas had been, or were being, emplaced at the time S4 formed. Deposition of S4w coincided with or followed termination of S3 emplacement (**Figure 11c**). Subunit 4w is most abundant at the base of the southwest caldera and we suggest that S4w formed when partial collapse of the caldera wall truncated Lavas G, H, and I. Evidence for partial caldera wall collapse following the emplacement of Lavas G, H, and I can be seen in the sharp truncation of these lavas along their northern edge by a scallop-shaped scarp (**Figure 1**). The collapse fed a debris avalanche, the deposits of which can be seen in bathymetry of the caldera floor (Carey et al., 2018). We suggest that the collapse permitted water interaction with the hot exposed cores of Lavas G, H, and I, and would have led to MFCI and quench fragmentation (Austin-Erickson et al., 2008), with the particles then deposited from suspension to form S4w.

Subunit 4e

Subunit 4e is present around Dome OP, extends downslope to the north (**Figures 10a, 11c**) and is composed of microcrystalline clasts. The spatial distribution of S4e indicates a source where Dome OP is located. No thinning or fining trends for S4e could be established. Dispersal is inferred to have been driven by weak sediment-gravity flows. Stratigraphically S4e overlies S1 and S2a, but its relationship to S3 and S4w is uncertain. Microcrystalline particles indicate that S4e was probably generated by fine fragmentation of Dome OP, and we infer that S4e represents the finest-grained fraction of material produced by fragmentation of Dome OP during its emplacement. Meter to decimeter scale blocks cover and extend beyond the slopes of Dome OP and indicate broad fracturing and fragmentation of the lava during extrusion. The exact mechanism driving fine-scale fragmentation in S4e remains unclear.

Eruption and Timing of Havre Depositional Events: Constraints From the AL Unit

Stage 1: The initial phase of the Havre eruption produced Lavas A–E on the caldera floor (**Figure 1**) at some time after the 2002 bathymetric survey of Wright et al. (2006) and prior to the raft pumice phase observed at the sea surface 18–19 July 2012 (Carey et al., 2018; **Figure 10b**). Lavas A–E are inferred to have been emplaced weeks prior to the generation of the pumice raft based on earthquake data (Carey et al., 2018).

Stage 2: Stage 2 includes the pumice raft, GP and ALB units, S1 and S2 subunits (**Figure 10b**). The pumice raft has been inferred to have been generated at the same time as the GP unit was deposited on the seafloor (Carey et al., 2018; Manga et al., 2018). Seafloor stratigraphy indicates that deposition of the

GP unit was followed, first, by deposition of S1 and the ALB. The precise stratigraphic relationship between S1 and ALB is uncertain, but both are overlain by S2a. Based on the similarities in vesicularity, ash shape, and clast groundmass microtextures, we infer that these deposits were erupted from a single vent now beneath Dome OP. The ALB unit, S1, and S2 all overlie the GP deposit, and were probably formed at the time of the pumice raft's generation, \pm days depending on the exact eruption mechanics. The deposition of the extremely fine-grained subunit S2a continued for longer because of the extremely slow settling rates of the extremely fine ash.

Stage 3: During late-stage deposition of S2, two ash subunits, S3 and S4, inferred to have been generated during lava effusion were deposited. Both are underlain by S2a. The inferred slow deposition of fine ash in S2a suggests a significant time break between the start of deposition of S2a and the deposition of S3 and S4. The 2 cm of S2a underlying S4w suggests that this time break may have been on the order of weeks. Subunit 3 was generated prior to S4w by ash venting that was probably simultaneous with effusion of lava G. The indication of a time break between the deposition of the ALB unit, S1, and S2 before the generation of S3 during the effusion of lava G is consistent with the observed lack of the AL unit overlying lavas F–O (Figures 2g–k). The effusion of lavas F–O is therefore inferred to have occurred days to weeks after the eruption that generated the ALB unit, S1, and S2.

The deposition of S4w resulted from gravitational collapse of the southwest caldera wall around lavas G, H, I. We suggest that the collapse of Lava G in this event terminated S3 deposition. Fine fragmentation to produce S4w is inferred to have occurred through interaction between the hot exposed cores of the lavas and ambient seawater.

Ash Generation During the Raft-Forming Phase

Subunits 1 and 2a overlie a seafloor deposit of giant pumice blocks and are composed of fine ash showing curvi-planar, angular, and fluidal morphologies that indicate a complex fragmentation environment. Ash grain size and shape data from S1 and S2 point to energetic fragmentation (Büttner et al., 2002; Zimanowski et al., 2003; Dürig et al., 2012a) driven dominantly by direct interaction of magma with water (e.g., Wohletz, 1983; Büttner et al., 1999, 2002; Austin-Erickson et al., 2008; Figures 3, 4), but with an important component of ash having fluidal surfaces that suggest primary hot-state fragmentation of magma isolated from direct water contact (Walker and Croasdale, 1971; Porritt et al., 2012). These inferences point toward the formation of S1 and S2 in an eruption with explosive fragmentation of a highly undercooled vesiculating magma. This eruption generated a vapor-rich eruptive jet and high convective plume from which dilute density currents were generated.

An effusive eruption style unique to the subaqueous environment has previously been inferred for the eruption of the pumice raft and the seafloor GP unit during the Havre eruption (Manga et al., 2018). The presence of S1 and S2 and evidence of their association with the pumice raft presented

here indicate that the eruption mechanism presented by Manga et al. (2018) needs to be expanded or modified to include explosive ash generation through both magma–water interaction and dry fragmentation. Ash generation through magma–water interaction may be compatible with the model proposed by Manga et al. (2018); the model's strain-induced fracturing of melt could provide conditions for induced fuel-coolant fragmentation (Austin-Erickson et al., 2008). The fluidal ash grains require a different process.

Limitations on Estimating the Volume of the Ash and Lapilli Unit

The stratigraphy of the AL unit presented in Figure 10 represents the intra-caldera and near-caldera deposits, but all ash subunits described here extend beyond the study area in one direction or another. A volume of $<0.1 \text{ km}^3$ was presented by Carey et al. (2018) for the AL unit within the 35 km^2 study area. There is no evidence of thinning in S1, S2, or even S4w, suggesting that these deposits extend well beyond the study area. Whole-deposit volumes are notoriously difficult to estimate even for comparatively well-understood subaerial dispersal systems (Bonadonna et al., 2015, 2016), and depend critically on treatment of the distal deposits for which we have no information at Havre. The ash component of the 2012 Havre eruption may represent a quite significant component of the overall eruptive volume. The plume of discolored water observed in MODIS imagery on 18–19 July 2012 (Carey et al., 2014, 2018; Jutzeler et al., 2014) also points to a significant population of fines that were carried away from the volcano.

Broader Implications

The 2012 Havre eruption constitutes a key laboratory in the study of large subaqueous silicic eruptions. The results of this study therefore have broader implications both for interpretations of the 2012 Havre eruption, and of other deep subaqueous silicic eruptions. Seafloor products of the 2012 Havre eruption have significant ash in proximal deposits, along with evidence that a substantial population of fines was transported off the volcano. The ash generated during the 2012 Havre constitutes a significant proportion of total fragmental material and represents an even larger proportion of eruptive energy; it must be accounted for in future eruption models.

Ancient subaqueous deposits often appear fines-poor, with ash forming only a minor component (Allen and McPhie, 2000; Kano, 2003; Raos and McPhie, 2003; Stewart and McPhie, 2004). Widespread dispersal of ash at Havre even from weakly explosive (e.g., S3) or non-explosive subaqueous eruptive events (e.g., S4e), along with reworking, provides a possible explanation for the observed lack of thick fines in ancient subaqueous proximal deposits.

A range of ash morphologies are observed in S1 and S2 produced by the higher intensity eruptive phase during which the 18–19 July 2012 pumice raft was generated. These ash morphologies display signatures of both phreatomagmatic and magmatic fragmentation processes during the same eruptive phase. This indicates a spatially and temporally varied

fragmentation environment for S1 and S2, and such variability may be typical of intense silicic eruptions in subaqueous environments.

CONCLUSION

Characteristics of the AL unit presented here constrain our interpretation of the 2012 Havre eruption. The ash-dominated AL unit comprises four subunits. The subunits were generated by different eruptive processes from three locations. Ash particles of subunits S1 and S2 formed from a highly undercooled vesiculating magma. Subunit S1 overlies a seafloor deposit of giant pumice blocks and contains curvilinear, angular, and fluidal particles indicating a complex fragmentation environment, from which water was excluded from places or at some times. Subunit 2, an extremely fine ash (6–5 ϕ) records highly effective fragmentation, with particles taking weeks to settle from the water column. Before 2 deposition was complete, lavas F–O were erupted and ash was generated first by ash venting from a vent also responsible for Lava G (S3), and then by interaction between the exposed hot lava and seawater (S4w) following gravitational collapse of the caldera wall, and related to the mass wasting event itself. At about the same time, S4e was dispersed around Dome OP and down into the caldera, probably as the result of extrusion, brecciation, and/or syn–post-eruption reworking.

More broadly, we find that these ash deposits provide information critical to reconstruction of the eruption sequence and processes. This suggests a way to strengthen work on modern submarine volcanoes, at which ash is systematically undercollected by dredging operations, and studies of ancient centers, where typical studies of the proximal deposits neglect detailed work on ash to focus on coherent rocks and breccias.

REFERENCES

- Allen, S. R., and McPhie, J. (2000). Water-settling and resedimentation of submarine rhyolitic pumice at Yali, eastern Aegean, Greece. *J. Volcanol. Geotherm. Res.* 95, 285–307. doi: 10.1016/S0377-0273(99)00127-4
- Allen, S. R., and McPhie, J. (2009). Products of neptunian eruptions. *Geology* 37, 639–642. doi: 10.1130/G30007A.1
- Allen, S. R., and Stewart, A. J. (2003). “Products of explosive subaqueous felsic eruptions based on examples from the Hellenic Island Arc, Greece,” in *Explosive Subaqueous Volcanism: Geophysical Monograph Series*, Vol. 140, eds J. D. L. White, J. L. Smellie, and D. A. Clague (Washington, DC: The American Geophysical Union), 285–298. doi: 10.1029/140GM19
- Austin-Erickson, A., Büttner, R., Dellino, P., Ort, M. H., and Zimanowski, B. (2008). Phreatomagmatic explosions of rhyolitic magma: experimental and field evidence. *J. Geophys. Res.* 113:11201. doi: 10.1029/2008JB005731
- Black, B. A., Manga, M., and Andrews, B. (2016). Ash production and dispersal from sustained low-intensity mono-ino eruptions. *Bull. Volcanol.* 78:57. doi: 10.1007/s00445-016-1053-0
- Blott, S. J., and Pye, K. (2001). Gradistat: a grain size distribution and statistics package for the analysis of unconsolidated sediments. *Earth Surf. Process. Landf.* 26, 1237–1248. doi: 10.1002/esp.261
- Bonadonna, C., Biass, S., and Costa, A. (2015). Physical characterization of explosive volcanic eruptions based on tephra deposits: propagation of

AUTHOR CONTRIBUTIONS

RC organized and led the cruise. All authors were present on the 2015 cruise and collected the samples. JW established the scope of the project. All sample analysis was conducted by AM. AM drafted the manuscript and produced all figures. All authors read through drafts and assisted in writing the final manuscript.

FUNDING

This research was funded by Australian Research Council Postdoctoral fellowships (DP110102196 and DE150101190 to RC), a short-term postdoctoral fellowship grant from the Japan Society for the Promotion of Science (to RC), National Science Foundation grants (OCE1357443 to BH, OCE1357216), and a New Zealand Marsden grant (U001616 to JW). JW and AM were supported by a research grant, Ph.D. scholarship, and postgraduate publishing bursary from the University of Otago.

ACKNOWLEDGMENTS

We thank the captain, operations teams, marine technicians, and crew of the R/V Roger Revelle for their expert help at sea. We thank the operations team of the ROV Jason and the AUV Sentry. This manuscript contains material included in the Ph.D. thesis of APM (Murch, 2018). Final revisions were completed while AM was supported by a NZ Marsden fund grant to JW.

SUPPLEMENTARY MATERIAL

The Supplementary Material for this article can be found online at: <https://www.frontiersin.org/articles/10.3389/feart.2019.00001/full#supplementary-material>

uncertainties and sensitivity analysis. *J. Volcanol. Geotherm. Res.* 296, 80–100. doi: 10.1016/j.jvolgeores.2015.03.009

Bonadonna, C., Cioni, R., Costa, A., Druitt, T., Phillips, J., Pioli, L., et al. (2016). MeMoVolc report on classification and dynamics of volcanic explosive eruptions. *Bull. Volcanol.* 78:84. doi: 10.1007/s00445-016-1071-y

Busby-Spera, C. J. (1986). Depositional features of rhyolitic and andesitic volcanoclastic rocks of the mineral king submarine caldera complex, Sierra Nevada, California. *J. Volcanol. Geotherm. Res.* 27, 43–76. doi: 10.1016/0377-0273(86)90080-6

Büttner, R., Dellino, P., La Volpe, L., Lorenz, V., and Zimanowski, B. (2002). Thermohydraulic explosions in phreatomagmatic eruptions as evidenced by the comparison between pyroclasts and products from molten fuel coolant interaction experiments. *J. Geophys. Res. Solid Earth* 107, 1–14. doi: 10.1029/2001JB000511

Büttner, R., Dellino, P., and Zimanowski, B. (1999). Identifying magma–water interaction from the surface features of ash particles. *Nature* 401, 688–690. doi: 10.1038/44364

Carey, R., Soule, S. A., Manga, M., White, J., McPhie, J., Wysoczanski, R., et al. (2018). The largest deep ocean silicic volcanic eruption of the past century. *Sci. Adv.* 4:e1701121. doi: 10.1126/sciadv.1701121

Carey, R. J., Wysoczanski, R., Wunderman, R., and Jutzeler, M. (2014). Discovery of the largest historic silicic submarine eruption. *EOS Trans. AGU* 95, 157–159. doi: 10.1002/2014EO190001

- Carlisle, D. (1963). Pillow breccias and their aquagene Tuffs, Quadra Island, British Columbia. *J. Geol.* 71, 48–71. doi: 10.1086/626875
- Cas, R. (1978). Silicic lavas in Paleozoic flyschlike deposits in New South Wales, Australia: behavior of deep subaqueous silicic flow. *Geol. Soc. Am. Bull.* 89, 1708–1714. doi: 10.1130/0016-7606(1978)89<1708:SLIPFD>2.0.CO;2
- Cas, R. A. F., and Giordano, G. (2014). Submarine volcanism: a review of the constraints, processes and products, and relevance to the Cabo de Gata volcanic succession. *Ital. J. Geosci.* 133, 362–377. doi: 10.3301/IJG.2014.46
- Cas, R. A. F., Yamagishi, H., Moore, L., and Scutter, C. (2003). Miocene submarine fire fountain deposits, Ryugasaki Headland, Oshoro Peninsula, Hokkaido, Japan: implications for submarine fountain dynamics and fragmentation processes. *Explosive Subaqueous Volcanism*, eds J. D. L. White, J. L. Smellie, and D. A. Clague (Washington, DC: The American Geophysical Union) 299–316.
- Cole, P. D., Smith, P., Komorowski, J.-C., Alfano, F., Bonadonna, C., Stinton, A., et al. (2014). Ash venting occurring both prior to and during lava extrusion at Soufriere Hills Volcano, Montserrat, from 2005 to 2010. *Geol. Soc. London Mem.* 39, 71–92. doi: 10.1144/M39.4
- Dimroth, E., and Demarcke, J. (1978). Petrography and mechanism of eruption of the archaean dalembert tuff, Rouyn-Noranda, Quebec, Canada. *Can. J. Earth Sci.* 15, 1712–1723. doi: 10.1139/e78-181
- Dimroth, E., and Yamagishi, H. (1987). Criteria for recognition of ancient subaqueous pyroclastic rocks. *Geol. Surv. Hokkaido* 58, 55–88.
- Dingwell, D. B., and Webb, S. L. (1990). Relaxation in silicate melts. *Eur. J. Miner.* 2, 427–449. doi: 10.1127/ejm/2/4/0427
- Druitt, T. H. (1995). Settling behaviour of concentrated dispersions and some volcanological applications. *J. Volcanol. Geotherm. Res.* 65, 27–39. doi: 10.1016/0377-0273(94)00090-4
- Dürig, T., Mele, D., Dellino, P., and Zimanowski, B. (2012a). Comparative analyses of glass fragments from brittle fracture experiments and volcanic ash particles. *Bull. Volcanol.* 74, 691–704. doi: 10.1007/s00445-011-0562-0
- Dürig, T., Zimanowski, B., Tobias, D., and Zimanowski, B. (2012b). “Breaking news” on the formation of volcanic ash: fracture dynamics in silicate glass. *Earth Planet. Sci. Lett.* 33, 1–8. doi: 10.1016/j.epsl.2012.05.001
- Edwards, D. A., Leeder, M. R., Best, J. L., and Pantin, H. M. (1994). On experimental reflected density currents and the interpretation of certain turbidites. *Sedimentology* 41, 437–461. doi: 10.1111/j.1365-3091.1994.tb02005.x
- Ferguson, R. I., and Church, M. (2004). A simple universal equation for grain settling velocity. *J. Sediment. Res.* 74, 933–937. doi: 10.1306/051204740933
- Fisher, R. V. (1984). Submarine volcanoclastic rocks. *Geol. Soc. London Spec. Publ.* 16, 5–27. doi: 10.1144/GSL.SP.1984.016.01.02
- Fiske, R. S., Cashman, K. V., Shibata, A., and Watanabe, K. (1998). Tephra dispersal from Myojinsho, Japan, during its shallow submarine eruption of 1952–1953. *Bull. Volcanol.* 59, 262–275. doi: 10.1007/s004450050190
- Gonnermann, H. M. (2015). Magma fragmentation. *Annu. Rev. Earth Planet. Sci.* 43, 431–458. doi: 10.1146/annurev-earth-060614-105206
- Gonnermann, H. M., and Manga, M. (2003). Explosive volcanism may not be an inevitable consequence of magma fragmentation. *Nature* 426, 432–435. doi: 10.1038/nature02138
- Head, J. W., and Wilson, L. (2003). Deep submarine pyroclastic eruptions: theory and predicted landforms and deposits. *J. Volcanol. Geotherm. Res.* 121, 155–193. doi: 10.1016/S0377-0273(02)00425-0
- Heiken, G. (1972). Morphology and petrography of volcanic ashes. *Bull. Geol. Soc. Am.* 83, 1961–1988. doi: 10.1130/0016-7606(1972)83[1961:MAPOVA]2.0.CO;2
- Jutzeler, M., Marsh, R., Carey, R. J., White, J. D. L., Talling, P. J., and Karlstrom, L. (2014). On the fate of pumice rafts formed during the 2012 Havre submarine eruption. *Nat. Commun.* 5:3660. doi: 10.1038/ncomms4660
- Jutzeler, M., McPhie, J., and Allen, S. R. (2015). Explosive destruction of a pliocene hot lava dome underwater: dogashima (Japan). *J. Volcanol. Geotherm. Res.* 304, 75–81. doi: 10.1016/j.jvolgeores.2015.08.009
- Kano, K. (2003). Subaqueous pumice eruptions and their products: a review. *Geophys. Monogr.* 140, 213–229. doi: 10.1029/140GM14
- Kano, K., Yamamoto, T., and Ono, K. (1996). Subaqueous eruption and emplacement of the Shinjima Pumice, Shinjima (Moesima) Island, Kagoshima Bay, SW Japan. *J. Volcanol. Geotherm. Res.* 71, 187–206. doi: 10.1016/0377-0273(95)00077-1
- Kennedy, L. A., and Russell, J. K. (2012). Cataclastic production of volcanic ash at Mount Saint Helens. *Phys. Chem. Earth* 4, 40–49. doi: 10.1016/j.pce.2011.07.052
- Kokelaar, P. (1986). Magma-water interactions in subaqueous and emergent basaltic volcanism. *Bull. Volcanol.* 48, 275–289. doi: 10.1007/BF01081756
- Liu, E. J., Cashman, K. V., Rust, A. C., and Gislason, S. R. (2015). The role of bubbles in generating fine ash during hydromagmatic eruptions. *Geology* 43, 239–242. doi: 10.1130/G36336.1
- Manga, M., Fauria, K. E., Lin, C., Mitchell, S. J., Jones, M., Conway, C. E., et al. (2018). The pumice raft-forming 2012 Havre submarine eruption was effusive. *Earth Planet. Sci. Lett.* 489, 49–58. doi: 10.1016/j.epsl.2018.02.025
- Manville, V., and Wilson, C. J. N. (2004). Vertical density currents: a review of their potential role in the deposition and interpretation of deep-sea ash layers. *J. Geol. Soc.* 161, 947–958. doi: 10.1144/0016-764903-067
- Mitchell, S. J., McIntosh, I. M., Houghton, B. F., Carey, R. J., and Sheaa, T. (2018). Dynamics of a powerful deep submarine eruption recorded in H 2 O contents and speciation in rhyolitic glass: the 2012 Havre eruption. *Earth Planet. Sci. Lett.* 494, 135–147. doi: 10.1016/j.epsl.2018.04.053
- Mulder, T., Zaragosi, S., Razin, P., Grelaud, C., Lanfumey, V., and Bavoil, F. (2009). A new conceptual model for the deposition process of homogenite: application to a cretaceous megaturbidite of the western Pyrenees (Basque region. SW France). *Sediment. Geol.* 222, 263–273. doi: 10.1016/j.sedgeo.2009.09.013
- Murch, A. P. (2018). *Ash Generation in the 2012 Eruption of Havre Volcano, Kermadec Arc: The Largest Deep Subaqueous Eruption of the Last Century*. Dunedin: University of Otago.
- Namiki, A., and Manga, M. (2008). Transition between fragmentation and permeable outgassing of low viscosity magmas. *J. Volcanol. Geotherm. Res.* 169, 48–60. doi: 10.1016/j.jvolgeores.2007.07.020
- Pickering, K. T., and Hiscott, R. N. (2009). Contained (reflected) turbidity currents from the middle ordovician cloridorme formation, Quebec, Canada: an alternative to the antidune hypothesis. *Deep Turbid Syst.* 32, 89–110. doi: 10.1002/9781444304473.ch7
- Pickering, K. T., Underwood, M. B., and Taira, A. (1992). Open-ocean to trench turbidity-current flow in the nankai trough: flow collapse and reflection. *Geology* 20, 1099–1102. doi: 10.1130/0091-7613(1992)020<1099:OOTTTC>2.3.CO;2
- Porritt, L. A., Russell, J. K., and Quane, S. L. (2012). Pele’s tears and spheres: examples from Kilauea Iki. *Earth Planet. Sci. Lett.* 334, 171–180. doi: 10.1016/j.epsl.2012.03.031
- Raos, A. M., and McPhie, J. (2003). The submarine record of a large-scale explosive eruption in the Vanuatu arc: ~ 1 Ma Efaté pumice formation. *Geophys. Monogr. Ser.* 140, 273–283. doi: 10.1029/140GM18
- Rotella, M. D., Wilson, C. J. N., Barker, S. J., Ian Schipper, C., Wright, I. C., and Wyszczanski, R. J. (2015). Dynamics of deep submarine silicic explosive eruptions in the Kermadec arc, as reflected in pumice vesicularity textures. *J. Volcanol. Geotherm. Res.* 301, 314–332. doi: 10.1016/j.jvolgeores.2015.05.021
- Rotella, M. D., Wilson, C. J. N., Barker, S. J., and Wright, I. C. (2013). Highly vesicular pumice generated by buoyant detachment of magma in subaqueous volcanism. *Nat. Geosci.* 6, 129–132. doi: 10.1038/ngeo1709
- Schipper, C. I., Castro, J. M., Tuffen, H., James, M. R., and How, P. (2013). Shallow vent architecture during hybrid explosive-effusive activity at Cordon Caulle (Chile, 2011–12): evidence from direct observations and pyroclast textures. *J. Volcanol. Geotherm. Res.* 262, 25–37. doi: 10.1016/j.jvolgeores.2013.06.005
- Schipper, C. I., White, J. D. L., Houghton, B. F., Shimizu, N., and Stewart, R. B. (2010). “Poseidic” explosive eruptions at Loihi Seamount. Hawaii. *Geology* 38, 291–294. doi: 10.1130/G30351.1
- Schmid, A., Sonder, I., Seegelken, R., Zimanowski, B., Büttner, R., Gudmundsson, M. T., et al. (2010). Experiments on the heat discharge at the dynamic magma-water-interface. *Geophys. Res. Lett.* 37, 2–5. doi: 10.1029/2010GL044963
- Simpson, K., and McPhie, J. (2001). Fluidal-clast breccia generated by submarine fire fountaining, Trooper Creek Formation, Queensland, Australia. *J. Volcanol. Geotherm. Res.* 109, 339–355. doi: 10.1016/S0377-0273(01)00199-8
- Staudigel, H., and Schmincke, H. U. (1984). The Pliocene Seamount Series of La Palma/Canary Islands. *J. Geophys. Res.* 89, 11195–11215. doi: 10.1029/JB089iB13p11195
- Stewart, A. L., and McPhie, J. (2004). An upper pliocene coarse pumice breccia generated by a shallow submarine explosive eruption, Milos, Greece. *Bull. Volcanol.* 66, 15–28. doi: 10.1007/s00445-003-0292-z

- Talling, P. J., Masson, D. G., Sumner, E. J., and Malgesini, G. (2012). Subaqueous sediment density flows: depositional processes and deposit types. *Sedimentology* 59, 1937–2003. doi: 10.1111/j.1365-3091.2012.01353.x
- van Otterloo, J., Cas, R. A. F., and Scutter, C. R. (2015). The fracture behaviour of volcanic glass and relevance to quench fragmentation during formation of hyaloclastite and phreatomagmatism. *Earth Sci. Rev.* 151, 79–116. doi: 10.1016/j.earscirev.2015.10.003
- Walker, G. P. L., and Croasdale, R. (1971). Characteristics of some basaltic pyroclastics. *Bull. Volcanol.* 35, 303–317. doi: 10.1007/BF02596957
- White, J. D. L., and Houghton, B. F. (2006). Primary volcanoclastic rocks. *Geology* 34, 677–680. doi: 10.1130/G22346.1
- White, J. D. L., Schipper, C. I., and Kano, K. (2015). *Submarine Explosive Eruptions*, 2nd Edn. New York, NY: Elsevier Inc. doi: 10.1016/B978-0-12-385938-9.00031-6
- White, J. D. L., Smellie, J. L., and Clague, D. A. (2003). “Introduction: a deductive outline and topical overview of subaqueous explosive volcanism,” in *Explosive Subaqueous Volcanism*, eds J. D. L. White, J. L. Smellie, and D. A. Clague (Washington, DC: American Geophysical Union).
- White, J. D. L., and Valentine, G. A. (2016). Magmatic versus phreatomagmatic fragmentation: absence of evidence is not evidence of absence. *Geosphere* 12, 1478–1488. doi: 10.1130/GES01337.1
- Wiesner, M. G., Wang, Y. B., and Zheng, L. F. (1995). Fallout of Volcanic Ash to the deep South China Sea induced by the 1991 eruption of Mount-Pinatubo (Philippines). *Geology* 23, 885–888. doi: 10.1130/0091-7613(1995)023
- Wohletz, K. H. (1983). Mechanisms of hydrovolcanic pyroclast formation: grain-size, scanning electron microscopy, and experimental studies. *J. Volcanol. Geotherm. Res.* 17, 31–63. doi: 10.1016/0377-0273(83)90061-6
- Wright, I. C., Worthington, T. J., and Gamble, J. A. (2006). New multibeam mapping and geochemistry of the 30°–35° S sector, and overview, of southern Kermadec arc volcanism. *J. Volcanol. Geotherm. Res.* 149, 263–296. doi: 10.1016/j.jvolgeores.2005.03.021
- Zimanowski, B., Buttner, R., and Lorenz, V. (1997). Premixing of magma and water in MFCI experiments. *Bull. Volcanol.* 58, 491–495. doi: 10.1007/s004450050157
- Zimanowski, B., Wohletz, K., Dellino, P., and Büttner, R. (2003). The volcanic ash problem. *J. Volcanol. Geotherm. Res.* 122, 1–5. doi: 10.1016/S0377-0273(02)00471-7

Conflict of Interest Statement: The authors declare that the research was conducted in the absence of any commercial or financial relationships that could be construed as a potential conflict of interest.

Copyright © 2019 Murch, White and Carey. This is an open-access article distributed under the terms of the Creative Commons Attribution License (CC BY). The use, distribution or reproduction in other forums is permitted, provided the original author(s) and the copyright owner(s) are credited and that the original publication in this journal is cited, in accordance with accepted academic practice. No use, distribution or reproduction is permitted which does not comply with these terms.



Structure of Lō'ihi Seamount, Hawai'i and Lava Flow Morphology From High-Resolution Mapping

David A. Clague^{1*}, Jennifer B. Paduan¹, David W. Caress¹, Craig L. Moyer², Brian T. Glazer³ and Dana R. Yoerger⁴

¹ Monterey Bay Aquarium Research Institute, Moss Landing, CA, United States, ² Department of Biology, Western Washington University, Bellingham, WA, United States, ³ Department of Oceanography, University of Hawai'i, Honolulu, HI, United States, ⁴ Applied Ocean Physics and Engineering, Woods Hole Oceanographic Institution, Woods Hole, MA, United States

OPEN ACCESS

Edited by:

Carles Soriano,
Instituto de Ciencias de la Tierra
Jaume Almera (ICTJA), Spain

Reviewed by:

Sharon Allen,
University of Tasmania, Australia
Alessandro Tibaldi,
University of Milano-Bicocca, Italy

*Correspondence:

David A. Clague
clague@mbari.org

Specialty section:

This article was submitted to
Volcanology,
a section of the journal
Frontiers in Earth Science

Received: 27 August 2018

Accepted: 08 March 2019

Published: 26 March 2019

Citation:

Clague DA, Paduan JB,
Caress DW, Moyer CL, Glazer BT and
Yoerger DR (2019) Structure of Lō'ihi
Seamount, Hawai'i and Lava Flow
Morphology From High-Resolution
Mapping. *Front. Earth Sci.* 7:58.
doi: 10.3389/feart.2019.00058

The early development and growth of oceanic volcanoes that eventually grow to become ocean islands are poorly known. In Hawai'i, the submarine Lō'ihi Seamount provides the opportunity to determine the structure and growth of such a nascent oceanic island. High-resolution bathymetric data were collected using AUV *Sentry* at the summit and at two hydrothermal vent fields on the deep south rift of Lō'ihi Seamount. The summit records a nested series of caldera and pit crater collapse events, uplift of one resurgent block, and eruptions that formed at least five low lava shields that shaped the summit. The earliest and largest caldera, formed ~5900 years ago, bounds almost the entire summit plateau. The resurgent block was uplifted slightly more than 100 m and has a tilted surface with a dip of about 6.5° toward the SE. The resurgent block was then modified by collapse of a pit crater centered in the block that formed West Pit. The shallowest point on Lō'ihi's summit is 986 m deep and is located on the northwest edge of the resurgent block. Several collapse events culminated in formation of East Pit, and the final collapse formed Pele's Pit in 1996. The nine mapped collapse and resurgent structures indicate the presence of a shallow crustal magma chamber, ranging from depths of ~1 km to perhaps 2.5 km below the summit, and demonstrate that shallow sub-caldera magma reservoirs exist during the late pre-shield stage. On the deep south rift zone are young medium- to high-flux lava flows that likely erupted in 1996 and drained the shallow crustal magma chamber to trigger the collapse that formed Pele's Pit. These low hummocky and channelized flows had molten cores and now host the FeMO hydrothermal field. The Shinkai Deep hydrothermal site is located among steep-sided hummocky flows that formed during low-flux eruptions. The Shinkai Ridge is most likely a coherent landslide block that originated on the east flank of Lō'ihi.

Keywords: caldera, pit crater, landslide, channelized flows, hummocky flows, Lō'ihi Seamount

INTRODUCTION

The timing of development of shallow sub-caldera magma chambers and their overlying calderas remains uncertain in basaltic volcanoes. In Hawai'i, this uncertainty reflects disagreement about whether the summit plateau of the submarine Lō'ihi Seamount is a caldera complex. Lō'ihi Seamount is the youngest volcano in the nearly 8000 km-long Hawaiian-Emperor volcanic

chain that stretches across the north Pacific (Clague and Dalrymple, 1987). The seamount is located at the southeastern end of the Hawaiian Islands (**Figure 1**). Emery (1955) named Lō'ihi and presented the first of several bathymetric charts showing the north-south elongate shape of the volcano and suggested that Lō'ihi and nearby Papa'u (**Figure 2**) might mark the locations of young submarine volcanoes related to the Hawaiian volcanic chain. It was not, however, until the Hawaiian Volcano Observatory's seismic network detected earthquake swarms in 1971–1972 and 1975 located beneath the volcano (Klein, 1982; Bryan and Cooper, 1995) that Lō'ihi was recognized as an active submarine volcano and the youngest in the Hawaiian-Emperor chain. That Lō'ihi was an active volcano was quickly confirmed when fresh, glassy lava samples were recovered (Moore et al., 1979, 1982; Frey and Clague, 1983; Garcia et al., 1989), and active hydrothermal vents and deposits were identified and sampled near the summit (Malahoff et al., 1982; De Carlo et al., 1983; Karl et al., 1988, 1989). Since that time, Lō'ihi has been the focus of intense study with numerous oceanographic expeditions and *Pisces IV and V*, *ALVIN*, *MIR*, and *Shinkai 6000* submersible and *Kaiko* and *Jason* remotely operated vehicle (ROV) dives that have collected samples and made visual and video observations. In 1996, an intense seismic swarm (Caplan-Auerbach and Duennebie, 2001a,b) accompanied the formation of a new pit crater named Pele's Pit (Lō'ihi Science Team, 1997) and initiation of sulfide/sulfate deposition inside it (Davis and Clague, 1998; Davis et al., 2003), and again invigorated scientific work at Lō'ihi. The formation of the summit pit crater in 1996 has renewed importance as summit collapse has recently occurred at Kilauea Volcano.

The uncertainty about whether the summit of Lō'ihi Seamount is a caldera complex results from the prior lack of high-resolution bathymetry of the summit. This study presents and discusses results from three surveys done at different resolutions. The first is a GPS-navigated bathymetric survey collected in 2014 using a Simrad EM302 0.5° × 1° system on the R/V *Falkor*, operated by the Schmidt Ocean Institute (**Figure 2**). The second is a high-resolution deep-tow Reson 8101 sonar survey done in 1997 (**Figure 3**) to plan the cable route for the Hawaii Undersea Geological Observatory (HUGO) (Duennebie et al., 2002). The third, and highest resolution, is surveys by AUV *Sentry*, operated by Woods Hole Oceanographic Institution (e.g., **Figure 4**). The deep-tow and *Sentry* surveys required extensive post-processing to clean noise and adjust for navigation offsets; all the data could not be recovered, especially for the deep-tow survey. These high-resolution surveys, coregistered to the GPS-navigated EM302 survey collected by the R/V *Falkor* for the entire volcano, allow us to take a new and more detailed look at the morphology and structure of Lō'ihi Seamount, including the formation of Pele's Pit in 1996.

PREVIOUS WORK

Lō'ihi Seamount has been mapped repeatedly as mapping and navigation technologies improved. Despite the intensity of scientific research on Lō'ihi, detailed descriptions and discussion

of its geomorphology and structure are largely based on visual or video observations and single sonar beam or low-resolution multibeam surveys. The earliest surveys were done by the U.S. Navy in the 1950s and formed the basis of the Emery (1955) identification and naming of Lō'ihi Seamount. The Navy also collected a multibeam survey using SASS (Malahoff et al., 1982; Malahoff, 1987). A single-beam survey in 1981 (Moore et al., 1982) located the seamount accurately and showed that the summit was generally flat at a depth slightly greater than 1000 m and had several collapse pits each several 100 m deep, as depicted in their **Figure 2** and in **Figures 6.3, 6.4** in Malahoff (1987). Two sidescan surveys followed using the towed Sea MARK II (Smith et al., 1994) and the GLORIA system (Holcomb et al., 1988; Holcomb and Robinson, 2004). Much of this work, as well as most sampling of lava flows and hydrothermal deposits, was done before GPS navigation was available or available 24-h per day (Moore et al., 1982; Malahoff, 1987; Fornari et al., 1988; Chadwick et al., 1993). The initial surveys by Moore et al. (1982) and Malahoff (1987) were superior to some later surveys in that navigation was done using triangulation with a radar-frequency transponder positioning system from shore-based stations on the Island of Hawaii.

Modern GPS or differential GPS navigated multibeam surveys (MBARI Mapping Team, 2000; Smith et al., 2002; Eakins et al., 2004) were an important advance. The survey done in 1998 (MBARI Mapping Team, 2000) used a Simrad EM300 multibeam system and differential GPS for navigation, but the system provided coverage only as deep as 4000 m. At the summit, the resolution is ~15–20 m. The seamount (**Figure 2**) was mapped again during a JAMSTEC program in 2000–2002 using Seabeam (Smith et al., 2002; Eakins et al., 2004), which provided GPS-navigated coverage of the entire seamount at similar resolution to the earlier EM300 survey.

The general structure of Lō'ihi Seamount was evident from the early surveys (Moore et al., 1982; Malahoff, 1987; Fornari et al., 1988; Karl et al., 1988; Chadwick et al., 1993). The volcano has a nearly flat summit platform at about 1000 m depth and two distinct rift zones that extend to the north and then northeast and to the south (**Figure 2**). The southern part of the summit platform was modified by two distinct collapse pits prior to the 1996 formation of Pele's Pit, a third summit pit crater (Lō'ihi Science Team, 1997). Constructional volcanic activity is concentrated along the rifts and at the summit, although rare volcanic cones occur away from the rift zones on the lower flanks, particularly the northwest flank (one was sampled by dredge 31 in Moore et al., 1982). The south rift extends ~19 km to a depth of about 5000 m (average plunge of 10°) whereas the north rift is ~11 km long and merges into the submarine slope of Mauna Loa volcano at a depth of about 2000 m (average plunge of 6°) (Fornari et al., 1988). The north rift zone consists of two roughly parallel ridges with the western one being the longer, more prominent one. Just north of the north rift zone, Papa'u (**Figure 2**) is not another young volcano as proposed by Emery (1955). It consists of uplifted and folded, poorly consolidated volcanoclastic sediments associated with the active Hilina fault zone on the south flank of Kilauea Volcano (Moore and Chadwick, 1995; Morgan et al., 2003).

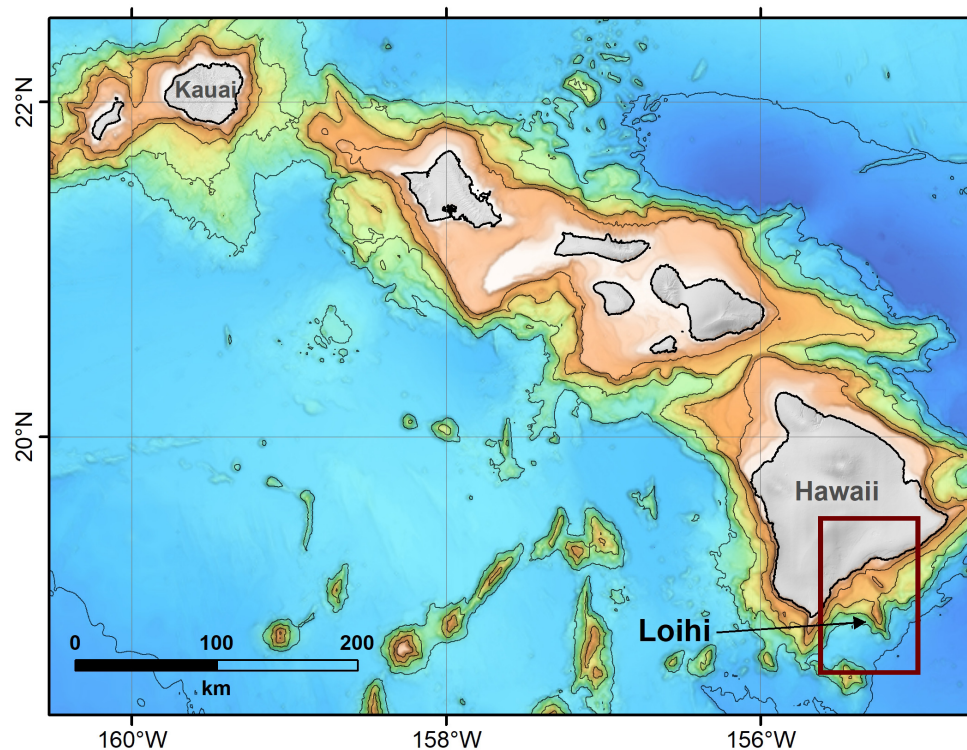


FIGURE 1 | Location map showing the Hawaiian Islands from Kaua'i to the northwest to Hawai'i at the southeast. Multibeam bathymetry around the islands is shown with one-km contours from 1 to 5 km below sea level. Lō'ihi Seamount is labeled and the box shows the extent of **Figure 2**.

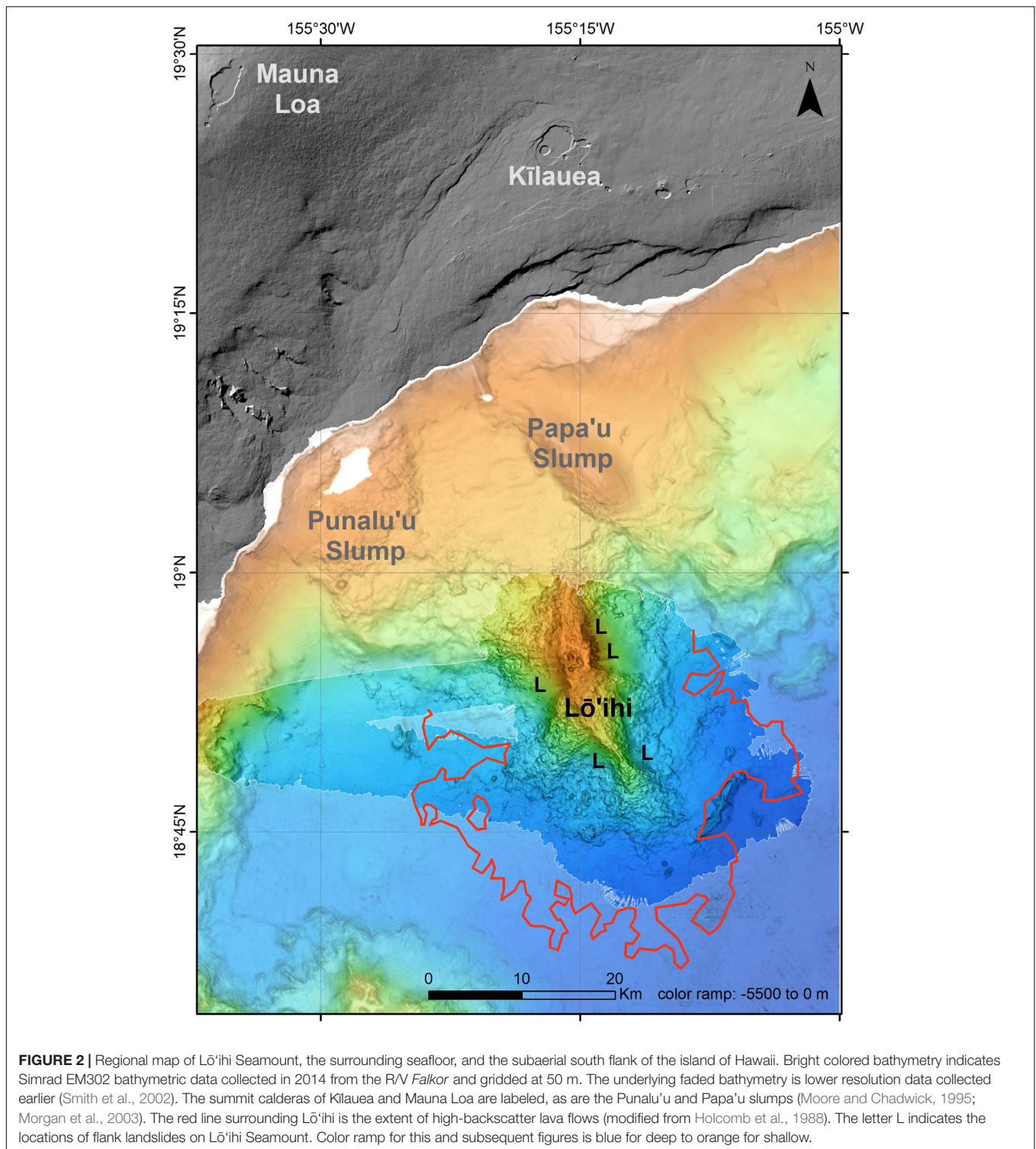
The outer rim of the summit is generally shallower than the center. Malahoff (1987) interpreted this broad summit depression as a caldera, and Fornari et al. (1988) interpreted the elevated rim as a series of cones erupted through ring faults on the margin of the summit platform. The three summit pit craters have been explored during numerous submersible dives that have shown that all are steep-walled and expose sequences of truncated lava flows (Garcia et al., 1993; Lō'ihi Science Team, 1997). Pele's Pit collapsed beneath the former location of the low-temperature (up to 30°C) Pele's Vents hydrothermal field (e.g., Sedwick et al., 1992, 1994), and high-temperature (about 200°C) venting was found around the base of the pit walls after the collapse (Lō'ihi Science Team, 1997; Davis and Clague, 1998; Wheat et al., 2000; Davis et al., 2003). More recent observations (Glazer and Rouxel, 2009) indicate that these vents have cooled significantly and are no longer depositing sulfides and sulfates. Part of the summit platform, particularly the eastern half, is covered by volcanoclastic deposits up to 11 m thick (Clague et al., 2000, 2003; Clague, 2009; Schipper et al., 2011), which obscure the underlying lava flows and smooth the relief of the summit platform.

The rift zones and summit platform have asymmetric slopes to the east and west, which Malahoff (1987); Fornari et al. (1988), Moore et al. (1989), and Garcia et al. (2006) interpreted to be the headwalls of landslides that modified Lō'ihi's flanks. Two slumps have modified the west flank of Lō'ihi, whereas a much larger slide or merged slides (**Figure 2**) has modified the eastern flank (Malahoff, 1987).

Lava flows on Lō'ihi are described as mainly pillow lava, but knobby 'a'a-like blocky flows are also present, based on shape and surface textures of dredged fragments (Moore et al., 1982; and references cited in Garcia et al., 2006). The only papers focused on lava flow morphology (Umino et al., 2000, 2002) described inflation features of lobate and hollow or drained lobate flows observed on the deep south rift zone during *Kaiko* ROV dives 94 and 96 between ~4050 and 4920 m depth. The deeper dive 96 (Umino et al., 2000, 2002) was located just uprift of a *Sentry* high-resolution survey of the FeMO hydrothermal site described below.

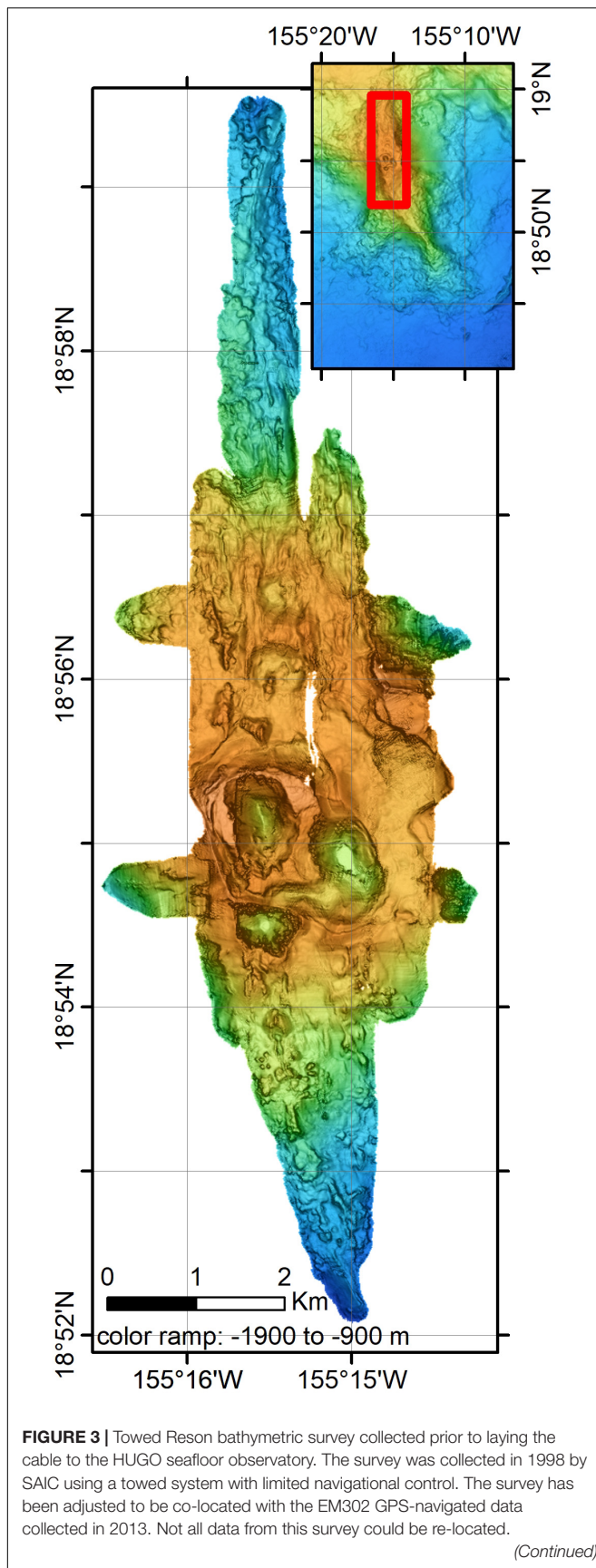
DATA AND DATA PROCESSING

We combine data from four surveys, each at different resolution. The broadest regional coverage of the deepest parts of the volcano (>4000 m depth) is based on several generations of SeaBeam data used in the Smith et al. (2002) compilation (**Figure 2**). Simrad EM302 bathymetric and backscatter data of the seamount collected from the R/V *Falkor* in 2014 are higher resolution than prior SeaBeam or the EM300 data (MBARI Mapping Team, 2000) and supplant those data. The EM302 survey mapped most of the edifice of Lō'ihi Seamount (**Figure 2**) at a resolution of ~17 m at the summit and ~85 m at 5000 m depth, but did not extend away from the base of the seamount nor cover the entire north rift or west flank, and in particular, the region of high-backscatter

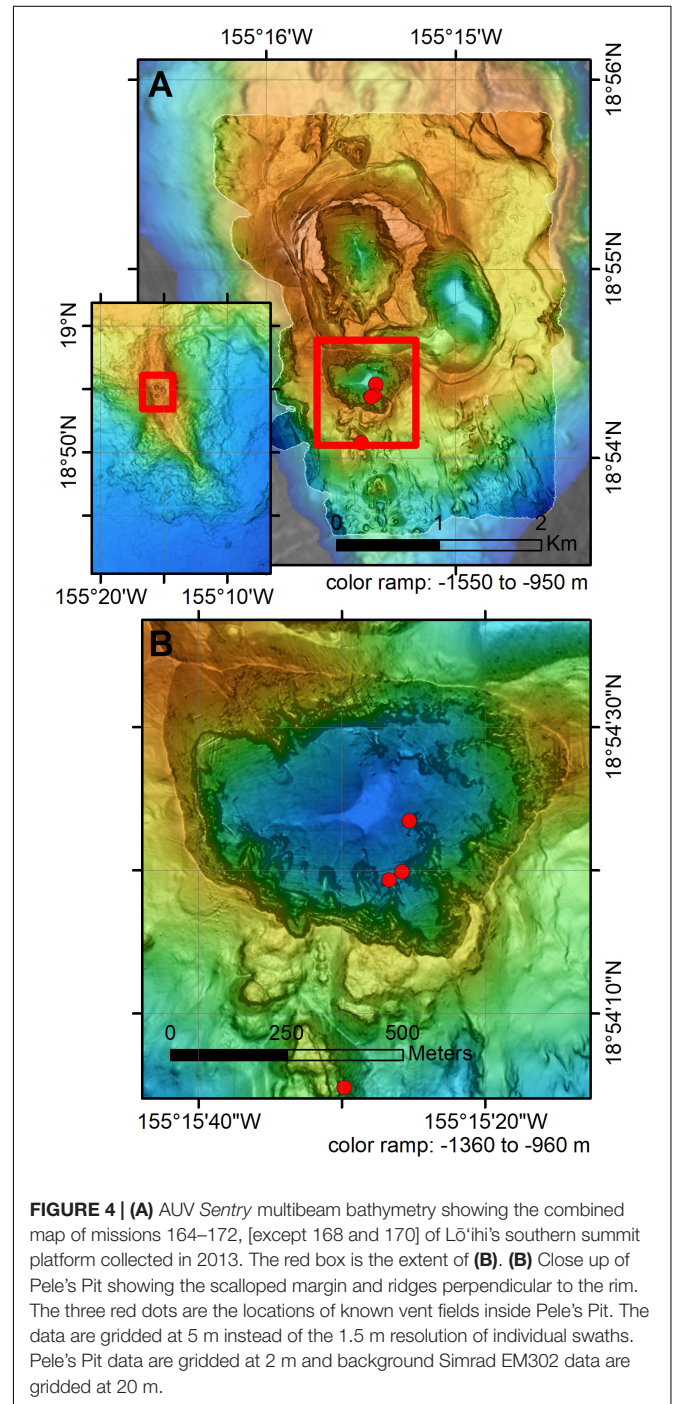


inferred by Holcomb et al. (1988), based on GLORIA side-scan data (**Figure 2**), to consist of extensive flows from Lō'ihi Seamount was only partly mapped. We have coregistered the higher resolution surveys to the EM302 data (see below). The higher-resolution survey for the HUGO cable route (Duennebie et al., 2002) suffers from poor navigation and noisy data, but

covers almost the entire summit and upper rift zones (**Figure 3**). These data were collected using a Reson 8101 (1.5° by 1.5° 240 kHz) multibeam mounted on a McCartney FOCUS steerable tow body operated by SAIC in 1997; only depth information could be recovered. The survey experienced abrupt depth and lateral offsets that could not be corrected and the navigation

**FIGURE 3 |** Continued

In addition, the swaths on the north rift could not be matched to the underlying ship data and are either mislocated by being too far west or have a depth offset of about 50 m to deeper depths. The map is gridded at 10 m.



coregistration to underlying EM302 data is less reliable than usually attained for AUV high-resolution map data, so it is best gridded at about 10 m cell size.

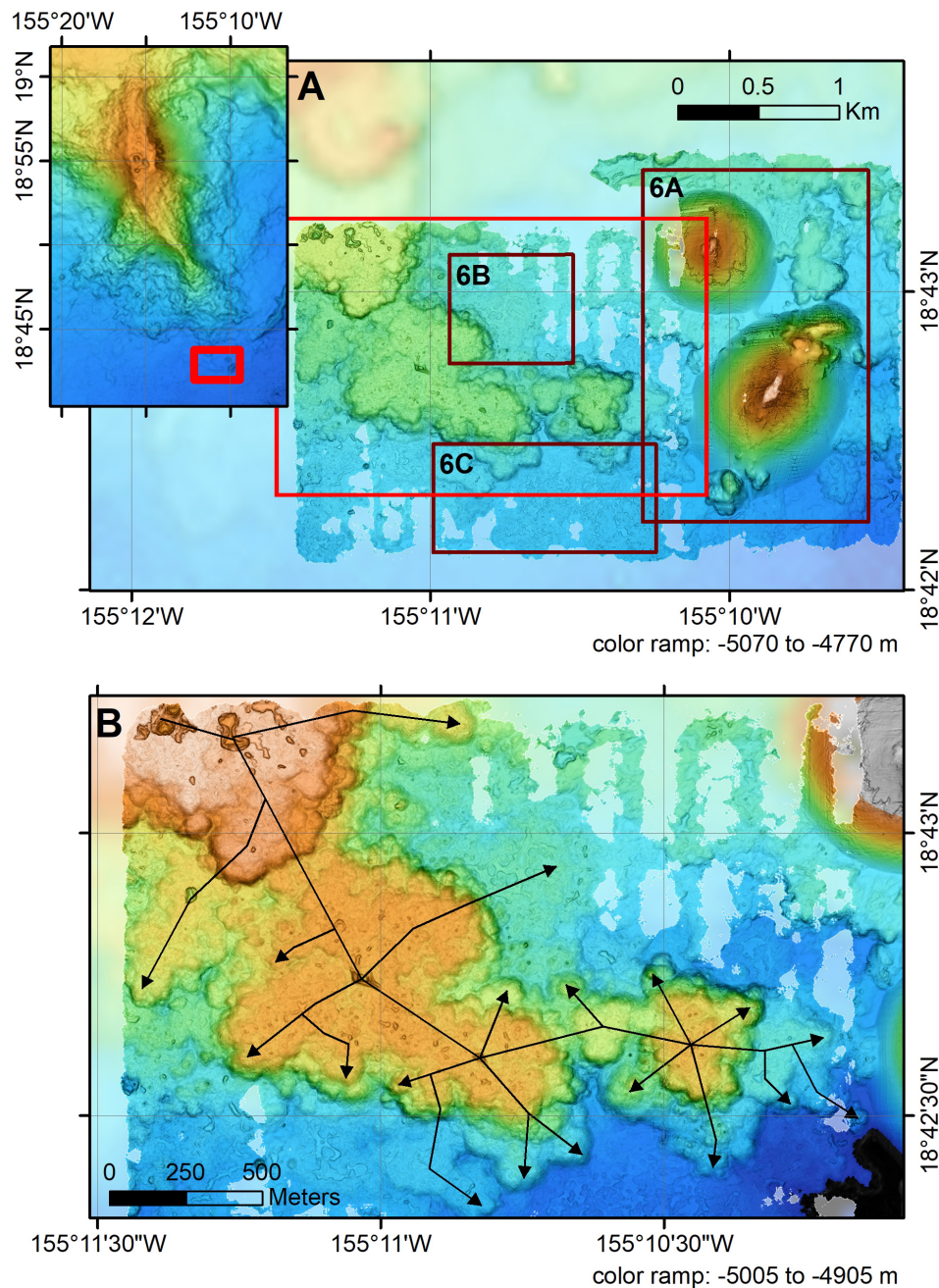


FIGURE 5 | (A) AUV *Sentry* multibeam bathymetry showing the combined map of missions 168, 264, and 265 of the FeMO hydrothermal site collected in 2013 and 2014. Boxes show extents of part **(B)** and **Figures 6A–C**. **(B)** Close-up of hummocky flows with arrows showing how lava advanced within the flow. The yellow-colored mound to the east has a shallower depth than the flows above the tube that fed it.

The highest resolution data for the southern portion of summit region were collected during 7 AUV surveys (164–172, except 168 and 170) using *Sentry* in 2013 (**Figure 4**). The Reson 7125 multibeam sonar on *Sentry* has a resolution of about 1.5 m when routinely flown at an altitude of ~60 m. Additional AUV *Sentry* surveys were conducted on the distal south rift zone at the FeMO hydrothermal site (Edwards et al., 2011) in 2013 and 2014 during *Sentry* missions 168, 264, and 265 (**Figures 5, 6**). Part of

survey 265 over the FeMO venting area, collected at an altitude of only 5 m, has roughly 5 cm resolution (**Figure 6D**) and collected overlapping bottom photographs (**Figure 7**). AUV *Sentry* surveys were also completed at the Shinkai Deep hydrothermal site during missions 266 and 270 and at the Shinkai Ridge site during missions 267 and 269 (**Figures 8, 9**). The increasingly higher-resolution surveys cover smaller and smaller areas nested within the Simrad EM302 surveys.

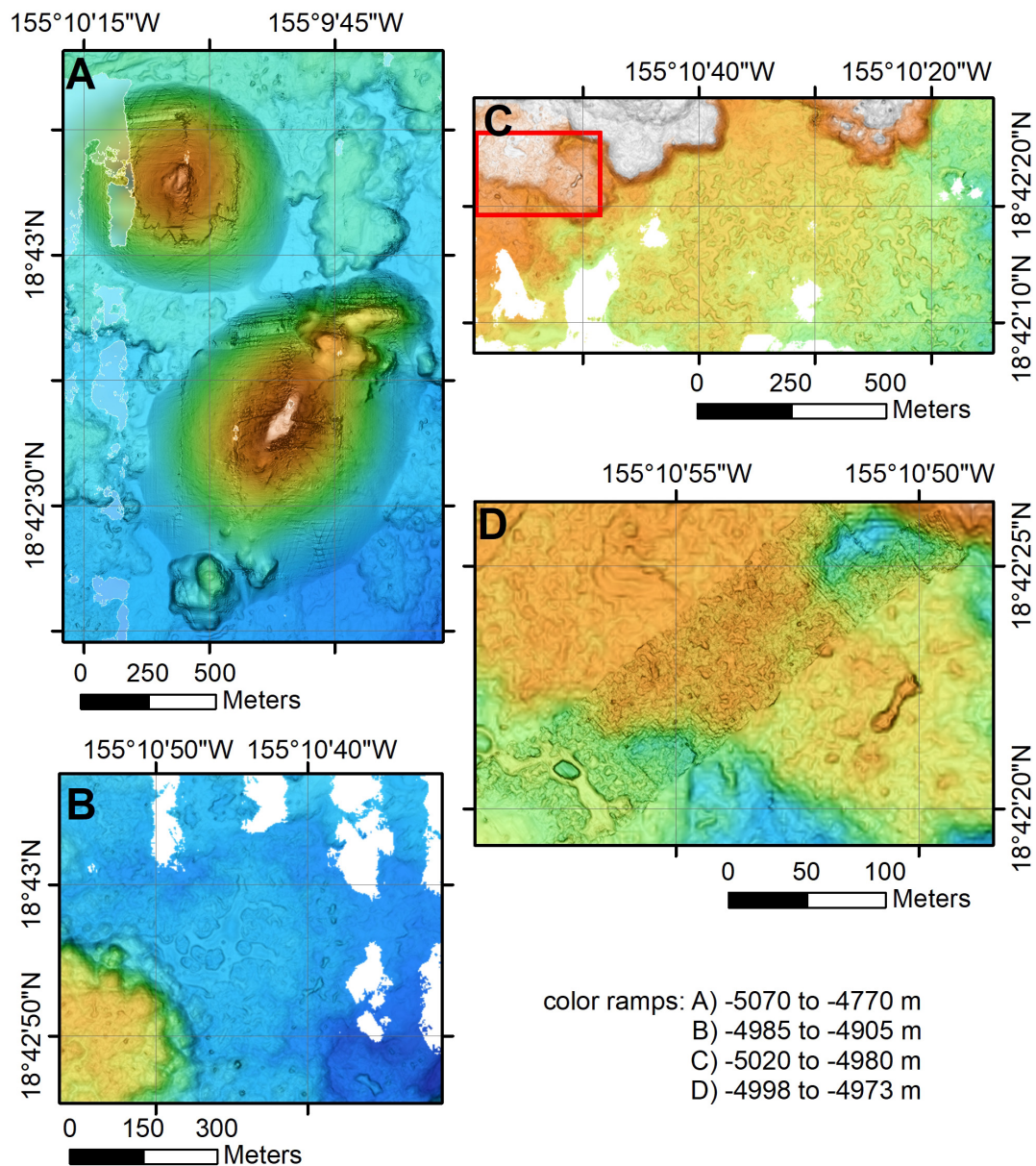


FIGURE 6 | (A) Detail of the two cones (southern one is ~300 m tall and 160 by 260 m across at the base) with smooth slopes located on the extension of the south rift. Resolution is 2 m. **(B)** Detail close-up of channelized flow with abundant drainback features. This flow originates at the edge of the hummocky flow lobe to the southwest. **(C)** Detail of another channelized flow with abundant drainback features that started from the hummocky flow lobe to the north. These rapidly emplaced flows are the molten cores of the hummocky flows that presumably reflect increased flux as the eruption proceeded. Extent of maps A, B, and C are shown by boxes on **Figure 5A**. **(D)** A portion of *Sentry* Reson bathymetric mission 265 of the FeMO hydrothermal site that was collected from an altitude of just 5 m. Bathymetry has about 5 cm resolution and overlapping photographic coverage (representative images in **Figure 7**). Individual lobate flow lobes a few m across can be seen, as can a small drained lava pond in a channelized flow in the southwest corner of the map. Extent of the map shown by box in part **(C)**. Each map is at a different scale and with a different depth range to highlight the details.

The *Sentry* and deep-tow data were reprocessed using MB-System (Caress and Chayes, 2011). Data editing used the 3-D mbeditviz tool and re-navigation used the mbnavadjust tool, first on individual surveys and then on combined surveys as multi-mission mbnavadjust projects for the summit and deep south rift, and then tying to points in the better-located EM302 survey.

RESULTS

General Bathymetric Characteristics

The overall structure of Lō'ihi Seamount (**Figure 2**) is largely as previously described (e.g., Malahoff, 1987; Fornari et al., 1988). The summit is a flat platform that connects to a ~15 km long northern rift and a 22-km long curved south rift. No radial

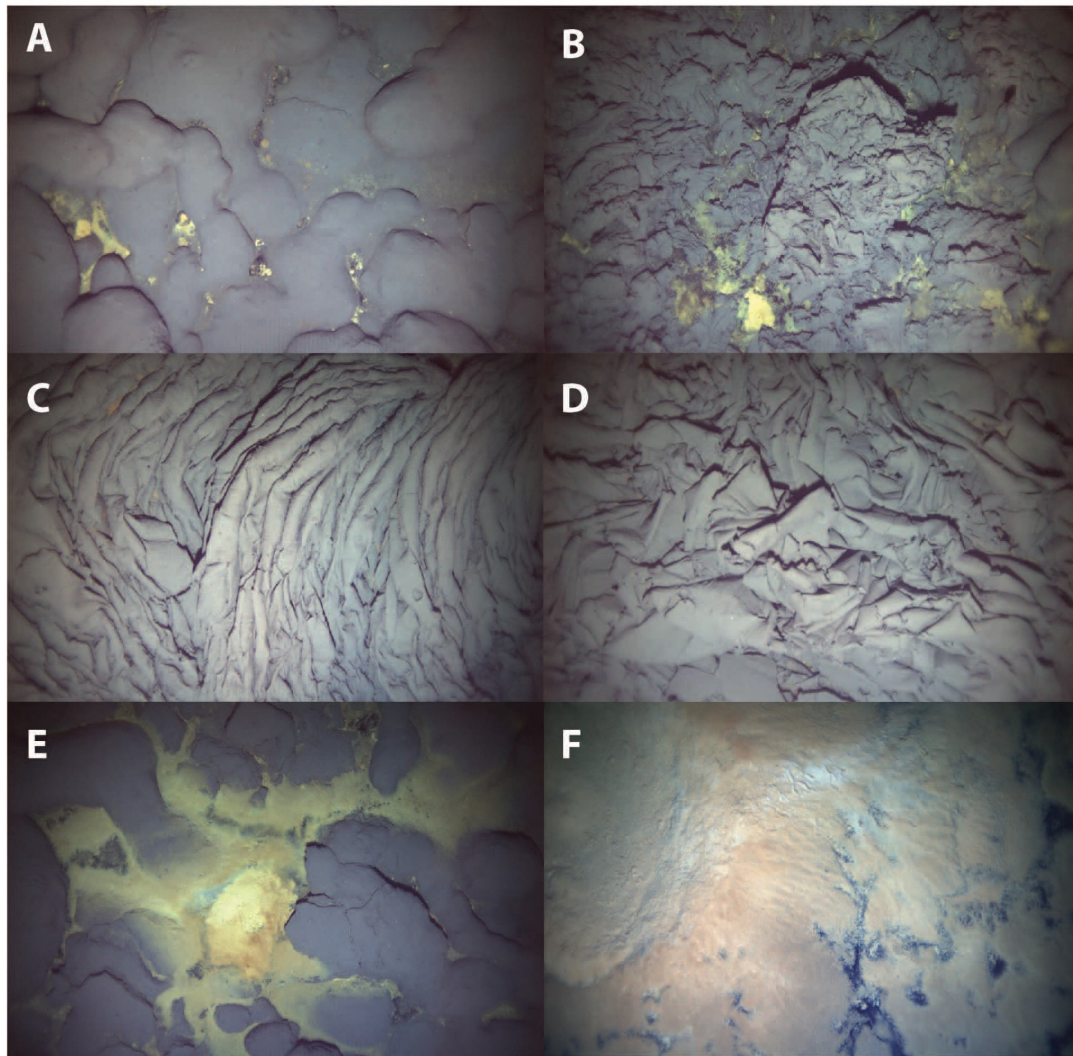
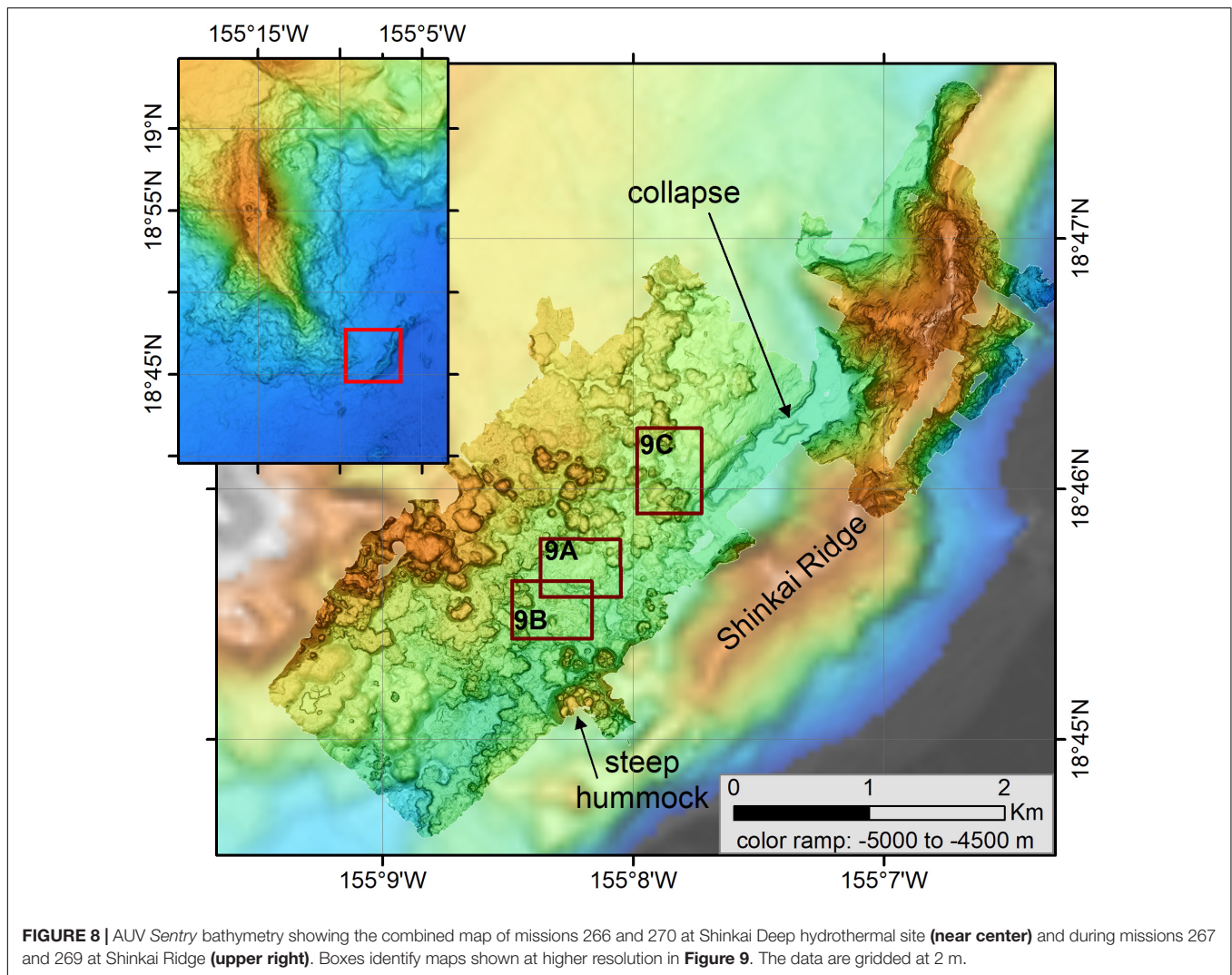


FIGURE 7 | Photographs collected by AUV *Sentry* during low-altitude portion of mission 168. No lasers were utilized to provide accurate scale, but the images are ~3–5 m across. **(A)** Pillow lava with minor hydrothermal sediment between pillows at 18.70781° latitude, –155.18420° longitude, and 4977 m depth. **(B)** Jumbled sheet flow with minor yellow hydrothermal sediment. 18.70795°, –155.18443°, 4975 m. **(C)** Drapery folded sheet flow at 18.70747°, –155.18493°, 4976 m. **(D)** Drapery folded to jumbled sheet flow. **(E)** Pillow lava with abundant yellow hydrothermal sediment and bacterial mat at 18.70769°, –155.18375°, 4978 m. **(F)** Thick white to light orange bacterial mat nearly covering sheet flow at 18.70751°, –155.18401°, 4981 m.

fissures have been identified, as occur on the northwest and north flanks of Mauna Loa (Wanless et al., 2006). The summit platform has three collapse pits in the southern part and is rimmed by a series of low cones/shields. The eastern portion of the summit platform and southeastern portion of the north rift ends at a steep cliff. This amphitheater has an upper rugged zone with spurs perpendicular to the upper break-in-slope and a smooth lower slope. A similar structure occurs on the west side of the southern summit platform, although the break-in-slope is not as steep as on the east side, nor the lower slope as smooth. Two additional amphitheaters occur on the east and west edges of the middle south rift, leaving a narrow ridge defining the rift zone. The lower slopes of both these amphitheaters are not as smooth as the others, nor are their upper slopes as steep. A NE-SW-oriented

ridge, named the Shinkai Ridge (**Figure 8**), is located to the southeast of Lō'ihī. It consists of lava flows, as observed during *Shinkai* submersible dives.

The north rift zone bifurcates into two ridges near ~1600 m depth where it appears to be built on top of the smooth Punalu'u slide structure (**Figure 2**; Moore and Chadwick, 1995). One rift is oriented north-south and the other roughly northeast-southwest. They intersect the south rift zone near West Pit (**Figure 2**). Such bifurcation of distal rift zones is also seen elsewhere in the Hawaiian Islands, such as the Haleakalā east rift zone (Smith et al., 2002). The distal south rift becomes ill-defined below ~3500 m depth and resembles the distal end of Puna Ridge on Kilauea (Clague et al., 1993, 1995) with lobes radiating from the inferred rift axis.



Backscatter Characteristics

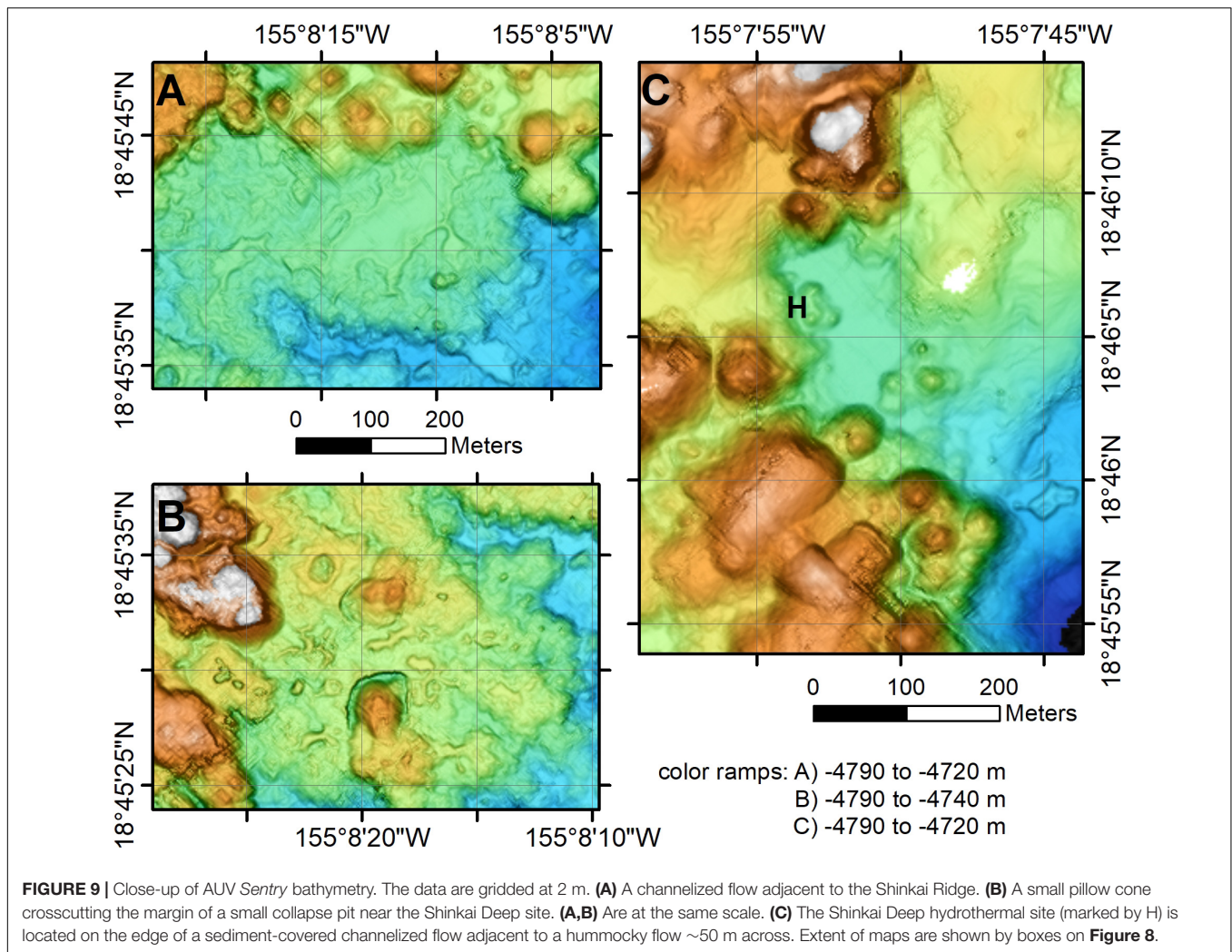
Holcomb et al. (1988), from the GLORIA side-scan sonar surveys, identified a region of high backscatter around the base of Lō'ihi Seamount that they inferred to be young, far-traveled, lava flows. The GLORIA data were poorly located and the outline of the flows they drew does not coincide with the new bathymetry. The flow boundary was redrawn (Figure 2) using mosaicked backscatter data from the GPS-navigated JAMSTEC cruises, guided by the outline of Holcomb et al. (1988). A SeaMark II sidescan survey of the south side of Hawaii Island (Fryer et al., 1987; Smith et al., 1994) also shows high-backscatter lava flows at the base of Lō'ihi Seamount and was also used in redrawing the outline of the high-backscatter flows (Figure 2). In many places the high-backscatter areas from the SeaBeam and SeaMark II data are not as clear as from the GLORIA imagery, suggesting that some of these flows are buried under sediment that the GLORIA sonar penetrated more deeply than either the SeaMark II or the SeaBeam sonars. Elsewhere around the Hawaiian Island chain, GLORIA penetrated at least three meters of sediment (Clague et al., 2002), so some of the high-backscatter flows may not be

recently emplaced. Some of these flows are located up to ~20 km from the summit or south rift zone.

High-Resolution Bathymetry of the Summit Caldera Complex

The summit of Lō'ihi has three pit craters between 0.8 and 1.2 km across: East Pit (EP, Figure 10), West Pit (WP) and Pele's Pit (PP) and four smaller pit craters (Figure 10). All have steep inward facing crater scarps. The uppermost south rift has two adjoined < 100-m diameter pit craters (P-A and P-B, Figure 10 and Table 1) that are ~40 m deep. These two small pit craters are aligned north-northwest with a low cone (C2, Figure 10), Pele's Pit, and West Pit; this trend defines the orientation of the upper south rift zone.

The southern summit displays a complex series of structures, most of which are nested collapse structures with inward-facing scarps (Figure 10). West Pit and Pele's Pit have numerous reentrants and spurs extending inward from the rim of the pits (Figure 4). The first scarp outside West Pit (R4, Figure 10 and Table 1) and concentric with the pit, has outward-facing scarps



more than 100 m high that bound an uplifted block. This is the only outward-facing scarp on the summit. East Pit (**Figure 10** and **Table 1**) is also nested within a more extensive series of inward-facing scarps that encircle both East and West Pits. High-flux lava flows with channels and shallow collapses cover the summit platform E and NE of East Pit (one is labeled “flow” on **Figure 10**), but were trapped inside the inward facing scarps (R1, **Figure 10**) that define part of the R1 summit caldera. These flows, and others north of North Pit are buried by volcanoclastic sediment (Clague et al., 2003; Clague, 2009; Schipper and White, 2010). Volcanoclastic sediment up to 11-m thick crop out at the tops of some of the outer caldera-bounding scarps (V, **Figure 10**), but were not observed on submersible dives inside the outermost caldera-bounding scarps.

The northern part of the summit platform was not mapped using AUV *Sentry*, but the deep-tow (**Figure 3**) and EM302 data show two shallow pit craters (P-C and P-D, **Figure 10** and **Table 1**) with the southern P-C about 600 m across and 103 m deep and the northern P-D about 450 m across and 91 m deep. They are aligned north-south with West Pit and the eastern of the two north rift zones and a cone (C1, **Figure 10**).

High-Resolution Bathymetry of Constructional Volcanic Features

Lō'ihi is characterized by having few identifiable constructional cones or shields, at the resolution of ship bathymetry. Most upper south rift eruptive vents consist of ramparts and haystack-like vents. The ramparts appear in the ship bathymetry as linear rift-parallel ridges. The summit and rifts generally have cones below the resolution of shipboard bathymetry. The constructional flanks of the rift zones consist of overlapping lobes of lava, presumably emplaced during fissure eruptions (**Figure 2**). The flanks of the summit are lacking overlapping lobes of flows, and instead are cut by steep cliffs to the E and W of the summit platform, which are discernable in ship bathymetry (**Figure 2**). Collapse structures truncate at least five pre-existing lava shields (S1–S5, **Figure 10**) whose remnants are at the S and N ends of East Pit, W of West Pit and surrounding Pele's Pit (**Figure 10** and **Table 1**). The two largest cones on the seamount occur near the south end of the south rift zone (**Figure 6A**) and are most likely monogenic. These two cones have smooth lower and middle slopes at the resolution of the *Sentry* data (**Figure 6A**) and summits of steeper knobby terrain. The southern cone is elongate

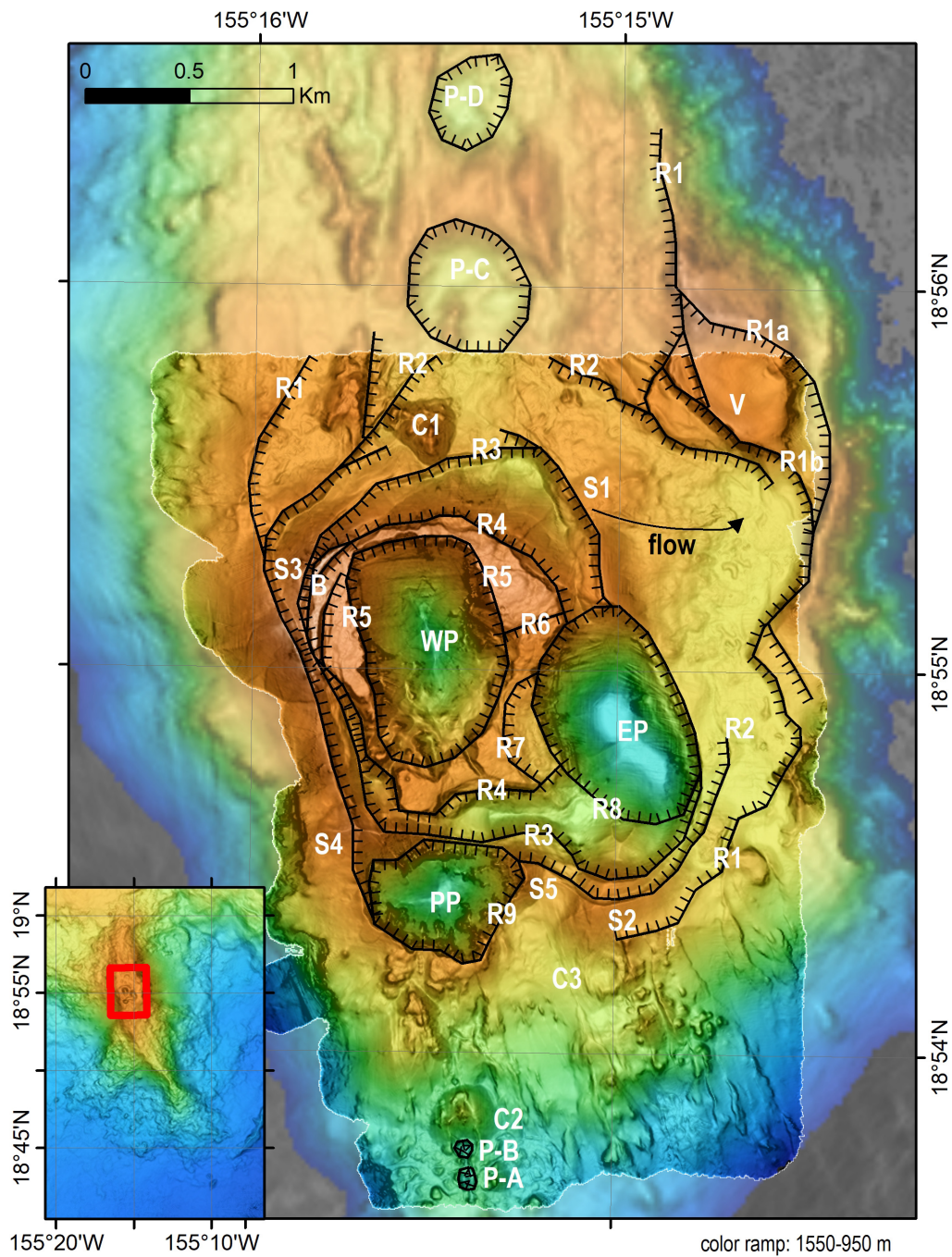


FIGURE 10 | Summit bathymetry with interpretive overlay of caldera and pit crater bounding scarps. *Sentry* data in foreground with Simrad EM302 data behind. Hatchures indicate down-thrown side of caldera or pit crater bounding scarps or ring faults R1 (oldest) to R9 (youngest). Exact sequence of formation for some collapse events cannot be determined. P-A to P-D are pit craters described in the text and in **Table 1**. EP is East Pit, WP is West Pit, PP is Pele's Pit, C1 to C3 indicate two cones described in the text, S1 to S5 indicate the remnants of five lava shields, B indicates 1996 basaltic breccia, and V indicates volcaniclastic sediment 5–11 m thick (Clague et al., 2003; Schipper and White, 2010) with a basal date of ~5900 years (Clague, 2009). Arrow labeled “flow” indicates direction of channelized flow from S1 to the east.

in a NE-SW orientation that is not parallel to the underlying rift orientation. Other constructional cones occur on the summit platform and upper south rift zone (C1 and C2, **Figure 10**), but are small compared to other submarine cones in Hawaii and lack

the flat tops commonly observed (Clague et al., 2000). A low cone with a large-diameter crater (C3, **Figure 10**) is located S of East Pit and low shield S2 and ~1 km E of the south rift zone. No other similar cones were identified.

TABLE 1 | Lō'ihi pit craters.

Feature	Diameter (m)	Long direction	Depth (m)
West pit	1100 × 700	N-S	299
East pit	1050 × 650	NW-SE	300
Pele's pit	700 × 500	E-W	332
P-A	100	Circular	41
P-B	90	Circular	40
P-C	580 × 610	NW-SE	103
P-D	480 × 365	NE-SW	91

Depth is from highest point on rim to deepest point.

High-Resolution Bathymetry of the FeMO Hydrothermal Site

The same AUV *Sentry* surveys that mapped the two smooth cones on the deep south rift zone also mapped a series of low hummocky lava flows that entered the mapped region from the northwest and stagnated just west of the southeastern smooth cone (**Figure 5B**). These hummocky flows display numerous small collapse structures indicative of molten interiors (see description of similar flows on Axial Seamount in Clague et al., 2017). Rapidly emplaced flows with channels and shallow drainout depressions appear to start at the margins of the thicker hummocky flows (**Figures 6B,C**). The hummocky mounds generally increase in depth along the flow (indicated by arrows on **Figure 5B**). In contrast, the easternmost mound is shallower than the mound just to the west from which it was fed. These lava flows host the FeMO low-temperature hydrothermal vents (Glazer and Rouxel, 2009). These hummocky and channelized flows (**Figure 7**) have very thin sediment, except in the vicinity of discharging low-temperature hydrothermal fluids (**Figures 7E,F**).

High-Resolution Bathymetry of the Shinkai Deep and Ridge Hydrothermal Sites

The map of the Shinkai Deep and Ridge on the south-southeast flank of Lō'ihi (**Figure 8**) illustrates a number of lava morphologies. Much of the mapped area is constructed of single steep-sided hummocky pillow flows lacking small collapse pits. The hummocks near the south-central part of the map (near 155°8'W, 18°45.2'N) are near the base of the northeast-southwest trending Shinkai Ridge and rise to shallower depths than the flows to the northwest that fed them. Many of these steep-sided flows, especially those in the northwestern part of the map, have smooth slopes around them or at their bases. A very few of the hummocky flows have small collapse pits indicative of molten cores (Clague et al., 2017). The central part of **Figure 8** shows some high-flux channelized flows which are characterized by subdued topography (**Figure 9A**). A 50-m diameter hummock (south-central **Figure 9B**) is surrounded by a shallow collapse structure in the surrounding channelized flow, indicating that the hummock was built on top of the channelized flow before it had solidified so that both the hummock and upper crust of the channelized flow could subside when magma was drained from within the channelized flow. A 50–70 m diameter low cone

with a 30–50 m-diameter crater is located a few hundred m to the north-northwest. The Shinkai Deep hydrothermal vent site (H, **Figure 9C**) is located at the edge of hummocky flows that overlie an older low-relief remnant of a channelized flow. Dive observations from the *Shinkai* submersible indicate that the flows are covered by thick sediment and are therefore inferred to be old.

AUV *Sentry* mapping of Shinkai Ridge is restricted to the northeastern part (**Figure 8**), but the ridge has no identifiable constructional volcanic characteristics. A channelized flow ponded at the northwestern base of the ridge and inflated, forming several large collapsed areas as lava drained from under the crust (labeled on **Figure 8** and in southeast corner of **Figure 9C**). This lava flow marks the southeastern edge of the high-backscatter flows (**Figure 2**) originally mapped by Holcomb et al. (1988), although the Shinkai Ridge also has high backscatter due to its steepness.

DISCUSSION

Structure and Evolution of the Summit

The relatively flat summit plateau has had a complex evolution consisting of multiple constructional and collapse structures that were unrecognized based on lower resolution surveys. These constructional and collapse structures have significant implications for defining the magma storage system within Lō'ihi Seamount. We use the nomenclature for calderas from Cole et al. (2005), which follows closely from Lipman (2000). The outermost inward-facing scarps are ring or caldera faults (R1, **Figure 10**) that define a caldera ~3 km across. It is therefore about half the average ~6 km diameter for basaltic calderas globally (Gudmundsson, 2008) and also about half the size of the summit calderas on Kilauea and Mauna Loa Volcanoes on Hawaii (**Figure 2**). The arcuate inward-facing ring fault on the northeast margin includes several steps (R1a and R1b, **Figure 10**) that may represent slumped portions of caldera walls, or two similar sized calderas. The base of an 11-m thick sequence of volcanoclastic sediment (V, **Figure 10**) exposed in the northeastern R1 scarp is 5900 years old (Clague, 2009), and formed before or during the collapse of the earliest and largest of the recognized calderas.

These R1 scarps define parts of a caldera that extended to the south, west and north margins of the summit, but portions of the northern, southern and eastern scarps are missing. The southern and northern bounding caldera scarps have probably been buried by subsequent lava whereas some of the western boundary and some parts of the eastern bounding fault scarps were likely removed during younger outward-directed landslides as discussed below.

Within this outermost inward-facing caldera scarp, four nested caldera scarps cut low lava shields and encircle West Pit. The outer two caldera scarps (R2 and R3, **Figure 10**) are inward-facing, but the next (R4, **Figure 10**) is a steeply dipping outward-facing fault scarp that bounds an uplifted block and suggests a period of resurgence prior to formation of the final inward-facing pit crater scarp (R5, **Figure 10**) that bounds West Pit. The collapses have progressively smaller diameters with the R2 caldera being 2.5 km in diameter, the R3 caldera 2 × 1.5 km,

the R4 resurgent block ~ 1.3 km in diameter, and the R5 pit crater (West Pit) 1×0.7 km. West Pit, as well as the younger East Pit and the youngest Pele's Pit are similar to other pit craters in being $< \sim 1$ km across (Gudmundsson, 2008). The progressive decrease in dimensions of these collapse and resurgent features suggest a shoaling of the magma reservoir beneath them (e.g., Acocella et al., 2000, 2001; Kusumoto and Takemura, 2005), while maintaining the general location of the reservoir beneath West Pit. The periods of collapse generally followed periods of summit eruptions that formed low lava shields that the collapses partially destroyed.

Based on cross cutting relations, three collapses (Okubo and Martel, 1998) centered on East Pit formed R6, R7, and R8 next (Figure 10). The final pit crater collapse event was the formation of Pele's Pit in 1996 defined by R9 (Figure 10; Lō'ihi Science Team, 1997; Davis and Clague, 1998). Pele's Pit is located at the former location of a lava shield constructed of an evolved alkalic basalt with 5.17 wt% MgO (sample 1804-19 in Garcia et al., 1993). The 1996 lava breccia (B, Figure 10) is a tholeiitic basalt with an average 6.85 wt% MgO (Garcia et al., 1998), so Pele's Pit did not form from the draining of alkalic magma stored beneath the shield. The serrated rims of West and Pele's Pits formed by numerous small landslides (each 50 to a few 100 m wide) into the pit. East Pit shows similar features on the west side, but the eastern and southern margins are smooth, and resemble Halema'uma'u pit crater on Kilauea prior to the 2018 collapse of Kilauea's summit from May to early August 2018 (Neal et al., 2019).

The timing of formation of pit craters P-A to P-D (Figure 10) is largely unknown, although P-C and P-D may well be located within the original caldera bounded by R1 caldera scarps. If this is the case, then the R1 caldera had an elongate N-S orientation and was about 2.5 by 4.5 km in size. An elongate caldera would be expected in an extensional setting (Acocella et al., 2004). Based on observed changes at Kilauea's summit in May–August 2018 (Neal et al., 2019), several of these collapse structures may have formed at the same time or in sequence during a single period of summit collapse.

The period of resurgence indicated by outward-facing scarp R4 is the first known from the Hawaiian Islands, but is known from other volcanoes such as Pantelleria and Ischia Island near Naples (Tibaldi and Vezzoli, 1998; Acocella and Funiciello, 1999; Acocella et al., 2001; Molin et al., 2003). The outward-facing scarps indicate uplift of a resurgent block. The diameter of the block should be roughly equal to the depth to the top of the magma reservoir (Acocella et al., 2001), in this case, ~ 1.3 km. The northwestern side of the resurgent block is the shallowest part of Lō'ihi's summit at 986 m depth, and the block is tilted about 6.5° with the northwestern edge uplifted relative to the southeastern edge.

Collapses to form calderas or pit craters on basaltic volcanoes, for example, have been documented previously in 1968 at Fernandina in the Galapagos Islands (Simkin and Howard, 1970; Filson et al., 1973; Munro and Rowland, 1996; Howard, 2010), in 2000 at Miyakejima in Japan (Kumagai et al., 2001), in 2007 at Piton de La Fournaise volcano on Reunion Island (Michon et al., 2007, 2009; Peltier et al., 2009), and in 2018 at Kilauea

Volcano (Neal et al., 2019). In each case the events were piston cylinder events, with incremental downdropping of the piston over periods lasting from 1 day (Piton de La Fournaise in 2007) to 77 days (Kilauea in 2018). The calderas and pit craters on the summit of Lō'ihi probably formed by a similar mechanism over similar time periods.

The sequence of collapse and one resurgent block confirm that Lō'ihi Seamount has had a crustal magma reservoir only one to a few km below the surface for much of the past 5900 years. This inference contrasts with prior interpretation that the magma reservoir was at 8–9 km depth, which was based on petrologic arguments for the 1996 glassy breccia samples (Garcia et al., 1998, and summarized in Garcia et al., 2006). The difference might be reconciled by having two magma reservoirs, one within or at the base of the underlying ocean crust as previously proposed (Clague, 1988; Garcia et al., 2006) and a second, much shallower reservoir that underlies the caldera and pit crater structures by just 1–2 km. That residence in the shallow reservoir was not identified petrologically is consistent with only brief residence of the 1996 magma in the shallowest reservoir, which in turn is consistent with its inferred small diameter and volume. The presence of a shallow sub-caldera magma reservoir at Lō'ihi Seamount establishes the early development of magma storage in Hawaiian volcanoes.

Rift Eruptions

Caldera formation on basaltic volcanoes is commonly inferred to be triggered by rapid magma withdrawal from the reservoir beneath the edifice (e.g., Pinel and Jaupart, 2005; Geshi et al., 2014) and observed at Kilauea in 2018 (Neal et al., 2019). This withdrawal of magma from beneath the summits was caused by flank eruptions coinciding with recent caldera and pit-crater forming eruptions discussed above, and formation of calderas and pit craters at Lō'ihi was probably triggered by the same mechanism.

Immediately following the 1996 collapse of Pele's Pit, six samples from a glassy breccia dated using ^{210}Po – ^{210}Pb (labeled B on Figure 10) were collected west and northwest of West Pit during *Pisces V* submersible dives 286 and 287 (Garcia et al., 1998), but no downrift lava flows were located. The glassy breccia fragments were erupted in 1996, most likely during brief activity of one of the many caldera-bounding faults nearby, as no eruption appears to have occurred within West Pit. Several additional dives within the 2000 m depth range of the *Pisces V* submersible were used in 1998 to search the south rift zone for young lavas that might be the “missing flow,” but no young flows were identified. Several sites of low-temperature fluid venting were found (Wheat et al., 2000), but the underlying and nearby flows were not young.

The deep south rift extension near the FeMO hydrothermal site (Figure 5) is characterized by channelized to hummocky flows with molten cores and drainbacks that are similar to flows erupted on Axial Seamount on the Juan de Fuca spreading center in 2015 (Clague et al., 2017). Likewise, similar complex advance of inflated hummocky flows was described in Clague et al. (2017) for part of the 2015 lava flow on Axial Seamount. Flows with this morphology form during moderate effusion-rate eruptions

lasting for weeks or longer. The flows surrounding the FeMO hydrothermal site are also almost free of non-hydrothermal sediment and have abundant low-temperature fluid venting that has deposited abundant yellow-orange hydrothermal sediment and supports active bacterial mats. These are characteristics seen on historical Axial Seamount lava flows (see e.g., Chadwick et al., 2013; Clague et al., 2017) where they have been observed for more than a decade following flow emplacement. Unfortunately, the lavas near the FeMO site on Lō'ihi have not been sampled, but we suspect that these flows were erupted in 1996 and that their emplacement on the deep rift zone led to the collapse of Pele's Pit at the summit.

The large flows that surround the base of Lō'ihi Seamount (Holcomb et al., 1988) appear to have erupted from the south rift axis and flowed long distances down relatively gentle slopes. The large volumes of these flows make them good candidates to have triggered summit collapses on Lō'ihi, but none have been sampled nor their ages determined to correlate with the summit caldera-forming events.

Formation of Volcanic Landforms

Lō'ihi Seamount is characterized by small-diameter cones (generally < 300 m in basal diameter) probably of monogenetic origin and linear spatter ramparts that are indicative of brief, small-volume eruptions. This is especially true for the summit of Lō'ihi where cones are very rare. As volcanoes grow and evolve, small cones and ramparts are supplanted by longer steadier eruptions that construct larger volume volcanic landforms such as shields or flat-topped cones (Clague et al., 2000).

The two largest cones on Lō'ihi Seamount (**Figure 6A**) are unusual in having very smooth flanks that elsewhere have been shown to consist of basaltic pillow talus deposited at the base of steep-sided hummocky pillow mounds. Such deposits formed during the 1996 North Gorda eruption (Paduan et al., 2014) and the 2011 Axial eruption on the distal south rift zone (Clague et al., 2017) and are indicative of very low eruption rate pillow mounds with the talus fragments forming during the eruption as pillows cascade over near-vertical scarps. Cones as large as the two near the base of the south rift on Lō'ihi likely took weeks to months of low-eruption rate activity to form. Many of the steep-sided hummocky flows around the Shinkai Deep (**Figure 9**) show similar smooth lower slopes and are also inferred to consist of talus formed during growth of the steep-sided flows.

Other lava flows, such as those on the summit platform east of East Pit are channelized flows that are inferred to have erupted at high effusion rates during brief eruptions as documented for several historical eruptions on Axial Volcano (Chadwick et al., 2013; Clague et al., 2017).

Landslides

The flank landslides (Fornari et al., 1988; Moore et al., 1989) on the east side of the summit (**Figure 2**) cut and removed part of the outermost caldera-bounding faults and therefore occurred or at least enlarged the headwall regions of the slides since formation of the largest outer summit caldera, inferred to be ~5900 years ago (Clague, 2009). We think it most likely that the landslide headwalls have simply stepped toward the summit

in that time period. These are the youngest of the landslides around the Hawaiian Islands that modify entire volcanoes (Moore et al., 1989).

The Shinkai Ridge may be a detached slide block that originated either on the east flank of Lō'ihi near the summit or from the southern margin of the Punaluu landslide from Mauna Loa prior to formation of Lō'ihi Seamount. JAMSTEC dive K96 of the ROV *Kaiko* recovered 5 picrite and olivine basalt samples and one mudstone from the ridge in 1998 and one volcanic breccia that was analyzed; it has a composition similar to Lō'ihi Seamount lavas, and distinct from Mauna Loa lavas, as expected if it were a block of the Punaluu slide (Coombs et al., 2004). The block most likely originated from the east flank of Lō'ihi and was emplaced near the southern end of Lō'ihi as a landslide block. To arrive at its present location, the block would have undergone a clockwise rotation of nearly 90° and slid, as a coherent block, about 45 km to the south-southeast.

The new mapping data provide an opportunity, beyond the scope of this paper, to evaluate what features were sampled during the many prior dives and dredges. Complete high-resolution mapping of the rest of the summit and the north and south rift zones would reveal more of the complex history of Lō'ihi Seamount. A new generation of submersible or ROV dives done with improved navigation would allow for construction of a detailed structural and magmatic evolution of Lō'ihi.

CONCLUSION

The new high-resolution summit bathymetry at Lō'ihi Seamount shows a nested series of eight caldera and pit crater collapses events, uplift of one resurgent block, and eruptions that formed at least five low lava shields. The oldest and largest caldera-bounding faults enclose almost the entire summit plateau. Resurgence that uplifted a fault-bounded block > 100 m was the fourth tectonic event at the summit and followed three caldera collapse events and preceded formation of five pit craters. The most recent collapse formed Pele's Pit in 1996. Each of the nine mapped collapse or resurgent structures indicates the presence of a shallow crustal magma chamber, ranging from depths between 1 km and perhaps 2 km. Shallow sub-caldera magma reservoirs therefore exist during the late pre-shield stage of Hawaiian volcanism. The structural history of caldera and pit crater formation on Hawaiian volcanoes, other basaltic volcanoes, and volcanoes in general, provides a framework for understanding the evolution, size, and depth of their magma storage systems.

The summit collapse events, including the last one in 1996, were probably triggered by draining the crustal magma reservoir to supply magma to eruptions on the deep south rift zone. Extensive young lavas that host the FeMO hydrothermal vent field (**Figure 6D**) at ~18°42.2'N, 155°10.55'W, likely erupted in 1996 and the low-temperature venting of heat extracted by fluids circulated in the thick lava field. The Shinkai Deep hydrothermal site is located among older sediment-covered steep-sided hummocky flows. These steep-sided mounds produced talus during their formation as advancing pillows broke

off and tumbled downslope. Two smooth-sloped cones on the deep south rift near the FeMO hydrothermal site formed by a similar process.

The summit and rift zones of Lō'ihi have been modified by landslides, with the youngest landslide activity occurring after formation of the oldest summit caldera about 5900 years ago. Most of the landslide activity produces smooth talus slopes below steep headwalls, but the Shinkai Ridge near the southern base of Lō'ihi is most likely a coherent landslide block that originated on the east flank of the volcano.

DATA AVAILABILITY

The multibeam datasets processed for this study can be found in the IDEA seafloor bathymetry archives.

AUTHOR CONTRIBUTIONS

CM and BG were chief scientists on the two cruises that collected the AUV *Sentry* data. DY designed the surveys and did initial processing of the data during the 2014 cruise. DWC did the initial processing of the HUGO cable-route survey and assisted and

advised JP and DAC on processing the AUV bathymetric data. JP did the extensive MB-System processing of the AUV data, constructed most of the figures, and contributed to editing the manuscript. DAC assisted with editing and processing the AUV data and wrote the manuscript.

FUNDING

Funding for the collection of the data was provided by the National Science Foundation OCE1155756 to CM and the Schmidt Ocean Institute to BG. Support for DC and JP to process the data and write the manuscript was provided by a grant from the David and Lucile Packard Foundation to MBARI.

ACKNOWLEDGMENTS

The 2013 AUV *Sentry* surveys were conducted off the R/V *Kilo Moana* and the 2014 surveys were conducted off the R/V *Falkor*. We would like to thank the crews of both ships and the AUV *Sentry* team from Woods Hole Oceanographic Institution, especially team leader Carl Kaiser in 2013, for their assistance at sea.

REFERENCES

- Acocella, V., Cifelli, F., and Funicello, R. (2000). Analogue models of collapse calderas and resurgent domes. *J. Volcanol. Geotherm. Res.* 104, 81–96. doi: 10.1016/S0377-0273(00)00201-8
- Acocella, V., Cifelli, F., and Funicello, R. (2001). The control of overburden thickness on resurgent domes: insights from analogue models. *J. Volcanol. Geotherm. Res.* 111, 137–153. doi: 10.1016/S0377-0273(01)00224-4
- Acocella, V., and Funicello, R. (1999). The interaction between regional and local tectonics during resurgent doming: the case of the islands of Ischia, Italy. *J. Volcanol. Geotherm. Res.* 88, 109–123. doi: 10.1016/S0377-0273(98)00109-7
- Acocella, V., Funicello, R., Marotta, E., Orsi, G., and de Vita, S. (2004). The role of extensional structures on experimental calderas and resurgence. *J. Volcanol. Geotherm. Res.* 129, 199–217. doi: 10.1016/S0377-0273(03)00240-3
- Bryan, C., and Cooper, P. (1995). Ocean-bottom seismometer observations of seismic activity at Loihi Seamount, Hawaii. *Mar. Geophys. Res.* 17, 485–501. doi: 10.1007/BF01204340
- Caplan-Auerbach, J., and Duennebie, F. K. (2001a). Seismicity and velocity structure of Loihi Seamount from the 1996 earthquake swarm. *Bull. Seismo. Soc. Am.* 91, 178–190. doi: 10.1785/0119990170
- Caplan-Auerbach, J., and Duennebie, F. K. (2001b). Seismic and acoustic signals detected at Loihi Seamount by the Hawaii Undersea Geo-Observatory. *Geochem. Geophys. Geosyst.* 2:1024. doi: 10.1029/2000GC000113
- Caress, D. W., and Chayes, D. N. (2011). *MB-System: Mapping the Seafloor*. Available at: <http://www.mbari.org/data/mbsystem>
- Chadwick, W. W. Jr., Clague, D. A., Embley, R. W., Perfit, M. R., Butterfield, D. A., Caress, D. W., et al. (2013). The 1998 eruption of Axial Seamount: new insights on submarine lava flow emplacement from high-resolution mapping. *Geochem. Geophys. Geosyst.* 14, 3939–3968. doi: 10.1002/ggge.20202
- Chadwick, W. W. Jr., Smith, J. R., Moore, J. G., and Fox, C. (1993). *Bathymetry of the South Flank of Kilauea Volcano, Hawaii*. Reston, VA: U.S. Geological Survey.
- Clague, D. A. (1988). Petrology of ultramafic xenoliths from Loihi Seamount, Hawaii. *J. Petrol.* 29, 1161–1186. doi: 10.1093/petrology/29.6.1161
- Clague, D. A. (2009). Accumulation rates of volcanoclastic sediment on Loihi Seamount, Hawaii. *Bull. Volcanol.* 71, 705–710. doi: 10.1007/s00445-009-0281-y
- Clague, D. A., Batiza, R., Head, J., and Davis, A. S. (2003). "Pyroclastic and hydroclastic deposits on Loihi Seamount, Hawaii," in *Explosive Subaqueous Volcanism, American Geophysical Union Monograph*, Vol. 140, eds J. D. L. White, J. L. Smellie, and D. A. Clague (Washington, DC: American Geophysical Union), 73–95. doi: 10.1029/140GM05
- Clague, D. A., and Dalrymple, G. B. (1987). "The hawaiian-emperor volcanic chain," in *Volcanism in Hawaii, US Geological Survey Professional Paper*, Vol. 1350, eds R. W. Decker, T. L. Wright, and P. H. Stauffer (Washington, DC: United States Government Publishing Office), 5–54.
- Clague, D. A., Hon, K. A., Anderson, J. L., Chadwick, W. W. Jr., and Fox, C. G. (1993). *Bathymetry of Puna Ridge, Kilauea Volcano, Hawaii*. Reston, VA: United States Geological Survey Miscellaneous Field Map MF-2237.
- Clague, D. A., Moore, J. G., Dixon, J. E., and Friesen, W. B. (1995). Petrology of submarine lavas from Kilauea's Puna Ridge, Hawaii. *J. Petrol.* 36, 299–349. doi: 10.1093/petrology/36.2.299
- Clague, D. A., Moore, J. G., and Reynolds, J. R. (2000). Formation of submarine flat-topped volcanic cones in Hawaii. *Bull. Volcanol.* 62, 214–233. doi: 10.1007/s004450000088
- Clague, D. A., Paduan, J. B., Caress, D. W., Chadwick, W. W. Jr., Le Saout, M., Dreyer, B., et al. (2017). High-resolution AUV mapping and targeted ROV observations of three historical lava flows at Axial Seamount. *Oceanography* 30, 82–99. doi: 10.5670/oceanog.2017.426
- Clague, D. A., Uto, K., Satake, K., and Davis, A. S. (2002). "Eruption style and flow emplacement in the submarine North Arch Volcanic Field, Hawaii," in *Hawaiian Volcanoes: Deep Underwater Perspectives*, Vol. 128, eds E. Takahashi, P. W. Lipman, M. O. Garcia, J. Naka, and S. Aramaki (Washington, DC: American Geophysical Union), 65–84. doi: 10.1029/GM128p0065
- Cole, J. W., Milner, D. M., and Spinks, K. D. (2005). Calderas and caldera structures: a review. *Earth Sci. Rev.* 69, 1–26. doi: 10.1016/j.earscirev.2004.06.004
- Coombs, M. L., Sisson, T. W., and Lipman, P. W. (2004). *Major-Element, S, and Cl Compositions of Submarine Kilauea Glasses Collected During the 1998–2002 JAMSTEC Hawaii cruises*. Reston, VA: U.S. Geological Survey 2004–1378.
- Davis, A. S., and Clague, D. A. (1998). Changes in the hydrothermal system at Loihi Seamount after the formation of Pele's pit in 1996. *Geology* 26, 399–402. doi: 10.1130/0091-7613(1998)026<0399:CITHSA>2.3.CO;2

- Davis, A. S., Clague, D. A., Zierenberg, R. A., Wheat, C. G., and Cousens, B. L. (2003). Sulfide formation related to changes in the hydrothermal system on Loihi Seamount, Hawaii, following the seismic event in 1996. *Can. Min.* 41, 457–472. doi: 10.2113/gscanmin.41.2.457
- De Carlo, E. H., McMurtry, G. M., and Yeh, H. W. (1983). Geochemistry of hydrothermal deposits from Loihi submarine volcano, Hawaii. *Earth Planet. Sci. Lett.* 66, 438–449. doi: 10.1016/0012-821X(83)90157-7
- Duennebie, F. K., Harris, D., Jolly, J., Caplan-Auerbach, J., Jordan, R., Copson, D., et al. (2002). HUGO: the Hawaii Undersea Geo-Observatory. *IEEE J. Ocean Eng.* 2, 218–227. doi: 10.1109/OE.2002.1002476
- Eakins, B. W., Robinson, J. E., Kanamatsu, T., Naka, J., Smith, J. R., Takahashi, E., et al. (2004). *Hawaii's Volcanoes Revealed*. Reston, VA: U.S. Geological Survey.
- Edwards, K. J., Glazer, B. T., Rouxel, O. J., Bach, W., Emerson, D., Davis, R. E., et al. (2011). Ultra-diffuse hydrothermal venting supports Fe-Oxidizing bacteria and massive umber deposition at 5000 m off Hawaii. *ISME J.* 5, 1748–1758. doi: 10.1038/ismej.2011.48
- Emery, K. O. (1955). Submarine topography south of Hawaii. *Pac. Sci.* 9, 286–291.
- Filson, J., Simkin, T., and Leu, L. K. (1973). Sesimicity of a caldera collapse: Galapagos Islands 1968. *J. Geophys. Res.* 78, 8591–8622. doi: 10.1029/JB078i035p08591
- Fornari, D. J., Garcia, M. O., Tyce, R. C., and Gallo, D. G. (1988). Morphology and structure of Loihi seamount based on seabeam sonar mapping. *J. Geophys. Res.* 93, 15227–15238. doi: 10.1029/JB093iB12p15227
- Frey, F. A., and Clague, D. A. (1983). Geochemistry of diverse basalt types from Loihi Seamount, Hawaii: petrogenetic implications. *Earth Planet. Sci. Lett.* 66, 337–355. doi: 10.1016/0012-821X(83)90150-4
- Fryer, P., Matsumoto, H., Duennebie, F., Cooper, P., Kellogg, J., Garcia, M., et al. (1987). Loihi Seamount: a reconnaissance Sea MARC II survey. *Geol. Soc. Am. Trans.* 19:380.
- Garcia, M. O., Caplan-Auerbach, J., De Carlo, E. H., Kurz, M. D., and Becker, N. (2006). Geology, geochemistry, and earthquake history of Loihi Seamount, Hawaii's youngest volcano. *Chem. Erde* 66, 81–108. doi: 10.1016/j.chemer.2005.09.002
- Garcia, M. O., Graham, D. W., Muenow, D. W., Spencer, K., Rubin, K. H., Norman, M. D., et al. (1998). Petrology and geochronology of basalt breccia from the 1996 earthquake swarm of Loihi Seamount, Hawaii: magmatic history of its 1996 eruption. *Bull. Volcanol.* 59, 577–592. doi: 10.1007/s004450050211
- Garcia, M. O., Irving, A. J., Jorgenson, B. A., Mahoney, J. J., and Ito, E. (1993). An evaluation of temporal geochemical evolution of Loihi summit lavas: results from Alvin submersible dives. *J. Geophys. Res.* 98, 537–550. doi: 10.1029/92JB01707
- Garcia, M. O., Muenow, D. W., Aggrey, K. E., and O'Neil, J. R. (1989). Major element, volatile, and stable isotope geochemistry of Hawaiian submarine tholeiitic glasses. *J. Geophys. Res.* 94, 10525–10538. doi: 10.1029/JB094iB08p10525
- Geshi, N., Ruch, J., and Acocella, V. (2014). Evaluating volumes for magma chambers and magma withdrawal for caldera collapse. *Earth Planet. Sci. Lett.* 396, 107–115. doi: 10.1038/ncomms12295
- Glazer, B. T., and Rouxel, O. J. (2009). Redox speciation and distribution within diverse iron-dominated microbial habitats at Loihi Seamount. *Geomicrobiol. J.* 26, 606–622. doi: 10.1080/01490450903263392
- Gudmundsson, A. (2008). Magma Chamber geometry, fluid transport, local stresses and rock behavior during caldera formation. *Dev. Volcanol.* 10, 313–349. doi: 10.1016/S1871-644X(07)00008-3
- Holcomb, R. T., Moore, J. G., Lipman, P. W., and Belderson, R. H. (1988). Voluminous lava flows from Hawaiian volcanoes. *Geology* 16, 400–404. doi: 10.1130/0091-7613(1988)016<400:VSLFFH>2.3.CO;2
- Holcomb, R. T., and Robinson, J. E. (2004). *Maps of the Hawaiian Islands Exclusive Economic Zone Interpreted from GLORIA Sidescan-Sonar Imagery*. Reston, VA: United States Geological Survey. doi: 10.3133/sim2824
- Howard, K. A. (2010). Caldera collapse: perspectives from comparing Galapagos volcanoes, nuclear-test sinks, sandbox models, and volcanoes on Mars. *GSA Today* 20, 4–10. doi: 10.1130/GSATG82A.1
- Karl, D. M., Brittain, A. M., and Tilbrook, B. D. (1989). Hydrothermal and microbial processes at Loihi Seamount, a midplate hot-spot volcano. *Deep Sea Res.* 36, 1655–1673. doi: 10.1016/0198-0149(89)90065-4
- Karl, D. M., McMurtry, G. M., Malahoff, A., and Garcia, M. O. (1988). Loihi Seamount, Hawaii: a mid-plate volcano with a distinctive hydrothermal system. *Nature* 335, 532–535. doi: 10.1038/335532a0
- Klein, F. W. (1982). Earthquakes at Loihi submarine volcano and the Hawaiian hot spot. *J. Geophys. Res.* 87, 7719–7726. doi: 10.1029/JB087iB09p07719
- Kumagai, H., Ohminato, T., Nakano, M., Ooi, M., Kubo, A., Unoue, H., et al. (2001). Very long-period seismic signals and caldera formation at Miyake Island, Japan. *Science* 293, 687–690. doi: 10.1126/science.1062136
- Kusumoto, S., and Takemura, K. (2005). Caldera geometry determined from depth of the magma chamber. *Earth Planets Space* 57, e17–e20. doi: 10.1186/BF03351879
- Lipman, P. W. (2000). in *Calderas, in Encyclopedia of Volcanoes*, ed. H. Sigurdsson (San Diego, CA: Academic Press), 643–662.
- Lō'ihi Science Team. (1997). Researchers rapidly respond to submarine activity at Lō'ihi volcano, Hawaii. *EOS Trans. AGU* 78, 229–233. doi: 10.1029/97EO00150
- Malahoff, A. (1987). "Geology of the summit of Loihi submarine volcano," in *Volcanism in Hawaii: USGS Professional Paper*, Vol. 1350, eds R. W. Decker, T. L. Wright, and P. H. Stauffer (Reston, VA: United States Geological Survey), 133–144.
- Malahoff, A., McMurtry, G. M., Wiltshire, J. C., and Hsueh-Wen, Y. (1982). Geology and chemistry of hydrothermal deposits from active submarine volcano Loihi, Hawaii. *Nature* 298, 234–239. doi: 10.1038/298234a0
- MBARI Mapping Team (2000). *Hawaii Multibeam Survey*. Moss Landing, CA: Monterey Bay Aquarium Research Institute
- Michon, L., Staudacher, T., Farrazzini, V., and Bachelory, P. (2007). April 2007 collapse of Piton de la Fournaise: a new example of caldera formation. *Geophys. Res. Lett.* 34:L21301. doi: 10.1029/2007GL031248
- Michon, L., Villeneuve, N., Catry, T., and Merle, O. (2009). How summit calderas collapse on basaltic volcanoes: new insights from the April 2007 caldera collapse of Piton de La Fournaise volcano. *J. Volcanol. Geotherm. Res.* 184, 138–151. doi: 10.1016/j.jvolgeores.2008.11.003
- Molin, P., Acocella, V., and Funicello, R. (2003). Structural, seismic, and hydrothermal features at the border of the active intermittent resurgent block: Ischia Island (Italy). *J. Volcanol. Geotherm. Res.* 121, 65–81. doi: 10.1016/S0377-0273(02)00412-2
- Moore, J. G., and Chadwick, W. W. (1995). "Offshore geology of Mauna Loa and adjacent area, Hawaii," in *Mauna Loa Revealed: Structure, Composition, History, and Hazards*, Vol. 92, eds J. M. Rhodes and J. P. Lockwood (Washington, DC: American Geophysical Union), 21–44.
- Moore, J. G., Clague, D. A., Holcolm, R., Lipman, P., Normark, W., and Torresan, M. (1989). Prodigious landslides on the Hawaiian ridge. *J. Geophys. Res.* 94, 17465–17484. doi: 10.1029/JB094iB12p17465
- Moore, J. G., Clague, D. A., and Normark, W. R. (1982). Diverse basalt types from Loihi seamount, Hawaii. *Geology* 10, 88–92. doi: 10.1130/0091-7613(1982)10<88:DBTFLS>2.0.CO;2
- Moore, J. G., Normark, W. R., and Lipman, P. W. (1979). "Loihi Seamount – a young submarine Hawaiian volcano," in *Proceedings of the Hawaii Symposium on Intraplate Volcanism and Submarine Volcanism*, Hilo, 127.
- Morgan, J. K., Moore, G. F., and Clague, D. A. (2003). Slope failure and volcanic spreading along the submarine south flank of Kilauea volcano, Hawaii. *J. Geophys. Res.* 108:2415. doi: 10.1029/2003JB002411
- Munro, D. C., and Rowland, S. K. (1996). Caldera morphology in the western Galapagos and implications for volcano eruptive behavior and mechanisms of caldera formation. *J. Volcanol. Geotherm. Res.* 72, 85–100. doi: 10.1016/0377-0273(95)00076-3
- Neal, C. A., Brantley, S. R., Antolik, L., Babb, J. L., Burgess, M., Calles, K., et al. (2019). The 2018 rift eruption and summit collapse of Kilauea Volcano. *Science* 363, 367–374. doi: 10.1126/science.aav7046
- Okubo, C. H., and Martel, S. J. (1998). Pit crater formation on Kilauea Volcano, Hawai'i. *J. Volcanol. Geotherm. Res.* 86, 1–18. doi: 10.1016/S0377-0273(98)00070-5
- Paduan, J. B., Clague, D. A., and Caress, D. W. (2014). "Constructional talus: built during eruption, not by later tectonism," in *Proceedings of the American Geophysical Union Fall Meeting*, San Francisco, CA.
- Peltier, A., Staudacher, T., Bachelery, P., and Cayol, V. (2009). Formation of the April 2007 caldera collapse at Piton de la Fournaise volcano: insights from GPS data. *J. Volcanol. Geotherm. Res.* 184, 152–163. doi: 10.1016/j.jvolgeores.2008.09.009

- Pinel, V., and Jaupart, C. (2005). Caldera formation by magma withdrawal from a reservoir beneath a volcanic edifice. *Earth Planet. Sci. Lett.* 230, 273–287. doi: 10.1038/ncomms12295
- Schipper, C. I., and White, J. D. L. (2010). No depth limit to hydrovolcanic limbo of Pele from Loihi Seamount, Hawaii. *Bull. Volcanol.* 72, 149–164. doi: 10.1007/s00445-009-0315-5
- Schipper, C. I., White, J. D. L., and Houghton, B. F. (2011). Textural, geochemical, and volatile evidence for a Strombolian sequence at Loihi Seamount, Hawaii. *J. Volcanol. Geotherm. Res.* 207, 16–32. doi: 10.1016/j.jvolgeores.2011.08.001
- Sedwick, P. N., McMurtry, G. M., Hilton, D. R., and Goff, F. (1994). Carbon dioxide and helium in hydrothermal fluids from Loihi Seamount, Hawaii, USA: temporal variability and implications for the release of mantle volatiles. *Geochim. Cosmochim. Acta* 58, 1219–1227. doi: 10.1016/0016-7037(94)90587-8
- Sedwick, P. N., McMurtry, G. M., and Macdougall, J. D. (1992). Chemistry of hydrothermal solutions from Pele's Vents, Loihi Seamount, Hawaii. *Geochim. Cosmochim. Acta* 56, 3643–3667. doi: 10.1016/0016-7037(92)90159-G
- Simkin, T., and Howard, K. A. (1970). Caldera collapse in the Galapagos Islands, 1968. *Science* 169, 429–437. doi: 10.1126/science.169.3944.429
- Smith, J. R., Satake, K., and Suyehiro, K. (2002). "Deepwater multibeam sonar surveys along the southeastern Hawaiian Ridge. Guide to the CD-rom," in *Hawaiian Volcanoes: Deep Underwater Perspectives*, Vol. 128, eds E. Takahashi, P. W. Lipman, M. O. Garcia, J. Naka, and S. Aramaki (Washington, DC: American Geophysical Union), 3–9. doi: 10.1029/GM128p0003
- Smith, J. R., Shor, A. N., Malahoff, A., and Torresan, M. E. (1994). *Southeast flank of island of Hawaii. Sheet 4, Hawaii Seafloor Atlas*. Honolulu: Hawaii Institute of Geophysics and Planetology.
- Tibaldi, A., and Vezzoli, L. (1998). The space problem of caldera resurgence: an example from Ischia Island. Italy. *Geologische Rundschau* 87, 53–66. doi: 10.1007/s005310050189
- Umino, S., Lipman, P. W., and Obata, S. (2000). Subaqueous lava flow lobes, observed on ROV dives off Hawaii. *Geology* 28, 503–506. doi: 10.1130/0091-7613(2000)28<503:SLFLOO>2.0.CO;2
- Umino, S., Obata, S., Lipman, P. W., Smith, J. R., and Shibata, T. (2002). "Emplacement and inflation structures of submarine and subaerial pahoehoe lavas from Hawaii," in *Hawaiian Volcanoes: Deep Underwater Perspectives*, Vol. 128, eds E. Takahashi, P. W. Lipman, M. O. Garcia, J. Naka, and S. Aramaki (Washington, DC: American Geophysical Union), 85–101.
- Wanless, V. D., Garcia, M. O., Truesdell, F. A., Rhodes, J. M., Norman, M. D., Weis, D., et al. (2006). Submarine radial vents on Mauna Loa Volcano, Hawaii. *Geochem. Geophys. Geosyst.* 7:Q05001. doi: 10.1029/2005GC001086
- Wheat, C. G., Sansone, F. J., McMurtry, G. M., Jannasch, H. W., Plant, J. N., and Moyer, C. L. (2000). Continuous sampling of hydrothermal fluids from Loihi Seamount after the 1996 event. *J. Geophys. Res.* 105, 19353–19367. doi: 10.1029/2000JB900088

Conflict of Interest Statement: The authors declare that the research was conducted in the absence of any commercial or financial relationships that could be construed as a potential conflict of interest.

Copyright © 2019 Clague, Paduan, Caress, Moyer, Glazer and Yoerger. This is an open-access article distributed under the terms of the Creative Commons Attribution License (CC BY). The use, distribution or reproduction in other forums is permitted, provided the original author(s) and the copyright owner(s) are credited and that the original publication in this journal is cited, in accordance with accepted academic practice. No use, distribution or reproduction is permitted which does not comply with these terms.



Internal Structures and Growth Style of a Quaternary Subaerial Rhyodacite Cryptodome at Ogariyama, Usu Volcano, Hokkaido, Japan

Yoshihiko Goto^{1*} and Akihiko Tomiya^{2*}

¹ Muroran Institute of Technology, Muroran, Japan, ² Geological Survey of Japan, National Institute of Advanced Industrial Science and Technology, Tsukuba, Japan

OPEN ACCESS

Edited by:

Guido Giordano,
Università degli Studi Roma Tre, Italy

Reviewed by:

Thomas R. Walter,
German Research Centre
for Geosciences, Helmholtz Centre
Potsdam, Germany
Claudio Antonio Tranne,
University of Bologna, Italy

*Correspondence:

Yoshihiko Goto
ygoto@mmm.muroran-it.ac.jp
Akihiko Tomiya
a.tomiya@aist.go.jp

Specialty section:

This article was submitted to
Volcanology,
a section of the journal
Frontiers in Earth Science

Received: 30 July 2018

Accepted: 14 March 2019

Published: 09 April 2019

Citation:

Goto Y and Tomiya A (2019)
Internal Structures and Growth Style
of a Quaternary Subaerial Rhyodacite
Cryptodome at Ogariyama, Usu
Volcano, Hokkaido, Japan.
Front. Earth Sci. 7:66.
doi: 10.3389/feart.2019.00066

Cryptodomes are shallow-level intrusions that cause updoming of overlying sediments or other rocks. Understanding the formation of cryptodomes is important for hazard assessment, as cryptodome-forming eruptions are one of the major triggering factors in sector collapse. This paper describes internal structures of a Quaternary subaerial rhyodacite cryptodome at Ogariyama, Usu volcano, Japan (the Ogariyama dome), and examines the textural differences between subaerial and subaqueous cryptodomes to extend our knowledge of these phenomenon. The Ogariyama dome, which is one of the youngest subaerial cryptodomes in the world (<0.4 ka), can be viewed in cross-section because a vertical fault formed during the 1977–1978 eruption and cut through the center of the cryptodome, exposing its interior. The morphology of the cryptodome is scalene triangular in shape, with rounded corners in cross-section, and it is 150 m across and 80 m high. The internal structure of the dome is concentrically zoned, with a massive core, jointed rim, and brecciated border, all of which are composed of uniform, feldspar-phyric rhyodacite (SiO₂ = 71–72 wt.%). The massive core (130 m across) consists of coherent rhyodacite that has indistinct, large-scale flow banding and rectangular joints that are spaced 50–200 cm apart. The jointed rim (8–12 m wide) surrounds the massive core and consists of coherent rhyodacite that is characterized by distinct rectangular joints that are 30–80 cm apart and radiate outward. The outermost brecciated border (7–10 m wide) comprises monolithological breccia, consisting of angular rhyodacite clasts (5–30 cm across) and a cogenetic matrix. These internal structures suggest that the Ogariyama dome was formed by endogenous growth, involving continuous magma supply during a single intrusive event and simple expansion from its interior. The massive core formed by slow cooling of homogeneous rhyodacite magma. The jointed rim formed by fracturing of solidifying rhyodacite magma in response to cooling–contraction and dynamic stress driven by continued movement of the less viscous core. The brecciated border formed by fragmentation of the solidified rim of the dome in response to dynamic stress. The growth style of the Ogariyama dome closely resembles that of subaqueous cryptodomes. However, the morphology and internal structures of the Ogariyama dome differ from those of subaqueous cryptodomes, given its asymmetric morphology and absence of radial columnar joints

and large-scale flow banding. These differences might reflect the well-consolidated and inhomogeneous physical properties of the host sediment and the slow cooling rate and high viscosity of the Ogariyama dome. The Ogariyama dome is probably the best cross-sectional example of a subaerial cryptodome in the world. Our descriptive study of the cryptodome provides invaluable information for hazard assessment.

Keywords: cryptodome, subaerial, rhyodacite, internal structure, endogenous growth

INTRODUCTION

Cryptodomes are shallow-level intrusions that cause updoming of overlying sediments or other rocks (Minakami et al., 1951; McPhie et al., 1993). They commonly form by the emplacement of silicic magma into poorly consolidated sediment (White et al., 2015). Cryptodomes are distinguished from lava domes in that magma does not appear on the ground surface. When a cryptodome partly breaks through the host sediment cover, the dome is termed a partly extrusive cryptodome (McPhie et al., 1993). Cryptodome-forming eruptions occur in both subaerial and subaqueous settings. The 1943–1945 eruption at Usu volcano, Hokkaido, Japan, produced the dacitic, partly extrusive cryptodome of Showa-Shinzan (Minakami et al., 1951; Mimatsu, 1962). The 1956 eruption at Bezymianny in Kamchatka produced a dacitic cryptodome during the pre-climactic stage, which led to a catastrophic sector collapse (e.g., Belousov, 1996). The 1980 eruption at Mount St. Helens in Washington, United States, also produced a dacitic cryptodome (bulge) on the volcano flank and caused a catastrophic sector collapse (e.g., Lipman et al., 1981; Voight et al., 1983). Marine geophysical studies of the Bay of Naples, Italy (Milia et al., 2012), suggest the presence of cryptodomes beneath the sea floor.

Understanding the formation of cryptodomes is important for hazard assessment and mineral exploration. Cryptodome-forming eruptions are one of the major triggering factors in sector collapse (e.g., Lipman et al., 1981; Voight et al., 1983; Siebert, 1984; Belousov, 1996; Riggs and Carrasco-Nunez, 2004). Cryptodome-forming eruptions cause ground deformation that is associated with major natural disasters (e.g., Mimatsu, 1962; Katsui et al., 1985; Ui et al., 2002). Submarine cryptodomes can be associated with the formation of volcanic-hosted massive sulfide deposits (e.g., Horikoshi, 1969; Allen, 1992; Allen et al., 1997; Doyle and McPhie, 2000). Internal fractures in submarine cryptodomes can be oil–gas reservoirs (e.g., the Katakai gas field, Japan; Yamada and Uchida, 1997; Nonaka et al., 2018).

Our knowledge of the nature and formation of cryptodomes remains limited. The morphology and internal structures of cryptodomes are poorly understood, because the silicic intrusions of most modern cryptodomes remain buried (e.g., the Usu-Shinzan dome in Japan; Katsui et al., 1985). Descriptive studies of the internal structures of cryptodomes have been based mainly on submarine examples in ancient successions (e.g., Horikoshi, 1969; Cas et al., 1990; Kurokawa, 1990; Allen, 1992; Hanson and Wilson, 1993; Hamasaki, 1994; Goto and McPhie, 1998; Doyle and McPhie, 2000; Stewart and McPhie, 2003; Páez et al., 2018). Few studies have provided detailed descriptions of the

internal structures of subaerial cryptodomes (Goto et al., 2004; Mattsson et al., 2018).

A Quaternary subaerial cryptodome at Ogariyama, Usu volcano, southwestern Hokkaido, Japan, displays well-preserved primary internal structures in a cross-sectional exposure. The Ogariyama dome was emplaced within the amphitheater at the summit of the volcano during a historic eruption that occurred after AD 1663 (probably AD 1769 or 1822; Soya et al., 2007; Matsumoto and Nakagawa, 2011). The cross-section of this young cryptodome is visible because a vertical fault formed during the 1977–1978 eruption and cut through the center of the cryptodome, exposing its interior. The Ogariyama dome is probably the best cross-sectional example of a subaerial cryptodome in the world. A detailed description of the internal structures of the Ogariyama dome and comparison with previously reported, well-studied subaqueous cryptodomes might significantly extend our understanding of cryptodomes, as our knowledge of these structures is based mainly on subaqueous examples. The objectives of this research are to: (1) describe in detail the morphology and internal structures of the Ogariyama dome based on field mapping; (2) interpret the formation of the internal structures; (3) constrain the growth mode of the dome; and (4) compare the Ogariyama dome with subaqueous examples.

GEOLOGICAL SETTING

Usu is a post-caldera volcano of Toya caldera that is located at the junction between the Kuril and NE Japan arcs (**Figures 1A,B**). The edifice of Usu volcano rises 733 m above sea level and the volcano has a basal diameter of ~6 km. It consists mainly of a basaltic to andesitic stratovolcano that is overlain by many silicic domes (**Figure 1C**; Yokoyama et al., 1973; Soya et al., 2007).

Previous geological studies (e.g., Soya et al., 2007; Goto et al., 2013; Goto and Danhara, 2018) suggest that the activity of Usu volcano commenced with an andesitic explosive eruption at 19–18 ka, followed by andesitic stratovolcano-building between 18 and 16 ka, and sector collapse at 16 ka. The sector collapse produced an amphitheater that is 1.5–2.0 km across at the summit of the stratovolcano (**Figure 1C**). Usu volcano was then dormant for ~15 kyr. Eruptive activity of Usu volcano resumed with a rhyolitic Plinian eruption in AD 1663 (Yokoyama et al., 1973). Silicic dome-forming eruptions occurred in AD <1769, 1769, 1822, 1853, 1910, 1943–1945, 1977–1978, and 2000 (Tomiya and Miyagi, 2002; Ui et al., 2002; Nakagawa et al., 2005; Soya et al., 2007). These eruptions produced more than eleven

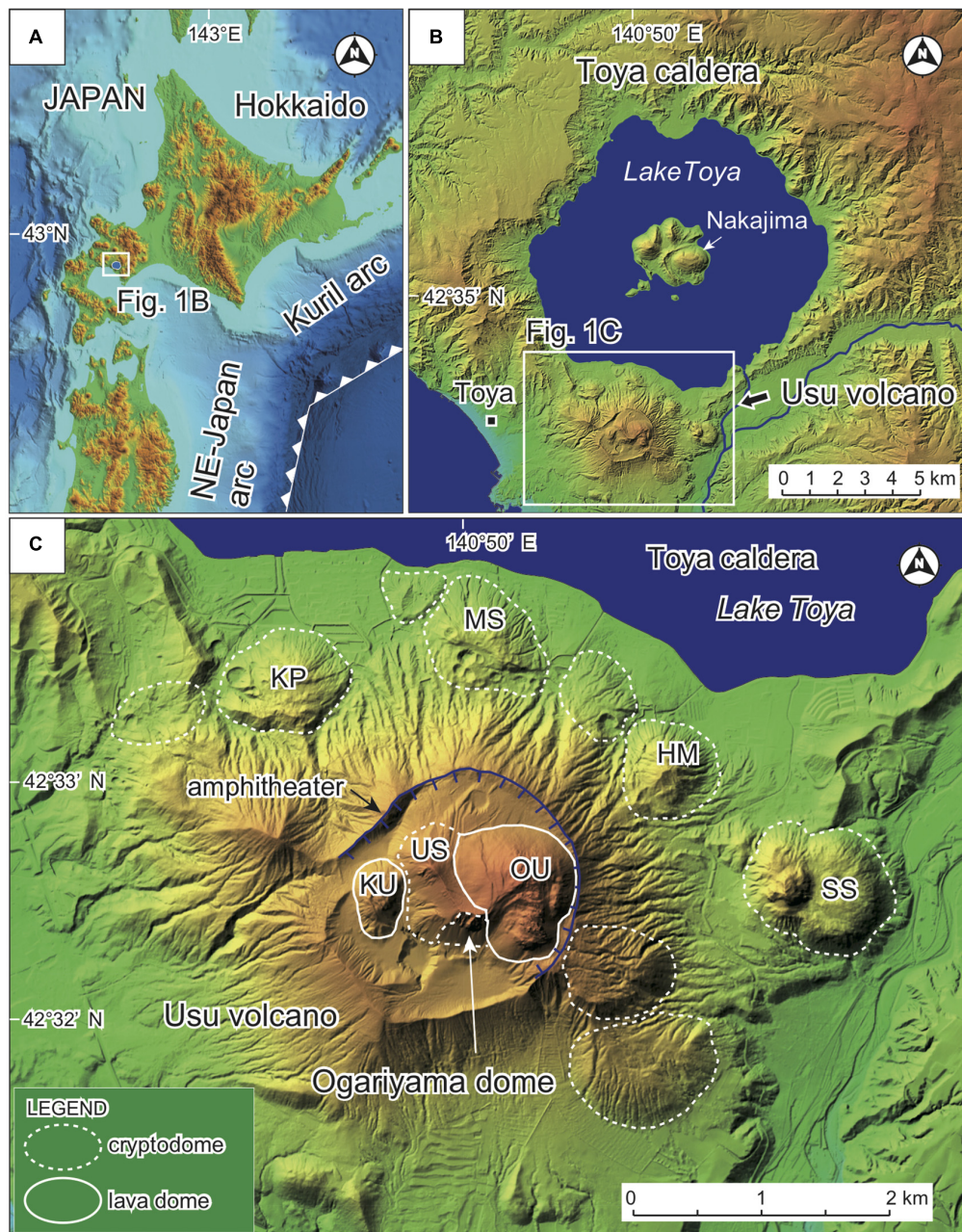


FIGURE 1 | (A) Tectonic setting of Usu volcano in southwestern Hokkaido, Japan. The volcano is located at the junction between the Kuril and NE Japan arcs. **(B)** Location of Usu volcano, which is a post-caldera volcano of Toya caldera. **(C)** Topographic map of Usu volcano, showing the location of the Ogariyama dome. Usu volcano comprises a basaltic to andesitic stratovolcano with an amphitheater at its summit, and contains many silicic cryptodomes and lava domes, including Kompira-yama (KP), Meiji-Shinzan (MS), Higashi-Maruyama (HM), Showa-Shinzan (SS), Ko-Usu (KU), Usu-Shinzan (US), O-Usu (OU), and Ogariyama. The base maps were produced by topographic data issued by the Geospatial Information Authority of Japan.

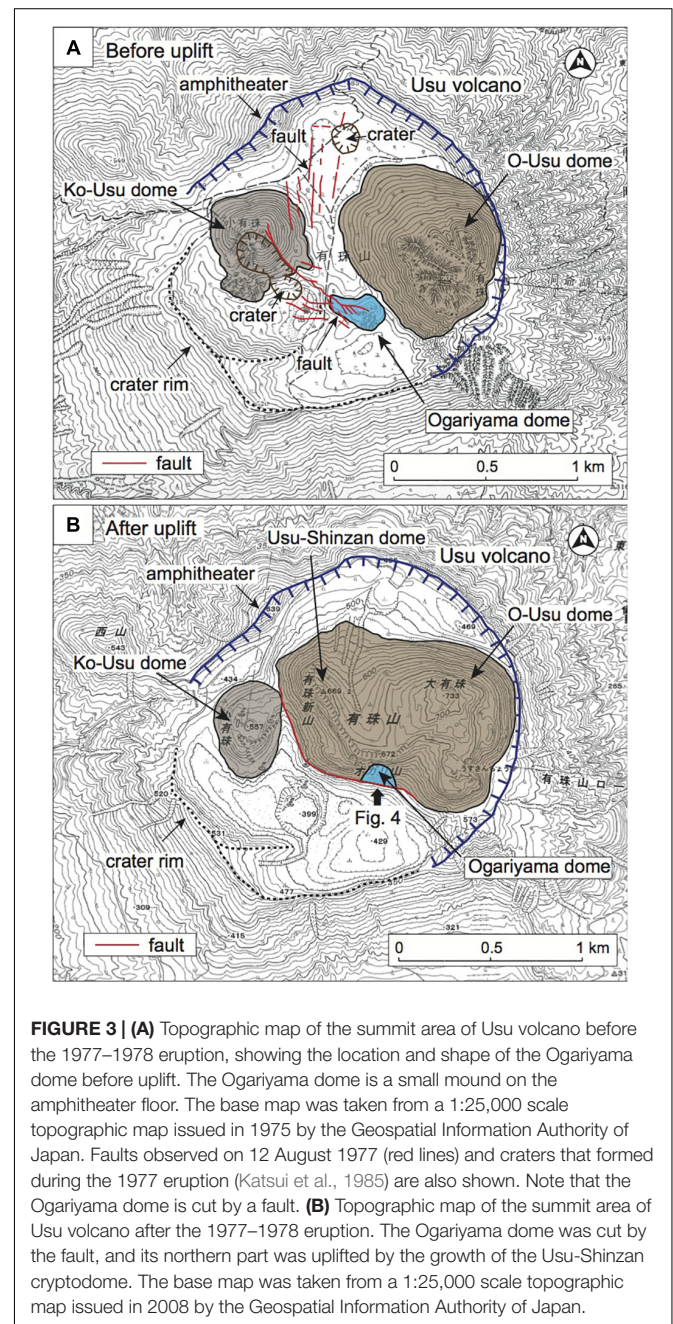
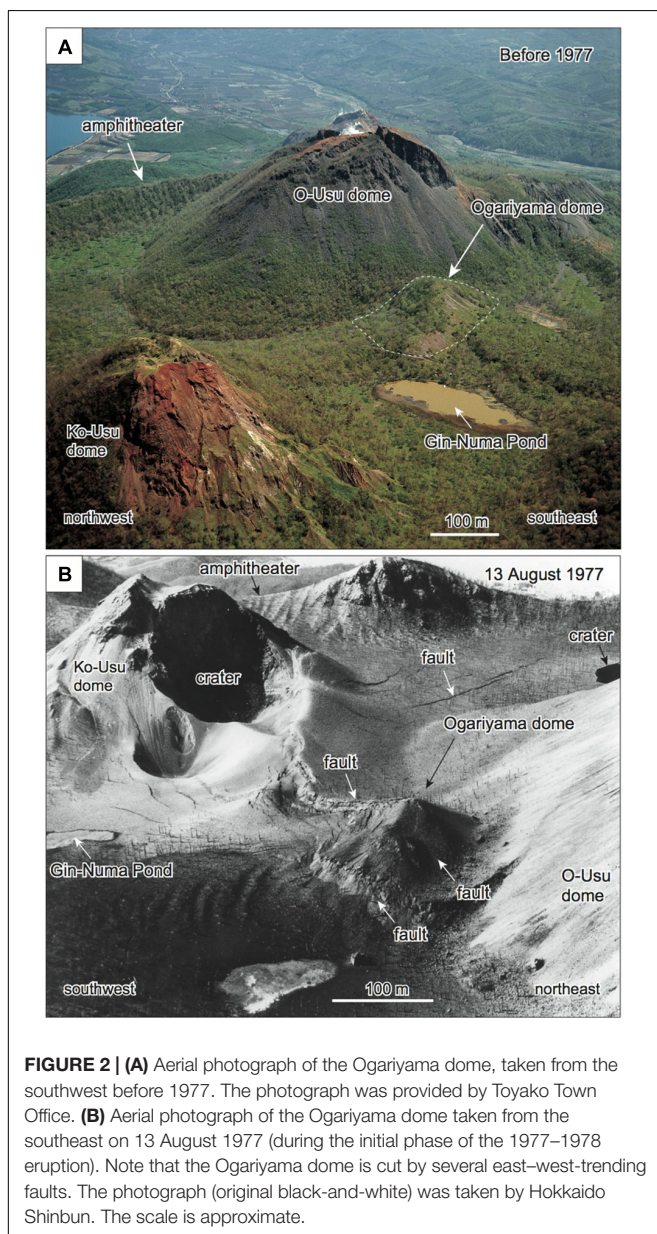
cryptodomes and two lava domes at the northern foot of the volcano and within the amphitheater (**Figure 1C**). Ogariyama is one of these cryptodomes and is located in the south-central part of the amphitheater (**Figure 1C**). The emplacement age of the Ogariyama cryptodome is considered to be AD 1769 based on petrological investigations (Matsumoto and Nakagawa, 2011), although Soya et al. (2007) suggested that the dome was emplaced

in AD 1822. Its absolute emplacement age is unknown, as no historic documents have been found describing the dome growth. The word *Ogariyama* in Japanese means “growing mountain.” Usu volcano is unique in terms of its frequency of cryptodome-forming eruptions (every 20–30 years; Soya et al., 2007). Such frequent cryptodome-forming eruptions can be attributed to the groundwater-rich environment of the volcano, which is located

nearby a caldera lake (Lake Toya; **Figure 1B**), and the intrusion of high-viscosity silicic magma during eruption.

Photographic records before AD 1977 (**Figure 2A**) indicate that the Ogariyama dome was a small mound (“roof mountain” of Mimatsu, 1962) standing on the amphitheater floor (Sobetsu Town, 2016). A topographic map published in 1975 (**Figure 3A**) indicates that the mound was 200–300 m across and 40 m high above the amphitheater floor. During the 1977–1978 eruption, large-scale ground deformation occurred within the amphitheater. The ground deformation was caused by the growth of a new cryptodome (Usu-Shinzan). Several east–west-trending faults appeared on the amphitheater floor (**Figures 2B, 3A**), and some of these faults cut the Ogariyama dome into three parts (Katsui et al., 1985). The northernmost part of the Ogariyama

dome was then gradually uplifted by ca. 180 m due to the growth of the Usu-Shinzan dome (**Figure 3B**). This uplift resulted in perfect exposure of the interior of the Ogariyama dome on the east–west-trending fault scarp along the southern perimeter of the Usu-Shinzan dome (**Figure 4**). Given that the fault vertically cut the Ogariyama dome through its center, a spectacular cross-section of the dome has been exhumed (**Figure 4**). During this ground deformation, volcanoclastic deposits on the amphitheater floor around the Ogariyama dome (“host sediment” of the Ogariyama dome) were also uplifted. The host sediment is presently exposed on the western side of the Ogariyama dome



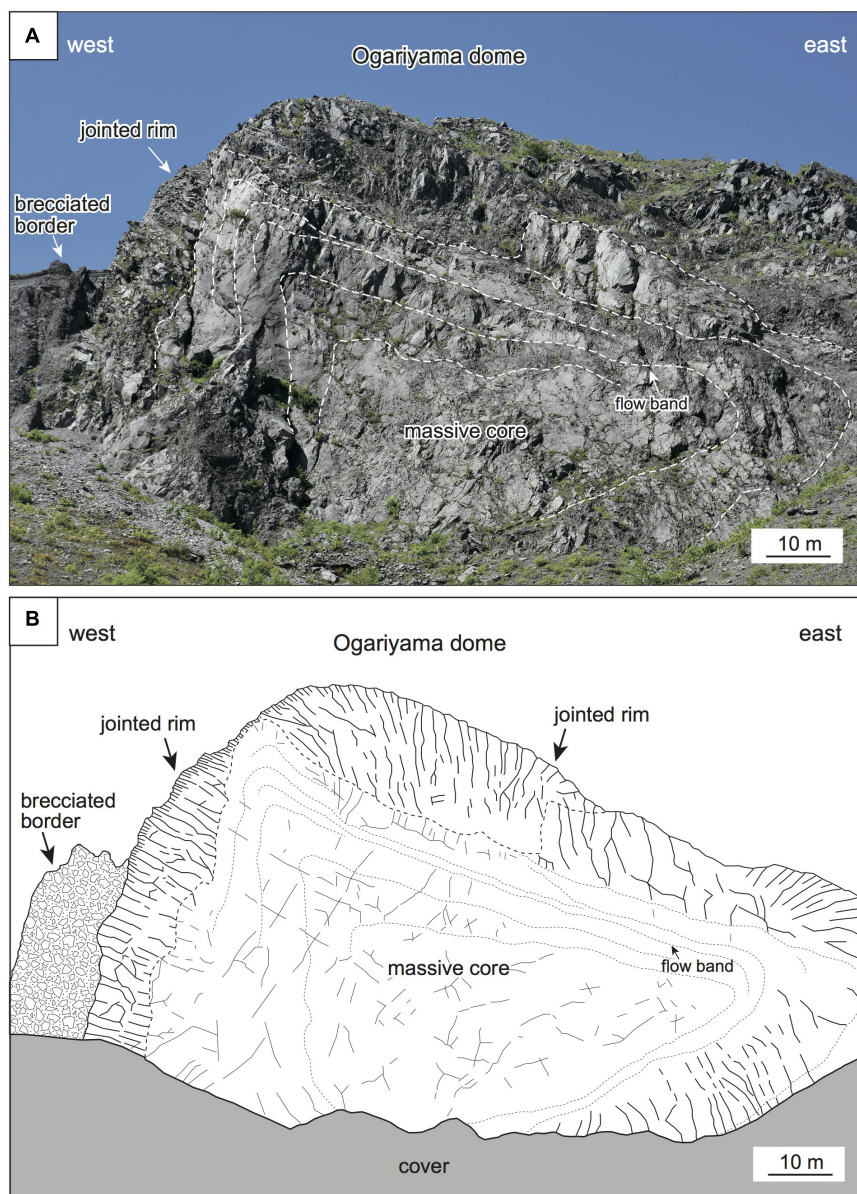


FIGURE 4 | (A) Photograph of a cross-section of the Ogariyama dome, viewed from the south. This cross-section is exposed on a fault scarp that formed in response to growth of the Usu-Shinzan cryptodome. A sketch of this outcrop is shown in **(B)**. The photograph was taken in 2018. **(B)** Sketch of the Ogariyama dome, viewed from the south. The Ogariyama dome has a scalene triangular shape, with rounded corners in cross-section, and is 150 m across and 80 m high. The Ogariyama dome is concentrically zoned, with a massive core, jointed rim, and brecciated border. The massive core comprises coherent rhyodacite that has indistinct, large-scale flow banding and poorly developed rectangular joints that are 50–200 cm apart. The jointed rim is characterized by many rectangular joints and irregular fractures. The brecciated border comprises monolithological breccia.

and is >50 m thick. It comprises rhyolitic to dacitic pyroclastic flow deposits, consisting of lithic clasts that are <50 cm in size set in a coarse-grained matrix, along with reworked deposits.

MATERIALS AND METHODS

Our geological survey of the Ogariyama dome focused on the morphology, internal structure, and lithology of the dome.

A detailed field survey of the Ogariyama dome was undertaken in 2017 and 2018 at the outcrop along the fault scarp along the southern perimeter of the Usu-Shinzan dome (**Figure 4**). The outcrop is subvertical, >80 m high, and extends horizontally in an east–west direction for >1 km. The survey locations of the Ogariyama dome were dependent on accessibility. As the outcrop is a subvertical cliff, only the base of the outcrop was accessible (i.e., the middle to upper parts of the outcrop were inaccessible). Detailed descriptions and rock

sampling of the Ogariyama dome were therefore carried out along its base. We collected more than 50 rock samples from the outcrop.

The lithological characteristics of the Ogariyama dome were determined by: (1) digital microscopy (Keyence VHX-2000) observations of collected samples; (2) optical microscopy observations of thin-sections; (3) bulk density measurements of rock samples; and (4) whole-rock geochemical analysis. The digital microscopy was used for observations of millimeter-sized rock fragments collected from the dome margin. Optical microscopy was used to determine the texture and mineralogy of the rock samples collected from various locations in the dome. Point counting was used to determine the modal abundances of phenocrysts. The bulk densities of rock samples were measured by the glass bead method of Sasaki and Katsui (1981). Whole-rock major element data were obtained by X-ray fluorescence spectrometry (XRF; Rigaku ZSX-Primus-II) at Okayama University, Japan, following the methods described by Kimura and Yamada (1996).

RESULTS

The morphology, internal structure, and lithology of the Ogariyama dome are described below, based on our field surveys and laboratory analyses.

Morphology of the Ogariyama Dome

The Ogariyama dome has a scalene triangular shape with rounded corners in an east–west cross-section (**Figure 4**). The dome has a pointed top on its western side and a steep western slope that dips at 70° – 80° and a gentle eastern slope that dips at 20° – 30° . Therefore, the Ogariyama dome has an asymmetric (anisotropic) shape. The exposed dome is 150 m wide and 80 m high (**Figure 4**), which might largely represent the original size of the intrusive body of the cryptodome, because the fault cut the dome through its center. The contact between the Ogariyama dome and its host sediment is not exposed.

Internal Structure of the Ogariyama Dome

The internal structure of the Ogariyama dome is concentrically zoned parallel to the dome margin (**Figure 4**) and comprises: (1) a massive core; (2) a jointed rim; and (3) a brecciated border.

Massive Core

The massive core occupies most of the central part of the Ogariyama dome and is ~ 130 m in diameter (**Figure 5A**). The core comprises pale gray, coherent (unbrecciated) rhyodacite with a uniform (homogeneous) texture (**Figure 5B**). The rhyodacite is dense and appears to be macroscopically non-vesicular, although it contains tiny cavities up to 0.1 mm across (described later). Indistinct, large-scale flow bands (Goto and McPhie, 1998; Stewart and McPhie, 2003) are present at the margin of the core (**Figure 5A**). The flow bands are approximately parallel to the outer surface of the core and comprise alternating darker and lighter bands, both of which

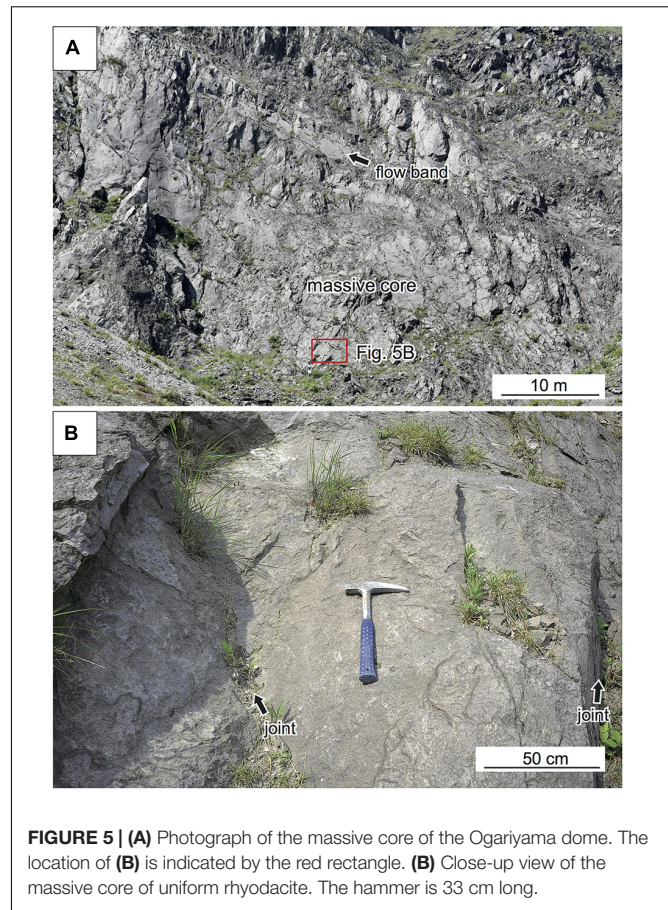


FIGURE 5 | (A) Photograph of the massive core of the Ogariyama dome. The location of **(B)** is indicated by the red rectangle. **(B)** Close-up view of the massive core of uniform rhyodacite. The hammer is 33 cm long.

range in thickness from 2 to 7 m. They show no systematic variation in thickness outward. Lithological differences between the darker and lighter bands are unknown because they are present in inaccessible parts of the outcrop. Similar banding has been reported from an experimentally simulated lava dome produced by the squeezing of viscous material (putty) through a narrow opening (Reyer, 1888). The massive core of the Ogariyama dome contains indistinct rectangular joints that overprint the flow bands. The joints are spaced at 50–200 cm intervals (**Figure 5B**). No columnar joints (i.e., prismatic joints with hexagonal or pentagonal outlines in cross-section) are present in the core.

The boundary between the core and jointed rim is distinct but gradual (**Figure 6A**). The core grades outward into the jointed rim and is marked by the appearance of a number of rectangular joints. Some joints in the core continue into the jointed rim. There is no glassy chilled contact (i.e., chilled margin) between the core and rim.

Jointed Rim

The jointed rim surrounds the core and is 8–12 m wide (**Figure 6A**). It comprises pale gray, coherent, uniform rhyodacite that contains many rectangular joints (**Figure 6B**). The rhyodacite is dense and appears to be macroscopically non-vesicular. No flow bands are visible in the rim. The rectangular

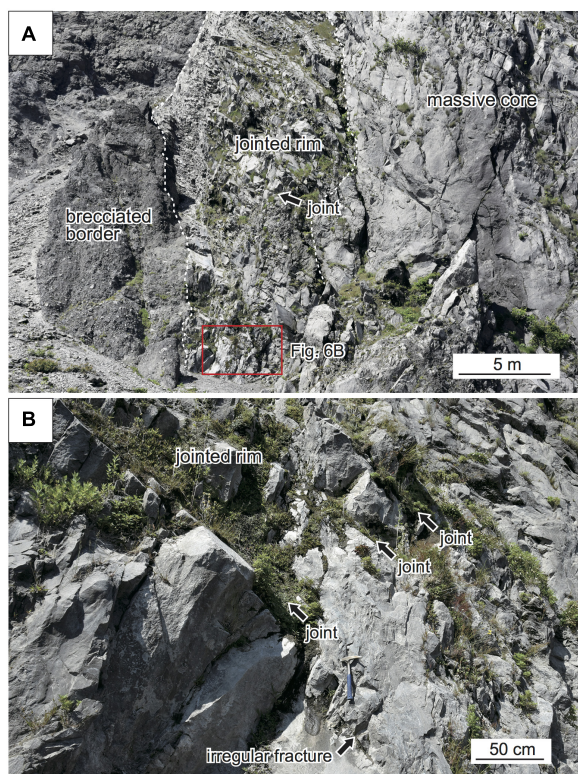


FIGURE 6 | (A) Photograph of the jointed rim of the Ogariyama dome, which occurs between the massive core and brecciated border. The location of **(B)** is indicated by the red rectangle. **(B)** Close-up view of the jointed rim, which contains numerous rectangular and parallel joints, as well as irregular fractures.

joints are approximately directed radially from the center to outer surface of the dome, but are not exactly perpendicular to the rim of the core (**Figure 6A**). The rectangular joints intersect the outer rim of the core at an angle of 60° – 80° (**Figure 6B**). The rectangular joints are generally sub-parallel with a spacing of 30–80 cm, and gradually decrease in spacing outward. Each rectangular joint extends for 8–12 m through the rim and has a curved-planar surface. The rim also contains irregular fractures between the rectangular joints (**Figure 6B**). The irregular fractures have developed in random directions with a spacing of 10–30 cm. The surfaces of the irregular fractures are rough. There are no columnar joints in the rim.

The boundary between the rim and brecciated border is distinct but gradual (**Figure 6A**). There is no glassy chilled contact between the rim and border. Compared with the boundary between the core and rim, the boundary between the rim and border is more distinct.

Brecciated Border

The brecciated border occurs at the outermost part of the Ogariyama dome and is 7–10 m wide (**Figure 6A**). It comprises a gray, monolithological (monomict) breccia that consists of

angular rhyodacite clasts that are 5–30 cm across set in a cogenetic matrix (**Figure 7A**). The breccia is massive (non-stratified), poorly sorted, and mostly shows a clast-rotated texture. Some domains also show a jigsaw texture. The clasts comprise more than 80 vol.% of the breccia. Each clast is a polyhedral rhyodacite fragment with sharp edges (**Figure 7A**). No glassy chilled margins were found on the clast surfaces. The rhyodacite of each clast is dense and macroscopically non-vesicular. The matrix of the breccia consists of angular rhyodacite fragments (<10 mm across) and fine ash (pulverized rhyodacite). Digital microscopy observations indicate that the rhyodacite fragments in the matrix have sharp edges (**Figure 7B**). Some small rhyodacite fragments (<1 mm across) have a flaky morphology (arrows in **Figure 7B**). There is no peperite (White et al., 2000; Skilling et al., 2002) within the brecciated border, suggesting that the host sediment was not fluidized during emplacement of the dome.

Lithology of the Ogariyama Dome

Texture and Mineral Assemblage

The rhyodacite of the massive core is uniformly porphyritic (**Figure 8A**). It contains euhedral plagioclase phenocrysts up to

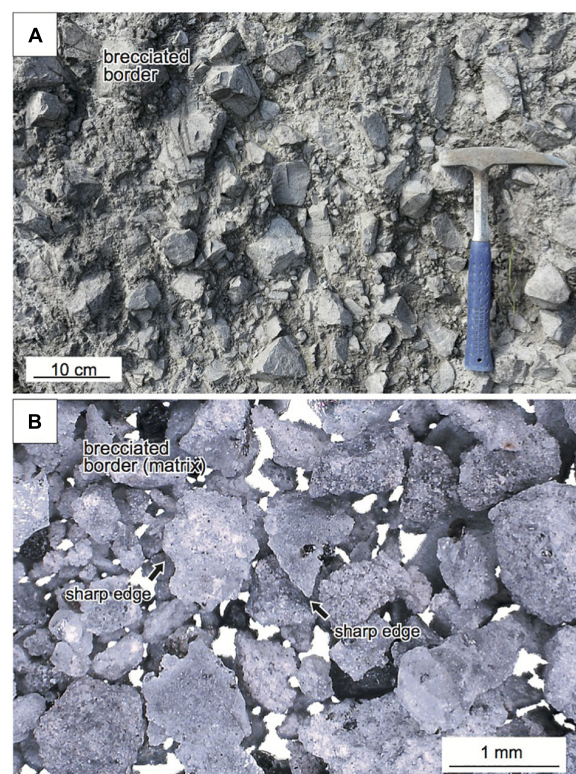


FIGURE 7 | (A) Photograph of the brecciated border of the Ogariyama dome, which comprises monolithological breccia consisting of angular rhyodacite clasts and a cogenetic matrix. **(B)** Close-up view of rhyodacite fragments in the matrix of the brecciated border. Some rhyodacite fragments have a flaky morphology with sharp edges (solid arrows). The photograph was taken with a digital microscope.

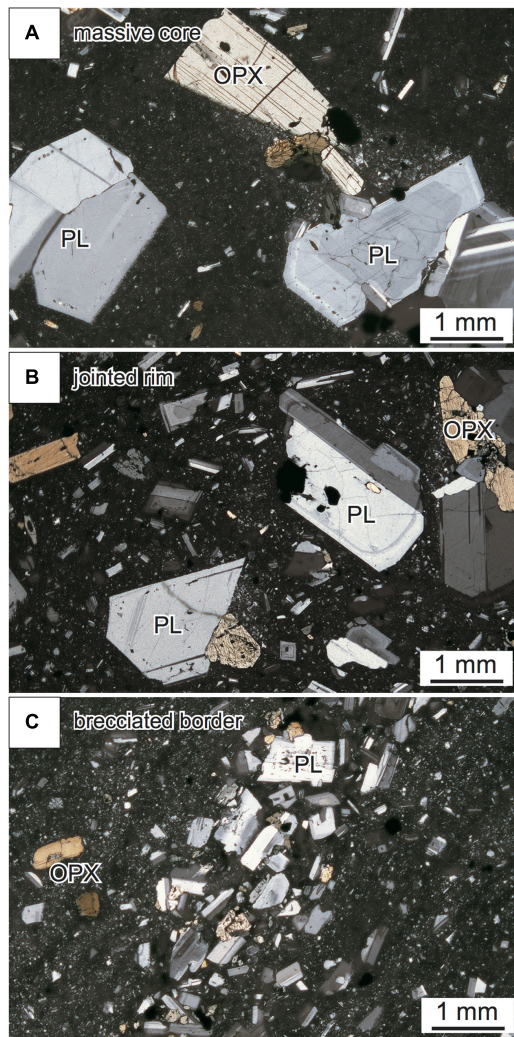


FIGURE 8 | Photomicrograph of rhyodacites from the (A) massive core, (B) jointed rim, and (C) brecciated border (cross-polarized light). Note that a phenocryst-rich zone occurs in the brecciated border. PL, plagioclase; OPX, orthopyroxene.

2 mm long (11–13 vol.% of the rhyodacite), hypersthene up to 2 mm long (1–2 vol.%), and opaque minerals up to 0.3 mm across (1 vol.%). Some phenocrysts are aggregated, forming “crystal clots” (Stewart, 1975) that are 1–3 mm across. The groundmass (~85 vol.%) of the rhyodacite has a microcrystalline texture and consists of plagioclase, hypersthene, silica minerals, and opaque minerals, all of which are up to 0.1 mm in size. Although no spherical vesicles are visible in the groundmass, irregularly shaped tiny cavities up to 0.1 mm across (“pores” of Zorn et al., 2018) occur sporadically among the crystals of the groundmass, in particular around the crystal clots.

The rhyodacite of the jointed rim is almost identical in terms of phenocryst assemblage, proportion, and size to the massive core (Figure 8B). It contains euhedral plagioclase phenocrysts up to 1.5–2.0 mm long (11–13 vol.%), hypersthene up to 2 mm

long (1–2 vol.%), and opaque minerals up to 0.3 mm across (1 vol.%). However, the groundmass (~85 vol.%) of this rhyodacite is more glassy and has a hyalopilitic texture (Bates and Jackson, 1984; Allaby, 2008), consisting of plagioclase, hypersthene, and opaque minerals, all of which are up to 0.1 mm across, set in volcanic glass that has been partly devitrified. No or few cavities were visible in the groundmass.

The rhyodacite of the brecciated border differs in texture from those of the massive core and jointed rim (Figure 8C). The rhyodacite has a micro-banded texture that is characterized by numerous, parallel, phenocryst-rich zones. Each phenocryst-rich zone is 1–2 mm wide and they are spaced at 2–5 mm intervals. The phenocryst-rich zone consists of phenocrysts of plagioclase (<2 mm long), hypersthene (<1.5 mm long), and opaque minerals (<0.3 mm across). Most phenocrysts are euhedral, but some are fragmented. The total phenocryst proportion of this rhyodacite is almost identical to those of the massive core and fractured rim. The groundmass of the rhyodacite has a hyalopilitic texture, consisting of sub-parallel laths of plagioclase and hypersthene, granular opaque minerals (all <0.1 mm across), and volcanic glass. Although no spherical vesicles are visible in the groundmass, irregularly shaped cavities up to 0.5 mm across occur sporadically in the phenocryst-rich zone.

Density

Bulk densities were determined for rhyodacite samples collected from the massive core, jointed rim, and brecciated border. Samples locations are shown in Figure 9. A total of 75 rhyodacite samples were analyzed. The bulk density of the Ogariyama dome ranges from 2.0 to 2.6 g/cm³ (Figure 9), which is consistent with the macroscopically non-vesicular texture of the three zones (cf. Zorn et al., 2018). The bulk densities of each zone are different. The massive core has the lowest bulk density (2.0–2.3 g/cm³), the brecciated border has an intermediate density (2.1–2.5 g/cm³), and the jointed rim has the highest density (2.4–2.6 g/cm³).

Geochemistry

Whole-rock major element compositions of rhyodacites collected from the massive core (sample US-81), jointed rim (US-17), and brecciated border (US-80) were determined (Table 1). The analyzed samples are fresh (unaltered) rhyodacites. The rhyodacites from the three zones are compositionally uniform and contain 71.3–71.7 wt.% SiO₂, 14.7–14.9 wt.% Al₂O₃, 4.5–4.6 wt.% Na₂O, and 1.0 wt.% K₂O. Data for the rhyodacites plot on the boundary between the dacite and rhyolite fields in the total alkalis versus SiO₂ (TAS) diagram of Le Maitre et al. (1989) (Figure 10).

DISCUSSION

Environment of Dome Emplacement

The location and geology indicate that the Ogariyama dome was intruded into poorly consolidated volcanoclastic deposits that were emplaced within an amphitheater of an andesitic stratovolcano in a subaerial environment (Figure 11A). The absence of glassy chilled margins and peperites in the brecciated

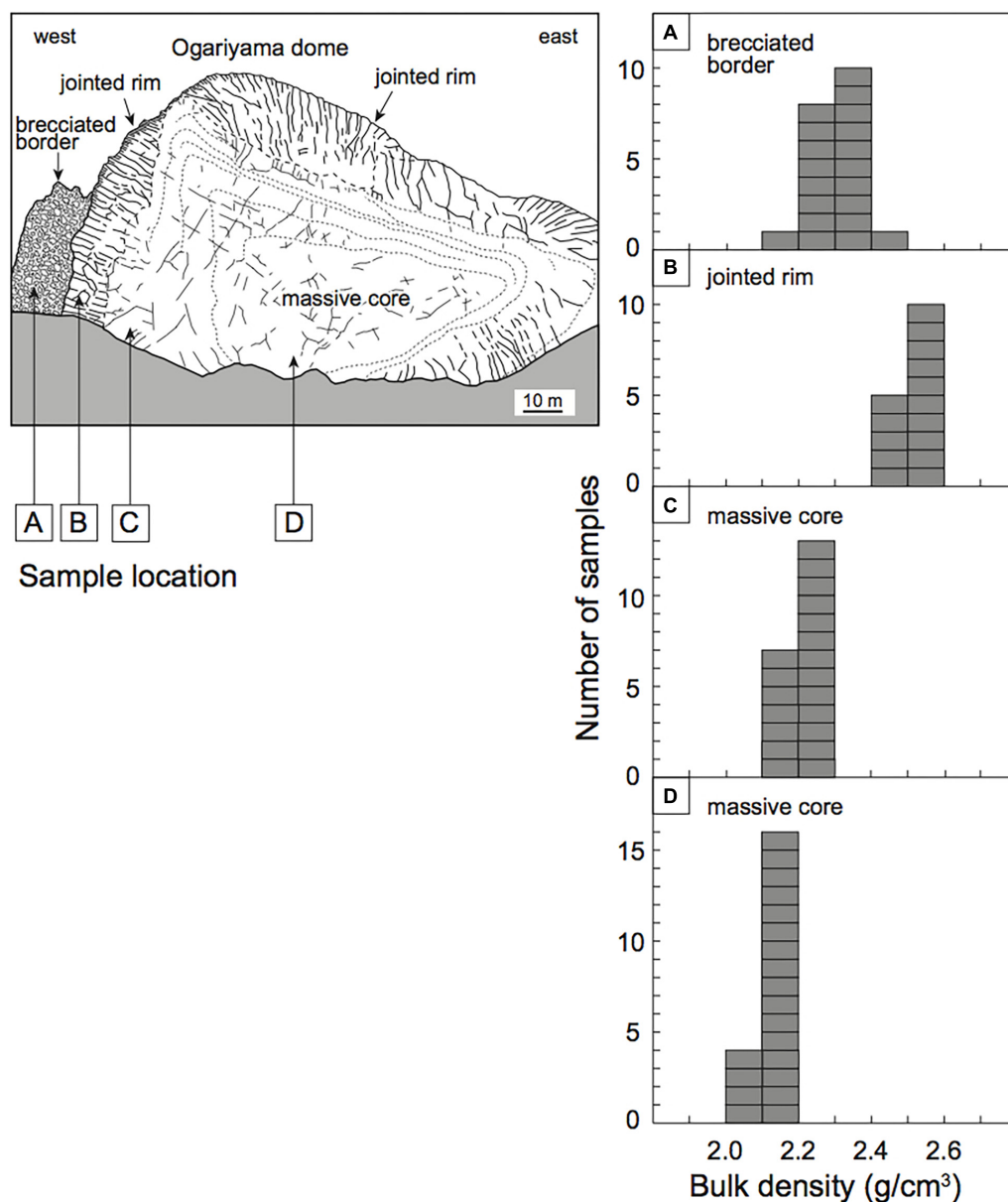


FIGURE 9 | Bulk densities of the rhyodacites from the (A) brecciated border, (B) jointed rim, and (C,D) massive core. Sampling positions (A–D) are shown in the sketch.

border demonstrates that the host sediment (i.e., volcanoclastic deposits) was not saturated with groundwater at the time of dome emplacement. However, we speculate that the host sediment contained some groundwater because photographic records (Figure 2A) show that a small pond (Gin-numa; 100–200 m across) was present on the amphitheater floor before the 1977–1978 eruption. No quantitative data are available to constrain the groundwater level at the time of dome emplacement, as no historic documents describe the growth of the Ogariyama dome. The morphology of the Ogariyama dome (i.e., not spherical; Figure 4) suggests that the cryptodome was not able to inflate in all directions, meaning it could not

push away the surrounding host sediment in all directions. This intrusion behavior can be attributed to the relatively hard (and non-homogeneous) physical properties of the host sediment in a subaerial environment.

Origin of the Concentric Zones in the Ogariyama Dome

The Ogariyama dome is characterized by a concentrically zoned structure comprising a massive core, jointed rim, and brecciated border (Figure 4). These three zones are inferred to be genetically related internal structures that developed

TABLE 1 | Whole-rock major element data for rhyodacites from the massive core, jointed rim, and brecciated border of the Ogariyama dome.

	Massive core	Jointed rim	Brecciated border
Sample No.	US-81	US-17	US-80
SiO ₂ (wt.%)	71.45	71.31	71.71
TiO ₂	0.32	0.31	0.32
Al ₂ O ₃	14.68	14.87	14.86
Fe ₂ O ₃ *	3.54	3.69	3.61
MnO	0.16	0.17	0.16
MgO	0.71	0.72	0.74
CaO	3.25	3.33	3.30
Na ₂ O	4.58	4.45	4.57
K ₂ O	1.03	1.00	1.02
P ₂ O ₅	0.09	0.09	0.10
Total	99.81	99.94	100.39
L.O.I.	0.08	0.04	0.05

Fe₂O₃*, total iron as Fe₂O₃. L.O.I., loss on ignition.

within a single intrusion. They do not represent three discrete injections of magma, as the contacts between the zones are gradual. In addition, phenocryst mineralogy and abundances, and geochemical compositions are identical in all three zones, indicating the zones were produced from the same rhyodacite magma.

The massive core comprises mainly texturally uniform (or weakly flow-banded) rhyodacite that has the widest joint intervals (<2 m apart) and highest groundmass crystallinity of the three zones. The spacing of cooling joints depends mainly on the rate of cooling (e.g., Grossenbacher and McDuffie, 1995), with slow cooling favoring more widely spaced joints. Groundmass crystallinity is also related to the rate of cooling, with slow cooling resulting in more complete crystallization. We thus infer that the massive core was formed by the slow cooling of relatively homogeneous rhyodacite magma.

The jointed rim comprises glassy rhyodacite that contains abundant rectangular joints in a zone surrounding the massive core, suggesting that they are syn-emplacement fractures. The rectangular joints have curved-planar surfaces, suggesting they formed in response to cooling-contraction (Kokelaar, 1986) and dynamic stress (Brooks et al., 1982; Kokelaar, 1986; Griffiths and Fink, 1993; Stewart and McPhie, 2003) in a viscous magma. The rectangular joints meet the outer rim of the massive core at an angle of 60°–80° (Figure 6B), indicating that dynamic stress played an important role in the joint formation. Therefore, we infer that the jointed rim was formed by the fracturing of solidifying rhyodacite magma around the massive core in response to cooling-contraction and dynamic stress due to continued movement of the less-viscous core of the actively growing dome (Figure 11B). During dome growth, both internal inflation and marginal shear might have occurred simultaneously in response to movement of the high-viscosity rhyodacite magma (Figure 11A). Similar syn-emplacement joints have been reported from a Miocene rhyolite cryptodome at Sandfell in Iceland (Mattsson et al., 2018).

The brecciated border is inferred to have formed by fragmentation of the rim of the cryptodome, as the rhyodacite clasts in the brecciated border are monolithological and lithologically identical to the jointed rim. Most rhyodacite clasts show a clast-rotated texture, suggesting that clasts of *in situ* breccia were rotated in response to shear stress due to continued movement of the less-viscous core. The angular morphology of the rhyodacite clasts (Figure 7A), absence of glassy chilled margins in the rhyodacite clasts, flaky rhyodacite fragments in the matrix (Figure 7B), and pulverized rhyodacite in the matrix all suggest that the brecciated border formed in response to dynamic stress (Figure 11B). Similar shear-induced breccia has been reported from the contact between the dacite intrusion (69 wt.% SiO₂) and host sediment of the Showa-Shinzan cryptodome (Goto et al., 2004). The phenocryst-rich zones in the rhyodacite clasts (Figure 8C) might have formed by strong shearing at the dome margins before fragmentation. Similar shear-induced textures have been reported from the marginal zone of dacitic lava spines at Mount St. Helens (Ryan et al., 2018).

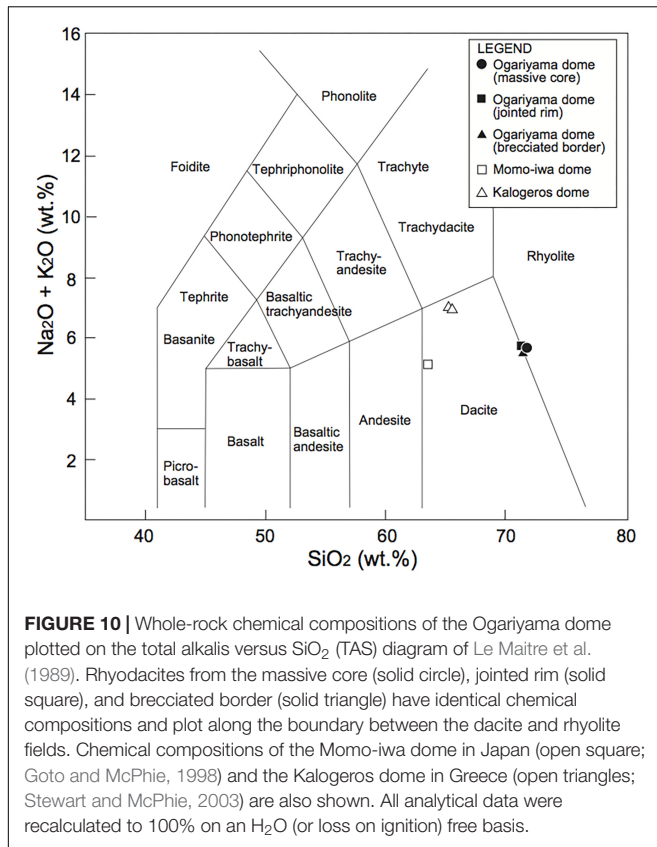
Growth Style of the Ogariyama Dome

The growth style of volcanic domes is thought to be either endogenous, when a dome grows by internal inflation in response to the injection of new lava into the dome interior, or exogenous, when new lava is added to the outer surface of a dome (Fink et al., 1990; Fink, 1993; Calder et al., 2015). We infer that the growth style of the Ogariyama dome was endogenous.

The internal structure of the Ogariyama dome is concentric, suggesting that the dome formed by simple expansion in response to a continuous supply of magma during a single extrusive phase. A pulsating magma supply and multiple injections of magma separated in time would have resulted in a more complicated internal structure, comprising multiple domes or lobes with highly variable flow-banding orientations and a more complex arrangement of textural domains (e.g., Hamasaki, 1994; Závada et al., 2009).

The joint systems in the Ogariyama dome are consistent with endogenous growth. The rectangular joints in the massive core are spaced at intervals of 0.5–2.0 m, and those in the jointed rim at 0.3–0.8 m, suggesting that the isotherms (Spry, 1962) within the dome during cooling were concentric, which is consistent with endogenous inflation of the dome. Exogenous growth or multiple discrete injections of magma would have resulted in highly variable isotherms and more complicated joint patterns.

The bulk density in the three zones is also consistent with endogenous growth. The differences in bulk density among the three zones might reflect the variable porosity (i.e., the total volume of micro-size pores) of the rhyodacites, as the three zones have almost identical total phenocryst proportions and chemical compositions (Table 1). The lowest bulk density of the massive core might reflect the highest porosity of the three zones. The highest bulk density of the jointed rim might reflect the lowest porosity of the three zones. We infer that the lowest porosity of the jointed rim was due to rapid cooling of rhyodacite magma at the dome rim, whereas the highest porosity of the massive core reflects delayed vesiculation in the slowly cooling magma, caused

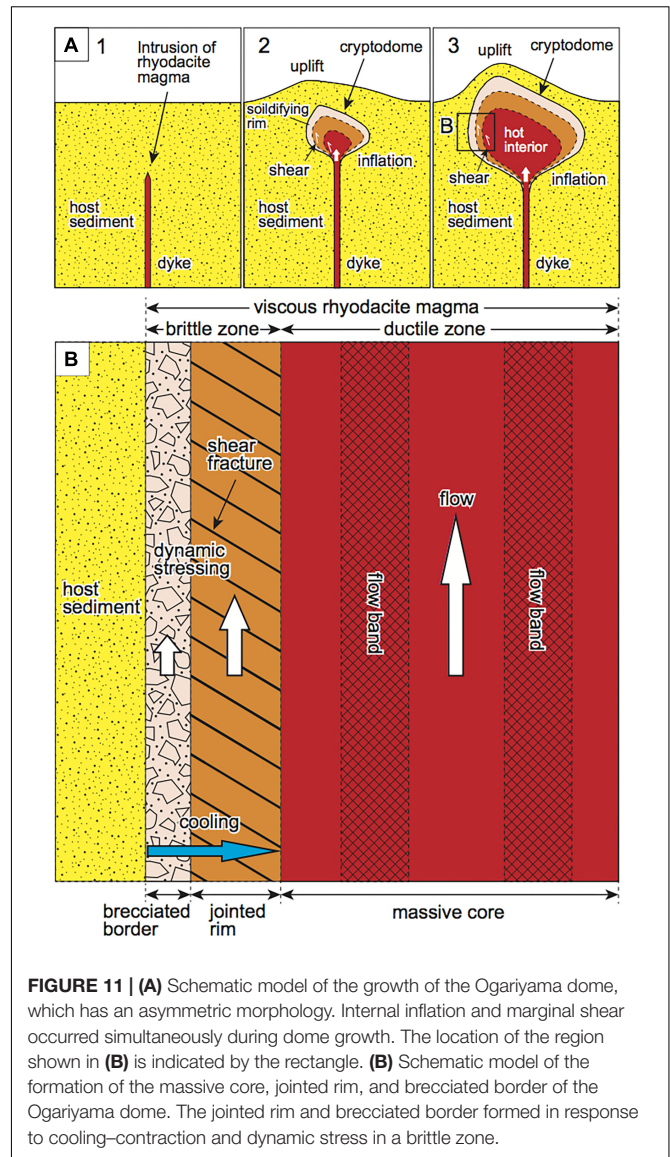


by incomplete degassing during ascent due to the high magma viscosity (e.g., Sato et al., 1992).

Endogenous growth is a common growth style of subaqueous cryptodomes (Goto and McPhie, 1998; Stewart and McPhie, 2003; White et al., 2015). Both subaerial and subaqueous cryptodomes favor endogenous growth because they form by the emplacement of silicic magma into poorly consolidated sediment, which is deformed during dome growth.

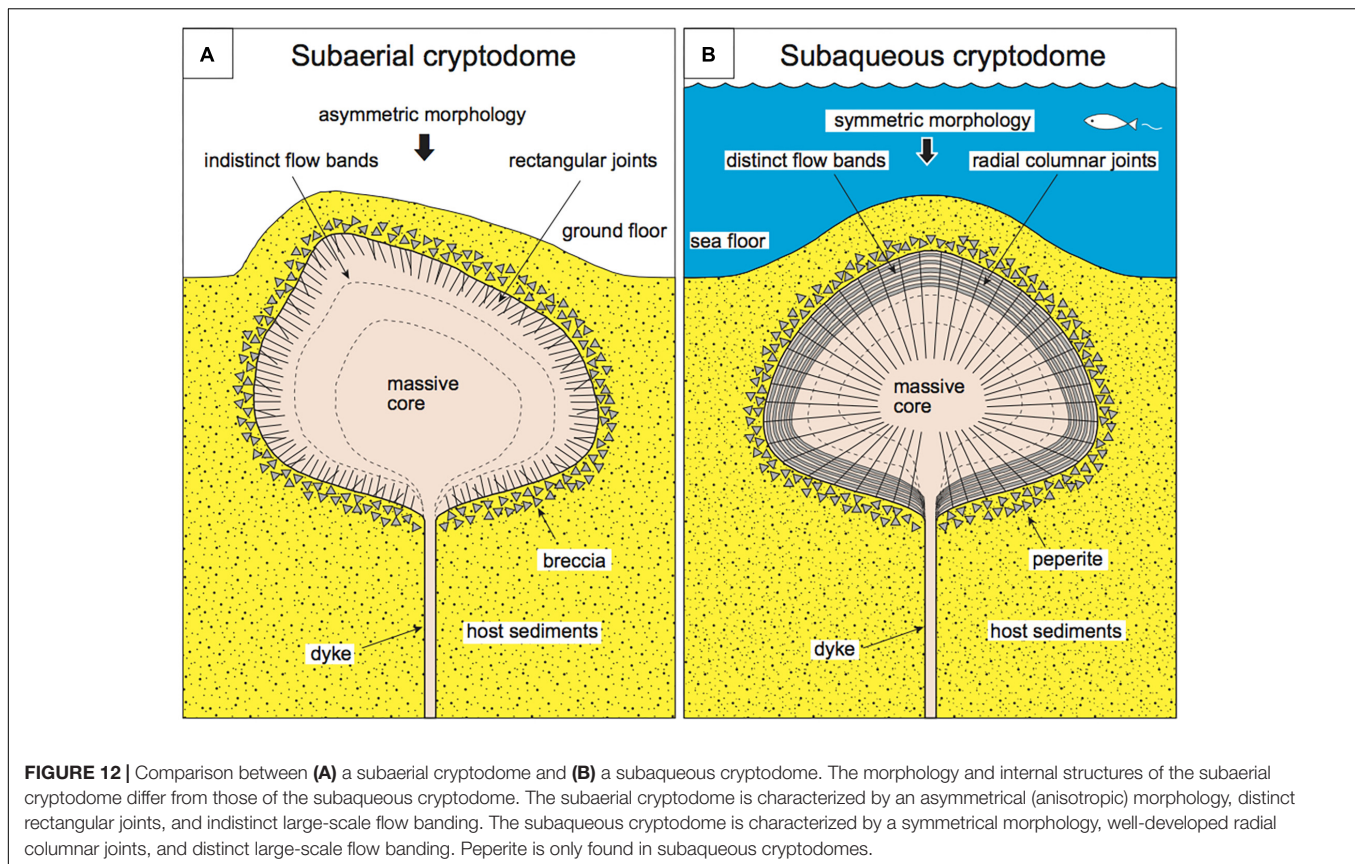
Comparison With Subaqueous Examples

We now compare the morphology and internal structures of the Ogariyama dome with those of well-described subaqueous cryptodomes to extend our understanding of these structures. Examples of subaqueous cryptodomes have been reported by Goto and McPhie (1998) and Stewart and McPhie (2003). Goto and McPhie (1998) described a Miocene submarine dacite cryptodome at Momo-iwa, Rebun Island, Hokkaido, Japan. The Momo-iwa dome has a hemispheric morphology with a diameter of 200–300 m and height of 190 m. The internal structure of the dome is concentric, with a massive core, flow banded rim, and brecciated border. Radial columnar joints are well-developed from core to rim. Peperite occurs in the brecciated border. Stewart and McPhie (2003) described a Pliocene submarine dacite cryptodome at Kalogeros, Milos Island, Greece. The Kalogeros dome has a flattened hemispheric morphology with a diameter of 800–1300 m and height of 120 m. The internal structure of the dome is concentric, with a massive core, flow-banded



rim, and brecciated border. The brecciated border comprises various types of breccias. Well-developed columnar joints occur from core to rim.

There are three differences between the Ogariyama dome and these subaqueous examples (Figure 12). The first difference is the asymmetric morphology of the Ogariyama dome, which has a scalene triangular shape, with rounded corners and a pointed top on its western side (Figure 4). In contrast, the morphology of submarine examples is simple, hemispherical, and symmetrical. This difference probably reflects the harder and non-homogeneous physical properties of the host sediments to the Ogariyama dome. The Ogariyama dome has an asymmetric (anisotropic) morphology because it was emplaced into relatively hard, non-water-saturated, coarse volcanoclastic deposits that were cut by faults or locally folded. Similar asymmetric morphologies of subaerial cryptodomes have been reported from the Showa-Shinzan



cryptodome (e.g., Minakami et al., 1951; Mimatsu, 1962; Goto and Johmori, 2014) and Usu-Shinzan cryptodome (Katsui et al., 1985). Subaqueous cryptodomes typically have a simple, symmetrical, and hemispherical morphology because they are emplaced into water-saturated, isotropic, very soft mud, which is easily deformed and pushed away during the emplacement of a cryptodome.

The second difference is the absence of radial columnar joints in the Ogariyama dome. Subaqueous cryptodomes commonly have well-developed columnar joints (Goto and McPhie, 1998; Stewart and McPhie, 2003; White et al., 2015). This difference probably reflects the slow cooling of the Ogariyama dome. Columnar joints form in response to cooling-contraction (e.g., Spry, 1962), and column diameter depends mainly on the cooling rate, with slow cooling favoring more widely spaced joints (e.g., Grossenbacher and McDuffie, 1995). The high cooling rate of subaqueous cryptodomes results in well-developed columnar joints.

The third difference is the absence of distinct, large-scale flow banding in the Ogariyama dome, whereas such banding is commonly observed in subaqueous cryptodomes (Goto and McPhie, 1998; Stewart and McPhie, 2003; White et al., 2015). This difference possibly reflects the high viscosity of the Ogariyama dome. In general, silicic magma undergoes Bingham flow rather than Newtonian flow (e.g., Harris and Rowland, 2015). Bingham flow comprises a rigid plug at the core and shear zones along the margins. Flow banding forms in response

to laminar shear in these shear zones (e.g., Cas and Wright, 1987). High-viscosity silicic magma is likely to behave as a rigid plug, which is not favorable for the development of flow bands. The Ogariyama dome has a higher SiO₂ content (71–72 wt.%) than the Momo-iwa dome (63 wt.%; Goto and McPhie, 1998) and Kalogeros dome (64–65 wt.%; Stewart and McPhie, 2003), indicating the higher viscosity of the former (Figure 10).

We propose that subaerial domes generally have higher viscosities than subaqueous domes because: (1) volcanic rocks in mature (continental) arcs have higher SiO₂ than those in immature (oceanic) arcs (e.g., Miyashiro, 1973); and (2) subaerial domes experience more complete degassing, resulting in a lower water content than subaqueous domes, as the confining pressure of subaerial domes is much lower than for subaqueous domes. The morphological and textural differences between the Ogariyama dome and subaqueous examples (i.e., the asymmetric morphology and the absence of well-developed radial columnar joints and large-scale flow banding in the Ogariyama dome) might reflect a combination of a harder host sediment, slower cooling rate, and higher viscosity of the Ogariyama dome. To our knowledge, the Ogariyama dome is the only example of a Quaternary subaerial cryptodome worldwide. The dome provides a rare opportunity to study the primary internal structure of a subaerial cryptodome. Further case studies are required to better understand the textural differences between subaerial and subaqueous cryptodomes.

SUMMARY

The subaerial Ogariyama cryptodome on Usu volcano has a scalene triangular shape in cross-section and is 150 m across and 80 m high. The cryptodome has a concentric internal structure, with a massive core, jointed rim, and brecciated border. The massive core formed by slow cooling of homogeneous rhyodacite magma. The jointed rim formed by fracturing of solidifying rhyodacite magma in response to cooling–contraction and dynamic stress due to continued movement of the less-viscous core. The brecciated border formed by dynamic stress. Compared with subaqueous cryptodomes, the Ogariyama dome is characterized by an asymmetric morphology and absence of radial columnar joints and large-scale flow bands. These morphological and textural differences might reflect the harder host sediment, slower cooling rate, and higher viscosity of the Ogariyama dome.

AUTHOR CONTRIBUTIONS

YG contributed to the conception and design of this work, performed field surveys, and led the writing of the manuscript

iteratively with AT. AT performed petrological investigations, advised YG on the geology of Usu volcano, and undertook revisions of the manuscript. YG and AT discussed and contributed to the final manuscript.

FUNDING

This work was supported by a grant from the Ministry of Education, Culture, Sports, Science and Technology of Japan (KAKENHI No. 16K05616 to AT) and the Muroran Institute of Technology (YG).

ACKNOWLEDGMENTS

We would like to thank H. Abe (Toya-Usu Geopark) for assistance with the geological field surveys. Toyako Town Office is thanked for providing a historic photograph. Hokkaido-Shinbun is thanked for allowing the use of an aerial photograph. Comments by the reviewers TW and CT, the editor GG, and the journal chief editor V. Acocella significantly improved the manuscript.

REFERENCES

- Allaby, M. (2008). *A Dictionary of Earth Sciences*. New York, NY: Oxford University Press.
- Allen, R. L. (1992). Reconstruction of the tectonic, volcanic and sedimentary setting of strongly deformed Zn-Cu massive sulfide deposits at Benambra, Victoria. *Econ. Geol.* 87, 825–854. doi: 10.2113/gsecongeo.87.3.825
- Allen, R. L., Wihed, P., and Svenson, S. A. (1997). Setting of Zn-Cu-Au-Ag massive sulfide deposits in the evolution and facies architecture of a 1.9 Ga marine volcanic arc, Skellefte district, Sweden. *Econ. Geol.* 91, 1022–1053. doi: 10.2113/gsecongeo.91.6.1022
- Bates, R. L., and Jackson, J. A. (1984). *Dictionary of Geological Terms*. Anchor Books: New York, NY.
- Belousov, A. (1996). Deposits of the 30 March 1956 directed blast at Bezymianny volcano, Kamchatka, Russia. *Bull. Volcanol.* 57, 649–662. doi: 10.1007/s004450050118
- Brooks, E. R., Wood, M. W., and Garbutt, P. L. (1982). Origin and metamorphism of peperite and associated rocks in the Devonian Elwell formation, northern Sierra Nevada, California. *Geol. Soc. Am. Bull.* 93, 1208–1231. doi: 10.1130/0016-7606(1982)93<1208:OAMOPA>2.0.CO;2
- Calder, E. S., Lavallée, Y., Kendrick, J. E., and Bernstein, M. (2015). “Lava domes eruptions,” in *Encyclopedia of Volcanoes*, 2nd Edn, ed. H. Sigurdsson (Amsterdam: Elsevier), 343–362. doi: 10.1016/B978-0-12-385938-9.00018-3
- Cas, R. A. F., Allen, R. L., Bull, S. W., Clifford, B. A., and Wright, J. V. (1990). Subaqueous, rhyolitic dome-top tuff cones: a model based on the Devonian Bunga beds, southeastern Australia and a modern analogue. *Bull. Volcanol.* 52, 159–174. doi: 10.1007/BF00334802
- Cas, R. A. F., and Wright, J. V. (1987). *Volcanic Successions: Modern and Ancient*. London: Allen and Unwin. doi: 10.1007/978-94-009-3167-1
- Doyle, M. G., and McPhie, J. (2000). Facies architecture of a silicic intrusion-dominated volcanic centre at Highway-Reward, Queensland, Australia. *J. Volcanol. Geotherm. Res.* 99, 79–96. doi: 10.1016/S0377-0273(00)00159-1
- Fink, J. H. (1993). “The emplacement of silicic lava flows and associated hazards,” in *Active Lavas*, eds C. J. Kilburn and G. Luongo (London: University College London Press), 5–24.
- Fink, J. H., Malin, M. C., and Anderson, S. W. (1990). Intrusive and extrusive growth of the Mount St. Helens lava dome. *Nature* 348, 435–437. doi: 10.1038/348435a0
- Goto, Y., and Danhara, T. (2018). Tectonics, trigger, and timing of the catastrophic sector collapse at Usu volcano, Hokkaido, Japan. *Abstract Cities Volcanoes* 10:327.
- Goto, Y., Ito, Y., Yokoyama, Y., Matsui, T., and Mimatsu, S. (2004). Internal structure of a subaerial dacite cryptodome at Usu volcano, Hokkaido, Japan. *Mem. Muroran Inst. Tech.* 54, 3–10.
- Goto, Y., and Johmori, A. (2014). Resistivity structure of the Showa-Shinzan dome at Usu volcano, Hokkaido, Japan. *Bull. Volcanol. Soc. Japan* 59, 1–11. doi: 10.18940/kazan.59.1_1
- Goto, Y., and McPhie, J. (1998). Endogenous growth of a Miocene submarine dacite cryptodome, Rebun Island, Hokkaido, Japan. *J. Volcanol. Geotherm. Res.* 84, 273–286. doi: 10.1016/S0377-0273(98)00040-7
- Goto, Y., Sekiguchi, Y., Takahashi, S., Ito, H., and Danhara, T. (2013). The 18–19 ka andesitic explosive eruption at Usu volcano, Hokkaido, Japan. *Bull. Volcanol. Soc. Japan* 58, 529–541. doi: 10.18940/kazan.58.4_529
- Griffiths, R. W., and Fink, J. H. (1993). Effects of surface cooling on the spreading of lava flows and domes. *J. Fluid Mech.* 252, 667–702. doi: 10.1017/S0022112093003933
- Grossenbacher, K. A., and McDuffie, S. M. (1995). Conductive cooling of lava: columnar joint diameter and stria width as functions of cooling rate and thermal gradient. *J. Volcanol. Geotherm. Res.* 69, 95–103. doi: 10.1016/0377-0273(95)00032-1
- Hamasaki, S. (1994). The internal structure of a rhyolite intrusion and the process of emplacement; an example from the Izumiyama porcelain stone deposit, Saga prefecture, southwestern Japan. *Bull. Volcanol. Soc. Japan* 39, 91–98.
- Hanson, R. E., and Wilson, T. J. (1993). Large-scale rhyolitic peperites (Jurassic southern Chile). *J. Volcanol. Geotherm. Res.* 54, 247–264. doi: 10.1016/0377-0273(93)90066-Z
- Harris, A. J. L., and Rowland, S. K. (2015). “Lava flows and rheology,” in *Encyclopedia of Volcanoes*, 2nd Edn, ed. H. Sigurdsson (Amsterdam: Elsevier), 321–342. doi: 10.1016/B978-0-12-385938-9.00017-1
- Horikoshi, E. (1969). Volcanic activity related to the formation of the Kuroko-type deposits in the Kosaka district, Japan. *Miner. Depos.* 4, 321–345. doi: 10.1007/BF00207161
- Katsui, Y., Komuro, H., and Uda, T. (1985). Development of faults and growth of Usu-Shinzan cryptodome in 1977–1982 at Usu volcano, north Japan. *Journal Faculty Sci. Hokkaido Univ.* 21, 339–362.

- Kimura, J., and Yamada, Y. (1996). Evaluation of major and trace element XRF analyses using a flux to sample ratio of two to one glass beads. *J. Mineral. Pet. Econo. Geol.* 91, 62–72. doi: 10.2465/ganko.91.62
- Kokelaar, B. P. (1986). Magma–water interaction in subaqueous and emergent basaltic volcanism. *Bull. Volcanol.* 48, 275–289. doi: 10.1007/BF01081756
- Kurokawa, A. (1990). Mode of occurrence and process of formation of subaqueous rhyolitic lavas in the Tadami province, Fukushima prefecture, Japan. *Earth Sci.* 44, 345–354.
- Le Maitre, R. W., Bateman, P., Dudek, A., Keller, J., Lameyre Le Bas, M. J., Sabine, P. A., et al. (1989). *A Classification of Igneous Rocks and Glossary of Terms*. Oxford: Blackwell.
- Lipman, P. W., Moore, J. G., and Swanson, D. A. (1981). Bulging of the north flank before the May 18 eruption: geodetic data. *US Geol. Surv. Prof. Pap.* 1250, 143–156.
- Matsumoto, A., and Nakagawa, M. (2011). Formation history of lava domes at the summit of Usu volcano, Hokkaido, Japan, inferred from petrological features of the volcanic rocks. *Abstract Volcanol. Soc. Japan* 97, B2–B20.
- Mattsson, T., Burchardt, S., Almqvist, B. S., and Ronchin, E. (2018). Syn-emplacement fracturing in the Sandfell laccolith, eastern Iceland—implications for rhyolite intrusion growth and volcanic hazards. *Front. Earth Sci.* 6:5. doi: 10.3389/feart.2018.00005
- McPhie, J., Doyle, M., and Allen, R. (1993). *Volcanic Textures: A Guide to the Interpretation of Textures in Volcanic Rocks*. Hobart: Centre for Ore Deposit and Exploration Studies, University of Tasmania.
- Milia, A., Torrente, M. M., and Bellucci, F. (2012). A possible link between faulting, cryptodomes and lateral collapses at Vesuvius Volcano (Italy). *Glob. Planet. Chang.* 90, 121–134. doi: 10.1016/j.gloplacha.2011.09.011
- Mimatsu, M. (1962). *Showa-Shinzan Diary*. Hokkaido: Mimatsu Masao Memorial Museum, Sobetsu.
- Minakami, T., Ishikawa, T., and Yagi, K. (1951). The 1944 eruption of Usu in Hokkaido, Japan. *Bull. Volcanol.* 11, 45–157. doi: 10.1007/BF02596029
- Miyashiro, A. (1973). The Troodos ophiolitic complex was probably formed in an island arc. *Earth Planet. Sci. Lett.* 19, 218–224. doi: 10.1016/0012-821X(73)90118-0
- Nakagawa, M., Matsumoto, A., Tajika, J., Hirose, W., and Ohtsu, T. (2005). Re-investigation of eruption history of Usu volcano, Hokkaido, Japan: finding of pre-Meiwa eruption (Late 17th century) between Kanbun (1663) and Meiwa (1769) eruptions. *Bull. Volcanol. Soc. Japan* 50, 39–52.
- Nonaka, M., Sugiyama, Y., Ohtani, T., Yagi, M., and Yamada, Y. (2018). Facies architecture of a felsic subaqueous volcano in the Katakai gas field, Niigata, Japan. *Abstract Cities Volcanoes* 10:565.
- Páez, G. N., Vidal, C. P., Galina, M., López, L., Jovic, S. M., and Guido, D. M. (2018). Intrusive hyaloclastite and peperitic breccias associated to sill and cryptodome emplacement on an Early Paleocene polymagmatic compound cone-dome volcanic complex from El guanaco mine, Northern Chile. *J. Volcanol. Geotherm. Res.* 354, 153–170. doi: 10.1016/j.jvolgeores.2018.02.011
- Reyer, E. (1888). *Theoretische Geologie*. Stuttgart: E. Schweizerbart'sche Verlagshandlung.
- Riggs, N., and Carrasco-Nunez, G. (2004). Evolution of a complex isolated dome system, Cerro Pizarro, central Mexico. *Bull. Volcanol.* 66, 322–335. doi: 10.1007/s00445-003-0313-y
- Ryan, A. G., Friedlander, E. A., Russell, J. K., Heap, M. J., and Kennedy, L. A. (2018). Hot pressing in conduit faults during lava dome extrusion: Insights from Mount St. Helens 2004–2008. *Earth Planet. Sci. Lett.* 482, 171–180. doi: 10.1016/j.epsl.2017.11.010
- Sasaki, T., and Katsui, Y. (1981). A new technique for measuring density of pumice using glass beads. *Bull. Volcanol. Soc. Japan* 26, 117–118.
- Sato, H., Fujii, T., and Nakada, S. (1992). Crumbling of dacite dome lava and generation of pyroclastic flows at Unzen volcano. *Nature* 360, 664–666. doi: 10.1038/360664a0
- Siebert, L. (1984). Large volcanic debris avalanches: characteristics of source areas, deposits, and associated eruptions. *J. Volcanol. Geotherm. Res.* 22, 163–197. doi: 10.1016/0377-0273(84)90002-7
- Skilling, I., White, J. D. L., and McPhie, J. (2002). *Peperites: Processes and Products of Magma-Sediment Mingling*. Amsterdam: Elsevier.
- Sobetsu Town. (2016). *Living Together With the Active Volcano*. Sobetsu: Sobetsu Town office.
- Soya, T., Katsui, Y., Niida, K., Sakai, K., and Tomiya, A. (2007). *Geological Map of Usu Volcano*, 2nd Edn. Tsukuba: Geol. Surv. Japan.
- Spry, A. (1962). The origin of columnar jointing, particularly in basalt flows. *Geol. Soc. Aust. J.* 8, 191–216. doi: 10.1080/14400956208527873
- Stewart, A. L., and McPhie, J. (2003). Internal structure and emplacement of an upper Pliocene dacitic cryptodome, Milos Island, Greece. *J. Volcanol. Geotherm. Res.* 124, 129–148. doi: 10.1016/S0377-0273(03)00074-X
- Stewart, D. C. (1975). Crystal clots in calc-alkaline andesites as breakdown products of high-Al amphiboles. *Contrib. Mineral. Petrol.* 53, 195–204. doi: 10.1007/BF0037260
- Tomiya, A., and Miyagi, I. (2002). The eruptive products and magma process of March 31, 2000 eruption of Usu volcano. *Bull. Volcanol. Soc. Japan* 47, 663–673.
- Ui, T., Nakagawa, M., Inaba, C., Yoshimoto, M., Geological Party, and Joint Research Group for the Usu 2000 Eruption (2002). Sequence of the 2000 Eruption, Usu volcano. *Bull. Volcanol. Soc. Japan* 47, 105–117.
- Voight, B., Janda, R. J., Glicken, H., and Douglass, P. M. (1983). Nature and mechanics of the Mount St. Helens rockslide-avalanche of 18 May 1980. *Geotechnique* 33, 243–273. doi: 10.1016/0148-9062(83)90666-6
- White, J. D. L., McPhie, J., and Skilling, I. (2000). Peperite: a useful genetic term. *Bull. Volcanol.* 62, 65–66. doi: 10.1007/s0044500050
- White, J. D. L., McPhie, J., and Soule, S. A. (2015). “Submarine lavas and hyaloclastite,” in *Encyclopedia of Volcanoes*, 2nd Edn, ed. H. Sigurdsson (Amsterdam: Elsevier), 363–375. doi: 10.1016/B978-0-12-385938-9.00019-5
- Yamada, Y., and Uchida, T. (1997). Characteristics of hydrothermal alteration and secondary porosities in volcanic rock reservoirs, the Katakai gas field. *J. Japanese Assoc. Petrol. Technol.* 62, 311–320. doi: 10.3720/japt.62.311
- Yokoyama, I., Katsui, Y., Oba, Y., and Ehara, Y. (1973). *Usuzan, Its Volcanic Geology, History of Eruption, Present State of Activity And Prevention of Disasters*. Sapporo: Committee for Prevention and Disasters of Hokkaido.
- Závada, P., Kratinová, Z., Kusbach, V., and Schulmann, K. (2009). Internal fabric development in complex lava domes. *Tectonophysics* 466, 101–113. doi: 10.1016/j.tecto.2008.07.005
- Zorn, E. U., Rowe, M. C., Cronin, S. J., Ryan, A. G., Kennedy, L. A., and Russell, J. K. (2018). Influence of porosity and groundmass crystallinity on dome rock strength: a case study from Mt. Taranaki, New Zealand. *Bull. Volcanol.* 80:35. doi: 10.1007/s00445-018-1210-8

Conflict of Interest Statement: The authors declare that the research was conducted in the absence of any commercial or financial relationships that could be construed as a potential conflict of interest.

Copyright © 2019 Goto and Tomiya. This is an open-access article distributed under the terms of the Creative Commons Attribution License (CC BY). The use, distribution or reproduction in other forums is permitted, provided the original author(s) and the copyright owner(s) are credited and that the original publication in this journal is cited, in accordance with accepted academic practice. No use, distribution or reproduction is permitted which does not comply with these terms.



Geochemistry of CO₂-Rich Gases Venting From Submarine Volcanism: The Case of Kolumbo (Hellenic Volcanic Arc, Greece)

Andrea Luca Rizzo^{1*}, Antonio Caracausi¹, Valérie Chavagnac², Paraskevi Nomikou³, Paraskevi N. Polymenakou⁴, Manolis Mandalakis⁴, Georgios Kotoulas⁴, Antonios Magoulas⁴, Alain Castillo², Danai Lampridou³, Nicolas Maruszczak² and Jeroen E. Sonke²

OPEN ACCESS

Edited by:

Guido Giordano,
Università degli Studi Roma Tre, Italy

Reviewed by:

Yuri Taran,
National Autonomous University
of Mexico, Mexico
Valerio Acocella,
Università degli Studi Roma Tre, Italy

*Correspondence:

Andrea Luca Rizzo
andrea.rizzo@ingv.it

Specialty section:

This article was submitted to
Volcanology,
a section of the journal
Frontiers in Earth Science

Received: 01 August 2018

Accepted: 12 March 2019

Published: 12 April 2019

Citation:

Rizzo AL, Caracausi A, Chavagnac V, Nomikou P, Polymenakou PN, Mandalakis M, Kotoulas G, Magoulas A, Castillo A, Lampridou D, Maruszczak N and Sonke JE (2019) Geochemistry of CO₂-Rich Gases Venting From Submarine Volcanism: The Case of Kolumbo (Hellenic Volcanic Arc, Greece). *Front. Earth Sci.* 7:60. doi: 10.3389/feart.2019.00060

¹ Istituto Nazionale di Geofisica e Vulcanologia, Sezione di Palermo, Palermo, Italy, ² Centre National de la Recherche Scientifique, Géosciences Environnement Toulouse, Toulouse, France, ³ Department of Geology and Geoenvironment, National and Kapodistrian University of Athens, Athens, Greece, ⁴ Hellenic Centre for Marine Research, Institute of Marine Biology, Biotechnology and Aquaculture, Heraklion, Greece

Studies of submarine hydrothermal systems in Mediterranean Sea are limited to the southern Italian volcanism, while are totally missing in the Aegean. Here, we report on the geochemistry of high-temperature fluids (up to 220°C) venting at 500 m b.s.l. from the floor of Kolumbo submarine volcano (Hellenic Volcanic Arc, Greece), which is located 7 km northeast of Santorini Island. Despite the recent unrest at Santorini, Kolumbo submarine volcano is considered more active due to a higher seismicity. Rizzo et al. (2016) investigated the He-isotope composition of gases collected from seven chimneys and showed that are dominated by CO₂ (>97%), with only a small air contamination. Here we provide more-complete chemical data and isotopic compositions of CO₂ and CH₄, and Hg(0) concentration. We show that the gases emitted from different vents are fractionated by the partial dissolution of CO₂ in water. Fractionation is also evident in the C-isotope composition ($\delta^{13}\text{C}_{\text{CO}_2}$), which varies between -0.04 and 1.15‰ . We modeled this process to reconstruct the chemistry and $\delta^{13}\text{C}_{\text{CO}_2}$ of intact magmatic gases before fractionation. We argue that the CO₂ prior to CO₂ dissolution in water had $\delta^{13}\text{C} \sim -0.4\text{‰}$ and CO₂/³He $\sim 1 \times 10^{10}$. This model reveals that the gases emitted from Kolumbo originate from a homogeneous mantle contaminated with CO₂, probably due to decarbonation of subducting limestone, which is similar to other Mediterranean arc volcanoes (e.g., Stromboli, Italy). The isotopic signature of CH₄ ($\delta^{13}\text{C} \sim -18\text{‰}$ and $\delta\text{D} \sim -117\text{‰}$) is within a range of values typically observed for hydrothermal gases (e.g., Panarea and Campi Flegrei, Italy), which is suggestive of mixing between thermogenic and abiotic CH₄. We report that the concentrations of Hg(0) in Kolumbo fluids are particularly high (~ 61 to 1300 ng m^{-3}) when compared to land-based fumaroles located on Santorini

and worldwide aerial volcanic emissions. This finding may represent further evidence for the high level of magmatic activity at Kolumbo. Based on the geo-indicators of temperature and pressure, we calculate that the magmatic gases equilibrate within the Kolumbo hydrothermal system at about 270°C and at a depth of ~1 km b.s.l.

Keywords: Hellenic Volcanic Arc, Kolumbo submarine volcano, submarine gases, gas–water interaction, hydrothermal system, CO₂, CH₄

INTRODUCTION

About 80% of Earth volcanism occurs on the ocean floor (Crisp, 1984), which has greatly hindered the understanding of the natural outgassing of volatiles from the Earth's interior and its impact on the environment. Several submarine volcanoes have been discovered in recent decades, and geochemical studies have investigated the current status of submarine magmatic-hydrothermal systems. These studies have focused either on midocean ridges (e.g., Butterfield et al., 1990; Lilley et al., 1993; Von Damm, 1995; Von Damm et al., 1995; Lupton et al., 1999) or subduction-related settings (Taran et al., 1992; Tsunogai et al., 1994; Caracausi et al., 2005; Chiodini et al., 2006; Lupton et al., 2006, 2008; Lan et al., 2010; Rizzo et al., 2016; Stucker et al., 2017; and references therein). To the best of our knowledge, Panarea (Aeolian Islands, Italy) is the only volcanic system in the Mediterranean basin characterized by active submarine emissions for which geochemical studies have provided detailed and comprehensive reconstructions of the gas–water interaction process, the origin of gases and the magmatic-hydrothermal system (Caliro et al., 2004; Caracausi et al., 2005 and references therein; Chiodini et al., 2006; Capaccioni et al., 2007; Tassi et al., 2009, 2014; and references therein). The submarine emissions at Panarea are mainly located at relatively shallow water depths (down to 30 m), thereby providing easy access for gas sampling.

In 2006, an extensive hydrothermal vent field was discovered at a depth of 500 m on the floor of Kolumbo submarine crater (Sigurdsson et al., 2006), 7 km off the northeast coast of the Santorini Island (**Figure 1**) in the southern Aegean Sea, Greece (Nomikou et al., 2012). Kolumbo volcano lies along the Christianna-Santorini-Kolumbo volcanic line (CSK; **Figure 1**) that is in the central part of the Hellenic Volcanic Arc (HVA; Nomikou et al., 2016, 2018). The CSK consists of 23 submarine cones and craters (Nomikou et al., 2012; Hooft et al., 2017), of which Kolumbo is the largest and most-active, and last erupted in 1650 (Cantner et al., 2014). The crater is 1.7 km in diameter and up to 500 m deep, with the shallowest point nowadays being at 18 m b.s.l. (below sea level) (Nomikou et al., 2012). All of these volcanoes belong to the modern HVA formed by the subduction of the African plate beneath the European plate (McKenzie, 1972; Le Pichon and Angelier, 1979). HVA began to form 3–4 My ago (Pe-Piper and Piper, 2007), and it stretches from the Gulf of Saronikos in the northwest to the Kos-Nisyros-Yali Islands complex in the east (**Figure 1**).

The Kolumbo hydrothermal vent field emits CO₂-dominated fluids at temperatures as high as 220°C (Sigurdsson et al., 2006; Carey et al., 2013) and with a clear mantle origin (Rizzo et al., 2016). However, the origin of CO₂ and CH₄, the extent of

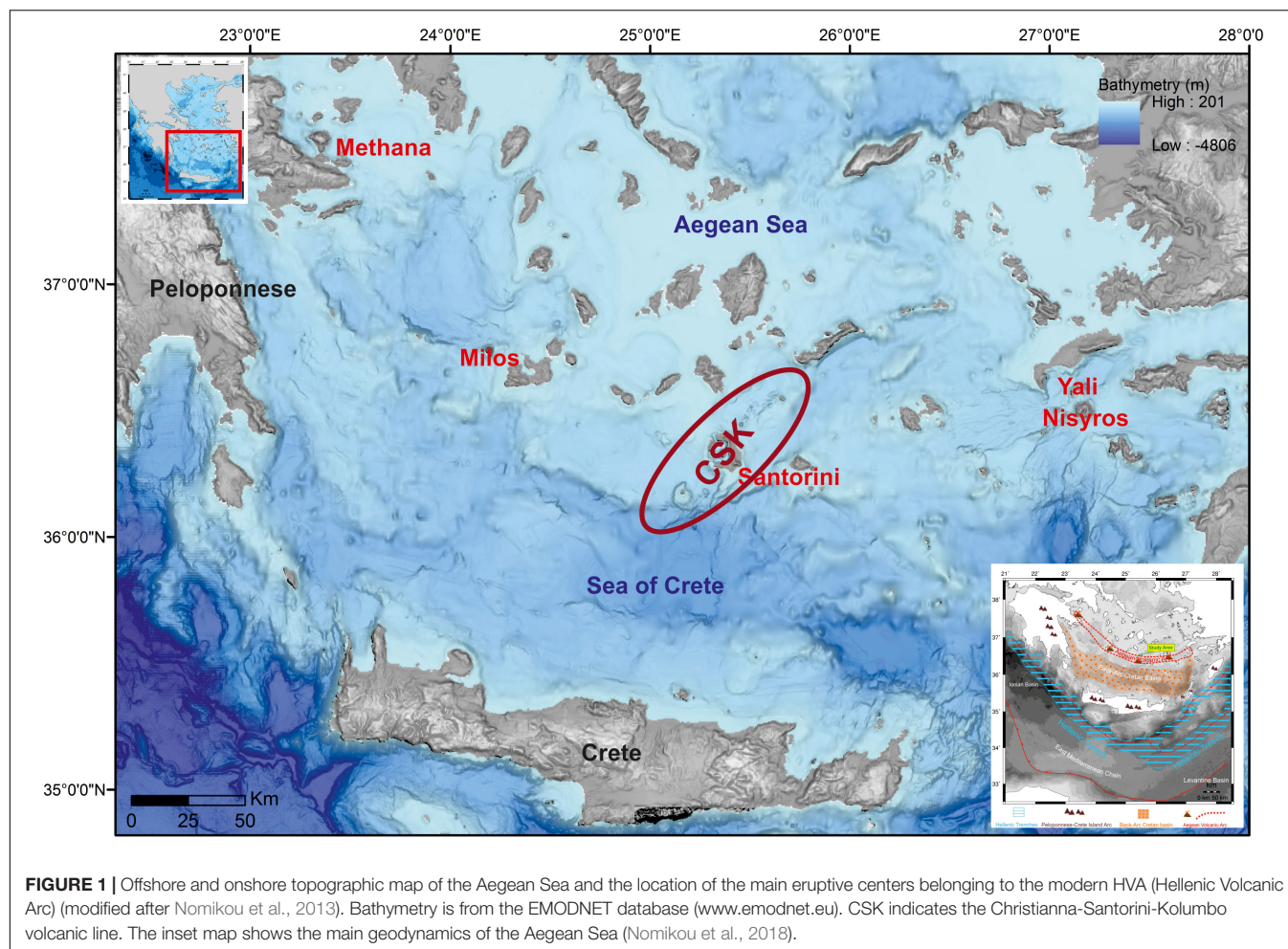
variability in the geochemistry of gases emitted from different chimneys, and the pressure and temperature conditions of the magmatic-hydrothermal system remain unclear.

This study aims to fill this gap in the knowledge by combining the chemical and isotopic data previously reported for noble gases by Rizzo et al. (2016) with new chemical data from the analysis of Hg(0) and the isotopic compositions of CO₂ and CH₄. We identified and modeled the main processes underlying the alterations in the isotopic composition of magmatic-hydrothermal fluids along the path of their ascent, in order to reconstruct the original chemistry of these gases at the earliest stages of their formation. Finally, we used geo-indicators to elucidate the pressure and temperature conditions of the hydrothermal system feeding the gas vents beneath Kolumbo volcano, and propose a conceptual scheme for the fluid circulation.

PRESENT KNOWLEDGE ABOUT KOLUMBO SUBMARINE VOLCANO

The Kolumbo submarine volcano developed next to Santorini Island (**Figure 1**), and several multidisciplinary studies have been carried out over the last decade to shed light on its plumbing system and activity state. The findings of volcanological and geochemical investigations suggest that there are two distinct plumbing systems beneath the Santorini and Kolumbo volcanic systems (Francalanci et al., 2005; Dimitriadis et al., 2009; Kiliyas et al., 2013). The depth of the magma chamber beneath Kolumbo has been constrained by seismological and petrological observations to lie at depths of 5–7 km (Dimitriadis et al., 2009, 2010; Konstantinou and Yeh, 2012; Cantner et al., 2014). A more recent petrological study revealed striking geochemical differences (e.g., in Nb/Yb, Zr/Nb, ²⁰⁶Pb/²⁰⁴Pb, ⁸⁷Sr/⁸⁶Sr, and ³He/⁴He) between Kolumbo and Santorini magmas despite their close temporal and spatial associations, supporting the hypothesis that the two magmatic systems have distinct mantle sources (Klaver et al., 2016).

Modern-day microseismicity along the CSK is concentrated beneath Kolumbo at depths of 6–9 km (Bohnhoff et al., 2006; Dimitriadis et al., 2009), with the exception of the unrest at Santorini during 2011–2012 when the seismicity focus migrated within its caldera (e.g., Parks et al., 2012). This confirms that Kolumbo is the most-active volcanic system in the region at the present time (Francalanci et al., 2005; Dimitriadis et al., 2009, 2010; Nomikou et al., 2012; Hubscher et al., 2015). Similar indications come from the presence of intense degassing of hydrothermal vents on the floor of Kolumbo submarine crater



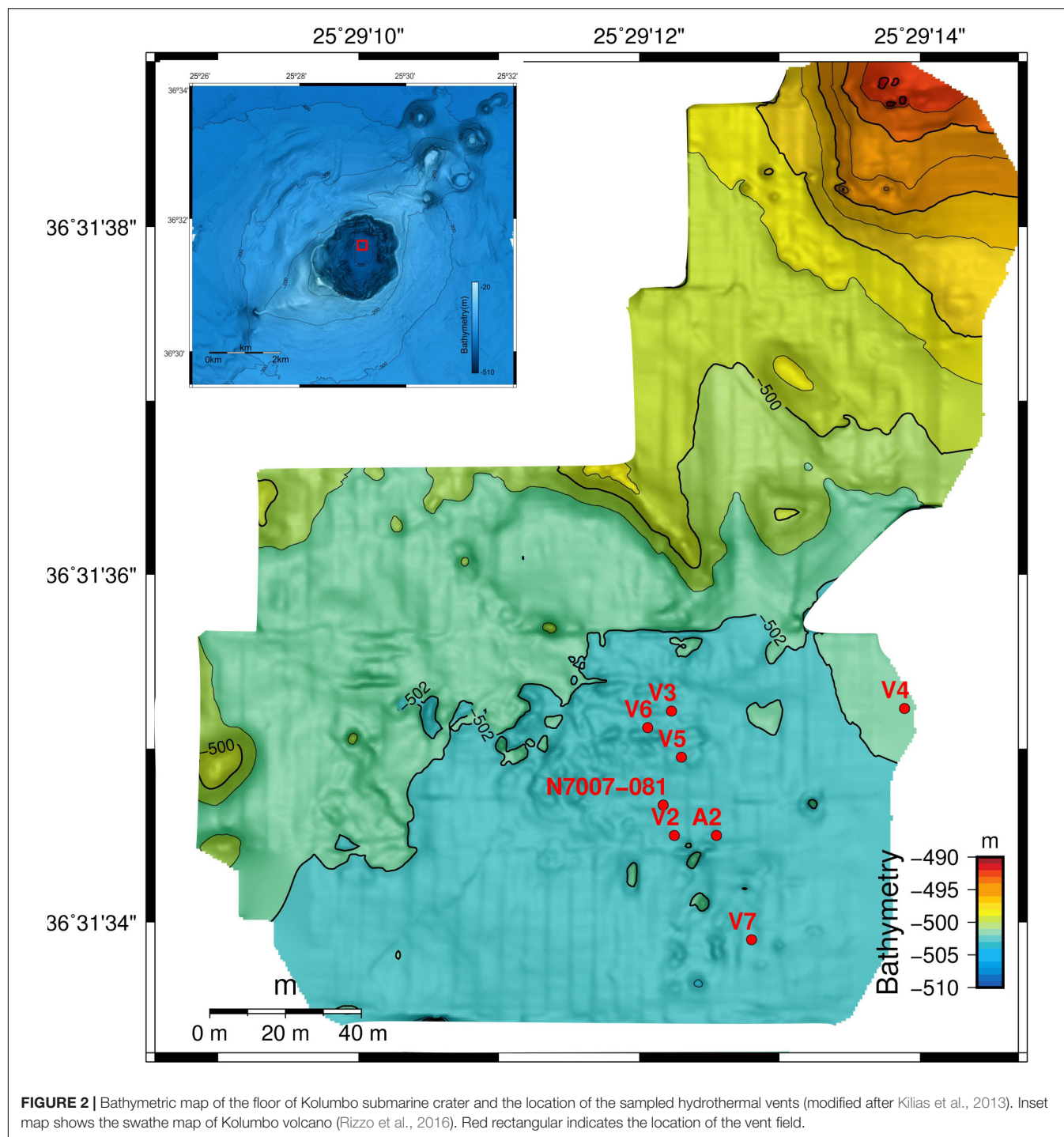
and the geochemistry of these fluids (Sigurdsson et al., 2006; Carey et al., 2013; Rizzo et al., 2016). This intense degassing contrasts with the low-temperature fumaroles observed in the Santorini caldera (Sigurdsson et al., 2006; Rizzo et al., 2015; and references therein).

Sigurdsson et al. (2006) were the first to describe the presence of a widespread hydrothermal vent field on the floor of Kolumbo submarine crater, but only two subsequent geochemical studies have investigated the chemistry of these fluids (Carey et al., 2013; Rizzo et al., 2016). Sigurdsson et al. (2006) and Carey et al. (2013) reported that fluids emitted from the Kolumbo floor are at temperatures up to 220°C and pH ~5 next to the vents, respectively. Carey et al. (2013) also reported the first data for the chemical composition of gas samples collected from two vents, which indicated that these gases are virtually pure CO₂. However, that study focused on the acidification-related hazards that may arise from the dissolution of CO₂ in seawater, which was found to occur within the first 10 m of the water column inside the bowl-shaped crater. This dissolution causes local increases in water density and favors the accumulation of CO₂-rich, acidic waters at the seafloor that do not permit the growth of macrofauna (Camilli et al., 2015), while additional hazards could arise from the abrupt release of gases at the surface.

Rizzo et al. (2016) reported on ³He/⁴He measurements of gas samples collected during May 2014 from seven chimneys. Briefly, they constrained the ³He/⁴He signature of Kolumbo gases and of the local mantle at 7.0 Ra (where Ra is the atmospheric ³He/⁴He equal to 1.39 × 10⁻⁶), which is indicative of a MORB-like mantle. It was subsequently revealed that these values are significantly lower than the ³He/⁴He values measured in Santorini fluids and rocks (~4 Ra; Rizzo et al., 2015 and references therein), whereas the observed decrease in the He-isotope signature was attributable to a crustal contamination below the Island. Finally, that study highlighted that ³He/⁴He values measured at Kolumbo were the highest ever measured across the entire HAV and indicative of the direct degassing through lithospheric faults.

SAMPLING AND ANALYTICAL TECHNIQUES

During the 4-SeaBioTech survey on RV AEGAEON (Hellenic Centre for Marine Research) during May 2014, seven chimneys bubbling gas phases with variable sustained fluxes were sampled on the floor of Kolumbo submarine crater with the Greek Max Rover remotely operated vehicle (ROV) (Figure 2).



These chimneys were selected based on a previous seafloor exploration of hydrothermal activity (Sigurdsson et al., 2006; Carey et al., 2013) and an oceanographic survey performed in 2014 (Figure 2). Although direct measurements of temperature were not possible during the 2014 survey, previous surveys found that the fluids discharged in the northern part of the crater floor had temperatures as high as 220°C, while those present along the northern and eastern margins were no hotter than 70°C, and

characterized by ephemeral bubble fluxes (Sigurdsson et al., 2006; Carey et al., 2013).

The present study collected bubbling hydrothermal gases at the seafloor and stored them in titanium gas-tight bottles equipped with funnels, as described in detail by Rizzo et al. (2016). The obtained gas samples were analyzed in the laboratories of INGV (Istituto Nazionale di Geofisica e Vulcanologia), Sezione di Palermo for their chemistry and

isotopic compositions of noble gases (He, Ne, and Ar), C of CO₂, and C and H of CH₄. The chemical composition of He, H₂, O₂, N₂, CO, CH₄, and CO₂ was measured by a gas chromatograph (Clarus 500, Perkin Elmer) equipped with a 3.5-m column (Carboxen 1000) and double detector (hot-wire detector and flame ionization detector [FID]), for which the analytical errors were < 3%. The concentrations of C₂H₆ and C₃H₈ were also measured in a few selected samples after hydrocarbon enrichment via bubbling pressurized gas in Giggenbach bottles filled with 4-M NaOH (Giggenbach, 1975). Higher hydrocarbons were analyzed using a gas chromatograph (Shimadzu, 2010) equipped with an FID and a capillary column (CP Poraplot) using He as the carrier gas. The analytical precision for these gas chromatography analyses was better than 5% for trace gases and 10% for alkanes.

The Hg(0) concentration in the gas samples was measured at the Geosciences Environment Toulouse laboratory in France. Titanium canisters filled with hydrothermal gases at a known pressure were connected to a 60-mL impinger (Saville) via a stainless steel valve, 6 mm of PTFE tubing and a 6-mm-long Pyrex bubbler tube. The impinger contained 30 mL of a strongly oxidizing 40 vol% inverse aqua-regia solution (HNO₃:HCl = 2:1). The canister was partly opened, which induced the hydrothermal gases to bubble in the aqua-regia solution and the oxidation of Hg(0) to Hg(II). The volume of hydrothermal gas sampled was measured with a ball flowmeter and a chronometer. The flow rate was approximately 80 mL min⁻¹, and trapping continued until atmospheric pressure equilibration occurred between the canister and the oxidizing solution trap. The total Hg concentrations were measured in accordance with the USEPA 1631 method. Aliquots of 0.1–1 mL were analyzed in duplicate using semiautomatic cold vapor atomic fluorescence spectrometry (CV-AFS; Brooks Rand Model III, United States) with a single gold trap. The analysis accuracy of CV-AFS was evaluated according to the standard analysis method for the NRC ORMS-4 certified reference material (22.0 ± 1.6 ng L⁻¹, mean ± SD), and satisfactory results were obtained (21.3 ± 2.4 ng L⁻¹, *n* = 7).

The ³He/⁴He and ⁴He/²⁰Ne ratios addressed in the present study have been reported together with the respective analytical methods by Rizzo et al. (2016). The ⁴⁰Ar/³⁶Ar and ³⁸Ar/³⁶Ar ratios were measured using a mass spectrometer (Argus GVI) with analytical errors of < 0.2%.

The C-isotope composition of CO₂ [expressed as δ¹³C ‰ vs. V-PDB (Vienna-Pee Dee Belemnite)] was determined using a continuous-flow isotope-ratio mass spectrometer (Thermo Delta Plus XP, Finnigan), connected to a gas chromatograph (Trace GC) and interface (Thermo GC/C III, Finnigan). The gas chromatograph and its column (length = 30 m and i.d. = 0.32 mm; Poraplot-Q) were operated at a constant temperature of 50°C using He as the carrier gas. The analytical errors were < 0.1‰. The C and H isotopes of CH₄ were analyzed using the same instrument. A combustion interface (Thermo GC III, Finnigan) was used to produce CO₂ from methane, while a gas-chromatograph/thermal-conversion interface provided on-line high-temperature conversion of CH₄ into H. The SDs for the δ¹³C and δD measurements of CH₄ were < 0.2 and < 2.5‰, respectively.

RESULTS

Gas Chemistry

The chemical composition of submarine gases collected at Kolumbo is presented in **Table 1**. These gases are dominated by CO₂, which is present at concentrations up to 99.1% (**Figure 3A**). The concentration of CH₄ ranges from 1052 to 5521 ppm, while C₂H₆ and C₃H₈ exhibit much narrow ranges of 95–128 and 14–20 ppm, respectively (values measured in the Giggenbach bottle; Giggenbach, 1975). He varies between 9 and 40 ppm, while H₂ and CO range from 170 to 716 ppm and from 2 to 7 ppm, respectively. The O₂ and N₂ contents varied depending on the degree of sample contamination by ambient air, with maximum values of 5.1 and 21%, respectively (**Figures 3B, 4A**). ²⁰Ne ranges between 0.082 and 4.2 ppm, while ⁴⁰Ar ranges between 69 and 834 ppm (**Figure 4B**). It should be noted that ⁴⁰Ar was not measured in the sample with the greatest air contamination (O₂ = 5.1%, N₂ = 21%, and ²⁰Ne = 4.2 ppm). In order to evaluate the extent of air or the presence of air-saturated water (ASW), O₂ and Ar are plotted versus ²⁰Ne in **Figures 4A,B**, respectively. All of the analyzed samples fell along the line representing air rather than ASW, indicating that this contamination is probably due to sampling or extraction procedures. In order to determine the gas composition before air contamination (*G_f*), data were corrected based on the O₂ content measured in each analysis as follows:

$$G_f = \frac{(G_s - (G_a \times F))}{(1 - F)}$$

where *G_s* is the concentration of the gaseous species measured in the sample (e.g., He), *G_a* is the concentration of the same gaseous species in air (e.g., He = 5.24 ppm) and *F* is the fraction of air calculated from the O₂ concentration measured in the sample divided by the atmospheric O₂ concentration (20.947%). We point out that even assuming that all of the ²⁰Ne or ⁴⁰Ar measured in our samples is of atmospheric origin (as for O₂), the recalculated percentages of air contamination would still be comparable. The back-corrected chemical composition of Kolumbo gases is reported in **Table 2**.

Furthermore, the concentration of gaseous Hg(0) differed markedly (and significantly) among the seven investigated chimneys, from 61 to 1301 ng m⁻³ (**Table 3**).

Isotopic Composition of Gases

Table 1 reports the isotopic compositions of CO₂, CH₄, and Ar in the analyzed gases. The C-isotope composition (δ¹³C_{CO₂}) varied between -0.04 and 1.15‰ V-PDB, whereas increasing ratios were positively correlated with the concentrations of He, H₂, CO, and CH₄. The CH₄-isotope composition varied over a narrow range for both C (δ¹³C = -18.8 to -17.6‰ V-PDB) and H (δD = -118.6 to -115.4‰ V-SMOW).

The ³He/⁴He and ⁴He/²⁰Ne ratios used in the present study were previously measured and discussed by Rizzo et al. (2016). Here we further measured the Ar-isotope composition, which was found to be close to the values typically encountered in atmospheric air (⁴⁰Ar/³⁶Ar = 295.5 and ³⁸Ar/³⁶Ar = 0.188; Ozima and Podosek, 1983). ⁴⁰Ar/³⁶Ar in hydrothermal gases varies between 296 and 316, while ³⁸Ar/³⁶Ar is between 0.187 and 0.189.

TABLE 1 | Chemical composition of major and minor gaseous components from Kolumbo hydrothermal vents. Ar, CO₂, and CH₄ isotope ratios are also reported.

Sample	Depth (m)	Latitude	Longitude	He (ppm)	Ne (ppm)	⁴⁰ Ar (ppm)	³⁶ Ar (ppm)	H ₂ (ppm)	O ₂ %	N ₂ %	CO (ppm)	CH ₄ (ppm)	C ₂ H ₆ ppm	C ₃ H ₈ ppm
A2	497	36°31.5700' N	25°29.2110' E	24.1	0.086	100	0.323	410.7	0.17	1.1	4.2	3270.6	95	14
V2	498	36°31.5700' N	25°29.2050' E	9.0	4.218	–	–	169.6	5.12	21.0	2.2	1052.2	–	–
V2	498	36°31.5700' N	25°29.2050' E	15.1	1.685	834	2.823	308.6	2.11	8.6	3.3	1938.6	–	–
V3	498	36°31.5843' N	25°29.2046' E	26.0	0.104	76	0.241	508.8	0.10	0.9	4.6	3689.1	128	18
V4	498	36°31.5846' N	25°29.2378' E	11.1	1.149	696	2.349	193.9	1.51	6.6	2.5	1519.4	–	–
V4	498	36°31.5846' N	25°29.2378' E	26.5	0.843	455	1.526	471.5	1.10	5.1	4.3	3119.2	–	–
V5	500	36°31.5790' N	25°29.2060' E	25.3	1.389	710	2.386	402.0	1.72	7.6	4.7	3391.8	–	–
V5	500	36°31.5790' N	25°29.2060' E	26.1	0.509	294	0.981	464.3	0.67	3.1	4.6	3077.5	–	–
V6	498	36°31.5824' N	25°29.2012' E	19.8	0.082	69	0.222	405.9	0.00	0.6	2.1	2848.2	118	20
V7	498	36°31.5580' N	25°29.2160' E	39.5	0.291	182	0.590	716.4	0.17	1.3	7.1	5521.5	100	15
NA007-081*	502	36°31.5735' N	25°29.2034' E	24.4	0.025	–	–	400.0	0.01	0.3	b.d.l.	2699.9	–	–
NA007-009*	502	36°31.6059' N	25°29.1969' E	–	–	–	–	299.9	0.01	0.2	b.d.l.	2598.7	–	–
ASSW				2.3	9.7	15936			34.30	62.6	0.2	3.8		
AIR				5.24	16.48	9300	31.5	0.53	20.95	78.084	0.25	1.7		

TABLE 1 | Continued

Sample	C ₁ /(C ₂ + C ₃)	CO ₂ %	F Air	⁴⁰ Ar/ ³⁶ Ar	Err _{40/36} + / –	³⁸ Ar/ ³⁶ Ar	Err _{38/36} + / –	⁴⁰ Ar* (ppm)	⁴ He/ ⁴⁰ Ar*	δ ¹³ C _{CO2} ‰ vs. PDB	δ ¹³ C-CH ₄ ‰ vs. PDB	δD-CH ₄ ‰ vs. SMOW
A2	1817	98.4	0.0081	310.2	0.052	0.1880	0.0001	4.8	5.0	0.60	–17.6	–115.4
V2	–	73.8	0.2443	–	–	–	–	–	–	–0.04	–	–
V2	–	89.1	0.1006	296.0	0.051	0.1870	0.0001	–	–	–	–	–
V3	1699	98.6	0.0048	315.9	0.060	0.1878	0.0001	5.0	5.3	0.75	–18.8	–116
V4	–	91.7	0.0723	296.0	0.065	0.1879	0.0001	–	–	–0.03	–	–
V4	–	93.4	0.0526	298.1	0.043	0.1872	0.0001	–	–	–	–	–
V5	–	90.3	0.0820	297.4	0.051	0.1891	0.0001	–	–	0.63	–	–
V5	–	95.9	0.0321	299.3	0.065	0.1876	0.0002	–	–	0.63	–	–
V6	1964	99.1	0.0000	311.6	0.059	0.1876	0.0001	3.6	5.5	0.46	–18.1	–118.6
V7	1948	97.9	0.0082	308.9	0.069	0.1875	0.0002	8.1	4.8	1.15	–	–
NA007-081*	–	99.4	0.0005	–	–	–	–	–	–	–	–	–
NA007-009*	–	99.5	0.0005	–	–	–	–	–	–	–	–	–
ASSW		1.4	1									
AIR		0.038	1	295.5		0.188				–8		

C₂H₆ and C₃H₈ were measured in Giggenbach bottles and then recalculated to the dry gas. *Sample from Carey et al. (2013). b.d.l., below detection limit. –, not determined.

However, ⁴⁰Ar was corrected for atmospheric contamination (⁴⁰Ar*) in the samples having ⁴⁰Ar/³⁶Ar > 308 as follows:

$$^{40}\text{Ar}^* = ^{40}\text{Ar}_{\text{sample}} - [^{36}\text{Ar}_{\text{sample}} \cdot (^{40}\text{Ar}/^{36}\text{Ar})_{\text{air}}]$$

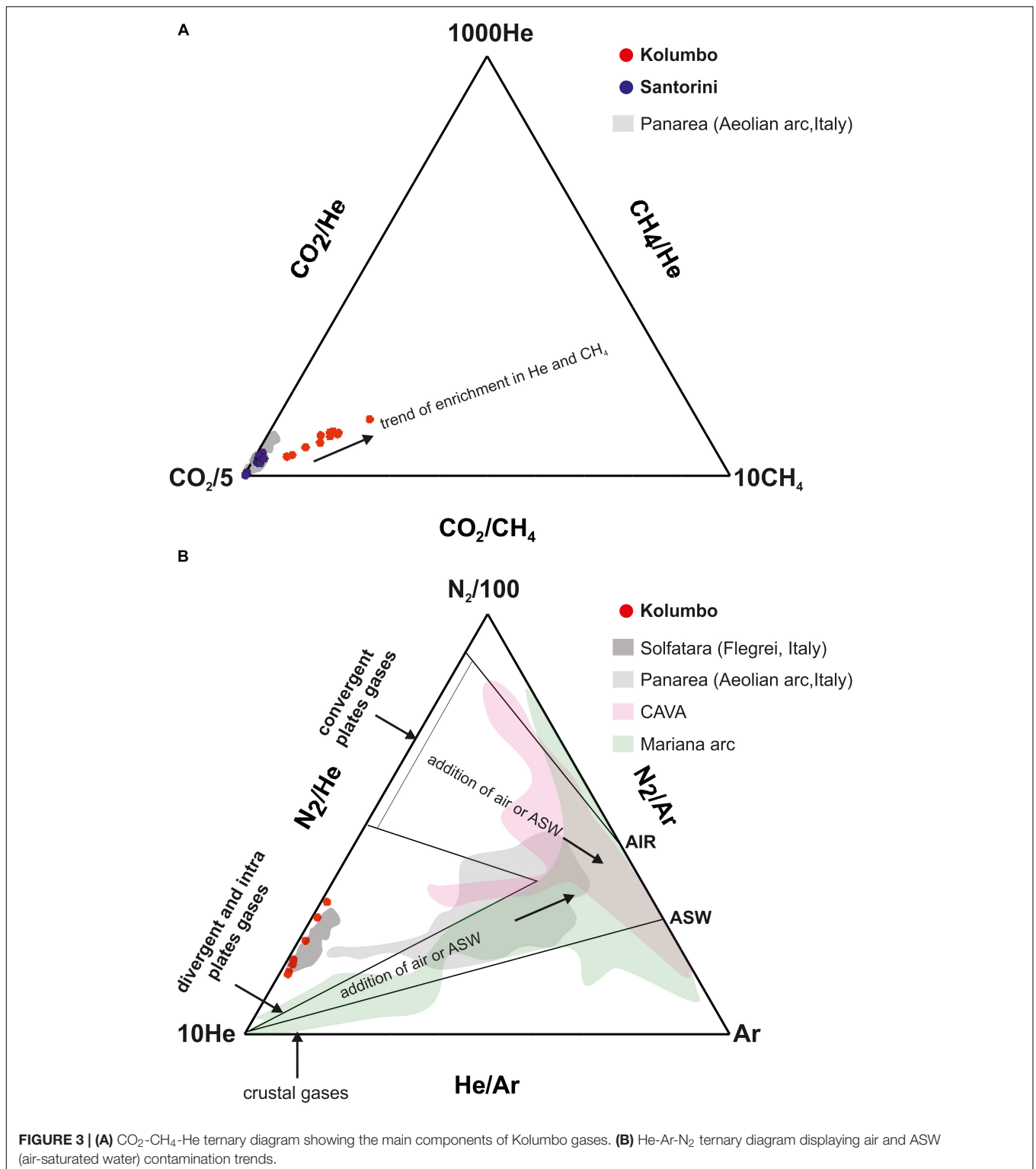
This correction is useful for obtaining accurate estimates of the ⁴He/⁴⁰Ar* ratio, which in Kolumbo gases vary between 4.8 and 5.5. These ratios are within the ratio range typical of the mantle (⁴He/⁴⁰Ar = 1–5; e.g., Ozima and Podosek, 1983; Marty, 2012), confirming that Kolumbo gases preserve the features that they have inherited from the magma.

DISCUSSION

Gas–Water Interaction of Magmatic Fluids

The chemical composition of gases corrected for air contamination as well as the δ¹³C_{CO2} show a variability

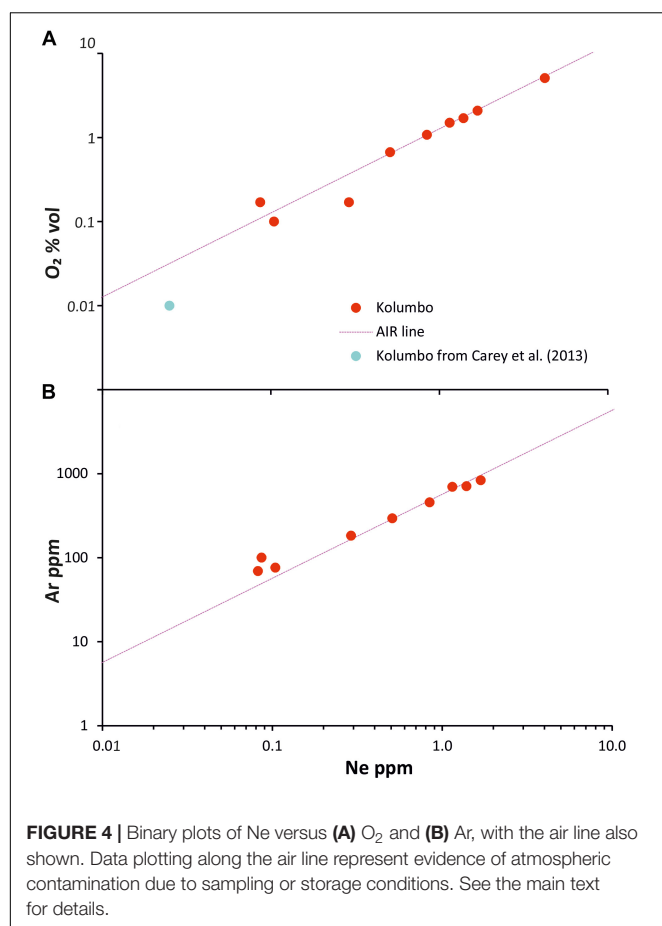
clearly modulated by a process of selective dissolution of gases in water driven by their different solubilities (Figures 5, 6). In order to determine the original composition of the intact gases, which is necessary for evaluating the origin of CO₂ and the pressure and temperature conditions of the hydrothermal system, we initially defined the boundary conditions for modeling. Due to the lack of direct measures of temperature in the fluids discharged from the Kolumbo chimneys, we assumed a homogeneous emission temperature of 220°C, as measured by Sigurdsson et al. (2006) (see section “Sampling and Analytical Techniques”). This assumption is reasonable because it is based on direct measurements made in the same part of the floor of Kolumbo submarine crater and from vents showing a sustained flux of gas bubbles, which indicates the concomitant release of high-temperature fluids (Sigurdsson et al., 2006). Regardless of the accuracy of this estimate, it should be remembered that any slight difference in temperature between vents would mostly influence the extent of the CO₂ dissolution in water rather than the path of fractionation of less-soluble species, especially when



considering elemental ratios. Since gases are emitted on the floor of Kolumbo submarine crater, which is at around 500 m b.s.l., we assumed a constant pressure of 50 bar. Based on the assumption of a temperature of 220°C , the saturated vapor pressure would be ~ 23 bar. This means that the partial pressure of CO_2 would be

~ 27 bar within a bubble of fluids exsolved from the vents located at the hydrostatic pressure of 50 bar.

Considering that we are dealing with submarine emissions, it is reasonable to assume that hydrothermal water condenses in the seawater together with the highly soluble acidic gases



(SO₂, HCl, and HBr). We cannot exclude that the CO₂ continued to dissolve in water inside the gas-tight bottles during the time that lapsed between sampling and gas extraction aboard the vessel, mostly because of cooling.

The residual gas phase that we studied comprised mainly CO₂ and secondarily N₂, H₂, CO and CH₄, as well as noble gases at low levels and trace gases. We ultimately assumed a geochemical system comprising CO₂, N₂, H₂, CO, CH₄, He, Ne and Ar, all of which dissolve in liquid water according to Henry's law. After the condensation of water vapors and highly soluble acidic gases, a further progression of gas dissolution would induce the preferential dissolution of CO₂ in water and the consequent enrichment of less-soluble species such as N₂, H₂, CO, hydrocarbons and noble gases (Sander, 2015). Since our dry gas mixture comprised > 97% CO₂, we deduce that the extent of fractionation was low. Therefore, this process can be better evaluated using other components such as CH₄ versus He (Figures 5, 6) rather than the CO₂ concentration.

Following the thermodynamic approach proposed by Fernandez-Prini et al. (2003 and references therein) and based on our pressure and temperature boundary conditions, we calculated Henry's constant k_H and the gas-liquid distribution constant K_D for each species included in our geochemical system. We simulated a condensation process under equilibrium conditions as expressed by the Rayleigh (1896) equation:

$$\frac{R_v}{R_{v0}} = f^{\alpha-1}$$

where R_{v0} is the initial ratio of the bulk composition (e.g., He/CO₂), R_v is the same instantaneous ratio in the residual gas phase (v), f is the fraction of the residual gas phase and α is the fractionation factor determined by the solubility ratio of the species under consideration (e.g., k_{H-He}/k_{H-CO_2}). We also assumed open-system conditions considering the continuous removal of gas-saturated parcels of water.

The initial composition applied in our model is reported in Table 2 and in the captions of Figures 5–7. Similarly to gas levels, the isotopic composition of gaseous CO₂ ($\delta^{13}C_{CO_2}$) changes as a result of its dissolution in water (Figure 7) and the

TABLE 2 | Restored chemical composition after correction for atmospheric contamination and pristine composition of gases after correction for CO₂ dissolution in water.

Sample	Depth (m)	Latitude	Longitude	He (ppm)	H ₂ (ppm)	N ₂ %	CO (ppm)	CH ₄ (ppm)	CO ₂ %	He/CO ₂	CH ₄ /CO ₂	CO ₂ / ³ He ⁺
A2	497	36°31.5700' N	25°29.2110' E	24.3	414.0	0.4	4.2	3297.2	99.2	2.44E-05	3.32E-03	4.19E+09
V2	498	36°31.5700' N	25°29.2050' E	10.2	223.6	2.5	2.8	1387.7	97.3	1.05E-05	1.43E-03	9.78E+09
V2	498	36°31.5700' N	25°29.2050' E	16.2	342.8	0.8	3.7	2153.1	98.9	1.64E-05	2.18E-03	6.22E+09
V3	498	36°31.5843' N	25°29.2046' E	26.1	511.2	0.5	4.6	3706.7	99.0	2.64E-05	3.74E-03	3.87E+09
V4	498	36°31.5846' N	25°29.2378' E	11.6	208.8	1.0	2.7	1636.5	98.8	1.17E-05	1.66E-03	8.79E+09
V4	498	36°31.5846' N	25°29.2378' E	27.7	497.5	1.1	4.5	3290.6	98.5	2.81E-05	3.34E-03	3.63E+09
V5	500	36°31.5790' N	25°29.2060' E	27.0	437.5	1.3	5.1	3691.4	98.3	2.75E-05	3.76E-03	3.72E+09
V5	500	36°31.5790' N	25°29.2060' E	26.8	479.6	0.6	4.8	3178.7	99.0	2.71E-05	3.21E-03	3.74E+09
V6	498	36°31.5824' N	25°29.2012' E	19.8	405.9	0.6	2.1	2848.2	99.1	2.00E-05	2.87E-03	5.13E+09
V7	498	36°31.5580' N	25°29.2160' E	39.7	722.3	0.7	7.1	5566.8	98.7	4.03E-05	5.64E-03	2.55E+09
NA007-081*	502	36°31.5735' N	25°29.2034' E	24.4	400.2	0.2	–	2701.2	99.4	2.45E-05	2.72E-03	4.29E+09
NA007-009*	502	36°31.6059' N	25°29.1969' E	–	300.0	0.2	–	2599.9	99.5	–	2.61E-03	–
Pristine composition of gases before CO ₂ dissolution in water				8	150	0.2	1.5	1150	99.8	8.02E-06	1.15E-03	1.26E+10

*Sample from Carey et al. (2013). ³He from Rizzo et al. (2016).

TABLE 3 | Hydrothermal gas Hg(0) concentrations of the seven chimneys where it was possible to make measurements.

Sample	Depth (m)	Latitude	Longitude	Hg0 concentration (canister) (ng/m ³)
A2	497	36°31.5700' N	25°29.2110' E	61
V1	498	36°31.5700' N	25°29.2050' E	1301
V2	498	36°31.5700' N	25°29.2050' E	612
V3	498	36°31.5843' N	25°29.2046' E	153
V5	500	36°31.5790' N	25°29.2060' E	73
V6	498	36°31.5824' N	25°29.2012' E	84
V7	498	36°31.5580' N	25°29.2160' E	819

isotopic fractionation between gaseous and dissolved inorganic CO₂ [CO₂(aq)]. CO₂(aq) is referred to as dissolved inorganic C (DIC) and is equal to the sum of the aqueous species H₂CO₃, HCO₃⁻, and CO₃²⁻. The fractionation process is modeled using the Rayleigh equation as follows (Clark and Fritz, 1997):

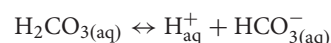
$$\delta^{13}\text{C}_{\text{CO}_2} = (\delta^{13}\text{C}_{\text{CO}_2})_0 + \varepsilon \ln(f)$$

where $(\delta^{13}\text{C}_{\text{CO}_2})_0$ is the initial CO₂-isotope composition, f is the fraction of the residual gas phase, and ε is the fractionation factor between DIC and gaseous CO₂ (CO₂(g)). This fractionation factor is obtained by summing up the fractionation factors of

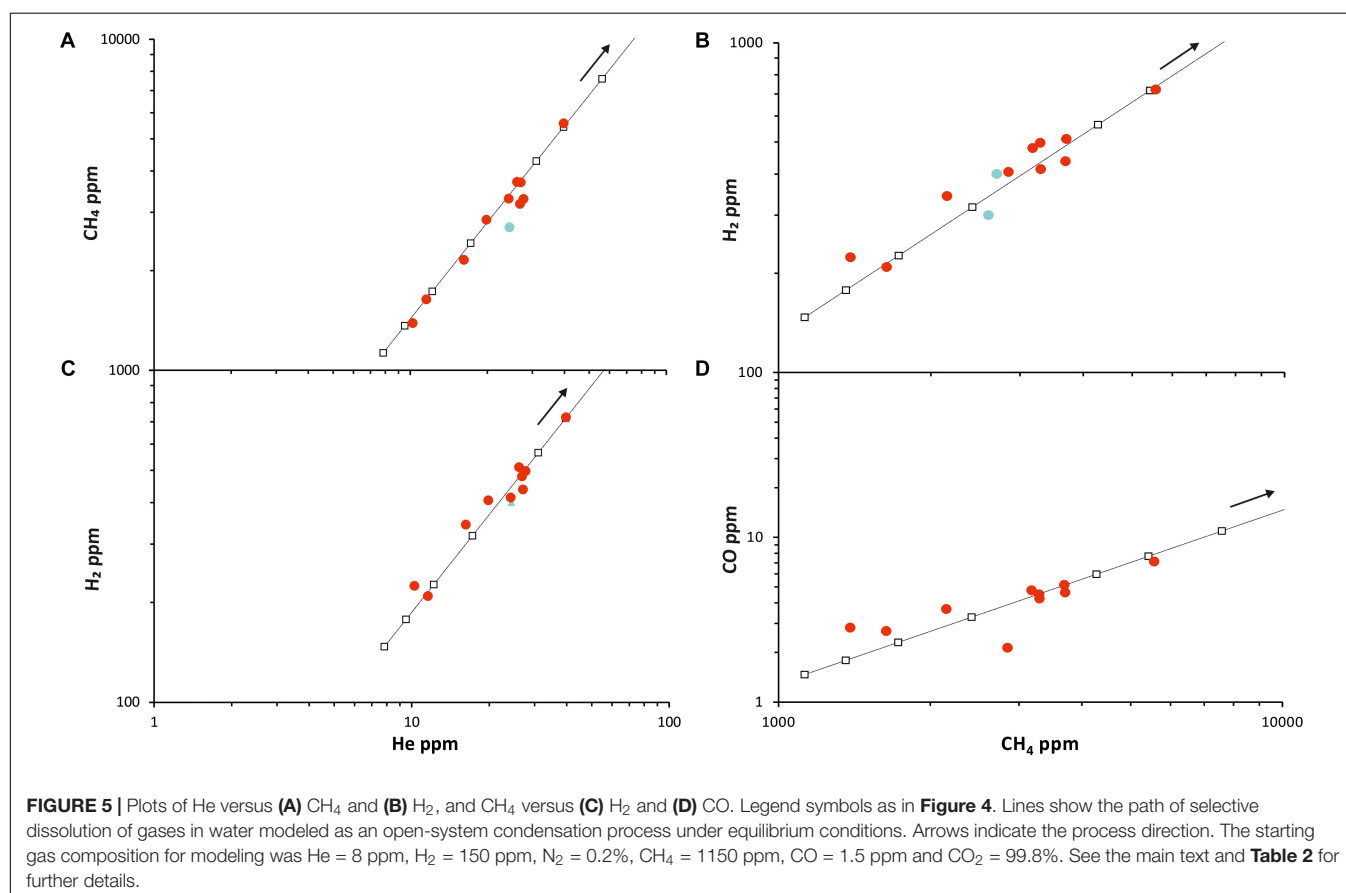
dissolved C species and CO₂(g) weighted for their molar fraction with respect DIC (Zhang et al., 1995; Allègre, 2008):

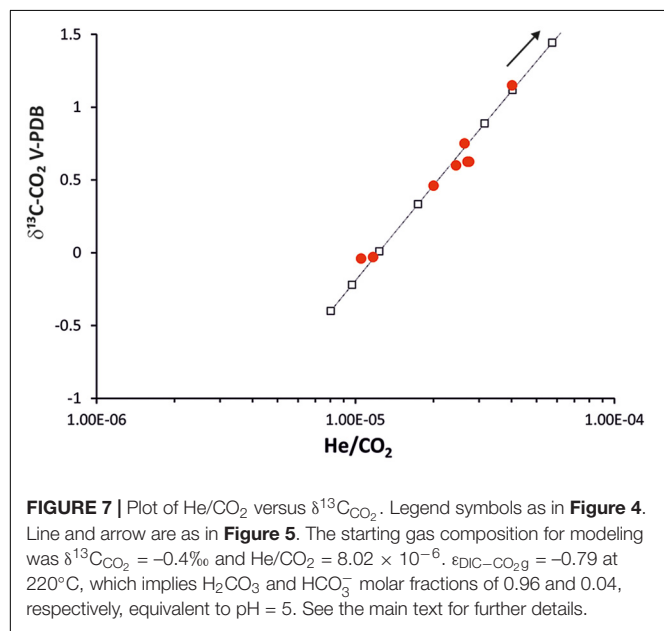
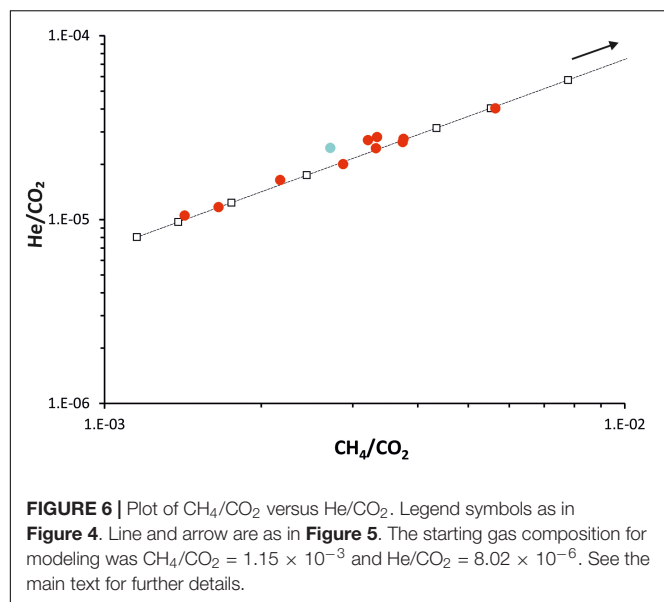
$$\varepsilon_{\text{DIC}-\text{CO}_2(\text{g})} = \frac{[\text{H}_2\text{CO}_3]\varepsilon_{\text{H}_2\text{CO}_3-\text{CO}_2(\text{g})} + [\text{HCO}_3^-]\varepsilon_{\text{HCO}_3^--\text{CO}_2(\text{g})} + [\text{CO}_3^{2-}]\varepsilon_{\text{CO}_3^{2-}-\text{CO}_2(\text{g})}}{[\text{H}_2\text{CO}_3] + [\text{HCO}_3^-] + [\text{CO}_3^{2-}]}$$

The molar fraction of each C species depends on the water temperature and pH. We calculated each fractionation factor at 220°C based on the approach of Zhang et al. (1995), while the molar fractions of H₂CO₃ and HCO₃⁻ were set to 0.96 and 0.04, respectively. We also assumed that the molar fraction of CO₃²⁻ was 0 given that the pH of water on the floor of Kolumbo submarine crater is typically lower than 8 (Mandalakis et al., 2019), which means that the terms involving [CO₃²⁻] can be neglected in the above equation. Under these conditions, $\varepsilon_{\text{DIC}-\text{CO}_2(\text{g})}$ was calculated to be -0.79. The molar fractions were also used in the following equation describing the dissociation of H₂CO₃ in order to estimate the pH of water in which CO₂ was dissolved:



$$K_{\text{A1}} = \frac{[\text{HCO}_3^-][\text{H}^+]}{[\text{H}_2\text{CO}_3]} = 4.3 \cdot 10^{-7}$$





The chemical and $\delta^{13}\text{C}_{\text{CO}_2}$ variability of gases emitted from Kolumbo (**Figures 7, 8**) is well-modeled by a trend of CO_2 dissolution in water having H_2CO_3 and HCO_3^- molar fractions of 0.96 and 0.04, respectively, which at 220°C corresponds to $\text{pH} \sim 5$. It is particularly interesting that this value is identical to that measured by Carey et al. (2013) in fluids emitted by a neighboring vent on the floor of Kolumbo submarine crater thereby further validating the boundary conditions selected for our model.

Origin of Gases Emitted at Kolumbo

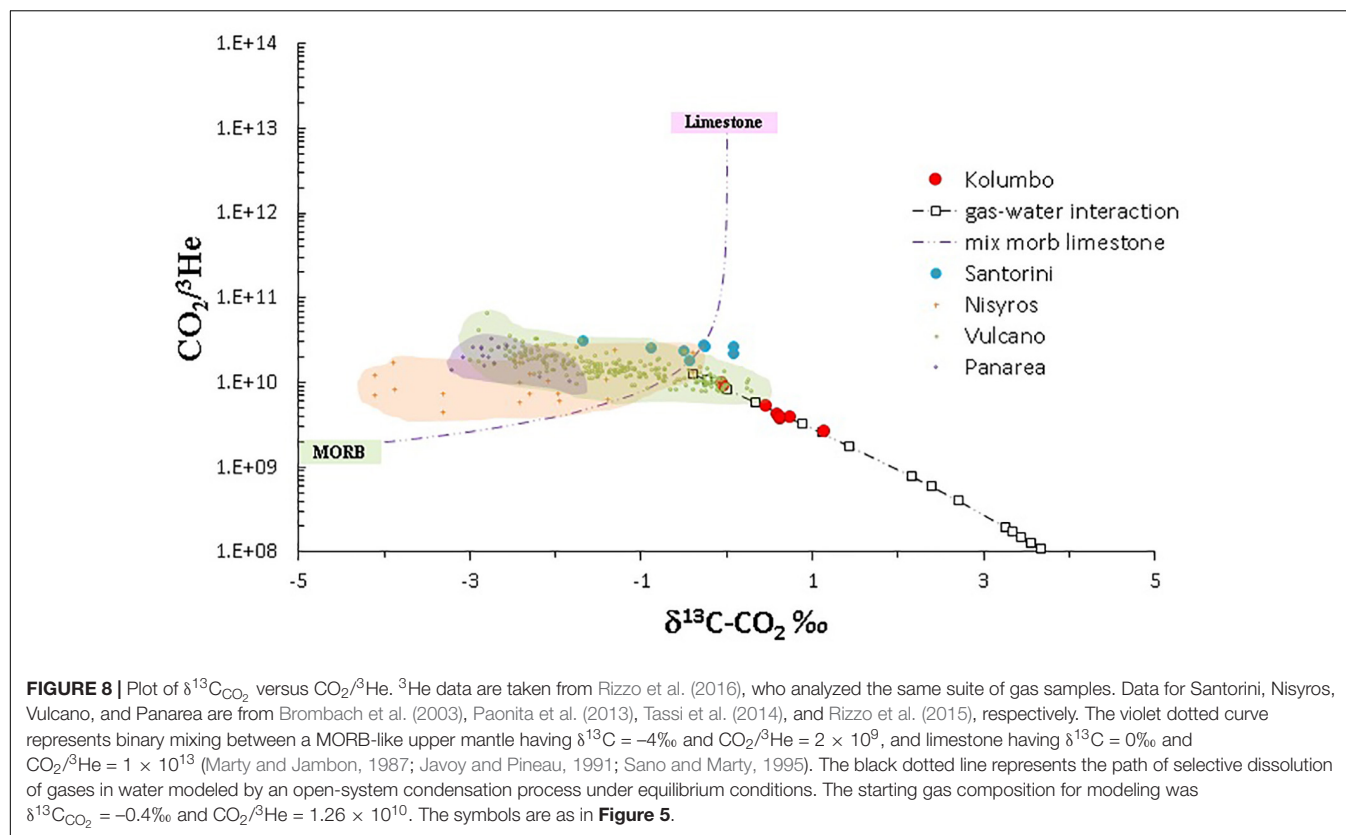
Origin of CO_2

Back-corrected calculations of the concentration and isotopic composition of gaseous CO_2 before its selective dissolution in water allow evaluation of its origin in the Kolumbo magmatic

system and the making of inferences about the local mantle. To our knowledge, this is the first study to provide data on $\delta^{13}\text{C}_{\text{CO}_2}$ emitted by Kolumbo submarine volcano.

We examined the origin of CO_2 by combining the $^3\text{He}/^4\text{He}$ values reported by Rizzo et al. (2016) with the CO_2 concentration and $\delta^{13}\text{C}_{\text{CO}_2}$ values measured in the present study. The plot of $\delta^{13}\text{C}_{\text{CO}_2}$ versus $\text{CO}_2/^3\text{He}$ is a convenient diagnostic for this purpose (Sano and Marty, 1995), although post-magmatic processes may strongly modify the original gas composition and thus compromise the accuracy of this approach (e.g., Oppenheimer et al., 2014). As discussed in Section “Gas–Water Interaction of Magmatic Fluids,” the trend of the variation of Kolumbo gases is modulated by the process of CO_2 dissolution in water, which can be observed in **Figure 8**. However, the back-corrected calculated values for the gas composition produced $\delta^{13}\text{C}_{\text{CO}_2}$ and $\text{CO}_2/^3\text{He}$ values of -0.4‰ and 1.28×10^{10} , respectively. This $\text{CO}_2/^3\text{He}$ ratio falls within the range of values reported for gases emitted from arc volcanoes worldwide ($\geq 10^{10}$; Hilton et al., 2002), while $\delta^{13}\text{C}_{\text{CO}_2}$ is within the range proposed for limestone ($\text{CO}_2/^3\text{He} \sim 1 \times 10^{13}$, $\delta^{13}\text{C} = -1$ to $+1\text{‰}$; Sano and Marty, 1995). **Figure 8** presents the binary mixing line between MORB ($\text{CO}_2/^3\text{He} = 2 \times 10^9$, $\delta^{13}\text{C} = -4\text{‰}$) and limestone (assuming $\text{CO}_2/^3\text{He} = 1 \times 10^{13}$, $\delta^{13}\text{C} = 0\text{‰}$), which highlights that gases emitted at Kolumbo have a MORB source contaminated by limestone. The main question arising from this evaluation is whether the contamination by carbonates occurs in the mantle (by subduction of limestone-bearing sediments) or in the crust (from carbonates in the basement). Unfortunately we have not performed any direct measurements of mantle fluids that could shed light on this question for Kolumbo, in contrast to the values measured for the mantle cumulates at Stromboli arc volcano (Gennaro et al., 2017). We therefore attempted to address this issue indirectly by comparing our data with those for fumarole gases emitted at Santorini (Nea Kameni Island) and Nisyros (**Figure 8**), which are the most-active volcanoes along HVA. Recent measurements of fumarole samples from Santorini (Rizzo et al., 2015) produced $\delta^{13}\text{C}_{\text{CO}_2}$ and $\text{CO}_2/^3\text{He}$ values that are comparable to those for Kolumbo gases, despite the considerable variability that may have been caused by gas–water interaction, similarly to our case study (**Figure 8**). In detail, $\delta^{13}\text{C}_{\text{CO}_2}$ as measured previously at Nea Kameni fumaroles was $-0.2 \pm 2.7\text{‰}$ (Dotsika et al., 2009; Parks et al., 2013; Tassi et al., 2013), which is consistent with the present results for Kolumbo (**Figure 8**). Similar $\delta^{13}\text{C}_{\text{CO}_2}$ and $\text{CO}_2/^3\text{He}$ values were also found by Brombach et al. (2003) for Nisyros fumaroles, although those data exhibited substantial variability. However, the reported range of values fell mainly within the binary mixing line between MORB and limestone, as observed for Santorini and Kolumbo gases.

Parks et al. (2013) proposed that the C-isotope signature of CO_2 emitted at Santorini and Nisyros is consistent with mixing between magmatic fluids and crustal basement limestone, the presence of which has been inferred by Nicholls (1971) and Spandler et al. (2012). This interpretation is plausible for two main reasons: (1) similar $\delta^{13}\text{C}_{\text{CO}_2}$ signatures characterize most of the Mediterranean volcanoes where there is evidence of the presence of a carbonate basement, and (2) the $\delta^{13}\text{C}_{\text{CO}_2}$ variability



observed in fumaroles at Santorini during the 2011–2012 unrest (Tassi et al., 2013) is not compatible with a mantle signature modified by subducted carbonates (Parks et al., 2013). In further support of the hypothesis of Parks et al. (2013), we highlight that there is strong evidence for the presence of Mesozoic carbonates within the crust beneath Kolumbo (Kiliass et al., 2013). However, Rizzo et al. (2016) reported that the ${}^3\text{He}/{}^4\text{He}$ signature of Kolumbo gases is indicative of the direct degassing of a MORB-like mantle, while those at Santorini are subsequently modified by crustal contamination. Those authors therefore argued that the mantle beneath Kolumbo and Santorini is homogeneous in terms of the He-isotope signature.

We consider that the consistency of the $\delta^{13}\text{C}_{\text{CO}_2}$ signatures at Santorini, Kolumbo, Nisyros, and most Mediterranean volcanoes with MORB and limestone mixing represents evidence of mantle metasomatism induced by decarbonation of subducting limestone-bearing sediments, rather than mixing of comparable proportions of magmatic and crustal fluids originating from local basement carbonates. Indeed, based on $\delta^{13}\text{C}_{\text{CO}_2}$ in fluid inclusions of mantle cumulates from Stromboli, Gennaro et al. (2017) revealed that the isotopic signature of local mantle reflected CO_2 contamination arising from the decarbonation of sediments carried by the subducting Ionian slab. We therefore argue that the mantle beneath Kolumbo and Santorini is reasonably homogeneous also in terms of $\delta^{13}\text{C}_{\text{CO}_2}$ signatures, and we cannot exclude that CO_2 is already contaminated by the decarbonation of slab sediments. Local crustal contamination may eventually further modify the isotopic composition of

metasomatized mantle C, as observed for He isotopes beneath Santorini (Rizzo et al., 2015, 2016).

Origin of CH_4

Some studies have focused on the origin of CH_4 in fluids emitted from submarine hydrothermal systems (Welhan, 1988; McCollom and Seewald, 2007; Proskurowski et al., 2008; Keir, 2010; McDermott et al., 2015; Wen et al., 2016; Xue-Gang et al., 2016; Wang et al., 2018; and references therein). Besides the difficulty of sampling at considerable water depths, the availability of CH_4 data is further impaired by the gases emitted from hydrothermal or magmatic systems generally being dominated by CO_2 (e.g., Yang et al., 2005; Lupton et al., 2006, 2008), with only trace levels of CH_4 . This compromises the ability to perform isotope analyses, especially those of H.

In this study we measured the stable C and H isotopes of CH_4 in Kolumbo hydrothermal gases and performed evaluations to ascertain the origin of CH_4 . In this context we plotted $\delta^{13}\text{C}_{\text{CH}_4}$ versus $\text{CH}_4/(\text{C}_2\text{H}_6 + \text{C}_3\text{H}_8)$, which is the most-common classification approach that was introduced by Bernard et al. (1978), and $\delta\text{D}_{\text{CH}_4}$ versus $\delta^{13}\text{C}_{\text{CH}_4}$, as introduced by Schoell (1980) and later modified by Mazzini et al. (2011), to distinguish CH_4 originating from thermogenic and microbial processes as well as sediment-free midocean ridges (Figure 9). It should be stressed that the CH_4 -isotope composition of Kolumbo gases (Table 1) varied within a narrow range for both C ($\delta^{13}\text{C} = -18.8$ to -17.6‰ V-PDB) and H ($\delta\text{D} = -118.6$ to -115.4‰ V-SMOW). The data points in the plot of $\delta^{13}\text{C}_{\text{CH}_4}$

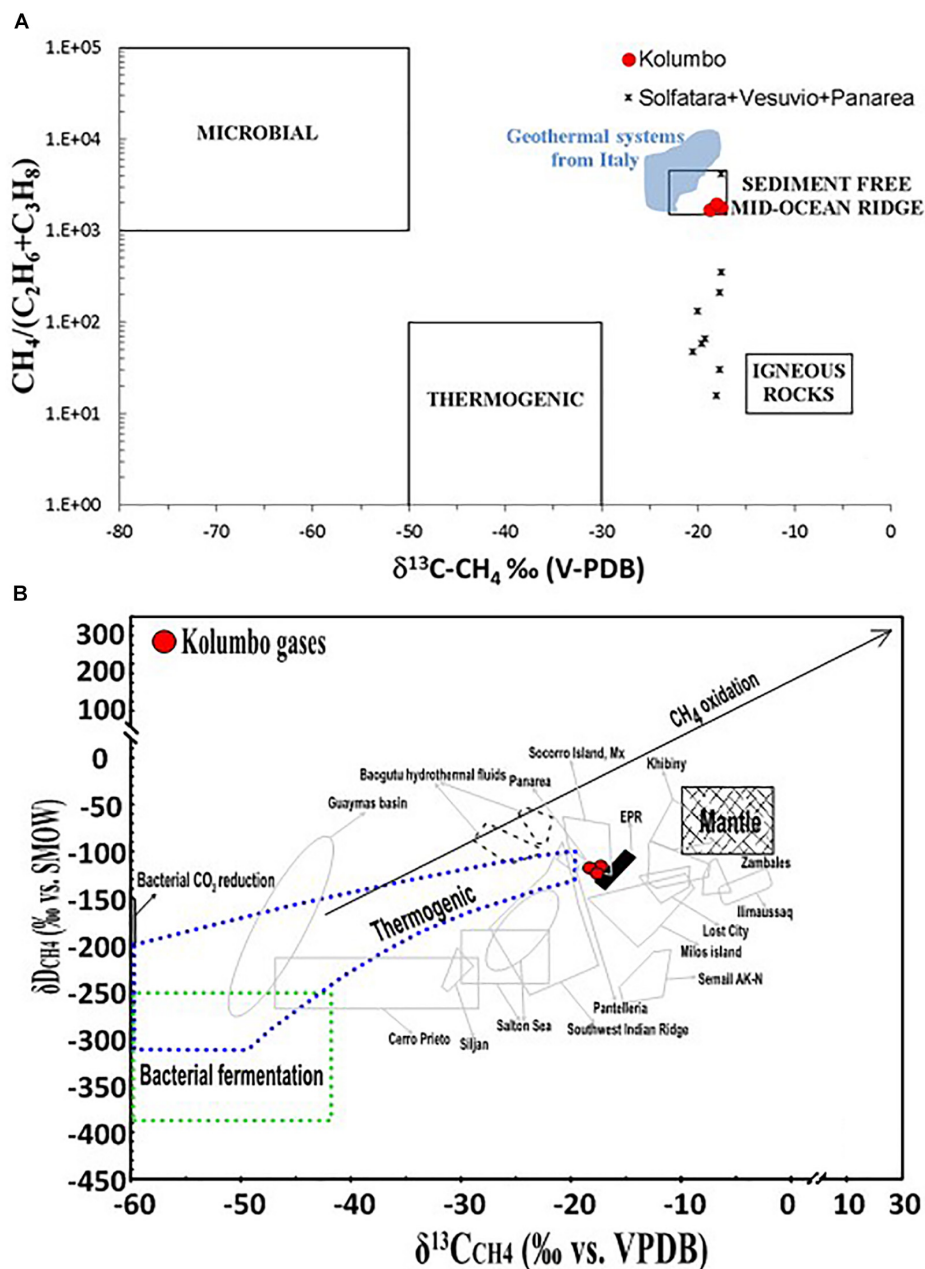


FIGURE 9 | (A) Plot of $\delta^{13}\text{C}_{\text{CH}_4}$ versus $\text{CH}_4/(\text{C}_2\text{H}_6 + \text{C}_3\text{H}_8)$ modified from Bernard et al. (1978). Field data for microbial and thermogenic gases and from sediment-free midocean ridges and for igneous rocks are from McCollom and Seewald (2007 and references therein). Data for Italian geothermal systems and hydrothermal systems from Campi Flegrei, Vesuvio and Panarea are from Tassi et al. (2012 and references therein). **(B)** Plot of $\delta\text{D}_{\text{CH}_4}$ versus $\delta^{13}\text{C}_{\text{CH}_4}$ as introduced by Schoell (1980) and modified by Mazzini et al. (2011). Field data are from Mazzini et al. (2011 and references therein). The symbols are as in Figure 5.

versus $\text{CH}_4/(\text{C}_2\text{H}_6 + \text{C}_3\text{H}_8)$ for Kolumbo samples (Figure 9A) fall within an origin area of the sediment-free midocean ridge, similar to other Italian geothermal and hydrothermal systems (e.g., Panarea and Pantelleria; Tassi et al., 2012). Such data are often classified as abiogenic (McCollom and Seewald, 2007 and references therein), meaning that methanogenesis does not involve a biogenic organic precursor (Welhan, 1988). Nevertheless, the accuracy of this approach can be significantly

compromised since the concentrations of light hydrocarbons and the isotopic composition of CH_4 can both be modified by oxidation and migration processes (Welhan, 1988). More specifically, $\delta\text{D}_{\text{CH}_4}$ and $\delta^{13}\text{C}_{\text{CH}_4}$ measured in Kolumbo gases may have been altered by thermogenic gas oxidation, as in the case of CH_4 from Salton Sea Geothermal Field (Mazzini et al., 2011). Alternatively, it is possible that abiogenic CH_4 is either formed in basalts and extracted into the circulating

fluids (Welhan, 1988) or produced by Fischer-Tropsch-type chemical reactions (e.g., Proskurowski et al., 2008; Keir, 2010 and references therein; Etiope and Sherwood-Lollar, 2013). However, the latter process was recently questioned by Taran et al. (2010a), who attributed the isotopic trends in the $\delta^{13}\text{C}$ and δD values of light hydrocarbons as mixing between two or more endmembers.

On the other hand, the plot of $\delta\text{D}_{\text{CH}_4}$ versus $\delta^{13}\text{C}_{\text{CH}_4}$ for Kolumbo samples (Figure 9B) falls within the area of Socorro gases (Mexico, Taran et al., 2010b), between the range of abiotic CH_4 (McCollom and Seewald, 2007 and references therein) and a thermogenic field, which is how most geothermal and hydrothermal systems worldwide are generally characterized (Whiticar, 1999; Mango, 2000; Taran et al., 2010b; Tassi et al., 2012). By combining He-isotope data (i.e., $^3\text{He}/^4\text{He}$ ratio of ~ 7 Ra for Kolumbo gases; Rizzo et al., 2016) with those of CH_4 (e.g., Hsin-Yi et al., 2016), we obtained an average $\text{CH}_4/^3\text{He}$ ratio of $\sim 1.4 \times 10^7$ (Table 1). This ratio falls within the range of values measured in fluids from the East Pacific Rise (e.g., Proskurowski et al., 2008; Keir, 2010; and references therein).

Christakis et al. (2018) analyzed the microbial community at Kolumbo sulfide chimneys using next-generation sequencing technologies, and did not find any microbial lineages closely related to CH_4 production processes. In addition, only a few phylotypes typically involved in CH_4 oxidation were identified. A further metagenomic investigation of the Kolumbo seafloor found negligible methanogenesis-related marker genes (Oulas et al., 2015), supporting the abiotic origin of CH_4 .

It was beyond the scope of this study to resolve the scientific controversies of the different theories about abiotic CH_4 . Overall, it is more likely that CH_4 in Kolumbo gases comprise a mixture of oxidized thermogenic and abiogenic CH_4 formed in high-temperature ($> 200^\circ\text{C}$) magmatic-hydrothermal systems.

Submarine Hydrothermal Hg(0) Emissions

The natural aerial volcanic emissions of Hg via passive degassing have been estimated at $76 \pm 30 \times 10^6 \text{ g yr}^{-1}$ (Bagnato et al., 2014). However, the quantity and impact of Hg released by submarine volcanoes and hydrothermal systems is less well-known due to a lack of observations (Varekamp and Buseck, 1981; Bagnato et al., 2017). In particular, there are severe logistical constraints in sampling submarine volcanic gas emissions on the floor of Kolumbo submarine crater, since it is at 500 m b.s.l. (Fitzgerald and Lamborg, 2004). Moreover, previous studies of submarine hydrothermal Hg have investigated dissolved Hg(II) concentrations but not dissolved gaseous Hg(0) (Lamborg et al., 2006).

The present study deployed gas-tight titanium syringes connected to inverted funnels above hydrothermal vents and activated by an ROV, which provided the unique opportunity to collect pristine bubbling gas emissions discharged from an active submarine volcano. The levels of gaseous Hg(0) in the gas samples varied from 61 to 1300 ng m^{-3} , which are roughly 10 times higher than the levels previously reported for on-land Santorini fumaroles (9 to 121 ng m^{-3} ; Bagnato et al., 2013) and also the worldwide aerial volcanic Hg(0) concentrations (4 to 125 ng m^{-3} ; Bagnato et al., 2014). These data seem to further highlight that the level of magmatic activity is higher at

Kolumbo volcano than at Santorini. It is also worth mentioning that the global average concentration of atmospheric Hg(0) in the northern hemisphere is 1.5 ng m^{-3} .

Hydrothermal Gas Equilibrium

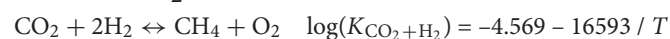
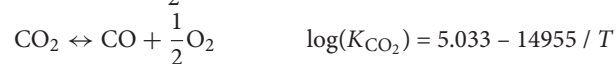
The temperature and pressure conditions at which gaseous species equilibrate in the hydrothermal system beneath the floor of Kolumbo submarine crater can be estimated from concentration data of minor reactive species together with CO_2 and H_2O (Chiodini and Marini, 1998 and references therein). The most-important assumptions in this approach are that the gaseous species have attained chemical equilibrium in the hydrothermal system and are quenched during their ascent to the sea surface. We evaluated two stability diagrams based on the concentrations of H_2 , CO , CH_4 , and CO_2 in the dry gas phase (Figure 10), following the approach proposed by Chiodini and Cioni (1989) and Chiodini et al. (2001) and subsequently modified by Chiodini et al. (2006) for submarine gases at Panarea. Because H_2O represents the main component of hydrothermal fluids, we assumed that pure water coexisted with vapor, whereas the fugacity of water vapor ($f_{\text{H}_2\text{O}}$) as a function of temperature (Giggenbach, 1987) can be expressed as follows:

$$\log(f_{\text{H}_2\text{O}}) (\text{bar}) = 5.510 - 2048/T$$

where T is the temperature in kelvin. It is also important to consider the fugacity of O_2 (f_{O_2}), since this controls the redox conditions at which hydrothermal systems are formed. Since the H_2O concentration of hydrothermal vapors in our samples was not available and we have no information on the mineral assemblage that could fix f_{O_2} , we considered the redox buffer typically proposed for hydrothermal systems by D'Amore and Panichi (1980):

$$\log(f_{\text{O}_2}) (\text{bar}) = 8.20 - 23643/T$$

Complementarily, we considered the following reactions and temperature-dependent equilibrium constants based on the thermodynamic data reported by Stull et al. (1969) and Giggenbach (1980, 1987):



Finally, the following equations derived by Chiodini et al. (2006) were taken into account:

$$\log(\text{H}_2/\text{CH}_4) = 8.811 - 4121.5/T - \log(P_{\text{CO}_2})$$

$$\log(\text{CO}/\text{CH}_4) = 5.786 - 4326.5/T$$

where P is the partial pressure. The plot of $\log(\text{CO}/\text{CH}_4)$ versus $\log(\text{H}_2/\text{CH}_4)$ in Figure 10A suggests that Kolumbo gases would have reached an equilibrium at $200\text{--}250^\circ\text{C}$ and $P_{\text{CO}_2} \sim 50$ bar. In comparison with the submarine hydrothermal system of Panarea and the high-temperature fumaroles of Vulcano (Aeolian Islands,

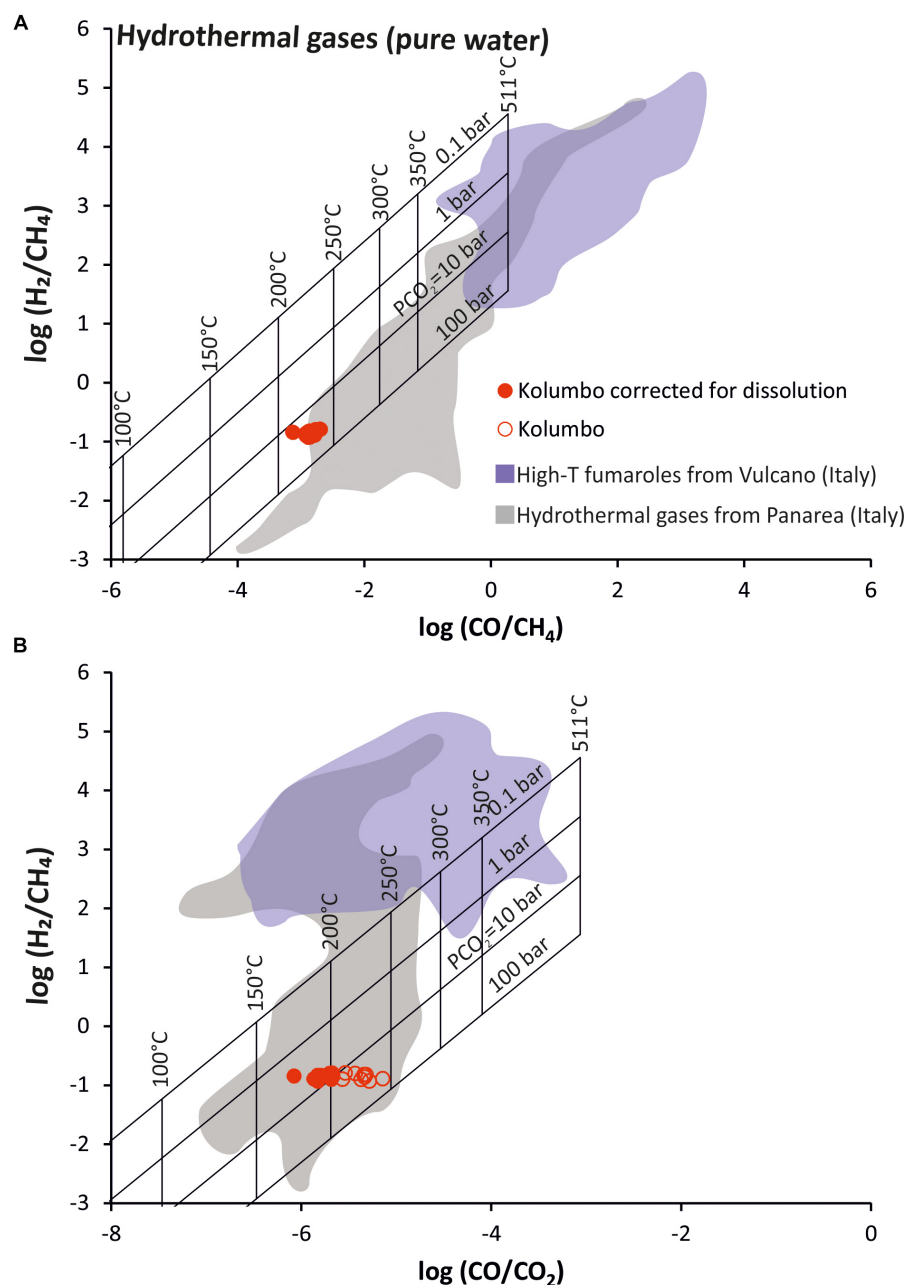


FIGURE 10 | Plots of (A) $\log(\text{CO}/\text{CH}_4)$ versus $\log(\text{H}_2/\text{CH}_4)$ and (B) $\log(\text{CO}/\text{CO}_2)$ versus $\log(\text{H}_2/\text{CH}_4)$. The theoretical grid for hydrothermal gases was calculated by assuming their coexistence with pure liquid water (Chiodini et al., 2006 and references therein). Data for Vulcano Island are from Paonita et al. (2013), and those for Panarea are from Caracausi et al. (2005), Chiodini et al. (2006), and Tassi et al. (2014). The symbols are as in Figure 5. See the main text for further details.

Italy), Kolumbo gases fall close to or within the range for Panarea gases, confirming their hydrothermal nature. The same pressure and temperature conditions were derived by examining the plot of $\log(\text{CO}/\text{CO}_2)$ versus $\log(\text{H}_2/\text{CH}_4)$ (Figure 10B). Given the compositional changes that may arise in hydrothermal gases due to the partial dissolution of CO_2 in water (see section “Gas–Water Interaction of Magmatic Fluids”), we recalculated the pressure and temperature conditions by applying the pristine composition

estimated for each gas vent. Based on the values of Henry’s law constant, CO_2 was found to differ considerably from H_2 , CO and CH_4 , with the former having a greater tendency to partition from the gas phase into the aqueous phase (Sander, 2015). Therefore, the correction for gas–water partitioning was deemed necessary only when considering ratios that involved CO_2 [e.g., $\log(\text{CO}/\text{CO}_2)$; Figure 10B]. By applying the pristine composition, we estimated a gas equilibrium temperature of

~200°C and $P_{\text{CO}_2} \sim 10$ bar. These values are slightly lower than the pressure and temperature conditions derived from the plot of $\log(\text{CO}/\text{CH}_4)$ versus $\log(\text{H}_2/\text{CH}_4)$, but they remain well within the typical values reported for hydrothermal gases. In general, the estimated temperature using CO/CH_4 , CO/CO_2 , and H_2/CH_4 was equal to or below the highest temperature measured on the floor of Kolumbo submarine crater vents by Sigurdsson et al. (2006) and Carey et al. (2013). This suggests that part or all of these gaseous species did not achieve equilibrium under the assumed redox conditions or that the magmatic activity has waned in recent years.

To investigate these two possibilities, we applied the approach proposed by Chiodini and Cioni (1989) and Chiodini et al. (2006), which is based on the reaction:



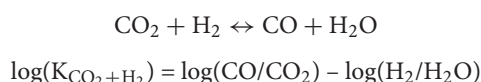
Since this reaction does not involve gaseous O_2 , Chiodini et al. (2006) suggested that this approach provides equilibrium pressure and temperature estimates that are independent of the redox conditions. The resulting equations that allow pressure and temperature to be determined are

$$T(K) \left[\frac{13606}{8065 - \log \left(\frac{\text{CO}^4}{\text{CO}_2^3 \cdot \text{CH}_4} \right)} \right]$$

$$\log P_{\text{CO}_2}(\text{bar}) = 3.573 - \frac{46}{T(K)} - \log \left(\frac{\text{H}_2}{\text{CO}} \right)$$

This specific approach revealed that Kolumbo gases equilibrated at 200–250°C and when P_{CO_2} was slightly below 50 bar (Figure 11A). The presence of CO_2 in one of the above equations prompted us to again consider the pristine composition of gases prior to the gas–water partitioning process. This yielded a slightly lower equilibrium temperature (189–216°C), whereas P_{CO_2} remained the same (Figure 11A). This temperature range is comparable to those estimated using CO/CH_4 , CO/CO_2 and H_2/CH_4 ratios, suggesting that the assumed redox conditions are not responsible for the difference in the estimated equilibrium temperatures.

The findings of previous investigations of crater fumaroles at White Island (Giggenbach, 1987) and Vulcano (Chiodini et al., 1993, 1995) suggest that the two most-reactive gaseous species in hydrothermal systems are H_2 and CO , while CH_4 is one of the least reactive (Giggenbach, 1991; Taran and Giggenbach, 2003). To evaluate if CH_4 measured in Kolumbo gases attained full equilibrium, we considered the following formation reaction and relative equilibrium constant:



In the gas phase, $\log(K_{\text{CO}_2+\text{H}_2}) = -2248/T + 2.485$

In a single saturated liquid phase, as assumed in our case, gas equilibrium contents are computed using the vapor–liquid

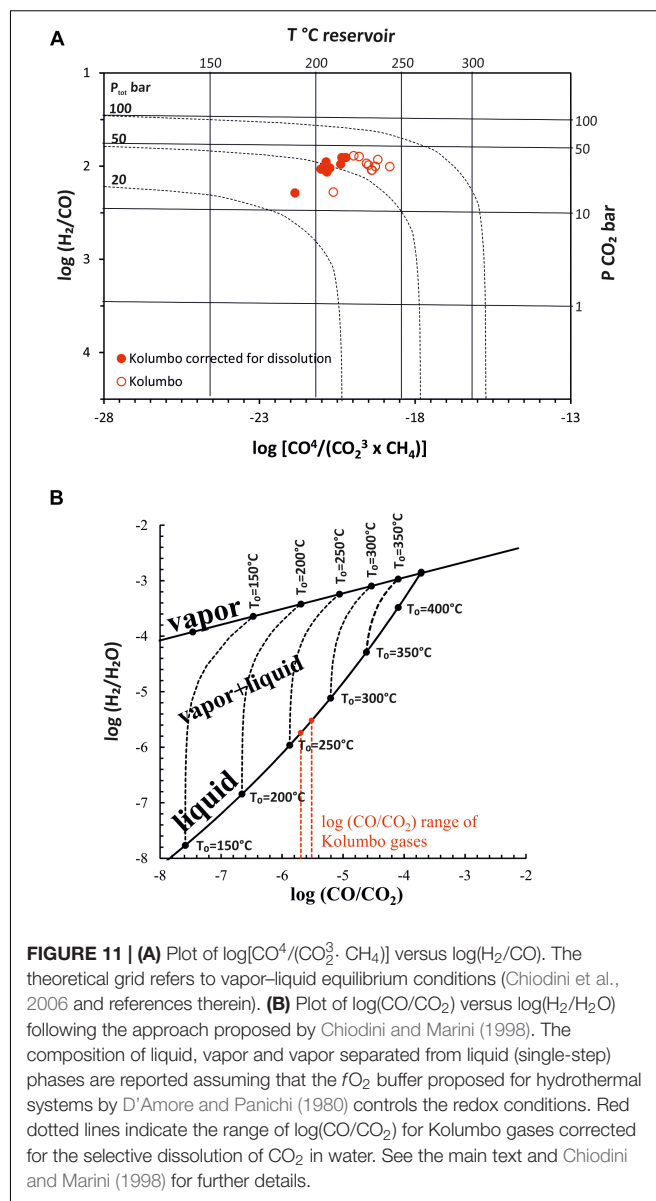


FIGURE 11 | (A) Plot of $\log[\text{CO}^4/(\text{CO}_2^3 \cdot \text{CH}_4)]$ versus $\log(\text{H}_2/\text{CO})$. The theoretical grid refers to vapor–liquid equilibrium conditions (Chiodini et al., 2006 and references therein). **(B)** Plot of $\log(\text{CO}/\text{CO}_2)$ versus $\log(\text{H}_2/\text{H}_2\text{O})$ following the approach proposed by Chiodini and Marini (1998). The composition of liquid, vapor and vapor separated from liquid (single-step) phases are reported assuming that the f_{O_2} buffer proposed for hydrothermal systems by D'Amore and Panichi (1980) controls the redox conditions. Red dotted lines indicate the range of $\log(\text{CO}/\text{CO}_2)$ for Kolumbo gases corrected for the selective dissolution of CO_2 in water. See the main text and Chiodini and Marini (1998) for further details.

distribution coefficient (B) (Giggenbach, 1980; D'Amore and Truesdell, 1988; Chiodini and Marini, 1998):

$$\log(B_{\text{CO}}) = 6.3173 - 0.01388 (T - 273.15)$$

$$\log(B_{\text{CO}_2}) = 4.7593 - 0.01092 (T - 273.15)$$

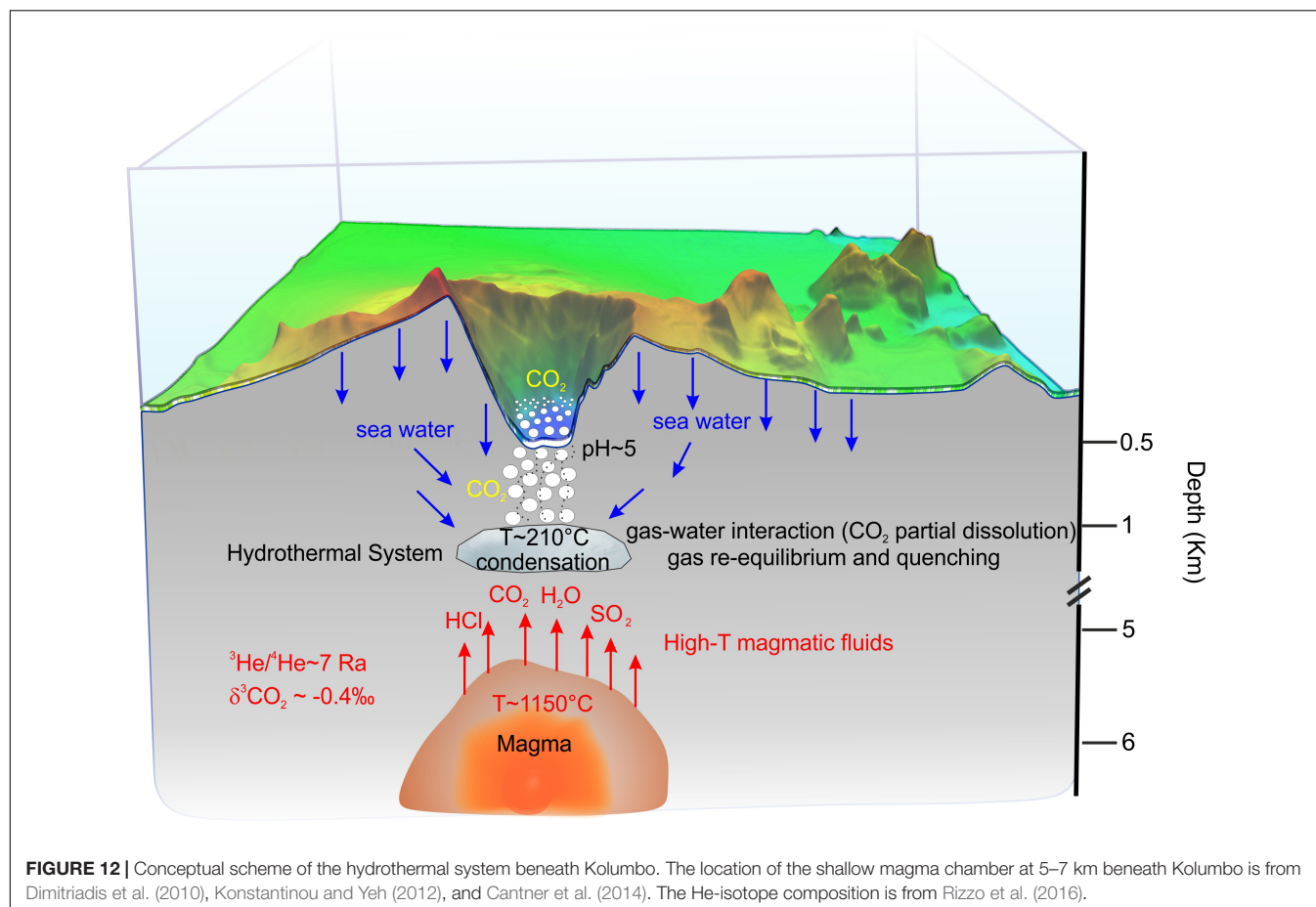
$$\log(B_{\text{H}_2}) = 6.2283 - 0.01403 (T - 273.15)$$

Therefore, the above reported reaction for the liquid phase becomes

$$\log(K_{\text{CO}_2+\text{H}_2}) - \log(B_{\text{CO}}/B_{\text{CO}_2}) + \log(B_{\text{H}_2})$$

$$= \log(\text{CO}/\text{CO}_2) - \log(\text{H}_2/\text{H}_2\text{O})$$

An equilibrium temperature of 250–300°C and $\log(K_{\text{CO}_2+\text{H}_2}) - \log(B_{\text{CO}}/B_{\text{CO}_2}) + \log(B_{\text{H}_2}) \approx 0.0 \pm 0.1$ implies $\log(\text{H}_2/\text{H}_2\text{O}) \approx \log(\text{CO}/\text{CO}_2)$. Thus, the $\log(\text{CO}/\text{CO}_2)$ values measured in our



samples and corrected for CO_2 dissolution can be used to roughly estimate the equilibrium temperature in liquid water, which varies in the narrow range of 263–276°C (**Figure 11B**). These values are higher than those previously calculated including CH_4 , and thus we deduce that the latter species was not in equilibrium with the other gases and led to underestimations of the equilibrium temperature.

Based on the relationships proposed by Chiodini and Cioni (1989), we can finally calculate $P_{\text{CO}_2} \sim 30$ bar and $P_{\text{H}_2\text{O}} \sim 36$ bar, which sum to a total pressure of ~ 66 bar. Considering that Kolumbo gases are emitted at 500 m b.s.l., which corresponds to a pressure of ~ 50 bar, the hydrothermal system must be located at a pressure of ~ 116 bar (~ 1000 m b.s.l.).

Conceptual Scheme of the Hydrothermal System Beneath Kolumbo

Based on this study and other previous findings (Sigurdsson et al., 2006; Carey et al., 2013; Kilias et al., 2013; Rizzo et al., 2016), in **Figure 12** we propose a physical and geochemical model for the Kolumbo magmatic-hydrothermal system. We made some assumptions in order to simplify the system: (1) the permeability of the system was considered uniform, isotropic and sufficiently high; (2) the shallow magma chamber located 5–7 km beneath Kolumbo (Dimitriadis et al., 2010; Konstantinou and Yeh, 2012; Cantner et al.,

2014) represents the source of magmatic gases feeding the hydrothermal system, (3) magmatic degassing does not or only weakly modifies these magmatic gases, and (4) seawater infiltrates from the sea bottom and favors condensation of magmatic gases both within and above the hydrothermal system.

At Kolumbo, magmatic gases (H_2O , CO_2 , S-bearing species, halogens and noble gases) having $^3\text{He}/^4\text{He} \sim 7$ Ra (Rizzo et al., 2016) and $\delta^{13}\text{C}_{\text{CO}_2} \sim -0.4\text{‰}$ ascend from the magma chamber and feed conduits up to the hydrothermal system (**Figure 12**). During the cooling of magmatic gases, H_2O and more-acidic species (S and halogens) condensate to form a hydrothermal system at $\sim 270^\circ\text{C}$ in which water at $\text{pH} \leq 5$ probably circulates. We cannot exclude that the hydrothermal system has multiple levels; however, we are able to reconstruct the upper level that feeds the bottom vents of the crater. Hydrothermal waters are probably fed by seawater infiltrating from the sea bottom and any brine formed from the adsorption of acidic gases in groundwater by rock dissolution.

The hydrothermal system has a total pressure of ~ 66 bar, corresponding to $\sim 1,160$ m b.s.l. and 650 m below the crater bottom, if the hydrostatic pressure is assumed at depth. Hydrothermal gases within the hydrothermal system undergo gas–water interactions along the fractures feeding the floor of

Kolumbo submarine crater and from the shallow vents that favor the removal of most of the acidic gases (S and halogens) and the partial dissolution of CO₂ (see section “Gas–Water Interaction of Magmatic Fluids”). This produces an excess of N₂, noble gases and reactive gases via migration paths that permit their rapid ascent under advective degassing. At the crater bottom, several vents discharge fluids at temperatures up to 220°C, variable gas fluxes and pH down to ~5 (Sigurdsson et al., 2006; Carey et al., 2013). Acoustic and visual imaging of the ascending bubbles suggests that CO₂ is being dissolved into seawater within ~10 m above the crater floor (Carey et al., 2013).

CONCLUSIONS

We have investigated the geochemistry of CO₂-rich gases venting at 500 m b.s.l. from Kolumbo submarine volcano, which is located 7 km northeast of Santorini Island. The main findings are as follows:

- Gases are dominated by CO₂ (>97%), with a small air contamination probably related to sampling conditions, but are fractionated by a process of gas–water interaction reasonably related to variable fluxes of gases emitted from the different vents. This process induces a partial dissolution of gaseous CO₂ in water, leading to substantial enrichment of the residual gas in those species that are much less soluble in water (i.e., He, H₂, CO, CH₄, and N₂). This fractionation also affects the C-isotope composition of CO₂.
- We modeled the gas–water interaction process (~220°C, ~50 bar and pH ~ 5) and reconstructed the chemistry and $\delta^{13}\text{C}_{\text{CO}_2}$ of magmatic gases before interaction. We assess that the pristine CO₂ is characterized by $\delta^{13}\text{C} \sim -0.4\text{‰}$. Combining our data with $^3\text{He}/^4\text{He}$ measurements carried out in the same gas samples by Rizzo et al. (2016) yields CO₂/ $^3\text{He} \sim 1 \times 10^{10}$. These data are in the same range as those obtained for the Santorini and Nisyros fumaroles. We argue that CO₂ emitted at Kolumbo could originate from a mantle contaminated by CO₂ via the decarbonation of subducting limestone.
- The CH₄-isotope composition falls within the range typical of hydrothermal gases, similar to other Mediterranean hydrothermal systems (Panarea and Campi Flegrei), suggesting that it originates from mixing between thermogenic and abiogenic CH₄.
- We found that the Hg(0) concentration in Kolumbo gases ranges from ~60 to 1300 ng m⁻³. These levels are particularly high when compared to those of

land-based fumaroles located on Santorini Island and worldwide aerial volcanic emissions, which suggests that the magmatic activity is higher at Kolumbo than at Santorini.

- Based on geo-indicators of pressure and temperature, we calculated that magmatic gases equilibrate within the Kolumbo hydrothermal system at about 270°C and 116 bar.

AUTHOR CONTRIBUTIONS

AR and PN conceived the study. AR, VC, PN, PP, MM, GK, AM, and AIC participated in the collection of gas samples. AR, VC, and AnC analyzed the gas samples and elaborated the data. DL helped in figures preparation. All of the authors contributed to the preparation and editing of the final manuscript.

FUNDING

The authors acknowledge financial support from the SeaBioTech project (spider.science.strath.ac.uk/seabiotech/) funded by the European Commission within its FP7 Programme (Grant No. 311932), as well as from INGV, Sezione di Palermo, which permitted the access to analytical facilities.

ACKNOWLEDGMENTS

We thank Giuseppe Riccobono and Paolo Cosenza for providing technical support to the project and constructing the gas-tight sampler at INGV, Sezione di Palermo that was used to collect some of the submarine fluid samples. The officers and crew of RV AEGAEON are especially acknowledged for their valuable help during sampling. We thank INGV, Sezione di Palermo for providing analytical support, particularly Francesco Salerno and Mauro Martelli for performing analyses of gases chemistry, and Mariano Tantillo for supporting the laboratory activities involving noble-gas isotopes. We also thank Fausto Grassa, Giorgio Capasso, Ygor Oliveri, and Aldo Sollami for their help with the analyses of CO₂ and CH₄ isotopes in the stable-isotope laboratory. We further thank Cinzia Federico and Fausto Grassa for useful discussions that helped in the elaborative and interpretative framework. Data reported in **Tables 1–3** are available by contacting the corresponding author. We thank the Chief Editor VA the Guest Associate Editor GG for handling and revising the manuscript, YT and an reviewer for suggestions that greatly improved the manuscript. English Science Editing revised the use of English in the manuscript.

REFERENCES

- Allègre, C. J. (2008). *Isotope Geology*. Cambridge: Cambridge University Press, 512. doi: 10.1017/CBO9780511809323
- Bagnato, E., Acquavita, A., Barra, M., Covelli, S., Italiano, F., Oliveri, E., et al. (2017). Hydrochemical and atmochemical mercury distribution over the submarine hydrothermal hot-spot sources of Panarea Island, Aeolian Archipelago. *Mar. Chem.* 194, 63–78. doi: 10.1016/j.marchem.2017.04.003
- Bagnato, E., Tamburello, G., Aiuppa, A., Sprovieri, M., Vougioukalakis, G. E., and Parks, M. (2013). Nea Kameni volcanic centre, Santorini (Greece). *Geochem. J.* 47, 437–450. doi: 10.2343/geochemj.2.0263

- Bagnato, E., Tamburello, G., Avard, G., Martinez-Cruz, M., Enrico, M., Fu, X., et al. (2014). Mercury Fluxes from volcanic and geothermal sources: an update. *Geol. Soc.* 410, 263–285. doi: 10.1144/SP410.2
- Bernard, B. B., Brooks, J. M., and Sackett, W. M. (1978). “A geochemical model for characterization of hydrocarbon gas sources in marine sediments,” in *Proceedings of the Offshore Technology Conference*, Houston, TX, 435–438.
- Bohnhoff, M., Rische, M., Meier, T., Becker, D., Stavrakakis, G., and Harjes, H.-P. (2006). Microseismic activity in the Hellenic Volcanic Arc, Greece, with emphasis on the seismotectonic setting of the Santorini–Amorgos zone. *Tectonophysics* 423, 17–33. doi: 10.1016/j.tecto.2006.03.024
- Brombach, T., Caliro, S., Chiodini, G., Fiebig, J., Hunziker, J., and Raco, B. (2003). Geochemical evidence for mixing of magmatic fluids with seawater, Nisyros hydrothermal system, Greece. *Bull. Volcanol.* 65, 505–516. doi: 10.1007/s00445-003-0278-x
- Butterfield, D. A., Massoth, G. J., McDuff, R. E., Lupton, J. E., and Lilley, M. D. (1990). Geochemistry of hydrothermal fluids from Axial Seamount Hydrothermal Emissions Study Vent Field, Juan de Fuca Ridge: subseafloor boiling and subsequent fluid-rock interaction. *J. Geophys. Res.* 95, 12,895–12,921. doi: 10.1029/JB095iB08p12895
- Caliro, S., Caracausi, A., Chiodini, G., Ditta, M., Italiano, F., Longo, M., et al. (2004). Evidence of a recent input of magmatic gases into the quiescent volcanic edifice of Panarea, Aeolian Islands, Italy. *Geophys. Res. Lett.* 31:L07619. doi: 10.1029/2003GL019359
- Camilli, R., Nomikou, P., Escartin, J., Ridao, P., Mallios, A., Kilias, S. P., et al. (2015). The kallisti limnes, carbon dioxide-accumulating subsea pools. *Sci. Rep.* 5:12152. doi: 10.1038/srep12152
- Cantner, K., Carey, S., and Nomikou, P. (2014). Integrated volcanologic and petrologic analysis of the 1650AD eruption of Kolumbo submarine volcano, Greece. *J. Volcanol. Geotherm. Res.* 269, 28–43. doi: 10.1016/j.jvolgeores.2013.10.004
- Capaccioni, B., Tassi, F., Vaselli, O., Tedesco, D., and Poreda, R. (2007). Submarine gas burst at Panarea Island (southern Italy) on 3 November 2002: a magmatic versus hydrothermal episode. *J. Geophys. Res.* 112:B05201. doi: 10.1029/2006JB004359
- Caracausi, A., Ditta, M., Italiano, F., Longo, M., Nuccio, P. M., Paonita, A., et al. (2005). Changes in fluid geochemistry and physico-chemical conditions of geothermal systems caused by magmatic input: the recent abrupt outgassing off the island of Panarea, Aeolian Islands, Italy. *Geochim. Cosmochim. Acta* 69, 3045–3059. doi: 10.1016/j.gca.2005.02.011
- Carey, S., Nomikou, P., Bell, K. C., Lilley, M., Lupton, J., Roman, C., et al. (2013). CO₂ degassing from hydrothermal vents at Kolumbo submarine volcano, Greece, and the accumulation of acidic crater water. *Geology* 41, 1035–1038. doi: 10.1130/G34286.1
- Chiodini, G., Caliro, S., Caramanna, G., Granieri, D., Minopoli, C., Moretti, R., et al. (2006). Geochemistry of the submarine gaseous emissions of Panarea (Aeolian Islands, southern Italy): magmatic vs. hydrothermal origin and implications for volcanic surveillance. *Pure Appl. Geophys.* 163, 759–780. doi: 10.1007/s00024-006-0037-y
- Chiodini, G., and Cioni, R. (1989). Gas geobarometry for hydrothermal systems and its application to some Italian geothermal areas. *Appl. Geochem.* 4, 465–472. doi: 10.1016/0883-2927(89)90004-8
- Chiodini, G., Cioni, R., and Marini, L. (1993). Reactions governing the chemistry of crater fumaroles from Vulcano Island, Italy, and implications for volcanic surveillance. *Appl. Geochem.* 8, 357–371. doi: 10.1016/0883-2927(93)90004-Z
- Chiodini, G., Cioni, R., Marini, L., and Panichi, C. (1995). Origin of the fumarolic fluids of Vulcano Island, Italy, and implications for volcanic surveillance. *Bull. Volcanol.* 57, 99–110. doi: 10.1007/BF00301400
- Chiodini, G., and Marini, L. (1998). Hydrothermal gas equilibria: the H₂O–H₂–CO₂–CO–CH₄ system. *Geochim. Cosmochim. Acta* 62, 2673–2687. doi: 10.1016/S0016-7037(98)00181-1
- Chiodini, G., Marini, L., and Russo, M. (2001). Geochemical evidence for the existence of high-temperature brines at Vesuvio volcano, Italy. *Geochim. Cosm. Acta* 65, 2129–2147. doi: 10.1016/S0016-7037(01)00583-X
- Christakis, C., Polymenakou, P., Mandalakis, M., Nomikou, P., Kristoffersen, J. B., Lampridou, D., et al. (2018). Microbial community differentiation between active and inactive sulfide chimneys of the Kolumbo submarine volcano. Hellenic Volcanic Arc. *Extremophiles* 22, 13–27. doi: 10.1007/s00792-017-0971-x
- Clark, I. D., and Fritz, P. (1997). *Environmental Isotopes in Hydrogeology*. Boca Raton, FL: CRC Press, 328.
- Crisp, J. A. (1984). Rates of magma emplacement and volcanic output. *J. Volcanol. Geotherm. Res.* 20, 177–211. doi: 10.1016/0377-0273(84)90039-8
- D’Amore, F., and Panichi, C. (1980). Evaluation of deep temperature of hydrothermal systems by a new gasgeothermometer. *Geochim. Cosmochim. Acta* 44, 549–556. doi: 10.1016/0016-7037(80)90051-4
- D’Amore, F., and Truesdell, A. H. (1988). A review of solubilities and equilibrium constants of chemical reactions for gaseous species of geothermal interest. *Sci. Geol. Bull.* 41, 309–332. doi: 10.3406/sgeol.1988.1801
- Dimitriadis, I., Karagianni, E., Panagiotopoulos, D., Papazachos, C., Hatzidimitriou, P., Bohnhoff, M., et al. (2009). Seismicity and active tectonics at Coloumbo Reef (Aegean Sea, Greece): monitoring an active volcano at Santorini Volcanic Center using a temporary seismic network. *Tectonophysics* 465, 136–149. doi: 10.1016/j.tecto.2008.11.005
- Dimitriadis, I., Papazachos, C., Panagiotopoulos, D., Hatzidimitriou, P., Bohnhoff, M., Rische, M., et al. (2010). P and S velocity structures of the Santorini–Coloumbo volcanic system (Aegean Sea, Greece) obtained by non-linear inversion of travel times and its tectonic implications. *J. Volcanol. Geotherm. Res.* 195, 13–30. doi: 10.1016/j.jvolgeores.2010.05.013
- Dotsika, E., Poutoukis, D., Michelot, J. L., and Raco, B. (2009). Natural tracers for identifying the origin of the thermal fluids emerging along the Aegean volcanic arc (Greece): evidence of arc-type magmatic water (ATMW) participation. *J. Volcanol. Geotherm. Res.* 179, 19–32. doi: 10.1016/j.jvolgeores.2008.09.024
- Etiopie, G., and Sherwood-Lollar, B. (2013). Abiotic methane on Earth. *Rev. Geophys.* 51, 276–299. doi: 10.1002/rog.20011
- Fernandez-Prini, R., Alvarez, J. L., and Harvey, A. H. (2003). Henry’s constants and vapor–liquid distribution constants for gaseous solutes in H₂O and D₂O at high temperatures. *J. Phys. Chem. Ref. Data* 32:903. doi: 10.1063/1.1564818
- Fitzgerald, W. F., and Lamborg, C. H. (2004). “Geochemistry of mercury in the environment,” in *Treatise on Geochemistry: Environmental Geochemistry*, Vol. 9, ed. B. S. Lollar (New York, NY: Elsevier, Inc).
- Francalanci, L., Vougioukalakis, G. E., Perini, G., and Manetti, P. A. (2005). “West-East traverse along the magmatism of the South Aegean volcanic arc in the light of volcanological, chemical and isotope data. Developments in Volcanology (Amsterdam, Olanda),” in *The South Aegean Active Volcanic Arc, Present Knowledge and Future Perspectives*, 7, eds M. Fitykas and G. E. Vougioukalakis (Amsterdam: Elsevier), 65–111. doi: 10.1016/S1871-644X(05)80033-6
- Gennaro, M. E., Grassa, F., Martelli, M., Renzulli, A., and Rizzo, A. L. (2017). Carbon isotope composition of CO₂-rich inclusions in cumulate-forming mantle minerals from Stromboli volcano (Italy). *J. Volcanol. Geotherm. Res.* 346, 95–103. doi: 10.1016/j.jvolgeores.2017.04.001
- Giggenbach, W. F. (1975). A simple method for the collection and analysis of volcanic gas samples. *Bull. Volcanol.* 39, 132–145. doi: 10.1007/BF02596953
- Giggenbach, W. F. (1980). Geothermal gas equilibria. *Geochim. Cosmochim. Acta* 44, 2021–2032. doi: 10.1016/0016-7037(80)90200-8
- Giggenbach, W. F. (1987). Redox processes governing the chemistry of fumarolic gas discharges from White Island, New Zealand. *Appl. Geochem.* 2, 143–161. doi: 10.1016/0883-2927(87)90030-8
- Giggenbach, W. F., (1991). “Geothermometry,” in *Isotopic and Chemical Techniques in Geothermal Exploration, Development and Use*, ed. S. Arnórsson (Vienna: International Atomic Agency), 119–142.
- Hilton, D. R., Fisher, T. P., and Marty, B. (2002). Noble gases and volatile recycling at subduction zones. *Rev. Mineral. Geochem.* 47, 319–370. doi: 10.2138/rmg.2002.47.9
- Hooft, E. E. E., Nomikou, P., Toomey, D. R., Lampridou, D., Getz, C., Christopoulou, M.-E., et al. (2017). Backarc tectonism, volcanism, and mass wasting shape seafloor morphology in the Santorini–Christiania–Amorgos region of the Hellenic Volcanic Arc. *Tectonophysics* 71, 396–414. doi: 10.1016/j.tecto.2017.06.005
- Hsin-Yi, W., Yuji, S., Naoto, T., Yama, T., Akizumi, I., Kentaro, T., et al. (2016). Helium and methane sources and fluxes of shallow submarine hydrothermal plumes near the Tokara Islands, Southern Japan. *Sci. Rep.* 6:34126. doi: 10.1038/srep34126
- Hubscher, C., Ruhnau, M., and Nomikou, P. (2015). Volcano-tectonic evolution of the polygenetic Kolumbo submarine volcano/Santorini (Aegean Sea). *J. Volcanol. Geotherm. Res.* 291, 101–111. doi: 10.1016/j.jvolgeores.2014.12.020

- Javoy, M., and Pineau, F. (1991). The volatiles record of a “popping” rock from the mid-Atlantic ridge at 14N: chemical and isotopic composition of gas trapped in the vesicles. *Earth Planet. Sci. Lett.* 107, 598–611. doi: 10.1016/0012-821X(91)90104-P
- Keir, R. (2010). A note on the fluxes of abiogenic methane and hydrogen from mid-ocean ridges. *Geophys. Res. Lett.* 37:L24609. doi: 10.1029/2010GL045362
- Kiliyas, S. P., Nomikou, P., Papanikolaou, D., Polymenakou, P. N., Godelitsas, A., Argyraki, A., et al. (2013). New insights into hydrothermal vent processes in the unique shallow submarine arc-volcano, Kolumbo (Santorini), Greece. *Sci. Rep.* 3:2421. doi: 10.1038/srep02421
- Klaver, M., Carey, S., Nomikou, P., Smet, I., Godelitsas, A., and Vroon, P. (2016). A distinct source and differentiation history for Kolumbo submarine volcano, Santorini volcanic field, Aegean arc. *Geochem. Geophys. Geosyst.* 17, 3254–3273. doi: 10.1002/2016GC006398
- Konstantinou, K. I., and Yeh, T.-Y. (2012). Stress field around the Coloumbo magma chamber, southern Aegean: Its significance for assessing volcanic and seismic hazard in Santorini. *J. Geodyn.* 54, 13–20. doi: 10.1016/j.jog.2011.09.003
- Lamborg, C. H., Von Damm, K. L., Fitzgerald, W. F., Hammerschmidt, C. R., and Zierenberg, R. (2006). Mercury and monomethylmercury in fluids from Sea Cliff submarine hydrothermal field. *Gorda Ridge Geophys. Res. Lett.* 33:L17606. doi: 10.1029/2006GL026321
- Lan, T. F., Sano, Y., Yang, T. F., Takahata, N., Shirai, K., and Pinti, D. (2010). Evaluating Earth degassing in subduction zones by measuring helium fluxes from the ocean floor. *Earth Planet. Sci. Lett.* 289, 317–322. doi: 10.1016/j.epsl.2010.07.049
- Le Pichon, X., and Angelier, J. (1979). The hellenic arc and trench system: a key to the neotectonic evolution of the eastern Mediterranean area. *Tectonophysics* 60, 1–42. doi: 10.1016/0040-1951(79)90131-8
- Lilley, M. D., Butterfield, D. A., Olson, E. J., Lupton, J. E., Macko, S. A., and McDuff, R. E. (1993). Anomalous CH₄ and NH₄⁺ concentrations at an unsedimented mid-ocean-ridge hydrothermal system. *Nature* 364, 45–47. doi: 10.1038/364045a0
- Lupton, J., Butterfield, D., Lilley, M., Evans, L., Ko-ichi, N., Chadwick, W., et al. (2006). Submarine venting of liquid carbon dioxide on a Mariana Arc volcano. *Geochem. Geophys. Geosyst.* 7:Q08007. doi: 10.1029/2005GC001152
- Lupton, J., Lilley, M., Butterfield, D., Evans, L., Embley, R., Massoth, G., et al. (2008). Venting of a separate CO₂-rich gas phase from submarine arc volcanoes: examples from the Mariana and Tonga-Kermadec arcs. *J. Geophys. Res.* 113, B08S12. doi: 10.1029/2007JB005467
- Lupton, J. D., Lilley, B. M., Ishibashi, J., Hey, D., and Evans, L. (1999). Gas chemistry of hydrothermal fluids along the East Pacific Rise, 5°S to 32°S (abstract). *Eos Trans.* 80:F1099. Fall Meet., Suppl.
- Mandalakis, M., Gavrilidou, A., Polymenakou, P. N., Christakis, C., Nomikou, P., Medvecký, M., et al. (2019). CO₂ vents at Kolumbo submarine volcano show microbial co-tolerance to high acidity and antibiotics. *Mar. Environ. Res.* in press.
- Mango, F. D. (2000). The origin of light hydrocarbons. *Geochim. Cosmochim. Acta* 51, 1549–1560. doi: 10.1016/S0016-7037(99)00389-0
- Marty, B. (2012). The origins and concentrations of water, carbon, nitrogen and noble gases on Earth. *Earth Planet. Sci. Lett.* 31, 56–66. doi: 10.1016/j.epsl.2011.10.040
- Marty, B., and Jambon, A. (1987). C/3He in volatile flux from the solid Earth: implications for carbon dynamics. *Earth Planet. Sci. Lett.* 83, 16–26. doi: 10.1016/0012-821X(87)90047-1
- Mazzini, A., Svensen, H., Etiope, E., Onderdonk, N., and Banks, D. (2011). Fluid origin, gas fluxes and plumbing system in the sediment-hosted Salton Sea Geothermal System (California, USA). *J. Volcanol. Geothermal Res.* 205, 67–83. doi: 10.1016/j.jvolgeores.2011.05.008
- McCormell, T. M., and Seewald, J. S. (2007). Abiotic synthesis of organic compounds in deep-sea hydrothermal environments. *Chem. Rev.* 107, 382–401. doi: 10.1021/cr0503660
- McDermott, J. M., Seewald, J. S., German, C. R., and Sylva, S. P. (2015). Pathways for abiotic organic synthesis at submarine hydrothermal fields. *PNAS* 112, 7668–7672. doi: 10.1073/pnas.1506295112
- McKenzie, D. (1972). Active tectonics of the Mediterranean region. *Geophys. J. R. Astron. Soc.* 30, 109–185. doi: 10.1111/j.1365-246X.1972.tb02351.x
- Nicholls, I. A. (1971). Petrology of Santorini Volcano. Cyclades, Greece. *J. Petrol.* 12, 67–119. doi: 10.1093/petrology/12.1.67
- Nomikou, P., Carey, S., Papanikolaou, D., Croff Bell, K., Sakellariou, D., Alexandri, M., et al. (2012). Submarine volcanoes of the Kolumbo volcanic zone NE of Santorini Caldera Greece. *Glob. Planet. Change* 9, 135–151. doi: 10.1016/j.gloplacha.2012.01.001
- Nomikou, P., Hübscher, C., Papanikolaou, D., Farangitakis, P. G., Ruhnau, M., and Lampridou, D. (2018). Expanding extension, subsidence and lateral segmentation within the Santorini - Amorgos basins during Quaternary: implications for the 1956 Amorgos events, central - south Aegean Sea. Greece. *Tectonophysics* 722, 138–153. doi: 10.1016/j.tecto.2017.10.016
- Nomikou, P., Hübscher, C., Ruhnau, M., and Bejelou, K. (2016). Tectonophysics Tectono-stratigraphic evolution through successive extensional events of the Anydros Basin, hosting Kolumbo volcanic field at the Aegean. *Tectonophysics* 671, 202–217. doi: 10.1016/j.tecto.2016.01.021
- Nomikou, P., Papanikolaou, D., Alexandri, M., Sakellariou, D., and Rousakis, G. (2013). Submarine volcanoes along the Aegean volcanic arc. *Tectonophysics* 59, 123–146. doi: 10.1128/AEM.01835-08
- Oppenheimer, C., Fischer, T. P., and Scaillet, B. (2014). “Volcanic degassing: process and impact” in *Treatise on Geochemistry, The Crust*, 2nd Edn, eds H. D. Holland and K. K. Turekian (Amsterdam: Elsevier), 111–179.
- Oulas, A., Polymenakou, P. N., Seshadri, R., Tripp, H. J., Mandalakis, M., Paez-Espino, A. D., et al. (2015). Metagenomic investigation of the geologically unique Hellenic Volcanic Arc reveals a distinctive ecosystem with unexpected physiology. *Environ. Microbiol.* 18, 1122–1136. doi: 10.1111/1462-2920.13095
- Ozima, M., and Podosek, F. A. (1983). *Noble Gas Geochemistry*. New York, NY: Cambridge University Press.
- Paonita, A., Federico, C., Bonfanti, P., Capasso, G., Inguaggiato, S., Italiano, F., et al. (2013). The episodic and abrupt geochemical changes at La Fossa fumaroles (Vulcano Island, Italy) and related constraints on the dynamics, structure, and compositions of the magmatic system. *Geochim. Cosmochim. Acta* 120, 158–178. doi: 10.1016/j.gca.2013.06.015
- Parks, M., Biggs, J., England, P., Mather, T., Nomikou, P., Palamartchouk, K., et al. (2013). The episodic and abrupt geochemical changes at La Fossa fumaroles (Vulcano Island, Italy) and related constraints on the dynamics, structure, and compositions of the magmatic system. *Geochim. Cosmochim. Acta* 120, 158–178. doi: 10.1016/j.gca.2013.06.015
- Parks, M. M., Caliro, S., Chiodini, G., Pyle, D. M., Mather, T. A., Berlo, K., et al. (2013). Distinguishing contributions to diffuse CO₂ emissions in volcanic areas from magmatic degassing and thermal decarbonation using soil gas 222Rn–813C systematics: application to Santorini volcano, Greece. *Earth Planet. Sci. Lett.* 377, 180–190. doi: 10.1016/j.epsl.2013.06.046
- Pe-Piper, G., and Piper, D. J. W. (2007). The South Aegean active volcanic arc: relationships between magmatism and tectonics. *Dev. Volcanol.* 7, 113–133. doi: 10.1016/S1871-644X(05)80034-8
- Proskurowski, G., Lilley, M. D., Seewald, J. S., Fruh-Green, G. L., Olson, E. J., Lupton, J. E., et al. (2008). Abiogenic hydrocarbon production at Lost City hydrothermal field. *Science* 319, 604–607. doi: 10.1126/science.1151194
- Rayleigh, J. W. S. (1896). Theoretical considerations respecting the separation of gases by diffusion and similar processes. *Philos. Mag.* 42:493. doi: 10.1080/14786449608620944
- Rizzo, A. L., Barberi, F., Carapezza, M. L., Di Piazza, A., Francalanci, L., Sortino, F., et al. (2015). New mafic magma refilling a quiescent volcano: evidence from He-Ne-Ar isotopes during the 2011–2012 unrest at Santorini, Greece. *Geochem. Geophys. Geosyst.* 16, 798–814. doi: 10.1002/2014GC005653
- Rizzo, A. L., Caracausi, A., Chavagnac, V., Nomikou, P., Polymenakou, P. N., Mandalakis, M., et al. (2016). Kolumbo submarine volcano (Greece): an active window into the Aegean subduction system. *Sci. Rep.* 6:28013. doi: 10.1038/srep28013
- Sander, R. (2015). Compilation of Henry's law constants (version 4.0) for water as solvent. *Atmos. Chem. Phys.* 15, 4399–4981. doi: 10.5194/acp-15-4399-2015
- Sano, Y., and Marty, B. (1995). Origin of carbon in fumarolic gases from island arcs. *Chem. Geol.* 119, 265–274. doi: 10.1016/0009-2541(94)00097-R
- Schoell, M. (1980). The hydrogen and carbon isotopic composition of methane from natural gases of various origins. *Geochim. Cosmochim. Acta* 44, 649–661. doi: 10.1016/0016-7037(80)90155-6
- Sigurdsson, H., Carey, S., Alexandri, M., Vougioukalakis, G., Croff, K., Roman, C., et al. (2006). Marine investigations of Greece's Santorini Volcanic Field. *EOS Trans. Am. Geophys. Union* 87:337. doi: 10.1029/2006EO340001

- Spandler, C., Martin, L. H. J., and Pettker, T. (2012). Carbonate assimilation during magma evolution at Nisyros (Greece), South Aegean Arc: evidence from clinopyroxenite xenoliths. *Lithos* 146, 18–33. doi: 10.1016/j.lithos.2012.04.029
- Stucker, V. K., Walker, S. L., de Ronde, C. E. J., Caratori Tontini, F., and Tsuchida, S. (2017). Hydrothermal venting at Hinepua submarine volcano, Kermadec arc: understanding magmatic-hydrothermal fluid chemistry. *Geochem. Geophys. Geosyst.* 18, 3646–3661. doi: 10.1002/2016GC006713
- Stull, D. R., Westrum, E. F., and Sinke, G. G. (1969). *The Chemical Thermodynamics of Organic Compounds*. Hoboken, NJ: Wiley.
- Taran, Y., Torokhov, P., Pokrovski, G., and Shabayeva, I. (1992). Isotopic composition of mineral precipitates and free gas associated with hydrothermal vents of Piip submarine volcano, Bering Sea. *Geochem. J.* 26, 291–297. doi: 10.2343/geochemj.26.291
- Taran, Y. A., and Gigenbach, W. F. (2003). “Geochemistry of light hydrocarbons in subduction-related volcanic and hydrothermal fluids,” in *Volcanic, Geothermal, and ore Forming Fluids: Rulers and Witnesses of Processes within the Earth*, Vol. 10, eds S. F. Simmons and I. J. Graham (Littleton, CO: Economic Geologists Special Publication), 61–74.
- Taran, Y. A., Kliger, G. A., Cienfuegos, E., and Shuykin, A. N. (2010a). Carbon and hydrogen isotopic compositions of products of open-system catalytic hydrogenation of CO₂: implications for abiogenic hydrocarbons in Earth's crust. *Geochim. Cosmochim. Acta* 74, 6112–6125. doi: 10.1016/j.gca.2010.08.012
- Taran, Y. A., Varley, N. R., Inguaggiato, S., and Cienfuegos, E. (2010b). Geochemistry of H₂- and CH₄-enriched hydrothermal fluids of Socorro Island, Revillagigedo Archipelago, Mexico. Evidence for serpentinization and abiogenic methane. *Geofluids* 10, 542–555. doi: 10.1111/j.1468-8123.2010.00314.x
- Tassi, F., Capaccioni, B., Caramanna, G., Cinti, D., Montegrossi, G., Pizzino, L., et al. (2009). Low-pH waters discharging from submarine vents at Panarea Island (Aeolian Islands, southern Italy) after the 2002 gas blast: origin of hydrothermal fluids and implications for volcanic surveillance. *Appl. Geochem.* 24, 246–254. doi: 10.1016/j.apgeochem.2008.11.015
- Tassi, F., Capaccioni, B., and Vaselli, O. (2014). Compositional spatial zonation and 2005–2013 temporal evolution of the hydrothermal-magmatic fluids from the submarine fumarolic field at Panarea Island. *J. Volcanol. Geothermal Res.* 277, 41–50. doi: 10.1016/j.jvolgeores.2014.03.010
- Tassi, F., Fiebig, J., Vaselli, O., and Nocentini, M. (2012). Origins of methane discharging from volcanic-hydrothermal, geothermal and cold emissions in Italy. *Chem. Geol.* 31, 36–48. doi: 10.1016/j.chemgeo.2012.03.018
- Tassi, F., Vaselli, O., Papazachos, C. B., Giannini, L., Chiodini, G., Vougioukalakis, G. E., et al. (2013). Geochemical and isotopic changes in the fumarolic and submerged gas discharges during the 2011–2012 unrest at Santorini caldera (Greece). *Bull. Volcanol.* 75, 1–15. doi: 10.1007/s00445-013-0711-8
- Tsunogai, U., Ishibashia, J., Wakita, H., Gamob, T., Watanabec, K., Kajimurac, T., et al. (1994). Peculiar features of Suiyo Seamount hydrothermal fluids, Izu-Bonin Arc: differences from subaerial volcanism. *Earth Planet. Sci. Lett.* 126, 289–301. doi: 10.1016/0012-821X(94)90113-9
- Varekamp, J. C., and Buseck, P. R. (1981). Mercury emissions from Mount St. Helens during September 1980. *Nature* 293, 555–556. doi: 10.1038/293555a0
- Von Damm, K. L. (1995). “Controls on the chemistry and temporal variability of seafloor hydrothermal fluids,” in *Seafloor Hydrothermal Systems: Physical, Chemical, Biological, and Geological Interactions*, Vol. 91, eds S. E. Humphris, R. A. Zierenberg, L. S. Mullineaux, and R. E. Thomson (Washington, DC: AGU), 222–247.
- Von Damm, K. L., Oosting, S. E., Kozlowski, R., Buttermore, L. G., Colodner, D. C., Edmonds, H. N., et al. (1995). Evolution of East Pacific Rise hydrothermal vent fluids following a volcanic eruption. *Nature* 375, 47–50. doi: 10.1038/375047a0
- Wang, D. T., Reeves, E. P., McDermott, J. M., Seewald, J. S., and One, S. (2018). Clumped isotopologue constraints on the origin of methane at seafloor hot springs. *Geochim. Cosmochim. Acta* 223, 141–158. doi: 10.1016/j.gca.2017.11.030
- Welhan, J. A. (1988). Origins of methane in hydrothermal systems. *Chem. Geol.* 71, 183–198. doi: 10.1016/0009-2541(88)90114-3
- Wen, H.-Y., Sano, Y., Takahata, N., Tomonaga, Y., Ishida, A., Tanaka, K., et al. (2016). Helium and methane sources and fluxes of shallow submarine hydrothermal plumes near the Tokara Islands, Southern Japan. *Sci. Rep.* 6:34126. doi: 10.1038/srep34126
- Whiticar, M. J. (1999). Carbon and hydrogen isotope systematics of bacterial formation and oxidation of methane. *Chem. Geol.* 161, 291–314. doi: 10.1016/S0009-2541(99)00092-3
- Xue-Gang, C., Hai-Yan, Z., Xiaohu, L., Chen-Tung, A., Chen, T., Frank, Y., et al. (2016). The chemical and isotopic compositions of gas discharge from shallow-water hydrothermal vents at Kueishantao, offshore northeast Taiwan. *Geochem. J.* 50, 341–355. doi: 10.2343/geochemj.2.0425
- Yang, T. F., Lan, T. F., Hsiao-Fen, L., Ching-Chou, F., Pei-Chuan, C., Ching-Hua, L., et al. (2005). Gas compositions and helium isotopic ratios of fluid samples around Kueishantao, NE offshore Taiwan and its tectonic implications. *Geochem. J.* 39, 469–480. doi: 10.2343/geochemj.39.469
- Zhang, J., Quay, P. D., and Wilbur, D. O. (1995). Carbon isotope fractionation during gas-water exchange and dissolution of CO₂. *Geochim. Cosmochim. Acta* 59, 107–114. doi: 10.1016/0016-7037(95)91550-D

Conflict of Interest Statement: The authors declare that the research was conducted in the absence of any commercial or financial relationships that could be construed as a potential conflict of interest.

Copyright © 2019 Rizzo, Caracausi, Chavagnac, Nomikou, Polymenakou, Mandalakis, Kotoulas, Magoulas, Castillo, Lampridou, Maruszczak and Sonke. This is an open-access article distributed under the terms of the Creative Commons Attribution License (CC BY). The use, distribution or reproduction in other forums is permitted, provided the original author(s) and the copyright owner(s) are credited and that the original publication in this journal is cited, in accordance with accepted academic practice. No use, distribution or reproduction is permitted which does not comply with these terms.



The Graham Volcanic Field Offshore Southwestern Sicily (Italy) Revealed by High-Resolution Seafloor Mapping and ROV Images

Danilo Cavallaro* and Mauro Coltelli

Istituto Nazionale di Geofisica e Vulcanologia, Sezione di Catania, Osservatorio Etneo, Catania, Italy

OPEN ACCESS

Edited by:

Guido Giordano,
Roma Tre University, Italy

Reviewed by:

Dario Pedrazzi,
Instituto de Ciencias de la Tierra
Jaume Almera (ICTJA), Spain
Claudia Romagnoli,
University of Bologna, Italy

*Correspondence:

Danilo Cavallaro
danilo.cavallaro@ingv.it

Specialty section:

This article was submitted to
Volcanology,
a section of the journal
Frontiers in Earth Science

Received: 07 April 2019

Accepted: 08 November 2019

Published: 26 November 2019

Citation:

Cavallaro D and Coltelli M (2019)
The Graham Volcanic Field Offshore
Southwestern Sicily (Italy) Revealed
by High-Resolution Seafloor Mapping
and ROV Images.
Front. Earth Sci. 7:311.
doi: 10.3389/feart.2019.00311

The understanding of submarine monogenetic volcanic fields, especially if located near to coastal areas, is fundamental for volcanic risk assessment. Using high-resolution bathymetric data and ROV images, the submarine Graham volcanic field, located 40–50 km offshore southwestern Sicily (Italy), has been described in detail. The field comprises a ten of monogenetic volcanic seamounts aligned along a N-S trending belt at 150–250 m water depths and includes the relict of the short-lived “Ferdinanda Island” produced during the well-documented 1831 “Surtseyan-type” eruption. The present-day morphology of the cones is the result of the interplay between volcanic activity, wave and current erosion, mass-wasting and depositional processes, in relationship with sea-level change, acting in both subaerial and submarine environments. The analysis of the morphometric parameters allowed a detailed morphological classification of the cones. The seamounts are composed of poorly consolidated tephra and show steep slopes and pointy or flat tops, often characterized by sub-vertical knolls. Taking into account analogies with other volcanic seamounts worldwide, the analysis of some morphological characteristics, such as presence and depth of terraces on top and along the slope of the cones in relationship with sea-level fluctuations, allowed us to hypothesize a Late Pleistocene-Holocene age for the volcanism forming the field. The probably older Terribile volcanic field was also identified on the adjacent Terribile Bank and analyzed. Numerous mass-transport deposits and pockmarks were identified in the surroundings of the volcanic fields, suggesting the occurrence of diffuse slope failures and fluid releases, respectively. The distribution and shape of the cones within the volcanic fields provided important insights into the interaction between volcanism and tectonics. The alignment of the cones and the main axis of the clusters in which they are grouped revealed two preferred directions, N-S and NW-SE, respectively, which are consistent with those of the main tectonic structures of the Sicily Channel. The detailed bathymorphological analysis of the cones proved the monogenetic nature of this volcanism, which represents a peculiarity since it took place outside the typical geodynamic settings of other volcanic fields worldwide such as subduction or oceanic rift zones, and far from long-lived volcanic systems.

Keywords: submarine volcanism, volcanic field, submarine terraces, bathymetric data, ROV images, Surtseyan-type eruption, Ferdinanda Island, Graham Bank

INTRODUCTION

Monogenetic volcanic fields occur in several areas worldwide and within different geodynamic settings such as subduction, intraplate and rift zones (Kereszturi and Németh, 2012; Cañón-Tapia, 2016). Nevertheless, they are mostly associated with extensional regimes and sometimes are located along transfer zones (e.g., Camargo volcanic field, Chihuahua, Mexico, Aranda-Gómez et al., 2003). Monogenetic volcanic fields are generally isolated from large composite volcanoes, however, they can form in the immediate surroundings of long-lived volcanic systems such as major calderas, stratovolcanoes and shield volcanoes, in both subaerial and submarine environments. While individual volcanoes within the fields have geologically short life spans and are generally monogenetic, the fields themselves can be active for several million years (Németh, 2010; Valentine and Connor, 2015). A monogenetic basaltic volcanic field may comprise from tens to hundreds of individual volcanic centers, generally erupting a small volume of magma (typically $< 1 \text{ km}^3$) as both pyroclastic products and lava flows (Németh and Kereszturi, 2015). Individual volcanic centers within a field are commonly arranged to form clusters and alignments, attesting a control by underlying tectonic structures and stress regime (Németh, 2010; Cañón-Tapia, 2016).

Underwater monogenetic volcanic fields are located on both deep and shallow waters. They often develop on ocean ridges, such as those identified within the Azores Archipelago (Casalbore et al., 2015) or near Easter Island in the southeastern Pacific (Rappaport et al., 1997), on subduction zones like the Aegean Volcanic Arc (Foutrakis and Anastakis, 2018) and in intraplate setting such as those surrounding Canary Islands (Romero Ruiz et al., 2000) or Bridge Point-Aorere Point volcanic center, offshore Otago, New Zealand (Cas et al., 1989). Shallow water submarine volcanic fields are usually originated by hydromagmatic eruptions known as “Surtseyan-type” (Kokelaar, 1983; White and Houghton, 2000), bearing the name from the 1963–67 eruption, which began at about -140 m , generating the small island (Surtsey) off South Iceland (Thorarinsson, 1967; Kokelaar and Durant, 1983). These explosive eruptions are characterized by the formation of small- to medium-size scoria cones, and generally, their intensity is progressively restricted with increasing water depth (Cas and Giordano, 2014). Recent shallow submarine volcanic activity also occurred at Capelinhos (Machado et al., 1962) and Baixa da Serreta Bank (Weston, 1964), offshore the Azores Islands; Kavachi volcano, Solomon Islands (Baker et al., 2002); Hunga Haapai, Tonga (Vaughan and Webley, 2010); offshore El Hierro, Canary Islands (Rivera et al., 2013); Socorro Island, offshore Mexico (Siebe et al., 1995); Nishima-Shima, Izu Volcanic Arc, Japan (Global Volcanism Program, 2013b).

The morphology of underwater volcanic edifices, especially if forming islands, since their formation and during their evolution, is strictly controlled by the competition between constructive (volcanic and depositional activity) and destructive processes (such as wave and current erosion, mass-wasting and subsidence) acting both in subaerial and submarine environments (Ramalho et al., 2013; Romagnoli and Jakobsson, 2015). This is particularly

important for short-lived cones made by pyroclastic rocks (White, 1996). Primary controls on the shape of volcanic seamounts are: tectonic setting; effusion rate and magma physical properties (mainly viscosity and gas content); shape, size and geometry of magma supply conduits; age and thickness of the lithosphere; thermal and compositional heterogeneities of the mantle, depth of the eruption site (Rappaport et al., 1997 and references therein). Water depth is one of the main controls of submarine eruptions since the hydrostatic pressure generally inhibits the amount of magma erupted and the explosivity of the eruption (Kokelaar, 1986; White, 1996; Cas and Giordano, 2014).

Once volcanic processes end, the scoria cones emerging above sea level are rapidly affected by wave-current erosion, resulting in formation of shoals; therefore, the existence of surtseyan cones maybe ephemeral (Schmidt and Schmincke, 2002).

Submarine volcanic cones within fields show a variety of morphologies ranging from pointy to flat-topped cones. The pointy cones reflect the lack of wave erosion processes affecting their summits, suggesting that they have not reached the near sea-surface during their life cycle. Conversely, the flat-topped cones can be formed either by wave-dominated erosive activity at wave base level (Cas et al., 1989; Trenhaile, 2000; Schmidt and Schmincke, 2002) or by lava infillings of early stage summit craters or calderas (Clague et al., 2000b), or else as continuously and long-lasting overflowing submarine lava ponds (Clague et al., 2000a). Moreover, many cones, during and after the time they were erupting often exhibit hydrothermal activity, highlighted by the presence of pockmark and fumarole fields.

The post-emplacement morphology of seamounts reflects several other processes, which interplay in a complex manner to modify their present-day shape: isostatism, tectonic deformation (e.g., uplift or subsidence), hydrothermal activity, subsidence due to compaction, slope failures, lithology and mechanical properties of the volcanic products, amplitude of eustatic change, wave and currents parameters, coral reef growth and biogenic production (Ramalho et al., 2013 and references therein).

Generally, on volcanic islands, particularly of polygenetic origin and recent formation, the timing and magnitude of relative sea-level change can be difficult to evaluate due to the possible occurrence of crustal vertical deformation induced by long-term regional tectonic and short-term volcano-tectonic processes (Lucchi et al., 2019). However, for scattered small monogenetic volcanic cones, as is the case of those forming a volcanic field, the deformation induced by volcanic processes are highly attenuated because of the lack of any long-lived volcanic center, plumbing system, magmatic reservoir, etc.; the subsidence for compaction is also minimized because of the generally low amount of pyroclastic material.

Summit abrasion platforms and submarine terraces result mainly from the combined work of wave erosion and sea-level change, and so their width and maximum depth experienced adjustments depending on the variability of the sea oscillations (Trenhaile, 1989, 2001). Summit abrasion platforms and submarine volcanoclastic terraces (SDTs) can be used, if supported by data on the vertical mobility affecting the area, as proxies for reconstructing relative sea-level positions with the purpose of constraining the age of the associated volcanism

(Casalbore et al., 2017). In particular, the depth of the summit abrasion platforms of truncated cones can be used to likely infer the age of the erosive activity flattening them, and thus may furnish a tool to reconstruct relative sea-level positions, taking into account the analogy with the present-day wave erosion level. Similarly, the inner margin of a marine terrace bounded by a paleo-cliff can be considered as a proxy of the shoreline position at the time of its formation.

SDTs are terrace-shaped sedimentary prograding wedges, found at variable water depths on continental and insular shelves characterized by high-energy marine settings. Their formation is associated with the downward transport of sediments from the surf zone and shoreface in stormy conditions during a highstand (interglacial) sea level peak (Hernández-Molina et al., 2000; Casalbore et al., 2017). The depositional edges (or rollover depth, Mitchell et al., 2012a) of the present-day SDTs lie at depths approximating the modern local storm-wave base level, and vary between 15 and 60 m bsl in the different areas of the world depending on the different wave climate conditions (in the western Mediterranean they were measured at about –32 m by Mitchell et al., 2012a, while in the Tyrrhenian Sea at 10–30 m below sea level (bsl) by Casalbore et al., 2017). Thus, they can be used for paleo sea-level estimation as modern analogs for relict terraces having depositional edges at greater depths, formed in the past (after the LGM – Last Glacial Maximum), when the sea level was lower, as well as to estimate local vertical movements (Casalbore et al., 2017).

Since volcanic activity in shallow water may result in explosive eruptions (Kokelaar and Durant, 1983) and tsunami generation (Latter, 1981), improving the knowledge of time-space activity forming submarine monogenetic volcanic fields, especially if located close to coastal areas, would be of great interest for volcanic risk assessment, which is mostly associated with the local navigation.

Based on multibeam echo-sounder data, Coltelli et al. (2016) recognized a small submarine volcanic field (hereby-named Graham volcanic field, GVF) in the surroundings of the Graham Bank (northwestern portion of Sicily Channel, Italy), the place of the 1831 submarine eruption, which originated the ephemeral “Ferdinandea Island.” In this study we present a new detailed bathy-morphological analysis of the cones composing the GVF with particular reference to the Ferdinandea shoal being the youngest of the field. Ferdinandea cone represents a well-documented example of a previous island turning into a seamount. Since its formation, “Ferdinandea Island” has suffered a strong wave and current erosive activity causing its rapid submersion, which substantially modified its original shape. The bathy-morphological analysis of another volcanic field (hereby-named Terribile volcanic field, TVF), identified on the near Terribile Bank, was also carried out.

In order to prove the monogenetic nature of the volcanism originating the fields, the relationship between the morphology of the seamounts and underwater volcanic processes was studied. Another goal was to verify a potential interaction between volcanism and tectonics in the formation and distribution of the seamounts within the volcanic field through an analysis of the main direction of the clusters in which they were grouped.

For the same aim, since the ellipticity of the base of cones is often influenced by the direction of the main stress axis acting at time of their formation (Tibaldi, 1995; Corazzato and Tibaldi, 2006; Németh, 2010), a morphologic classification, focused on measuring the main dimensions and morphometric associated parameters of the seamounts, was carried out.

Finally, we inferred the possible age of formation of GVF, by comparing the post-eruptive morphological characteristics of other short-lived pyroclastic cones worldwide (such as the satellite volcanic centers formed during the 1963 eruption at Surtsey; Romagnoli and Jakobsson, 2015) to the Ferdinandea seamount and then to the other seamounts of the field in relationship with sea-level change.

This study may also provide a key to better understand the volcano-tectonic setting of this region and furnish a useful comparison for other submarine areas affected by monogenetic volcanism.

GEOLOGICAL SETTING

The study area is located in the northwestern sector of the Sicily Channel, Central Mediterranean Sea (**Figure 1**). The Sicily Channel belongs to the northern margin of the African continental plate, called the Pelagian Block (Burlot et al., 1978), which corresponds to the foreland area of the Sicilian sector of the Apenninian-Maghrebian fold-and-thrust belt. Its geodynamic setting is the product of the Neogene collision between the African and European plate margins associated with the NW-SE oriented Late Miocene–Quaternary continental rifting, which produced the Pantelleria, Linosa, and Malta grabens (Jongsma et al., 1985; Boccaletti et al., 1987; Reuther et al., 1993). The Sicily Channel consists of a 6–7 km thick Mesozoic-Cenozoic shallow-to deep-water carbonate sedimentary successions with repeated intercalations of volcanic deposits, covered by Upper Tortonian–Lower Messinian siliciclastic deposits and Plio-Quaternary clastic sequences (Torelli et al., 1995).

The northern side of the Sicily Channel is characterized by a very uneven bathymetry, being a composite array of shallow continental shelves (the Siculo-Maltese Shelf and the Adventure, and Malta plateau), deep depressions, such the fault-controlled Pantelleria, Linosa, and Malta grabens and a foredeep depocenter (the Gela Basin), and topographic highs, such as several small- to middle-scale banks of sedimentary origin (e.g., the Nerita, Terribile, Nameless, and Madrepora banks) (Colantoni, 1975; Calanchi et al., 1989; Cavallaro et al., 2017; **Figure 1**). Within the Sicily Channel, a widespread and scattered volcanism is known to have occurred during Upper Miocene to Pleistocene times, building up the alkaline volcanic islands of Linosa and Pantelleria and several other volcanic centers (e.g., Anfitrite, Tetide Galatea, Cimotoc banks) (Beccaluva et al., 1981; Calanchi et al., 1989; Rotolo et al., 2006; Civile et al., 2008, 2015; Lodolo et al., 2012, 2019a,b; Pensa et al., 2019; **Figure 1**). Volcanism occurred up to historical times, with the 1831 submarine eruptions of Ferdinandea Island (Gemmellaro, 1831; Marzolla, 1831; Colantoni et al., 1975; Dean, 1980) and the 1891 eruption off NW Pantelleria Island (Washington, 1909;

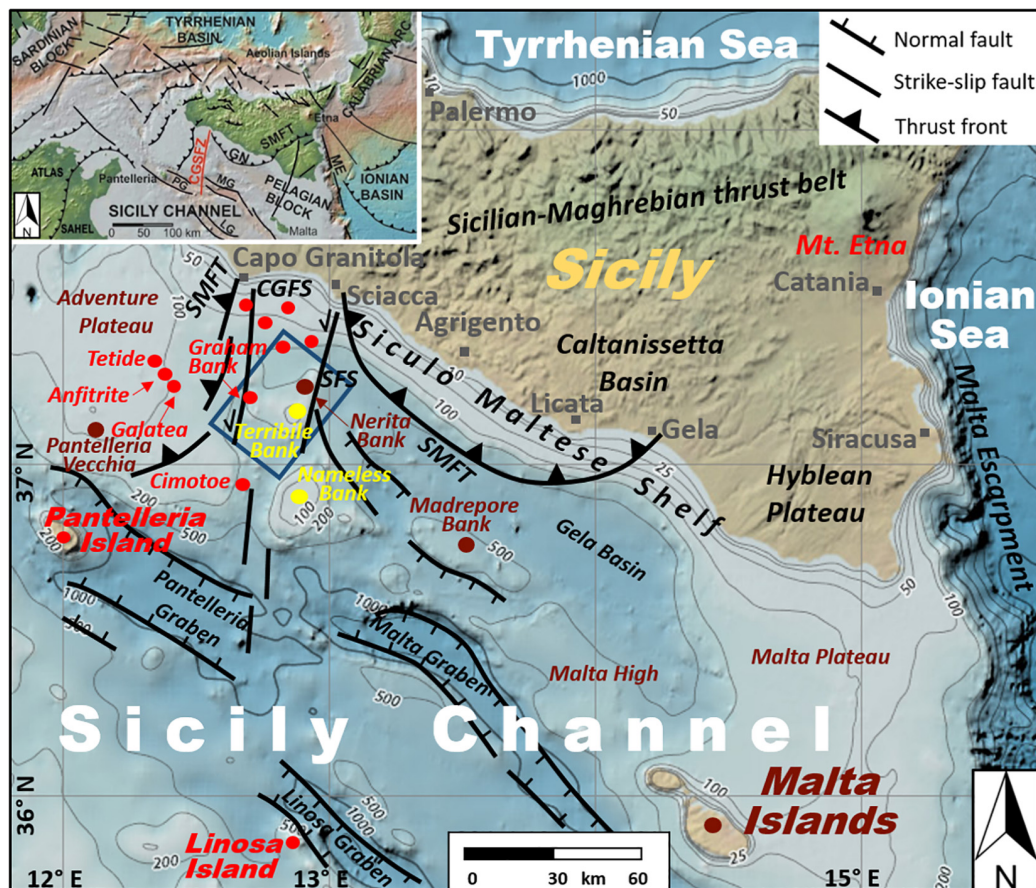


FIGURE 1 | Shaded-relief bathymetric map of the northern portion of the Sicily Channel (from GEBCO-General Bathymetric Chart of the Oceans-Digital Atlas). The blue box shows the study area; the red, brown and yellow circles indicate the location of volcanic centers, sedimentary banks and sedimentary banks with scattered volcanic manifestations on top, respectively (from Calanchi et al., 1989; Civile et al., 2015, 2018; Lodolo et al., 2019a). CGFS, Capo Granitola fault system; SFS, Sciaccia fault system; SMFT, Sicilian-Maghrebian fold-and-thrust belt front (from Civile et al., 2018). The inset shows the geodynamic setting of the Central Mediterranean; GN, Gela Nappe; ME, Malta Escarpment; PG, Pantelleria Graben; LG, Linosa Graben; MG, Malta Graben; CGSFZ, Capo Granitola-Sciaccia Fault Zone (from Civile et al., 2018).

Conte et al., 2014). Some of these volcanic centers are sited in an area extending from the Adventure Plateau to the Nameless Bank, informally known as the “Campi Flegrei del Mar di Sicilia” (Global Volcanism Program, 2013a).

The volcanic centers of the GVF, those on the Nameless Bank and in the nearshore of Capo Granitola-Sciaccia coast, together with Cimotote volcanic seamount (Civile et al., 2015, 2018; Coltelli et al., 2016; Lodolo et al., 2019a), are aligned along a nearly N-S oriented belt extending southwards for almost 200 km up to Linosa Island. This belt was related to a lithospheric-scale transpressive transfer zone (the Capo Granitola-Sciaccia Fault Zone, CGSFZ; see inset in Figure 1) between the western and eastern sectors of the Sicily Channel Rift Zone, characterized by different amount of rifting (Argnani, 1990; Civile et al., 2014, 2018). The CGSFZ is also positioned between two tectonically independent sectors of the offshore part of the Sicilian-Maghrebian Chain, characterized by different deformation ages, structural trends and tectonic evolution, playing a key role in the Neogene-Quaternary geodynamic

evolution of the region (Argnani, 1990; Corti et al., 2006; Civile et al., 2008, 2014, 2018; Ghisetti et al., 2009; Calò and Parisi, 2014; Cavallaro et al., 2017; Fedorik et al., 2018; Ferranti et al., 2019). The CGSFZ is composed of two major left-lateral strike-slip systems: the Capo Granitola fault system (CGFS) to the west, which affects the GVF area, and the Sciaccia fault system (SFS) to the east (Figure 1), which bounds the eastern extent of the Nerita and Terribile banks (Civile et al., 2018; Fedorik et al., 2018; Ferranti et al., 2019). Ferranti et al. (2019), based on seismic reflection profiles, inferred that folds and faults offshore Capo Granitola and Sciaccia are different scale expression of the CGFS and SFS, which were active in left transpression since the Latest Miocene-Early Pliocene and are still active; transpressional deformation along the southern segments of the CGFS and SFS inverted the previous Late Tortonian-Early Messinian extensional or transtensional basins with an uplift rate of about 2 mm/yr during the Plio-Quaternary. The CGSFZ is also characterized by moderate seismicity (Coltelli et al., 2016) with large seismic

gaps in the proximity of the Graham Bank, associated with the geothermal and volcanic activity (Calò and Parisi, 2014), and by remarkable magnetic anomalies (Colantoni et al., 1975; Lodolo et al., 2012).

Other volcanic seamounts are arranged to form minor clusters with different orientations, like the three small volcanic shoals, Tetide (summit depth at -18 m), Anfitrite (-35 m) and Galatea (-74 m), located on the Adventure Plateau along a nearly 10 km long NW-SE oriented alignment (Calanchi et al., 1989; Civile et al., 2014, 2015; Pensa et al., 2019; **Figure 1**).

Despite such diffuse volcanism affecting the northern Sicily Channel, no quaternary volcanism occurs onshore in south-west Sicily.

The study area includes three banks: Nerita, Terribile and Graham (**Figures 1, 2**).

The Nerita Bank is a morphological high, elongated in a NNE-SSW direction (**Figure 2**). On the basis of seismic reflection profiles, it was interpreted as an almost symmetrical push-up structure of carbonate origin, generated along strike-slip tectonic faults (i.e., SFS), lacking volcanic structures on it (Argnani, 1990; Civile et al., 2015, 2018; Fedorik et al., 2018).

The Terribile Bank is a carbonate submarine plateau (Colantoni, 1975), with several small conical-shaped structures on top (**Figure 2**); seismic profiles indicate that it is made of an Upper Cretaceous-Eocene to Lower Miocene carbonate succession, overlapped to the west by Tortonian-Messinian sediment missing the Pliocene-Quaternary sequence (Civile et al., 2018).

The Graham Bank includes two volcanic seamounts, the smallest of which is the relict of the short-lived “Ferdinanda Island,” originated during the 1831 Surtseyan-type eruption, which represents the only well-documented volcanic event occurred in the study area; other volcanic activities were uncertainly reported in the surroundings of Graham Bank during the first Punic war (264–241 BC) (Guidoboni et al., 2002; Bottari et al., 2009), in 1632, 1833, and 1863 (Antonoli et al., 1994; Falzone et al., 2009). Moreover, numerous episodes of strong gas releases in the Graham Bank area were observed in 1816 (Mercalli, 1883), 1845, 1942 and more recently in 2003.

The emersion and disappearance of the island during and after the 1831 submarine eruption are well-described in literature (Gemmellaro, 1831; Marzolla, 1831; Dean, 1980). The eruption was preceded, between the end of June and the first days of July 1831, by an intense seismic activity, which produced damage in the Sciacca area. On July 16–17 the island emerged; during the following weeks it grew up rapidly in size, reaching 600 m in diameter and about 60 m in height. The eruption ceased on August 16, after about 6 weeks of activity. During the following months, the island was rapidly dismantled by the sea: at the end of September it was some 20 m high; 1 month later it consisted of a less than a one-meter-high islet, and finally, between December 1831 to January 1832, it completely disappeared. Two bathymetric surveys carried out in 1883 and 1914 by the Istituto Idrografico Regia Marina described the top of the shoal at 3 and 8 m bsl, respectively (Falautano et al., 2010). While the bathymetric survey carried out in 2012 (this paper) and those in 2012 and 2014

by the Istituto Idrografico della Marina (IIM) (Sinapi et al., 2016) measured the top at about 9 m bsl.

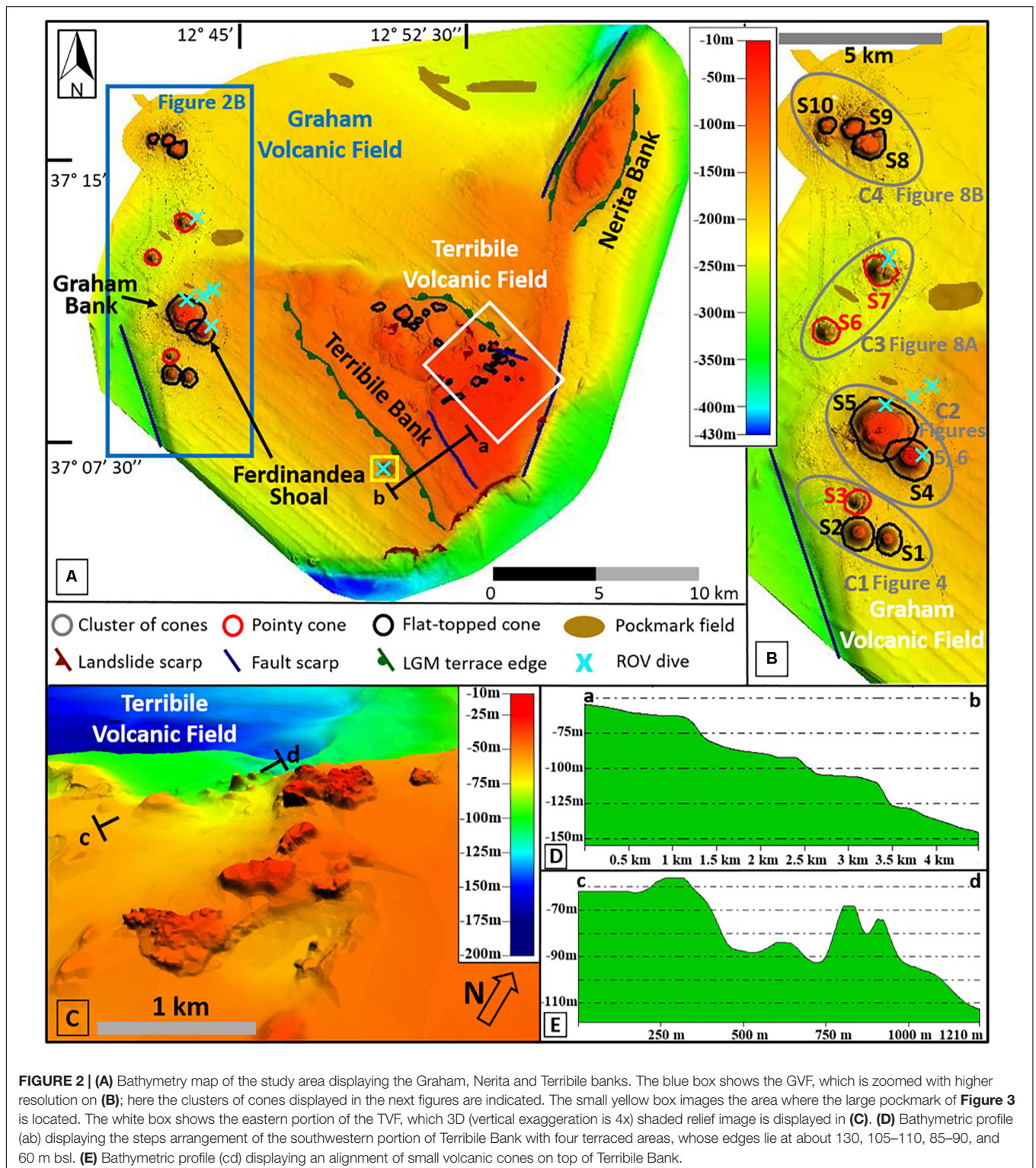
Dredged rocks from the Graham Bank consist mainly of poorly evolved alkali basalts (Calanchi et al., 1989; Rotolo et al., 2006). A piece of a palagonitized tephra layer was sampled at the base of the northern side of the Graham Bank, likely representing the consolidated deposit of the final surtseyan explosive activity of the 1831 eruption (Coltelli et al., 2016).

The composition of a gas sample, collected within a fumarole filed at 155 m water depth near the base of the eastern cone of the Graham Bank, revealed a significant mantle component; helium and carbon isotope compositions of gas emitted from the seafloor reflect a clear magmatic/crustal origin (Coltelli et al., 2016). Petrological data suggest that all the volcanic centers of the Sicily Channel lack a shallow-level magma chamber, where primitive magmas could pond and fractionate and crustal contamination is generally absent (Rotolo et al., 2006).

Finally, in the proximity of the GVF, three deposits of dead red coral have been discovered (Di Geronimo et al., 1993). They may have accumulated, during the post-LGM, as consequence of periodic collapses, possibly associated with volcanic and/or seismo-volcanic activity, dislodging living (or dead) corals from the steep flanks of volcanoes on which they lived (Di Geronimo et al., 1993; Lodolo et al., 2017).

MATERIALS AND METHODS

The dataset used for this work consists of multibeam bathymetric data and Remotely Operated Vehicle (ROV) images. Data were collected during the multidisciplinary oceanographic cruise “Ferdinanda 2012” carried out in 2012 by INGV (Istituto Nazionale di Geofisica e Vulcanologia) offshore southwestern Sicily on the Research Vessel Astrea of ISPRA (Istituto Superiore per la Protezione e la Ricerca Ambientale) (Coltelli et al., 2016). The latter paper focused on the preliminary results of the oceanographic cruise giving a short and general description of the main morpho-structural features of the area, describing seafloor and gas samples and the local underwater seismic monitoring, which was carried out by means of OBS/Hs (ocean bottom seismometer with hydrophone). The high-resolution seafloor mapping covered an area of nearly 70 km², focusing on the GVF (**Figures 1, 2A,B**). It was performed by using an EM 2040 Kongsberg multibeam sonar system with a frequency range of 200–400 kHz supported by GPS-RTK positioning. SIS software by Kongsberg was used for data acquisition. Daily sound velocity profiles and repeated calibration of transducers were applied to get the best possible data resolution. CARIS Hips & Sips software package was utilized for data processing (calibration and processing of navigation, correction for sound velocity and tide variation, noise filtering and removal of erroneous beams), producing a very high-resolution Digital Terrain Model of the seafloor, with a bin size of 5 m, which, for some peculiar areas (e.g., the Ferdinanda seamount), reached 0.7 m. The bad sea conditions during the survey created wave-like artifacts on the bathymetries, somewhere still visible, despite noise



filtering, and more apparent on the 3D views of smooth surfaces because of the high vertical exaggeration. Our bathymetry was merged with lower resolution bathymetric data related to the Nerita and Terribile banks (about 600 km²), courteously provided by the IIM.

Furthermore, the repeated bathymetric surveys (single- and multi-beam echo sounders data) carried out from 1890 to 2014 by IIM (Sinapi et al., 2016), together with those realized in 1883 and 1914 by the Istituto Idrografico Regia Marina and that in 1972 by Consiglio Nazionale delle Ricerche

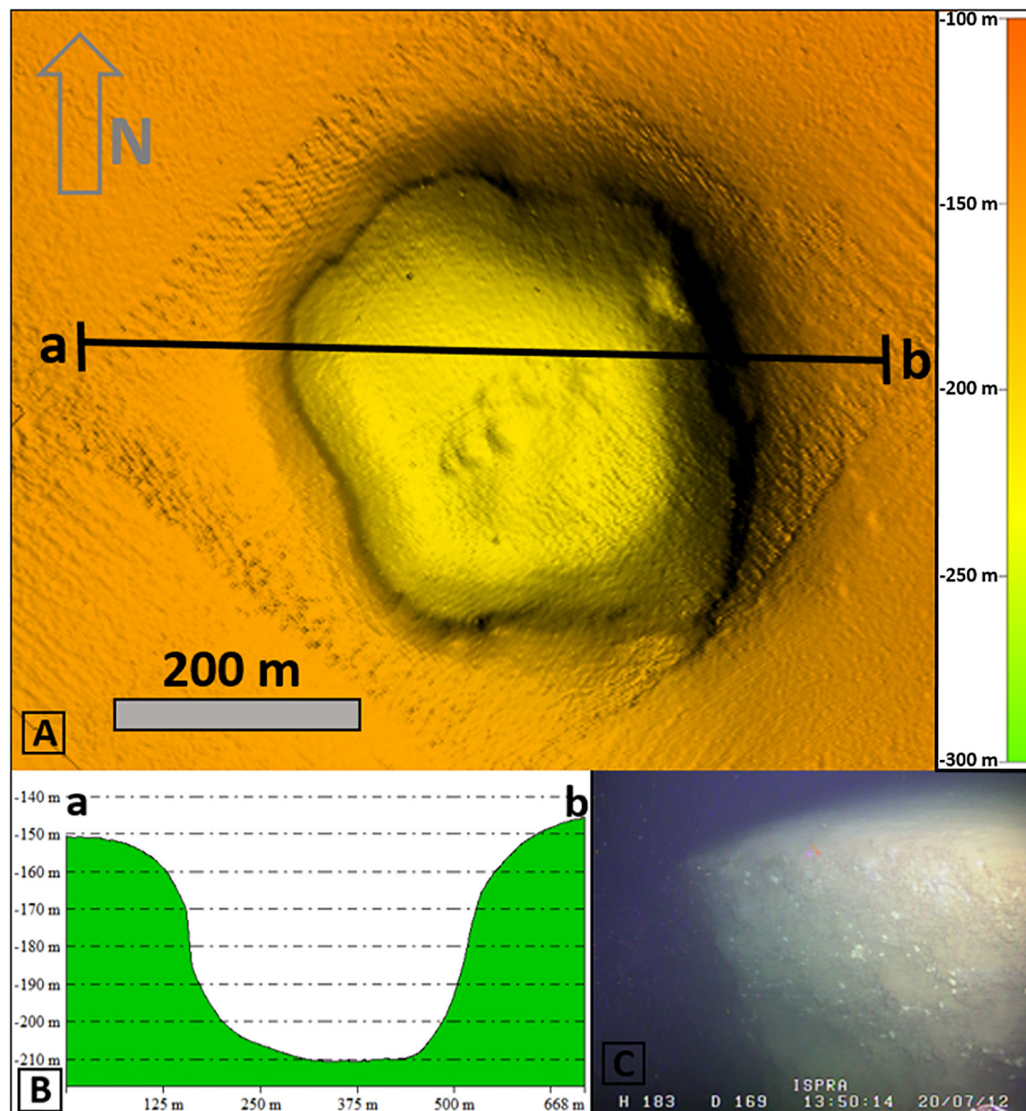


FIGURE 3 | (A) High-resolution shaded-relief image displaying a large pockmark south of the Terribile Bank (location in **Figure 2**). **(B)** Bathymetric profile across the pockmark well displays its sub-vertical and deep walls imaged in the ROV photo of **(C)**.

(Falautano et al., 2010), allowed us to estimate, even if by means of old and low-quality measurements, the depth changes of the summit abrasion platform of the Ferdinanda cone, in order to compare its post-eruptive morphological evolution with that of the others of the field.

Following the definition by Wessel et al. (2010), “Seamounts are active or extinct undersea volcanoes with heights exceeding about 100 m,” we interpreted the cones within the GVF as seamounts. Moreover, since their tops lie in shallow water, we also referred to them as shoals.

For the morphological analysis used to describe the cones of the GVF, we adopted the following criterion. Based on the spatial separation between the cones (Cañón-Tapia, 2016), all the seamounts were grouped in clusters. For each volcanic seamount, we indicated location (in geographic coordinates)

and local name, if already known. The main morphometric parameters, including summit depth, minimum and maximum basal diameters, cone height, slope gradients and basal area, were measured (**Table 1**). In order to avoid overestimation in case of steep basal surfaces, cone height and width were determined by fitting a line to the inflection points on either side of each cone profile using the method proposed by Mitchell et al. (2012b), as illustrated in **Supplementary Figure S3**; the height of the cone has been measured as the elevation difference between the peak and the basal plane of the cone reconstructed through bathymetric profiles. Unfortunately, the cone bases were not easily identified everywhere because of the presence of talus and/or erosive features. Moreover, the gradient changes locally, and thus the topography can be confused by rugged pre-existing reliefs; hence, individual measurements could have been

TABLE 1 | Main morphological dimensions and morphometric associated parameters of the cones of the GVF.

Cluster id (local name)	Seamount id (local name)	Lat	Long	Cone shape	Summit depth (m bsl)	H (m)	Summit terrace depth (m bsl)	Max D (m)	Min D (m)	Average D (W) (m)	Basal ratio	Basal shape (Max axis direction)	BS (Km ²)	H/W aspectratio	Volume (Km ³)	Average slope gradient (°)
C1	S1	37° 08' 55" N	12° 42' 46" E	FT	76	117	90–100	870	710	821	1.22	C	0.45	0.14	0.033	26
	S2	37° 09' 00" N	12° 42' 11" E	FT	66	144	90–100	1050	870	924	1.20	C	0.67	0.16	0.045	25
	S3	37° 09' 27" N	12° 42' 10" E	P	105	100	/	800	680	730	1.17	C	0.38	0.14	0.018	27
C2 (Graham Bank)	S4 (Ferdinanda)	37° 10' 10" N	12° 42' 09" E	FT	9	141	25–30	1450	1050	1220	1.38	E (N130)	1.17	0.12	0.056	29
	S5 (Secca del Corallo)	37° 10' 35" N	12° 42' 34" E	FT	33	137	50–60	1850	1780	1807	1.04	C	2.40	0.07	0.169	18
C3	S6	37° 12' 04" N	12° 41' 28" E	P	122	118	/	750	720	731	1.04	C	0.42	0.16	0.028	24
	S7 (Secchitella)	37° 13' 03" N	12° 42' 28" E	P	98	132	/	990	780	874	1.27	E (N115)	0.60	0.15	0.041	23
C4 (Bancazzo)	S8	37° 14' 57" N	12° 42' 14" E	FT	83	113	85–95	1280	900	1022	1.42	E (N122)	0.82	0.11	0.058	26
	S9	37° 15' 12" N	12° 41' 55" E	FT	75	109	80–90	1345	750	855	1.79	E (N55)	0.57	0.13	0.035	24
	S10	37° 15' 14" N	12° 41' 23" E	FT	83	88	90–95	1020	710	821	1.44	E (N30)	0.53	0.11	0.031	23
MEDIAN						120				980			0.80	0.13	0.051	24

FT, Flat-topped; P, Pointy; C, Circular; E, Elliptical; D, Diameter; BS, Basal surface; H/W, aspect ratio (height vs. average basal diameter).

affected by significant uncertainty. These parameters were used to obtain the aspect ratio (height vs. average basal diameter, H/W) of the cone, a morphometric index widely used in both subaerial (Favalli et al., 2009) and submarine (Mitchell et al., 2012b) settings to characterize volcanic cones. The volume of the seamounts was also estimated by using gridded bathymetric profiles and apposite tools of dedicated software. In some locations, individual seamounts consist of overlapping cones, making classification with these parameters difficult. The overlapping basal area represents a minor component of the total area, thus, according to Rappaport et al. (1997), overlapping regions were reasonably included in the basal area of both adjacent seamounts. The same *modus operandi* was used for measuring the cone diameters and volume.

Based on their summit morphology, the cones were divided into two main types: pointy or flat-topped (flattened and/or truncated) cones. Average slope gradient was calculated by averaging the slope gradients of lines connecting the border of the basal plane with the cone top (if pointy cones) or with the border of the summit terrace (if flat-topped cones).

Finally, we classified the basal shape of the cones as circular if the Max axis/Min axis ratio = 1.0–1.25, and elliptical if it is >1.25. This classification is important to define a possible tectonic control, even if the shape of the seamounts also depends on erosive and depositional activity of the post-emplacement processes, which are, in turn, subject to the local wave-current conditions.

We used the depth of the wave-cut summit platforms of the different flat-topped cones within GVF, which is related to the local wave erosive level, as a marker of relative paleo sea levels (e.g., LGM and younger stillstands during the last sea-level rise), with the purpose of inferring the possible age of the volcanism creating the cones of the field, taking into account data on the vertical mobility affecting the area. Similarly, even though the position of the SDTs' depositional edges (or rollover depth, Mitchell et al., 2012a) is not a direct measure of paleo sea-level positions, because their depth depends on a complex interplay of several factors (such as the storm-wave base level and the occurrence of subsequent erosional or depositional processes), we can use it as useful tool for paleo sea-level reconstructions (Casalbore et al., 2017). The Ferdinanda depositional terrace has its edge at depths approximating the modern local storm-wave base level, which is defined as the water depth beyond which wave action ceases to stir the sediment bed (Cowell et al., 1999), especially during stormy conditions. Thus, following the model of Casalbore et al. (2017), the Ferdinanda SDT edge was used as analog for deeper terraces located on the other cones of the GVF and formed in the past (but after the LGM), when the sea level was relatively stable and lower than the modern one, with an uncertainty of a few meters (due to the impossibility to distinguish the depositional shelf edge from the erosive one, because of lacking of seismic profiles). Within this approach, we assumed that past meteo-marine and oceanographic circulation conditions were similar to the present ones (see **Supplementary Material**) and adopted the post-LGM curve proposed by Lambeck et al. (2011).

Some ROV dives were also carried out (**Figures 2A,B**) by using a ROV PolluxII (400 m depth rated), which allowed the shooting of several high-resolution videos along the slopes of the GVF cones.

RESULTS

Physiography of the Study Area

The GVF is located between 43 and 51 km offshore Sciacca on the western side of a relatively shallow (maximum depth of about 350 m) submarine morphological high, which rises for more than 200 m from the surrounding seafloor (**Figures 1, 2**). The high covers an area of about 600 km² and includes, in addition to the GVF, the Terribile and Nerita banks.

The Nerita Bank is an ellipse-shaped morphological high with a summit depth of ~50 m, a nearly 10 km long major axis with a NNE-SSW direction and a 3 km long minor axis. The bathymetric data confirmed the lack of morphological irregularities ascribable to volcanic structures on top of it, as previously indicated by seismic reflection profiles for its subsurface (Civile et al., 2018; Fedorik et al., 2018).

The Terribile Bank is a triangle-shaped submarine plateau with a summit at 28 m water depth. Its top shows a terrace-like morphology, very smooth in the eastern sector, but rugged in the western one, where numerous landslide scars and associated deposits were identified.

The inter-bank areas are characterized by a nearly flat seafloor ranging in depth between 150 and 250 m, occasionally interrupted by fields of circular depressions interpreted as pockmarks related to fluid escape (**Figures 2A,B**). They either occur as isolated features or grouped in WNW to NW-SE oriented clusters. A giant pockmark (300 m large and 65 m deep) was recognized south of the Terribile Bank (**Figures 3A,B**); here, ROV videos (**Figure 3C**) show the very steep walls cutting the seafloor.

Morphological Analysis of the GVF

The GVF is composed of a ten of cones, arranged along a N-S trending belt, nearly 12 km long and 3 km wide (**Figures 2A,B**). The seamounts are distributed on a flat or gently westwardly sloping seafloor, ranging in water depths of 140–250 m. The field is bounded to the west by a NW-SE trending and nearly 100 m high steep scarp, well visible in the southern part of the study area. The volcanic cones are isolated or organized in clusters, which are elongated in a NW-SE preferential direction (**Figure 2A**). Taking into account the spatial separation between the cones (Cañón-Tapia, 2016), all the seamounts were grouped in four clusters (numbered from C1 to C4) (**Figure 2B**). C1 and C3 are composed of isolated cones, while C2 and C4 are composite shoals resulting from the coalescence of two or more simple cones that together make up larger morphological features.

Based on HR multibeam bathymetry data, the seamounts are hereinafter numbered from S1 to S10 and morphologically described in detail moving from south to north.

All the seamounts consist of tephra/tuff cones lacking a summit crater or collapse pit.

C1, the southernmost cluster of the field, is composed of S1, S2, and S3 seamounts lying in water depths of 190–210 m (Figures 2B, 4). S1 and S2 are two flat-topped cones which are very similar to each other with an almost perfect circular shape and very regular and steep slopes (gradient range of 25–26°), without evidence of significant channelized erosive features. S1 has a maximum base diameter of 870 m and a summit located 76 m bsl, while S2 has a base diameter of 1050 m and presents the top at 66 m bsl. Both the tops are constituted by sub-vertical small-scale (about 5 m high) reliefs, similar to plugs or knolls, consisting in the highest part of the volcanic necks highlighted by selective erosion; the plugs are located in the middle of flat or gently sloping (gradient of 6–8°) narrow summit terraces lying between 90 and 100 m water depths. No lava flows were identified along the slopes or around their basis. Their relative proximity (800 m of distance each other) and their very similar morphological features allow us to infer a probable coeval formation, along a nearly N100° oriented eruptive fissure. S3 is a pointy seamount located some 800 m to the north with respect to S2. The summit is located at 105 m bsl while the average basal diameter is about 700 m. It is the only seamount of the field showing an amphitheater-shaped rim around the cone (Figures 4A,B); this is 40–55 m high and opened northwestward with, at its base, a 400–600 m large and 20–25 m deep canyon head (Figures 4A,C). The canyon runs for nearly 1.5 km in a nearly E-W direction up to the base of the fault scarp bounding westward the volcanic field (Figures 2A,B, 4A); the presence of such a developed channelized feature suggests an intense erosive activity affecting the cone. Finally, numerous isolated blocks, up to 10 m high, likely related to collapse processes, are scattered on the seafloor around C1.

C2 (the Graham Bank, Figures 2B, 5), shows a N130° oriented major axis and is composed of the coalescence of two simple cones, S4 (the remnant of the short-lived “Ferdinandea Island”)

and S5, which lie on a seafloor between 140 and 180 m bsl (Figures 5, 6). S4 appears as a truncated cone that rises up to 150 m from the surrounding seafloor. It shows an elliptical-shaped base with a N140° direction, and a maximum axis longer than 1.4 km (although it is difficult to exactly measure it due to the coalescence with S5). Its aspect ratio is 0.12 (Table 1). The shoal top consists of a sub-vertical volcanic plug, which reaches 9 m bsl (the shallowest point of the whole GVF), being part of a 25 × 10 m elliptical-shaped structure (the knoll), which is elongated in a SW-NE direction. ROV dives carried out on S4 (Figure 7A) filmed the knoll abundantly colonized by algae like *Sargassum*¹ (Figure 7B). The knoll (Figures 5, 6) is placed in the middle of a 500 × 380 m elliptical-shaped terrace, which lies between 25 and 30 m water depths. The summit terrace shows a very uneven morphology being characterized by sub-vertical ridges/furrows composed of consolidated pyroclastic material, arranged in a sub-concentric asset and dipping away from the top (Figures 6, 7D); according to Calanchi et al. (1989) they consist of interbedded cinder and ash, with abundant lithic fragments, confirming the explosive activity of the 1831 eruption. Outwardly, a flat or gently sloping (gradient range of 4–8°) seabed occurs, likely corresponding to the top of a depositional terrace, below which the slope sharply steepens. The terrace is up to 70 m large in the NW and SE sectors, narrowing to 30 m in NE and SW ones: its edge lies at water depths of 40–43 m in the N and E sectors, shallowing to 36–38 m in the S and W ones (Figure 6). It is likely composed of the black volcanic sediment produced by combined wave/current erosion and wave-driven deposition. The occurrence of sand ripples, imaged by ROV dives (Figure 7C), witnesses the active role of waves and currents on the shoal, as

¹<https://storage.googleapis.com/planet4-italy-stateless/2018/11/81b16db4-81b16db4-i-tesori-sommersi-del-canale-di-sicilia.pdf>

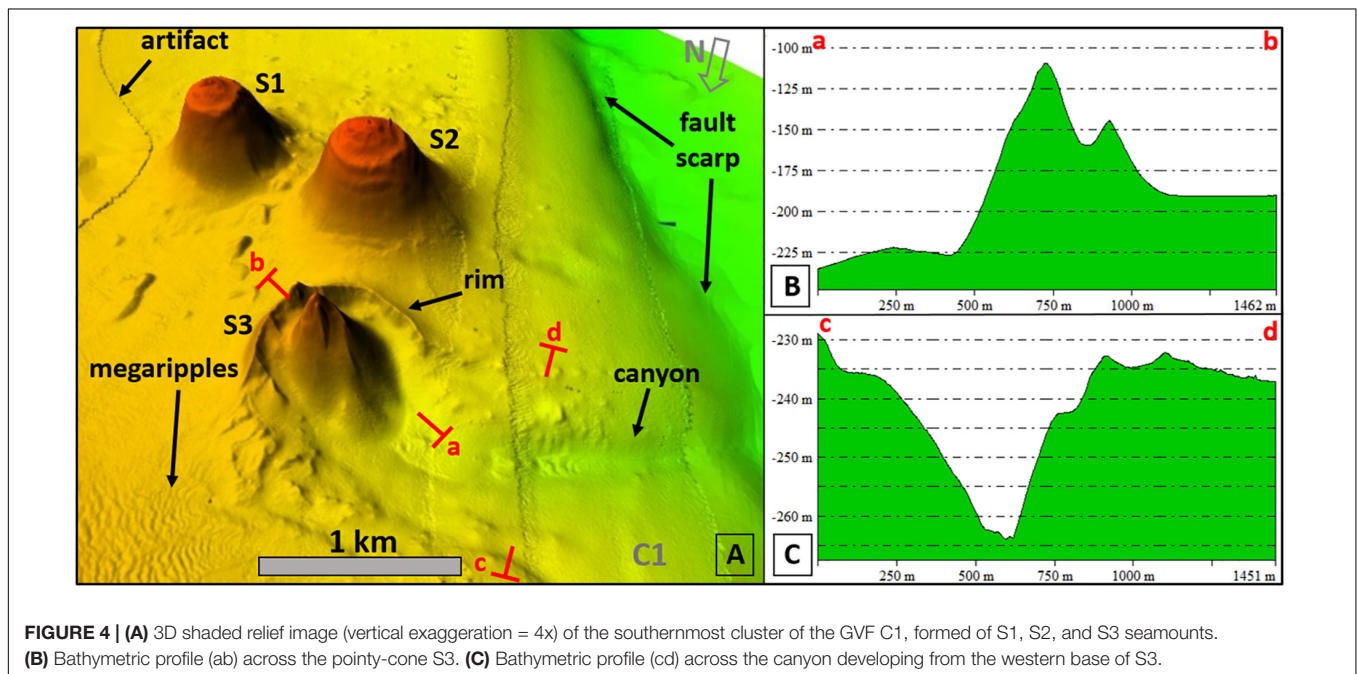


FIGURE 4 | (A) 3D shaded relief image (vertical exaggeration = 4x) of the southernmost cluster of the GVF C1, formed of S1, S2, and S3 seamounts. **(B)** Bathymetric profile (ab) across the pointy-cone S3. **(C)** Bathymetric profile (cd) across the canyon developing from the western base of S3.

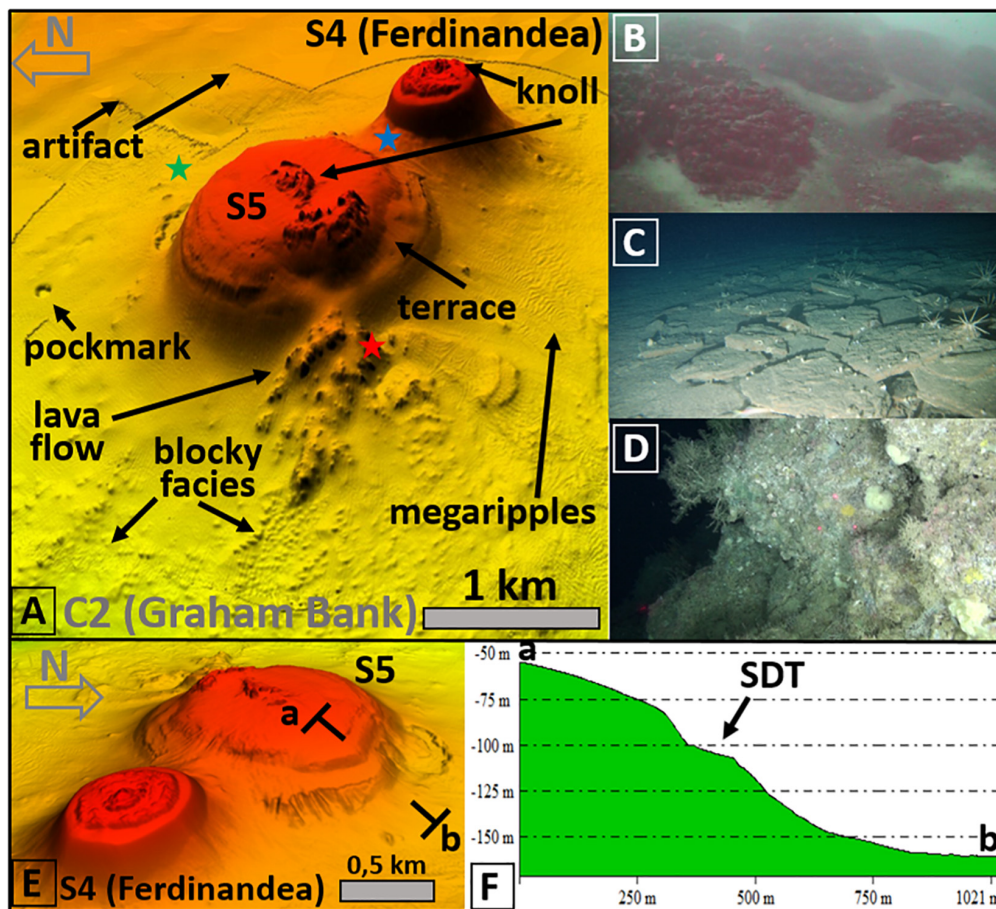


FIGURE 5 | (A) 3D view (vertical exaggeration = 4x) of the Graham Bank (C2 cluster) viewed from the west; the blue star indicates the location a ROV photo **(B)** displaying a group of mounds on the saddle between S4 (the Ferdinandea shoal) and S5 seamounts; the green star indicates the location of the ROV photo **(C)** displaying pieces of semi-consolidated pyroclastic layers on the seafloor; the red star indicates the location of the ROV photo **(D)** displaying the lateral front of a lava flow on the low western side of S5. **(E)** 3D view (vertical exaggeration = 2x) of the Graham Bank from the east showing a 200–300 m wide terrace at about 100 m bsl along the slope of S5, which bathymetric profile (ab) is displayed in **(F)**.

also observed through scuba dives (Colantoni, 1975; Antonioli et al., 1994). The slopes of S4 appear very steep (gradient of 30°, the highest observed in the entire volcanic field, **Table 1**) and regular, without evidence of active erosive process (e.g., gullies or scars), in agreement with its very young age. No lava flows were identified along the slopes or around the base of the cone.

The Ferdinandea cone lies to the SE next of a bigger cone, S5 seamount (**Figures 5A,E**), giving origin to a 200–300 m long and 80–90 m deep saddle among them. On the northern side of the saddle several rounded mounds, up to 5 m high and 10 m large, were observed on both bathymetric data and ROV images (**Figure 5B**). S5, locally called “Secca del Corallo,” represents the largest edifice of the field since its circular-shaped base area encompasses some 2.4 km² with a maximum basal diameter of 1.8 km (**Table 1**). Its aspect ratio is 0.07, the lowest of the volcanic field. The top (minimum depth of 33 m bsl) is formed by several prominent rocky structures (volcanic plugs/knolls) located in the central and southwestern portions of a nearly flat or gently sloping northwestward terrace lying at 50–60 m

water depths. At 100–115 m water depths, the cone shows a break in slope associated with another terrace, which is more developed (200–300 m wide) on the southeastern side of the edifice (**Figures 5A,E,F**). The slopes exhibit abundant evidence of erosive activity proving an older age with respect to the Ferdinandea cone. In fact, the lowest part of the eastern flank is cut by several gullies, up to 150 m long and 6 m deep, which are indicative of slope failures and sediment transport into deeper water in form of debris flows or turbidity currents. The northeastern flank and its base are characterized by a few scars, up to 5 m deep (**Figures 5A,E**), likely enhanced by hydrothermal activity of a fumarole field, whose presence is confirmed by gas bubbles recorded by multibeam sonar echos in the water column (Falzone et al., 2009) and by ROV images and gas samples (Coltelli et al., 2016). Here, ROV images show the presence on the seafloor of few cm thick sharp-cornered plates of consolidated pyroclastic sediment (**Figure 5C**). The seafloor at the base of the western flank shows an irregular morphology due to the presence of a 1 km long and 1 km wide fan-shaped lava field,

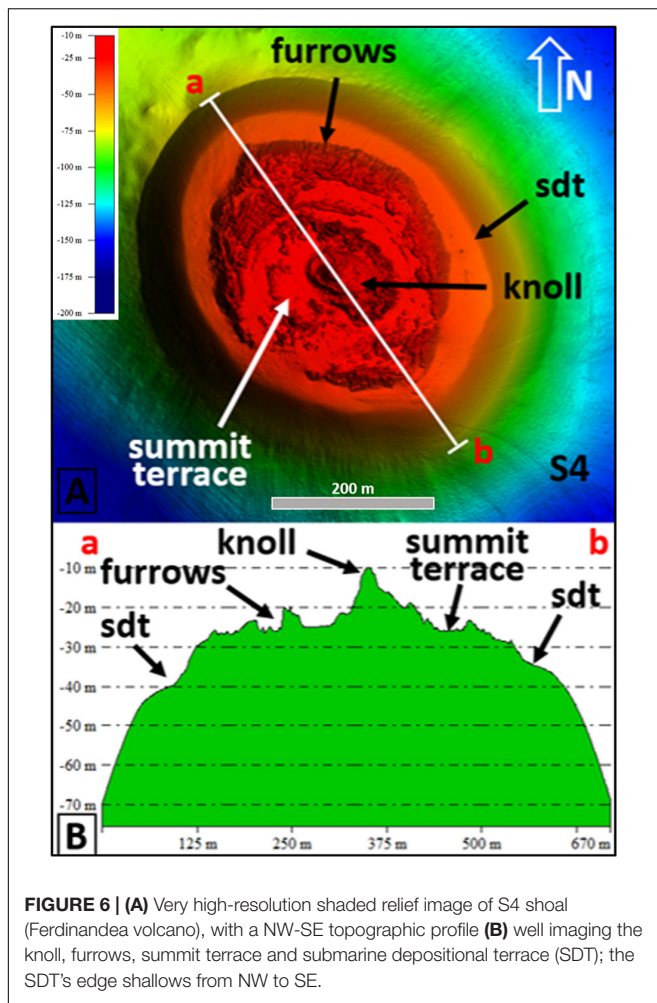


FIGURE 6 | (A) Very high-resolution shaded relief image of S4 shoal (Ferdinandea volcano), with a NW-SE topographic profile **(B)** well imaging the knoll, furrows, summit terrace and submarine depositional terrace (SDT); the SDT's edge shallows from NW to SE.

the only one well-recognized in all the mapped area, composed of three or four different blocky-lava flow units (**Figures 5A,D**). The southernmost portion of the lava field shows a smoothed morphology likely due to the partial covering by both the eroded material of the cone flanks and pyroclastic fallout deposit erupted by the adjacent Ferdinandea cone in 1831. Westwards, a blocky facies extends for more than 1 km from the front of the lava flow, partially buried by sediments. A field of megaripples (up to 2 m high) occurs in water depths between 160 and 200 m, on the southern side of C2 (**Figure 5A**), witnessing an intense reworking activity. Finally, a pockmark is located to the north of the Graham Bank showing a width of 100 m and a depth of 7 m (**Figure 5A**).

C3 is composed of S6 and S7, two isolated pointy seamounts, located 3 and 4.5 km northwards from the Graham Bank, respectively (**Figures 2B, 8A**). The tops lie at 122 and 98 m bsl while the average basal diameters are 730 and 870 m large, respectively (**Table 1**). S6 is 118 m high and shows an almost perfect circular basal shape. S7, locally called “Secchitella” (“small shoal” in Italian), has a NW-SE trending elliptical-shaped base. Both the seamounts show several important evidence of mass wasting processes, confirmed by hundred-meter-wide scars along the slopes and hummocky morphologies at their bases. In

particular, the seafloor around S7 is covered by a blocky facies of boulder deposits extending up to 700 m far from the southeastern side of the cone.

C4, locally called “Bancazzo,” is the northernmost cluster of the field (**Figure 8B**), being located only 44 km offshore Sciacca. It is composed of at least three coalescent truncated cones (S8–S10), aligned along a NW-SE direction. The shape of the three seamounts is irregular with basal diameters ranging from 1000 to 1350 m (**Table 1**), although an accurate estimation is difficult due to their partial overlying. The summit depth ranges from 75 m for S9 to 83 m for both S8 and S10; it was measured at the prominent knolls, lying in the middle of the top platforms at around 85 and 90 m, for S9 and S8–S10, respectively. On the northern side of S8 a small cone with a summit at –82 m is observed, together with another one between it and S9, as belonging to the same edifice (see also Civile et al., 2018). The seafloor around C4 shows a rugged morphology due to the presence of deposits of boulders (up to 200 m large), which are spread up to 1 km far from the cones.

Morphological Analysis of the Terribile Bank

The southwestern side of the Terribile Bank displays an overall step arrangement with three, NW-SE oriented main scarps, up to 20 m high, and four terraces, whose edge lies at about 130, 105–110, 85–90, and 60 m bsl (**Figures 2A,C,D**). Based on the depth of its inner margin the deepest terrace might be related to the sea level reached during the LGM, even if the lack of seismic reflection images limits the reliability of our interpretation. It almost continuously bounds the whole Terribile Bank (slightly shallowing from NW to SE, likely due to tectonic tilting produced by the proximity to the fault on the eastern side of the bank, see Ferranti et al., 2019). Similar features were recognized on the Anfitrite Bank at 120–130 m bsl and associated with the LGM paleo-coastal cliff by Civile et al. (2015) on the basis of seismic reflection profiles. The shallowest step lying at 65–85 m bsl was interpreted by Civile et al. (2018) as a NW trending currently active normal fault developed during late Miocene and later reactivated by the transpressive tectonics affecting the Terribile and Nerita Bank, although a correlation with a paleo-coastal cliff related to younger stillstands during the last sea-level rise (e.g., Younger Dryas stadial) could not be ruled out (see Zecchin et al., 2015).

On top of the Terribile Bank, a field of numerous (ca 30) flattened truncated cones, isolated or clustered, sometimes coalescent, are spread over a 25 km² wide area ranging in depth from 100 to 40 m bsl (**Figures 2A,C,E**), giving origin to the TVF. Few of these cones were also identified in previous studies (i.e., Falzone et al., 2009; Coltelli et al., 2016; Civile et al., 2018; Lodolo et al., 2019b), while most of them are recognized for the first time in this work. Although the lack of high-resolution bathymetric data does not allow a detailed morphological analysis of the TVF, generally the cones show a smaller size in comparison with those of the GVF; indeed their width ranges between 100 and 300 m, while height from 10 to 50 m. The cones have a circular or elliptical (with maximum axis showing a predominant NW-SE

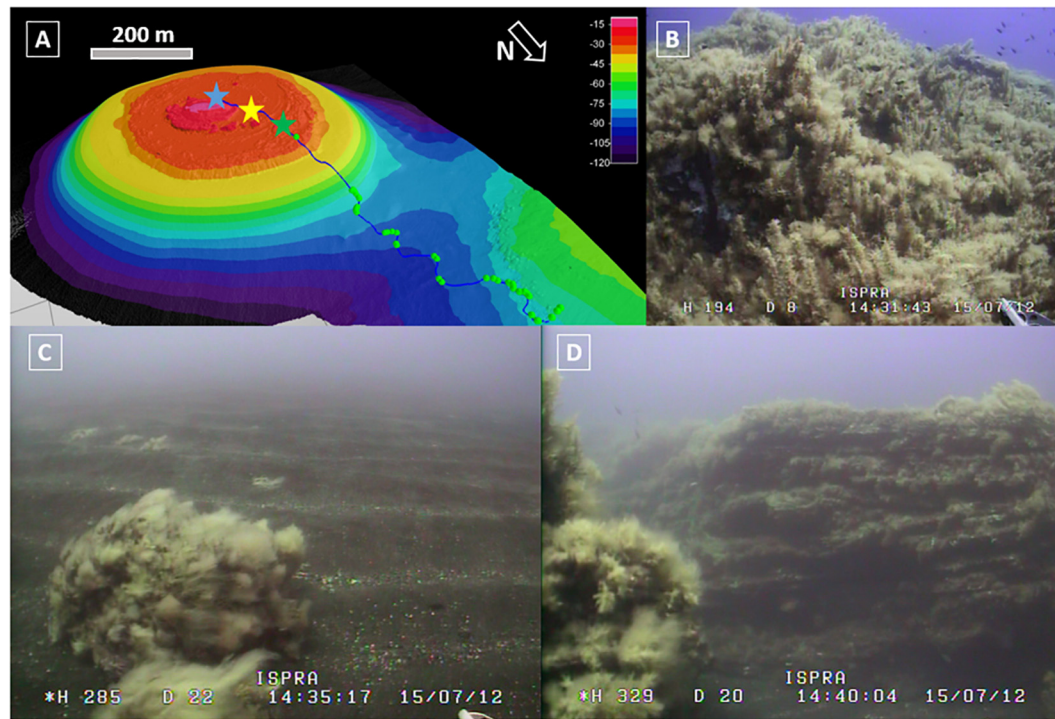


FIGURE 7 | (A) ROV dive on top of the Ferdinandea shoal (S4). The blue star indicates the location of **(B)** showing the volcanic knoll, which represents the shallowest point (−9 m) of the whole field, completely colonized by gorgonians. The yellow star points to the location of **(C)** displaying the seafloor of the summit terrace characterized by black sand ripples. Finally, the green star indicates the location of **(D)** where the furrows are imaged.

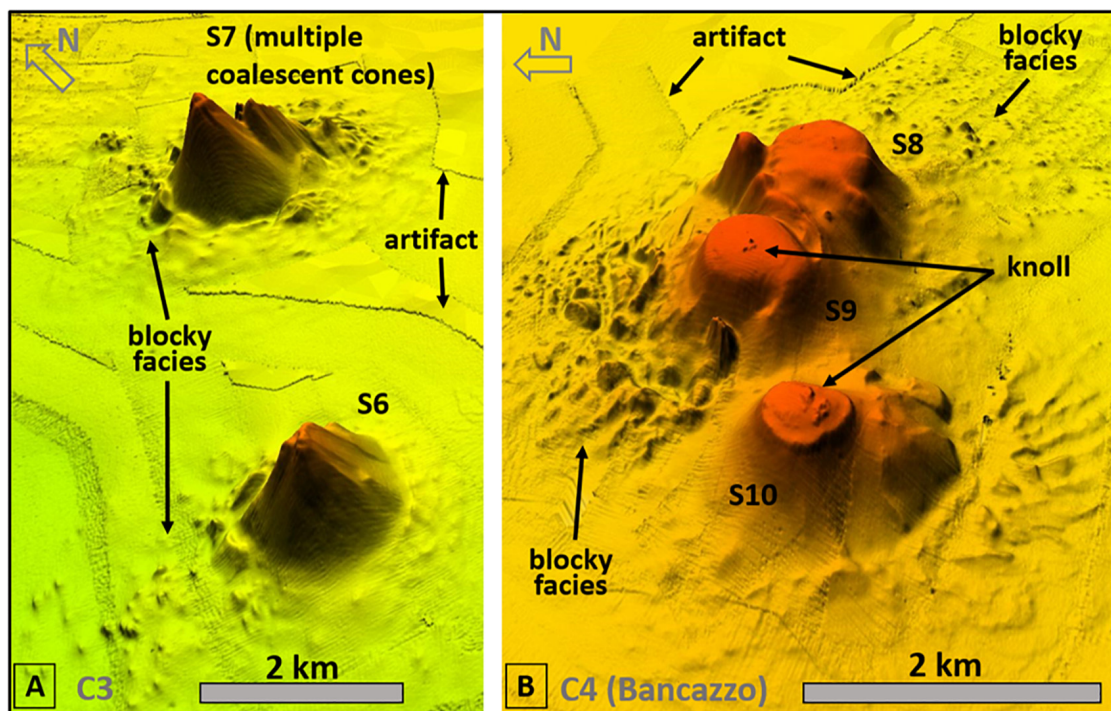


FIGURE 8 | 3D view (vertical exaggeration = 4x) of **(A)** C3 Cluster – **(B)** C4 cluster (Bancazzo).

direction) basal shape. Summit depth ranges from 28 to 100 m bsl. The great part of the cones is flat-topped with summit terraces between 40 and 80 m water depths.

DISCUSSION

Morphological Evolution of the Seamounts and Relationship With Underwater Volcanic Processes

The seamounts of the GVF show heights from 88 to 144 m, maxima basal diameters ranging from 750 to 1850 m and planimetric basal areas from 0.42 to 2.40 km², with a median value of 0.8 km² (Table 1). The depth of their summits varies between 9 and 122 m. They have steep flanks, with gradients ranging between 18 and 29°, except for the Ferdinanda cone (S4), which shows steeper flanks being the youngest and best-preserved volcanic edifice of the field. The occurrence of such steep gradients, together with the non-cohesive nature of the sediments, explains the numerous slope failures identified within the volcanic field. The cone slopes show abundant evidence of widespread flank failures suggesting a long-lasting and intense erosive activity (e.g., C3 and C4 clusters); this process is confirmed by the rugged seabottom at their bases highlighted by blocky deposits, which were transported gravitationally downwards. Instability triggering processes may include syn-eruptive shaking and volcano-tectonic activity as well as cyclic loading due to storm-waves.

The aspect ratio (H/W) of the cones ranges between 0.07 and 0.16, with a median value of 0.13, which is within the range (0.1–0.3) reported for other submarine cones worldwide (e.g., Romero Ruiz et al., 2000; Stretch et al., 2006; Tempera et al., 2013). The estimated volume ranges from 0.018 to 0.169 km³ with a median value of 0.051 km³, which is a little smaller than that reported for other monogenetic volcanic field (e.g., Romero Ruiz et al., 2000). This value confirms the relative low amount of lava erupted during underwater monogenetic eruptions. Correlations were observed between maximum and minimum diameters and between height and average basal diameter; seamount height increases with increasing of minimum basal diameter, as well as volume with basal surface and with average basal diameter, as expected. A general increase in volume with increasing height was also observed. The lack of linear relationships between some other morphometric parameters (i.e., between water depth and cone height) suggests that the cones did not develop in a simple self-similar way (Stretch et al., 2006).

The GVF cones likely grew in shallow water and thus are related to Surtseyan-type eruptions. The lack of summit craters on the pointy cones indicates a low explosivity due to the significant water load, allowing to discriminate the very shallow water eruptions (Surtseyan-type) from the deeper ones (submarine-type) (Kokelaar, 1983, 1986; Cas and Giordano, 2014).

Some seamounts are isolated, whilst others form coalescent cones. Although the occurrence of multiple cones could be interpreted as due to polygenetic activities, we infer that it is

due to cones superimposition related to the same eruption, where different vents interfere with each other (as evidenced by Corazzato and Tibaldi, 2006 in subaerial environment). This inference is based on several evaluations on the cone features, which are discussed in the following. The ellipticity of the S7's base, could be explained as due to syn-eruption sector collapses affecting the eastern flank of the cone or alternatively as the result of the coalescence of two or three volcanic vents (see Tibaldi, 1995); this latter interpretation entails the need of a NW-SE oriented fissure. Similarly, the presence of the amphitheater-shaped rim around S3 could be interpreted as the combined effect of a syn-eruption slope failure and bottom-current erosion, instead of a secondary intra-crater activity (Figure 4A). The particularly similar morphology (i.e., size, slope gradient, level of erosive dismantlement) between cones located at relative short distance each other (i.e., S1–S2 seamounts and those forming the C4 cluster), together with the comparable depth of their summit terraces, could be explained as generated during the same eruption along nearly WNW-ESE trending volcanic fissures. The lack of morphological evidence for such fissures connecting the cones could be ascribed to pyroclastic/epiclastic deposits, produced during the explosive activity and/or transported by erosive-depositional waves-currents processes mantling them. Lineaments of isolated cones may be due to the rapid cooling of the eruptive fissure during the same eruption, favoring the progressive blocking of magma ascent through the entire dyke and leading to the emission of lava from separate vents along the same feeder dyke (see Bruce and Huppert, 1989; Head et al., 1996). This process is enhanced in submarine environment due to the very high heat conduction through water.

All these considerations confirm the monogenetic nature of the GVF seamounts. In this condition, according to Coltelli et al. (2016), the extremely regular morphology of the Ferdinanda slopes and the lack of any secondary crater, fissure or simple volcanic vent, allowed us to rule out the occurrence of any other eruptive activity after the 1831 eruption, in contrast with some chronicles that reported new volcanic activities in 1833 and 1863 on the same cone (Antonoli et al., 1994; Falzone et al., 2009).

Within the GVF some cones show a pointy shape, whereas others exhibit a terraced top. With the exception of the shoals composing the C2 cluster, the depth of the terraces of the flat-topped cones ranges between 80 and 100 m. Generally, morphometric parameters (height, H/W ratio, and basal diameter ratio) of flat-topped cones show correlations with depth (e.g., Clague et al., 2000a; Mitchell et al., 2012b; Casalbore et al., 2015), suggesting that the latter plays an important role in their formation. Although the wave erosion is the predominant process responsible for modeling flat-topped cones, other factors come into play: (1) lava infillings of summit craters or calderas (Clague et al., 2000b); (2) long-lasting overflowing submarine lava ponds (Clague et al., 2000a); (3) high effusive rates associated with areas of high magma supply (McClinton et al., 2013); (4) the combined effect of forced spreading of the eruptive submarine plume upon reaching the water-air density barrier and wave erosion (Mitchell et al., 2012b; Casalbore et al., 2015).

The seamounts recognized within the GVF and in other shallow-water submarine areas worldwide, such as

the Syrtlingur, Jólnir and Surtla satellite shoals of Surtsey (Kokelaar and Durant, 1983; Romagnoli and Jakobsson, 2015), consist of spatter/tuff cones, typical of the Surtseyan-type eruptions. The large amount of scarcely cohesive pyroclastic material forming the cones could have been easily eroded by wave action during Late-Quaternary sea-level change, leading to the formation of summit planar surfaces. The summit of the flat-topped seamounts composing the GVF is often characterized by sub-concentric furrows and ridges (see for example the Ferdinandea shoal, **Figures 5–7**), as also observed at Surtla (Kokelaar and Durant, 1983), or at the Princess Alice Bank and Terceira (Azores, Casalbore et al., 2015; Mitchell et al., 2016), where these features are likely the result of differential erosion of the coarse-fine and/or more-less consolidated volcanic strata. Selective erosion of individual pyroclastic layers with varying resistance may leave the concentric furrows and ridges (Mitchell et al., 2016). Similarly, the knolls, often found on the cone summits, represent the remnants of the conduit supplying the volcanic vent exposed by selective erosion. Analogously to those identified on the tops of Surtsey' satellite shoals (Jakobsson et al., 2009), knolls rise vertically to heights of 5–15 m above the surroundings with a diameter of about 20–50 m. These structures represent semi-consolidated spatter deposits, which have undergone palagonitization near the volcanic vent; the high temperature led to palagonite-tuff formation to a higher level than elsewhere (Norrman and Erlingsson, 1992; Jakobsson et al., 2009).

Distribution of Volcanic Seamounts and Tectonic Control

The GVF and TVF volcanic fields, identified offshore southwestern Sicily, prove the repeated occurrence of a

monogenetic volcanism, which is part of a wider and scattered one affecting the northwestern Sicily Channel since the Upper Miocene (Calanchi et al., 1989, among others). This volcanism represents a peculiarity since it took place within a tectonic transpressive transfer zone associated with a continental rifting, outside of the typical geodynamic settings of other volcanic fields such as subduction or oceanic rift zones, and far from long-lived volcanic systems.

The distribution and shape of seamounts within the volcanic fields, as well as the orientation of the main axis of the cluster in which they are grouped, provide important insights into the interaction between volcanism and tectonics in the formation of the fields, since tectonic structures furnish a preferential pathway for magma ascent. Indeed, the alignment of pyroclastic cones and vents as well as the elongation of cone base are generally related to the magma-feeding plane, and the strike of the latter is in turn strongly influenced by the main tectonic stress axis (Tibaldi, 1995). A similar interaction was observed in other submarine volcanic areas, such as offshore the Azores (Casalbore et al., 2015) and Canary islands (Romero Ruiz et al., 2000).

The cones of the GVF are generally grouped into clusters or merged to form coalesced edifices, both aligned along NW-SE to WNW-ESE preferential directions (**Figure 9A**). The base of the cones varies from circular- to elliptical-shaped. Although the distribution of both syn- and post-eruptive deposits on the slopes of the cones down to their bases is considerably influenced by the main currents direction, it also strongly depends on the shape and strike of the volcanic conduit/feeder dykes. Thus, the ellipticity of the volcanic cones reflects the orientation of preferential tectonic stress axis controlling their emplacement. The elliptical cones of the GVF have their main axes preferentially aligned NW-SE (**Figure 9B**). The interaction between volcanism and NW-SE tectonic structures in controlling

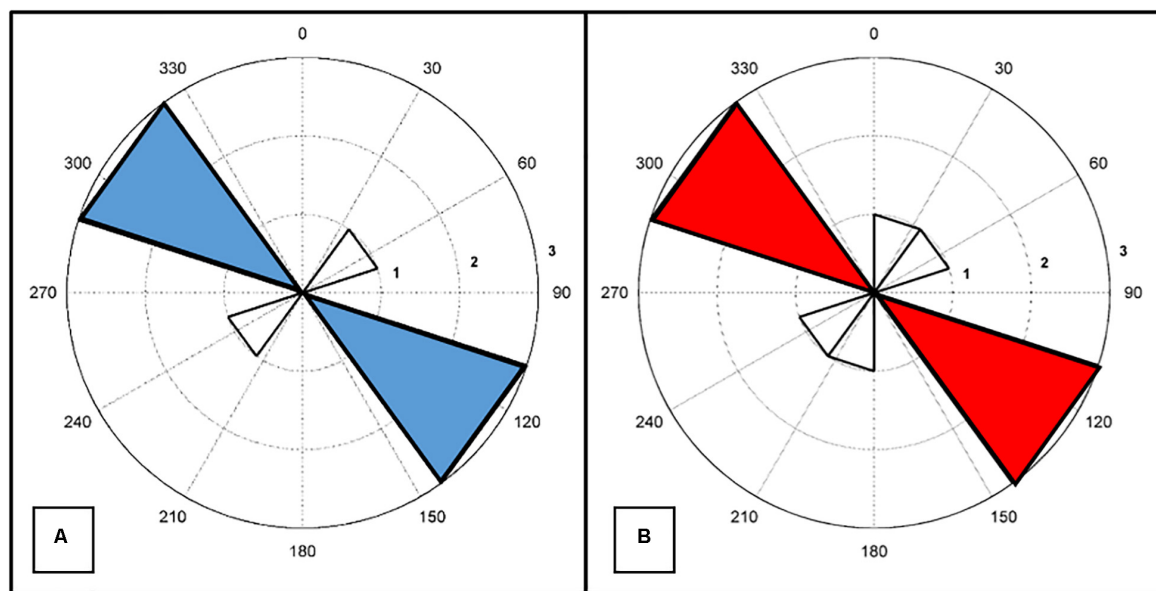


FIGURE 9 | Rose diagrams related to the trend of maximum elongation axis of the clusters of cones **(A)** and cone bases **(B)**.

the distribution and shape of the volcanic cones is also confirmed by the maximum axis direction of some elliptical-shaped cones forming the TVF. Finally, the role of the NW-SE preferential structural direction is corroborated by the alignment of three other volcanic centers (Tetide, Anfritrite, and Galatea) located on the adjacent Adventure Plateau (**Figure 1**) and by the alignments of several pockmarks observed within the study area (**Figure 2**) and to the west of the GVF (Spatola et al., 2018). Some of the above-discussed pockmarks could be also responsible for the recent strong gas releases observed within the area and may have been inaccurately associated with the repeated volcanic activities of the last few centuries reported by several authors (Antonioli et al., 1994; Guidoboni et al., 2002; Bottari et al., 2009; Falzone et al., 2009). The NW-SE direction is associated with the Pliocene-Quaternary continental rift-related processes that generated the three NW-SE oriented and fault-controlled grabens of Pantelleria, Malta and Linosa, characterizing the central part of Sicily Channel.

The overall N-S alignment of the GVF cones, together with the other volcanic centers identified south (i.e., Cimotoc volcano, Calanchi et al., 1989; Civile et al., 2015) and north (a few small isolated cones, Civile et al., 2015, 2018; Lodolo et al., 2019a) of the field, reflects the orientation of the Capo Granitola-Sciacca Fault Zone (Fedorik et al., 2018; **Figure 1**). Based on seismicity data, Calò and Parisi (2014) interpreted this transfer zone as the shallow expression of a sub-vertical lithospheric shear zone favoring magma ascent in this region.

Thus, two main tectonic systems, N-S and NW-SE trending, consistent with the main regional tectonic lineaments affecting the Sicily Channel, seem to control the arrangement of the volcanic fields and the other volcanic centers of the surrounding area (as also inferred by Civile et al., 2018; Spatola et al., 2018; Lodolo et al., 2019a,b). These two preferential orientations are also confirmed by the occurrence of magnetic (Colantoni et al., 1975; Lodolo et al., 2012) and gravity (Civile et al., 2008; Lodolo et al., 2019b) anomalies.

Relationship With Sea-Level Change

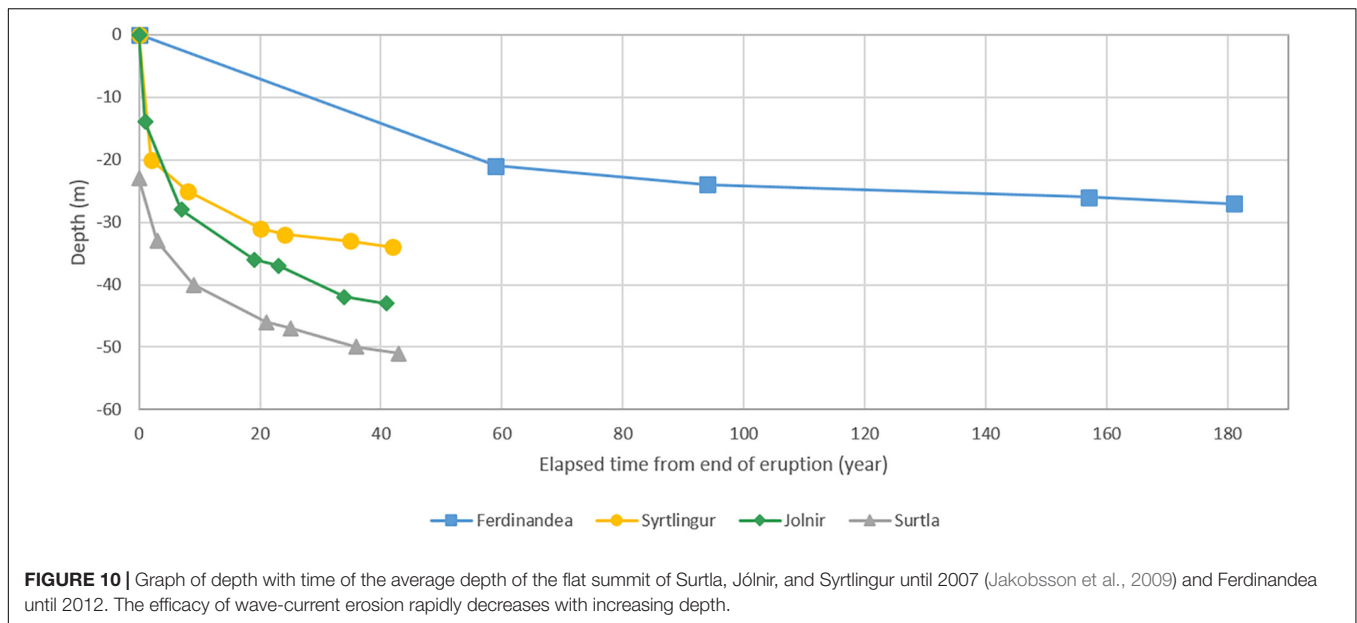
Wave erosion is very efficient in shoaling volcanic islands and flattening their summits, especially if made of poorly consolidated materials such as those built by Surtseyan-type eruptions. The flattening process is more efficient for volcanic cones without topping lava flows, which may represent a resistant cap protecting the island from wave erosion (Schmidt and Schmincke, 2002). On the other hand, erosive processes will slow considerably once the much more resistant volcano interior, composed of the feeder dyke and palagonite tuff, is reached (Jakobsson et al., 2000). Together with surface waves, the intensity and recurrence of extreme-wave events, like storms and even tsunamis, should have a very high impact in both flattening the tops of volcanic shoal, and creating SDTs along their slopes. In fact, strong storms and tsunamis constitute high-energy and low-frequency events that cause extensive erosion, sediment transport and deposition in a very short time and over large areas (Paris et al., 2009).

Wave-induced shear stresses and currents on the bottom are efficient down to considerable depths, at least down to storm-wave base (Cas et al., 1989; Ramalho et al., 2013), creating shallow marine abrasion surfaces (White, 1996; Schmidt and Schmincke, 2002). The depth to which the top platform is abraded is the result of the interplay of different factors and processes, including depth of sea level at the time of eruption, vertical movements due to volcano-tectonic deformation, sediment compaction, wave/current energy, time and direction of exposure to wave/current attack, rock resistance, lava and sediment progradation, coral reef growth and biogenic production (Quartau et al., 2010; Ramalho et al., 2013). Sea-level oscillations significantly influence the depth to which the top wave-cut platform is abraded; this depth represents the local wave base level (Ramalho et al., 2013).

Following the models by Cas et al. (1989) and Corcoran and Moore (2008), relative to the post-eruptive degradational phase of monogenetic shallow marine volcanoes, a wave-planned top is developed on the submarine volcanic edifice becoming gradually stable and colonized. Wave and current activity, together with periodic storms, sweep material off the platform, spreading over its edge the eroded debris, which is re-deposited along the slopes of the cone and down there; steep progradational wedges are thus formed at the edge of the platform, causing its gradual enlargement (Romagnoli and Jakobsson, 2015).

“Ferdinandea Island” is a well-documented example of the post-eruptive transitional stage from volcanic island to shoal. Since its formation, destructive forces have been active for almost 200 years, during which the cone has suffered rapid and severe subaerial and submarine erosion due to strong wave and current activity causing significant modification of its original size and shape: i.e., a reduction from nearly 210 to 140 m of height from the seafloor and an enlargement of its basal surface. Scuba (Colantoni et al., 1975; Antonioli et al., 1994) and ROV dives (this work, **Figure 7**) revealed that the flat seafloor of the summit terrace between the volcanic plugs (25–28 m bsl), is made up of black coarse loose tephra organized in sand waves. A similar sedimentary facies characterizes the top of the underlying SDT, whose edge lies between 36 and 43 m (corresponding to the local storm wave base-level), suggesting that wave and current erosion is still quite strong at that depth. The morphological asset of the Ferdinandea’s SDT reflects the distribution of wave force since its edge shallows from NNW to SSE (**Figure 6**) in agreement with the prevailing wave direction, which is toward ESE, being strongly influenced by the northwesterly winds (Arena et al., 2015, **Supplementary Material** and **Figure 2** therein).

The summit of the Ferdinandea cone was eroded down to –28 m over nearly 200 years following its eruption. The bathymetric surveys carried out by IIM from 1890 to 2014 (Sinapi et al., 2016) allow us to document a faster erosive rate during the first 50–60 years (**Figure 10**), as expected. This has been also observed at the satellite centers of Surtsey, Surtla, Syrtlingur and Jólnir (**Figure 10**), which represent excellent modern analogs for understanding the post-eruptive phase of the Ferdinandea shoal and others cones of the GVF. Syrtlingur and Jólnir reached a maximum height of 70 m asl at the end of the 1963–67 eruption, while Surtla only approached the sea surface; a few weeks after



the eruption ceased they were washed away by wave action (Romagnoli and Jakobsson, 2015). Successively, the shoals were further abraded by the sea, producing summit platforms, which were gradually enlarged and lowered (Jakobsson et al., 2009) as the result of the reworking of volcanoclastic sediments due to erosion by waves and bottom currents. In 2007, the measured depths of the Surtla, Jólnir and Syrtlingur top terraces were 51, 43, and 34 m, respectively (Romagnoli and Jakobsson, 2015). In particular, the summit of Surtla was eroded down to 45 m depth over nearly 18 years following its eruption (Kokelaar and Durant, 1983) and down to 51 m depth over the next 26 years (Figure 10), suggesting that the wave erosion depth level is deeper here, if correlated to the more energetic wave climate of North Atlantic Ocean with respect to the Sicily Channel (see **Supplementary Material**).

A similar process occurred at the Baixa da Serreta Bank (offshore Terceira Island, Azores), the probable site of the 1867 submarine eruption (Weston, 1964), where the planar surface identified in 2011 at $-30/-40$ m was interpreted as the result of wave erosion of scarcely cohesive volcanic products (Quartau et al., 2014).

On the basis of the present-day maximum depth of the summit abrasion terrace (28 m bsl) of the Ferdinandeia shoal, which has to be considered still under development, and taking into account the trend of its erosive rate (Figure 10), the local wave base level can be reasonably placed at least at 30 m bsl. Considering the differences in the respective wave climates (see **Supplementary Material**), this value is lower than that observed in Atlantic Ocean, where the Surtsey's volcanic satellites and Baixa da Serreta Bank are placed, but higher than the value relative to the Mediterranean. This latter assumption is based on two evidence: (1) the wave climate of the study area is more energetic than the average climate of the Mediterranean (Drago et al., 2010; Arena et al., 2015; **Supplementary Material**); (2) the value of the local storm wave base-level, estimated between

36 and 43 m bsl on the basis of the depth of Ferdinandeia SDT depositional edge (or rollover depth) (Figure 6), is higher than that calculated in other areas of the Mediterranean, e.g., 20 ± 10 m bsl in the Tyrrhenian Sea, Casalbore et al., 2017; $20-25$ m bsl Hernández-Molina et al., 2000 and 32 m bsl, Mitchell et al., 2012a in western Mediterranean. Moreover, it is worth noting that these latter values are referred to a coastal environment, while the GVF cones are shoals and thus the erosion affecting them is to be considered omnidirectional.

Based on seismic reflection profiles, Ferranti et al. (2019) estimated a relatively moderate growth rate of 0.2 mm/yr during the Plio-Quaternary for the southern segments of the CGFS and SFS, along which the GVF and Terribile bank are respectively aligned. This rate is also confirmed by GPS data of the Campobello di Mazara station (about 10 km NW of Capo Granitola, Figure 1), which recorded an uplift rate of 0.2 mm/yr between 2009 and 2015 (Valentina Bruno personal communication). As above discussed, based on the depth of its inner edge (130 m bsl), the flat terraced surface, identified at the base of the SW portion of the Terribile Bank (Figures 2A,D), may be related to the sea-level reached during the LGM ($19-20$ ka B.P. when sea level was -125 ± 5 m below the modern one, Fleming et al., 1998; Siddall et al., 2003; Clark et al., 2009), by considering an overall tectonic uplift of nearly 4 m over the last 20 ka. Moreover, such a small uplift is to be considered within the level of uncertainty related to the estimation of LGM sea level. These data suggest the lack of significant tectonic variations affecting the study area in the last 20 ka. The compaction of the tephra deposits through time may have contributed, even if in a small proportion, to lower the Ferdinandeia shoal and thus to increase the depth of its summit terrace. Surtsey Island could represent a good analog, since a series of GPS surveys were carried out during the years following its recent formation. Surtsey was affected by a general subsidence (including the crustal sagging due to the load of the erupted material and

possible compaction of the seabed sediments) of about 1.0–1.5 m during the 35 years following the end of the eruption, with a rate decreasing from 15–20 cm/yr for 1967–1968, to 1 cm/yr for 1992–2000 and finally to 0.5 cm/yr for 2000–2002 (Moore et al., 1992; Sturkell et al., 2009). Although Surtsey and GVF lie in different geodynamic settings, we can reasonably apply this subsidence rate to the Ferdinanda cone; moreover, this rate is probably overestimated for the Ferdinanda case, because of its lower load in comparison with that of Surtsey, having the two volcanic centers different size and stratigraphy (succession of lava flows and pyroclastic units vs. pyroclastic material). Thus, the Ferdinanda subsidence associated with compaction could be estimated in less than 1 m since its formation, and thus its contribution in lowering its summit as well as the other cones of the GVF considered negligible.

On the basis of the above considerations and assuming uniform rates for the tectonic uplift during the post-LGM, we can reasonably discount the minimum contribution of tectonic deformations and subsidence affecting the GVF; moreover, these processes compensate each other and their values could be considered within the level of uncertainty related to precisely measure the depth of the summit terrace of the Ferdinanda volcanic cone. Moreover, the deformation induced by volcanic processes (i.e., inflation-deflation) for scattered small monogenetic volcanic cones, as the case of those forming the GVF, is highly attenuated because of the lack of any plumbing system, magmatic reservoir, etc., and thus considered negligible as well.

Consequently, any submarine structure shallower than ca. –155 m (125 ± 5 = depth of LGM + 30 ± 5 m = depth of the wave erosion depth) below present sea level was potentially affected by wave erosion during the LGM, if created before the LGM. Therefore, following the model proposed by Mitchell et al. (2012b) and taking into account the Global mean sea level curve for the study area (Lambeck et al., 2011), the cones with a top shallower than ca. –155 m and lacking a flat summit surface typical of a wave-eroded platform (i.e., S3, S6, and S7 seamounts, **Table 1**) have survived erosion during the LGM; otherwise, they should have been flattened during the LGM. Thus, they are likely younger than the LGM (**Figure 11**).

S1, S2, S8, S9, and S10 seamounts show summit terraces, at around 90–100 m water depths. Thus, they were likely eroded during the transgressive phase following the LGM (**Figure 11**). Taking into account the analogy with the wave erosion depth of Ferdinanda shoal (–30 m), we can reasonably hypothesize that they were mostly eroded when sea level was at least –60/–70 m below present sea level and thus during the interstadial stillstand of the Younger Dryas (YD), a geologically short period of cold climatic conditions, which occurred between 12.8 and 11.5 ka (Muscheler et al., 2008), when sea level was 60–65 m below the present level. This stadial would have favored the development of restricted abrasion platforms in several regions worldwide (see Salzmann et al., 2013; Green et al., 2014, among others) including the Sicily Channel (Civile et al., 2015; Zecchin et al., 2015), like that recognized at about 60 m bsl on the Terribile Bank (**Figures 2A,C,D**). Civile et al. (2015) recognized along the flanks of several sedimentary banks of the

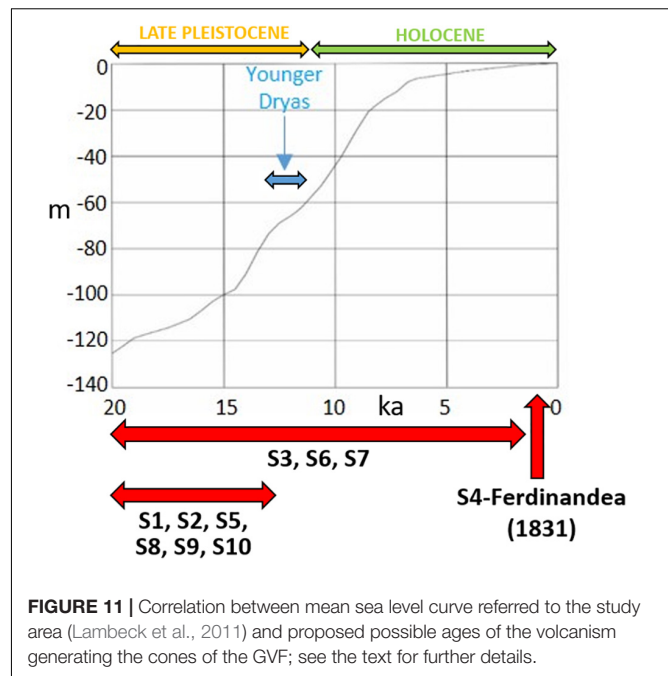


FIGURE 11 | Correlation between mean sea level curve referred to the study area (Lambeck et al., 2011) and proposed possible ages of the volcanism generating the cones of the GVF; see the text for further details.

Sicily Channel (e.g., Pantelleria Vecchia) a relatively flat surface between 60 and 75 m water depths connecting two scarps, that might have formed during episodes of rapid relative sea level rise (i.e., Melt-Water Pulse MWP-1A and MWP-1B, Liu and Milliman, 2004), following the cliff overstep transgressive model by Zecchin et al. (2011).

The summit terrace of S5 shallows from NW to SE, confirming the relationship with the main NW-SE oriented wave provenance (Arena et al., 2015; **Supplementary Material and Figure 2** therein) as also observed on the Ferdinanda's SDT. The lowest values of slope gradient and aspect ratio of the GVF (**Table 1**) reveal an ancient age; this is also confirmed by the morphological aspect of S5, which suggests that it suffered a longer-lasting severe erosion (probably amplified by the presence of a large amount of pyroclastic material) in comparison with the other cones of the field. Its summit terrace lies between 50 and 60 m of depth suggesting that S5 was flattened during the sea level rise of the current Holocene interstadial. Moreover, S5 shows a restricted depositional terrace, which is well-developed on the southeastern sector of the cone (**Figure 5**); its outer edge lies at about 100–110 m water depths. Consequently, by applying the storm-wave base level relative to the Ferdinanda shoal (36–43 m bsl) to the S5, we can hypothesize (taking into account that the lack of seismic reflection profiles limits the reliability of our interpretation of these marine terraces) that its SDT likely formed when sea level was about 60–70 m lower than the modern one, and thus during the YD. Therefore, we speculate that S5 may have erupted after the LGM, giving origin to a nearly 1 km large island. Successively, it was partially eroded during the YD (when the middle-slope SDT formed) and finally was flattened during rising sea level following the YD, more precisely between 6 and 8 ka, when the sea level was nearly 20 m below present sea level (**Figure 11**).

Among all seamounts of the GVF, S5 cone is clearly oversize (3 times larger in volume than the Ferdinanda shoal and

at least 5 times larger than the average value of the other cones, **Table 1**). Taking into account that the S5 eruption likely occurred in shallower water with respect to the 1831 Ferdinandea eruption, and, consequently, it was subjected to a significantly minor hydrostatic pressure, a stronger Surtseyan-type activity (Kokelaar, 1983, 1986; White, 1996) could justify such a larger volume in comparison with those of the other cones of the field.

On the basis of the above-described analysis, we can reasonably hypothesize a post-LGM age for the monogenetic submarine volcanism forming the GVF (**Figure 11**), without any clear migrating pattern with age.

Moreover, paleontological analysis of faunal elements associated with sub-fossil coral deposits found between C3 and C4, indicated a post-LGM emplacement (Di Geronimo et al., 1993); while radiocarbon dating of these corals span the last 10 ka, indicating that they were accumulated during the Holocene (Lodolo et al., 2017). The latter authors associated the origin of the coral deposit to periodic slope failures, possibly triggered by volcanic and/or seismo-volcanic activity (like that reported during Ferdinandea eruption; Gemmellaro, 1831), dislodging corals (dead or alive) from the steep flanks of volcanoes on which they lived, hypothesizing the occurrence of an active volcanism in the area during the last 10 ka.

Finally, as regards the Terrible volcanic field, it includes at least 30 small (height from 10 to 50 m) truncated and multiple coalescent cones. Most of them likely consist of the volcanic necks or the hard volcano-interiors representing the remnants of severely eroded volcanic edifices. This suggests that a likely older submarine volcanism affected this area before migrating westward to create the GVF. Although the lack of high-resolution bathymetric data does not allow a detailed morphological analysis of these cones, many of them show a summit terrace between 40 and 80 m water depths, suggesting that they were presumably flattened during the Holocene interstadial.

Similarly to what observed for the GVF, the morphological asset of the TVF suggests the occurrence of a diffuse monogenetic volcanism, which however does not support the presence of a large common magmatic reservoir, as also confirmed by petrological studies of volcanic samples collected in the region (Rotolo et al., 2006).

CONCLUSION

High-resolution bathymetric data and ROV images allowed new detailed morphological analysis of the present-day setting of the Graham submarine volcanic field located offshore southwestern Sicily.

Another volcanic field, the TVF, was also identified on the adjacent Terribile Bank and analyzed.

The relationship between the morphology of the seamounts and underwater volcanic processes proved the monogenetic nature of this volcanism, which is part of a wider and scattered volcanism affecting the northwestern Sicily Channel. This volcanism represents a peculiarity, since it took place outside of the typical geodynamic settings of other fields such as subduction or oceanic rift zones, and far from long-lived volcanic systems.

The ten of cones forming the GVF is likely the witnesses of a Late Pleistocene to Holocene submarine volcanism. This age is reasonably hypothesized by means of the analysis of some morphological parameters (i.e., depth and shape of the tops, presence and depth of abrasion and depositional terraces, level of erosive dismantlement) in relationship with sea-level fluctuations and taking into account analogies with the post-eruptive morphological evolution of Ferdinandea shoal formed during the 1831 eruption and other volcanic seamounts worldwide, such as the satellite shoals of Surtsey formed during the 1963–67 eruption.

The shape of the seamounts and their distribution within the GVF attested to the interaction between volcanism and tectonics in the formation of the field itself. The overall N-S trend of the volcanic field reflects the orientation of the Capo Granitola-Sciacca transpressive transfer zone, which favored the volcanism in this region. The cones within the fields are generally grouped into clusters or merged to form coalesced edifices, both aligned along NW-SE to WNW-ESE preferential directions, consistent with the main regional tectonic structures associated with the Plio-Quaternary continental rifting of the Sicily Channel.

This paper could furnish a key to better understand the volcano-tectonic complexity of this region and provide a useful comparison for other submarine areas affected by monogenetic volcanism.

The improvement of the knowledge of this shallow submarine volcanism would be also of great interest in determining volcanic risk in the area.

DATA AVAILABILITY STATEMENT

The datasets generated for this study are available on request to the corresponding author.

AUTHOR CONTRIBUTIONS

DC processed the multibeam bathymetric data. DC and MC conceived and designed the research and acquired the multibeam bathymetric data and ROV images, interpreted the dataset integrating it with the available information concerning the study area and conceived the morphological evolution of the Graham volcanic field, discussing methods, analyses, results and conclusion of the manuscript.

ACKNOWLEDGMENTS

We thank for their contribution during the “Ferdinandea 2012” research cruise, the captain of the R/V ASTREA Massimo Saporito and his crew, Simone Pietro Canese and the C.L.C. Luigi Manzueto of ISPRA, and Andrei Diaconov of SoProMar. Moreover, we are grateful to Alessandro Bosman of CNR for his support during the multibeam data processing and to our colleague William Moreland for improving the English style. Finally, we are grateful to the Chief Editor Valerio Acocella,

Guest Associate Editor GG and two reviewers for providing useful suggestions in improving the manuscript quality. The oceanographic cruise “Ferdinandea 2012” was supported by “Studi e Ricerche” 2012-grant of INGV-Osservatorio Etneo.

REFERENCES

- Antonoli, F., Donadio, C., Ferranti, L., Margottini, C., and De Vita, A. (1994). Il Banco Graham: storia, sismica storica, petrologia e geomorfologia subacquea. Nascita e scomparsa del vulcano sommerso nel Canale di Sicilia. *Mem. Descr. Carta Geol. d'It.* 52, 99–102.
- Aranda-Gómez, J. J., Luhr, J. F., Housh, T. B., Connor, C. B., Becker, T., and Henry, C. D. (2003). Synextensional pliocene–pleistocene eruptive activity in the camargo volcanic field, Chihuahua, México. *Geol. Soc. Am. Bull.* 115, 289–313.
- Arena, F., Laface, V., Malara, G., Romolo, A., Viviano, A., Fiamma, V., et al. (2015). Wave climate analysis for the design of wave energy harvesters in the Mediterranean Sea. *Renew. Energy* 77, 125–141. doi: 10.1016/j.renene.2014.12.002
- Argnani, A. (1990). The Strait of Sicily rift zone: foreland deformation related to the evolution of a backarc basin. *J. Geodyn.* 12, 311–331. doi: 10.1016/0264-3707(90)90028-s
- Baker, E. T., Massoth, G. J., de Ronde, C. E. J., Lupton, J. E., and McInnes, B. I. A. (2002). Observation sand sampling of an ongoing subsurface eruption of Kavachi volcano, Solomon Islands, May 2000. *Geology* 30, 975–978.
- Beccaluva, L., Colantoni, P., Di Girolamo, P., and Savelli, C. (1981). Upper Miocene submarine volcanism in the Strait of Sicily (Banco Senza Nome). *Bull. Volcanol.* 44, 573–581. doi: 10.1007/bf02600587
- Boccaletti, M., Cello, G., and Tortorici, L. (1987). Transensional tectonics in the Sicily Channel. *J. Struct. Geol.* 9, 869–876. doi: 10.1016/0191-8141(87)90087-3
- Bottari, C., Stiros, S. C., and Teramo, A. (2009). Archaeological evidence for destructive earthquakes in Sicily between 400 B.C. and A.D. 600. *Geoarchaeology* 24, 147–175. doi: 10.1002/geo.20260
- Bruce, P. M., and Huppert, H. E. (1989). Thermal control of basaltic fissure eruptions. *Nature* 342, 665–667. doi: 10.1038/342665a0
- Burrollet, P. F., Mugniot, J. M., and Sweeney, P. (1978). “The geology of the pelagian block: the margins and basins of southern Tunisia and Tripolitania,” in *The Ocean Basins and Margins. The Western Mediterranean*, Vol. 4b, eds A. E. M. Nairn, W. H. Kanes, and F. G. Stelhi, (New York, NY: Plenum), 331–359. doi: 10.1007/978-1-4684-3039-4_6
- Calanchi, N., Colantoni, P., Rossi, P. L., Saitta, M., and Serri, G. (1989). The Strait of Sicily continental rift systems: physiography and petrochemistry of the submarine volcanic centres. *Mar. Geol.* 87, 55–83. doi: 10.1016/0025-3227(89)90145-X
- Calò, M., and Parisi, L. (2014). Evidences of a Lithospheric fault zone in the Sicily Channel (Southern Italy) from instrumental seismicity data. *Geophys. J. Int.* 199, 219–225. doi: 10.1093/gji/ggu249
- Cañón-Tapia, E. (2016). Reappraisal of the significance of volcanic fields. *J. Volcanol. Geotherm. Res.* 310, 26–38. doi: 10.1016/j.jvolgeores.2015.11.010
- Cas, R. A. F., and Giordano, G. (2014). Submarine volcanism: a review of the constraints, processes and products, and relevance to the cabo de gata volcanic succession. *Ital. J. Geosci.* 133, 362–377. doi: 10.3301/ijg.2014.46
- Cas, R. A. F., Landis, C. A., and Fordyce, E. (1989). A monogenetic, surlta-type, surtseyan volcano from the eocene-oligocene waiareka-deborah volcanics, otago, New Zealand: a model. *Bull. Volcanol.* 51, 281–298. doi: 10.1007/bf01073517
- Casalbore, D., Falese, F., Martorelli, E., Romagnoli, C., and Chiocci, F. L. (2017). Submarine depositional terraces in the Tyrrhenian Sea as a proxy for paleo-sea level reconstruction: problems and perspective. *Q. Int.* 439, 169–180. doi: 10.1016/j.quaint.2016.07.051
- Casalbore, D., Romagnoli, C., Pimentel, A., Quartau, R., Casas, D., Ercilla, G., et al. (2015). Volcanic, tectonic and mass-wasting processes offshore Terceira island (Azores) revealed by high-resolution seafloor mapping. *Bull. Volcanol.* 77:24. doi: 10.1007/s00445-015-0905-3
- Cavallaro, D., Monaco, C., Polonia, A., Sulli, A., and Di Stefano, A. (2017). Evidence of positive tectonic inversion in the north-central sector of the Sicily Channel (Central Mediterranean). *Nat. Hazards* 86, S233–S251. doi: 10.1017/s11069-016-2515-6
- Civile, D., Lodolo, E., Accaino, F., Geletti, R., Schiattarella, M., Giustiniani, M., et al. (2018). Capo granitola-sciacca fault zone (Sicilian Channel, Central Mediterranean): structure vs magmatism. *Mar. Pet. Geol.* 96, 627–644. doi: 10.1016/j.marpetgeo.2018.05.016
- Civile, D., Lodolo, E., Alp, H., Ben-Avraham, Z., Cova, A., Baradello, L., et al. (2014). Seismic stratigraphy and structural setting of the Adventure Plateau (Sicily Channel). *Mar. Geophys. Res.* 35, 37–53. doi: 10.1007/s11001-013-9205-5
- Civile, D., Lodolo, E., Tortorici, L., Lanzafame, G., and Brancolini, G. (2008). Relationships between magmatism and tectonics in a continental rift: the Pantelleria Island region (Sicily Channel, Italy). *Mar. Geol.* 251, 32–46. doi: 10.1016/j.margeo.2008.01.009
- Civile, D., Lodolo, E., Zecchin, M., Ben-Avraham, Z., Baradello, L., Accetella, D., et al. (2015). The lost adventure archipelago (Sicilian Channel, Mediterranean Sea): morpho-bathymetry and late quaternary palaeogeographic evolution. *Glob. Planet. Change* 125, 36–47. doi: 10.1016/j.gloplacha.2014.12.003
- Clague, D. A., Moore, J. G., and Reynolds, J. R. (2000a). Formation of submarine flat-topped volcanic cones in Hawaii. *Bull. Volcanol.* 62, 214–233. doi: 10.1007/s004450000088
- Clague, D. A., Reynolds, J. R., and Davis, A. S. (2000b). Near ridge seamount chains in the northeastern Pacific Ocean. *J. Geophys. Res.* 105, 16541–16561. doi: 10.1029/2000jb900082
- Clark, P. U., Dyke, A. S., Shakun, J. D., Carlson, A. E., Clark, J., Wohlfarth, B., et al. (2009). The last glacial maximum. *Science* 325, 710–714. doi: 10.1126/science.1172873
- Colantoni, P. (1975). Note di geologia marina sul Canale di Sicilia. *Giorn. Geol.* 40, 181–207.
- Colantoni, P., Del Monte, M., Galignani, P., and Zarudsky, E. F. K. (1975). Il Banco Graham: un vulcano recente nel Canale di Sicilia. *Giorn. Geol.* 40, 141–162.
- Coltelli, M., Cavallaro, D., D’Anna, G., D’Alessandro, A., Grassa, F., Mangano, G., et al. (2016). Exploring the submarine graham bank in the sicily channel. *Ann. Geophys.* 59:S0208. doi: 10.4401/ag-6929
- Conte, A. M., Martorelli, E., Calarco, M., Sposato, A., Perinelli, C., Coltelli, M., et al. (2014). The 1891 submarine eruption offshore Pantelleria Island (Sicily Channel, Italy): identification of the vent and characterization of products and eruptive style. *Geochem. Geophys. Geosyst.* 15, 2555–2574. doi: 10.1002/2014GC005238
- Corazzato, C., and Tibaldi, A. (2006). Fracture control on type, morphology and distribution of parasitic volcanic cones: an example from Mt. Etna Italy. *J. Volcanol. Geotherm. Res.* 158, 177–194. doi: 10.1016/j.jvolgeores.2006.04.018
- Corcoran, P. L., and Moore, L. N. (2008). Subaqueous eruption and shallow-water reworking of a small-volume Surtseyan edifice at Kakanui, New Zealand. *Can. J. Earth Sci.* 45, 1469–1485. doi: 10.1139/e08-068
- Corti, G., Cuffaro, M., Doglioni, C., Innocenti, F., and Manetti, P. (2006). Coexisting geodynamic processes in the Sicily Channel. *Geol. Soc. Am. Spec. Pap.* 409, 83–96.
- Cowell, P. J., Hanslow, D. J., and Meleo, J. F. (1999). “The shoreface,” in *Handbook of Beach and Shoreface Morphodynamics*, ed. A. D. Short, (Chichester: Wiley and Sons), 39–71.
- Dean, D. R. (1980). Graham island, charles lyell, and the craters of elevation controversy. *Isis* 71, 571–588. doi: 10.1086/352593
- Di Geronimo, I., Rosso, A., and Sanfilippo, R. (1993). “The corallium rubrum fossiliferous banks off sciacca (Strait of Sicily),” in *Il Corallo Rosso in Mediterraneo: Arte, Storia e Scienza*, eds F. Cicogna, and R. Cattaneo Vietti (Roma: Ministero Risorse Agricole Alimentari Forestali), 75–107.

SUPPLEMENTARY MATERIAL

The Supplementary Material for this article can be found online at: <https://www.frontiersin.org/articles/10.3389/feart.2019.00311/full#supplementary-material>

- Drago, A., Sorgente, R., and Olita, A. (2010). Sea temperature, salinity and total velocity climatological fields for the south-central Mediterranean Sea. GCP/RER/010/ITA/MSM-TD-14. *MedSudMed Tech. Doc.* 14:35.
- Falautano, G., Falzone, G., Lanzafame, G., Macaluso, D., Niosi, M., and Rossi, P. (2010). *Primi Tentativi di monitoraggio dei resti sottomarini dell'eruzione che nel 1831 costruì l'Isola Ferdinandea nel Canale di Sicilia. Rapporti tecnici INGV*. Rome: Istituto Nazionale di Geofisica e Vulcanologia.
- Falzone, G., Lanzafame, G., and Rossi, P. L. (2009). Il vulcano Ferdinandea nel Canale di Sicilia. *Geoitalia* 29, 15–20.
- Favalli, M., Karátson, D., Mazzarini, F., Pareschi, M. T., and Boschi, E. (2009). Morphometry of scoria cones located on a volcano flank: a case study from Mt. Etna (Italy), based on high-resolution LiDAR data. *J. Volcanol. Geotherm. Res.* 186, 320–330. doi: 10.1016/j.jvolgeores.2009.07.011
- Fedorik, J., Toscani, G., Lodolo, E., Civile, D., Bonini, L., and Seno, S. (2018). Structural analysis and Miocene-to-Present tectonic evolution of a lithospheric-scale, transcurrent lineament: the Sciacca Fault (Sicilian Channel, Central Mediterranean Sea). *Tectonophysics* 722, 342–355. doi: 10.1016/j.tecto.2017.11.014
- Ferranti, L., Pepe, F., Barreca, G., Meccariello, M., and Monaco, C. (2019). Multi-temporal tectonic evolution of Capo Granitola and Sciacca foreland transcurrent faults (Sicily Channel). *Tectonophysics* 765, 187–204. doi: 10.1016/j.tecto.2019.05.002
- Fleming, K., Johnston, P., Zwart, D., Yokoyama, Y., Lambeck, K., and Chappell, J. (1998). Refining the eustatic sea-level curve since the Last Glacial Maximum using far- and intermediate-field sites. *Earth Planet. Sci. Lett.* 163, 327–342. doi: 10.1016/S0012-821X(98)00198-8
- Foutarakis, P. M., and Anastasakis, G. (2018). Bathymorphological setting of the submarine pausanias volcanic field, south aegean active volcanic arc. *J. Maps* 14, 341–347. doi: 10.1080/17445647.2018.1473816
- Gemmellaro, C. (1831). *Relazione dei fenomeni del nuovo vulcano sorto dal mare fra la costa di Sicilia e l'Isola di Pantelleria nel mese di luglio 1831*. Catania: ne' torchi della Regia Università Carmelo Pastore 48:25.
- Ghissetti, F. C., Gorman, A. R., Grasso, M., and Vezzani, L. (2009). Imprint of foreland structure on the deformation of a thrust sheet. The Plio-Pleistocene Gela Nappe (southern Sicily, Italy). *Tectonics* 28:TC4015. doi: 10.1029/2008TC002385
- Global Volcanism Program (2013a). *Campi Flegrei del Mar di Sicilia (211070) in Volcanoes of the World*, 4.7.6, ed. E. Venzke, (Washington, DC: Smithsonian Institution), doi: 10.5479/si.GVP.VOTW4-2013
- Global Volcanism Program (2013b). *Izu-Oshima (284010) in Volcanoes of the World*, 4.7.6, ed. E. Venzke, (Washington, DC: Smithsonian Institution), doi: 10.5479/si.GVP.VOTW4-2013
- Green, A. N., Cooper, J. A. G., and Salzmann, L. (2014). Geomorphic and stratigraphic signals of postglacial meltwater pulses on continental shelves. *Geology* 42, 151–154. doi: 10.1130/g35052.1
- Guidoboni, E., Muggia, A., Marconi, C., and Boschi, E. (2002). A case study in archaeoseismology. The collapses of the Selinunte temples (Southwestern Sicily): two earthquakes identified. *Bull. Seismol. Soc. Am.* 92, 2961–2982. doi: 10.1785/0120010286
- Head, J. W., Wilson, L., and Smith, D. K. (1996). Mid-ocean ridge eruptive vent morphology and substructure: evidence for the dike widths, eruption rates, and axial volcanic ridges. *J. Geophys. Res.* 101, 28265–28280. doi: 10.1029/96jb02275
- Hernández-Molina, F. J., Fernández-Salas, L. M., Lobo, F. J., Somoza, L., Díaz del Río, V., and Alveirinho Dias, J. M. (2000). The infralittoral prograding wedge: a new largescale progradational sedimentary body in shallow marine environments. *Geo Mar. Lett.* 20, 109–117. doi: 10.1007/s003670000040
- Jakobsson, S. P., Gudmundsson, G., and Moore, J. G. (2000). Geological monitoring of Surtsey, Iceland, 1967–1998. *Surtsey Res.* 11, 99–108.
- Jakobsson, S. P., Thors, K., Vésteinsson, Á. T., and Ásbjörnsdóttir, L. (2009). Some aspects of the seafloor morphology at Surtsey volcano: the new multibeam bathymetric survey of 2007. *Surtsey Res.* 12, 9–20.
- Jongsma, D., Van Hinte, J. E., and Woodside, J. M. (1985). Geologic structure and neotectonics of the North African continental margin south of Sicily. *Mar. Pet. Geol.* 2, 156–179. doi: 10.1016/0264-8172(85)90005-4
- Kereszturi, G., and Németh, K. (2012). “Monogenetic basaltic volcanoes: genetic classification, growth, geomorphology and degradation,” in *Updates in Volcanology New Advances in Understanding Volcanic Systems*, ed. K. Németh, (Rijeka: InTech), doi: 10.5772/51387
- Kokelaar, B. P. (1983). The mechanism of surtseyan volcanism. *J. Geol. Soc. Lond.* 140, 939–944. doi: 10.1144/gsjgs.140.6.0939
- Kokelaar, B. P. (1986). Magma–water interactions in subaqueous and emergent basaltic volcanism. *Bull. Volcanol.* 48, 275–289. doi: 10.1007/bf01081756
- Kokelaar, B. P., and Durant, G. P. (1983). The submarine eruption and erosion of Surtla (Surtsey), Iceland. *J. Volcanol. Geotherm. Res.* 19, 239–246. doi: 10.1016/0377-0273(83)90112-9
- Lambeck, K., Antonioli, F., Anzidei, M., Ferranti, L., Leoni, G., Scicchitano, G., et al. (2011). Sea level change along the Italian coast during the Holocene and projections for the future. *Quat. Int.* 232, 250–257. doi: 10.1016/j.quaint.2010.04.026
- Latter, J. H. (1981). Tsunamis of volcanic origin. *Bull. Volcanol.* 44, 467–490. doi: 10.1007/BF02600578
- Liu, J. P., and Milliman, J. D. (2004). Reconsidering melt-water pulses 1A and 1B: global impacts of rapid sea-level rise. *J. Ocean Univ. China* 3, 183–190. doi: 10.1007/s11802-004-0033-8
- Lodolo, E., Civile, D., Zanolli, C., and Geletti, R. (2012). Magnetic signature of the Sicily Channel volcanism. *Mar. Geophys. Res.* 33, 33–44. doi: 10.1007/s11001-011-9144-y
- Lodolo, E., Civile, D., Zecchin, M., Zampa, L. S., and Accaino, F. (2019a). A series of volcanic edifices discovered a few kilometers off the coast of SW Sicily. *Mar. Geol.* 416:105999. doi: 10.1016/j.margeo.2019.105999
- Lodolo, E., Zampa, L., and Civile, D. (2019b). The Graham and Terrible volcanic province (NW Sicilian Channel): gravimetric constraints for the magmatic manifestations. *Bull. Volcanol.* 81:17. doi: 10.1007/s00445-019-1274-0
- Lodolo, E., Sanfilippo, R., Rajola, G., Canese, S., Andaloro, F., Montagna, P., et al. (2017). The red coral deposits of the Graham Bank area: constraints on the Holocene volcanic activity of the Sicilian Channel. *Geo. Res. J.* 13, 126–133. doi: 10.1016/j.grj.2017.04.003
- Lucchi, F., Ricchi, A., Romagnoli, C., Casalbone, D., and Quartau, R. (2019). Late Quaternary paleo sea level geomorphological markers of opposite vertical movements at Salina volcanic island (Aeolian Arc). *Earth Surf. Process. Landforms* 44, 2377–2395. doi: 10.1002/esp.4651
- Machado, F., Parsons, W. H., Richards, A. F., and Mulford, J. W. (1962). Capelinhos eruption of Fayal Volcano, Azores, 1957–1958. *J. Geophys. Res.* 67, 3519–3529. doi: 10.1029/jz067i009p03519
- Marzolla, B. (1831). *Descrizione dell'Isola Ferdinandea al mezzogiorno della Sicilia*. Napoli: Reale Ufficio Topografico.
- McClinton, T., White, S. M., Colman, A., and Sinton, J. M. (2013). Reconstructing lava flow emplacement processes at the hot spot-affected Galápagos Spreading Center, 95° W and 92° W. *Geochem. Geophys. Geosyst.* 14, 2731–2756. doi: 10.1002/ggge.20157
- Mercalli, G. (1883). *Geologia d'Italia: Vulcani e fenomeni vulcanici*. Milano: Vallardi editore.
- Mitchell, N. C., Masselink, G., Huthnance, J. M., Fernández-Salas, L. M., and Lobo, F. J. (2012a). Depths of modern coastal sand clinoforms. *J. Sed. Res.* 82, 469–481. doi: 10.2110/jsr.2012.40
- Mitchell, N. C., Stretch, R., Oppenheimer, C., Kay, D., and Beier, C. (2012b). Cone morphologies associated with shallow marine eruptions: east Pico Island, Azores. *Bull. Volcanol.* 74, 2289–2301. doi: 10.1007/s00445-012-0662-5
- Mitchell, N. C., Stretch, R., Tempera, F., and Ligi, M. (2016). “Volcanism in the Azores: a marine geophysical perspective,” in *Volcanoes of the Azores*, eds U. Kueppers, and C. Beier, (Berlin: Springer-Verlag).
- Moore, J. G., Jakobsson, S. P., and Hólmjárn, J. (1992). Subsidence of Surtsey volcano, 1967–1991. *Bull. Volcanol.* 55, 17–24. doi: 10.1007/bf00301116
- Muscheler, R., Kromer, B., Björck, S., Svensson, A., Friedrich, M., Kaiser, K. F., et al. (2008). Tree rings and ice cores reveal 14C calibration uncertainties during the Younger Dryas. *Nat. Geosci.* 1, 263–267. doi: 10.1038/ngeo128
- Németh, K. (2010). “Monogenetic volcanic fields: origin, sedimentary record, and relationship with polygenetic volcanism,” in *What Is a Volcano?*, eds E. Canon-Tapia, and A. Szakacs, (Boulder, CO: Geological Society of America), 43–66. doi: 10.1130/2010.2470(04)
- Németh, K., and Kereszturi, G. (2015). Monogenetic volcanism: personal views and discussion. *Int. J. Earth Sci.* 104, 2131–2146. doi: 10.1007/s00531-015-1243-6
- Norrmann, J. O., and Erlingsson, U. (1992). The submarine morphology of Surtsey volcanic group. *Surtsey Res. Prog. Rep.* 10, 45–56.

- Paris, R., Wassmer, P., Sartohadi, J., Lavigne, F., Barthomeuf, B., Desgages, E., et al. (2009). Tsunamis as geomorphic crises: lessons from the December 26, 2004 tsunami in Lhok Nga, West Banda Aceh (Sumatra, Indonesia). *Geomorphology* 104, 59–72. doi: 10.1016/j.geomorph.2008.05.040
- Pensa, A., Pinton, A., Vita, L., Bonamico, A., De Benedetti, A. A., and Giordano, G. (2019). ATLAS of Italian submarine volcanic structures. *Mem. Descr. Carta Geol. d'It.* 104, 77–183.
- Quartau, R., Hipolito, A., Romagnoli, C., Casalbone, D., Madeira, J., Tempera, F., et al. (2014). The morphology of insular shelves as a key for understanding the geological evolution of volcanic islands: insights from Terceira Island (Azores). *Geochem. Geophys. Geosyst.* 15, 1801–1826. doi: 10.1002/2014gc005248
- Quartau, R., Trenhaile, A. S., Mitchell, N. C., and Tempera, F. (2010). Development of volcanic insular shelves: insight from observations and modelling of Faial Island in the Azores Archipelago. *Mar. Geol.* 275, 66–83. doi: 10.1016/j.margeo.2010.04.008
- Ramalho, R. S., Quartau, R., Trenhaile, A. S., Mitchell, N. C., Woodroffe, C. D., and Ávila, S. P. (2013). Coastal evolution on volcanic oceanic islands: a complex interplay between volcanism, erosion, sedimentation, sea-level change and biogenic production. *Earth Sci. Rev.* 127, 140–170. doi: 10.1016/j.earscirev.2013.10.007
- Rappaport, Y., Naar, D. F., Barton, C. C., Liu, Z. J., and Hey, R. N. (1997). Morphology and distribution of seamounts surrounding Easter Island. *J. Geophys. Res.* 102, 24713–24728. doi: 10.1029/97jb01634
- Reuther, C. D., Ben-Avraham, Z., and Grasso, M. (1993). Origin and role of major strike-slip transfers during plate collision in the central Mediterranean. *Terra Nova* 5, 249–257. doi: 10.1111/j.1365-3121.1993.tb00256.x
- Rivera, J., Lastras, G., Canals, M., Acosta, J., Arrese, B., Hermida, N., et al. (2013). Construction of an oceanic island: insights from the El Hierro (Canary Islands) 2011–2012 submarine volcanic eruption. *Geology* 41, 355–358. doi: 10.1130/G33863.1
- Romagnoli, C., and Jakobsson, S. P. (2015). Post-eruptive morphological evolution of island volcanoes: surtsey as a modern case study. *Geomorphology* 250, 384–396. doi: 10.1016/j.geomorph.2015.09.016
- Romero Ruiz, C., García-Cacho, L., Araña, V., Yanes Luque, A., and Felpeto, A. (2000). Submarine volcanism surrounding Tenerife, Canary Islands: implications for tectonic controls, and oceanic shield forming processes. *J. Volcanol. Geotherm. Res.* 103, 105–119. doi: 10.1016/s0377-0273(00)00218-3
- Rotolo, S. G., Castorina, F., Cellura, D., and Pompilio, M. (2006). Petrology and geochemistry of submarine volcanism in the Sicily Channel Rift. *J. Geol.* 114, 355–365. doi: 10.1086/501223
- Salzmann, L., Green, A., and Cooper, J. A. G. (2013). Submerged barrier shoreline sequences on a high energy, steep and narrow shelf. *Mar. Geol.* 346, 366–374. doi: 10.1016/j.margeo.2013.10.003
- Schmidt, R., and Schmincke, H. U. (2002). From seamount to oceanic island, Porto Santo, central east-Atlantic. *Int. J. Earth Sci.* 91, 594–614. doi: 10.1007/s00531-001-0243-x
- Siddall, M., Rohling, E. J., Almogi-Labin, A., Hemleben, C., Meischner, D., Schmelzer, I., et al. (2003). Sea-level fluctuations during the last glacial cycle. *Nature* 423, 853–858. doi: 10.1038/nature01690
- Siebe, C., Komorowski, J. C., Navarro, C., McHone, J. Z., Delgado, H., and Cortes, A. (1995). Submarine eruption near Socorro Island, Mexico: geochemistry and scanning electron microscopy studies of floating scoria and reticulite. *J. Volcanol. Geotherm. Res.* 68, 239–271. doi: 10.1016/0377-0273(95)00029-1
- Sinapi, L., Lamberti, L. O., Pizzeghello, N. M., and Ivaldi, R. (2016). The Graham Bank: hydrographic features and safety of navigation. *Int. Hydrogr. Rev.* 15, 7–20.
- Spatola, D., Micallef, A., Sulli, A., Basilone, L., Ferreri, R., Basilone, G., et al. (2018). The Graham Bank (Sicily Channel, central Mediterranean Sea): seafloor signatures of volcanic and tectonic controls. *Geomorphology* 318, 375–389. doi: 10.1016/j.geomorph.2018.07.006
- Stretch, R., Mitchell, N. C., and Portaro, R. A. (2006). A morphometric analysis of the submarine volcanic ridge of Pico Island. *J. Volcanol. Geotherm. Res.* 156, 35–54. doi: 10.1016/j.jvolgeores.2006.03.009
- Sturkell, E., Einarsson, P., Geirsson, H., Tryggvason, E., Moore, J. G., and Ólafsdóttir, R. (2009). Precision levelling and geodetic GPS observations performed on Surtsey between 1967 and 2002. *Surtsey Res.* 12, 39–74.
- Tempera, F., Hipolito, A., Madeira, J., Vieira, S., Campos, A., and Mitchell, N. C. (2013). Condor seamount (Azores, NE Atlantic): a morphotectonic interpretation. *Deep Sea Res. Part II Top. Stud. Oceanogr.* 98, 7–23. doi: 10.1016/j.dsr2.2013.09.016
- Thorarinsson, S. (1967). *Surtsey. The New Island in the North Atlantic*. New York, NY: Viking Press Inc.
- Tibaldi, A. (1995). Morphology of pyroclastic cones and tectonics. *J. Geophys. Res.* 100, 24521–24535. doi: 10.1029/95jb02250
- Torelli, L., Grasso, M., Mazzoldi, G., Peis, D., and Gori, D. (1995). Cretaceous to Neogene structural evolution of the Lampedusa shelf (Pelagian Sea, Central Mediterranean). *Terra Nova* 7, 200–212. doi: 10.1111/j.1365-3121.1995.tb00689.x
- Trenhaile, A. S. (1989). Sea level oscillations and the development of rock coasts. *Elsevier Oceanogr. Ser.* 49, 271–295. doi: 10.1016/s0422-9894(08)70129-6
- Trenhaile, A. S. (2000). Modeling the development of wave-cut shore platforms. *Mar. Geol.* 166, 163–178. doi: 10.1016/s0025-3227(00)00013-x
- Trenhaile, A. S. (2001). Modelling the Quaternary evolution of shore platforms and erosional continental shelves. *Earth Surf. Process. Landforms* 26, 1103–1128. doi: 10.1002/esp.255
- Valentine, G. A., and Connor, C. B. (2015). “Basaltic volcanic fields,” in *Encyclopedia of Volcanoes*, 2nd Edn, eds H. Sigurdsson, B. F. Houghton, S. R. McNutt, H. Rymer, and J. Stix, (London: Academic Press), 423–439. doi: 10.1016/b978-0-12-385938-9.00023-7
- Vaughan, R. G., and Webley, P. W. (2010). Satellite observations of a surtseyan eruption: hunga Ha’apai. *Tonga. J. Volcanol. Geotherm. Res.* 198, 177–186. doi: 10.1002/2017GL076621
- Washington, H. S. (1909). The submarine eruption of 1831 and 1891 near Pantelleria. *Am. J. Sci.* 27, 131–150. doi: 10.2475/ajs.s4-27.158.131
- Wessel, P., Sandwell, D. T., and Kim, S. S. (2010). The global seamount census. *Oceanography* 23, 24–33. doi: 10.5670/oceanog.2010.60
- Weston, F. S. (1964). List of recorded volcanic eruptions in the Azores with brief reports. *Bol. Mus. Lab. Min. Geol. Fac. Ciênc. Lisboa* 10, 3–18.
- White, J. D. L. (1996). Pre-emergent construction of a lacustrine basaltic volcano, Pahvant Butte, Utah (USA). *Bull. Volcanol.* 58, 249–262. doi: 10.1007/s004450050138
- White, J. D. L., and Houghton, B. (2000). “Surtseyan and related phreatomagmatic eruptions,” in *Encyclopedia of Volcanoes*, ed. H. Sigurdsson, (London: Academic Press), 495–511.
- Zecchin, M., Ceramicola, S., Gordini, E., Deponte, M., and Critelli, S. (2011). Cliff overstep model and variability in the geometry of transgressive erosional surfaces in high-gradient shelves: the case of the Ionian Calabrian margin (southern Italy). *Mar. Geol.* 281, 43–58. doi: 10.1016/j.margeo.2011.02.003
- Zecchin, M., Ceramicola, S., Lodolo, E., Casalbone, D., and Chiocci, F. L. (2015). Episodic, rapid sea-level rises on the central Mediterranean shelves after the last glacial maximum: a review. *Mar. Geol.* 369, 212–223. doi: 10.1016/j.margeo.2015.09.002

Conflict of Interest: The authors declare that the research was conducted in the absence of any commercial or financial relationships that could be construed as a potential conflict of interest.

Copyright © 2019 Cavallaro and Coltelli. This is an open-access article distributed under the terms of the Creative Commons Attribution License (CC BY). The use, distribution or reproduction in other forums is permitted, provided the original author(s) and the copyright owner(s) are credited and that the original publication in this journal is cited, in accordance with accepted academic practice. No use, distribution or reproduction is permitted which does not comply with these terms.

Advantages of publishing in Frontiers



OPEN ACCESS

Articles are free to read
for greatest visibility
and readership



FAST PUBLICATION

Around 90 days
from submission
to decision



HIGH QUALITY PEER-REVIEW

Rigorous, collaborative,
and constructive
peer-review



TRANSPARENT PEER-REVIEW

Editors and reviewers
acknowledged by name
on published articles

Frontiers

Avenue du Tribunal-Fédéral 34
1005 Lausanne | Switzerland

Visit us: www.frontiersin.org

Contact us: info@frontiersin.org | +41 21 510 17 00



REPRODUCIBILITY OF RESEARCH

Support open data
and methods to enhance
research reproducibility



DIGITAL PUBLISHING

Articles designed
for optimal readership
across devices



FOLLOW US

[@frontiersin](https://twitter.com/frontiersin)



IMPACT METRICS

Advanced article metrics
track visibility across
digital media



EXTENSIVE PROMOTION

Marketing
and promotion
of impactful research



LOOP RESEARCH NETWORK

Our network
increases your
article's readership